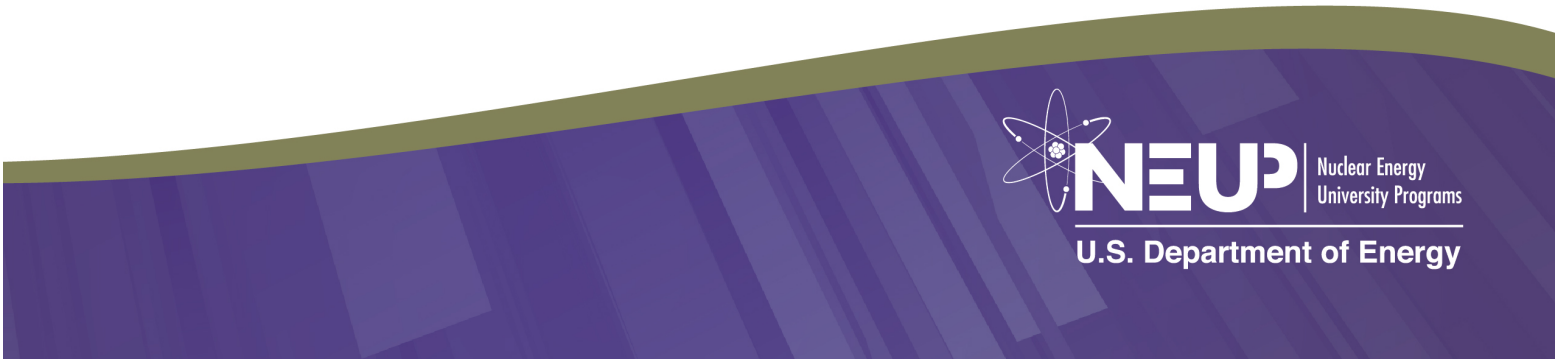
Project No. 14-6909

Effect of Metallic Li on the Behavior of Metals in Molten Salts

Fuel Cycle Research and Development

Dev Chidambaram
University of Nevada, Reno

Stephen Kung, Federal POC
Perry Motsegood, Technical POC



FINAL REPORT DOE-UNR-08262

Project Title: Effect of Metallic Li on the Behavior of Metals in Molten Salts

Award No.: DE-NE0008262

Project Locations: Materials Science and Engineering;
University of Nevada, Reno, Reno, NV 89557-0388

Project Start Date: 10/01/2014

Reporting Period: Oct 1, 2014 – Sept 30, 2017

Date of Report: Dec 29, 2017

Project Contacts: Dev Chidambaram, Ph.D.,
Ormat Technologies Scholar of Materials and Interfaces
Professor of Materials Science and Engineering,
University of Nevada, Reno, Reno, NV 89557,
(775) 784-7066, dcc@unr.edu

Collaborator: James Willit, Ph.D.
Argonne National Laboratory

Financial Contact: Ella Chavez-Harbrecht
Grants and Projects Analyst, Sponsored Projects MS 325
University of Nevada, Reno, Reno, NV 89557-0001
(775) 784-4158, chaveze@unr.edu

DOE Contacts:

Technical Monitor: Stephen Kung
Technical Project manager: David Kamerman
HQ Program Manager: Kenny Osborne

Technical POC: Perry Motsegood
Contract Specialist: Coleman Dieger
Contracting Officer: Jeffrey Fogg

Table of Contents

Final Report 3

1 Executive Summary 3

2 Personnel Involved 3

3 Abstract of the proposed project 4

4 Introduction 5

5 Synopsis of this report 7

6 Products 8

7 References 11

8 Technical Appendices 14

A1 Short term interaction of materials with $LiCl\text{-}Li_2O\text{-}Li^0$

A2 Long term exposure of stainless steel and Inconel with $LiCl\text{-}Li_2O\text{-}Li^0$

A3 Corrosion behavior of Monel 400 and electrochemical performance of Li-Bi reference electrode in $LiCl\text{-}Li_2O\text{-}Li$

Final Report

1 Executive Summary

The deleterious effect of Li0 on the reactor container materials has not been studied. Exposure to liquid Li^0 results in material degradation primarily through lithium intercalation, leaching of specific alloying elements, and decarburization. The objective of this research is to understand how the presence of Li^0 in molten LiCl-Li_2O affects the degradation of two classes of alloys by correlating their accelerated and long term electrochemical behavior to the surface chemistry of the alloys and the chemistry of the electrolyte.

This study has completed all the proposed tasks. The project led to the design and development of unique experimental setups and protocols. Several groundbreaking findings resulted from this study. The project had several products in terms of student education, thesis and dissertation, publications and presentations.

2 Personnel Involved

All are from Materials Science and Engineering, University of Nevada, Reno

Augustus Merwin	PhD	Graduated with his PhD.
William Phillips	MS	Graduated with his MS
William Phillips	PhD student	Also supported by NRC Fellowship
Vick Singh	PhD Student	Also supported by NRC Fellowship
Aaron Unger	BS student	Also supported by NEUP scholarship
Jeremy Moon	BS student	
Dev Chidambaram	Principal Investigator	

3 Abstract of the proposed project

In order to integrate current stockpiles of used nuclear fuel into a pyroprocessing based fuel cycle, oxide fuel must be reduced to a metallic form. During the process of reducing uranium oxide, significant quantity of metallic lithium (Li^0) is generated and unless measures are taken to remove Li^0, Li^0 will accumulate in the molten LiCl-Li_2O electrolyte. While, the formation and accumulation of Li^0 in the molten salt electrolyte is well documented, the effect of so formed Li^0 on the degradation of the system materials has not been studied in detail. *Thus, there is a knowledge gap in understanding the effects of metallic lithium, present in the molten salt electrolyte, on materials. Specifically, the deleterious effect of Li^0 on the reactor container materials has not been studied.* Exposure to liquid Li^0 results in material degradation primarily through lithium intercalation, leaching of specific alloying elements, and decarburization. *The research objective of this proposal is to understand how the presence of Li^0 in molten LiCl-Li_2O affects the degradation of two classes of alloys by correlating their accelerated and long term electrochemical behavior to the surface chemistry of the alloys and the chemistry of the electrolyte.* These studies will focus on the role of Li^0 in altering the chemistry at the molten salt and material interface, and its resultant effects on oxide film stability and material longevity.

Specific Objectives: Specialized laboratory molten salt reactors with automated control and a suite of spectroscopic analytical techniques available in the PI's laboratory and the Co-PI's expertise AC/DC impedance methods uniquely qualify this team to execute the above study. Specific objectives include: (i) Electrochemical studies on materials in molten LiCl-Li_2O-Li^0, electrolyte, with varying Li_2O (0-8wt%) and Li^0 (0-1.0 mol%) concentrations (ii) Understanding of surface chemistry, (iii) Long term exposure studies, and (iv) Evaluation of surface mechanical properties. Quantification of these changes will help predict container material behavior and longevity more accurately.

4 Introduction

The electrolytic reduction of uranium oxide in molten LiCl-Li_2O is a viable feed-in process for integrating ceramic used nuclear fuel into a pyroprocessing based fuel cycle (1-8). Recent observations have shown the accumulation of metallic lithium in the molten electrolyte used in this process (8-10). This fundamental change to the solution chemistry combined with the critical importance of material longevity to the safety of process operations, is the driving force behind this investigation.

Based on Gibbs free energy of reduction reactions, electrochemical methodologies can be successfully be employed in the reduction of nuclear fuel due to the roughly 70mV difference in reduction potential between UO_2 and Li_2O (2, 7, 11). Despite this theoretical difference in reduction potential, it has become increasingly clear that in practice significant overpotential is required to achieve high process throughput, and as a result a cell potential exceeding the Li_2O electrochemical window is required (6, 9, 10, 12-14). Principle investigators at the Korean Atomic Energy Research Institute (KAERI) (9), Central Research Institute of Electric Power Industry (CRIEPI) (15), and the Idaho National Laboratory (INL) (14) have independently stated that the reduction takes place via both the direct mechanism and the electrochemical mechanisms shown as reactions (1) and (2), respectively.

$$4Li + UO_2 \rightarrow U + 2Li_2O \qquad (1)$$

$$UO_2 + 4e^- \rightarrow U + 2O^{2-} \qquad (2)$$

The accumulation of excess metallic lithium has been reported to occur due to continued electrolysis of Li_2O after the depletion of UO_2, and the diffusion limited kinetics of the reaction between metallic lithium and UO_2 (8, 16). The goal of the current research is to investigate the effect of the inclusion of metallic lithium on material corrosion exposed to molten mixtures of LiCl-Li_2O-Li to evaluate material longevity for various applications in this process.

Extensive research on the corrosion of materials exposed to molten salts has led to an understanding of material interactions with LiCl-Li_2O (17-21). The most successful model used to describe corrosion in this system is based on the basicity of the salt, defined as the negative log

of the activity of the O^{2-} ion in the electrolyte (18, 22-24). Using this model, acidic salts containing little to no Li_2O, corrode materials through the oxidation and subsequent dissolution of metal atoms from the material. Alternatively, in basic salts where the concentration of Li_2O is high, the basic dissolution of anion complexes, such as CrO_4^{2-}, is the primary mode of material degradation. Between the two extremes a salt composition of optimal basicity exists such that material dissolution is minimized. For example, in the extensively researched and analogous molten $NaSO_4$ system an optimal concentration of Na_2O is known to result in the formation of a stable and protective $NaCrO_2$ surface film on stainless steel alloys (22).

Considering the presence of metallic lithium in the molten electrolyte used in the electrolytic reduction of UO_2, it is further beneficial to review aspects of fluid mixtures of metals and conjugate salts containing the same cation. Bredig *et al.* was highly successful in classifying these mixtures into two categories, although it is important to emphasize that the two models are not mutually exclusive, and aspects of both have been simultaneously observed in non-ideal conditions (25-27). The first model applies most directly to mixtures of alkali metals and alkali – halide salts, such as Li in LiCl (28, 29). These solutions are known to exhibit true solution behavior in the salt rich region of the phase diagram, and rapidly change their physical properties with the inclusion of a minor quantity of metal (30, 31). Such phases have been successfully described using an adopted version of the F^- model of ionic crystals. In this model the metallic atoms are treated as anion vacancies, replaced by an excess electron. A key indication of mixtures of this type is a sharp rise in electron mobility, indicating a transition from a nonmetallic to a metallic state, with the inclusion of a small percentage of metal in the solution.

The second classification of metal salt mixtures applies to more complicated systems, for example Bi in BiI (25, 32). In these mixtures, chemical interactions between the metal atoms and the salt anions results in the formation of abnormally reduced complexes referred to as subhalides. In such situations, the change in physical properties that accompanies the nonmetal – metal transition does not occur until much higher concentrations of metals are present in the mixture. The larger amount of metal required to induce this change is due to the consumption of excess electrons in the formation of the subhalides. While Li in LiCl has been successfully

described using the first model, the experimental observation and theoretical prediction of Li_2Cl as a subhalide in molten LiCl-KCl-Li_2O-Li system suggests that the ternary solution currently under investigation may be more readily described by the second model (29, 33, 34).

To investigate the above, the following tasks were identified:

(i) Electrochemical studies on materials in molten LiCl-Li_2O-Li^0, electrolyte, with varying Li_2O and Li^0 concentrations

(ii) Understanding of surface chemistry

(iii) Long term exposure studies

(iv) Evaluation of surface mechanical properties.

5 Synopsis of this report

The tasks are described briefly below. The comprehensive details of all the experiments conducted under this project and the results from those are provided as technical appendices 1, 2 and 3. The reason for attaching them as technical appendices is that each system was studied separately and the work was conducted independently of others and at different times. Since there is very little literature on effect of Li present in molten salt as Li^0, many of the protocols used here are developed by us and to maintain the comprehensive nature and its meaning, it was decided to maintain them as separate scientific studies rather than combine the three systems which will likely lead to errors due transcribing and formatting as well.

Task 1: Electrochemical studies on materials in molten LiCl-Li_2O-Li^0

Various materials and alloys were studied in this salt environment. Materials studied include stainless steels, high-nickel based Inconels, ceramics such as magnesia and alumina, and high purity metals such as tungsten, molybdenum, and platinum. Studies were conducted in salts containing varying amounts of Li_2O and Li to understand the effect of those two species.

Task 2: Surface Characterization

Several techniques were used for characterization of materials. Techniques used include microscopy techniques such as optical and scanning electron microscopy, spectroscopy techniques such as Raman, Infrared and UV-Visible spectroscopy, and X-ray techniques such as X-ray diffraction and X-ray photoelectron spectroscopy. Additionally, the solution chemistry was analyzed using inductively coupled plasma optical emission spectroscopy. Some of these techniques were custom built as described in their particular sections.

Task 3: Long Term Exposure Studies

Long term exposure studies were conducted on the primary materials of interest; namely, stainless steels and the high nickel based Inconel alloys. Exposure tests were conducted using specially built apparatus as described in that section. Tests were conducted for 500 and 1000 hours,

Task 4: Degradation of Surface Mechanical Properties

Degradation of surface mechanical properties was analyzed using microhardness and nano-indentation. It was determined that significant surface preparation is required to obtain meaningful nano-indentation results but that surface preparation itself leads to degradation of Li affected surface. Microhadness testing was considered to be somewhat useful. These results are provided in those respective sections as well.

6 Products

This funded project resulted in several notable accomplishments that are described below:

Theses and Dissertations:

1. William Phillips, MS Thesis, entitled "*Corrosion behavior of Monel 400 and electrochemical performance of Li-Bi reference electrode in molten LiCl-Li_2O-Li*' December 2015.

2. Augustus Merwin, PhD Dissertation, entitled "*Material Interactions with Molten LiCl-Li_2O -Li*', May 2016.

3. William Phillips, PhD Dissertation, expected December 2018/May 2019.

Peer reviewed publications:

1. A. Merwin and D. Chidambaram, "*Corrosion of Inconel 625 in Molten LiCl-Li_2O-Li*", Nuclear Technology, 195, 204 (2016).

2. A. Merwin, W. C. Phillips, M. A. Williamson, J. L. Willit, P. N. Motsegood, and D. Chidambaram, "*Presence of Li Clusters in Molten LiCl-Li*", Nature Scientific Reports, 6, 25435 (2016). DOI: 10.1038/srep25435.

3. A. Merwin, M. A. Williamson, J. L. Willit, and D. Chidambaram, "*Metallic Lithium and the Reduction of Actinide Oxides: A Review*" Journal of the Electrochemical Society, 164, 8, H5236 (2017).

4. A. Merwin and D. Chidambaram, "*The effect of Li^0 on the corrosion of stainless steel alloy 316L exposed to molten LiCl-Li_2O-Li*," Corrosion Science, 126, 1 (2017).

5. W. C. Phillips, A. Merwin and D. Chidambaram, *"On the corrosion performance of Monel 400 in molten LiCl-Li_2O-Li at 923K"*, Under Review Metallurgical and Materials Transactions.

Meeting Presentations:

1. W. Phillips and D. Chidambaram, *"Long-Term Corrosion Performance of Stainless Steel 316 in Molten LiCl-Li2O-Li"* in session C03: State-of-the-Art Surface Analytical Techniques in

Corrosion 3: In Honor of Hugh Isaacs, of the 232nd Meeting of the Electrochemical Society, National Harbor, MD, October 1-5 (2017).

2. D. Chidambaram, '*Evaluating Materials for Use in Pyroprocessing of Used Nuclear Fuel*', 11th International Symposium on Advances in Electrochemical Science and Technology (iSAEST-11) 09 December (2016). INVITED

3. A. Merwin and D. Chidambaram, '*Corrosion of Stainless Steel 316L in Molten LiCl-Li_2O-Li*' in session C03 High Temperature Corrosion and Materials Chemistry 12– Molten Salt Corrosion Reactions of the Prime 2016 Meeting of the Electrochemical Society, Honolulu, HI, October 2-7 (2016).

4. A. Merwin, W. Phillips, and D. Chidambaram, '*On the Formation of Clusters of Li_8 in Molten Solutions of LiCl-Li*' in session L02: Molten Salts and Ionic Liquids 20 – Solute and Solvent Properties II of the Prime 2016 Meeting of the Electrochemical Society, Honolulu, HI, October 2-7 (2016).

5. W. Phillips, A. Merwin, V. Singh, and D. Chidambaram, '*Characterization of the Electrochemical Behavior of a Li-Bi Reference Electrode for the Molten LiCl-Li*' in session L02: Molten Salts and Ionic Liquids 20 – Materials of the Prime 2016 Meeting of the Electrochemical Society, Honolulu, HI, October 2-7 (2016).

6. D. Chidambaram, '*Understanding the Electrochemical Behavior of a Material in terms of its Surface Chemistry*', Presented at the University of Idaho, Moscow, ID, June 23rd (2016). INVITED

7. W. Phillips, A. Merwin, and D. Chidambaram, '*Corrosion behavior of Monel 400 in Molten LiCl-Li_2O-Li*' in session C01: General Corrosion-Corrosion in Harsh and Complex Environments II, Session of the 229th Meeting of the Electrochemical Society, San Diego, May 29th-June 2nd (2016).

8. W. Phillips, A. Merwin, and D. Chidambaram, '*Electrochemical Performance of the Li-Bi Reference Couple in Molten LiCl-Li_2O-Li*' in session C01: General Corrosion-Corrosion in

Harsh and Complex Environments II, Session of the 229th Meeting of the Electrochemical Society, San Diego, May 29th-June 2nd (2016).

9. D. Chidambaram, Presentation at the Annual Progress Meeting for Pyroprocessing, organized by DOE, Germantown, MD, February 25-26 (2016).

10. D. Chidambaram, "*Understanding Materials, Interfaces and Electrochemical Behavior*", Presented at the Western University, Ontario, Canada, Dec 8th (2015). INVITED

11. D. Chidambaram, "*Understanding Materials, Interfaces and Electrochemical Behavior*", Presented at the Nuclear Waste Management Organization, Toronto, Canada, December 7th (2015). INVITED

12. D. Chidambaram, *"Behavior of Materials in Molten LiCl-Li_2O-Li"*, Presented at the Western University, Ontario, Canada, June 25 (2015). INVITED

13. D. Chidambaram, *"High Temperature Corrosion of Materials"*, Presented at the Engineering Physics Department, University of Wisconsin-Madison, Madison, WI, May 27 (2015). INVITED

14. A. Merwin and D. Chidambaram, *"Material Interactions with LiCl-Li_2O-Li"* presented at the Idaho National Laboratory, Idaho Falls, ID, November 6th (2014). INVITED

7 References

1. S. M. Jeong, B. H. Park, J.-i.-m. Hur, C.-S. Seo, H. Lee and K.-C. Song, *Nuclear Engineering and Technology*, **42**, 183 (2010).

2. S. Herrmann, S. Li and M. Simpson, *Journal of Nuclear Science and Technology*, **44**, 361 (2007).

3. T. Shimada, N. Tedzuka, Y. Shimizu and M. Miyake, *J. Alloys Compd.*, **204**, 1 (1994).

4. M. Gibilaro, L. Cassayre, O. Lemoine, L. Massot, O. Dugne, R. Malmbeck and P. Chamelot, *J. Nucl. Mater.*, **414**, 169 (2011).

5. M. Iizuka, Y. Sakamura and T. Inoue, *Journal of Nuclear Materials*, **359**, 102 (2006).

6. J.-M. Hur, C.-S. Seo, S.-S. Hong, D.-S. Kang and S.-W. Park, *Reaction Kinetics and Catalysis Letters*, **80**, 217 (2003).

7. B. H. Park, I. W. Lee and C. S. Seo, *Chemical Engineering Science*, **63**, 3485 (2008).

8. W. Park, J.-M. Hur, S.-S. Hong, E.-Y. Choi, H. S. Im, S.-C. Oh and J.-W. Lee, *Journal of Nuclear Materials*, **441**, 232 (2013).

9. W. Park, J.-K. Kim, J.-M. Hur, E.-Y. Choi, H. S. Im and S.-S. Hong, *Journal of Nuclear Materials*, **432**, 175 (2013).

10. E.-Y. Choi, C. Y. Won, J.-S. Cha, W. Park, H. S. Im, S.-S. Hong and J.-M. Hur, *Journal of Nuclear Materials*, **444**, 261 (2014).

11. O. Research, Chemical Reaction and Equilibrium Software with Extensive Thermochemical Database, Version 5.1, in, HSC Chemistry (2002).

12. B. Park, S. Park, S. Jeong, C. Seo and S. Park, *J. Radioanal. Nucl. Chem.*, **270**, 575 (2006).

13. S. Phongikaroon, S. Herrmann and M. Simpson, *Nucl. Technol.*, **174** (2010).

14. S. Herrmann, S. Li and B. Serrano-Rodriguez, in *GLOBAL 2007* (2007).

15. Y. Sakamura, *Electrochimica Acta*, **80**, 308 (2012).

16. E. Karell, K. Gourishankar, J. Smith, L. Chow and L. Redey, *Nucl. Technol.*, **136**, 343 (2001).

17. J. E. Indacochea, J. L. Smith, K. R. Litko, E. J. Karell and A. G. Rarez, *Oxid. Met.*, **55**, 1 (2001).

18. S. H. Cho, J. S. Zhang, Y. J. Shin, S. W. Park and H. S. Park, *J. Nucl. Mater.*, **325**, 13 (2004).

19. S. Cho, J. Lim, K. Yun and S. Park, *Korean Journal of Materials Research*, **14** (2004).

20. S. H. Cho, S. B. Park, J. H. Lee, J. M. Hur and H. S. Lee, *Mater. Chem. Phys.*, **131**, 743 (2012).

21. J. Indacochea and J. Smith, *J. Mater. Res.*, **14**, 1990 (1999).

22. Y. S. Zhang, *J. Electrochem. Soc.*, **133**, 655 (1986).

23. M. Spiegel, P. Biedenkopf and H. J. Grabke, *Corros. Sci.*, **39**, 1193 (1997).

24. R. Rapp, in *Corrosion: fundamentals, testing and protection*, ASM International, Materials Park, OH (2003).

25. M. A. Bredig, in *Molten Salt Chemistry*, J. W. a. Sons Editor (1964).

26. G. M. Haarberg and J. Thonstad, *J Appl Electrochem*, **19**, 789 (1989).

27. J. D. Corbett, in *Fused Salts*, M. Hill Editor (1964).

28. H. R. Bronstein and M. A. Bredig, *J. Am. Chem. Soc.*, **80**, 2077 (1958).

29. A. S. Dworkin, H. R. Bronstein and M. A. Bredig, *The Journal of Physical Chemistry*, **66**, 572 (1962).

30. W. W. Warren, in *Advances in Molten Salt Chemistry*

R. Publishing Editor (1983).

31. W. Freyland, *Journal of Non-Crystalline Solids*, **117**, 613 (1990).

32. L. F. Grantham and S. J. Yosim, *The Journal of Chemical Physics*, **38**, 1671 (1963).

33. P. Hébant and G. S. Picard, *Electrochimica Acta*, **43**, 2071 (1998).

34. P. Hébant and G. S. Picard, *Journal of Molecular Structure: THEOCHEM*, **426**, 225 (1998).

8 Technical Appendices

A1 Short term interaction of materials with $LiCl\text{-}Li_2O\text{-}Li^0$

Contents

Chapter 1 Metallic Lithium and the Reduction of Actinide Oxides 1
1.1 Introduction: 1
1.2 Experience with the Reduction Process: 4
1.3 The Formation of Li During the Electrolytic Reduction of UO_2: 8
1.4 Physical Chemistry of Molten LiCl-Li_2O-Li: 15
1.5 LiCl-Li_2O-Li and the Reduction of Actinide Oxides: 22
1.6 Summary: 31
1.7 Corrosion in Molten Salts and Liquid Metals: 32
1.7.1 Corrosion in Molten Alkali-Halide Salts: 33
1.7.2 Corrosion in Molten Salts Containing Oxides: 35
1.7.3 Corrosion in Liquid Lithium: 40
1.8 Outline Material Interactions with Molten LiCl-Li_2O-Li: 42
Chapter 2 Experimental Methods 46
2.1 Glove Boxes: 46
2.2 Materials: 52
2.3 The Li-Bi Reference Electrode in Molten LiCl-Li_2O-Li: 54
2.4 Gas Chromatography: 57
2.5 Scanning Electron Microscopy / Energy Dispersive X-ray Spectroscopy: 57
2.6 X-ray Diffraction: 60
2.7 Micro-Hardness Testing: 63
2.8 Inductively Coupled Plasma – Optical Emission Spectroscopy: 64
2.9 Raman Spectroscopy: 65
2.10 X-ray Photoelectron Spectroscopy: 67
Chapter 3 Development of Experimental Protocol for Molten LiCl-Li_2O-Li 69
3.1 Introduction: 69
3.2 Materials: 71

3.3 Crucible Materials: 72
3.3.1 Degradation of Ceramic Materials in Molten LiCl-Li_2O-Li: 74
3.3.2 The Use of Metal Crucibles for Containing Molten LiCl-Li_2O-Li: 78
3.4 Corrosion of Inconel 625 and 718 in Molten LiCl-Li_2O-Li: 82
3.4.1 Experimental: 82
3.4.2 Results and Discussions: 83
3.4.3 Summary: 93
3.5 Exposure Studies of Stainless Steel in Alternative Crucibles: 94
3.6 Corrosion of Hastelloy N in Molten LiCl-Li_2O-Li: 98
3.8 Investigations of Reagent Grade vs. Anhydrous LiCl: 103
3.9 Extended Exposure Studies: 109
3.10 Sample Baking: 130
3.11 Conclusions: 133
Chapter 4 Dispersion of Li in Molten LiCl-Li_2O 136
4.1 Chemical Analysis of LiCl-Li_2O-Li: 137
4.2 Concentric Inductor Magnetization Sensor: 141
4.2.1 Theory: 142
4.2.2 Experimental Setup: 144
4.2.3 Simulation and Calibration Results: 145
4.2.4 Results: 148
4.3 Anomalous Physical Properties of Molten LiCl-Li_2O-Li: 151
4.4 Presence of Li Clusters in Molten LiCl-Li: 156
4.4.1 Methods: 157
4.4.2 Results: 158
4.4.3 Discussions: 166
4.5 Conclusions: 169
Chapter 5 Effect of Li on the Corrosion Stainless Steel Alloy 316L Exposed to Molten LiCl-Li_2O 171
5.1 Results and Discussion: 171
5.1.2 Hardness: 171

5.1.2 SEM / EDS: 173
5.1.3 XRD: 177
5.1.4 Raman: 178
5.1.5 XPS: 179
5.2 Conclusions: 195
Chapter 6 Electroless Deposition of Titanium Compounds on Stainless Steel Alloy 316L in Molten LiCl-Li_2O-Li 197
6.1 Introduction: 197
6.2 Ti Compounds Formed as a Function of Li_2O Concentration: 199
6.3 Interactions of TiO_2 with Molten LiCl-Li_2O-Li: 208
6.4 Ti Compounds Formed as a Function of Li Concentration: 211
6.5 Conclusions: 215
Chapter 7 Conclusions and Future Work 217
7.1 Conclusions: 217
7.2 Future Work: 221
7.3 Scholarly Work from this Study: 223
References: 225

Chapter 1 Metallic Lithium and the Reduction of Actinide Oxides

1.1 Introduction:

The reduction of uranium, plutonium and minor actinide oxides to a metallic form is an important nuclear fuel cycle process [2-8]. The ability of metallic lithium to reduce various uranium oxides, importantly UO_2 and U_3O_8, has been known for many years [9]. A molten salt metalothermic reduction process employing metallic lithium (Li) as a reductant dissolved in molten LiCl was first developed by Argonne National Laboratory (ANL) to consolidate a variety of forms of actinide oxides for integration into a single electrometallurgical reprocessing system [10-12]. An electrolytic process, often referred to as electro-deoxidation, was subsequently developed as a more controllable method of reducing metal oxides [13-16]. It was demonstrated that metal oxides could be reduced electrochemically in molten salts as long as the reduction potential of the metal oxide in question was more noble than the cation of the electrolyte [17]. This methodology was later adapted by Fray, Farthing and Chen (FFC) to a variety of metal production industries and has been the subject of several literature reviews [18-21]. While these reviews address the processes associated with the reduction of nuclear fuel in LiCl, they focused on the electro-deoxidation phenomena and the $CaCl_2$-CaO system. Additionally, the process engineering of the electrolytic reduction of nuclear fuel, and experience in incorporating oxide fuel into pyroprocessing, has been the focus of a recent review [22]. The current review will focus on the role metallic lithium plays in the electrolytic reduction of actinide oxides in LiCl-Li_2O.

The primary difference between the direct lithium reduction process and the electrolytic reduction process is that the molten salt used in the former begins as LiCl saturated with Li. During the reduction process, the oxide concentration in the salt increases up to its solubility limit of 11.6mol% at 650°C as reaction (1) progresses [23-25].

$$4Li + MO_2 \rightarrow M + 2Li_2O \qquad \text{Reaction (1)}$$

Alternatively, in the electrolytic process, Li_2O is added as an oxide ion transport species intentionally, and its concentration remains constant throughout the process. In this process the reduction of the metal oxide, MO_x, occurs via reaction (2a) and oxygen gas is evolved at the anode via reaction (2b).

$$MO_x + 2ne^- \rightarrow MO_{x-n} + nO^{2-} \qquad \text{Reaction (2a)}$$

$$nO^{2-} \rightarrow \frac{n}{2}O_{2(g)} + 2ne^- \qquad \text{Reaction (2b)}$$

The electrolytic process is a noted improvement compared to the direct lithium reduction method [12, 14, 16, 26-28]. The reaction between dissolved Li and the metal oxide is difficult to control under Li saturated conditions, especially at the surface of the melt due to the lower density of Li compared to LiCl. Corrosion of the container materials used to hold the electrolyte in the direct reduction process proved to be difficult due to the presence of reducing Li, and oxidizing LiCl. Additionally, the concentration of Li_2O in the melt cannot be controlled in the direct reduction process other than by controlling the oxide/salt ratio. In both processes, the concentration of Li_2O in the salt must be maintained below certain levels due to the decrease in the Gibbs free energy of

reducing actinide oxides with increasing oxygen ion activity. Lithium reduction of PuO_2 and AmO_2 was demonstrated by Usami *et al.*, however only at less than 3 and 1.8wt% Li_2O in the melt, respectively [25, 29]. The electrolytic reduction process is highly advantageous in this respect, as the concentration of Li_2O, in theory, remains at a controlled level throughout the reduction process. The adaptation of the electrochemically driven reduction process has been highly successful, resulting in reduction yields exceeding 99% [30].

Electrolytic reduction in LiCl-Li_2O has been successfully used to reduce MOX, as well as simulated high burnup SIMFUEL [31, 32]. In a non-nuclear context, electrolytic reduction in LiCl-Li_2O has been adapted to TiO_2 [33], SiO_2 [34], Ta_2O_5 [35] and Nb_2O_5 [36]. The electrolytic reduction of actinide oxides in LiCl-Li_2O is unique compared to transition metal oxides in that the reduction potential of the primary components of interest, namely UO_2 and PuO_2, are so close to the reduction potential of Li_2O that the mechanisms of reduction are significantly more complex.

Due to the roughly 70mV difference in reduction potential between UO_2 and Li_2O, electrolytic methodologies can theoretically be employed in the reduction of nuclear fuel [37-39]. Experience with the process has shown however, that in practice significant overpotential is required to achieve high process throughputs, and as a result a cell potential exceeding the Li_2O electrochemical window is required [26, 40-44]. Principle investigators at the Korean Atomic Energy Research Institute (KAERI) [44], Central Research Institute of Electric Power Industry (CRIEPI) [45], and the Idaho National Laboratory (INL) [43] have independently reported that the electrolytic

reduction cell is operated with the cathode at a more cathodic potential than the lithium reduction potential, and that the reduction takes place via both the direct, and the electrochemical reduction mechanisms shown as reactions (1) and (2), respectively.

It will be shown in the following review that significant quantities of metallic lithium form on the cathode during the reduction of actinide oxides. Despite its presence in the system, and the important role it plays in the reduction, the nature and chemical form of metallic lithium in this process is not well understood. This review attempts to discuss the role of metallic lithium in this process; both, how it is formed and how it interacts with the system, in an attempt to emphasize its critical importance in understanding the oxide reduction process.

1.2 Experience with the Reduction Process:

Extensive fundamental research and engineering scale experience with the reduction of actinide oxides has yielded critical information regarding the mechanics of the process [26, 40]. The process fundamentals, adopted by virtually all researchers, are as follows: polarization between an inert anode material, usually platinum, and a stainless steel cathode basket containing the metal oxide to be reduced is conducted at a cell voltage of approximately 3V in a molten bath of LiCl containing 0.5-3wt%Li_2O at 650°C. Studies have demonstrated that optimal process conditions include a Li_2O concentration of approximately 2wt%, and a cathode to anode surface area ratio of 2.6 [7, 46]. Research into the anodic behavior of platinum under these conditions has demonstrated that platinum can operate as a nearly inert anode if the concentration of Li_2O is maintained above 0.5wt% and the anode potential is less than +2.6V vs LiPb

[47]. If the activity of the O^{2-} ion decreases significantly the dissolution of platinum occurs via reaction (4). However, the anode corrodes via the formation of Li_2PtO_3, as shown in reaction (5), if the anode potential is too high [46, 47]. Alternative anode materials have been proposed, however none have been widely adopted [44, 48-50].

$$Pt \rightarrow Pt^{2+} + 2e^- \qquad \text{Reaction (4)}$$

$$2Li^+ + Pt + 3O^{2-} \rightarrow Li_2PtO_3 + 4e^- \qquad \text{Reaction (5)}$$

Sakamura *et al.* compared the electrolytic reduction of UO_2 in LiCl and $CaCl_2$ and found that experiments conducted in LiCl exhibited significantly superior current efficiencies and higher yields compared to those conducted in $CaCl_2$ [51]. Metallic Ca was formed on the cathode during the polarization in $CaCl_2$, but it did not penetrate the exterior U metal that was reduced initially. It was observed that a dense metal surface formed on the exterior of the UO_2 which prevented the discharge of O^{2-} from the remaining oxide, inhibiting the continuation of the reduction process. As a result, UO_2 in the center of the fuel pellets was found to be not reduced. This effect has driven research in the electrolytic reduction of UO_2 to be conducted almost exclusively in LiCl-Li_2O.

Voloxidation of used nuclear fuels is considered as a head-end process prior to oxide reduction to separate the fuel from the cladding, remove volatile fission products, and to reduce the particle size of the fuel [52-55]. Voloxidation is achieved by reacting nuclear fuel with an oxidizer, typically O_2 gas, at high temperature to promote the oxidation of UO_2 to U_3O_8. The removal of volatile and salt soluble fission products from the fuel by this process is desirable as it reduces the activity of the pyroprocessing

electrolyte salts [56]. Reducing the particle size of the oxide fuel through voloxidation has been shown to increase the kinetics of the oxide reduction process [57]. However, research into the reduction behavior of U_3O_8 has shown that it reduces to intermediate lithium uranates, and UO_2 prior to reducing to metallic uranium [40, 58, 59]. Furthermore, it has also been demonstrated the reduction of U_3O_8 to UO_2 occurs spontaneously upon exposure to molten LiCl-Li_2O [40, 60]. Therefore, because the reduction of U_3O_8 progresses via the reduction of UO_2, the reduction of the latter remains the primary energy barrier to the electrochemical process. The current review will focus on the reduction of UO_2 specifically, as the aspects that are demonstrated to occur during its reduction will inevitably occur during the reduction of U_3O_8.

Despite being capable of high reduction yields, the electrolytic reduction process is known to exhibit low current efficiencies and, in some instances, consume Li_2O. Table 1.1 shows reported process parameters associated with the reduction of UO_2 conducted by various organizations. For previously stated reasons, the reduction yields and current efficiencies reported for the reduction of U_3O_8 cannot be compared to those of UO_2, and are therefore emitted from the following discussion.

Table 1.1 Reported process parameters of the electrolytic reduction process

Institution	Initial wt% Li_2O	Final wt%Li_2O	Charge Transfer (%)	Reduction Yield	Mass (g)	Reference	Comments
CRIEPI	-	-	150	Complete**	18	[5]	
CRIEPI	1	-	160	Complete**	103.5	[61]	Observed anode potential increase before adding 0.3wt%Li_2O
CRIEPI	-	-	135	99.2**	100	[62]	
KAERI	1	-	150	100	18	[57]	
KAERI	1.01	.97	150	>95	20	[41]	
KAERI*	1	0.89	200	100	5	[63]	
KAERI	1	0.98	150	98.9	20	[64]	
KAERI	1.37	-	177	98	17,000	[7]	Lost ~0.47wt%Li_2O in 12 hours before adding ~0.8wt%Li_2O
KAERI	1	-	150	88	4.1	[32]	
KAERI	1	-	170	99	29.7	[65]	
INL	1	-	220	99.7	50	[66]	Ended with anode potential increase (~0.5wt%Li_2O)
INL	1	0.8	150	67	50	[43]	
INL	1	-	263	98	50	[38]	Ended with anode potential increase (~0.5wt%Li_2O)
INL	1	-	220	99.7	45	[67]	Ended with anode potential increase (~0.5wt%Li_2O)

* Denotes the use of a LiCl-KCl-Li_2O electrolyte. ** Denotes reduction yield quantification based strictly on visual observation. Note that at least ~150% of the theoretical charge transfer is required to surpass a quantitative reduction yield of 95%.

Table 1.1 demonstrates that no research to date has quantitatively demonstrated a current efficiency of greater than 66%. Additionally, it has to be demonstrated that the process kinetics and efficiency are deteriorated as the process proceeds due to the accumulation of soluble fission products in the electrolyte [4]. These deleterious effects, associated primarily with the accumulation of KCl and CsCl in the LiCl-Li_2O, were attributed to a decrease in the solubility limit of Li_2O in the melt. Decreasing the transport of O^{2-} in the electrolyte suppresses the reaction kinetics by limiting Reaction 2b. Additionally, the data in Table 1.1 demonstrates the loss of measurable quantities of Li_2O

during the process. Quantification of the consumption of Li_2O during the process is complicated due to the presence of Li in the electrolyte, for reasons that will be discussed subsequently. Furthermore, it has been demonstrated that oxides of salt soluble fission products, primarily Cs, Ba, Rb, and Sr, will react LiCl to form their respective chlorides and Li_2O [4, 26]. By producing Li_2O, these reactions would result in an apparent rate of Li_2O consumption that is considerably lower than the true value. While the consumption of minor quantities of Li_2O may appear insignificant on a bench scale, the loss of large quantities during industrial scale operations is seen as a major process impediment [68].

1.3 The Formation of Li During the Electrolytic Reduction of UO_2:

Preliminary attempts to avoid the reduction of Li^+ during the reduction of actinide oxides employed modest currents to avoid the cathode from reaching the $Li|Li^+$ reduction potential. Figure 1.1 shows the cathode potential recorded as a function of current passed through the salt during the reduction of $(U\text{-}40Pu\text{-}5Np)O_2$ fuel in LiCl-0.51%Li_2O [69]. This investigation had intended to maintain a cell current of 70mA, but was forced to reduce the current after exceeding the $Li|Li^+$ potential of -0.75V vs Bi-Li. The cell had to be interrupted after 108% of the theoretical charge required to reduce the specified quantity of material was passed, a quantity recognized to be insufficient to result in significant reduction yields. After the initial interruption, each successive polarization approached the $Li|Li^+$ potential more rapidly, indicating that the $Li|Li^+$ potential had to be exceeded in order to achieve sufficient reduction yields.

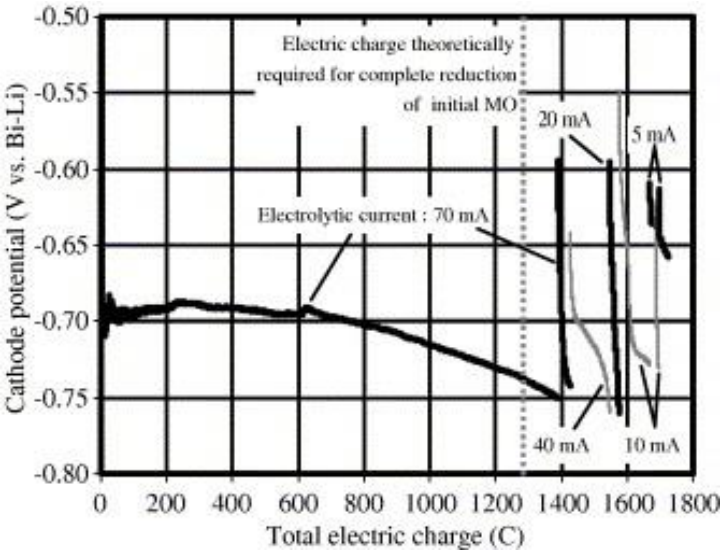


Figure 1.1: The cathode potential measured during galvanostatic polarization of (U-40Pu-5Np)O_2. The electrolysis was periodically interruped after the cathode achieved the Li|Li^+ potential at -0.75V vs Bi-Li. Dispite these attempts the Li|Li^+ potential was rapidly re-established in each successive polarization [69].

Galvanostatic polarization of U_3O_8 at minimal current densities, as low as 26.5 mA/cm^2, resulted in a cathode potential more cathodic than the Li|Li^+ reduction potential of -1.75V vs Pt after approximately 30% of the theoretical charge was passed through the cell [39, 58]. The authors further noted that following the reduction experiments, the cathode basket vigorously produced gas bubbles when rinsed in water; an observation they attributed to the presence of metallic lithium in and on the cathode. These two examples demonstrate that avoiding the Li|Li^+ potential during the reduction process is impractical if the process is to be conducted at an industrially viable rate.

It should be noted that Li forms in the oxide reduction process at potentials more noble than the Li|Li^+ standard potential. Li is soluble in LiCl at 650°C, and as a result it has an activity as solvated Li that is less than unity until the melt is saturated [1, 70-74]. Therefore, according to the Nernst equation, Li^+ can be reduced at potentials more noble

than the $Li|Li^+$ standard potential as long as the activity of Li in the melt is not unity. This is important to note considering the proximity of the $U|U^{4+}$ and $Li|Li^+$ potentials. Li will form at the $U|U^{4+}$ standard potential, however at an activity that is in accordance with the Nernst equation. Recent approaches to the reduction process have employed potentiostatic polarization to maintain the cathode potential below the $Li|Li^+$ potential, as opposed to the galvanostatic polarization previously discussed in which the cathode potential is not controlled. Figure 1.2 (c&e) shows electrical responses recorded during the reduction of SIMFUEL and of UO_2, reported by KAERI and INL, respectively [32, 67, 75]. Cathodic cyclic voltammograms (CVs) conducted by the respective researchers

are also included in Figure in 1.2 (a&d) for comparison.

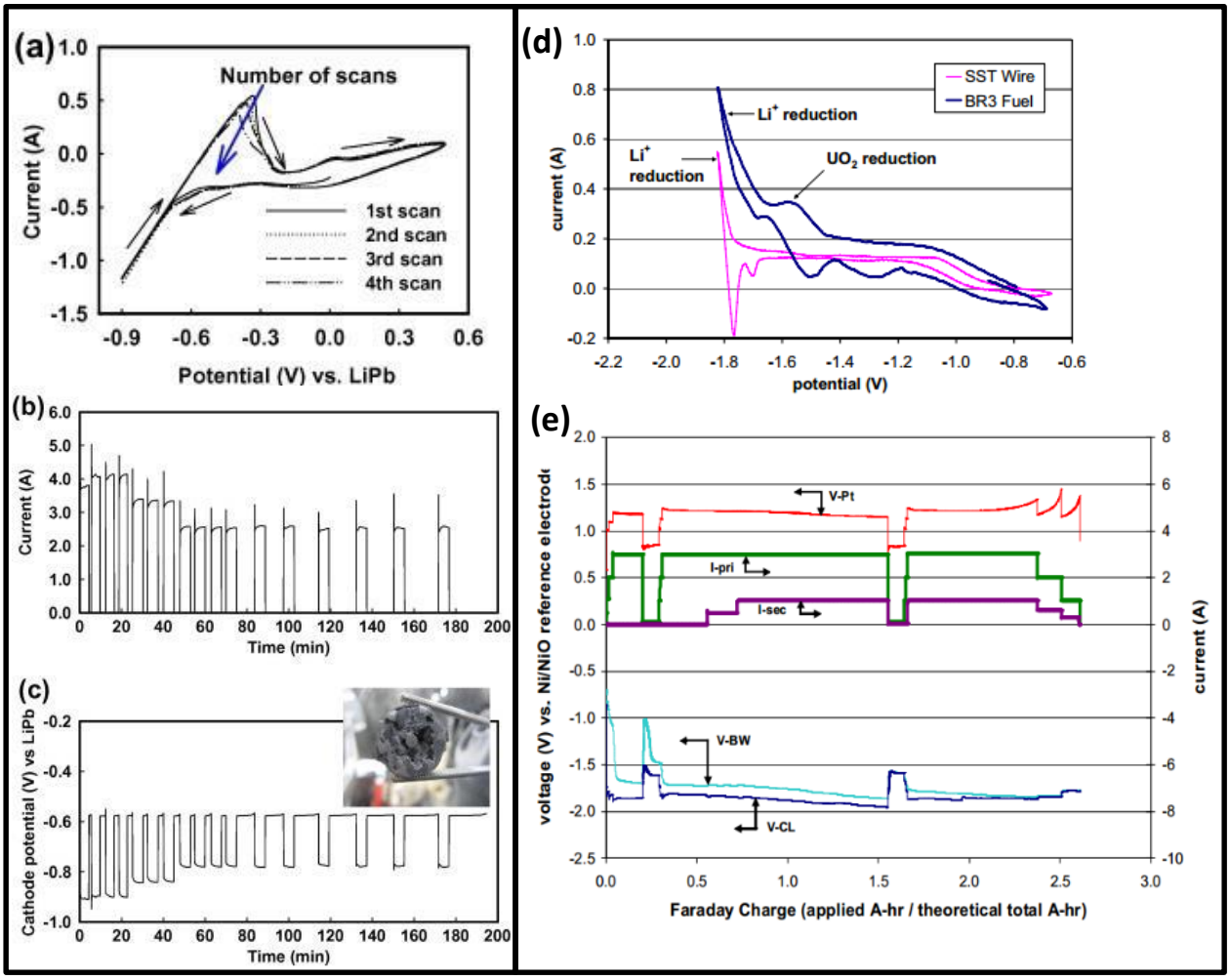


Figure 1.2: Electrical responses recorded during the reduction of SIMFUEL and UO_2 published by KAERI (left) and INL (right). (a) CV of SIMFUEL polarized vs a LiPb reference. (b) and (c) Cell current and cathode potentials recorded during the reduction of SIMFUEL. (d) CVs of a stainless steel wire and UO_2 polarized against a Pt refericne (e) Cell current and and electrode potential responses recorded during the reduction of UO_2. It is apparent in both studies that the the OCP of the cathode is that of $Li|Li^+$ when the polarization is ceased [32, 67, 75].

The electrical circuit was periodically interrupted during the electrolytic reduction studies shown in Figure 1.2 (c&e) specifically to avoid the deposition of excessive quantities of Li. During these periods of cell interruption it is important to note that the cathode open circuit potential (OCP) is observed to be the $Li|Li^+$ potential demonstrated

by the respective CV's shown in Figures 1.2 (a&d). This effect has been noted by numerous studies, and is attributed to the measurement of the OCP of metallic lithium existing on the cathode at unit activity [5, 32, 38, 41, 48, 62-64, 66, 76, 77]. Due to the presence of Li on the cathode it can be concluded that the process proceeded via both reactions (1) and (2). It is important to note that metallic lithium must be in physical contact with the cathode and the molten LiCl-Li_2O electrolyte in order for the electrochemical potential of the cathode to be measured at the $Li|Li^+$ potential.

Interpretations of electrode potentials made while passing current though the cell can lead to false conclusions due to omic potential drop effects. In the oxide reduction process, the cathode is in physical contact with electrically insolating oxide matierals, such as UO_2, and as a result current flowing through the cathode can exhibit a potential drop equivelnt to the product of the cell current and the electrical resistance of the insolator (iR). However, OCP measurements, such as those shown in Figures 1.2 C&E, are not subjected to such effects. As a result, it is noted that OCP measurements provide more acurate information than electrode potentials made during cell operation.

Reduction of actinide oxides has also been achieved in molten LiCl-KCl-Li_2O [44, 63]. The electrical response of a reduction experiment conducted in LiCl-KCl-Li_2O is shown in Figure 1.3. It is observed that two separate cathode OCPs were recorded when the cell was interrupted, a fact that Hur *et al.* attributed to the measurement of the $Li|Li^+$ and the $K|K^+$ potentials at -1.27V and -1.42V vs Li-Pb, respectively [63]. It is noted that the solubility of Li_2O in LiCl-KCl has been reported to be 4mol% at 520°C

[24], less than half of the solubility in LiCl at 650°C [23-25]. Therefore the use of a LiCl-KCl electrolyte is expected to lower process kinetics by limiting Reaction 2b.

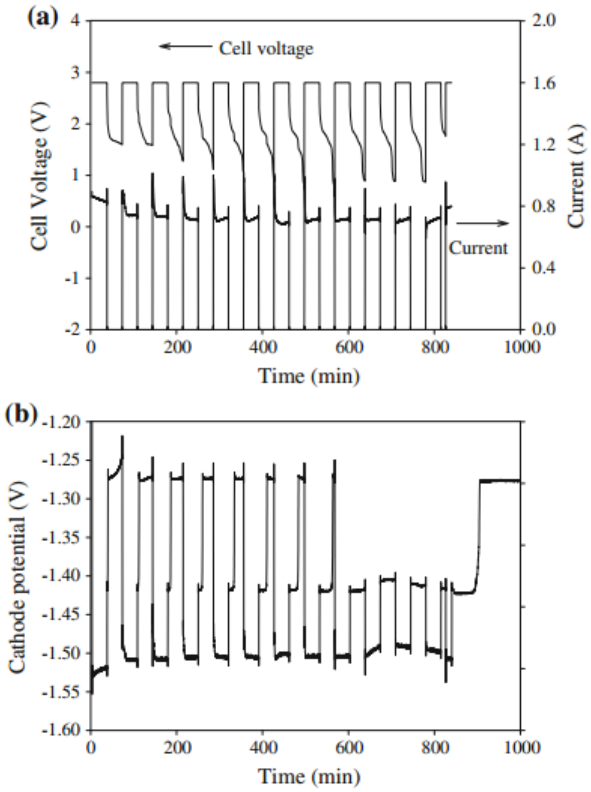


Figure 1.3: Cell voltage, current and cathode potentials measured during the reduction of UO_2 in LiCl-KCl-Li_2O at 520°C using a LiPb referince electrode. The recording of both the $K|K^+$ and the $Li|Li^+$ potentials when the cell was interupted demonstrates the presence of metallic K and Li on the cathode [63].

In research conducted by Choi *et al.* the electrical circuit was held open during the periods of cell interruptions as long as the cathode remained at the $Li|Li^+$ potential [32]. The departure from the $Li|Li^+$ potential is demonstrated by the gradual increase in cathode potential at the end of each cell interruption in Figure 1.3 (c). The length of time that the basket remains at the $Li|Li^+$ potential increases with polarization time; indicating that the time required for the activity of metallic lithium at the molten salt / cathode interface to dissipate increases as the process proceeds. (Note that as reduction proceeds

the reduced uranium metal shell on the feed material is in electrical contact with the cathode, effectively extending the cathode area across the fuel bed, albeit with a voltage drop across the bed due to iR.) There are two plausible ways for the metallic lithium phase to dissipate: by reacting with UO_2 through reaction (1), or via dissolution into the salt.

The kinetics of the oxide reduction process are known to be diffusion limited; as the reduction rate decreases asymptotically as the process progresses to completion [42, 43, 57, 77]. Recent modeling of the process employed a diffusion model using the production of Li at the cathode as the source term according to Faraday's law of electrolysis [42]. Interestingly, this model successfully fit numerous data sets by employing the direct reduction mechanism as the sole reduction pathway, neglecting the electro-deoxidation mechanism. It was reported that during the initial stages of reduction, the kinetics were limited by the production of Li due to the cell current; however, as the process proceeded towards completion, the diffusion through the exterior shell of metallic uranium limited the reaction kinetics.

The reduction process initiates with the rapid reduction of the exterior shell of each oxide pellet, forming a porous metallic layer surrounding the oxide center. The process kinetics is then limited by two potential mechanisms; the diffusion of Li to the UO_2, and the diffusion of the O^{2-} to the bulk electrolyte. Diffusion through the exterior metallic shell has been shown to be the rate limiting step in the process, due to the relatively rapid diffusion of the O^{2-} in the fluid salt phase [43, 57]. However, significant disagreement exists in the literature as to whether the process is limited by the diffusion

of Li into, or O^{2-} out of, the pellet [4, 32, 42]. The diffusion of Li^{+} through the porous metallic phase is unlikely to occur without the prior reduction of Li^{+} because the metallic phase is held below the $Li|Li^{+}$ potential. As a result of the oxide being incased in a metallic phase that is in electrical contact with the cathode held below the $Li|Li^{+}$ potential, the reduction of Li^{+} is expected to occur at the metallic surface of the pellets. Once formed on the exterior of the metallic phase, Li^{0} can undergo oxidization and lead to the reduction of U^{4+}. This process can occur nearly spontaneously because both phases are in physical contact with electrically conducting U metal. However, in order to conserve charge neutrality, this process is kinetically limited by the recombination of O^{2-} with the oxidized Li^{+}. This results in the process reduction kinetics being limited by diffusion O^{2-} out of the pellet. Many authors have attributed observations of increased reduction kinetics to altering process variables that would result in increased O^{2-} transport out of the cathode assembly such as; decreasing the UO_2 pellet size, increasing the UO_2 porosity, rotating the cathode assembly, and changing the material of the cathode assembly [5, 6, 15, 21, 22, 40, 43, 57, 78]. These observations strongly suggest that the diffusion of O^{2-} out of the oxide pellet, through the metal phase, is the rate limiting step of the electrolytic reduction process.

1.4 Physical Chemistry of Molten LiCl-Li_2O-Li:

Due to the previously discussed formation of metallic lithium during the reduction of actinide oxides, and the known solubility of Li in LiCl at 650ºC, it can be concluded that metallic lithium dissolves in-to the electrolyte during the oxide reduction process [1, 70-74]. Considering the presence of Li in the molten LiCl-Li_2O electrolyte, it is necessary

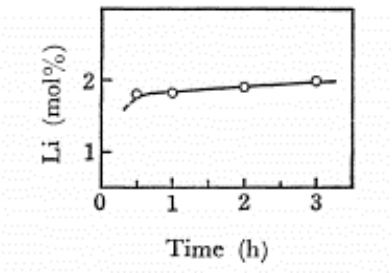
to review aspects of fluid mixtures of metals and conjugate salts containing the same cation. Bredig *et al.* were highly successful in classifying these mixtures into two categories, although it is important to emphasize that the two models are not mutually exclusive, and aspects of both have been observed simultaneously under non-ideal conditions [79-82]. The first model applies most directly to mixtures of alkali metals and alkali-halide salts, such as Na in NaCl [70, 83]. These solutions are known to exhibit true, microscopically homogenous, solution behavior in the salt rich region of the phase diagram, and rapidly change their physical properties with the inclusion of a minor quantity of metal [84, 85]. Such phases have been successfully described using an adapted version of the F^- model of ionic crystals. In this model, the metallic atoms are treated as anion vacancies, replaced by an excess electron. A key indication of mixtures of this type is a sharp rise in electron mobility, with the inclusion of a small percentage of metal in the solution, demonstrating a transition from a nonmetallic to a metallic state. The second classification of metal-salt mixtures applies to more complicated systems, for example Bi in BiI [79, 86]. In these mixtures, chemical interactions between the metal atoms and the salt anions results in the formation of abnormally reduced complexes referred to as subhalides. In such situations, the change in physical properties that accompanies the nonmetal-metal transition does not occur until much higher concentrations of metal are present in the mixture. The larger amount of metal required to induce this change is due to the consumption of excess electrons in the formation of the subhalides. The properties of the LiCl-Li_2O-Li electrolyte will be discussed in the context of fitting into these two models.

Despite numerous investigations, the solubility limit of Li in molten LiCl is still widely debated [1, 70-72, 87]. Initial investigations by Dworkin *et al.* at Oak Ridge National Laboratory (ORNL) measured the solubility limit using thermal analysis to be 0.5±0.2mol% at 640°C [70]. Researchers at ORNL were highly successful in developing phase diagrams of numerous metal-salt solutions, yet they noted exceptional difficulty in characterizing the LiCl-Li system [70, 79, 83, 88-90]. Attempts to characterize the electrical conductivity of LiCl-Li solutions, data that were used to support alternative metal-salt phase diagrams, were unsuccessful due to chemical reactions between Li and the crucibles. Park *et al.* reported the solubility limit of Li in LiCl to be 0.22mol% at 650°C, however no reference to the experimental data supporting this conclusion could be found [26].

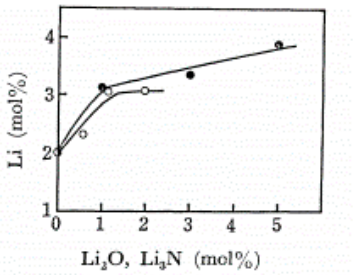
Nakajima *et al.* reported significantly different observations regarding the quantity of Li that could be dispersed in LiCl [1, 73, 74, 91]. In a series of experiments, metallic lithium was added in excess to one side of a U shaped crucible full of LiCl, while the salt on the opposite side was sampled. The quantity of lithium that was found to be dispersed in LiCl in these experiments was observed to be much higher in comparison to previous reports. Figure 1.4 shows the quantity of lithium observed in LiCl as a function of equilibration time, agitation time, as well as concentrations of Li_2O and Li_3N in the salt.

The concentrations of lithium observed to be dispersed in molten LiCl shown in Figure 1.4 depart from a general understanding of the electrolyte used in the oxide reduction process. It was hypothesized that the quantity of lithium per unit volume of

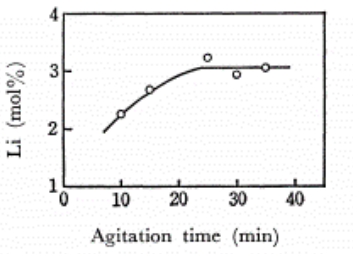
molten LiCl was the sum of two different forms; true solution and colloidal suspension. The true (physical) solubility limit was reported as 0.66mol%, a value within the margin of error reported by separate investigators [70, 74]. It is noted that the additional quantity of Li suspended in the molten salt in the form of a colloid would not be detectable in thermal analysis because the metallic lithium would not undergo a phase change during dispersion. The metal rich portion of the LiCl-Li system, if present, is not expected to contain large quantities of LiCl or O, as their solubility limits in liquid lithium are reported to be approximately 0.005mol% and 2mol%, respectively [92, 93]. Alternatively, the solubility limit of Li_2O is relatively high in LiCl at 11.6mol% at 650°C [23-25].



(a) Concentration of lithium vs time in the absence of agitation.



(b) Effects of lithium oxide and nitride on the lithium concentration at 650°C, agitation:1000rpm. ○=Li_2O ●=Li_3N



(c) Effect of agitation time on the lithium concentration at 650°C. Agitation: 1000 rpm with 1.14mol%Li_2O added.

Figure 1.4: Measured concentrations of dispersed Li in molten LiCl as a function of (a) time in the absence of agitation (b) Li2O and Li3N concentration and (c) agitation time [1].

Liu *et al.* investigated the seemingly anomalous behavior of the LiCl-Li system, and the reasons it behaved significantly differently compared to other alkali metal-alkali halide solutions [71, 72]. In these studies, the solubility of Li in LiCl was measured using potentiometry via

observation of the electrochemical potential of a lithium deposit as it dispersed into solution. The solubility limit recorded using this technique was 1.8mol% at 650°C. It should be noted that the salt used in this experiment was dried at 500°C prior to melting, and that no agitation was employed during the solubility measurements. These experimental parameters are important for characterizing unperturbed molten LiCl-Li as opposed to melts that contain impurities or exist under forced convection. The solubility limit of 1.8mol% is in agreement with data reported by Nakajima *et al.* in Figure 1.4 (a), and due to the nature of the experiment, appears to be representative of the total quantity of Li that disperses in LiCl in the absence of agitation. Two important facts were stated by Liu *et al.*: the observation that the thermodynamic activity of metallic Li is not unity when in contact with molten LiCl, and that an intermediate and momentarily stable electrochemical potential was observed between that of the lithium deposit and that of the bare electrode OCP [72]. The first observation has significant implications regarding the $Li|Li^+$ reduction potential and will be discussed later. The observation of an intermediate OCP, between the potentials of metallic lithium and the working electrode, was suggested as evidence of the formation of a lithium rich compound that was soluble in molten LiCl. This hypothesis proposes the formation of a Li_xCl compound with a value of X greater than one, in contrast to the accepted miscibility gap phase diagram behavior of alkali metal-alkali halide solutions proposed by Bredig [79]. The formation of an additional, subhalide, compound may be in agreement with the observation of the two seemingly different dissolution mechanisms previously discussed. Nakajima *et al.* attributed the dissolution of excessive quantities of lithium to the formation of suspended Li colloids, emulsified by impurity level quantities of Li_2O and Li_3N; however, it can be observed in

Figure 1.4 (b) that the amount of Li dispersed in LiCl was not highly dependent upon the concentration of either [1]. It is therefore reasonable to suggest that the quantity of dispersed lithium observed in these studies, up to 2-3mol%, was present in the form of an unidentified complex or subhalide in addition to the quantity physically dissolved in the solution.

Hébant *et al.* reached the conclusion that Li_2Cl is formed at the interface of molten lithium and eutectic LiCl-KCl salt [87, 94]. This research employed density functional theory to determine the most thermodynamically stable subhalide possible in the molten LiCl-KCl-Li_2O-Li-K system, and subsequently used electrochemical techniques for experimental validation of this hypothesis. These reports noted that the formation of Li_2Cl was independent of the presence of KCl, and was detectable at the LiCl-Li interface, although experimental data was not provided. The presence of Li_2Cl as a subhalide in molten LiCl-Li_2O-Li suggests that the solution may be readily described by the second of Bredig's models [70, 87, 94].

In addition to being termed a subhalide, Li_2Cl can be classified as a hyperlithiated compound. Hyperlithiated compounds have been experimentally observed by several researchers and are of significant academic interest due to their apparent departure from the octet rule of quantum mechanics [95-97]. Additionally, experimental observation of hyperlithiated oxygen, in the form of Li_3O and Li_4O has been reported, a fact that is potentially important to the LiCl-Li_2O-Li electrolyte in question [97-100]. The role of Li_2O in the LiCl-Li_2O-Li system is largely unknown. It has been demonstrated that Li_2O

dissociates nearly completely in LiCl, however how the O^{2-} ion interacts with Li is not yet understood [101].

The electrical conductivity of the LiCl-Li system is exceedingly small compared to other metal-salt solutions, specifically the other alkali-alkali halides [71, 82-84, 102]. This behavior has been attributed to the formation of a high population of bound F-centers in the LiCl-Li system, as opposed to the loosely bound electrons that are more probable in alternative systems; for example Na-NaI. The low electrical conductivity of the LiCl-Li system is further evidence that the system is more adequately described by the more complicated model of metal-salt solutions where chemical interactions between the metal and salt result in the consumption of what would be free electrons, thereby suppressing electrical conductivity under metal saturated conditions. This conclusion was recently stated in a review of molten salt electrolytic processes by Masset *et al.* [103]. Similar conclusions were reached during the studying "metal fog" formed during the electrolysis of lithium from LiCl-KCl where authors stated: *"The metal fog generated in the Li electrolysis with larger cathodic current is hardly explained by simple dissolution" [104]*. This report further hypothesized that the phenomena observed could be explained by the formation of a salt soluble compound other than that of metallic lithium.

Recent research conducted in our laboratory has reported evidence that molten LiCl-Li, in the presence or absence of Li_2O, exhibits the Raman spectroscopic characteristics of the lithium nanoclusters Li_8 [105]. Should Li clusters be miscible with molten LiCl, a well-defined solubility limit of Li in LiCl may not exist due to the dispersion mechanism of colloidal suspension in addition to physical dissolution. In this

case, the quantity of Li that may be suspended or dispersed under a given set of conditions would be highly dependent upon experimental factors such as thermally induced mixing of the melt or mechanical agitation. Furthermore, the presence of a second Li phase, in addition to bulk metallically bonded Li, would complicate the thermodynamics of the LiCl-Li system as each phase would possess separate activities. It is suggested that such effects are the cause of the previously unattributed physical properties of molten LiCl-Li.

In summary, it is suggested that the nature of the LiCl-Li_2O-Li electrolyte is likely a superposition of multiple dispersion phenomena, and does not fit exclusively into either of Bredig's models. While the true dissolution of ~0.5mol% Li in LiCl may be successfully described by the F- center model, in accordance with alternative alkali–alkali halide solutions, the formation of subhalides and or dispersion of Li nanoclusters suggests that the second model is more adequate. Therefore, it is suggested that the LiCl-Li_2O-Li electrolyte is a complex solution consisting of at least two phases; Li dissolved in LiCl-Li_2O, and a dispersed Li rich phase.

1.5 LiCl-Li_2O-Li and the Reduction of Actinide Oxides:

Evidence of the formation of LiCl-Li_2O-Li during the electrolytic reduction process includes the coloring of the molten salt from the formation of "metal fog": dark purple ribbons in the relatively transparent LiCl-Li_2O solution, and the bubbling of salt samples upon contact with water [104, 106-108]. These observations, along with the low current efficiencies reported throughout the electrolytic reduction literature, are indicative of the presence of metal-salt solutions, and similar to the observations that led their study

in the first half of the 20th century [79, 80, 82, 84]. As will be shown in the following examples, the generation of a complex LiCl-Li_2O-Li electrolyte during the reduction of actinide oxides has significant implications regarding the oxide reduction process.

A method of electrochemically recycling metallic Li throughout successive UO_2 reduction runs has been developed specifically to control the excess Li that accumulates in the cathode assembly [68]. This investigation noted that the accumulation of excess Li in the cathode assembly could be detrimental to post reduction processes such as salt vaporization and electrorefining. In these experiments a typical reduction run of UO_2 was completed by passing 190% of the theoretical charge through the electrolytic reduction cell for the given quantity of UO_2. The reduced U cathode assembly that contained excess Li was then polarized as the anode against a stainless steel rod at +0.3V; to oxidize the Li from the metallic U deposit and reduce Li^+ at the stainless steel rod. The deposited Li was then used as a reducing agent in the reduction of a new batch of UO_2, where it reacted chemically with the UO_2 to regenerate the Li_2O lost in the initial UO_2 reduction run. This study successfully demonstrated all of these steps in succession, and proved that excess Li could be recycled in subsequent electrolytic reductions of UO_2. It is important to note however, that Park *et al.* stated numerous times that the electrolyte was saturated with Li and that losses of charge transfer, along with Li and Li_2O, occurred during the separate stages of the recycling process.

Alternatively, Herrmann *et al.* have employed a secondary circuit to oxidize Li prior to its dissolution in an attempt to suppress Li attack of the Pt anode [38, 66, 67, 109]. A power supply was connected between the cathode lead, a stainless steel rod at the

center of the cathode, and the exterior of the stainless steel basket of the cathode assembly. This power supply was energized in a galvanostatic mode when the cathode lead approached the $Li|Li^+$ potential. The current passed through this secondary power supply, I-sec, the potential of the basket wall, V-BW, and the potential of the cathode lead, V-CL, are shown in Figure 1.2 (e). Although the basket wall is maintained at a positive potential with respect to the cathode lead, it is observed that the OCP of both exhibit the $Li|Li^+$ potential during the cell interruption at approximately 1.5 A-hr. No quantitative information regarding the success of this configuration in the containment of Li could be found in the published literature, however it was noted that the 1 mm diameter Pt wire anode was used in six successive reduction runs without exhibiting extensive corrosion [67].

The generation of excess Li during the reduction process could result in decreased current efficiencies by several mechanisms: reduction of Li^+ consuming an electron and dissolving into solution without reacting with an actinide oxide, dissolved Li reacting with $O_{2(g)}$ prior to complete evolution resulting in the regeneration of Li_2O, oxidation of dissolved Li at the anode, side reactions of Li with alternative materials exposed to the melt, as well facilitating electrical conductivity in the melt. Two technical difficulties exist in the published literature regarding the parasitic reactions of Li that could be used to characterize the low current efficiency of the process. First, the concentration of Li_2O in samples of the electrolyte is commonly quantified by titrating a sample of the salt; assuming that Li_2O in the salt reacts with water to produce basic LiOH. However, if Li is present in the salt sample as well, it will react with water to form $H_{2(g)}$ and LiOH. As a

result, careful analysis of the quantity of $H_{2(g)}$ that results from contacting a sample of the electrolyte with water must be taken into account, and the quantity of LiOH that results from the presence of Li must then be subtracted from the titration measurement. Unfortunately, numerous researchers have employed such a titration methodology without explicitly stating that $H_{2(g)}$ evolution was accounted for [4-6, 39, 68]. As a result, it is difficult to quantify to what degree these measurements are accurate. The technical difficulties associated with quantifying the production of $H_{2(g)}$ and discerning the correct concentration of Li_2O have been previously emphasized [110]. Furthermore, the validity of salt sampling techniques based on freezing salt on a dipstick is questionable due to the highly temperature dependent phase stability of LiCl-Li solutions [70, 72].

The second difficulty in quantifying the degree to which Li is present in the LiCl-Li_2O electrolyte is that Li is known to react with nearly all molecular compounds, many of which are frequently in contact with the electrolyte during the reduction process. Dworkin *et al.* first noted that LiCl-Li was observed to react with, and physically degrade both synthetic sapphire and single crystal MgO [70]. Commercial grade MgO is widely employed as a crucible material and as an electrode shroud in the oxide reduction process [41, 76]. Li dispersed in LiCl-Li_2O has additionally been reported to degrade Y_2O_3 stabilized ZrO_2 [111]. Furthermore, if present as a colloid in the electrolyte, metallic lithium is known to react spontaneously with nearly all commercial ceramics [112]. All of these potential reactions would result in the consumption of Li and a loss in current efficiency. Significantly, recent research by Choi *et al.* into the development of anode shrouds noted degradation of MgO during the reduction of UO_2 [41]. Figure 1.5 shows

two anode shrouds fabricated of MgO and MgO (3wt%)-ZrO_2 before and after being used to reduce UO_2 in LiCl-Li_2O. Considering the physical separation of the anode shroud and the cathode assembly, the degradation of the materials was attributed to reactions with Li dissolved in the electrolyte.

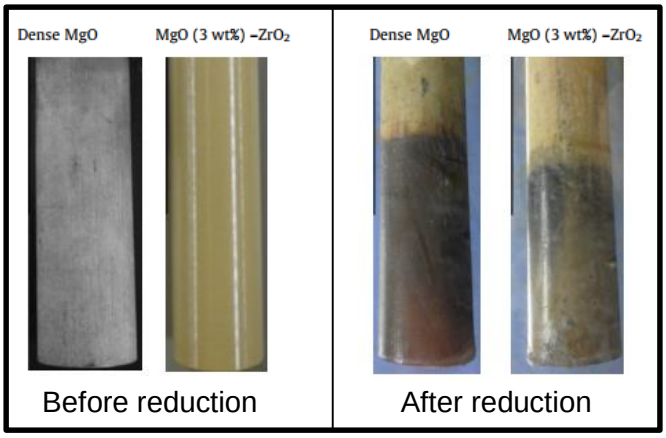


Figure 1.5: MgO and MgO (3wt%)-ZrO_2 anode shrouds before and after being employed for reducing UO_2 in LiCl-Li_2O at 650°C. The visable degradation was atributed to chemcial attack by disolved Li in the electrolte [41].

MgO-ZrO_2 coated stainless steel mesh (STS) was investigated as an alternative anode shroud material [41]. As shown in Figure 1.6, MgO-ZrO_2 coated STS was shown to be stable when exposed to molten LiCl-Li_2O at 650°C over the course of 21 days; however, it was found to be degraded when employed as the anode shroud during the electrolytic reduction of 20g of UO_2 over the course of 1.5 hours. The degradation that occurred when the material was employed as an anode shroud, and not during the extended period of exposure, was attributed to the accumulation of Li in the electrolyte during the reduction of UO_2. Similar degradation was reported when MgO-ZrO_2 coated STS was exposed to LiCl-Li_2O containing 0.3wt%(~2mol%)Li. Interestingly, the authors noted explicitly that the degradation resulting from exposure to the LiCl-Li_2O-0.3wt%Li

solution was similar to the damage experienced during the reduction run, however the data was not provided.

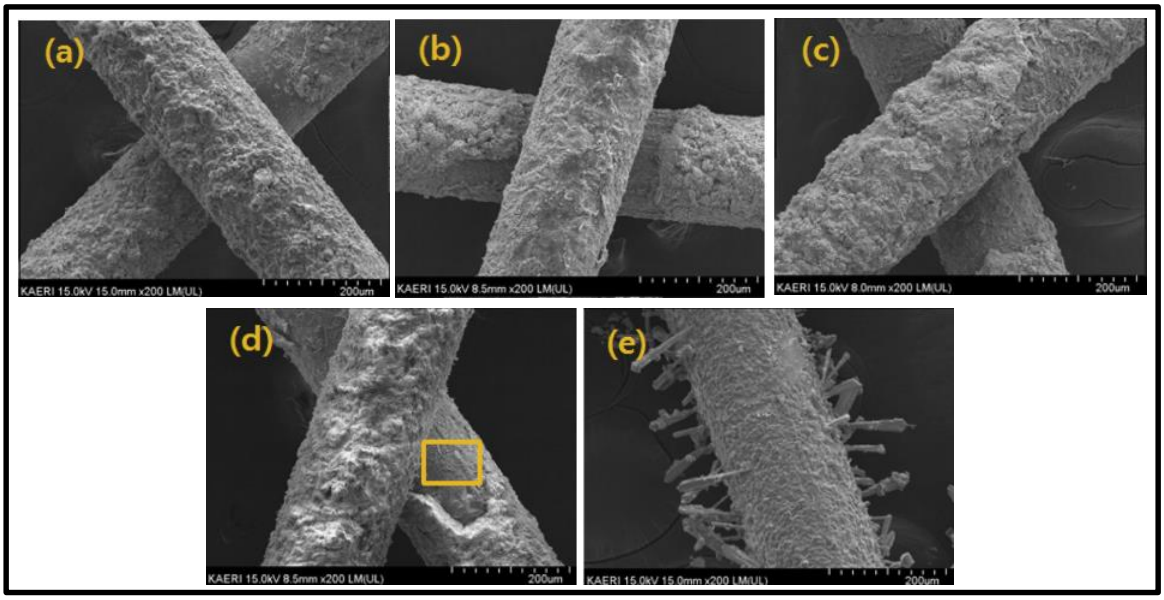


Figure 1.6: SEM micrographs of MgO-ZrO_2 coated STS meshes (a) origional, and exposed to LiCl-Li_2O at 650°C for (b) 7 days, (c) 14 days, (d) 21 days, and (e) after bening employed as an anode shroud during the electrolytic reduction of 20 g of UO_2 over the cource of 1.5 hours. The damage to the ceramic coatings of the steel shown in (e), and not as a result of extended period sof exposure, was atributed to the presince of Li in the molten salt acumulated during the operation of the reduction cell [41].

These observations suggest that Li disperses into the electrolyte during the reduction process up to the limit of physical solubility. The rate at which LiCl-Li_2O-Li reacts with MgO is currently unknown, and as a result it is impossible to suggest to what degree Li is consumed by MgO throughout the electrolytic reduction process. The reaction of dissolved Li and MgO is suggested to be a significant loss of current efficiency and a source of experimental error in numerous reports; specifically those employing MgO crucibles.

Lithium has been recovered from molten LiCl-Li_2O by reducing Li^+ at a cathode inside a porous MgO shroud [27]. After accumulating Li in the cathode container, the

container was lifted out of the melt and the Li was extracted using a vacuum syphon. It was suggested that the fluid salt drained from the porous ceramic while the Li was contained inside the MgO. It was reported that greater than 95% of the reduced Li was recovered using this method; however, this study falls victim to the previously mentioned experimental uncertainties associated with quantification of the concentration of Li and Li_2O in molten LiCl. Furthermore, the containment of reasonably pure Li in MgO is questionable due to the chemical reactivity of liquid Li.

Sakamura *et al.* noted that the oxide reduction process's current efficiency decreased, and the Li_2O loss rates increased, when a cathode assembly was rotated during reduction [5]. This observation was attributed to the agitation of the electrolyte causing accelerated dissolution of Li from the cathode. Similar phenomena were reported by INL where consistent Li_2O concentrations were recorded for a number of reduction runs that employed stationary electrodes, but became less repeatable, and with greater losses of Li_2O, when the cathode basket was rotated [43]. Further investigations into these effects are suggested to suppress losses of current efficiency and Li_2O consumption.

Simpson *et al.* were successful in modeling literature data on the kinetics of the lithium reduction process, not electrochemically driven, using a shrinking core model of the UO_2 pellets by employing literature data of the Li solubility limit as $1.7x10^{-4}$ mol/cm^3 (~0.5mol%) [77, 113]. This report explicitly stated that the diffusivity of the melt in the porous uranium metal was found to be exceedingly high at $9.7x10^{-4}$ cm^2/s, and suggested that the concentration of lithium in the salt might have been significantly greater than the solubility limit implied. Subsequent modeling of the electrolytic reduction process, also

conducted by INL, reported an effective diffusion coefficient considerably closer to analogous systems by employing a higher concentration of lithium in the salt, citing the solubility limit as 0.0058 g/cm^3 (~2.3mol%) [42]. This value is in agreement with the higher concentrations of dispersed lithium previously discussed, however the origin of this solubility limit could not be found in the cited reference by Park *et al.* [39]. While the adaptation of diffusion limited kinetic models has been shown to be effective in predicting process kinetics, the inconsistency in the values of lithium concentration employed should be further investigated.

The accumulation of excess Li has been stated to coincide with a loss of Li_2O as a result of the continued electrolysis of Li_2O after the intended reduction of the actinide oxides, due to the inability of the operator to know when the reduction of the actinide oxide is complete [68]. This conclusion is conspicuous however, as the depletion of Li_2O has been observed to be continuous throughout the reduction process [43, 60]. The reported rates of Li_2O consumption during the reduction process vary widely between references; an inconsistency that is attributed to the previously mentioned difficulties in quantifying the concentration of Li and Li_2O in the salt, the quantity of Li that is lost to side reactions, and the quantity of Li and Li_2O that remain in the cathode basket [6, 38, 63, 75, 114]. Furthermore, the concentration of Li_2O in the electrolyte can be diminished if the rate of O^{2-} oxidation at the anode exceeds the transport of O^{2-} from the UO_2 out of the cathode assembly. Continued oxidation of O^{2-} at a greater rate than the electrolyte can be replenished from the reduction of UO_2 would result in the direct electrolysis of Li_2O without inducing the reduction of further UO_2.

The final aspect of the role of lithium in the electrolytic reduction of actinide oxides to be discussed is the underpotential deposition (UPD) of Li^+. UPD is the formation of single monolayers of atoms on a foreign substrate at a potential more noble than is required to reduce successive bulk metal onto the initial monolayer [115-118]. The UPD of Li^+ from molten LiCl has been reported to occur on the surface of U_3O_8 as well as numerous other substrates [19, 119-121]. Application of modern theory of UPD is beyond the scope of this review; however it is illuminating to note the following basic effects. UPD occurs when the binding energy between a deposited species and a substrate is greater than the binding energy of the pure metallic species. As a result, there is an energetic benefit to the deposition of a monolayer of metal onto the foreign material compared to the subsequent reduction of the species onto like atoms. This effect manifests itself in a thermodynamic activity of the reduced metal being less than unity as long as the foreign substrate is exposed. As predicted by the Nernst equation, this results in the first monolayer being deposited at a more noble electrochemical potential.

While the UDP of Li^+ from LiCl-Li_2O has been shown to occur on U_3O_8, it was explicitly not observed on a Ni wire in the same study [121]. Numerous alternative CV's of metal electrodes in LiCl-Li_2O have also not detected any UPD current [59, 66, 122]. It has been demonstrated that the activity of Li in LiCl is significantly less than unity, even under Li saturated conditions [72]. This observation is highly supportive of the feasibility of Li^+ UPD, as it would raise the $Li|Li^+$ reduction potential. Similar low activity behavior of Li in LiCl was reported when investigating the deposition and intercalation of Li from LiCl into graphite [120]. This work is of specific interest as the authors noted that both

the kinetics of Li deposition, and the reduction potential itself, were highly dependent upon the porosity of the graphite substrate. This effect could play an analogous role in the UPD of Li^+ on porous uranium oxides.

Despite these observations, the UPD of Li^+ on U_3O_8 is interesting because metallic Li reacts spontaneously with U_3O_8 [39]. In order for UPD of Li^+ to occur on the surface of U_3O_8, an electron would be required to transport through the U_3O_8 to the electrolyte interface, and reduce the Li^+ ion. This is exceedingly unlikely as the reduction potential of U_3O_8 is more noble than that of Li^+. If this process were to occur, the recently formed Li would then immediately react with the U_3O_8. Significant theoretical difficulties exist in this respect due to the non-unit activity of Li in LiCl and the complex valance structure of U_3O_8 and intermediately reduced lithium uranates. Further investigations, both theoretical and experimental, are required before an understanding of these effects can be presented. Therefore it is probably not accurate to discuss reduction of Li^+ at U_3O_8 in terms of UPD.

1.6 Summary:

Metallic lithium is inevitably formed during the electrolytic reduction of actinide oxides in LiCl-Li_2O. Polarization of the cathode below the reduction potential of Li^+ is required to facilitate efficient and high yield reductions. As a result, metallic lithium is deposited on the cathode basket throughout the reduction process. Li has been observed to be in physical contact with the cathode and the molten LiCl-Li_2O electrolyte. The solubility of Li in molten LiCl-Li_2O is well documented, and yet the amount of Li that disperses into the electrolyte during the reduction process has not been quantified.

Dispersion of Li in molten LiCl is reported to occur via multiple possible mechanisms: true physical dissolution, the formation of subhalide complexes, and colloidal suspension as nanoclusters. The true dissolution of Li in LiCl appears to have a solubility limit of ~0.5mol%, while the limit of dispersion may not be well defined.

The effect of the generation of a LiCl-Li_2O-Li electrolyte on the operation of the electrolytic reduction process is not known due to the experimental difficulties associated with isolation of potential variables. It is suggested that dispersed Li is a likely cause for the reported low current efficiencies of the process due to recombination of Li with oxygen to form Li_2O. Additionally, the loss of Li dissolved into the electrolyte and via reactions with unintended materials represents a possible consumption mechanism of Li_2O and electric charge. The degradation of ceramic materials exposed to the electrolyte, notably MgO, have been reported to occur due to the presence of dispersed Li, however the reaction rates associated with the consumption of Li are yet unknown. Further research regarding these effects is essential to understand the role of lithium in the electrolytic reduction of actinide oxides.

1.7 Corrosion in Molten Salts and Liquid Metals:

Previous research and literature reviews have demonstrated that material degradation proceeds through separate mechanisms in molten salts [123, 124], molten salts containing dissolved oxides [125, 126] and liquid metals [127]. As the mechanisms of material interactions with the LiCl-Li_2O-Li system are widely unknown, but are likely to contain aspects observed in each of these three systems, the following section discusses the general corrosion phenomena associated with these systems independently.

The term corrosion is used throughout this dissertation to refer the degradation of a material that results from interactions with a given environment. This definition is therefore applied to chemical, electrochemical, and physical alterations to materials that results from being exposed to a given set of conditions.

1.7.1 Corrosion in Molten Alkali-Halide Salts:

Corrosion of metals or alloys in pure alkali-halide molten salts, for example LiCl, is governed nearly exclusively by the presence of impurities [124]. These strongly ionically bound salts are typically lower in free energy of formation than transition metal halides [125]. Therefore, in the absence of impurities no significant corrosion reaction will occur between an engineering alloy and a molten alkali-halide salt. However, impurities are always present in practical systems and as a result completely dictate corrosion in molten alkali-halide salts. H_2O is by far the most important contaminant regarding corrosion in molten salts containing LiCl due to the highly hygroscopic nature of LiCl. The effects of the presence of H_2O on the electrochemistry of molten LiCl-Li_2O as it applies to the electrolytic reduction of actinide oxides has been the subject of recent research for this reason [106, 128]. Molten LiCl reacts with H_2O to form hydrochloric acid and lithium hydroxide as governed by the reaction 6.

$$LiCl_{(molten)} + H_2O \rightarrow LiOH + HCl \qquad \text{Reaction (6)}$$

As a result of Reaction 6, when H_2O is present in molten LiCl, the oxidation of an alloying element M can result in the formation of a salt soluble chloride via reaction 7.

$$M + nHCl \rightarrow M^{n+}Cl_n + \frac{n}{2} H_{2(g)} \qquad \text{Reaction (7)}$$

Obtaining molten LiCl in the complete absence of H_2O is not practical for industrial scale processes [106, 125, 129-131]. As a result, it can be expected that corrosion of materials as a result of reactions 6 and 7 will occur to some degree in all melts containing LiCl. Methods employed in the current study to dry LiCl, adopted from findings by Gese *et al.* [106, 128], are discussed in Chapter 2. Additionally, examples of the effect of the presence of residual H_2O on the corrosion of materials exposed to molten LiCl-Li_2O-Li are demonstrated in Chapter 3.

It has been demonstrated by previous authors as well in the current study that the standard reduction potential of Li^+ is more cathodic than LiOH and HCl in molten LiCl at 650°C [106, 132]. As a result, the formation of a molten solution of LiCl-Li_2O containing dissolved Li will not occur until reactions 8 and 9 have progressed to completion.

$$Li + LiOH \rightarrow Li_2O + \tfrac{1}{2}H_2 \qquad \text{Reaction (8)}$$

$$Li + HCl \rightarrow LiCl + \tfrac{1}{2}H_2 \qquad \text{Reaction (9)}$$

Therefore, the addition of metallic Li will result in the purification of molten LiCl-Li_2O via the progression of reactions 8 and 9. These reactions will suppress the driving forces for the previously discussed corrosion mechanism (reactions 6 and 7) by removing the oxidizing and reducing agents from the melt. A similar effect was employed extensively to inhibit corrosion during the molten salt reactor (MSR) program at Oak Ridge National Laboratory (ORNL) [133]. Metallic Be was added to molten fluoride salts in the MSR where it functioned as a dissolved sacrificial anode to scrub impurities from the system. This approach, termed “redox control”, was observed to be

highly effective at mitigating corrosion in the MSR program as well as in alternative molten fluoride salts [134, 135].

It has been reported that LiH is stable in molten salts containing LiCl at temperatures of both 500 and 650°C [106, 132, 136]. Evidence suggesting the presence of dissolved Li in molten LiCl prior to the complete reduction of LiOH has also been reported [128]. Therefore, the possibility exists that reaction 10 will occur in molten LiCl in the presence of H_2O and excess Li.

$$2Li + LiOH \rightarrow Li_2O + LiH \qquad \text{Reaction (10)}$$

The effect of the presence of LiH on the corrosion of materials exposed to molten salts is currently unknown. It is hypothesized that the presence of LiH in impure melts of LiCl-Li_2O-Li is the mechanism behind certain results presented in Chapter 3 of this study.

1.7.2 Corrosion in Molten Salts Containing Oxides:

Corrosion processes in molten salts containing dissolved oxides, or in the presence of O_2, are different than in pure alkali-halide melts in that materials exposed to these melts will oxidize to some degree in the absence of impurities [125]. As a result, corrosion in these systems is governed by the degree to which alloys form stable surface oxides that protect against continued oxidation of the underlying alloy. Prior to exposure to molten salts, the surface of engineering alloys is typically comprised of transition metal oxides that suppress corrosion [137]. Stainless steel possessing a surface film of chromium oxides (Cr_2O_3 will be used as representative chromium oxide) will be used as a

prototypical example in this discussion due to its relevance to the current work. Under typical operating conditions, for example exposure of stainless steel to a dilute aqueous solution of H_2SO_4, the corrosion of bulk material will not occur before the Cr_2O_3 surface film is compromised. Prior to the destruction of the Cr_2O_3 film, the corrosion of the underlying alloy is kinetically limited by diffusion through the surface oxide. As a result, corrosion suppression in oxidizing environments is typically achieved through the formation of stable and protective surface films.

The solubility of transition metal oxides in molten salts containing dissolved oxides is non-zero. As a result, there is a thermodynamic driving force for the dissolution of protective surface films from engineering alloys. The rate at which dissolution occurs is governed by the chemistry of the melt / material interface. The principle goal of corrosion protection in these environments is therefore the identification of alloys that form protective surface films with minimal solubility under a certain set of conditions.

The corrosion of stainless steel by molten salts containing oxides proceeds though the destruction and dissolution of Cr_2O_3 by either acidic or basic dissolution, shown as Reactions 11 and 12, respectively.

Acidic dissolution: $Cr_2O_3 \rightarrow 2Cr^{3+} + 3O^{2-}$ Reaction (11)

Basic dissolution: $Cr_2O_3 + 2O^{2-} + 3/2O_2 \rightarrow 2CrO_4^{2-}$ Reaction (12)

The most successful model used to describe corrosion in molten salts containing oxides, governed by the stability of surface films, is derived from the Lux-Flood theory of basicity. In this model, the basicity (pO^{2-}) is defined as the negative log of the activity of the O^{2-} ion in the melt [126, 138-140]. Molten salt constituents can be classified as O^{2-}

acceptors or donors in an analogous manner to acids and bases in aqueous electrochemistry. Acidic molten salts containing little to no O^{2-} corrode materials through the oxidation and subsequent dissolution of metal cations in a manner similar to Reaction 11. Alternatively, in basic salts containing excessive quantities of O^{2-} the primary mode of material degradation is the basic dissolution of anion complexes, shown as Reaction 12. An optimal basicity exists between these two corrosion mechanisms such that material dissolution is minimized. Optimal basicity is a colloquial phrase for the salt chemistry that results in the minimum solubility of corrosion products in the melt, and therefore minimizes the thermodynamic force for dissolution of surface films.

Corrosion in molten sulfate salts has been researched extensively due to its relevance to the coal power industry, and is commonly used as an example of molten salt corrosion chemistry [125, 126, 139, 141] . The basicity in molten sulfate systems is typically discussed based on the equilibrium of Reaction 13.

$$SO_4^{2-} \leftrightarrow SO_3 + O^{2-} \qquad \text{Reaction (13)}$$

With a basicity of: $pO^{2-} = -\log a_{O^{2-}} = -\log \frac{K}{P_{SO_3}}$

Where K is a temperature dependent equilibrium constant of Reaction 13. In this example, SO_3 is an acid or O^{2-} acceptor, while SO_4^{2-} is a base or an O^{2-} donor. The corrosion rate of stainless steel exposed to molten Na_2SO_4 is then discussed based on the basicity of the melt and how it governs the balance between the acidic and basic dissolution mechanisms. This methodology has resulted in the use of plots similar to the one shown as Figure 1.7 for predicting corrosion rates in melts of varying basicity.

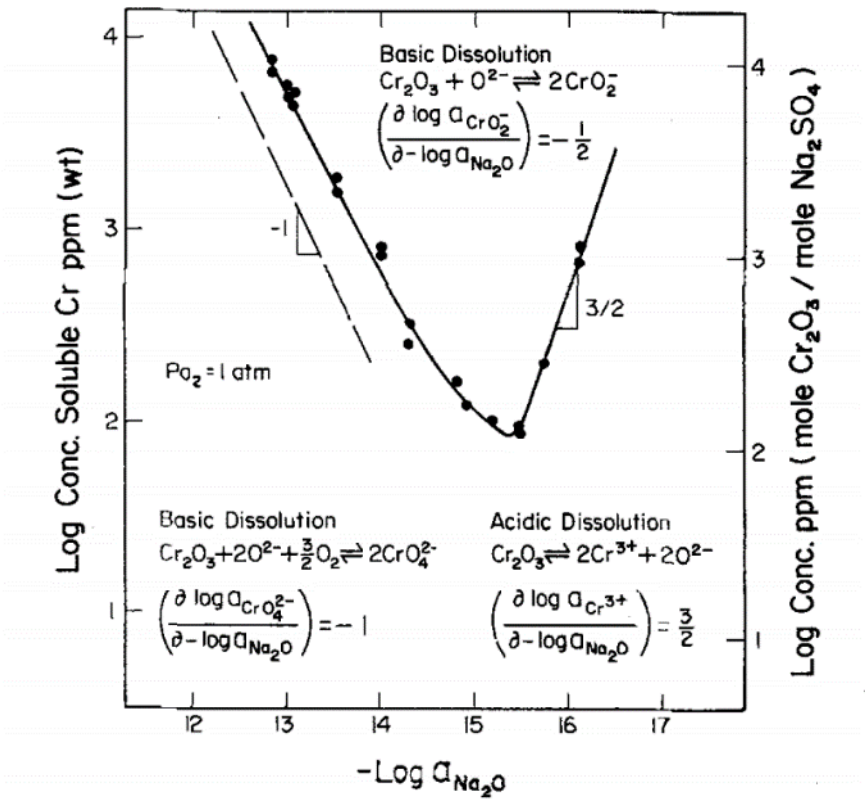


Figure 1.7: Solubility of Cr_2O_3 in fused Na_2SO_4 at 1200K and $1.01x10^5$ Pa oxygen [139].

As shown in Figure 1.7, the solubility of Cr_2O_3 in molten Na_2SO_4 is not zero at any basicity. Therefore, some quantity of the Cr_2O_3 surface film on stainless steel will dissolve into molten Na_2SO_4 in the presence or absence of O_2. In oxygen deficient melts the acidic fluxing mechanism is observed to drive the dissolution of Cr_2O_3, while at higher basicity (approximately greater than pO^{2-}=15), the basic fluxing mechanism is observed to dominate. Corrosion mitigation in this system is typically achieved by the formation of a protective $NaCrO_2$ surface film that minimizes the rate of both dissolution mechanisms over an intermediate range of pO^{2-} [126, 139].

An important difference between corrosion in molten salts containing oxides and aqueous systems should be clarified to avoid confusion. In aqueous corrosion, the pH of

the electrolyte can generally be directly related to the driving force for the oxidation or reduction of an element in contact with the solution. In a basic aqueous electrolyte (containing a high concentration of OH^-) the system has a driving force for oxidizing O^{2-} to form $O_{2(g)}$. This oxidation reaction liberates electrons to drive reduction reactions in alternative elements. As a result, corrosion products formed in basic aqueous electrolytes tend to be more reduced. For the same reason corrosion products formed in acids tend to have higher oxidation states as their electrons get consumed by the reduction of H^+. However, it can be observed in Reaction 12 as well as in Figure 1.7 that this is not the case in molten salts containing oxides. The thermodynamic driving force in these systems is the activity of O^{2-} in the melt; as a posed to the balance of H^+ and OH^- that dictates pH in aqueous systems. Basic molten salts will tend to donate O^{2-} ions and *increase* the oxidation state of corrosion products. Again this can be observed in Reaction 12 where Cr^{3+} is oxidized to Cr^{6+} via the basic dissolution mechanism. This distinction is important in understanding the role of O^{2-} in the electrochemistry of the molten LiCl-Li_2O-Li system.

Extensive research on the corrosion of engineering alloys exposed to molten LiCl-Li_2O has indicated that corrosion in these systems is governed by the basicity of the melt in an analogous manner to the Na_2SO_4 system [138, 142-145]. $LiCrO_2$ has been reported to be the primary surface film formed on austenitic Fe-Cr-Ni alloys exposed to molten LiCl-Li_2O [138]. Li_2O is known as a basic metal oxide and therefore the basicity in the molten LiCl-Li_2O system is based on Reaction 14.

$$Li_2O \rightarrow 2Li^+ + O^{2-} \qquad \text{Reaction (14)}$$

With a basicity of: $pO^{2-} = -\log a_{O^{2-}} = -\log \frac{K}{P_{2Li^+}}$

While the Lux-Flood model of molten salt basicity has been shown to be applicable to the molten LiCl-Li_2O system, little is known regarding how the accuracy of this model is effected by the inclusion of Li in the melt. It is anticipated that key information regarding the mechanisms of material degradation in molten LiCl-Li_2O-Li can be obtained by understanding whether or not the system behaves as an extremely basic salt. Chapters 3 and 6 of this dissertation investigate this hypothesis to determine if the inclusion of Li in LiCl-Li_2O has the effect of varying the activity of the O^{2-} ion (pO^{2-}), or if it behaves independently of the LiCl-Li_2O molten salt at a fixed basicity.

1.7.3 Corrosion in Liquid Lithium:

Lithium chemistry is a complex field in its own right and has been the subject of multiple texts and reviews [112, 146-148]. Notable examples of Li chemistry include that it is the only element that spontaneously reacts with N_2 at standard temperatures, and that despite not having a 2p electron orbital Li frequently is observed in molecular bonding characterized by 2p electron states, for example Li_6C [149]. Material interactions with liquid Li have been investigated primarily by NASA and the fusion reactor community due to the low density of liquid Li and its desirable neutronic properties [112, 127, 150]. No commercial molecularly bound material (oxide, nitride, carbide etc.) has been identified that is stable upon exposure to Li significantly above its melting point (approximately 180°C) [70, 112, 144]. Material interactions with liquid Li have been primarily investigated through the study of interactions of ultra-pure Li with various

transition and refractory metals. Interactions between liquid Li and Fe as well as the refractory metals is nearly undetectable when ultra-high precursors and strict atmospheric controls are employed [127, 151-153]. Alternatively, exceptionally low (ppm) levels of non-metallic impurities such as nitrogen, oxygen and or carbon have been found to lead to rapid liquid metal attack. An illuminating example of the extreme dependence of such properties on impurity concentrations is the observation of the corrosion rate of vanadium being 100 times greater in liquid sodium (an alkali metal analogous to lithium) containing 5-15ppm oxygen compared to liquid sodium containing <1ppm oxygen [150].

Attack by liquid Li is often caricaturized by softening effects, decarburization, intergranular cracking and the formation of low melting point alloys [150]. The differences between these modes of degradation and the previously discussed oxidation phenomena associated with molten salt corrosion are important to note when considering material interactions with molten LiCl-Li_2O-Li.

Significant theoretical challenges arise when attempting to consider molten solutions of LiCl-Li_2O-Li as liquid metal. It is not clear to what degree liquid metal corrosion theories can be applied to the LiCl-Li_2O-Li system due to the abundance of non-metallic impurities, specifically oxygen, present in the melt. Should liquid Li exist as metal in the molten LiCl-Li_2O-Li system, it is likely saturated with oxygen and chlorine. It is currently unknown if liquid Li under these conditions is as reactive or degrading as it is in a more purified form.

1.8 Outline Material Interactions with Molten LiCl-Li_2O-Li:

The molten electrolyte formed during the electrolytic reduction of actinide oxides is a ternary molten solution of LiCl containing varying quantities of dissolved Li_2O and Li. Investigation of material interactions with molten solutions of LiCl-Li_2O-Li requires an understanding of both the corrosive effects of molten salts as well as liquid metals. The different degradation mechanisms that govern material interactions with these systems require a new theory to be developed specific to molten LiCl-Li_2O-Li. Such a theory must account for the unusual physical properties of molten solutions of metals and salts. It must be discerned to what degree the mechanisms of corrosion in LiCl-Li_2O-Li are based on molten salt electrochemistry or on liquid metal effects. Specifically, it is unknown if Li_2O and Li dissolved in molten LiCl behave independently as dissolved oxides and liquid metals, or if they participate in synergistic effects not observed in pure systems of either molten salts or liquid metals.

The aim of this dissertation is to characterize the mechanisms of material degradation during exposure to LiCl-Li_2O-Li, and to discern between electrochemical and liquid metal effects

Chapter 1 reviews the role of lithium in the electrolytic reduction process and the unusual nature of the LiCl-Li_2O-Li electrolyte. This chapter discusses why the formation of metallic Li is necessary to produce high process yields in the electrolytic reduction of actinide oxides. A summary of previous research into the physical chemistry of molten solutions of LiCl and elemental Li is included with a specific focus on the dispersion of Li in the solution. Furthermore, issues regarding the effect of the presence of lithium on

the electrolytic reduction process are discussed. Finally, a review of material degradation in molten salts and liquid metals is included with emphasis applied to the potential corrosion processes that may occur in the LiCl-Li_2O-Li system.

Experimentation in the molten LiCl-Li_2O-Li system, as well as on materials exposed to molten LiCl-Li_2O-Li, poses unique challenges due to the highly impurity dependent and reactive nature of molten solutions containing Li. Chapter 2 discusses the development and operation of the experimental and analytical techniques used in this study.

The processes associated with material interactions with LiCl-Li_2O-Li were largely unknown at the initial stages of this study. Numerous experiments were designed and conducted throughout this study to determine the most accurate and reliable methods of characterizing material interactions with molten solutions of LiCl-Li_2O-Li. Chapter 3 contains preliminary studies conducted to evaluate the generalized effects of the presence of Li on the corrosion of materials exposed to molten LiCl-Li_2O. The principle goal of these studies was quantification of the range of Li concentrations that can be included in molten LiCl-Li_2O before fundamentally altering the corrosion processes that occur in the melt. These studies included exposure testing of stainless steel alloy 316L, nickel-based Inconel alloys 625 and 718, as well as Hastelloy N. General observations presented in this chapter include the formation of protective Cr based surface oxides in melts containing small quantities of Li and the preferential leaching of Cr and Mo by molten solutions containing high concentrations of Li. Observations regarding the sensitivity of corrosion in the molten LiCl-Li_2O-Li system on the presence of trace quantities of

moisture are discussed. Further, the efficacy of methods used to dry the salt to an acceptable level such that these effects are not observed is demonstrated. Finally, it was observed during extended exposure testing that no detectable material dissolution occurs from stainless steel alloy 316L or Inconel 625 as a result of exposure to molten LiCl-1wt%Li2O containing up to 0.3wt% for 50 or 100 hours.

Chapter 4 focuses on evaluation of the dispersion of Li in molten LiCl to assess the range of Li concentrations that are relevant to subsequent corrosion studies. Preliminary experiments were based on chemical analyses of quenched salt, however this methodology was found to result in large experimental errors. Subsequent investigations involved the design, development and operation of a magnetic susceptibility measurement device for characterizing molten solutions of LiCl-Li_2O-Li. Finally, a study employing *in-situ* Raman spectroscopy was conducted in an attempt to characterize the physical chemistry of molten solutions of LiCl and Li with and without the presence of Li_2O.

Characterization of the effect of the presence of Li on the corrosion of stainless steel alloy 316L exposed to molten LiCl-Li_2O, the main focus of this dissertation, is presented in Chapter 5 as the culmination of this dissertation. The results presented in this chapter examine this effect by systematically characterizing the corrosion of stainless steel that resulted from exposure to melts of varying chemistry; molten LiCl containing varying concentrations of Li_2O as well as Li.

The electroless deposition of Ti compounds on materials exposed to molten LiCl-Li_2O-Li was observed during the course of characterizing materials from studies

conducted as part of this dissertation research and the results are presented in Chapter 6. Characterization of these compounds and the dependence of their composition on the chemistry of the LiCl-Li_2O-Li melts were conducted using X-ray photoelectron spectroscopy. This study yielded important information demonstrating the ternary nature of the LiCl-Li_2O-Li system.

Chapter 2 Experimental Methods

2.1 Glove Boxes:

Two glove boxes were used throughout this study; each one retrofitted with equipment to conduct specific experiments. Both glove boxes maintained an Ar atmosphere with impurities of less than 5ppm O_2 and 1ppm H_2O. The first glove box was equipped with a computer controlled LabVIEW program that was previously developed in this laboratory to conduct precision electrochemical experimentation in molten salts without human interactions [49, 154]. This glove box was used for all electrochemical experimentation, as well as those that employed *in situ* Raman spectroscopy.

A mounting assembly was designed and constructed to facilitate the simple exchange of electrode assemblies without deconstructing the computer controlled translation stage used to actuate the system. The improved mounting system is shown in Figure 2.1 as assembled for electrochemical studies. The mounting bracket attached to the translation stage provides a stable platform for adapting specific experimental setups to the system through a simple four bolt attachment observed behind the electrode holding assembly shown in Figure 2.1.

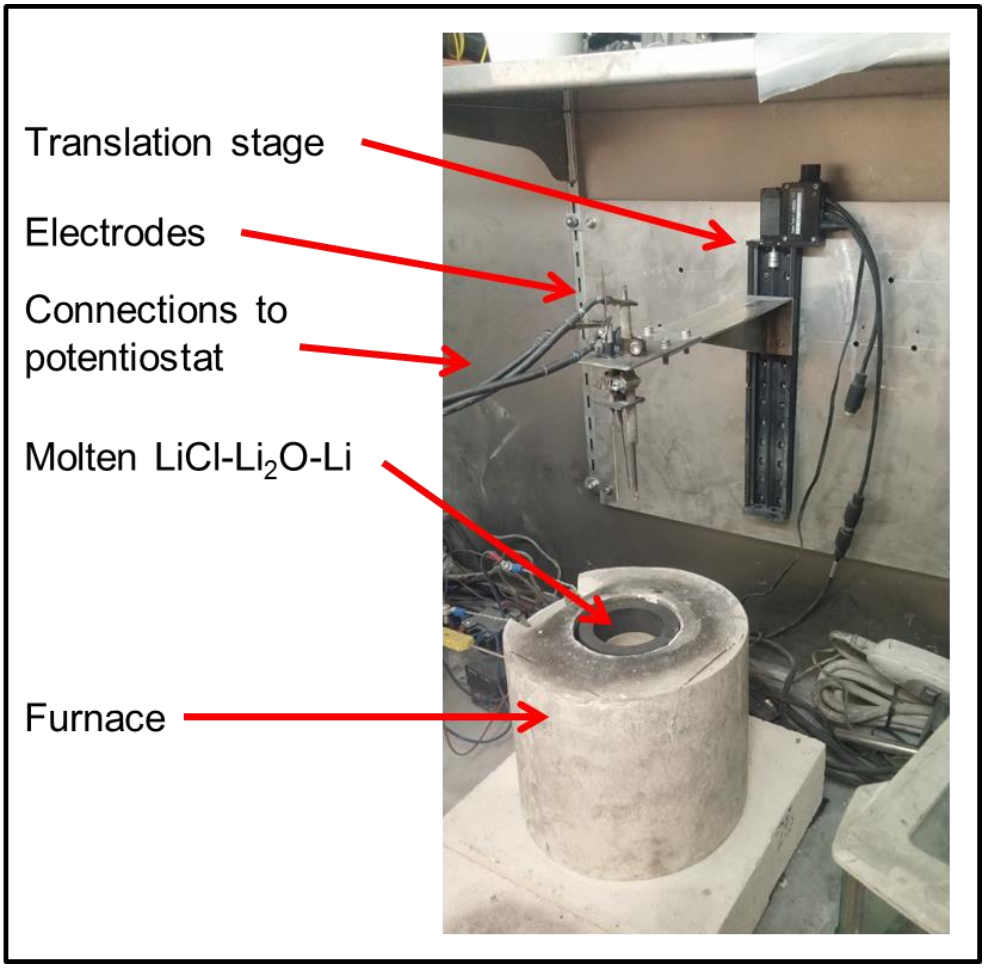


Figure 2.1: Image of the apparatus used to conduct electrochemical testing in molten LiCl-Li_2O-Li. The system was developed with a mounting bracket that can be used to connect to the electrode holding assembly shown here, or the *in situ* Raman telescope shown in Figure 2.2.

A mounting assembly was developed to attach an optical system to the translation stage bracket to facilitate *in situ* Raman spectroscopy of molten LiCl-Li_2O-Li. The ability to adapt a new experimental apparatus to the translation stage mounting bracket without deconstructing the LabVIEW controlled stage highlights the modular nature of this system. The bracket mounting system ensured the Raman optics would be positioned directly above the experimental furnace in such a manner that the beam could be focused into the melt using the translation stage. A custom fiber optic probe and accompanying 20 cm focal length telescope were designed and procured from InPhotonics. This fiber

optic system was coupled to an existing Thermo-Fisher DXR Raman spectrometer (Section 2.9) to facilitate Raman spectroscopy in the glove box / molten salt system. The telescope was constructed out of high temperature tolerant materials capable of functioning at 250˚C for extended periods of time. Temperature calibration experiments were conducted to ensure that the telescope system could be positioned at the focal length of the telescope directly above molten solutions while at 650°C without exceeding the operating constraints of the system. The telescope functioned as the incident and receiving optic to avoid the experimental complexities associated with aligning separate beam paths into and out of the molten salt. This system was employed to conduct spectroelectrochemistry in molten LiCl-Li_2O-Li while the electrodes were positioned in the melt. Images of the Raman assembly are shown in Figure 2.2.

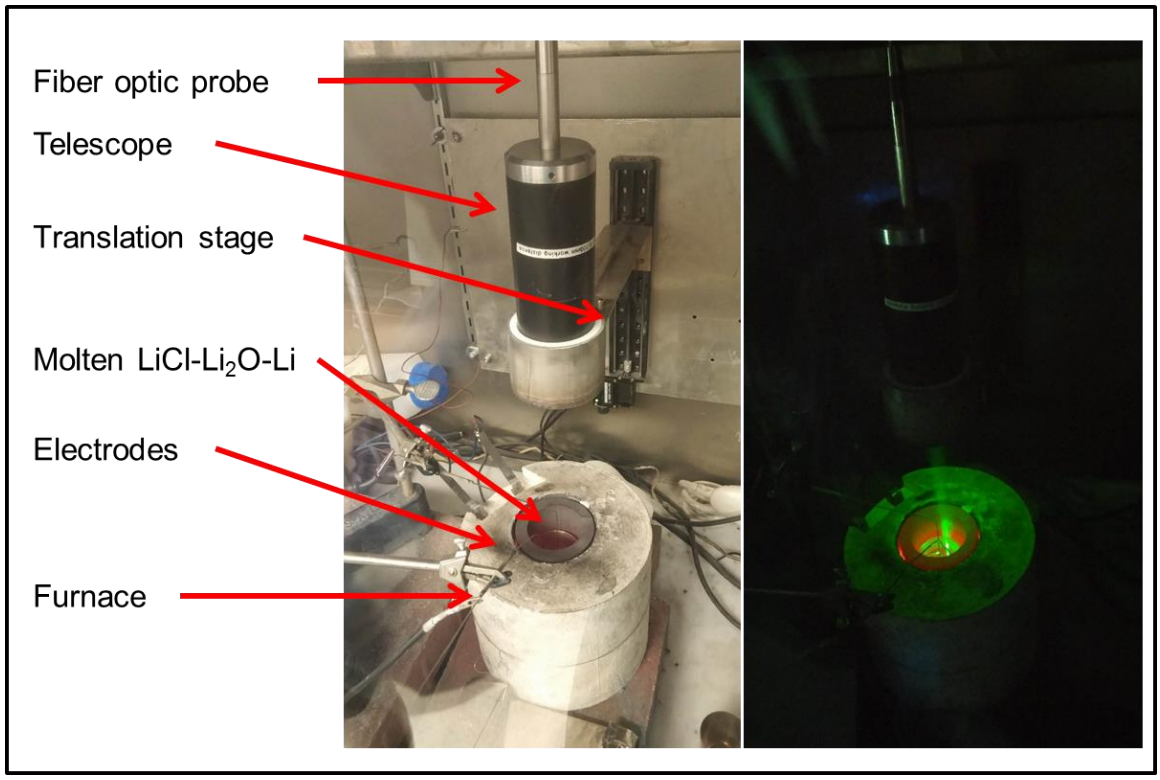


Figure 2.2: The experimental setup used to conduct *in situ* Raman spectroscopy of molten LiCl-Li_2O-Li while conducting electrochemical experiments in the molten salts. An annotated figure is included on the left while an image of the system taken while conducting spectroelectrochemistry is included on the right.

The second glove box used in this study was adapted to facilitate long term exposures of materials to high temperature molten salts in a safe and repeatable manner. Two separate but identical exposure testing systems were constructed in a single glove box to increase experimental throughput. The system was designed to operate two molten salt furnaces simultaneously in order to conduct extended exposure studies (thousands of hours) without significant down time.

In order to operate two furnaces in one glove box without exceeding the temperature limits of the system it was necessary to maintain excellent thermal insulation on top of the furnaces. The critical component that was required to facilitate these

experiments was a sample holder that could operate within the numerous design constraints imposed by the LiCl-Li_2O-Li system. The positioning of the sample coupons in the high temperature environment had to be accurate and repeatable in order to ensure that a consistent sample surface area was exposed during separate experiments. For reasons discussed in Section 3.3, non-metallic or electrically insolating materials could not contact the molten solutions containing metallic Li. As a result, the samples had to be suspended into the melt by a sample holder positioned above the melt in order to avoided galvanic coupling of the samples to the metal crucibles. Furthermore, the system had to be capable of being inserted and removed from the furnace while at temperature. Finally, the use of high temperature tolerant and non-reactive materials was required so that the sample holder assembly could be maintained in the furnace without reacting with the environment or degrading mechanically.

The exposure testing system shown in Figure 2.3 was fabricated in accordance with the previously stated design constraints. Alumina was used as the material in direct contact with the samples for electrical insulation, while low alloy steel and graphite were used for high temperature mechanical support. The system employed redundant container crucibles to mitigate thermal gradients and to protect the furnace incase molten salt spilled from the primary crucible. Two furnace systems analogous to the one depicted in Figure 2.3 were installed in the exposure glove box so that two independent exposure tests could be conducted simultaneously.

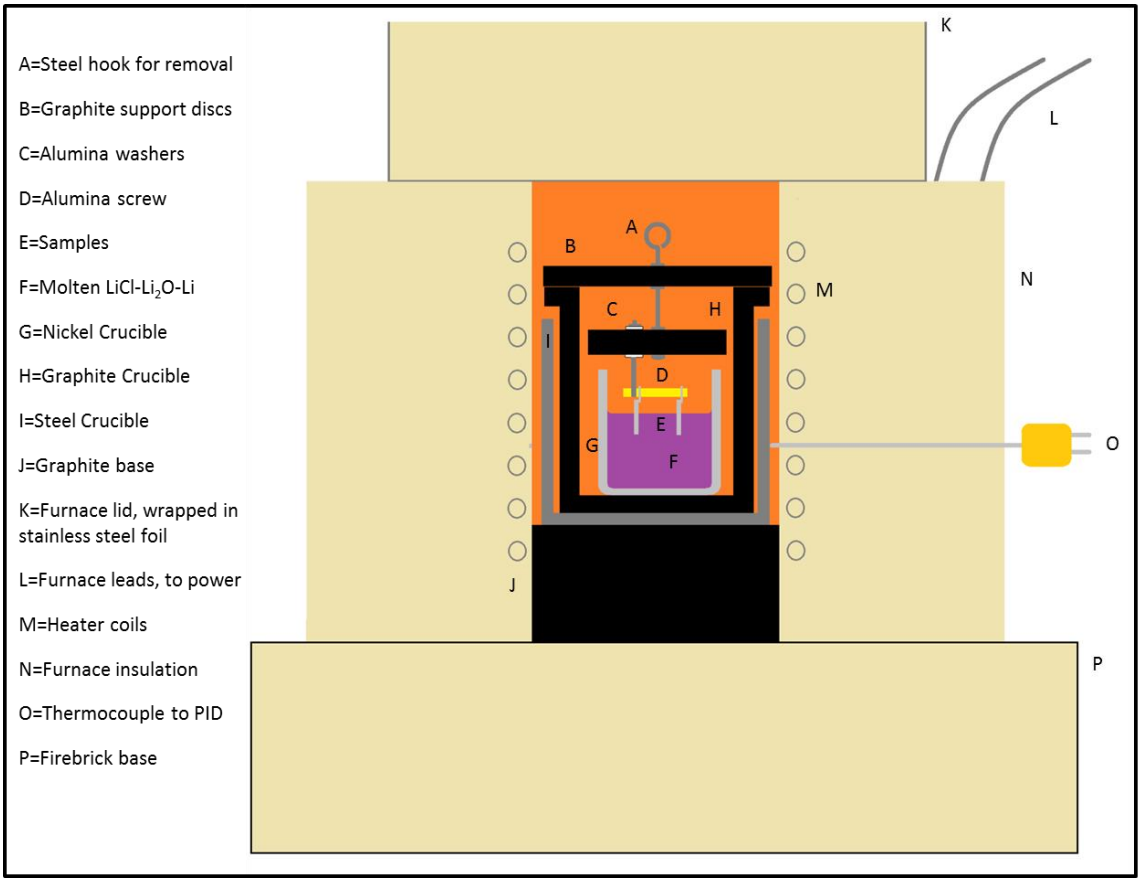


Figure 2.3: Schematic depiction of the experimental configuration used in exposure experiments. The system was duplicated in a single glove box to facilitate extended exposure testing in two melts of LiCl-Li_2O-Li simultaneously [155].

Except where specified otherwise, samples were laser cut into square coupons of 1.2 cm dimension, spot welded to wire hooks of similar alloying compositions and suspended on an alumina screw. A schematic depiction of a spot welded sample is shown in Figure 2.4. This geometry resulted in a surface area of 3.6cm^2±5% per sample exposed to the molten solution. Typically two samples were exposed to each melt for a total sample surface area of 7.2cm^2. The hooks were looped onto an alumina screw where they rested in the screw threads to secure the samples in place. This method was found to limit the motion of the samples sufficiently such that the assembly could be inserted and removed from the furnace without disturbing the placement of the samples.

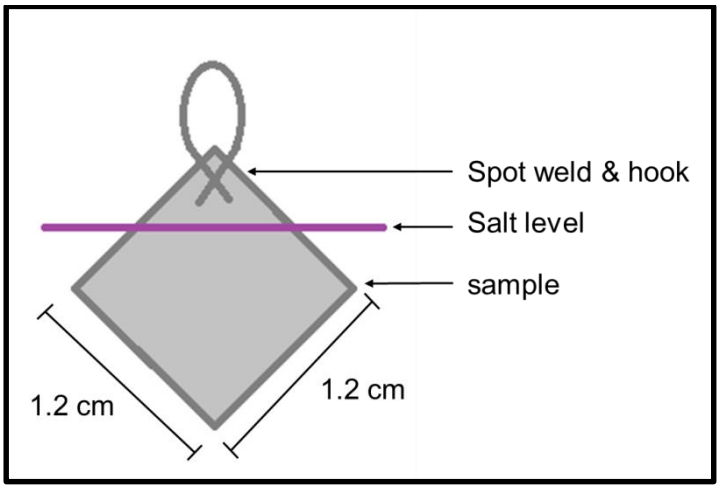


Figure 2.4: The sample geometry used during exposure testing. 1.2 cm square samples were spot welded to hooks of similar alloying composition and suspended from Al_2O_3 in the melt such that the spot weld was not exposed to the molten solution.

The exposure testing glove box was further equipped with a circulating water chiller physically contacting the exterior of the glove box to assist in cooling the system. A limit controller was installed so that should the temperature of the glove box exceed 45˚C (5˚C bellow design specifications) all electrical power to the furnaces would be cut off. This limit system was actively engaged so that should the system over heat, or alternative "beyond design base scenario" occur, the system could not apply power to the furnaces without being re-set. The combination of the experimental apparatus and systems described above allow the exposure testing glove box to be capable of exposing two sets of materials to two separate high temperature (<1,000°C) molten salts in a rigorous electrochemical manner for extended periods of time (thousands of hours).

2.2 Materials:

The primary materials investigated in this study were austenitic stainless steel alloy 316L (SS316L), nickel-chromium based Inconel alloys 625 (I625) and 718 (I718),

as well as the nickel-molybdenum alloy Hastelloy N. The composition of these materials as provided by the commercial suppliers is given in Table 2.1.

Table 2.1 The composition of stainless steel alloy 316L, Inconel alloys 625 as well as 718, and Hastelloy N used in this study.

Alloy	Ni	Cr	Fe	Mo	Nb	Mn	Cu	Al	Ti	Si
SS316L	10	18	Bal.	3		< 2				
I625	58	20-23	5	8.0-10	3.2-4.2	0.5		0.4	0.4	0.5
I718	50-55	17-21	19	2.8-3.3	4.8-5.5	0.35	0.2-0.8	0.65-1.15	0.3	0.35
Hastelloy N	71	7	4.2	17		0.5				

All chemicals were procured from VWR Scientific. Reagent grade LiCl of 99wt% purity, Li_2O of 99.5wt% purity and Li of 99wt% purity were used in all experiments, except in ultra-high purity melts where LiCl of 99.995wt% purity and Li of 99.9wt% purity were employed. To dry LiCl before use in corrosion studies a quantity of LiCl was heated to 550°C for two hours, then the temperature was raised to 650°C and equilibrated for 30 minutes before Li_2O and Li were added [106]. These melts were additionally allowed to equilibrate for 30 minutes following the addition of Li_2O and Li to allow for their dissolution before sample coupons were exposed to the final melt [43]. In melts that employed ultra-high purity precursors, anhydrous LiCl was procured in a sealed glass container and was exposed to the glove box atmosphere for less than 5 minutes prior to heating. Melts were typically contained in Ni crucibles supplied by Alfa Aesar and used 50 g of salt.

2.3 The Li-Bi Reference Electrode in Molten LiCl-Li_2O-Li:

Electrochemical studies were employed for investigating the physical chemistry of molten LiCl-Li_2O containing metallic Li. The development of a reference electrode that maintains a stable electrochemical potential in molten LiCl-Li_2O-Li is required in order to employ electro-analytical techniques in these molten solutions. The motivation for, and theory of, the Li-Bi reference electrode has been presented elsewhere and only a brief description is included here for brevity [155].

For a reference electrode to exhibit a stable potential in molten LiCl-Li_2O-Li, a redox couple ($M|M^+$) must be identified that does not vary in Gibbs free energy as a result of a change in the composition of the melt. The identification of such a couple is exceedingly difficult in molten solutions containing metallic Li as well as Li_2O. In theory, any oxidized species, M^+, that would not be reduced by metallic Li would have a metallic component, M, that would be oxidized by Li_2O, or vice versa. Stated mathematically, for a theoretical $M|M^+$ reference redox couple the difficulty is stated as follows:

$$\text{If } \Delta G_{M|M^+} > \Delta G_{Li|Li^+} \text{ then } \; 2M + Li_2O \rightarrow M_2O + 2Li$$

$$\text{However, if } \Delta G_{M|M^+} < \Delta G_{Li|Li^+} \text{ then } \; M_2O + 2Li \rightarrow 2M + Li_2O$$

It is proposed that no rigorously defined reference electrode can be employed in molten LiCl-Li_2O-Li without the identification of a redox couple that avoids this paradox. A liquid metal reference electrode containing Li is therefore suggested to be the best candidate for obtaining a stable redox couple in the in molten the LiCl-Li_2O-Li system.

By employing a liquid alloy of Li and an electronegative, low melting point metal that has a high solubility of Li, the Li|Li+ potential will be at equilibrium at the interface between the liquid metal and the molten LiCl-Li_2O-Li. This approach has been successfully employed in molten LiCl-Li_2O using eutectic alloys of Li-Pb [47] and Li-Bi [69] contained in thin walled MgO cells. It has been theorized that in these cells Li preferentially wets the porous MgO walls, facilitating a Li|Li+ couple to be measured between the salt phase and the electrically conducting liquid alloy. In the present work, Li-Bi was chosen to avoid the use of chemically toxic Pb.

The reference electrode developed in the current work consisted of a graphite cylinder with a 500 µm wall thickness, sealed at one end, containing 3 g of 30at%Li-Bi. Prior to its use in molten LiCl-Li_2O-Li, this electrode was heated to 900ºC for 3 hours to saturate the graphite with the liquid alloy. An image of the Li-Bi reference electrode constructed in this manner is shown in Figure 2.5.



Figure 2.5: The Li-Bi reference electrode used in Chapter 4 of this study. The thin walled graphite tube that contained the molten alloy was held via ceramic insulation outside of the melt and electrical contact to the potentiostat was made through a Ni wire. A red arrow is included indicating the level of the Li-Bi alloy within the reference electrode.

Research conducted in our laboratory demonstrated the stability of Li-Bi in LiCl-Li_2O [155]. However, it should be noted that the activity of Li in Li-Bi is dependent upon the concentration of Li in the liquid alloy and as a result the stability of the Li-Bi potential in molten LiCl-Li_2O solutions varying in Li concentration is currently unknown [156, 157]. Furthermore, the current work employed a thin walled graphite cell as the ion bridge between the liquid alloy and the molten salt phase and the stability of graphite in the LiCL-Li_2O-Li system is also unknown. Future investigations are necessary to verify

the Nernstian behavior and stability of the Li-Bi reference electrode as well as the effect of the use of graphite in the system.

2.4 Gas Chromatography:

An SRI instruments gas chromatograph (GC) with a thermal conductivity detector was used to quantify the content of N_2 in the Ar atmosphere of the glove box. GC analysis measured the concentration of N_2 to be 2% of the Ar glove box atmosphere in which the experiment was conducted. It is noted that the glove box purification system used in this study is designed to remove H_2O and O_2 but not N_2, and as a result the accumulation of N_2 in the glove box over time is expected. The quantification of N_2 in the glove box atmosphere is thought to be variable with time as purging of the glove box with Ar was conducted periodically (approximately every 6 months) to regenerate the glove box gas purification system. The effect of the presence of N_2 on material interactions with molten LiCl-Li_2O-Li are presented in Chapter 6 of this study.

2.5 Scanning Electron Microscopy / Energy Dispersive X-ray Spectroscopy:

A Hitachi S-4700 field-emission scanning electron microscope (SEM) was used to study the morphology of material surfaces following exposure to molten LiCl-Li_2O-Li. Micrographs were recorded at 45x, 2,000x, 10,000x and 25,000x magnifications to display morphology at various levels of magnification. The elemental composition of the surface was obtained using energy dispersive X-ray spectroscopy (EDS) coupled to the SEM. The SEM was operated at 20 kV during imaging, and EDS measurements were made using accelerating voltages of 10 kV and 20 kV to observe differences in elemental

composition as a function of relative depth. The SEM used in this study is shown in Figure 2.6.



Figure 2.6: Hitachi S-4700 field emission scanning electron microscope, equipped with an energy dispersive spectrometer.

Samples were exposed to atmosphere before entering the vacuum chamber of the SEM due to mechanical limitations of the instrument. Samples were maintained under an Ar atmosphere in a sealed container for all but approximately 30 seconds when transferring them from the glove box to the SEM chamber. To investigate the effect of this period of exposure to atmosphere samples were analyzed after approximately 30 seconds of atmospheric exposure, removed from the vacuum, exposed to atmosphere for one minute, and analyzed again. Coupons of SS316L exposed to molten LiCl-1wt%Li_2O containing 0, 0.1 and 0.3wt%Li at 650°C for 50 hours were analyzed in this manner to investigate the effect of variation in melt composition on the atmospheric stability of the surfaces. This experiment was conducted to study the morphological alteration that results from exposure to atmosphere and to understand the degradation that may occur

during the 30 seconds of exposure that transpires before the samples are analyzed. The micrographs recorded from the surface of these samples following the first brief exposure to atmosphere are shown in Figure 2.7 (A) and micrographs of the same samples following a subsequent one minute period of exposure to atmosphere are shown in Figure 2.7 (B).

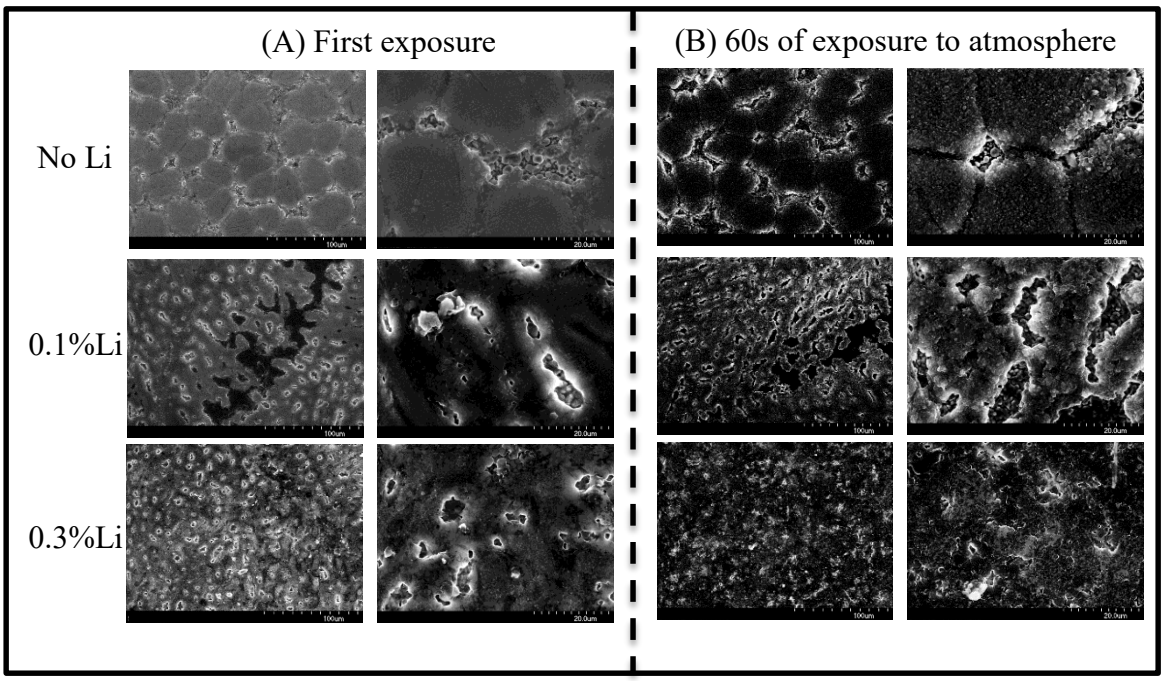


Figure 2.7: SEM micrographs of SS316L exposed to molten LiCl-Li_2O containing 0, 0.1 and 0.3wt%Li at 650°C for 50 hours. Samples were analyzed (A) after approximately 30 seconds of exposure to atmosphere and (B) after an additional one minute of exposure to atmosphere.

By comparing the micrographs of SS316L after the first and second period of exposure to atmosphere it can be observed that the surfaces maintain their macroscopic morphology, on the order of 10's of µm, upon brief periods of exposure. However, smaller features observed at higher magnification, on the order of µm, are observed to become increasingly rough and less uniform following the second period of exposure to atmosphere. The degree to which the roughening occurs is observed to be more severe on

samples exposed to molten solutions containing higher concentrations of Li. This is attributed to the increased reactivity of Li compared to LiCl and Li_2O, and indicates that the compounds present on the sample surfaces reflect the increased reactivity of the melt. It is concluded that while alteration to the sample morphology does occur during exposure to atmosphere before being analyzed in the SEM, the bulk morphology is not fundamentally altered by the initial 30 seconds of exposure.

2.6 X-ray Diffraction:

X-ray diffraction (XRD) was conducted to determine what crystalline phases were present on samples following exposure to LiCl-Li_2O-Li. Additionally, XRD analysis was conducted to investigate the alteration to the lattice parameter of the base materials that occurred as a result of exposure. XRD analysis was conducted using the Rigaku SmartLab X-ray diffractometer shown in Figure 2.8. XRD data was analyzed using PDXL2 software. Unless otherwise stated, XRD analysis was conducted as described below. Specimens were analyzed using a parallel beam optical configuration across a 2θ range of 10-90° with a step width of 0.05° at a scan rate of 0.5°/min. Parallel beam optics were employed in these studies due to their superior reliability in resolving peak shifting compared with Bragg-Brentano optical configurations. However, parallel beam optics are incapable of quantitative analysis due to susceptibility of preferential grain orientation causing skewed intensity ratios of diffraction peaks. Peak sifting due to such effects as lattice expansion or contraction has been utilized for quantifying liquid Li attack on materials [158]. The benefit of parallel beam optics in resolving these effects of liquid Li attack was chosen despite the known drawbacks of using a non-quantitative XRD

analyses method. Furthermore, the use of parallel beam optics allowed for grazing incident angle diffraction (GI-XRD) analysis to be conducted for surface sensitive diffraction studies.

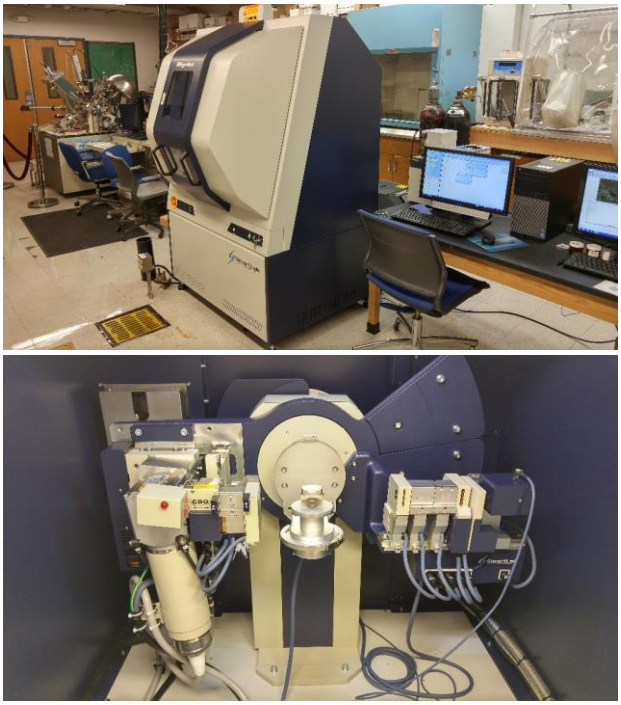


Figure 2.8: Rigaku SmartLab 3kW XRD used throughout these studies.

Specimens were sealed in plastic bags in the glove box and maintained under Ar during XRD analysis. The efficacy of maintaining the samples in plastic bags throughout XRD analysis is demonstrated in Figure 2.9. Figure 2.9 shows the XRD patterns obtained from a sample of SS316L exposed to ultra-high purity LiCl-1wt%Li_2O in the absence of Li for 20 hours at 650°C recorded when the sample was in a plastic bag, as well as during exposure to atmosphere.

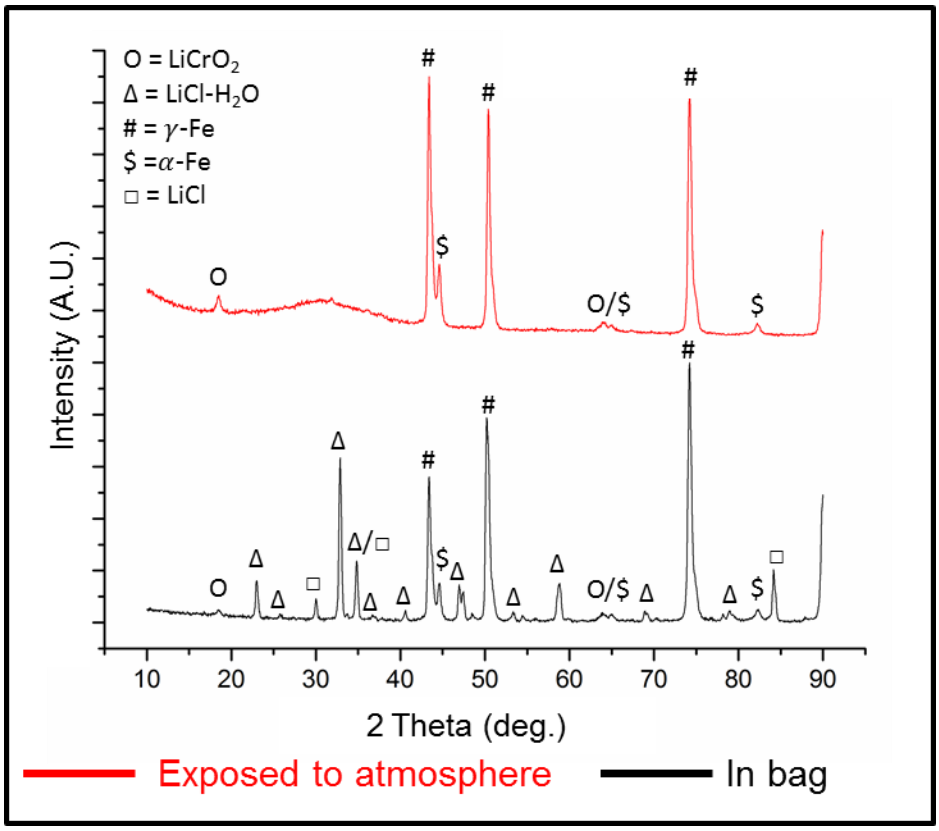


Figure 2.9: X-ray diffraction patterns obtained from a coupon of SS316L exposed to ultra-high purity LiCl-1wt%Li_2O at 650°C for 20 hours recorded in a plastic bag (Bottom) and during exposure to atmosphere (Top). Diffraction from the (0,0,3) plane of $LiCrO_2$ at $2\theta = 18.4^{\circ}$ 2θ is observed in both patterns while the removal of LiCl and LiCl-H_2O occurred as a result of exposure to atmosphere.

XRD analysis identified phases of $LiCrO_2$, LiCl, LiCl-H_2O, γ-Fe, and α-Fe on SS316L exposed to molten LiCl-1wt%Li_2O when analyzed in a plastic bag, however only $LiCrO_2$, γ-Fe, and α-Fe were present following exposure to atmosphere. It is observed that by exposing the sample to atmosphere the hygroscopic phases of LiCl, and LiCl-H_2O are removed from the sample surface and replaced by a broad amorphous feature spanning approximately 2θ=20-40°. The detection of these phases when analyzed in the plastic bag, and their disappearance upon exposure to atmosphere, demonstrates that to some extent the samples are protected from atmospheric exposure when maintained in the plastic bag. However, the presence of LiCl-H_2O on the sample analyzed in the plastic bag

demonstrates that the bag is at least semi-permeable and the samples are exposed to minor quantities of moisture during XRD analysis.

2.7 Micro-Hardness Testing:

The hardness of the surface of materials following exposure to molten LiCl-Li_2O-Li was evaluated using micro-indentation. The Shimadzu Seisakusho LTD NT-M001 micro-Vickers indenter and Leica MC170 optical microscope used in this study are shown in Figure 2.10. Prior to analysis samples were rinsed with methanol for 10 minutes to remove residual salt from their surface. Indentations were made by applying a 500 g load to the samples for 30 seconds. Subsequently, the dimensions of the resulting indentations were measured using the optical microscope. The dimensions of the indentation were related to the hardness of the material surface by equation 1.

$$\text{Micro-Vickers hardness: HV} = \frac{1854.4 * L}{d^2} \qquad \text{Equation (1)}$$

Where d is the diagonal of the rectangular indentation in µm, and L is the load in g. A total of 10 indentations were made on each sample surface. The evaluated hardness is the average of the 10 observed values and is reported with error bars according to the standard deviation of the 10 measurements.



Figure 2.10: The Shimadzu Seisakusho LTD NT-M001 micro-Vickers indenter (left) and the Leica MC170 optical microscope (right) used in this study to evaluate the hardness of samples.

2.8 Inductively Coupled Plasma – Optical Emission Spectroscopy:

Inductively coupled plasma – optical emission spectroscopy (ICP-OES) was used extensively thought this study to quantify the amount of a given element that was leached from samples into the molten LiCl-Li_2O-Li during the periods of exposure testing. ICP-OES is a strictly elemental analytical tool, capable of detecting the concentrations of elements in aqueous solutions with a detection limit on the order of 100 ppb. To detect the elements that were present in each salt melt, the salt ingots were allowed to cool after each experiment, dissolved in 750 mL of 18 MΩ deionized water and analyzed using a Perkin Elmer Optima 8000 ICP-OES. The Optima 8000 spectrometer used in this study is shown in Figure 2.11. Spectroscopic standards were purchased from SCP Scientific. All identified concentrations resulted in relative standard deviations less than 10%. To ensure the complete dissolution of the elements of interest, individual samples were acidified

using hydrochloric acid, or adjusted to a pH of 13 using sodium hydroxide as specified in specific studies.

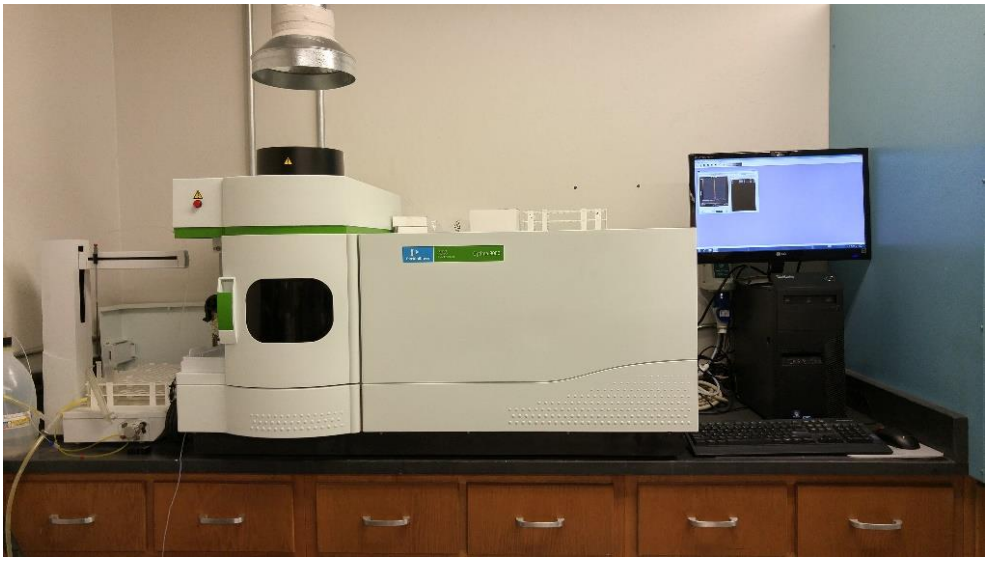


Figure 2.11: Perkin Elmer Optima 8000 ICP-OES used to conduct quantitative analysis of alloying elements present in salt ingots following exposure testing.

2.9 Raman Spectroscopy:

A Thermo-Scientific DXR Raman microscope was used to characterize the Raman active modes of the surface of samples exposed to molten solutions of LiCl-Li_2O-Li. The DXR, shown in Figure 2.12, was operated with a 532nm laser at 10mW. It is noted that in certain circumstances in this study, Raman spectroscopy was conducted while samples were exposed to atmosphere. Additionally, the DXR was equipped with a custom fiber optic probe procured from InPhotonics that facilitated Raman spectroscopy of sample surfaces in the glove box atmosphere. The fiber optic was used to pass the 532nm excitation laser to the sample surface and the receiving fiber optic collected light with a spectral shift of 250-3900cm^{-1} from 532nm. The fiber probe had a 5mm focusing length. While the use of this fiber probe facilitates

spectroscopy of samples without contacting atmosphere, the incident intensity of the excitation laser beam was observed to be roughly 10% of that employed in the DXR microscope. As a result, Raman spectroscopy conducted in the glove box was typically of reduced intensity and increased spectroscopic noise. Raman spectroscopic analysis of samples following shorter period of exposure, for example 20 hours, required being analyzed in the microscope to achieve appreciable levels of signal. Surface films that possessed fully developed surface films, formed during hundreds of hours of exposure, were analyzed using the fiber optic probe without contacting atmosphere to confirm that the films were present prior to contacting atmosphere.



Figure 2.12: Thermo Fischer DXR Raman microscope. The DXR was equipped coupled to a fiber optic probe (not shown) to facilitate Raman spectroscopic analysis of samples in the experimental glove box.

2.10 X-ray Photoelectron Spectroscopy:

X-ray photoelectron spectroscopy (XPS) was used extensively throughout this study. XPS is unique in its ability to characterize the atomic and chemical characteristics of surface films on the order of nanometers thick. This ability makes XPS ideally suited for the current study, as the films formed on alloys exposed to molten LiCl-Li_2O containing Li are exceedingly thin. As shown in Chapters 5 and 6, XPS analysis offered the sole analytical method for characterizing the chemistry of surface films formed in molten LiCl-Li_2O-Li. Relying on this analytical technique to such an extent required the near mastery of the XPS system as well as its underlying physics before it could be confidently utilized to its full potential.

XPS analysis was conducted using a PHI 5600 with both monochromatic Al K_α radiation as well as achromatic Mg K_α radiation. The spectrometer was calibrated to the Ag $3d_{5/2}$ line at 368.3±0.05 eV. Internal charge correction of XPS spectra was accomplished using the oxide bonding state (O^{2-}) of the O 1s line to 530 eV due the overlap of the adventitious C 1s line with the Cl 2s line on specimens containing large quantities of Cl**.** XPS spectra were collected from an analysis area of 1.6 mm^2. Ar^+ ion sputtering was conducted at a current density of approximately 0.1 mA/cm^2, which was shown to remove ~7 nm of Ta_2O_5 per minute, across an area of 9 mm^2. Samples were transferred from the Ar glove box atmosphere to the vacuum chamber of the XPS using a sealed transfer chamber to avoid exposure to the atmosphere. XPS spectra underwent 3 points of smoothing, were analyzed using SDP v4.6 Gaussian fitting software and were

normalized to the highest intensity peak. The XPS used throughout this study is shown in Figure 2.13.

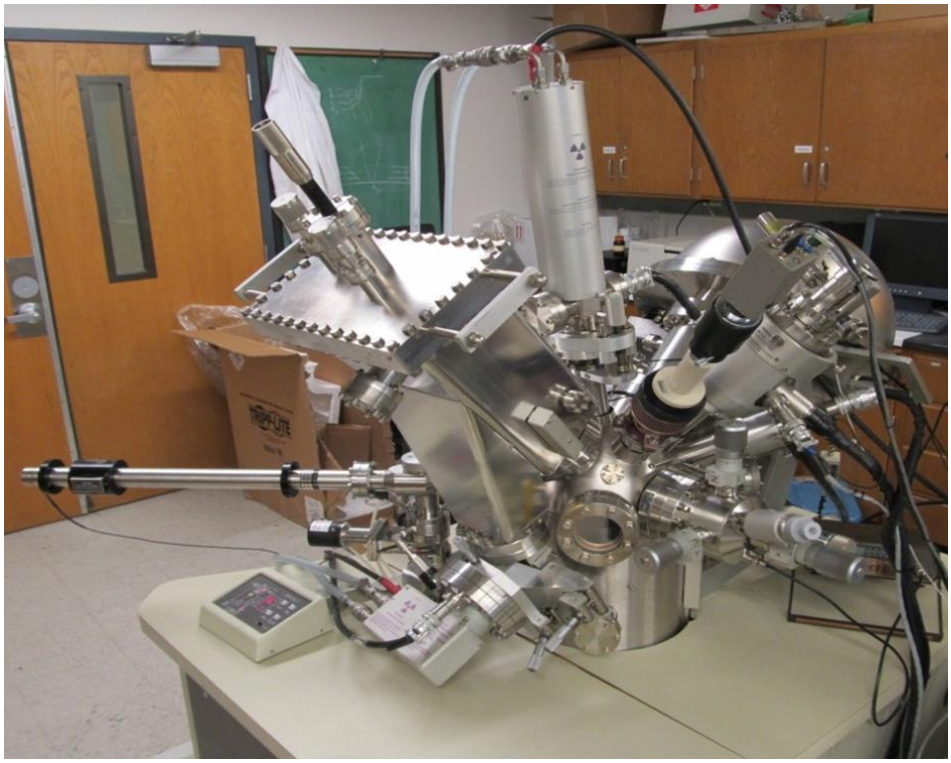


Figure 2.13: PHI 5600 X-ray photoelectron spectrometer used extensively throughout this study to characterize the chemistry of material surfaces following exposure to molten solutions of LiCl-Li_2O-Li.

Chapter 3 Development of Experimental Protocol for Molten LiCl-Li_2O-Li

3.1 Introduction:

Numerous constraints are imposed on the experimentalist investigating the molten LiCl-Li_2O-Li system due to the confluence of various characteristics in these systems such as: high chemical reactivity, oxidizing as well as reducing nature, electrical instability, toxicity and extreme sensitivity to nature and amount of impurities, in addition to the high temperature of these systems. The following quote is included to summarize the difficulties encountered in these studies. It should be noted that the authors, Bredig *et al.,* were highly successful in studying numerous alternative metal-salt solutions including every alkali metal–alkali halide system with the exception of lithium and its respective halides [88].

> *"Attempts to measure the conductivity of Li systems were unsuccessful because of reactions between the lithium solutions and the synthetic sapphire or single crystal magnesia cells…No insulating material has yet been found which will withstand attack by these solutions" [70]*

In addition to material challenges, the very nature of the LiCl-Li_2O-Li system eliminates the ability to employ standard experimental techniques. For example, the low ionization potential of the dissolved metallic lithium makes the melt highly susceptible to polarization by electric fields [159]. The polarization of molten solutions of metals and salts has the effect of shifting the localized concentration of conduction, or solvated, electrons in the melt, altering the physical properties of the molten solution [80, 160]. This in fact reduces the ability of electrochemical techniques to gain quantitative information regarding molten LiCl-Li_2O-Li without altering the solution. Furthermore,

optical probing of LiCl-Li_2O-Li via transmission is not feasible as liquid lithium metal reacts with all existing commercial molecular compounds that could be used for viewports [112]. Furthermore, the LiCl-Li_2O-Li phase in question is only stable above the melting point of LiCl-Li_2O (approximately 600°C depending on the concentration of Li_2O) [70]. As a result, any investigation into the solution chemistry of the melt that is relevant to the electrolytic reduction process has to be conducted at the process temperature (650°C), to avoid possible phase separations upon cooling. Additional challenges exist regarding chemical analysis of corrosion products formed on materials exposed to molten LiCl-Li_2O-Li. The low atomic number of Li precludes the use of X-ray analytical techniques that employ Be windows, such as energy dispersive X-ray spectroscopy (EDS) or X-ray fluorescence spectroscopy (XRF), for characterizing Li on corroded materials. Finally, the chemical reactivity of Li intercalated transition metal oxides requires that strict atmospheric control be maintained to preserve the corrosion products formed in molten solutions containing Li. The atmospheric instability of these corrosion products further limits the post exposure analytical techniques that can be employed to only those that can be conducted while maintaining the sample in a controlled atmosphere throughout analysis.

The study of material interactions with LiCl-Li_2O-Li is non-trivial and required the development of first of a kind experimental techniques in terms of the corrosion experiments themselves, as well as the analytical methods that employed to study the materials post exposure. Numerous experiments were conducted throughout this study to develop experimental procedures that were capable of yielding a more accurate and

repeatable characterization of material interactions with molten LiCl-Li_2O-Li. This chapter discusses the development and operation of the experimental and analytical methodologies used throughout this study. Preliminary studies were conducted to evaluate the generalized effects that the presence of Li has on the corrosion of materials exposed to molten LiCl-Li_2O. The principle goal of this study was to evaluate an approximate range of Li concentrations that can be included in molten LiCl-Li_2O before fundamentally altering the corrosion processes that occur in the melt. These studies included exposure testing of stainless steel alloy 316L, as well as nickel based Inconel alloys 625, 718 and Hastelloy N.

3.2 Materials:

The primary materials investigated in this study were austenitic stainless steel alloy 316L (SS316L), nickel-chromium based Inconel alloys 625 (I625) and 718 (I718), as well as the nickel-molybdenum alloy Hastelloy N. SS316L is a common engineering alloy frequently employed as the material of construction for molten salt containing crucibles and has shown acceptable corrosion resistance in molten LiCl-Li_2O [124, 138, 142, 145, 161]. Chapter 5 of this dissertation focuses specifically on the corrosion resistance of SS316L in molten LiCl-Li_2O-Li as it is the crucible material used in UO_2 electrolytic reduction studies at Argonne [162].

Nickel based super alloys I625 and I718 were chosen for their previously demonstrated excellent corrosion resistance in molten chloride salts in the presence and absence of dissolved oxides [163-166]. As shown in Table 2.1, while I625 is primarily composed of Ni, Cr, and Mo, I718 contains a relatively high concentration of Fe and

lower contents of Cr and Mo. These two alloys were studied in parallel to facilitate a study of corrosion behavior as a function of Fe content in the alloy. Fe is less expensive than Ni, Cr and Mo, and as a result high Fe content alloys are commonly employed to reduce the cost associated with the use of expensive superalloys. Consequently, investigation of the corrosion performance of high Fe content alloys such as I718 was desirable.

Hastelloy N was chosen for investigation due to its fundamentally different mechanism of corrosion protection in molten salts. Counter to the corrosion protection of common alloys, Hastelloy N was developed specifically to remain inert in highly oxidizing molten salts without relying on the formation of protective surface films [123, 167-169]. While stainless steels and Ni based superalloys typically require the formation of stable surface films to protect the bulk alloy from exposure to oxidizing environments, Hastelloy N was designed to depend on its intrinsic electrochemical nobility for corrosion protection. This mechanism of corrosion suppression has proven highly successful in molten fluoride salts where transition metal surface films are not stable and bare alloy is in contact with the molten salt. Due to the instability of transition metal oxides in contact with liquid Li, it was hypothesized that this mechanism of corrosion protection may be applicable in molten LiCl-Li_2O-Li.

3.3 Crucible Materials:

Ideally corrosion experimentation in a given environment is conducted using a vessel that contains the environment without interacting with it or altering its chemical nature. However, the principle goals of the current research are (A) the identification of

materials that are resistant to corrosion in molten solutions of LiCl-Li_2O-Li and (B) characterizing the mechanisms by which these materials corrode in these systems. By deductive logic, it is therefore impossible to identify a crucible material that will remain inert while containing molten solutions of LiCl-Li_2O-Li prior to the completion of this study. The principle challenge in identifying such a container material for the LiCl-Li_2O-Li system is the presence of both reducing metallic Li as well as oxidizing Li_2O. Material selection is complicated significantly by the fact that molten solutions of LiCl-Li_2O-Li possess thermodynamic driving forces for both oxidation and reduction reactions simultaneously. Prior to the completion of the investigations presented in this study it was unknown to what extent oxidized materials (ceramics) would be reduced by Li, or if alloys would be oxidized by Li_2O. These potential reactions would not only degrade the crucible material and introduce corrosion products into the melt, but would have unquantifiable effects on the solution chemistry of the molten LiCl-Li_2O-Li itself. Should a crucible material oxidize or reduce when in contact with molten LiCl-Li_2O-Li, it would have an opposing effect on the melt. These reactions would alter the concentration of either Li_2O or Li in the melt, resulting in an inaccurate assessment of melt composition.

Preliminary studies were conducted on a wide array of crucible materials in an attempt to quantify to what degree various materials interacted with molten solutions of LiCl-Li_2O-Li. This was principally achieved by quantifying the concentration of the elements that were leached from the crucibles into molten LiCl-Li_2O-Li during extended periods of exposure using ICP-OES analysis (methodology provided in Section 2.8). This

analysis served as a rough estimation of the corrosion rate of these materials in the LiCl-Li_2O-Li environment as well as to what degree the reactions altered the molten solution.

3.3.1 Degradation of Ceramic Materials in Molten LiCl-Li_2O-Li:

A wide array of ceramic materials has been used in molten salt research for a variety of reasons. Alumina (Al_2O_3) and magnesia (MgO) are commonly used in molten salt electrochemical studies involving LiCl due to their minimal chemical reactivity with molten chlorides and electrically insulating properties [8, 41, 170, 171]. However, liquid Li at the temperatures employed in this study has been shown to react with and degrade all commercially available ceramic materials, including high purity Al_2O_3 and single crystal MgO [70, 144]. Importantly, recent work by Choi *et al.* noted that when a molten solution of LiCl-Li_2O-Li was formed during the electrolytic reduction of UO_2, the melt was found to degrade both MgO and MgO-ZrO_2 [41]. It was reported that these materials did not degrade upon exposure to molten LiCl-Li_2O in the absence of Li, however no data was provided on the corrosion rate of these materials as a function of Li concentration in the melt. Preliminary investigations were conducted on the degradation of both Al_2O_3, and MgO in the current work to verify the inability of these materials to function as inert materials in LiCl-Li_2O-Li.

A digital image of an Al_2O_3 tube exposed to LiCl-2wt%Li_2O-1wt%Li for 20 hours at 650°C is shown in Figure 3.1. While Al_2O_3 is known to be relatively inert in molten LiCl-Li_2O [170], the degradation that occurred during this test yielded a corrosion rate exceeding 50 mm/year. This observation is one of several dramatic examples included in

this dissertation of the alteration of melt chemistry that occurs when metallic Li is added to molten LiCl-Li_2O. The observed reaction rate of Al_2O_3 with molten LiCl-Li_2O-Li is far too great to employ this material in these systems. Substantial alterations to both the Al_2O_3 as well as the melt can be expected should this material contact molten solutions containing Li.

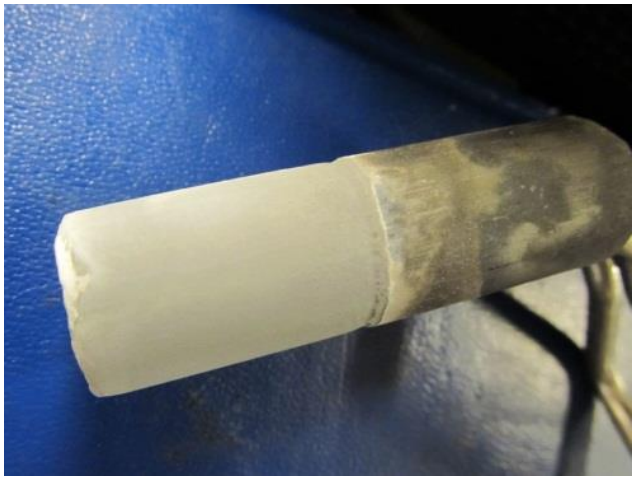


Figure 3.1: A digital image of Al_2O_3 after 20 hours of exposure to LiCl-2wt%Li2O-1wt%Li at 650°C. The recorded corrosion rate exceeded 50 mm/yr indicating the highly reactive nature of Al_2O_3 with melts containing metallic Li.

The stability of MgO in molten solutions of LiCl-Li_2O-Li was investigated over a range of metallic Li concentrations. Approximately 1.2g of 99.95wt% purity MgO crystals were submerged in LiCl-2wt%Li_2O containing 0, 0.5, 1 and 2wt%Li at 650ºC for 50 hours. ICP-OES analysis of the melt following the period of exposure was used to quantify the amount of Mg that was leached into the molten solutions. It should be noted that the density of MgO is greater than that of LiCl, which is greater than liquid Li. As a result, if the solubility limit of Li in LiCl is exceeded, excess Li will float on molten LiCl-Li_2O-Li. Therefore, the MgO crystals in this experiment were only exposed to a mixture of LiCl-Li_2O-Li during the duration of the experiment and were not exposed to

bulk metallic Li. The mass of Mg in each melt following the separate periods of exposure is shown, as detected by ICP-OES, is shown in Figure 3.2.

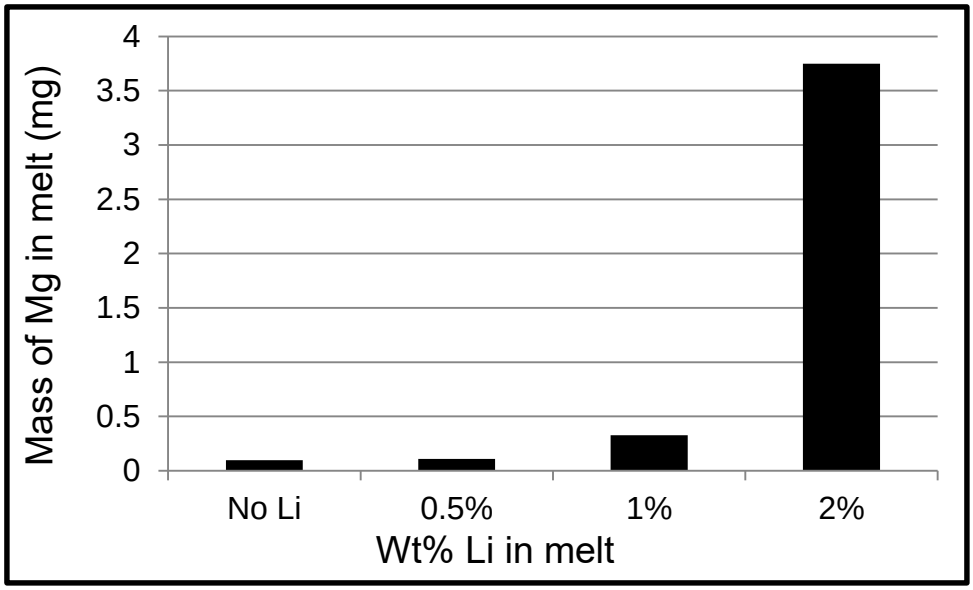


Figure 3.2: Mass of Mg detected by ICP-OES analysis of LiCl-2wt%Li2O containing 0, 0.5, 1 and 2wt%Li when approximately 1.2g of MgO was exposed to each melt for 50 hours. The observation of high leaching rates of Mg from exposure to melts containing greater than 0.5wt% is indicative of the instability of this material to molten solutions containing high concentrations of Li.

A sharp shift in Mg leaching from MgO contacting molten LiCl-Li_2O-Li can be observed in Figure 3.2. The increase in Mg in the melts containing greater than 0.5wt%Li is the first evidence shown in this dissertation of a fundamental alteration in material interactions with material in solutions of LiCl-Li_2O containing greater than 0.5wt%Li. The dissolution of MgO into molten LiCl-Li_2O-Li has significant implications considering the electrolytic reduction of UO_2, as MgO is commonly employed as an electrical insulator, electrode shroud, and crucible material in the process [8, 41]. The dissolution of more than 3.5mg from 1.2g of MgO in 50 hours is considered unacceptable for applications of MgO to function as a melt containing crucible. Furthermore, the

corresponding consumption of Li or Li_2O that results in the dissolution of Mg would represent a major alteration to the intended chemistry of the molten solution.

Preliminary investigations on the corrosion of SS316L in molten LiCl-Li_2O-Li employed MgO crucibles to contain the melt. A maximum of 1wt%Li was included in the molten solutions investigated in these studies and the duration of the exposures was limited to 20 hours to minimize the interactions of the melt with the crucibles. It was observed that the quantity of yttrium leached from the MgO crucibles saturated the ICP-OES detector, indicating the presence of thousands of ppm of yttrium in the melt. Yttrium was included as a stabilizer in the MgO crucibles employed in these studies at less than 3at%. The observation of preferential leaching of the yttrium stabilizing agent into the melt over the course of 20 hours indicates the inability of commercial MgO to maintain mechanical integrity following exposure to molten LiCl-Li_2O-Li.

Nitride ceramics have been employed for electrical insolation in highly reducing molten fluoride salts [172]. For example, boron nitride has been successfully employed as an ion bridge in reference electrodes due to the unique ability of this material to function as a chemically stable form of electrical insolation in highly reducing molten salts [172, 173]. However, Li is reactive with N, and previous research has shown that molten Li reacts with BN highly exothermically [112]. The use of nitride based ceramics for containing molten solutions of LiCl-Li_2O-Li was not pursued for this reason.

3.3.2 The Use of Metal Crucibles for Containing Molten LiCl-Li_2O-Li:

In contrast to molten salts, materials research involving liquid metals typically employ metals or alloys as container materials due to their inability to be reduced by contact with molten metal [174, 175]. Specifically, liquid Li is not reactive with a wide variety of engineering alloys, including low alloy steel, provided strict impurity controls are followed [152]. However, as discussed in Chapter 1, material interactions with liquid Li are notorious for being extraordinary dependent upon the presence of minor quantities of non-metallic impurities [127, 150, 174, 175]. Due to the abundance of oxygen in the LiCl-Li_2O-Li system, it is not clear to what degree liquid metal corrosion theories can be applied to the current research.

Vitreous carbon, also referred to as glassy carbon, was briefly investigated for its ability to contain molten solutions of LiCl-Li_2O-Li. This material was investigated due its advertised chemical resistance to acidic as well as alkaline melts and liquid metals . A vitreous carbon crucible was purchased from SPI supplies. The vitreous carbon crucible was observed to fail catastrophically as a result of a single 20 hour exposure to molten LiCl-2wt%Li_2O-1wt%Li at 650°C. An image of the failed crucible is shown in Figure 3.3. Localized corrosion was observed on the material indicating that chemical interactions occurred during exposure to the molten solution. Similar interactions between highly reducing molten fluoride salts containing dissolved Cr metal and vitreous carbon have been previously reported [177].



Figure 3.3: A shard of a vitreous carbon crucible that failed during a 20 hour exposure to molten LiCl-2wt%Li_2O-1wt%Li at 650°C. Localized corrosion was observed (indicated by the red arrow) suggesting that the material was chemically attacked by the molten solution.

Preliminary evaluations of the corrosion rate of refractory metals in molten solutions of LiCl-Li_2O-Li were conducted. Crucibles of Ta, Mo and W were chosen due to their commercial availability, previously demonstrated corrosion resistance in liquid lithium as well as reducing molten salts, and reported data on their corrosion properties in molten solutions of LiCl-Li_2O-Li [145, 178]. Ta, and Mo crucibles of 99.9wt% purity were procured from Kurt J. Lesker, and W crucibles of 99.9wt% purity were procured from Stanford Materials. Each crucible was independently exposed to LiCl-2wt%Li_2O in the absence of Li at 650°C for 20 hours. These exposure tests were intentionally conducted in molten solutions of LiCl-Li_2O in the absence of Li due to the typically superior corrosion behavior of refractory metals under reducing conditions. It should be noted that the electrolyte used in the electrolytic reduction process begins as LiCl-Li_2O, and only accumulates metallic Li as the process is conducted for a period of time. Therefore, any material used to contain the electrolyte used in the electrolytic reduction

process must be capable of withstanding exposure to molten LiCl-Li_2O in the presence, as well as the absence, of Li. ICP-OES analysis was used to quantify the mass of each element that leached into the LiCl-2wt%Li_2O melts during the exposure testing. The corrosion rate of each crucible was calculated from this mass, the surface area of the crucible exposed to the melt, and the time period which the crucibles contacted the molten solutions. The observed corrosion rate of the W crucible was 0.66mm/yr, while the corrosion rate of the Mo crucible was 0.23mm/yr. The corrosion rate of Ta could not be determined, however visual inspection showed that significant corrosion occurred as a result of the brief period of exposure. Previous research on the degradation of Ta in molten solutions of LiCl-Li_2O-Li demonstrated a high rate of uniform material dissolution resulting in visual thinning of samples [178]. These rates of material dissolution into the melt were determined to be too great for any of these materials to function as a relatively inert crucible material in the current studies. As a result, the use of refractory metals proved to be too expensive, difficult to clean, and unstable to be used as robust crucible materials for containing molten LiCl-Li_2O-Li.

Further investigations evaluated the corrosion performance of Ni crucibles for containing molten LiCl-Li_2O-Li. It was qualitatively observed that the leaching rate of Ni from Inconel and stainless steel alloys during preliminary corrosion studies was low and did not vary significantly when exposed to molten solutions of LiCl-Li_2O-Li varying in Li content [179]. Ni crucibles were found to be relatively cost effective and commercially available in a multitude of physical dimensions from Alfa Aesar. The use of Ni crucibles to contain molten LiCl-Li_2O-Li during the corrosion studies included in Chapters 3-6 was

found to result in an approximately uniform rate of Ni dissolution into the melts despite variation in melt composition. Figure 3.4 shows the Ni concentration observed by ICP-OES analysis to have leached into molten LiCl-Li_2O-Li as a result of 20 hours of exposure testing of SS316L at 650°C. The data included in Figure 3.4 was recorded from exposure testing of SS316L in melts of LiCl with 1 and 2wt%Li_2O, each containing between 0 and 1wt%Li, employing as-received LiCl and reagent grade LiCl dried at 550°C. The results of these experiments are presented in Section 3.5 and Chapter 5.

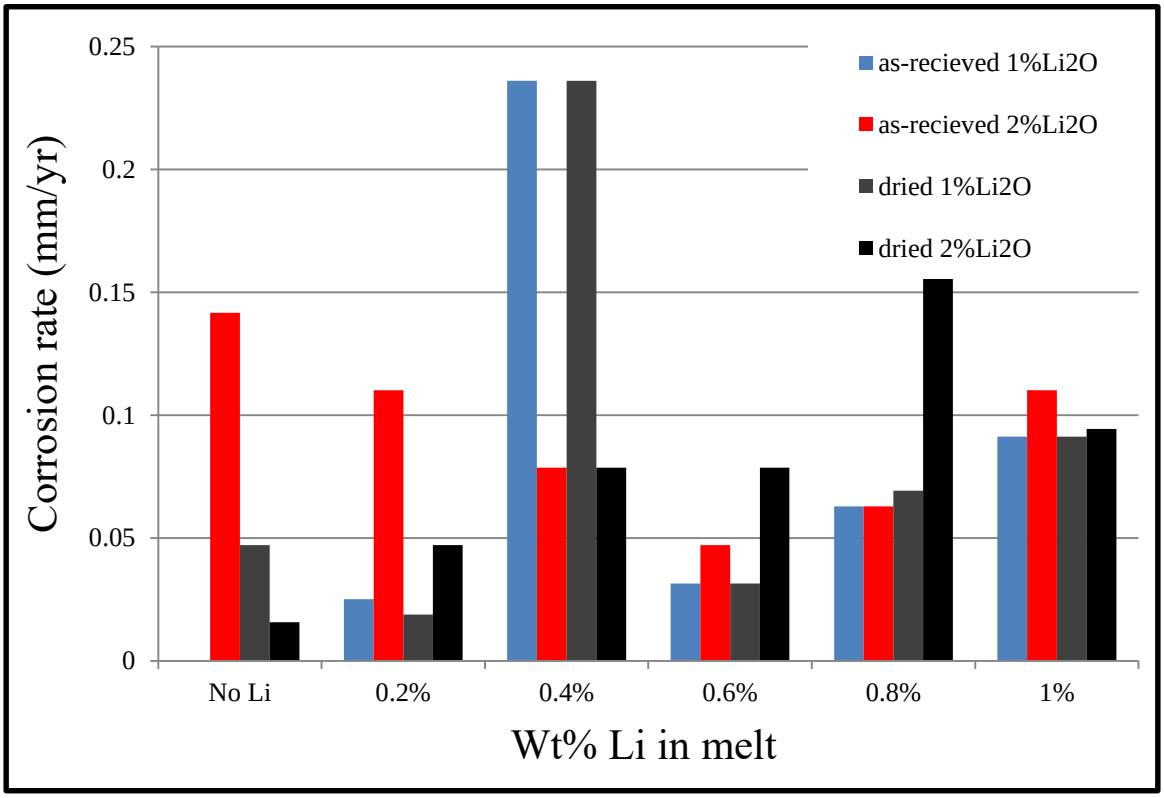


Figure 3.4: Corrosion rate of Ni detected by ICP-OES analysis following 20 hours exposure of SS316L to molten LiCl-Li_2O-Li contained in Ni crucibles. A reasonably consistent and low rate of Ni leaching is observed in melts of varying concentration of Li_2O as well as Li, and irrespective of the removal of impurity H_2O from the LiCl.

The concentrations of Ni leached by molten LiCl-Li_2O-Li shown in Figure 3.4 are observed to be relatively low and consistent despite variations in moisture content as well

as the concentrations of Li_2O and Li. The average mass of Ni detected by ICP-OES analysis in the melts from the 24 experiments was used to calculate an approximate corrosion rate of Ni across this range of melt compositions. The average observed corrosion rate was 0.08mm/year. This is an impressive level of corrosion resistance considering the range of LiCl-Li_2O-Li systems studied. Using this data, it was concluded that while Ni is not a perfectly inert crucible material for containing molten solutions of LiCl-Li_2O-Li, its rate of degradation remains constant over the range of conditions studied. This is an important behavior for the current study, as it allows for the effect of varying the concentration of Li in the melt on the corrosion of sample alloys to be studied nearly independently without having to account for variations in crucible interactions. Considering this benefit, the amount of Ni that leached into the molten LiCl-Li_2O-Li systems during exposure testing was accepted as a background impurity level in the system. Ni crucibles were utilized as the primary crucible material throughout the remainder of this study.

3.4 Corrosion of Inconel 625 and 718 in Molten LiCl-Li_2O-Li:

3.4.1 Experimental:

Samples of both I625 and I718 were exposed to molten solutions of LiCl-Li_2O-Li in the manner discussed in Chapter 2. Separate exposure tests were conducted in solutions of LiCl containing: 1 and 2wt%Li_2O with 0, 0.5 and 1wt%Li. Additionally, tests were conducted in LiCl containing 9wt%Li_2O and no metallic lithium. The solution containing 9wt%Li_2O was assumed to be saturated with Li_2O as the solubility limit of

Li_2O in LiCl at 650ºC has been reported to be 8.2wt% [23]. 50g of each mixture was ground in a mortar and pestle prior to heating. The salt melt was contained in a nickel crucible. Samples were exposed to the molten salt mixture after the salt was heated to 650ºC and equilibrated for 30 minutes. Samples remained in the salt at temperature for 20 hours. After being subjected to the exposure, one of the two samples was rinsed for 60 seconds in methanol to remove salt deposits, and was transferred via a sealed vessel in to the X-ray photoelectron spectrometer vacuum chamber to avoid atmospheric exposure. The second sample was characterized without rinsing using scanning electron microscopy.

3.4.2 Results and Discussions:

SEM micrographs of sample surfaces after exposure to LiCl containing 1, 2, and 9(saturated) wt%Li_2O, as well as saturated with Li_2O are shown in Figure 3.5. An increase in the percent surface area covered by oxide formations follows an increase in the concentration of Li_2O in the molten salt. The surface exposed to LiCl saturated with lithium oxide appears covered with a thick oxide layer, with little to no underlying alloy surface observable.

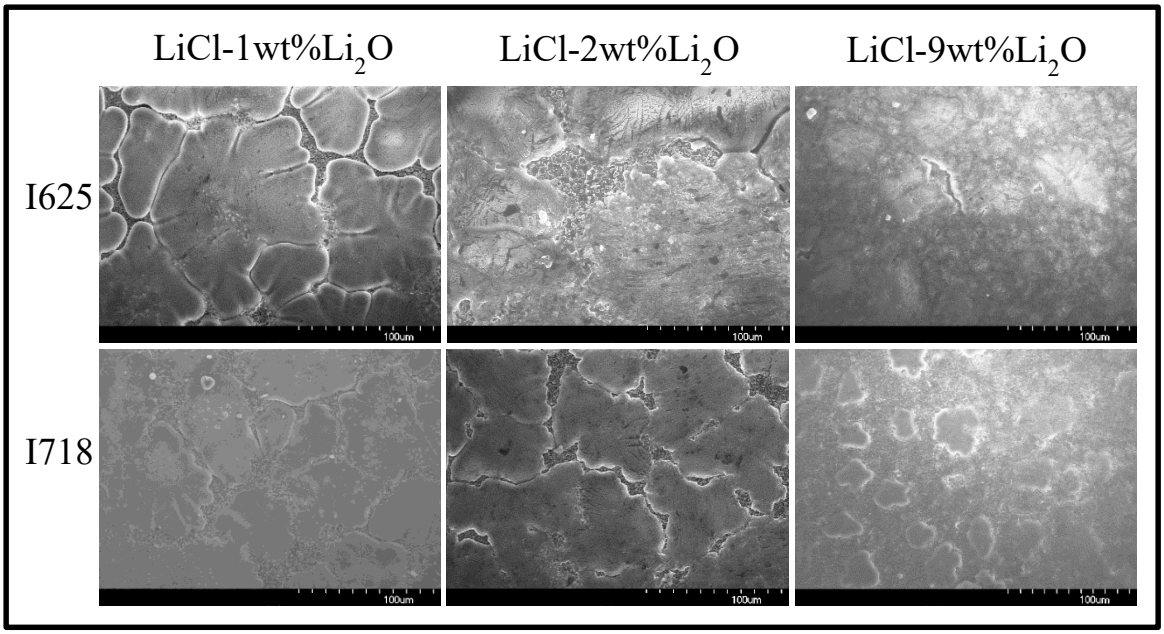


Figure 3.5: SEM micrographs of Inconel 625 and 718 after exposure to LiCl with 1, 2, and 9 (saturated) wt%Li_2O for 20 hours at 650°C. The increase in the extent of the oxide film formation with increasing Li_2O concentration is evident.

As shown in Figure 3.6, the surface of I625 and I718 exposed to molten LiCl-Li_2O-Li mixtures containing 0.5 wt% Li is different than those formed in LiCl containing an equivalent concentration of Li_2O without the presence of lithium metal. The surfaces exposed to LiCl-1 wt% Li_2O-0.5 wt% Li exhibit more uniform oxide formations compared to other melts. Alternatively, the morphology of samples exposed to LiCl-2 wt% Li_2O-0.5 wt% Li is seen to have isolated island oxide formations, characteristic of less stable films compared to those formed in lower concentrations of Li_2O.

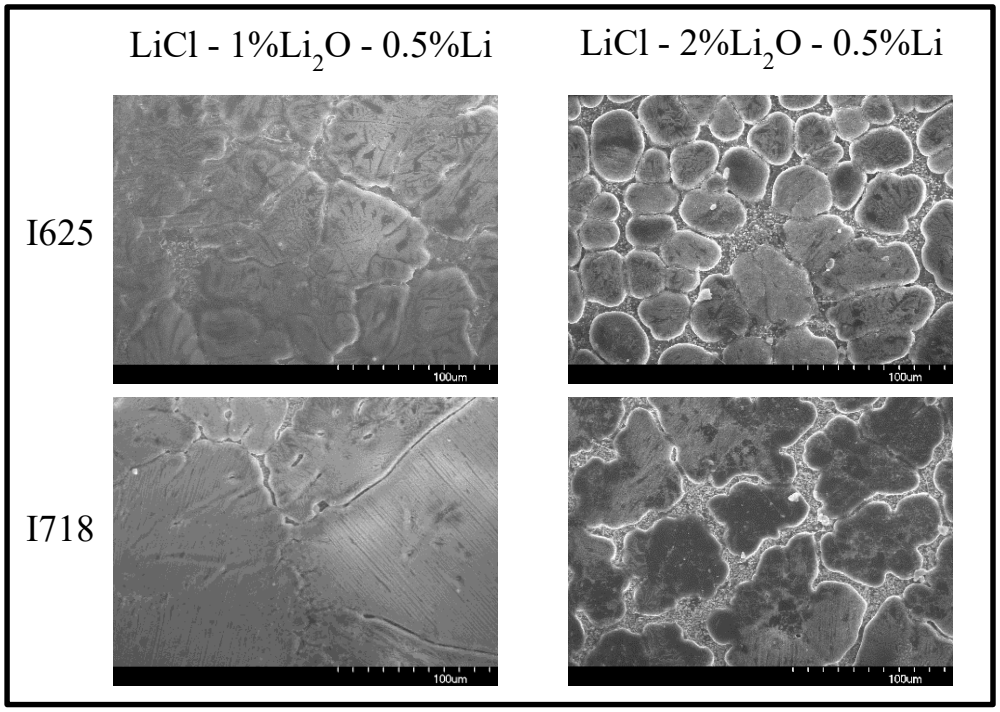


Figure 3.6: SEM micrographs of Inconel 625 and 718 after exposure to LiCl-1wt%Li_2O-0.5wt%Li and LiCl-2wt%Li_2O-0.5wt%Li for 20 hours at 650°C. The surfaces formed in mixtures with lower Li_2O concentration appear to be uniformly coated, while islands of coatings are seen to be formed in mixtures containing 2wt%Li_2O and 0.5%wtLi.

The surfaces of samples exposed to LiCl-Li_2O-1 wt% Li are shown in Figure 3.7, and are different than those formed under any of the previously discussed conditions. The surfaces resemble a bare alloy surface, lacking an indication of an oxide film cover. The bulk of the surfaces exposed to solutions containing 1 wt% Li appear flat with extensive surface blemishes. The size and severity of these blemishes appear to increase as the concentration of Li_2O in the salt increased from 1 to 2 wt%. The dependence of Li_2O concentration on the extent of these blemishes is evidence that the O^{2-} concentration in the solution, and not just the content of metallic Li, affects material interactions. It is hypothesized that the observed blemishes are the result of localized corrosion occurring at discontinuities in the surface films formed in melts containing 1 wt% Li.

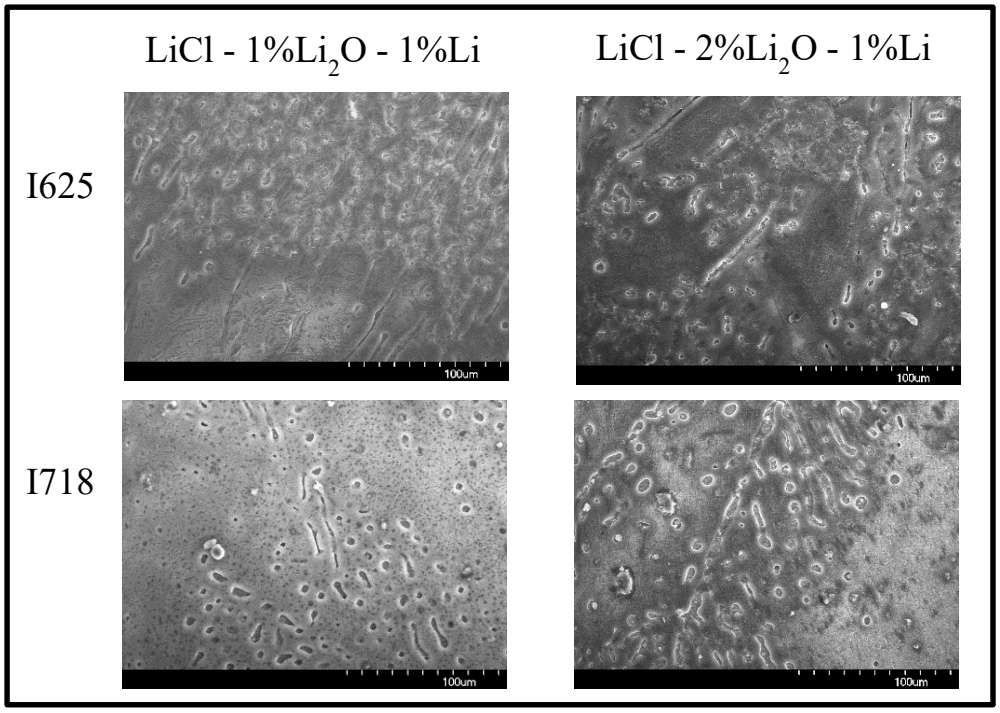


Figure 3.7: SEM micrographs of Inconel 625 and 718 after exposure to LiCl-1wt%Li_2O-1wt%Li and LiCl-2wt%Li_2O-1wt%Li for 20 hours at 650°C. The surfaces appear to not have formed a stable oxide film, and are rather characterized as bare alloy with extensive surface blemishes.

ICP-OES analysis was used to identify and quantify the alloying elements that leached out of each sample during exposure testing in the various molten salts. The concentrations of the primary alloying elements leached from the samples into the salt are shown in Figure 3.8.

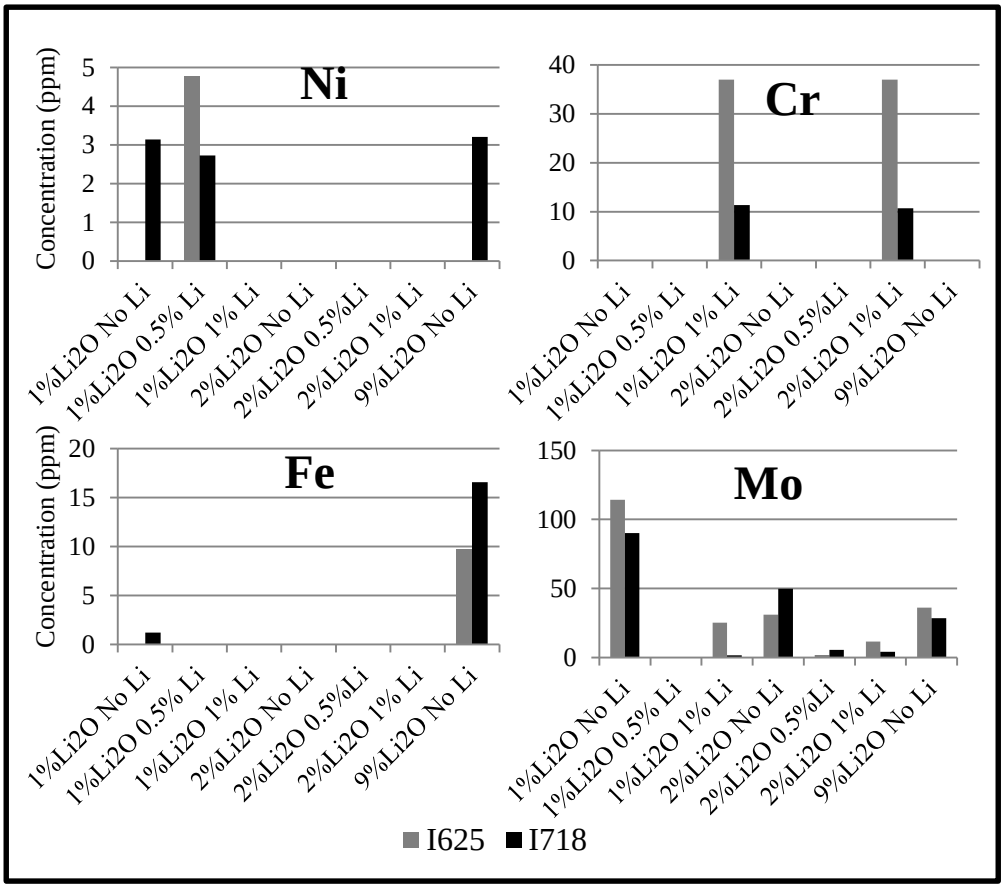


Figure 3.8: Concentrations of alloying elements found in the salt melts after each experiment, recorded by ICP analysis. The dissolution of Cr was only observed in significant quantities when 1wt%Li was present in the melt.

Information regarding the interactions of Inconel with the various molten salt mixtures can be obtained by comparing the dissolution of the constituent elements that occurred as a result of each exposure [50, 51]. The dissolution of Mo followed an interesting relation to the basicity of the salt. In the most acidic salt studied, LiCl-1 wt% Li_2O, the concentration of Mo leached from I625 exceeded 100 ppm. The loss of Mo was suppressed by the increase in basicity of the salt when the content of Li_2O was increased from 1 to 2 wt%. The loss of Mo continued to be suppressed to below the level of detection with the inclusion of 1 wt% Li_2O and 0.5 wt% Li in the melt, which may indicate that this solution was more basic than the LiCl-2 wt% Li_2O mixture. Resurgence

in Mo dissolution was observed with the inclusion of 2 wt% Li_2O-0.5 wt% Li or 1 wt% Li, and become increasingly severe in solutions saturated with Li_2O. This trend suggests that the LiCl-1 wt% Li_2O-0.5 wt% Li solution supports a balance between acidic and basic dissolution of Mo from Inconel. Fe was only observed to have dissolved in significant quantities when the alloys were exposed to solutions saturated with Li_2O. Significant dissolution of Ni was observed only in the LiCl-1 wt% Li_2O-0.5 wt% Li melt. However, it should be re-emphasized that all experiments were conducted in Ni crucibles, and that the dissolution of minor quantities of Ni during the experiments is expected. The strongest effect molten salt chemistry had on material dissolution was the absence of a detectable quantity of Cr in all melts, except those with 1wt%Li, where roughly 10 and 35ppm Cr was recorded for exposures of I718 and I625, respectively. This result suggests a fundamental change in corrosion processes that occur when a significant concentration of metallic Li is present in the solution.

The different dissolution processes that occurred as a result of exposure to the solutions containing the three different concentrations of metallic Li indicate that separate mechanisms drive material degradation during exposures to the various solutions. This observation is significant considering the solubility limit of Li in LiCl has been reported to not exceed 0.3 wt% [37, 41, 52-54]. The observation of material interaction dependence on Li concentration beyond 0.3 wt% is therefore attributed to the ternary nature of the LiCl-Li_2O-Li system. As a result of this ternary dependence it is evident that LiCl-Li_2O-Li solutions cannot be completely described by the F^- center model of metal salt solutions discussed in Chapter 1.

The observation that the minimum material loss rates for every element except Ni were recorded in molten LiCl solutions containing 1 wt% Li_2O and 0.5 wt% Li, corroborated by the uniform surfaces observed through SEM analysis, suggests that Inconel alloys are most stable in this solution chemistry. According to the acid-base description of molten salt chemistry, this observation coincides with optimal solution basicity. Samples exposed to solutions containing either a higher concentration of Li_2O and or Li, were significantly more degraded indicating a departure from optimal basicity. It is important to note that while increasing the concentration of either Li_2O or Li beyond this point resulted in more aggressive material interactions with the melt, the results of increasing either concentration independently were different. Increasing the concentration of Li_2O to 2 wt% and maintaining 0.5 wt% Li resulted in less uniform oxide formations across the surface, yet only a minor change in the dissolution of alloying elements occurred. This suggests that the basic corrosion rate is not significant in these solutions, and that the partial oxide film does not protect the bare alloy. However, it is noted that the observation of Ni in the LiCl-1 wt% Li_2O-0.5 wt% Li melt may indicate that Ni is unstable under these conditions. The lack of detectable quantities of Ni and only minimal quantities of Mo in the LiCl-2 wt% Li_2O-0.5 wt% Li melt indicates that optimal basicity is between 1 wt% Li_2O-0.5 wt% Li and 2 wt% Li_2O-0.5 wt% Li. Alternatively, when the concentration of metallic Li was increased to 1 wt%, the surfaces formed no stable surface films and large quantities of Cr dissolved into the salt. Finally, the dissolution processes that occurred during exposure to solutions containing 1 wt% Li were different compared to the melt of extreme basicity, where the activity of the O^{2-} ion can be approximated as unity. The observation of significant quantities of Fe and Mo in

solutions saturated with Li_2O demonstrates the non-protective nature of the surface films formed under these conditions. Further, the lack of surface film formation during exposure to mixtures containing 1 wt% Li appears to have only had the effect of removing Cr from the surface. It can therefore be suggested that excess amounts of metallic Li in the salt alters the chemistry of the solution in a different manner other than, or in addition to, the basicity of the salt.

X-ray photoelectron spectroscopy was used to further characterize the chemistry of the surfaces that resulted from exposure to the various test solutions. Due to the necessity of rinsing the samples with methanol to remove residual salt from the sample surface prior to analysis, only elemental information obtained from XPS analysis can be relied upon. The elemental compositions of the surface of both I625 and I718 after exposure to the separate test mixtures, corrected by the respective elemental photoemission cross section, are given in Figure 3.9.

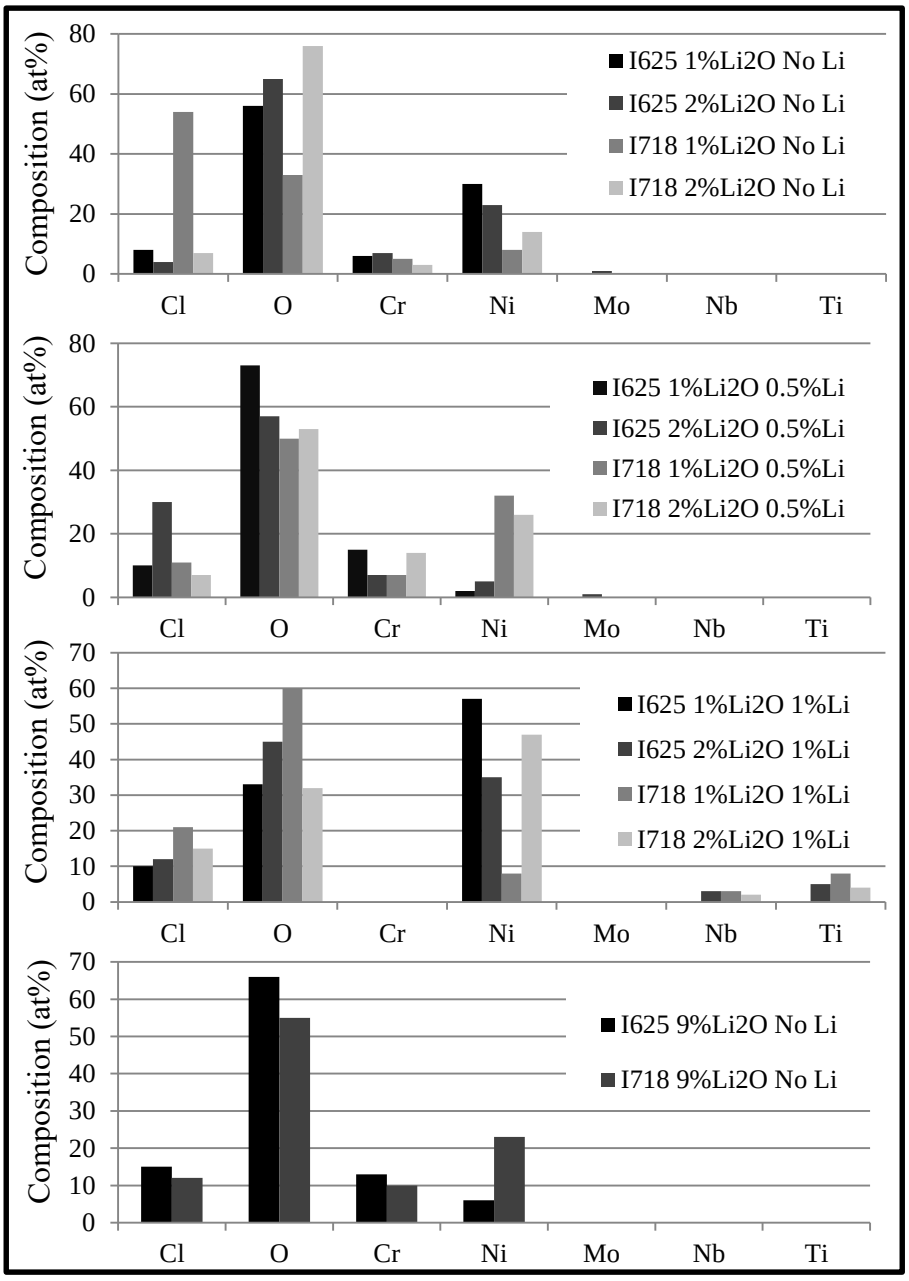


Figure 3.9: Elemental composition, given in atom %, of each sample surface obtained by XPS. The ratio of intensity of Cr to Ni remains constant or increases with the inclusion of 0.5wt%Li for a given concentration of Li_2O. Further, no Cr was observed on a sample surface exposed to mixtures containing 1wt%Li.

The elemental composition of the surfaces that formed as a result of exposure to the separate test solutions support the previously stated hypotheses of material interactions with LiCl-Li_2O-Li. The ratio of Cr to Ni on the surface was found to increase

with the inclusion of 0.5 wt% Li in the melt for a given concentration of Li_2O. This indicates that the stability of Cr oxides is at least equal to, if not enhanced by, the addition of 0.5 wt% Li to LiCl-1 wt% Li_2O. The surface exposed to LiCl saturated with Li_2O consisted of a higher amount of Cr compared to other samples.

The difference in the success of the separate Cr based films at suppressing material dissolution is significant. The films formed in LiCl saturated with Li_2O were observed to encase the surface completely and had the highest Cr content, yet they facilitated the dissolution of significant quantities of Fe and Mo. Alternatively, the films formed in LiCl-1 wt% Li_2O-0.5 wt% Li had comparable Cr contents but were highly protective against the dissolution of alloying elements.

Chromium was not present in detectable quantities on the surface of either alloy exposed to molten mixtures containing 1 wt% Li, in agreement with the observation of the Cr depletion effect detected by ICP-OES analysis. Minor alloying elements, Nb and Ti, were only observed on the surfaces exposed to solutions containing 1 wt% Li, indicating that the bulk material was being analyzed. Contrastingly, these elements were not detectable on surfaces exposed to solutions containing less than 1 wt% Li, where oxide films were present. The surface of an I625 sample exposed to LiCl-1 wt% Li_2O-1 wt% Li was subjected to Ar sputtering for 50 minutes, approximately equivalent to the removal 350 nm of Ta_2O_5, to investigate the depth to which Cr leaching occurred. The XPS spectrum recorded after this sputtering, shown in Figure 3.10, is that of nearly pure Ni metal without detectable quantities of major alloying elements. The complete depletion of Cr from its initial content of 20 wt% Cr at a depth of hundreds of nm

represents severe degradation through a mechanism that is not analogous to corrosion in LiCl-Li_2O.

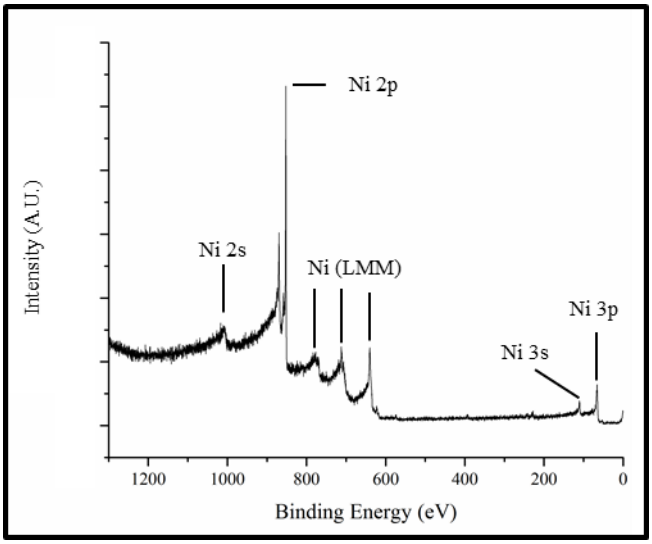


Figure 3.10: XPS survey spectrum obtained from I625 after exposure to LiCl-1wt%Li_2O-1wt%Li at 650°C for 20 hours and Ar milled for 50 minutes. It is apparent that only Ni is present in detectable quantities, and that Cr is depleted from the alloy surface.

3.4.3 Summary:

The effect of including metallic lithium in molten LiCl-Li_2O on material degradation was investigated. Both Inconel 625 and 718 suffered significant loss of molybdenum in the most acidic salt studied, LiCl-1wt%Li_2O. The completeness and protective abilities of oxide films formed as a result of exposure, was found to increase when these materials were exposed to more basic LiCl-2wt%Li_2O. The most protective and uniform surface films formed on both alloys during exposure to LiCl-1wt%Li_2O-0.5wt%Li. It is suggested that this solution therefore is close to the optimal solution chemistry for the suppression of material degradation.

The stability of the surface films was degraded by increasing the concentration of either metallic Li, or Li_2O, beyond LiCl-1wt%Li_2O-0.5wt%Li. The surfaces of both alloys exposed to LiCl saturated with Li_2O were coated with thick non-protective Cr based oxides. Samples exposed to mixtures containing 1wt%Li did not form surface films, independent of the concentration of Li_2O in the mixture. Significant dissolution of Cr into the melt only occurred as a result of the exposure of materials to solutions containing 1wt%Li. It is reported that fundamentally different chemical interactions occur in solutions containing excess metallic lithium other than or in addition to, the activity of the O^{2-} ion in the molten mixture.

3.5 Exposure Studies of Stainless Steel in Alternative Crucibles:

As discussed in Chapter 2, a variety of crucible materials were investigated for containing molten LiCl-Li_2O-Li. While, it was known that practically any crucible material would interact with the melts to some degree, the effect of the presence of corrosion products from the crucible on the corrosion of alloy samples exposed to the melt was unknown. Experiments were conducted to evaluate the effect of varying the crucible material on the corrosion of alloys exposed to molten LiCl-Li_2O-Li. Coupons of SS316L were exposed to molten LiCl-2wt%Li_2O containing 0 and 1wt%Li in increments of 0.2wt% at 650˚C for 20 hours. Replicate exposures were conducted in nickel and tungsten crucibles. The dissolution of alloying elements that occurred during these exposures, obtained by ICP-OES analysis, is shown in Figure 3.11.

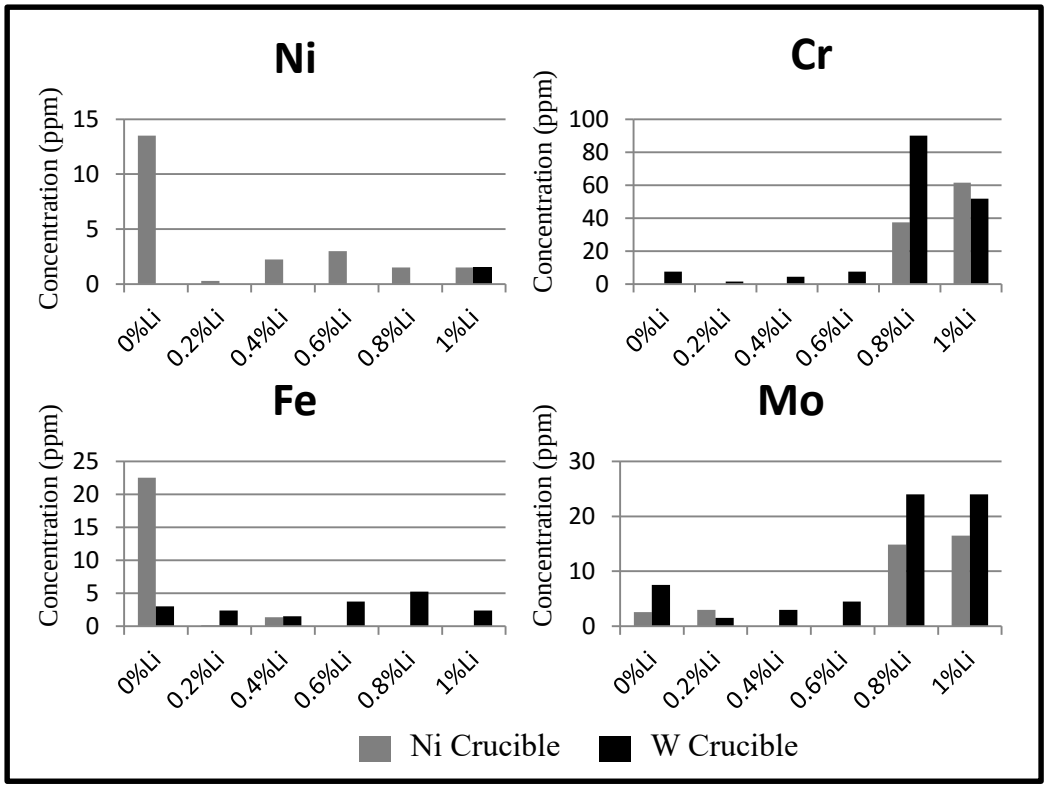


Figure 3.11: Concentrations of alloying elements detected in the salt melts after exposure of SS316L to LiCl-Li_2O-Li, recorded by ICP analysis. The dissolution of Cr and Mo were observed when greater than 0.6wt%Li was present in the melt.

The trends in material dissolution from SS316L by molten LiCl-Li_2O-Li detected by ICP-OES analysis, shown in Figure 3.11, are observed to agree with the conclusions of Section 3.4. It is observed that, in the absence of Li, LiCl-Li_2O preferentially leaches Fe and Ni. However, Mo and Cr are preferentially leached by melts containing high concentrations of Li. Furthermore, as was observed in the corrosion study of Inconel in molten LiCl-Li_2O (Section 3.4), the inclusion of low concentrations of Li (between 0.2 and 0.6wt%) suppresses the rate of material dissolution.

The concentration of W detected in the LiCl-Li_2O-Li melts contained in W crucibles was sufficient to saturate the ICP-OES detector, thereby indicating the presence of hundreds of ppm in the salt. Furthermore, W oxide was visually observed to flake off

the walls of the crucibles following each exposure test, nearly independent of the concentration of Li in the melt. As a result, it can be concluded that a large concentration of oxidized W was present in the molten LiCl-Li_2O-Li used in these studies. However, as seen in the ICP-OES data in Figure 3.11, the presence of this large quantity of W in the melts did not significantly affect the dissolution of Cr and Mo from the SS316L samples. Therefore it is concluded that the inclusion of a high concentration of a given element in molten LiCl-Li_2O-Li may not affect the rate of dissolution of alternative elements.

The compositions of the surfaces of SS316L samples exposed to molten LiCl-Li_2O-Li obtained from XPS analysis, following a 10 minute methanol rinse, are shown in Figure 3.12. The XPS data shown in Figure 3.12 is restricted to the samples exposed in Ni crucibles as the samples exposed to melts contained in W crucibles were observed to be coated with oxidized W.

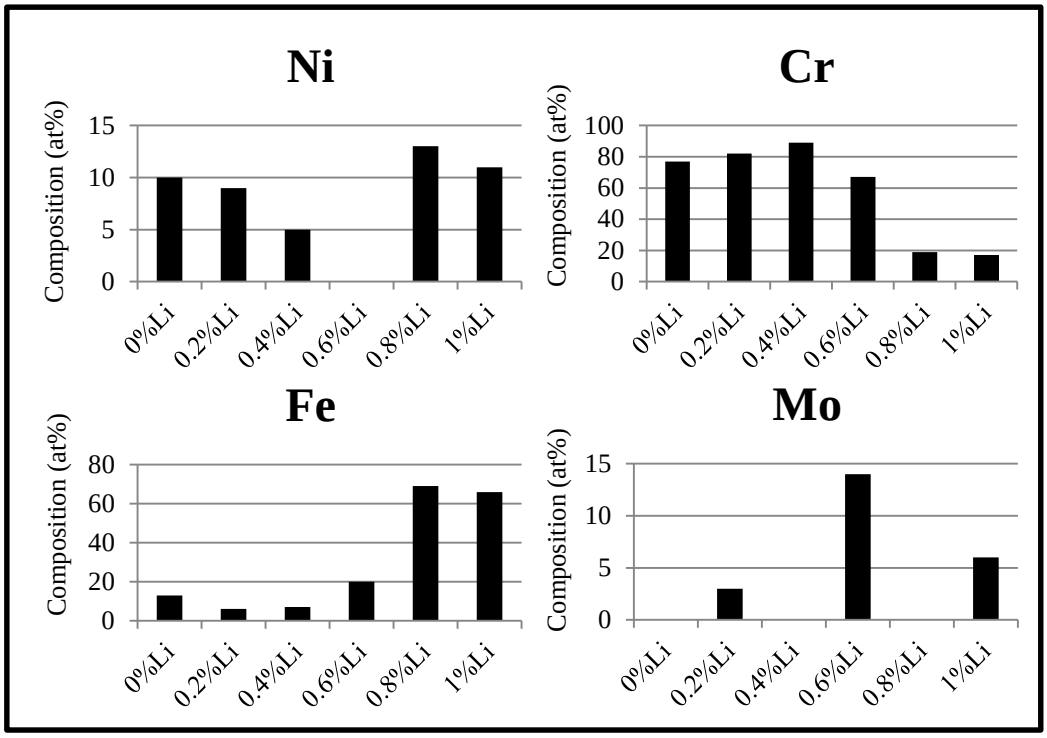


Figure 3.12: Elemental composition, given in atom %, of the surfaces of SS316L obtained by XPS after exposure to LiCl-Li_2O-Li at 650°C for 20 hours.

The elemental compositions obtained XPS analysis shown in Figure 3.12 demonstrates that Cr is stable on the surface of SS316L upon contact to molten LiCl-Li_2O containing low concentrations of Li. On the other hand, the surfaces of samples exposed to melts containing greater than 0.6wt%Li are observed to be depleted of Cr, and are comprised nearly exclusively of Ni and Fe. The surface of the sample exposed to LiCl-2wt%Li_2O-0.6wt%Li possessed a high concentration of Mo and was depleted of Ni.

The data obtained from the degradation of SS316L upon exposure to LiCl-Li_2O-Li, as shown in Figures 3.11 and 3.12 support the findings presented in the Inconel study of Section 3.4. While the rate of material dissolution from SS316L is suppressed by presence of low concentrations of Li, Cr and Mo are preferentially leached by melts containing greater than 0.6wt%Li. This data is in agreement with the detection of a

primarily Cr based surface following exposure of SS316L to melts containing up to 0.6wt%Li. Similarly, the surfaces of samples exposed to molten LiCl-Li_2O-Li containing either 0.8 or 1wt%Li are observed to be depleted of Cr. Coupled with the results of Section 3.4, these data indicate that common alloying elements are similarly stable in austenitic stainless steels and nickel based alloys when exposed to molten LiCl-Li_2O-Li. It is observed that a protective Cr based surface develops on these alloys in molten LiCl-Li_2O containing less than 0.8wt%Li. Alternatively, material degradation is observed to follow a different mechanism, leaching Li where Cr and Mo preferentially, in melts containing greater than 0.8wt% Li.

3.6 Corrosion of Hastelloy N in Molten LiCl-Li_2O-Li:

The corrosion resistance of Hastelloy N in molten LiCl-Li_2O-Li was studied to investigate the behavior of an alloy that does not typically rely on the formation of Cr based surface oxides for corrosion protection. Hastelloy N (7% Cr; 4.2% Fe; 17% Mo; balance Ni) was developed during the molten salt reactor program at Oak Ridge National Laboratory specifically to suppress corrosion in molten fluoride salts [123, 167-169]. Corrosion in molten fluoride salts is different than corrosion in molten chloride salts in that corrosion in the latter case relies on the formation of stable surface films that protect the bulk alloy from contacting the melt (Section 1.7.2). However, transition metal oxides are highly soluble in molten fluoride salts, and as a result molten fluorides typically contact bare metallic alloys directly [124]. The direct contact of structural alloys with molten fluorides requires the employment of materials that do not rely on the formation of protective surface films for corrosion suppression, but instead rely on the

electrochemical nobility of the alloy to prevent oxidation. Hastelloy N was therefore designed specifically to contain a minimal quantity of the electrochemically active element Cr, and consists primarily of the noble elements Ni and Mo.

Hastelloy N's mechanism of corrosion protection, based on the avoidance of oxidation and surface film formation, was the motivation for investigating Hastelloy N's behavior in molten LiCl-Li_2O-Li. As shown in Chapter 5, the surface of alloys exposed to molten solutions of LiCl-Li_2O containing high concentrations of Li are metallically bonded. Furthermore, melts containing certain concentrations of Li were observed to preferentially leach Cr. Therefore, it was anticipated that Hastelloy N may be capable of sustaining a metallic surface without reacting with molten LiCl-Li_2O-Li in a manner similar to its mechanism of stability in molten fluorides.

Coupons of Hastelloy N were supplied by Haynes Alloys. Samples were cut in to 1 cm wide strips and suspended in molten solutions of LiCl-2wt%Li_2O in the absence of Li, as well as LiCl-2wt%Li_2O containing 0.5 and 1wt%Li at 650°C for 20 hours. The quantity of alloying elements that were leeched into each melt as a result of the exposures was characterized using ICP-OES analysis. Post exposure surface analysis was conducted using XPS following a 10 minute methanol rinse.

The concentration of alloying elements leached from Hastelloy N during exposure to molten LiCl-Li_2O-Li, as determined ICP analysis of the solidified salt melts, is shown in Figure 3.13. It is observed that Mo was preferentially leached from Hastelloy N during exposure to molten LiCl-Li_2O irrespective of whether it contained Li or not. The preferred dissolution of Mo by molten LiCl-Li_2O in the absence of Li is in agreement

with the study of Inconel in this system. However, the preferential leaching of Mo from I625 and I718 was suppressed dramatically by the inclusion of 0.5wt% Li in the melt which is in contrast to the observation of similar leaching rates of Mo from Hastelloy N in melts in the presence, as well as in the absence of Li is counter to what was observed in previous studies of alternative alloys.

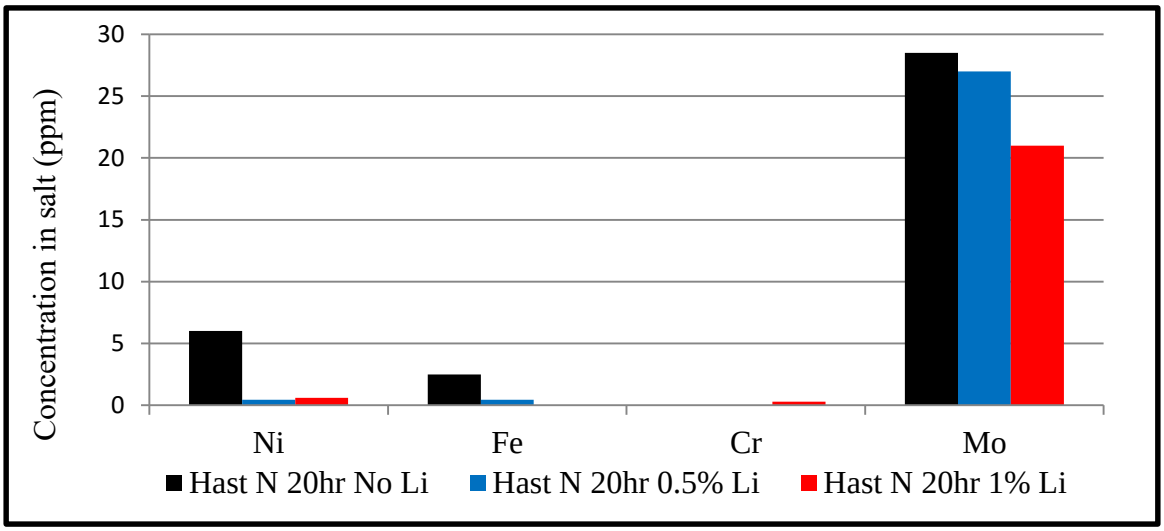


Figure 3.13: Concentration of alloying elements detected in the salt following 20 hours of exposure of Hastelloy N to molten LiCl-2wt%Li_2O containing 0, 0.5 and 1wt%Li, recorded by ICP analysis. The dissolution of large quantities of Mo was observed to occur as a result of exposure to these molten solutions independent of the presence or concentration of Li.

The XPS spectra obtained from the surfaces of Hastelloy N samples independently subjected to 20 hours of exposure to molten LiCl-2wt%Li_2O containing 0, 0.5 and 1wt% Li are shown in Figure 3.14. The relative composition of the alloying elements detected on the alloy surface following exposure to the molten solutions, obtained from XPS analysis, are shown in Table 3.1.

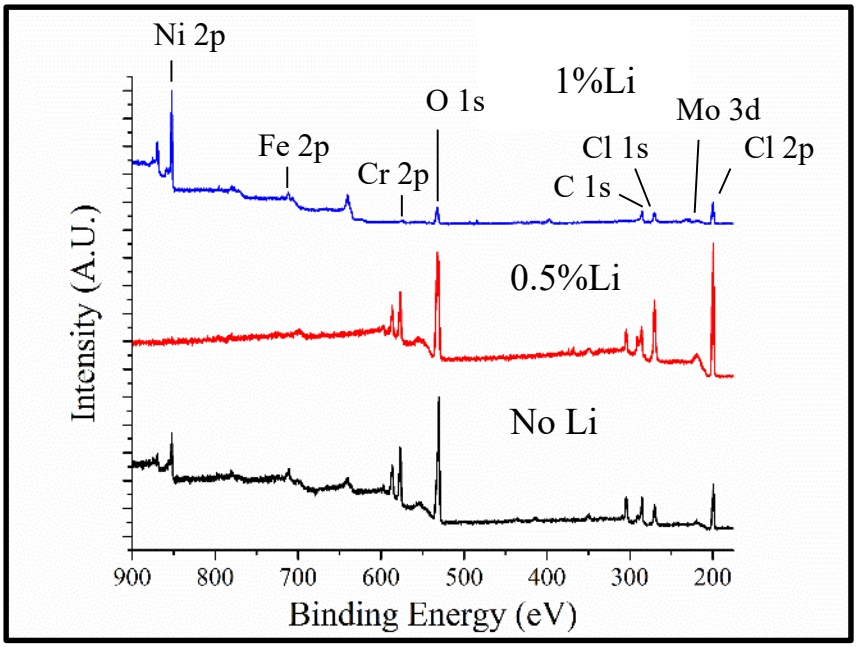


Figure 3.14: XPS survey scans obtained from the surface of Hastelloy N exposed to molten LiCl-2wt%Li_2O containing 0, 0.5 and 1wt%Li at 650˚C for 20 hours. The increase in Cr content on the sample exposed to the melt containing 0.5wt%Li, and the lack of Cr on the sample exposed to the melt containing 1wt%Li are in agreement with the findings of the study of Inconel corrosion in molten LiCl-Li_2O-Li shown in Section 3.4.2.

The XPS spectra obtained from the surface of Hastelloy N, shown in Figure 3.14, corroborate the findings of the previous studies of the corrosion of Inconel and stainless steel in molten LiCl-Li_2O-Li. It can be observed that the surface of Hastelloy N exposed to molten LiCl-2wt%Li_2O in the absence of Li primarily consists of Cr and Ni. Alternatively, the surface of Hastelloy N exposed to molten LiCl-2wt%Li_2O-0.5wt%Li is observed to be almost completely comprised of Cr. The detection of a nearly exclusively Cr surface on Hastelloy N is similar to the results obtained from the surface of I625, I718 and SS316L following exposure to molten solutions containing low concentrations of Li. The ability of Hastelloy N to form a Cr based surface is surprising due to the low Cr content (7wt%) in the as-received alloy. Furthermore, Cr was observed to be below the level of detection by XPS on the surface of Hastelloy N exposed to LiCl-2wt%Li-

1wt%Li. Interestingly, Mo was below the level of detection by XPS analysis on the surface of Hastelloy N exposed to molten LiCl-Li_2O in the absence, as well as the presence, of Li. Mo constitutes 17% of the as-received alloy and the observation of complete removal of this element from the surface of the alloy as a result of 20 hours of exposure is indicative of sever preferential corrosion.

Table 3.1 Relative proportions of Ni and Cr on the surface of Hastelloy N, as observed by XPS, exposed to molten LiCl-2wt% Li_2O containing 0, 0.5 and 1wt%Li at 650°C for 20 hours. Samples were rinsed with methanol following exposure to the molten solution.

Wt% Li in melt	Ni %	Cr %
No Li	30	70
0.5%	N.D.	100
1%	99	1

The results obtained from XPS analysis of Hastelloy N are in agreement with analysis of I625, I718 and SS316L exposed to melts of the same composition. The trends in the behavior of Cr and Mo in the three categories of alloys studied, Ni-Mo-Cr, Ni-Cr-Fe, and Fe-Cr-Ni, indicate a general trend of the chemistry of material interactions with molten LiCl-Li_2O-Li. While the presence of a low concentration of Li in the melt increases the Cr content on material surfaces, materials exposed to melts containing high concentrations of Li are depleted of Cr. Furthermore, Mo is depleted from the surface as a result of exposure to molten LiCl-Li_2O in the presence as well as the absence of Li.

As previously stated, the Hastelloy N's mechanism of corrosion protection in molten salts is typically not reliant upon the formation of protective surface films, but the intrinsic nobility of the alloy itself. The dissolution of large quantities of Mo into molten LiCl-Li_2O in the presence and absence of Li suggests that the nobility of this alloy is

insufficient to provide corrosion protection in these molten systems. While the surface of Hastelloy N exposed to LiCl-2wt%Li-0.5wt%Li was observed to be comprised of oxidized Cr, these surface films were not protective against preferential dissolution of Mo. Alternatively, neither SS316, I625 nor I718 leached Mo when a primarily Cr surface film was formed during exposure to molten LiCl-Li_2O-Li. The difference in ability of these films to protect the underlying alloy is attributed to the low Cr content in Hastelloy N compared to the other alloys investigated. It is hypothesized that of the minimal content of Cr in Hastelloy N does not allow for the development of fully protective surface films when exposed to molten solutions of LiCl-Li_2O containing small quantities of Li. As will be shown in Chapter 6, the presence of O^{2-} is molten solutions of LiCl-Li_2O-Li oxidizes material surfaces in a manner typical of molten salts containing oxides despite the presence of the reducing agent Li. It is therefore proposed that while some portion of the surface of Hastelloy N may form protective Cr based surface films, these films are not fully developed and allow for the continued oxidation and dissolution of Mo. Thus, the corrosion rate of Hastelloy N in molten LiCl-Li_2O-Li was too high and did not warrant further investigations.

3.8 Investigations of Reagent Grade vs. Anhydrous LiCl:

For reasons discussed in Chapter 1, the presence of trace levels of impurities in molten alkali-halide salts has a profound effect on the corrosive properties of the melt [124, 125]. The highly hygroscopic nature of LiCl offers a unique challenge in this respect as chemical stocks of anhydrous LiCl can absorb large quantities of water during shipping or storage [103, 180]. For example, it has been shown that LiCl-2wt%Li_2O

accumulated an equivalent of 0.75wt% H_2O by being stored in a 425L volume Ar glove box that contained 15ml of H_2O in an open beaker for 8 hours [106]. For this reason, the effect of the presence of varying levels of moisture in molten LiCl-Li_2O-Li on the corrosive properties of the molten solutions was investigated.

Three levels of H_2O content as impurity were studied: as-received reagent grade LiCl, reagent grade LiCl dried at 550°C, and ultra-high purity LiCl dried at 550°C. To dry LiCl before use in corrosion studies a quantity of LiCl was heated to 550°C for two hours, then the temperature was raised to 650°C and equilibrated for 30 minutes before Li_2O and Li were added [106]. These melts were additionally allowed to equilibrate for 30 minutes following the addition of Li_2O and Li to allow for their dissolution before sample coupons were exposed to the final melt [43]. This approach was adopted due to the findings of Gese *et al.* who demonstrated that while LiCl is hygroscopic it does not react with H_2O to form LiOH and HCl until after it is molten [106]. On the other hand, Li_2O is not hygroscopic but forms LiOH at ambient temperature when exposed to H_2O. As a result, by drying LiCl at a temperature below its melting point prior to the addition of Li_2O, impurity H_2O in the LiCl can be evaporated and the formation of LiOH can be avoided. By removing excess hydroxide ions from the molten salt, this drying procedure suppresses the basic fluxing mechanism discussed in Chapter 1. The efficacy of this drying procedure was demonstrated through electrochemical analysis, as well as by comparing the results of corrosion experiments conducted in the melts containing varying levels of impurity H_2O.

Cyclic voltammetry (CV) is an effective tool for studying the purity and electrochemical properties of molten salts. CV was used extensively by Gese *et al.* to characterize how the presence of trace levels of H_2O effects the electrochemistry of molten LiCl-Li_2O [106]. In this study, CV was used to qualitatively analyze the purity of molten LiCl-Li_2O. It was demonstrated that precurrents (reduction currents observed at more anodic potentials than the $Li^+|Li$ reduction potential) could be dramatically suppressed by adding Li_2O to LiCl after it had been heated to a temperature of several hundred degrees Celsius. The observation of a precurrent is a direct indication of the presence of impurities in molten LiCl-Li_2O, as a pure melt would ideally contain a single cation. For this reason, cathodic cyclic voltammograms of pure LiCl-Li_2O will contain a single reduction peak corresponding to the $Li|Li^+$ potential. Any current observed prior to this (at a more anodic potential) must derive from the reduction of an impurity cation, in this case H^+. Furthermore, as per the Randles–Sevcik equation, the peak current density of a redox reaction in a CV is directly related to the concentration of the analyte that is undergoing oxidation or reduction. In the case of impurity moisture in molten LiCl-Li_2O, the magnitude of the precurrent peak is proportionate to the quantity of LiOH in the melt. This effect can be observed in the cyclic voltammograms shown in Figure 3.15. The two CV curves shown in Figure 3.15 are polarizations of a Mo wire measured against a $Ni|Ni^{2+}$ quasi-reference electrode using a Ni counter electrode in molten LiCl-2wt%Li_2O at 650°C. Duplicate experiments were conducted employing as-received LiCl, shown in red, and in LiCl that was dried in the previously described manner prior to the addition of Li_2O, shown in black. It is noted that the CV conducted in dried LiCl possess a minor precurrent peak corresponding to the reduction of LiOH, however, the peak current is

dramatically less than that observed in the as-received reagent grade LiCl. The flat current density observed between -1.1 and -1.2 V vs $Ni|Ni^{2+}$ in the as-received salt is the result of maximizing the current output of the potentiostat employed in this study.

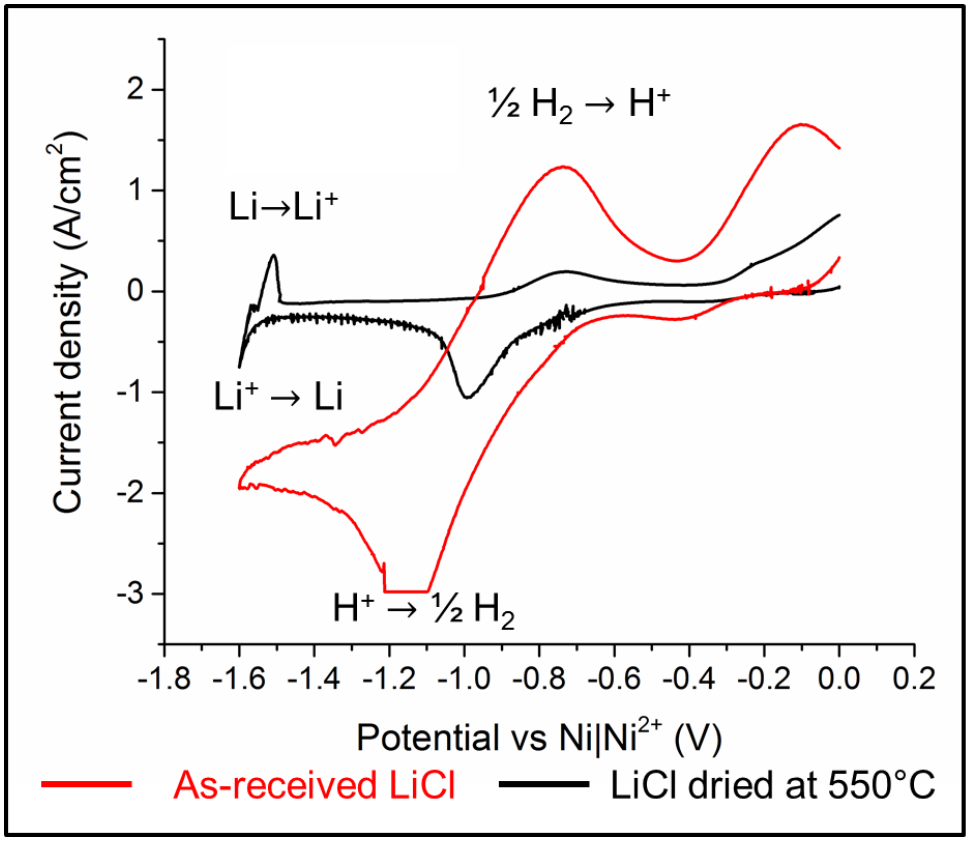


Figure 3.15: Cathodic cyclic voltammograms of Mo vs a Ni quasi-reference electrode using a Ni counter electrode in molten LiCl-2wt%Li_2O at 650°C using (Red) as-received reagent grade LiCl and (Black) reagent grade LiCl that was dried at 550˚C for two hours before Li_2O was added. The reduction in the precurrent observed (corresponding to the oxidation and reduction of LiOH) that occurs as a result of the drying process indicates the removal of a large portion of the residual H_2O in the melt.

While the data shown in Figure 3.15 demonstrates that the previously described baking procedure removes the majority of impurity H_2O from reagent grade LiCl, it does not quantify the effect that the presence of the residual moisture has on corrosion in this system.

The effect of the presence of residual moisture on the corrosion of materials exposed to molten LiCl-Li_2O-Li was evaluated by exposing coupons of SS316L to molten LiCl-Li_2O-Li containing the three levels of H_2O impurity previously discussed. The concentrations of Cr and Mo that leached during 20 hours of exposure of SS316L to molten solutions of as-received LiCl-Li_2O-Li, as detected by ICP-OES analysis, are shown in Figure 3.16. The quantity of Cr detected by ICP-OES following exposures of SS316L to melts that were dried prior to the addition of Li_2O and Li is shown in Figure 3.17. The quantity of Mo in dried melts was below the level of detection by ICP-OES. Fe and Ni were below the level of detection in melts containing Li following all exposures regardless of the purity or composition of the melt. As discussed in Section 3.4, high levels of Cr and Mo were leached from SS316L during exposure to undried LiCl-2wt%Li_2O when 0.8 or 1wt%Li was present in the melt. Alternatively, the quantity of Cr detected in melts that were dried prior to the addition of Li_2O and Li, shown in Figure 3.17, was significantly suppressed compared to melts that were not dried. Melts containing LiCl dried at 550°C only leached significant quantities of Cr when 0.6wt%Li was included in the solution. The concentrations of Cr and Mo were below the levels of detection in melts of ultra-high purity LiCl. It can be concluded that removal of residual H_2O from reagent grade LiCl by baking at 550˚C prior to the addition of Li_2O and Li is effective at suppressing preferential leaching in the molten LiCl-Li_2O-Li system. Material leaching rates in reagent grade LiCl melts dried in this manner are low with the exception of melts containing 0.6wt%Li.

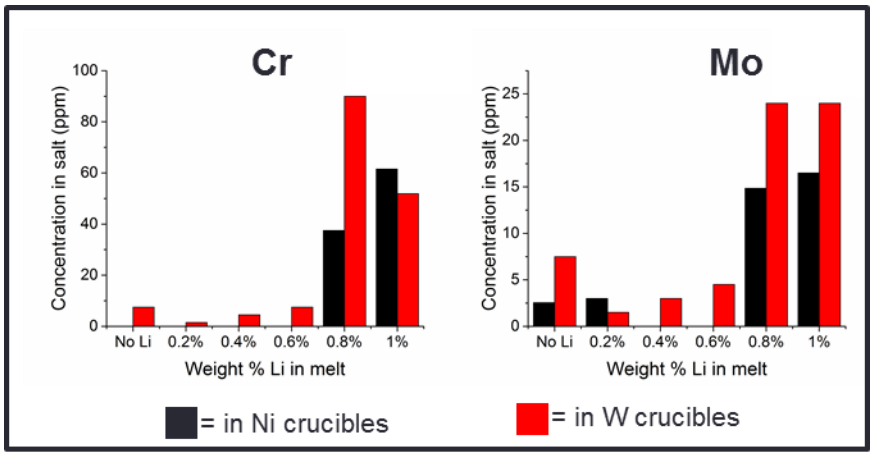


Figure 3.16: Concentration of Cr (Left) and Mo (Right) detected by ICP-OES analysis of salt ingots following 20 hours of exposure of SS316L to as-received LiCl-2wt%Li_2O with 0, 0.2, 0.4, 0.6, 0.8, and 1wt%Li at 650°C. Data resulting from duplicate exposures contained in W and Ni crucibles is shown. Large quantities of Cr and Mo are observed to have been leached by melts containing 0.8 and 1wt%Li.

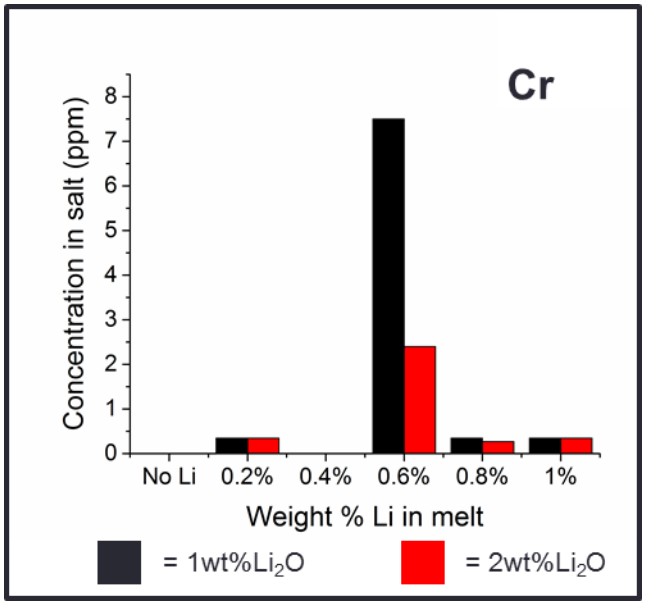


Figure 3.17: Concentration of Cr detected by ICP-OES analysis of salt ingots following 20 hours of exposure of SS316L to dried molten LiCl-2wt%Li_2O with 0, 0.2, 0.4, 0.6, 0.8, and 1wt%Li at 650°C with melts containing in Ni crucibles. Cr was observed to have been leached in appreciable quantities by melts containing 0.6wt%Li.

The subsequent investigations of the effect that metallic Li has on corrosion in molten LiCl-Li_2O were conducted using LiCl dried at 550°C prior to the addition of Li_2O and Li. It is noted that the LiCl-Li_2O electrolyte used in the electrolytic reduction process

will not contain Li until it is electrolytically formed during polarization. It has been reported that the reduction of LiOH precludes the formation of bulk Li [106]. For this reason, the following studies investigated the effect of the accumulation of Li in dry LiCl-Li_2O as it is expected to be representative of process conditions. Finally, the principle findings obtained from studies using dried reagent grade LiCl melts were confirmed in duplicate experiments employing ultra-high purity LiCl.

3.9 Extended Exposure Studies:

Corrosion testing of two alloys was conducted for extended periods of time to verify that the previously discussed findings are accurate representations of the degradation that occurs in molten LiCl-Li_2O-Li over longer periods of exposure. Inconel 625 and stainless steel alloy 316L were chosen for this study as they represent model Ni and Fe based alloys for which the data were presented in Sections 3.4 and 3.5, respectively. Sample coupons were exposed to molten LiCl-1wt%Li_2O containing 0, 0.1 and 0.3wt%Li at 650˚C for 50 and 100 hours. These melt compositions were chosen to represent the range of concentrations that would be most relevant to the electrolytic reduction process; containing Li concentrations up to the approximate limit of physical dissolution in LiCl at 650˚C (see Chapter 4). The LiCl used in this study was dried for two hours at 550ºC prior to the addition of Li_2O and Li in the manner described in Section 3.8. The surfaces of the samples used in this study were polished to a 1µm finish prior to exposure. With the exception of these specified details, the exposure experiments were conducted in an identical manner to the procedures discussed in Chapter 2. Post exposure surface analysis was conducted using Raman and X-ray photoelectron

spectroscopies, X-ray diffraction was used for crystallographic analysis, micro-Vickers hardness testing was used to evaluate surface mechanical properties, and scanning electron microscopy was used to analyze the sample morphology.

It should be noted that the series of experiments included in this section was conducted in an intermediate phase of this research program. These studies were undertaken and completed after the effects of residual H_2O in the melt were identified (Section 3.8), but before the sample baking procedure (described in Section 3.10 and employed in Chapters 5 and 6) was developed. As a result, the characterization in this section is restricted in comparison to the analyses employed in Chapters 5 and 6. This is specifically relevant to EDS and XPS analyses of the post exposure surfaces in this section. As demonstrated in Section 3.10, the baking procedure facilitates the redistribution of the salt on the sample surfaces such that EDS and XPS measurements of the surface chemistry can be conducted without excessive interference from residual salt. Unfortunately, the EDS analysis included here captured considerable signal from residual salt as this procedure was not developed prior to conducting the experiments in the current section. The EDS data shown in this section is normalized to the Fe, Ni, Cr and Mo signals to avoid the effects of the presence of salt on the sample surfaces. Further, post exposure surface analysis using XPS was conducted after the samples were rinsed in methanol for 10 minutes to remove residual salt. The nanometer scale interaction volume of XPS resulted in the inability of this technique to detect material surfaces unless the salt was removed prior to analysis. The effects of rinsing the post exposure surfaces with methanol are unknown, however it is likely that the Li intercalated surface films formed

in molten LiCl-Li_2O-Li are unstable in the room temperature solvent. For this reason, the characterization of the surface chemistry of samples exposed to molten LiCl-Li_2O-Li is restricted in the current section. A more in-depth analysis of post exposure surface chemistry is included in Chapter 5.

Material dissolution from both I625 and SS316L as a result of exposure to LiCl-1wt%Li_2O containing up to 0.3wt%Li for either 50 or 100 hours was below the level of detection by ICP-OES analysis. The lack of detectable material leaching in these experiments is important as it indicates the low level of material dissolution that is expected to occur in the electrolytic reduction process. Such low levels of material dissolution can be expected assuming that the conditions employed in this set of experiments accurately replicate the process; namely that relatively moisture-free LiCl is employed, and the limit of physical dissolution of Li in the melt is not exceeded.

Morphological analysis was of the surface of samples exposed to LiCl-1wt%Li_2O with 0, 0.1 and 0.3wt%Li for 50 and 100 hours was conducted using SEM. The micrographs of SS316L and I625 samples are shown in Figures 3.18 and 3.19, respectively.

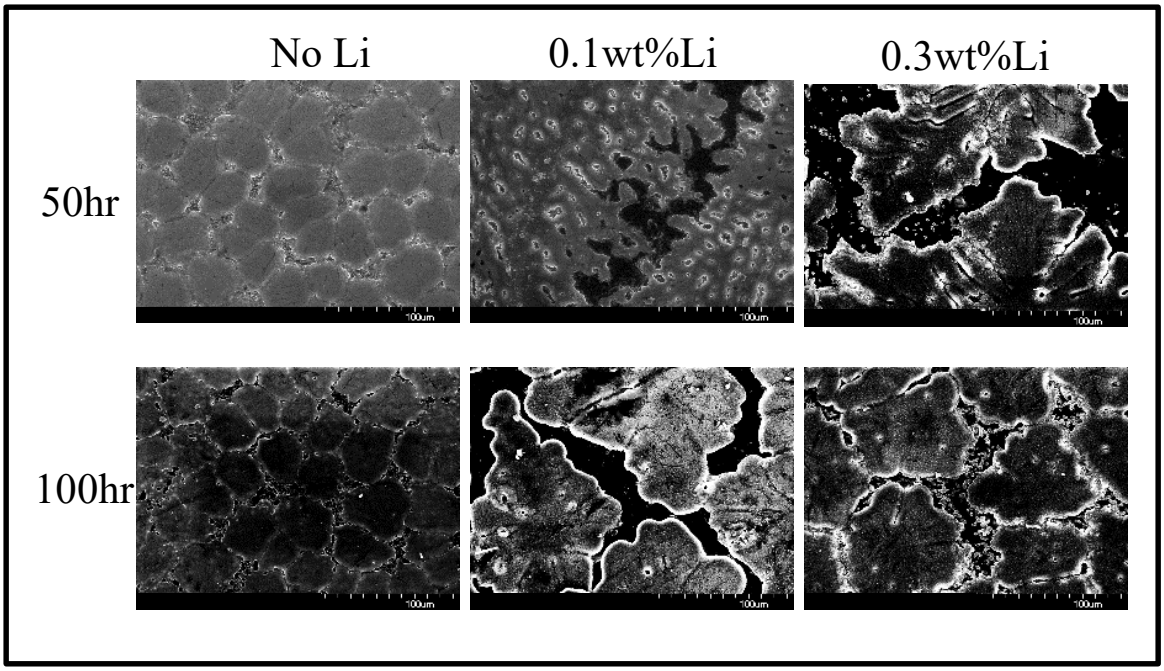


Figure 3.18: SEM micrographs of SS316L subjected to 50 and 100 hours of exposure to molten LiCl-1wt%Li_2O containing 0, 0.1 and 0.3wt%Li at 650°C.

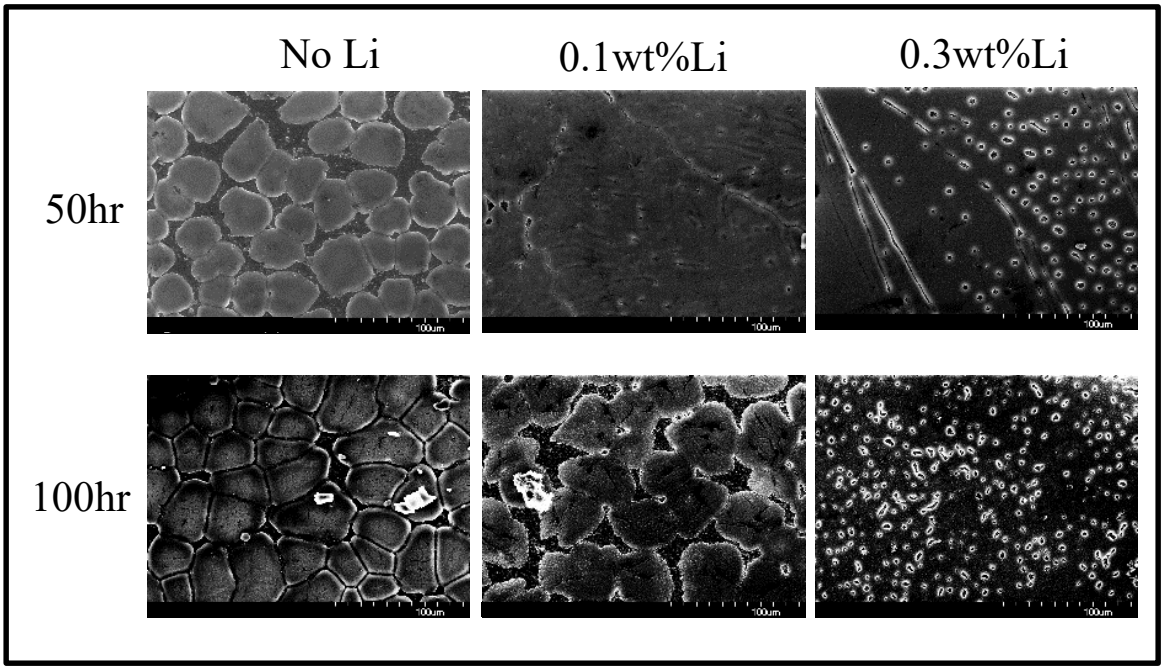


Figure 3.19: SEM micrographs of I625 subjected to 50 and 100 hours of exposure to molten LiCl-1wt%Li2O containing 0, 0.1 and 0.3wt%Li at 650°C.

Analysis of the morphologies of SS316L and I625, shown in Figures 3.18 and 3.19, is limited due to the presence of residual salt on the sample surfaces. Confirmation

of this statement is demonstrated in Section 3.10 were EDS analysis concluded that these surface features consist primarily of Cl and not alloying elements. The only observations that can be made from the micrographs shown in Figures 3.18 and 3.19 are regarding the adherence of the salt to the alloy surface. The adherence of residual salt on the surfaces of both SS316L and I625 exposed to molten LiCl-Li_2O in the absence of Li is fairly regular; exhibiting salt formations that look like islands of ~40 μm. The morphology of salt adhered to the surfaces of samples exposed to melts containing Li is less repeatable and tends to be characterized by larger areas of coverage. Uniform surface coverage with localized blemishes, similar to the morphology discussed in Section 3.4.2, is observed on multiple samples exposed to melts containing Li.

Quantification of the alteration to the surface mechanical properties of SS316L and I625 that occurred as a result of exposure to molten LiCl-Li_2O-Li was conducted using micro-hardness testing. Figure 3.20 shows the surface hardness of both alloys measured after subjecting samples to the previously discussed exposure conditions. The hardness of the as-received alloys is included for comparison.

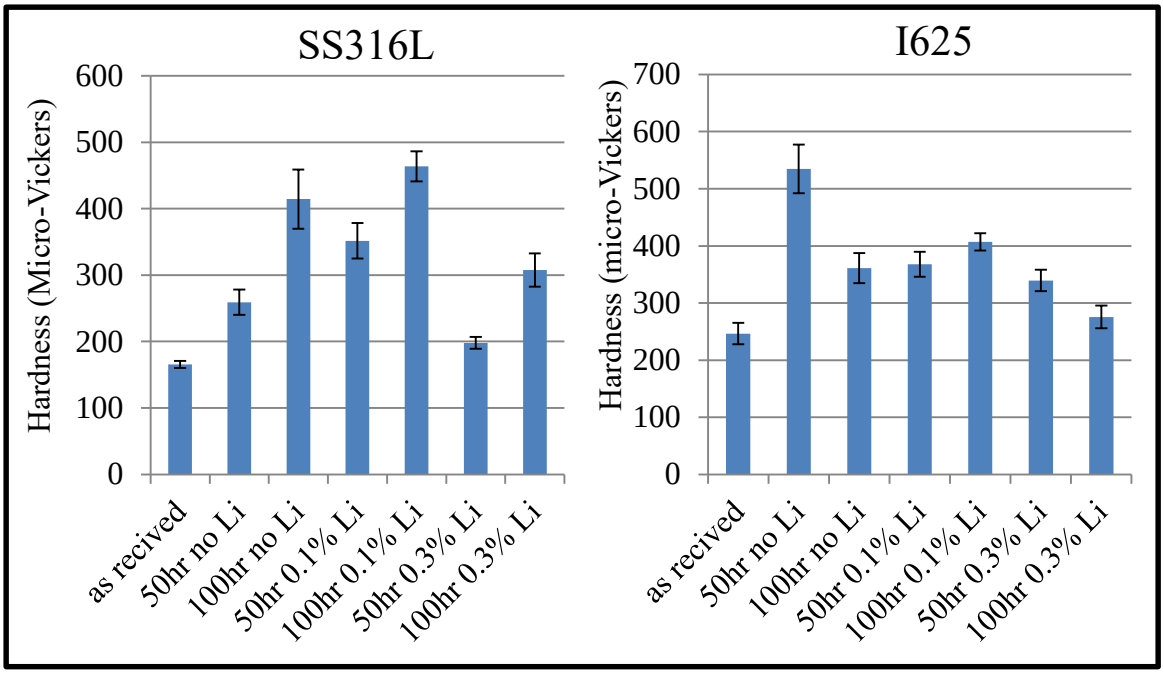


Figure 3.20: Micro-Vickers hardness of SS316L and I625 following exposure to LiCl-1wt%Li_2O with 0, 0.1 and 0.3wt%Li at 650°C compared to an as received samples.

As shown in Figure 3.20, the hardness of both SS316L and I625 following exposure to molten LiCl-Li_2O-Li exceeded that of the as-received alloy. An unexpected trend of an increase in hardness with increasing exposure time is observed for SS316L. The hardening effect appears to be suppressed by the inclusion of increased Li concentration in the system; with the relative hardening after a given length of exposure decreasing with increasing Li concentration. Alternatively, the surface of I625 exhibited hardening in all cases, compared to the unexposed material, without an obvious trend to length of exposure or Li content in the melt.

The increase in hardness of SS316L that resulted from exposure to LiCl-Li_2O-Li is counter to the softening effects that typically results from material interactions with liquid Li [112, 127, 153, 181, 182]. Alternatively, various molten salt based case hardening treatments, such as nitriding of steels, are accomplished by the diffusing

nitrogen into the alloy causing an expansion of the crystal lattice [183-186]. XRD was conducted on the SS316L samples exposed to molten LiCl-Li_2O-Li in an attempt to investigate the mechanism behind of hardening observed in Figure 3.20. This analysis was conducted using parallel beam optics to quantify diffraction peak shifting; a phenomenon associated with unit cell expansion and or contraction. The d-spacing of the three principle planes of austenite (γ-Fe) of the SS316L samples, as determined by XRD, is shown in Figure 3.21.

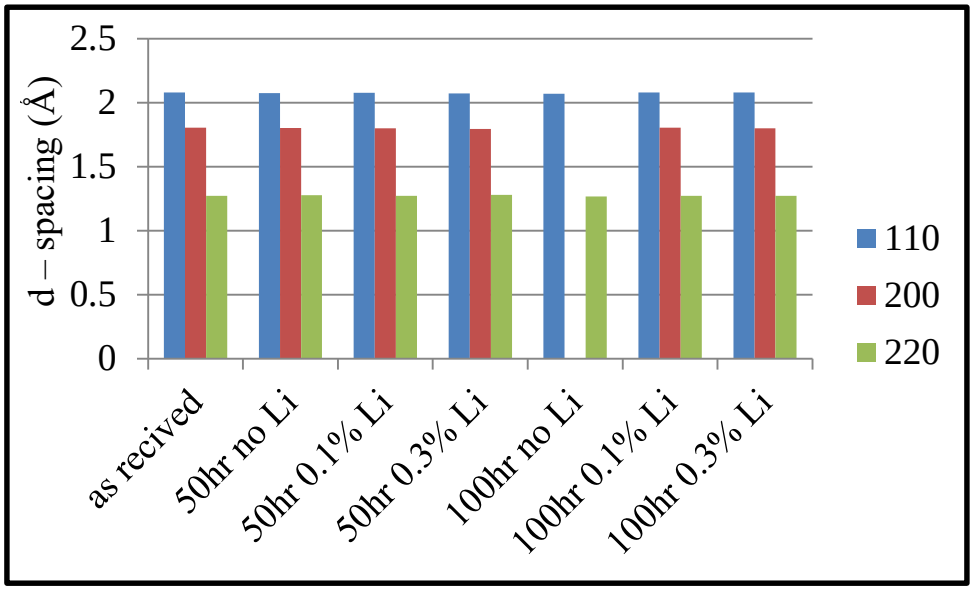


Figure 3.21: The d-spacing of three crystal places of austenite recorded from SS316L by XRD following exposure to LiCl-1wt%Li_2O with 0, 0.1 and 0.3wt%Li at 650°C for 50 and 100 hours. The d-spacing of an as-received sample measured by XRD is included for reference.

It is evident that no significant expansion or contraction of the austenite unit cell occurred as a result of the exposure to molten LiCl-Li_2O-Li. It is therefore concluded that the hardening effect demonstrated in Figure 3.20 is not a result of alteration to the austenite phase of the steel, and therefore is not strictly analogous to either molten salt induced case hardening.

XRD analysis of SS316L following exposure to molten LiCl-Li_2O-Li demonstrated that no significant change in the lattice parameter of the austenite phase occurred as a result of exposure. Alternatively, significant quantities of BCC ferrite, α-Fe, were observed by XRD analysis of SS316L samples exposed to molten LiCl-Li_2O-Li. The diffraction pattern of an unexposed sample of SS316L and that of SS316L exposed to LiCl-1wt%Li_2O for 50 hours is shown in Figure 3.22. Diffraction from the principle planes of ferrite as well as austenite are observed in the pattern obtained from the sample exposed to molten LiCl-Li_2O-Li, while only diffraction from FCC austenite is observed from the as-received sample. This observation demonstrates that some amount of austenite to ferrite transformation occurred during the exposure of SS316L to molten LiCl-Li_2O-Li.

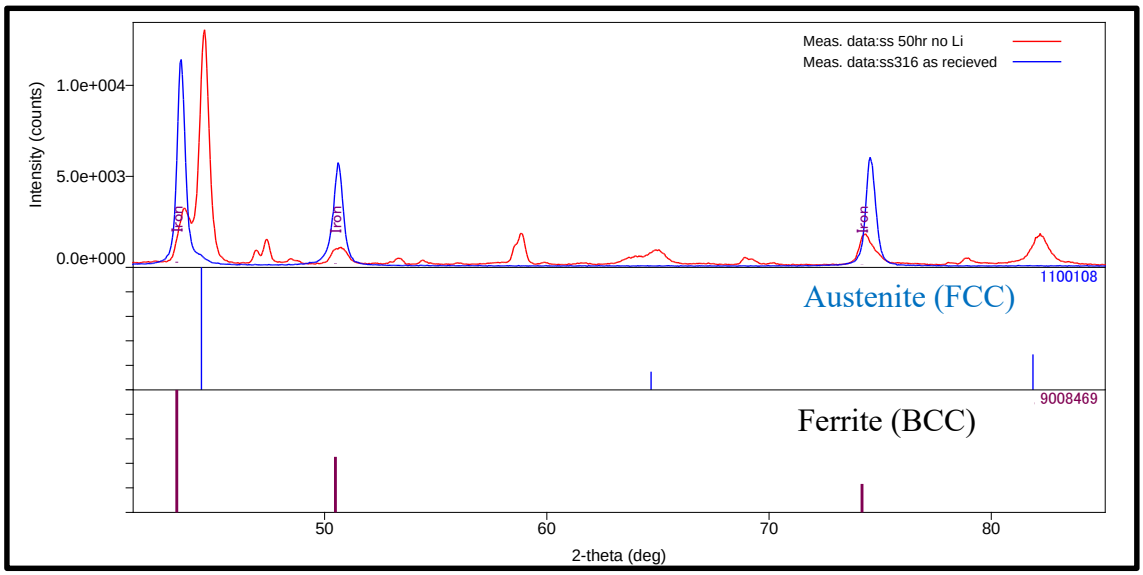


Figure 3.22: X-ray diffraction patters of as-received SS316L compared to SS316L exposed to LiCl-1wt%Li_2O at 650°C for 50 hours. The formation of significant quantities of the BCC ferrite phase (α-Fe) was observed in SS316L samples exposed to molten LiCl-Li_2O-Li.

The transition of portions of the SS316L samples from austenite to ferrite as a result of exposure to molten LiCl-Li_2O-Li observed in Figure 3.22 is potentially of

interest. Liquid Li has been demonstrated to preferentially alloy with Ni in austenitic stainless steels, drawing the Ni from the matrix to the alloy / liquid Li interface [187]. The removal of the austenite stabilizer, Ni, from the matrix results in the formation of a porous ferrite bulk diffusion layer that is characteristic of liquid Li attack. XRD analysis employing a Bragg-Brentano optical configuration was conducted on samples of SS316L to quantify the relative proportions of austenite and Ferrite present in the samples. As discussed in Chapter 2, Bragg-Brentano optics were chosen for this analysis due to the inability of parallel beam optics to yield quantitative information from relative diffraction intensities. The diffraction peaks from the austenite (111) and the ferrite (110) planes of SS316L exposed to molten LiCl-Li_2O-Li for 50 and 100 hours are shown in Figure 3.23.

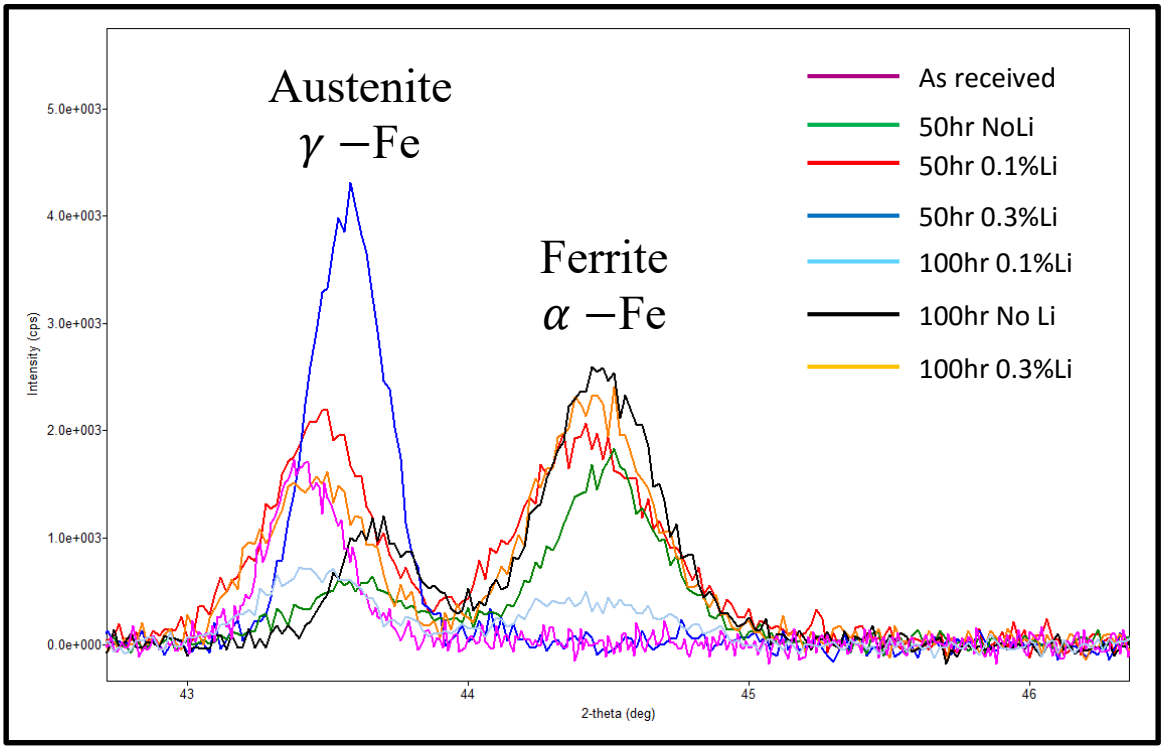


Figure 3.23: X-ray diffraction patters of as received SS316L compared to SS316L exposed to LiCl-1wt%Li_2O containing 0, 0.1 and 0.3wt%Li at 650°C for 50 and 100 hours. The formation of ferrite phase (α-Fe) did not follow an obvious trend with Li concentration in the melt or length of exposure.

It can be observed in Figure 3.23 that no trend in ferrite formation followed either the concentration of Li in the melt or the length of exposure. The diffraction pattern yielded from SS316L exposed to molten LiCl-1wt%Li_2O for 50 hours is a notable example as this sample was exposed to a melt in the absence of Li for a shorter period of time and yet contained a high concentration of ferrite. Furthermore, the sample exposed to the melt containing 0.1wt%Li for 100 hours exhibited the greatest hardness of the tested samples and yet only minor signal of diffraction from ferrite was detected. Extensive attempts to observe a relationship between the formation of ferrite and various experimental variables regarding exposure to molten LiCl-Li_2O-Li have been unsuccessful.

The diffraction patterns obtained from the samples of SS316L and I625 exposed to molten LiCl-1wt%Li_2O in the absence of Li are shown in Figure 3.24 and 3.25, respectively. Diffraction from the characteristic (0,0,3) plane of $LiCrO_2$ at $2\theta=18.4°$ (JCPDS 01-072-7839) was detected on all samples exposed to melts that did not contain Li. Alternatively, no transition metal oxide or chloride was detected by XRD following exposure to melts containing Li.

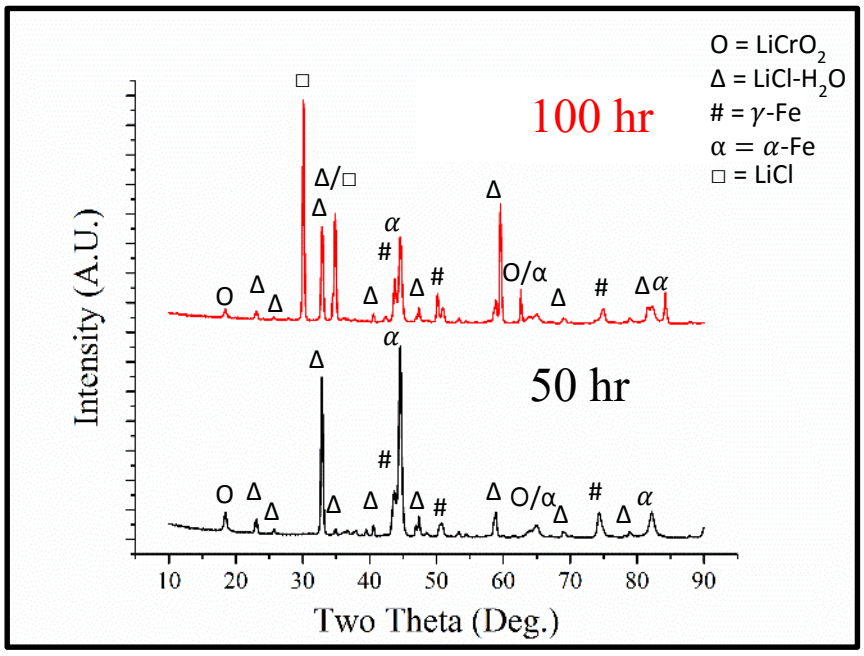


Figure 3.24: X-ray diffraction patterns of SS316L exposed to molten LiCl-1wt%Li_2O at 650°C for 50 (bottom) and 100 (top) hours. Diffraction from $LiCrO_2$ is observed in the pattern from both samples.

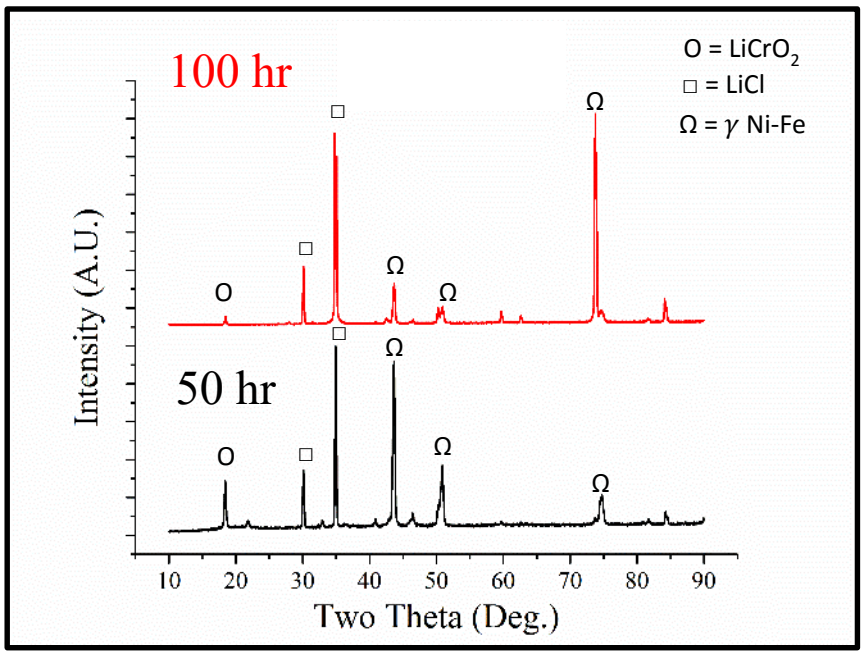


Figure 3.25: X-ray diffraction patterns of I625 exposed to molten LiCl-1wt%Li_2O at 650°C for 50 (bottom) and 100 (top) hours. Diffraction from $LiCrO_2$ is observed in the pattern from both samples.

Raman spectroscopy was conducted to further characterize the chemistry of post exposure sample surfaces. The Raman spectra obtained from the surface of SS316L and

I625 exposed to molten LiCl-1wt%Li_2O in the absence of Li for 50 and 100 hours are shown in Figures 3.26 and 3.27, respectively. The characteristic Raman mode of $LiCrO_2$ at~590cm^{-1} is observed in the spectra obtained from both SS316L and I625 after exposure to LiCl-1wt%Li_2O for 50 as well as 100 hours [188]. Only qualitative information regarding the concentration of $LiCrO_2$ in the spectra shown in Figures 3.26 and 27 can be presented due to the limitations of the fiber optic based sampling system. It is clear that the signal of the characteristic feature of $LiCrO_2$ recorded from I625 is of greater intensity compared to those obtained from SS316. The signal obtained from the sample of SS316L exposed to LiCl-1wt%Li_2O for 50 hours is only slightly detectable above the background noise. The presence of $LiCrO_2$ on this sample is only deemed reportable due to the corroborative analysis by XRD, shown in Figure 3.24.

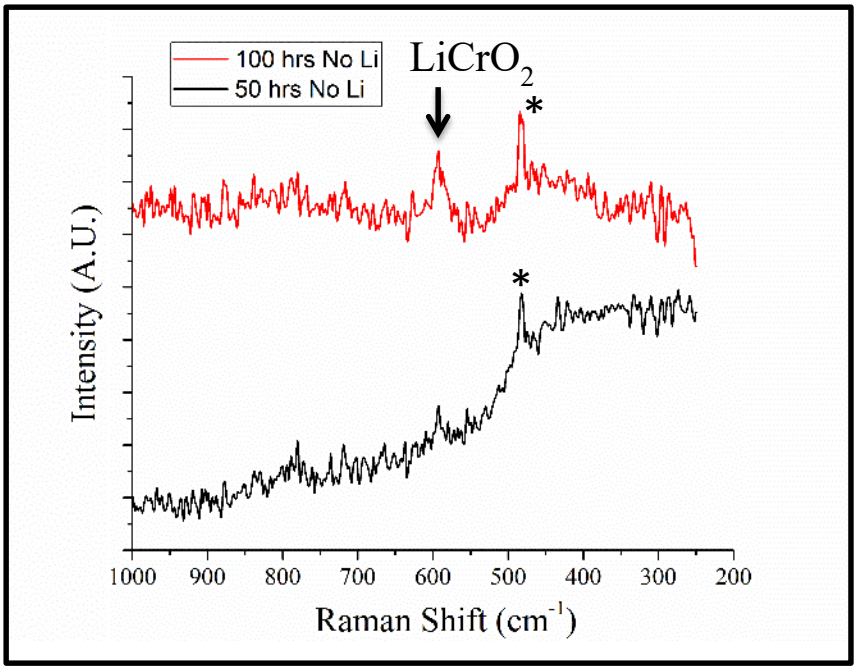


Figure 3.26: Raman spectra obtained from the surface of SS316L after exposure to LiCl-1wt%Li_2O at 650˚C for 50 and 100 hours. The characteristic Raman mode of $LiCrO_2$ is identifiable in both spectra. An artifact feature is labeled (*) due to ambient light in the laboratory.

No Raman features were observed on the surfaces of either I625 or SS316L exposed to molten solutions containing Li. This result is in agreement with the XRD analysis of sample surfaces where $LiCrO_2$ was only present in detectable quantities following exposure to melts that did not contain Li.

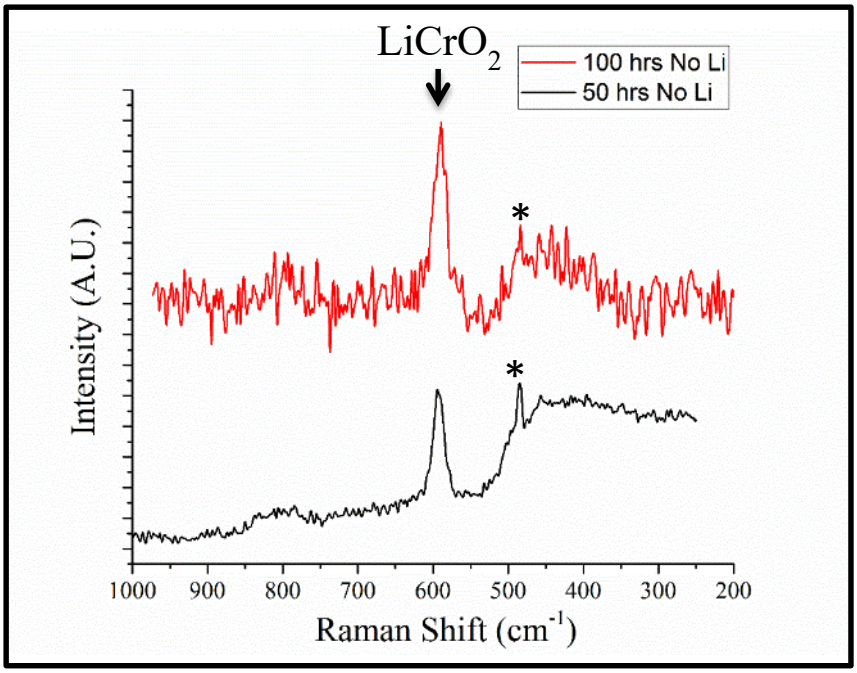


Figure 3.27: Raman spectra obtained from the surface of I625 after exposure to LiCl-1wt%Li2O at 650˚C for 50 and 100 hours. The characteristic Raman mode of $LiCrO_2$ is identifiable in both spectra. An artifact feature is labeled (*) due to ambient light in the laboratory.

Post exposure surface analysis was conducted using EDS to quantify the elemental composition of SS316L and I625 after being subjected to 50 and 100 hours of exposure to LiCl-1wt%Li_2O containing 0, 0.1 and 0.3wt%Li. Figures 3.28 and 3.29 show the elemental composition of SS316L and I626 after exposure to the separate test conditions as observed by EDS analysis, respectively. As previously stated, the elemental compositions determined by EDS in this section are normalized to the sum of the signals from the alloying elements Fe, Ni, Cr and Mo.

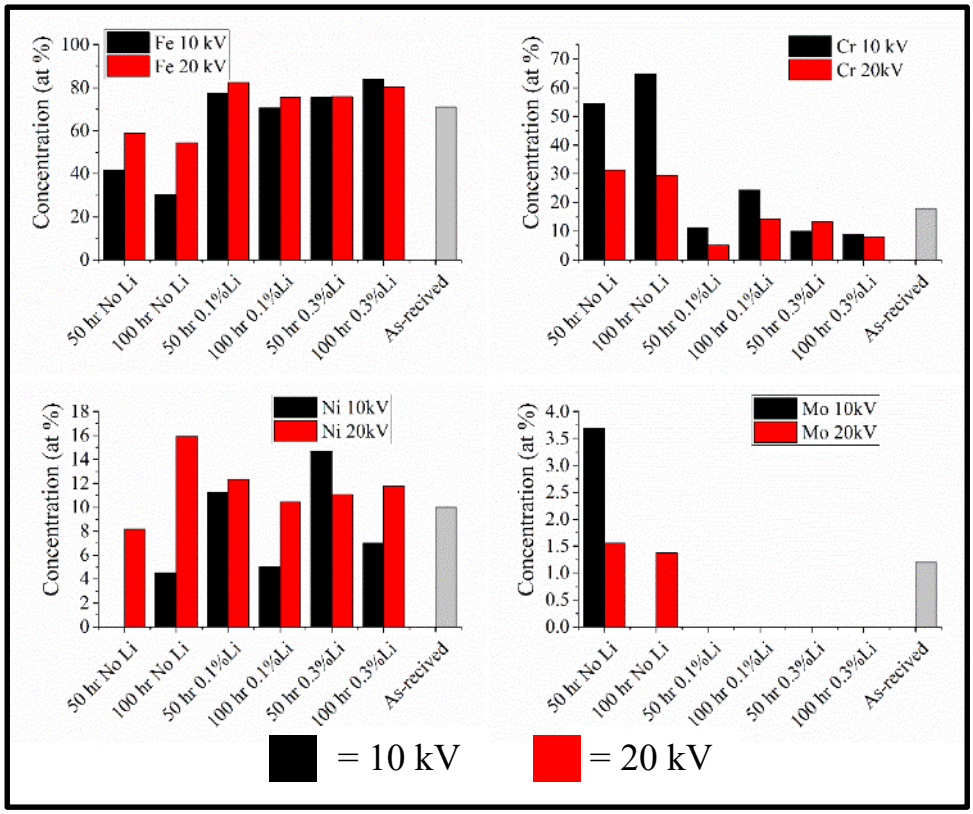


Figure 3.28: Elemental composition of SS316L, as observed from EDS analysis, following exposure to LiCl-1wt%Li_2O with 0, 0.1 and 0.3wt%Li at 650°C. EDS analysis was conducted using accelerating voltages of 10 and 20 kV to yield information regarding the composition as a relative function of depth.

The EDS analysis of the surface of SS316L exposed to molten LiCl-Li_2O-Li for 50 and 100 hours, shown in Figure 3.28, demonstrates a preferential enrichment in Fe on the samples exposed to melts containing Li. Compared to the as-received composition, Cr and Mo were detected in relatively high percentages on samples exposed to melts that did not contain Li. This observation is attributed to the formation of a $LiCrO_2$ surface film in these melts; a hypothesis that is supported by the previously discussed Raman and XRD analyses of these samples. This is further supported by the higher concentration of Cr detected when an accelerating voltage of 10 kV was employed (shallower depth of analysis) compared to the lower Cr content when 20 kV was used. All samples exposed to molten LiCl-Li_2O containing Li exhibited a decreased Cr concentration compared to

the as-received alloy. Furthermore, Mo was not present in detectable quantities on the surface of any sample exposed to a melt containing Li. As previously stated, no detectable quantity of the alloying elements Fe, Ni, Cr and Mo leached into the melts during the periods of exposure testing. These observations suggest that Ni and Fe are enriched on the sample surface, as opposed to the preferential leaching of Cr and Mo from the alloy.

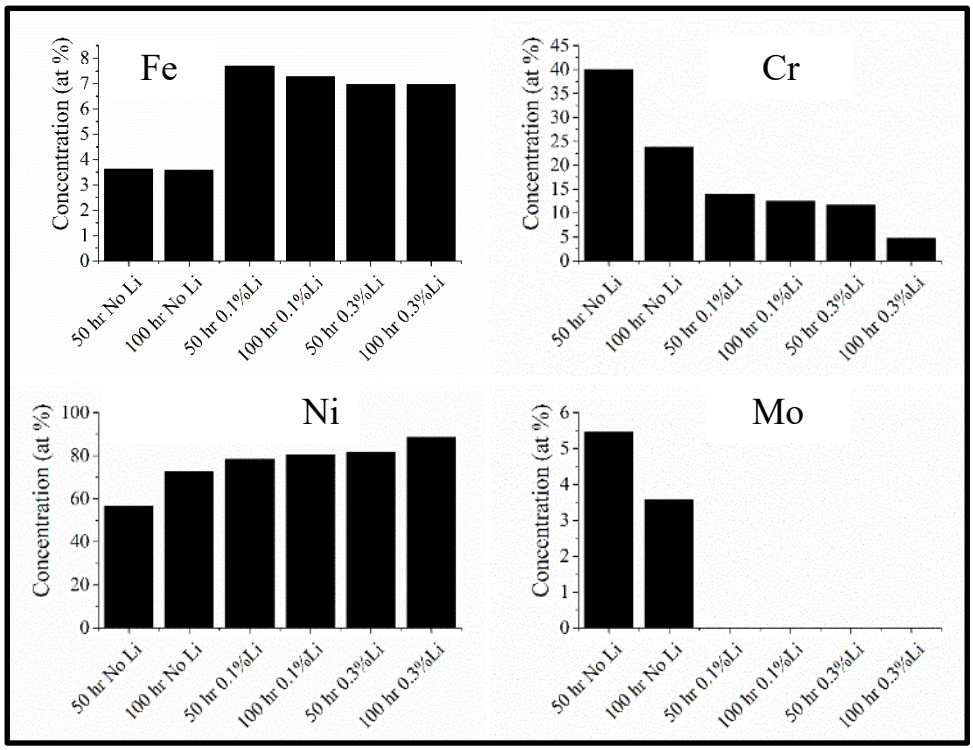


Figure 3.29: Elemental composition of I625, as observed from EDS analysis, following exposure to LiCl-1wt%Li_2O with 0, 0.1 and 0.3wt%Li at 650°C. EDS analysis was conducted using an accelerating voltage of 20 kV.

The compositions of I625 samples exposed to molten LiCl-1wt%Li_2O containing 0, 0.1 and 0.3wt%Li for 50 and 100 hours, as detected by EDS, are shown in Figure 3.29. It is observed that higher concentrations of Ni and Fe, and less Cr and Mo, were detected with increasing exposure time and Li content in the melt. These findings are in similar to

the results obtained from EDS analysis of SS316L. The reduced quantity of Cr on the surface, along with the complete depletion of Mo, upon exposure to melts containing Li represents a significant alteration to I625 as these elements account for roughly 30% of the unexposed material. This mode of degradation is not analogous to corrosion by molten salts or liquid Li, as Fe and Cr are preferentially oxidized in the former and Ni is leached in the later [112, 138, 143, 144, 164, 189, 190].

X-ray photoelectron spectroscopy was used to further characterize the chemistry of the surfaces of SS316L and I625 following exposure to molten LiCl-Li_2O-Li. The XPS survey scans obtained from the surfaces of I625 exposed to molten LiCl-1wt%Li_2O containing 0, 0.1 and 0.3wt%Li for 50 and 100 hours are shown in Figure 3.30. The XPS spectra of the SS316L samples exposed to molten LiCl-1wt%Li_2O containing 0, 0.1 and 0.3wt%Li for 50 hours are shown in Figure 3.31.

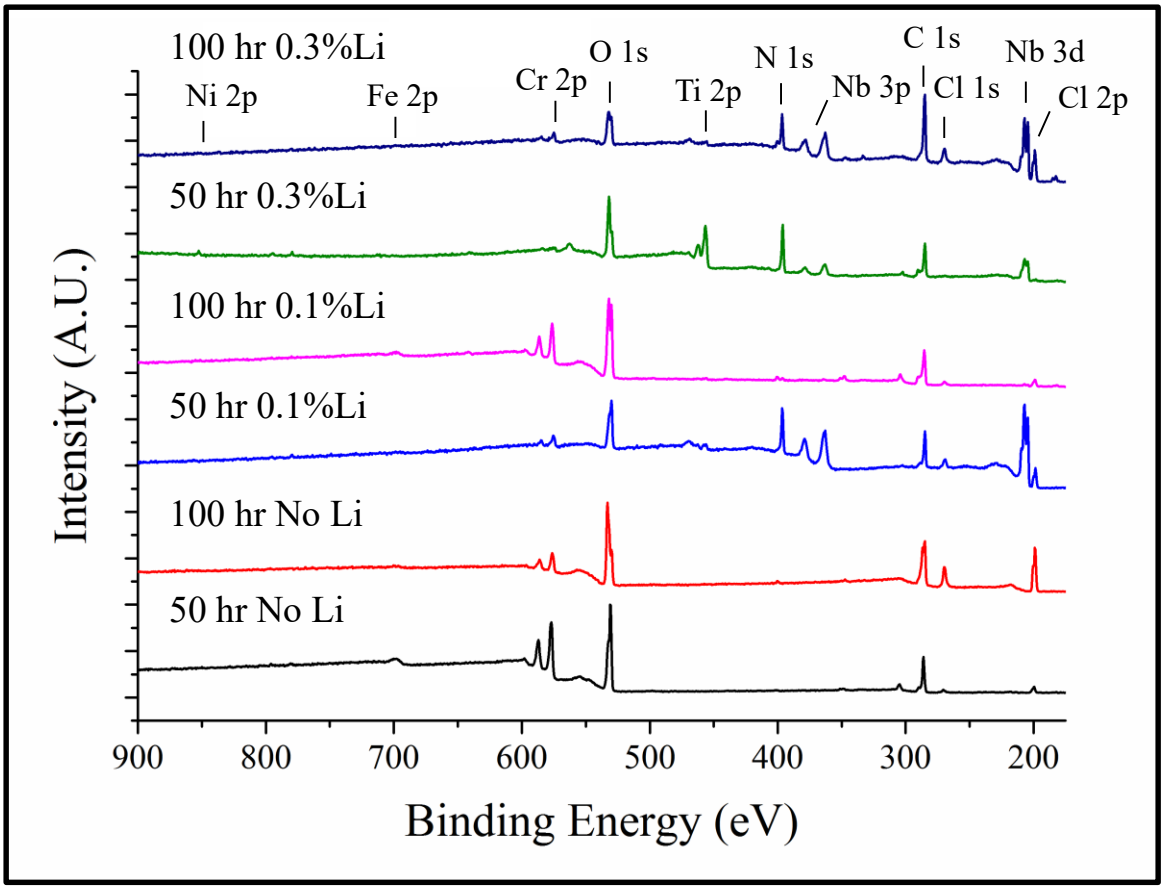


Figure 3.30: XPS survey scans of I625 following exposure to LiCl-1wt%Li_2O with 0, 0.1 and 0.3wt%Li at 650°C for 50 and 100 hours followed by a 10 minute rinse in methanol.

The XPS spectra obtained from the surfaces of I625 exposed to molten LiCl-Li_2O-Li shown in Figure 3.30 exhibit unexpected results. The relative intensity of the elements detected by XPS follows no significant trend and possess seemingly unexplainable data points. Notable results include the very high concentration of Nb detected on the surface of I625 exposed to molten LiCl-1wt%Li_2O-0.1wt%Li for 50 hours, and the lack of Nb on the sample exposed to a melt of the same composition for 100 hours. Additionally, the surface of I625 exposed to LiCl-1wt%Li_2O-0.3wt%Li for 50 hours contained a large amount of Ti, and yet the sample exposed to the melt containing 0.3wt%Li for 100 hours did not contain a measureable quantity of Ti. It is emphasized

that these samples were subjected to a methanol rinse prior to XPS analysis to remove residual salt from the sample surfaces. It is anticipated that alterations to the surfaces of the samples occurred during this rinsing procedure as Li, Li intercalated oxides, and alternative compounds formed in the high temperature molten salt are not expected to be stable in room temperature solvents. Additional examples of the erratic nature of rinsed samples are shown in Figures 3.31 and 3.32.

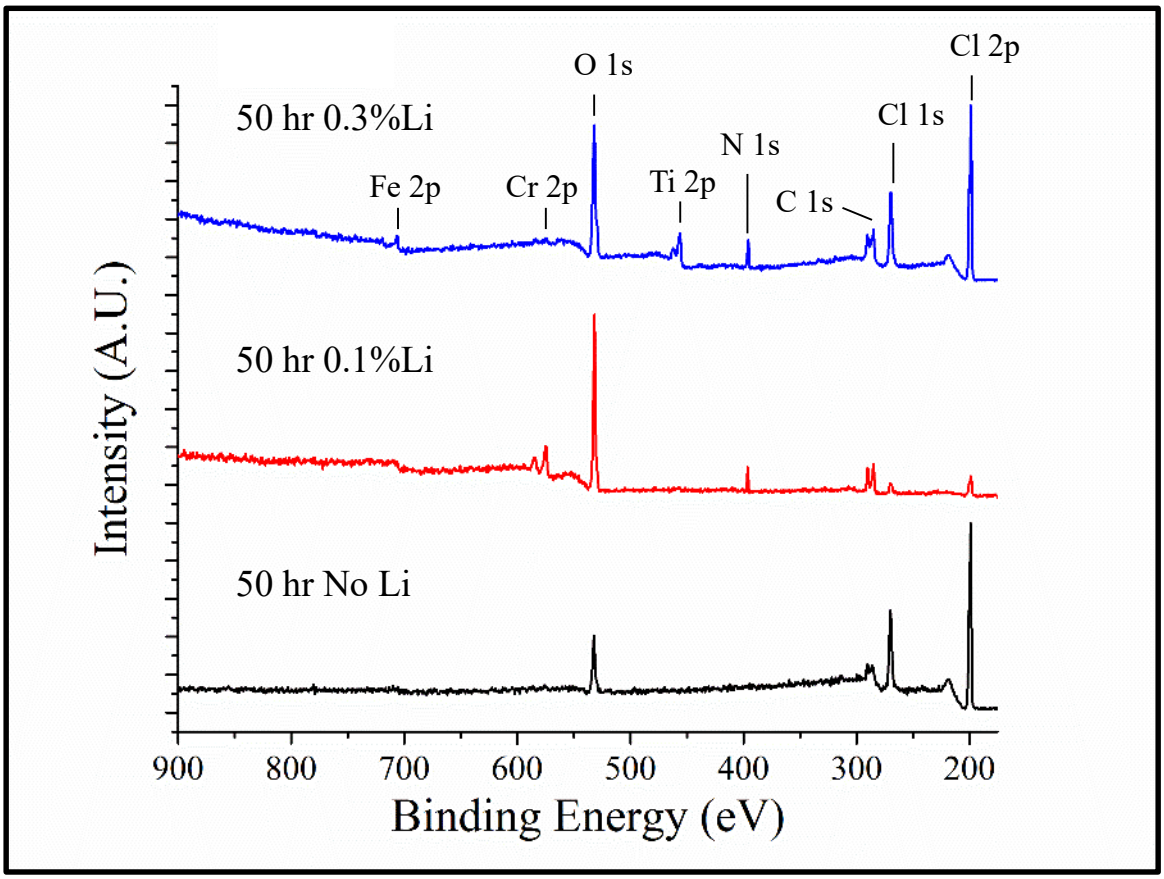


Figure 3.31: XPS survey scans of SS316L following exposure to LiCl-1wt%Li_2O with 0, 0.1 and 0.3wt%Li at 650°C for 50 hours followed by a 10 minute rinse in methanol.

The XPS spectrum obtained from SS316L exposed to LiCl-1wt%Li_2O, shown in Figure 3.31, does not exhibit significant Cr signal, however EDS, XRD and Raman analysis demonstrated the presence of Cr based surface film on this sample. The results

obtained from XPS should be carefully considered for two reasons: (i) the alternative three analytical techniques characterized the sample without significantly altering its surface chemistry (such as exposing it to methanol) and (ii) since XPS only analyzes the top ~10nm, the methanol rinse modified surface is what would be observed rather than a native surface after exposure. XPS spectra obtained from triplicate experiments were compared in an attempt to verify the accuracy and repeatability of XPS analysis. Figure 3.32 shows the XPS survey spectra obtained from three samples of SS316L exposed to separate melts of LiCl-1wt%Li_2O-0.3wt%Li for 50 hours. All samples were subjected to 10 minutes of methanol rinse to remove the excess salt from the sample surfaces prior to XPS analysis.

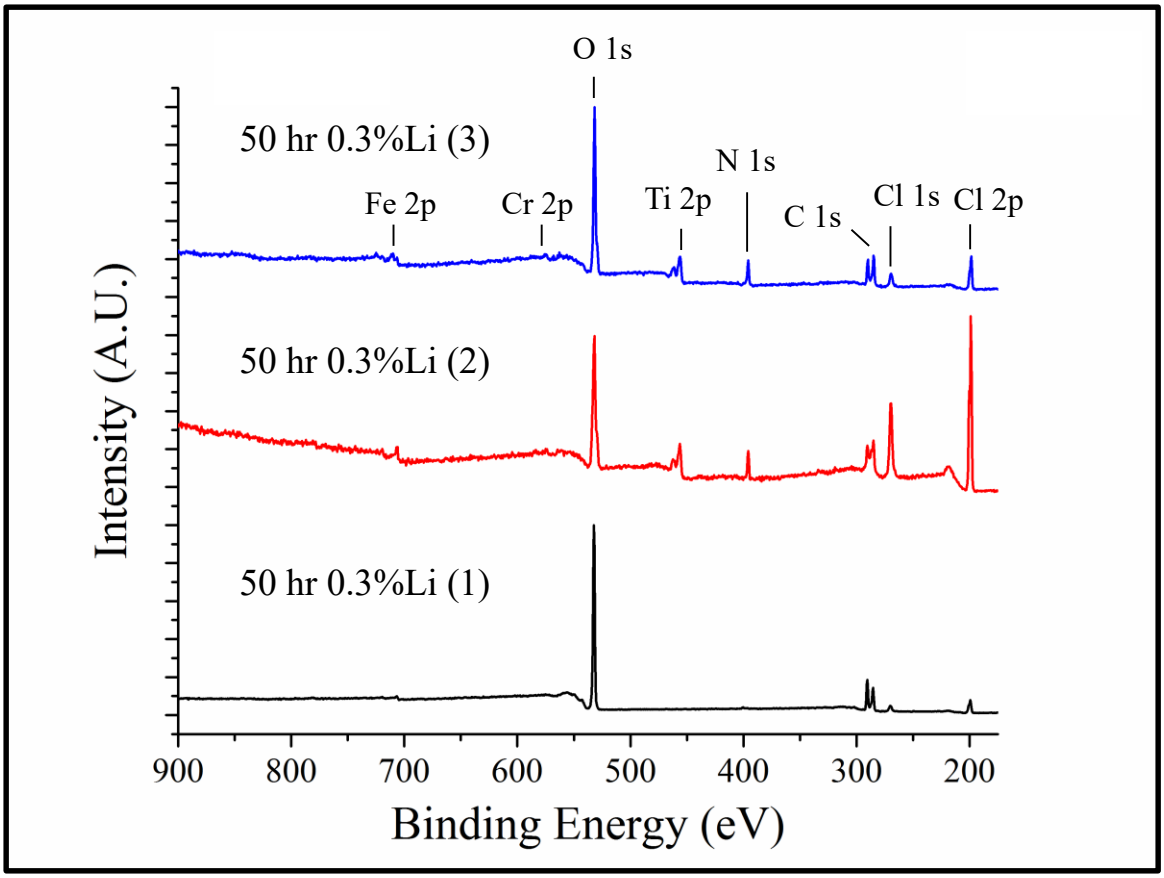


Figure 3.32: XPS survey scans of SS316L following exposure to LiCl-1wt%Li_2O-0.3wt%Li at 650°C for 50 hours followed by a 10 minute rinse in methanol.

The inability of XPS to yield repeatable information regarding the surface chemistry of samples exposed to molten LiCl-Li_2O-Li that have been rinsed with methanol can be observed in the XPS spectra shown in Figure 3.32. The variance in the spectra obtained from the triplicate experiments observed in Figure 3.32 is likely due to the nature of XPS which analyzes ~ top 10nm and is highly sensitive to the surface preparation procedure. The observed variations here would indicate that the surface was modified significantly and in a non-repeatable manner during methanol rinse procedure. The relative signal intensities from Fe, Cr, Ti and N vary considerably between each

spectra. It is concluded that XPS analysis employing the above experimental methodologies used in this section does not warrant further continuation.

3.10 Sample Baking:

The surfaces of materials exposed to molten salts are typically encased in residual bulk salt following removal from the melt. This salt layer tends to cover any surface films that lie between the material and the molten solution during exposure, impeding characterization of these films. As a result, surface sensitive analytical techniques commonly used in corrosion studies cannot typically characterize surface films formed in molten salts. Similar to the studies in Sections 3.4 – 3.9, the majority of research conducted on corrosion in molten LiCl-Li_2O has employed some form of organic solvent rinsing procedure to remove solidified salt from the material surface prior to post exposure analysis [138, 144, 163, 164, 189, 191, 192]. These surface cleaning procedures potentially remove or alter surface films that are less stable in common solvents at standard temperatures. However, analyses using alternative methodologies have demonstrated the formation of lithiated transition metal oxide such as $LiCrO_2$, $LiFeO_2$, and $Li_2Ni_8O_{10}$, that may not be stable upon exposure to atmosphere or mild solvents [138, 142, 178]. The employment of surface rinsing procedures was avoided in the studies included in Chapters 5 and 6 of the current work by baking the samples above the liquidus temperature of the melt to facilitate the re-distribution of the salt on the sample surfaces [193, 194]. To accomplish this, following removal from molten LiCl-Li_2O-Li, the samples were hung vertically on the sample holder and baked in an Ar atmosphere at

650°C for two hours. The efficacy of this process to remove bulk salt without destruction of the underlying surface films is shown in Figures 3.33 and 3.34.

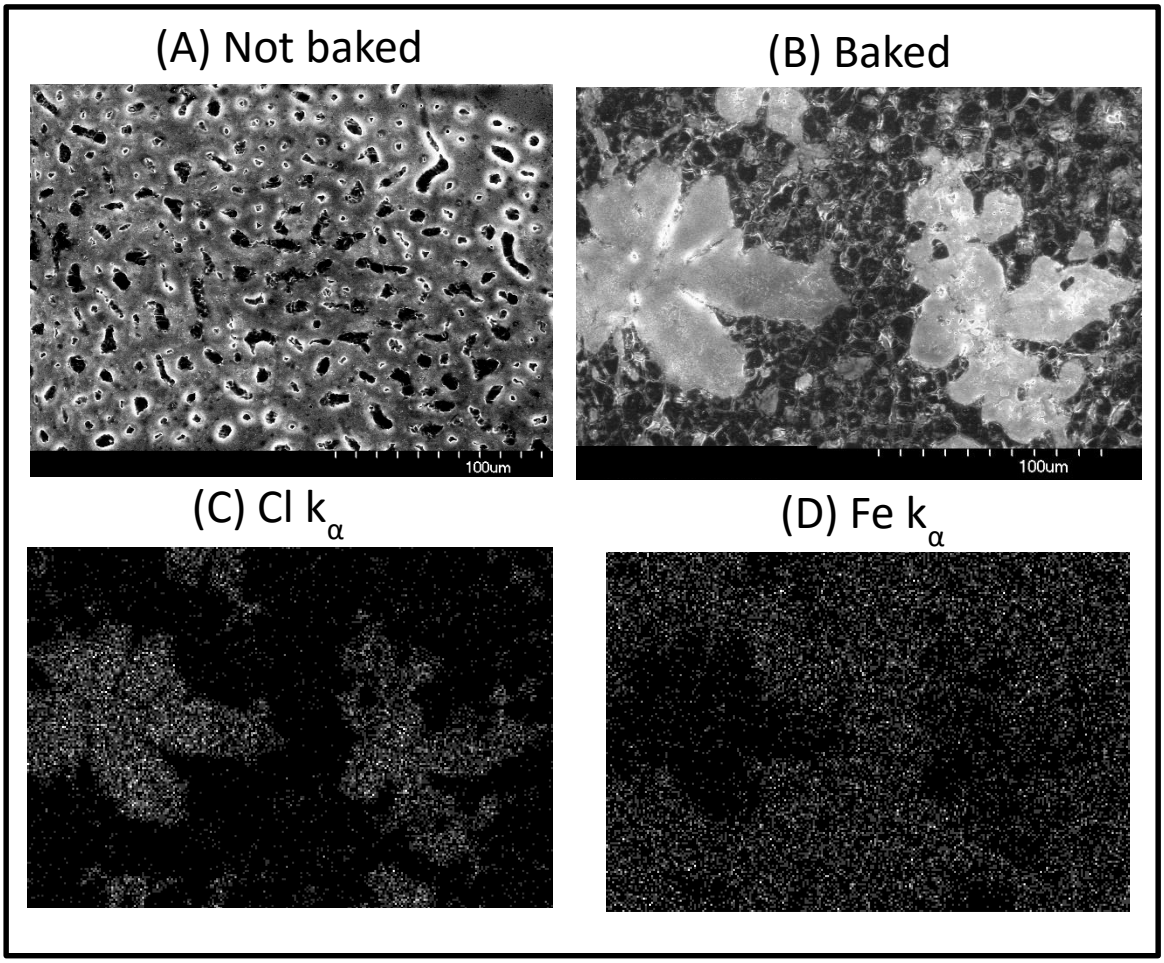


Figure 3.33: SEM micrographs recorded at 500x of the surface of SS316L subjected to 20 hours of exposure to molten LiCl-2wt%Li_2O-0.2wt%Li (A) without baking and (B) after 2 hours of baking at 650°C in Ar. EDS mapping of (C) Cl K_α and (D) Fe K_α signal obtained from the surface of the baked sample shown in (B). A separation between the alloy and the residual salt is observed to result from the baking procedure.

The morphological alteration to the material surface that occurred as a result of the baking procedure can be observed in the SEM micrographs shown in Figure 3.33. The surface of SS316L following 20 hours of exposure to molten LiCl-2wt%Li_2O-0.2wt%Li before and after baking is shown in Figures 3.33 (A) and (B), respectively. It is observed that the baking process consolidates the salt on the surface from the approximately

uniform coating shown in Figure 3.33 (A) to an island like morphology shown in Figure 33 (B). EDS mapping of the sample following the baking procedure, shown in Figure 3.33 (C) and (D), demonstrates the separation between the exposed alloy and the residual islands of LiCl by clear distinction between the Fe and Cl signals. The baking process is observed to lead to the formation of islands of salt with dimensions of approximately 100μm on the alloy surface. This morphology facilitates the use of surface sensitive analytical techniques such as EDS and XPS, to study the alloy surface, without having to employ solvent based rinsing procedures that may alter the film chemistry.

The ability of corrosion products formed in molten LiCl-Li_2O-Li to be unaffected by this baking procedure was verified in the following manner. A sample of SS316L exposed to LiCl-2wt%Li_2O in the absence of Li at 650°C for 20 hours was characterized by X-ray diffraction before and after being subjected to the baking procedure. The diffraction patterns yielded by these experiments are shown in Figure 3.34. As shown in Chapter 5, SS316L exposed to molten solutions of LiCl-Li_2O develops a protective $LiCrO_2$ surface film. Multiple diffraction peaks attributed to the presence of $LiCrO_2$ are observed in both patterns, indicating the stability of this lithiated transition metal oxide in the baking process. The low intensity of this peak when recorded from un-baked surfaces is attributed to the minimal relative abundance of this compound compared to residual LiCl and LiCl-H_2O on the sample surface.

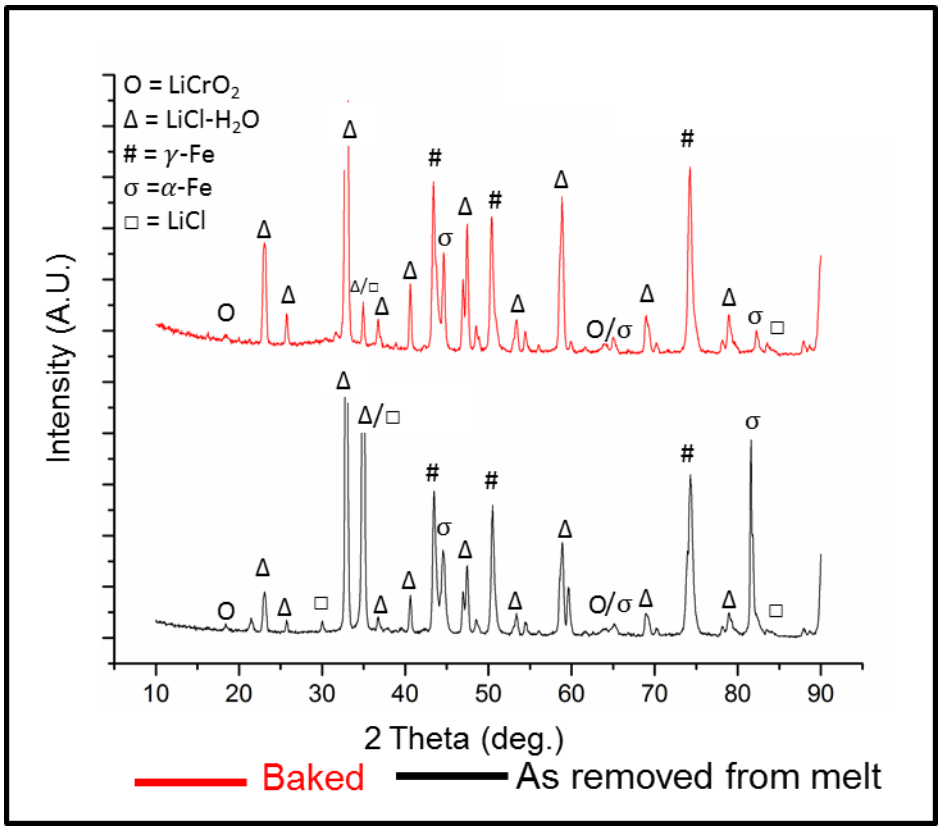


Figure 3.34: X-ray diffraction patterns obtained from a coupon of SS316L exposed to LiCl-2wt%Li_2O in the absence of Li before baking (Bottom) and after 2 hours of baking at 650°C in Ar (Top). Diffraction from the (0,0,3) plane of $LiCrO_2$ at $2\theta = 18.4^{\circ}$ 2θ is observed in both patterns demonstrating that the baking procedure did not remove surface oxides formed in molten LiCl-Li_2O.

3.11 Conclusions:

Samples of Inconel 625 and 718 were exposed to solutions of LiCl with 1 and 2wt% Li_2O, each with 0, 0.5 and 1wt% metallic lithium at 650ºC for 20 hours. Additional experiments exposed samples to LiCl saturated with Li_2O to investigate the mechanisms of material interactions with melts of varying chemistry. Post exposure surface analysis was conducted using scanning electron microscopy and X-ray photoelectron spectroscopy; additionally ICP-OES was used to analyze the alloy constituents that dissolved out of the material during the exposure. The inclusion of 0.5wt% metallic lithium in the solution was found to increase the stability of chromium rich surface films

and suppress the dissolution rate of alloying elements, compared to melts of LiCl-Li_2O. Alternatively, samples exposed to solutions containing 1wt% metallic lithium did not form surface films and demonstrated evidence of chromium depletion. The degradation of materials exposed to solutions containing 1wt% metallic lithium was observed to be fundamentally different than samples exposed to solutions saturated with lithium oxide, demonstrating a chemical effect other than, or in addition to, salt basicity.

Subsequent experiments exposed coupons of stainless steel alloy 316L and Hastelloy N to molten solutions of LiCl-Li_2O-Li to confirm that the observations obtained from scoping studies of Inconel 625 and 718 are general phenomena and not restricted to Inconel alloys. Investigations of the degradation of SS316L demonstrated that the preferential leaching of Mo and Cr occurrea in melts containing greater than 0.6wt%Li. Corrosion testing of SS316L conducted in Ni as well as W crucibles demonstrated the independence of these corrosion processes on the separate materials that were exposed to the melt. Despite its different intended mechanism of corrosion protection Hastelloy N was observed to behave similarly to Inconel and stainless steel when exposed to molten LiCl-Li_2O-Li, with the exception of a tendency of Hastelloy N to preferentially leach Mo in the presence as well as the absence of Li. The trends in the behavior of Cr and Mo in the three categories of alloys studied, Ni-Mo-Cr, Ni-Cr-Fe, and Fe-Cr-Ni, indicate a general trend of the chemistry of material interactions with molten LiCl-Li_2O-Li.

Extended exposure studies of Inconel 625 and stainless steel alloy 316L in molten LiCl-Li_2O-Li were conducted to verify that the corrosion analyzed in the previous

sections is representative of the degradation that occurs during longer terms of duration. No material leaching was detected from either SS316L or I625 exposed to molten LiCl-1wt%Li_2O containing 0, 0.1 or 0.3wt%Li at 650°C for 50 or 100 hours. The surface of SS316L was observed to be hardened as a result of the exposure; however the cause of the hardening is currently unknown. No alteration to the austenite crystal lattice perimeter, nor trend in ferrite phase transformation was observed by XRD analysis. EDS analysis demonstrated a preferential enrichment of Fe and Ni, accompanied by a depletion in Cr and Mo, on the surface of SS316L and I625 following exposure. With the exception of the hardening effect, all findings obtained from these studies were in agreement with the results obtained from 20 hour exposures.

Chapter 4 Dispersion of Li in Molten LiCl-Li_2O

Quantification of the solubility limit of Li in LiCl-Li_2O is of paramount interest to the current study as the electrolytic reduction of actinide oxides has been noted to operate under Li saturated conditions. As a result, evaluations of corrosion that occurs in the molten electrolyte used in the actinide oxide reduction process cannot be simulated without knowledge of the concentration of Li that is present in the melt under these conditions. As discussed in Chapter 1, the reported values of the solubility limit of Li in LiCl measured by different methods of analyses vary significantly and are in disagreement [1, 70-74, 91]. The solubility limit of Li in LiCl detected by thermal analysis has been reported to be 0.5±0.2mol% at 913 K [70], while electrochemical analysis quantified the limit to be 1.8mol% at 923 [71, 72]. Furthermore, chemical analysis of LiCl-Li quenched at 923 K has been reported to contain greater than 3mol% Li [1, 73, 74, 91]. To complicate matters further, little is known regarding the alteration to the solubility limit of Li in LiCl that occurs when Li_2O is present in the system [1]. Without quantification of the variation in Li solubility in LiCl-Li_2O as a function of Li_2O concentration, it would be impossible to replicate the conditions encountered during the electrolytic reduction of UO_2. Understanding of the range of concentrations that are relevant to the ternary LiCl-Li_2O-Li system is therefore critical to the investigation of material degradation in this process. This chapter employs a variety of methods for analyzing the solubility limit of Li in LiCl in the presence and absence of Li_2O.

4.1 Chemical Analysis of LiCl-Li_2O-Li:

An experimental procedure was developed to quantify the amount of metallic lithium in molten LiCl-Li_2O-Li. Melts of LiCl-Li_2O-Li were contained in Ni crucibles and allowed to equilibrate for 30 minutes prior to analysis. The molten solution was then sampled by submerging a cupped scoopula into the middle of a melt, maintaining its position until it was thermally equilibrated with the melt, removing the scoopula and dripping a sample of LiCl-Li_2O-Li (while still molten) onto a graphite plate. By dripping a sample of LiCl-Li_2O-Li while still molten, it is hypothesized that potential phase separation due to cooling would be minimized. This technique is suggested to yield a more representative sample of the melt compared to a typical "salt freeze" method for the reasons discussed in Chapter 1. Once a sample of the salt was obtained, it was weighed and reacted with DI water in a sealed glass reaction vessel. The quantity of H_2 gas produced via the reaction with water was measured using an attached 5ml burette. A leveling bulb was attached to the apparatus to maintain a constant pressure. Assuming that metallic Li reacted with H_2O to form LiOH and H_2 gas, the quantity of Li present in the sample of quenched LiCl-Li_2O-Li was determined by measuring the expansion of gas that occurred at a constant pressure in the volumetric burette. The apparatus used in this experiment consisted of a sealed glass reaction vessel, a 5ml volumetric burette and a leveling bulb shown in Figure 4.1.

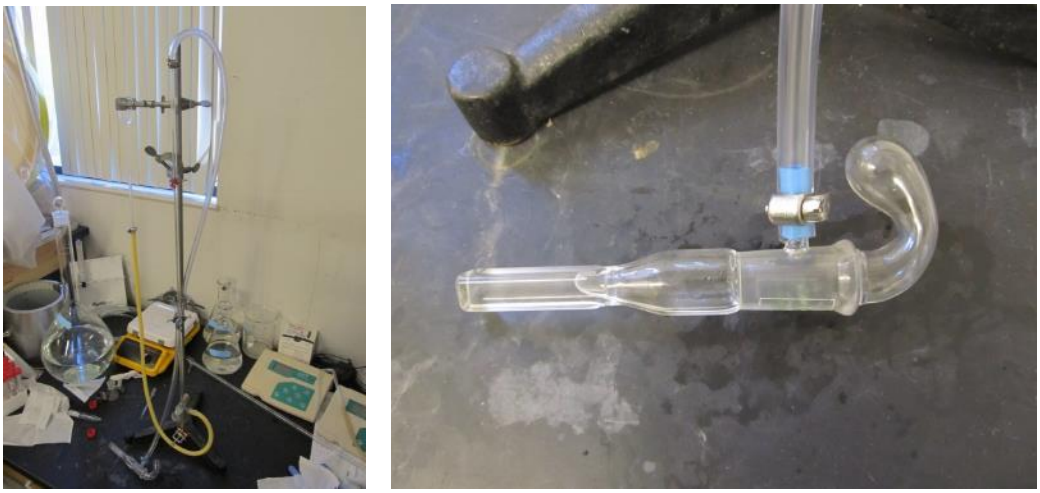


Figure 4.1: Images of the H_2 gas quantification apparatus employed to measure the concentration of Li in quenched LiCl-Li_2O-Li. Left: the complete constant pressure volumetric burette apparatus. Right: the reaction chamber where samples contacted water in a sealed container.

Using the previously described procedure, the solubility limit of Li in molten LiCl-Li_2O at 650ºC was investigated. Analysis of the quantity of Li in the quenched salt was conducted as a function of Li_2O concentration in the melt, and as a function of the concentration of metallic Li that was initially added. Figure 4.2 shows the concentration of Li measured in wt% as a function of Li_2O concentration for all melts where greater than 0.3wt%Li was added.

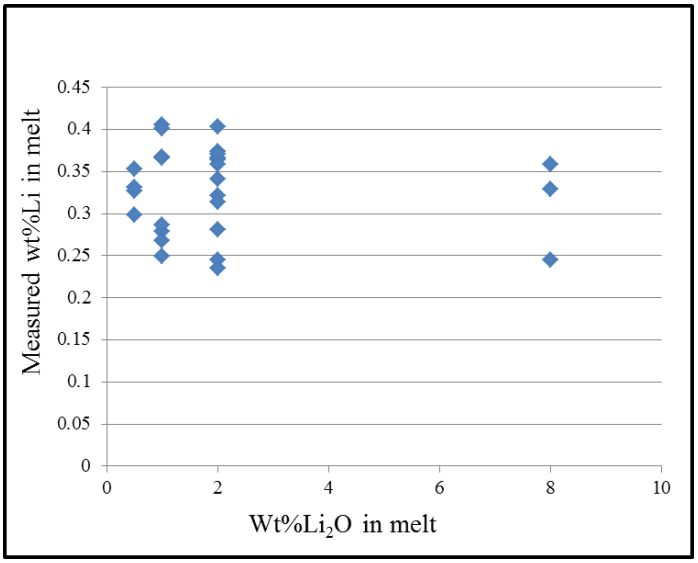


Figure 4.2 Concentration of Li measured in quenched samples of LiCl-Li_2O-Li as a function of Li_2O concentration when greater than 0.3wt%Li was added to the melt.

The concatenations of Li measured in wt% as a function of Li_2O concentration for all melts where less than 0.3wt%Li was added are shown in Figure 4.2. Circles indicating the actual composition of the as prepared melt are included to indicate the deviation of the experimental results from the actual melt composition.

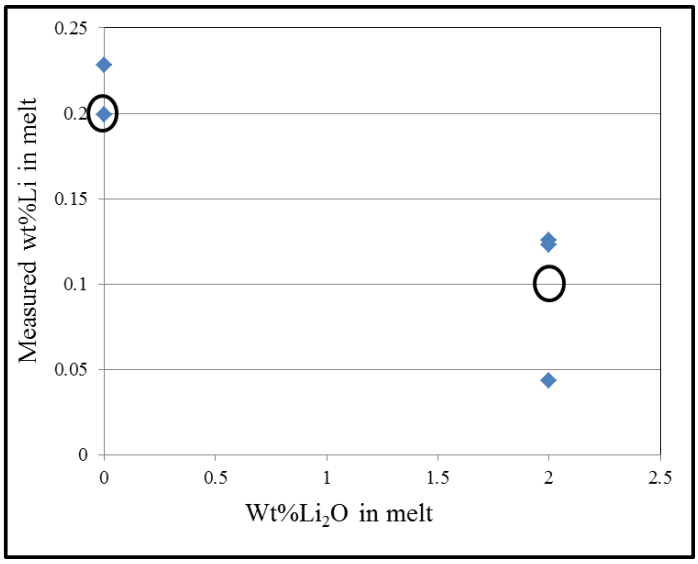


Figure 4.3 Concentration of Li measured in quenched samples of LiCl-Li_2O-Li as a function of Li_2O concentration when less than 0.3wt%Li was added to the melt. Circles indicating the actual composition of the as prepared melt are included for reference.

The data included in Figures 4.2 and 4.3 are averaged to the tabulated form shown in Table 4.1. In this analysis three samples of salt were removed from each melt, and the concentrations presented in Table 4.1 are the average of the three measurements. The only exception to this analysis is for the molten solution of LiCl-0.2wt%Li in the absence of Li_2O in which only two measurements were made. The reported error for all other melt compositions is the standard deviation (in wt% Li) observed between the separate measurements conducted in each melt.

Table 4.1 Composition of molten solutions containing varying quantities of added Li_2O and Li, yielding various measured concentrations of Li in the melts.

wt%Li2O	wt%Li added	wt%Li measured	Error (wt%)
8	1	0.31	0.1
2	1	0.33	0.05
2	0.5	0.3	0.07
2	0.1	0.1	0.05
1	1	0.27	0.02
0.5	0.5	0.32	0.02
0	1	0.27	0.02
0	0.2	0.2	N/A

As shown in Table 4.1, for solutions containing below 0.3wt%Li the quantity of Li that had been added to the melt and the quantity measured to be in solution are in excellent agreement. These data points serve as controls, demonstrating the validity of the experimental methodology. The maximum measured quantity of dissolved Li was approximately 0.3wt% when greater than 0.3wt% Li was added to the melt. This value is interpreted as the limit of physical dissolution of Li in LiCl at 650˚C recorded using this experimental approach. It is noted that this value is approximately independent of Li_2O concentration in the LiCl-Li_2O-Li system. The data yielded from this study is in

agreement with previously published data that used similar sampling techniques and greater than those that employed thermal analysis by approximately a factor of 4 [1, 70, 73].

It should be emphasized that the reported concentrations of Li in Table 4.1 are the average of three samples obtained from each melt, and that large relative standard errors were observed in each data set. Multiple individual measurements recorded a Li concentration exceeding 0.4wt%. The source of this experimental error will be discussed subsequently in this chapter.

4.2 Concentric Inductor Magnetization Sensor:

Due to the inability of electrochemical experimental techniques to yield quantitative information regarding the LiCl-Li_2O-Li system, and the large relative error of chemical analysis of quenched LiCl-Li_2O-Li, an alternative method of measuring the solubility of Li in LiCl-Li_2O was developed. As previously noted, the nature of the ternary solution is highly delicate, and fundamentally altered when subjected an electric field, or exposed to electrically insolating and impure materials that are prone to liquid metal interactions in any way. The need to probe the fundamental properties of the solution without subjecting it to an electric field, quenching it, or exposing it to molecular compounds led to the motivation to employ magnetic fields as a tool for determining the solubility limit of Li in molten LiCl.

4.2.1 Theory:

The physical operating principles of the concentric inductor magnetization sensor (CIMS) is as follows. Fundamentally, the CIMS acts as an electric transformer, transferring an AC current between two wire coils submerged in the molten LiCl-Li_2O-Li. The primary coil is driven by a high frequency AC current which produces a magnetic field, B, through its coil internals governed by the law of induction in a solenoid, shown as Equation 2 [195].

$$\boldsymbol{B} = \mu_0(1+\chi)\boldsymbol{H} \tag{2}$$

Where μ_0 is the permeability of free space, χ is the magnetic susceptibility of the medium inside the solenoid, and **H** is the magnetizing field vector. **B** is the sum of two components: μ_0**H** derives from the magnetic field produced strictly by the current in the solenoid, and $\mu_0\chi$**H** is produced by the magnetization of the medium. **H** in a solenoid is defined by Ampere's law, shown here as Equation (3).

$$\mathbf{H}=\mu_0 * n_1 * \mathrm{I(t)} \tag{3}$$

Where n_1 is the number of turns in the solenoid, and I(t) is the time dependent current. Faraday's law of induction, shown as Equation (4), states that for a given magnetic flux, ϕ, through a solenoid, an electromotive force (EMF), ε, is induced between the ends of the coil windings.

$$\varepsilon = -n_2 \frac{d\phi}{dt} \tag{4}$$

Where n_2 is the number of turns in the second solenoid. The CIMS is operated at a fixed geometry in all experiments, and as a result the magnetic flux through the fixed coil area, A, is normalized by the approximation shown as equation (5).

$$\phi = \int \boldsymbol{B} dA \approx c * \boldsymbol{B} \quad (5)$$

Where c is a proportionality constant depending upon the geometry of the CIMS coils. Therefore, when the primary coil is driven by an AC current, $I(t) = Asin(\omega t)$, where A is the amplitude of the current, ω is the frequency and t is time, an EMF, or voltage, is induced in the second coil governed by Equation 6.

$$\varepsilon = kn_1 n_2 A\,(1 + \chi)\omega\cos(\omega t) \quad (6)$$

Where k is a coupling constant dependent upon the coupling efficiency of the two inductors determined by their respective geometries. It is now observed that when the AC potential, ε, is measured across the leads of the second coil and is plotted as a function of the driving current frequency, ω, a linear relation results with a slope equal to $kn_1 n_2 A(1 + \chi)$. Furthermore, for a CIMS that employs a fixed geometry, and is driven by a constant amplitude current, the slope will be a constant plus a value that is exclusively dependent upon the magnetic susceptibility of the medium inside of the coils.

By submerging the CIMS in solutions of LiCl-Li_2O-Li with varying concentration of Li and recording the potential induced in the secondary coil of the CIMS at various driving frequencies, the magnetic susceptibility of the solution can be measured. Furthermore, it is proposed that this measurement will be dependent upon the concentration of Li in the system only up to the solubility limit of Li in the melt. Beyond this concentration, a metal rich phase of LiCl-Li_2O-Li will separate out and the magnetic susceptibility of the solution will be independent of further addition of Li. Thus, by measuring the concentration of dissolved Li at which the magnetic Li of the LiCl-Li_2O-Li remains unaltered with the addition of greater quantities of lithium, the CIMS would measure the solubility limit of Li in LiCl-Li_2O-Li.

4.2.2 Experimental Setup:

The CIMS is constructed of two nickel wires, wrapped in concentric coils to form coupled solenoids with maximum inductive coupling efficiency. The concentric coils are submerged in the solution where they act as a transformer: a driving current in the primary coil induces a voltage in the secondary coil. The efficiency at which the transformer operates is dependent upon the magnetic susceptibility of the medium between the coils. Since the coil material chosen for this application is high purity nickel, and no current flows between the two coils, the measurement of magnetic susceptibility can be made without disturbing the LiCl-Li_2O-Li solution. An image of a prototype CIMS used to attain the results discussed in a subsequent portion of this report is shown in Figure 4.4.

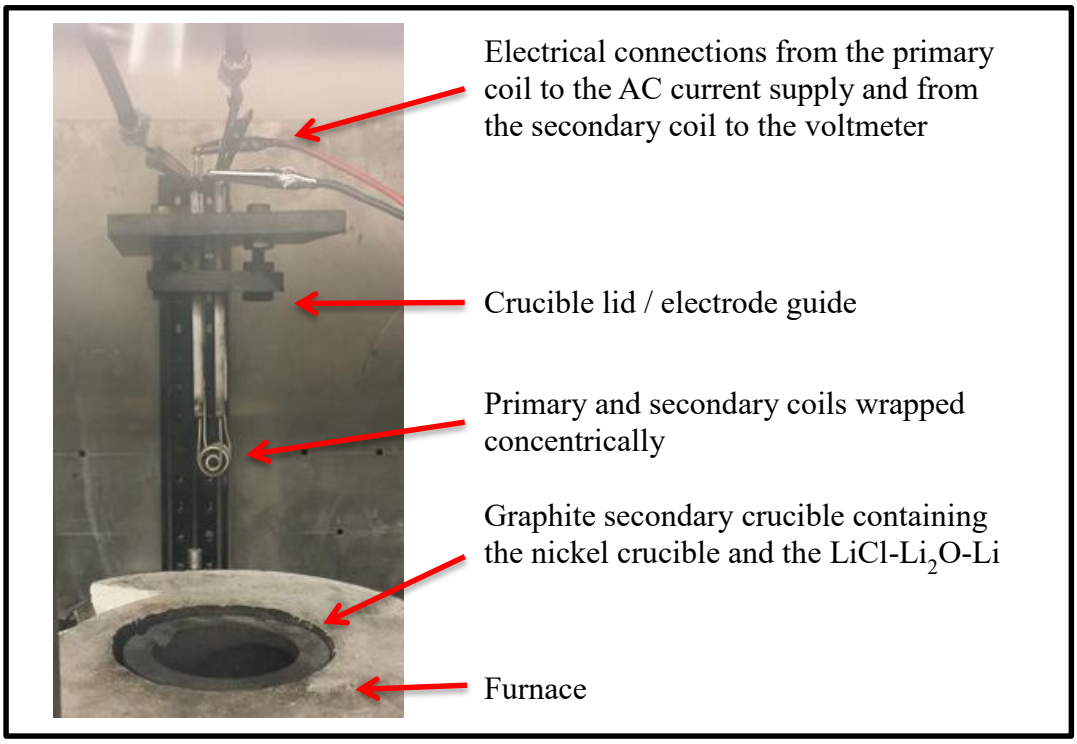


Figure 4.4: A prototype CIMS with labeling of its separate components.

The CIMS was fabricated out of 1mm diameter nickel wire of procured from GoodFellow, and was of greater than 99.9% purity. Separate exposure tests were conducted in solutions of LiCl-2wt% Li_2O containing: 0, 0.5, 1, 1.5, 2 and 3wt%Li. 50g of each mixture was ground in a mortar and pestle prior to heating. The salt melt was maintained at 650ºC in all tests, and less than a ±5ºC temperature gradient was recorded along the submersion depth of the CIMS.

A single CIMS was used in all experiments in the following discussion. Prior to each experiment, the CIMS was boiled in DI water for 5 minutes, rinsed with acetone, and dried at 200°C for 2 hours. The CIMS was then connected to a computer controlled translation stage in the glove box and connected to the primary and secondary circuits. The primary coil was driven by a Keithley 6221 AC current source, and the induced voltage in the secondary coil was measured by a Keithley 2100 multimeter. The primary coil was driven by a 100mA AC current with frequency varying between 10-100kHz. Each experiment was run in triplicate to reduce the experimental uncertainty associated with the measurements. To reduce the possibility of contamination effects between the separate salt compositions, successive experiments were conducted in a randomized order of Li concentration.

4.2.3 Simulation and Calibration Results:

To demonstrate the validity of this concept, a simplistic coupled inductor circuit model was employed using PSPICE and MultiSIM software. The inductors were modeled by adhering to the definition of inductance, L, given in equation (7).

$$L = \frac{\mu N^2 A}{l} \tag{7}$$

Using the measured length, l, and area, A, of the CIMS coils and the permeability, μ, of argon gas, equation (7) predicts an inductance of 2.89×10^{-7} H and 1.18×10^{-7} H in the primary and secondary CIMS coils, respectively. The operation of the CIMS in the argon atmosphere of the glove box was modeled using these inductance values, and an arbitrarily chosen coupling constant, k, of 0.5, in the coupled inductor circuit shown in Figure 4.5, and simulating driving the circuits with frequencies between 10-100kHz. The simulated induced voltages in the secondary coil as a function of frequency are shown in Figure 4.5.

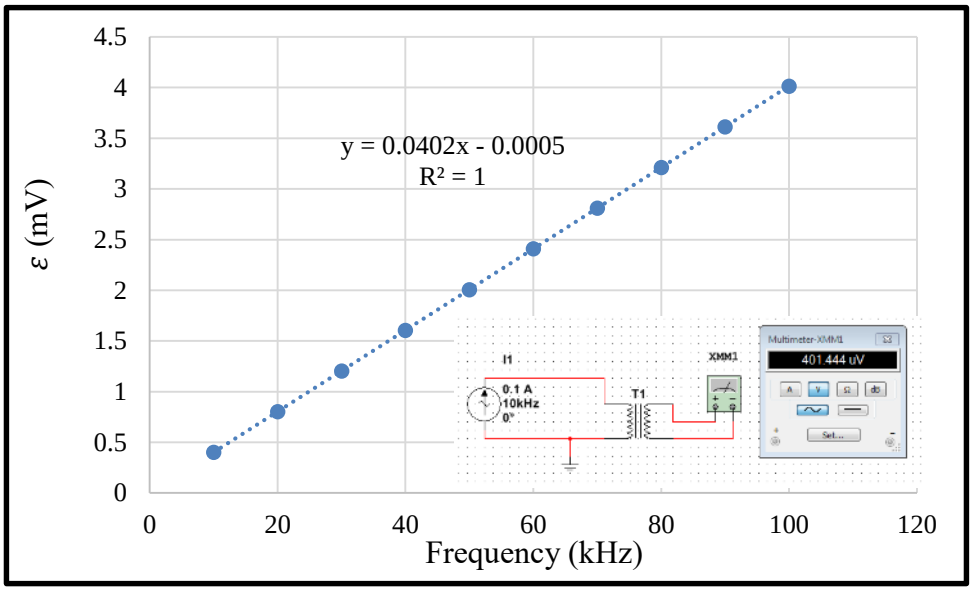


Figure 4.5: Simulated operation of the CIMS in Ar with μ=0.99. The induced voltage as a function of driving frequency is shown along with a schematic of the simulated circuit. The displayed equation shows the slope, proportionate to the magnetic susceptibility, to be 0.0402, and an R^2 value of 1 indicating a perfectly linier fit.

The perfect linearity of the data shown in Figure 4.5, quantified by an R^2 value of unity, indicates the theoretically linear dependence of the coupled inductor circuit on driving frequency. To demonstrate the linear relation of the slope of the ε vs ω plot on

magnetic susceptibility, the simulation was re-run using a permeability of μ=99.999, compared to the μ=0.999 of argon. The response of the modeled system under these conditions is shown in Figure 4.5. It should be noted that magnetic susceptibility is defined as $\chi = \mu - 1$ and as a result, the simulation dependence on permeability is assumed to be equivalent to its dependence upon the magnetic susceptibility.

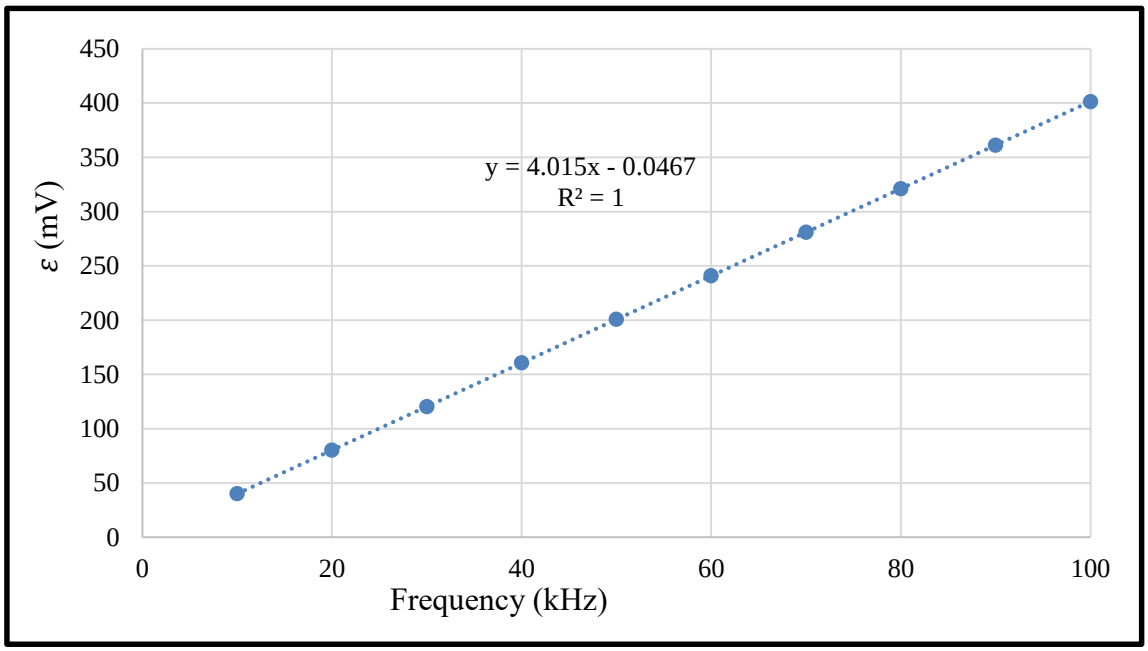


Figure 4.6: Simulated response of the CIMS with μ=99.99

The observed slope of the ε vs ω plot in Figure 4.6 is 100 times that of Figure 4.5, exactly proportionate to the permeability used in the respective models. It can therefore be concluded that the relationship between induced voltage and frequency, ε and ω, of coupled inductors is linear with a slope proportionate the magnetic susceptibility of the medium inside the inductors.

Prior to each experiment, the CIMS was calibrated in the argon atmosphere of the glove box to ensure repeatability. The data obtained in these calibration tests are shown in Figure 4.7 in comparison to the response predicted by the previously discussed model.

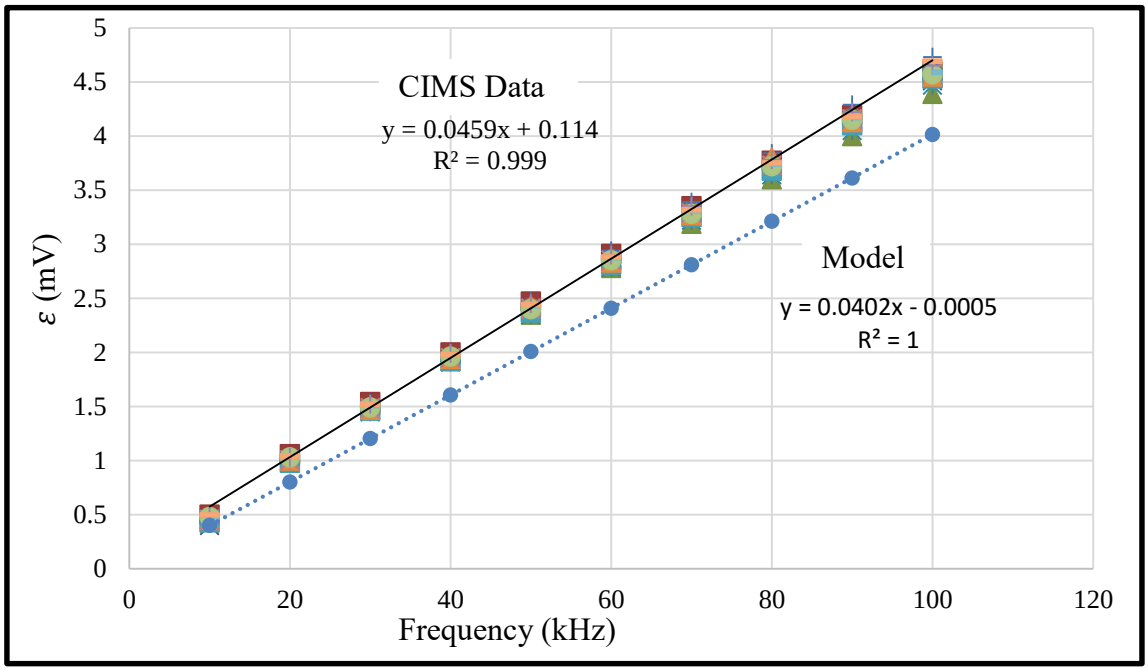


Figure 4.7: Recorded calibration data recorded before each test using the CIMS compared to the response modeled in Ar.

The linearity of the calibration data of the CIMS, and the agreement of this data with the modeled equivalent circuit, serves as proof of the operating principle of the CIMS. Furthermore, Figure 4.7 demonstrates the minimal system degradation that occurred throughout the 18 testing cycles the CIMS was subjected to.

4.2.4 Results:

To ensure the stability of the CIMS in LiCl-2wt%Li_2O-1wt%Li, the frequency response was recorded after exposure to the molten solution for 30 seconds as well as 10

and 30 minutes. The induced voltage recorded as a function of driving frequency under these conditions is shown in Figure 4.8.

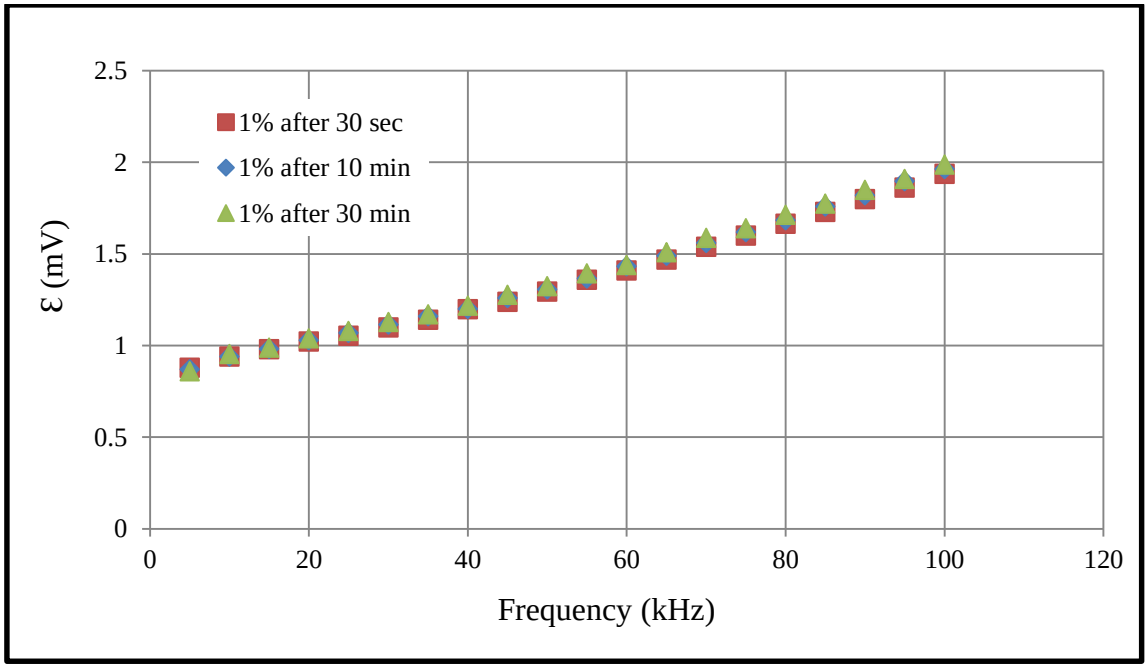


Figure 4.8: Frequency of the CIMS on LiCL-2wt%Li_2O-1wt%Li after exposure to the solution for 30 seconds as well as 10 and 30 minutes.

The results shown in Figure 4.8 demonstrate the stability of the CIMS system in the highly aggressive LiCl-Li_2O-Li environment. Additionally, the repeatability of the data after multiple operations in the same melt demonstrates that the operation of the CIMS does not significantly alter the nature of the LiCl-Li_2O-Li solution.

The slopes of the frequency response of the CIMS in LiCl-2wt%Li_2O-Li with respect to Li concentration are shown in Figure 4.9. Each experiment was conducted in triplicate, in a randomized order to ensure that no unintentional system alterations affected the measurements. The average of the magnetic susceptibility recorded at each concentration, the slope of ε vs ω, has been displayed with error bars according to the

standard deviation of the three data points. The linearity of all data recorded in each test produced an R^2 value greater than 0.998.

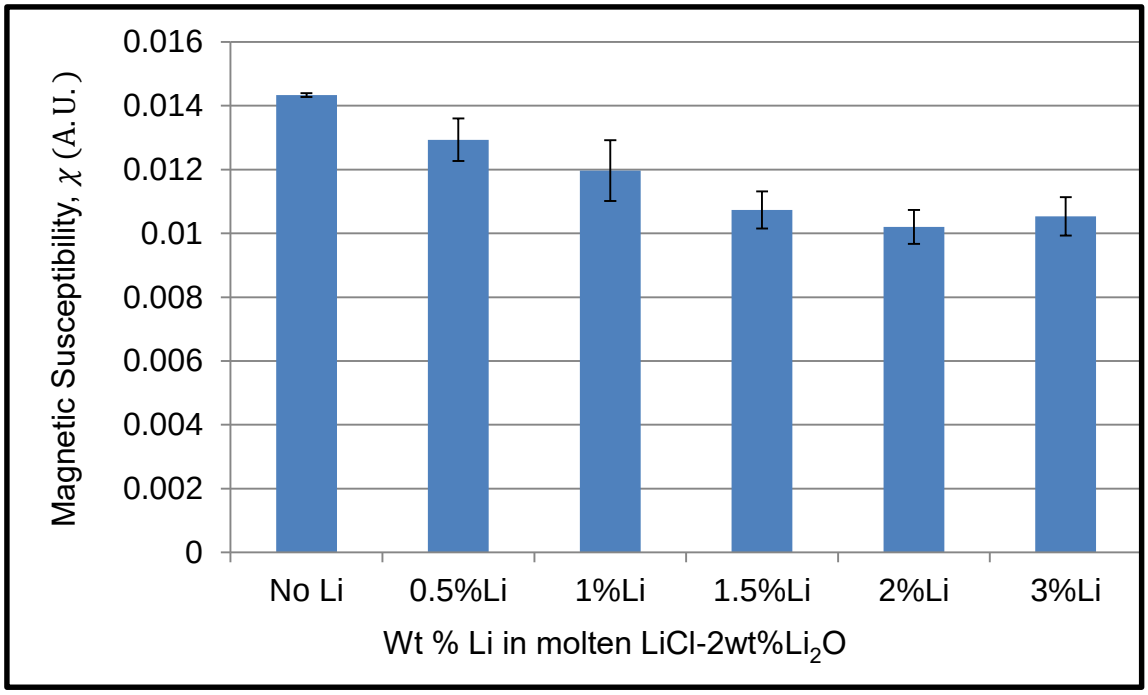


Figure 4.9: Recorded magnetic susceptibility of LiCl-2wt%Li_2O with the inclusion of 1-3wt%Li at 650°C.

Figure 4.9 demonstrates the ability of the prototype CIMS to quantify the solubility limit of Li in molten LiCl-Li_2O. The observation of the magnetic susceptibility becoming nearly independent of Li concentration above 1wt% indicates, as predicted, that the solution is saturated. The experimental uncertainty in these measurements is significant, however a definite trend can be observed.

It should be noted that LiCl is highly diamagnetic, having $\chi < 1$, due to the noble gas configuration of its constituent atoms. The observation of a decrease in magnitude of the magnetic susceptibility of LiCl-Li_2O with the addition of Li suggests that the valence electron of the solvated lithium exists in a paramagnetic, $\chi > 1$, state. This is strong

evidence that excess electrons in the system do not form spin paired states, as the formation of such states would increase the overall diamagnetic nature of the solution. Previous research has utilized the magnetic susceptibility of metal salt solutions to discern the nature of solvated Bi in BiCl, Cd in CdCl and Na in NaCl solutions [196]. As discussed in further detail subsequently, the interpretation of this data gives key insight into the bonding of lithium and electronic structure of the LiCl-Li_2O-Li solution.

4.3 Anomalous Physical Properties of Molten LiCl-Li_2O-Li:

Molten solutions of LiCl and Li, as well as the interface of Li and molten solutions of LiCl in the presence or absence of Li_2O or KCl, has been the subject of extensive research [1, 70-74, 87, 91, 104, 108]. Even so, a knowledge gap still exists in the understanding of the true nature of these molten solutions. Previous research has demonstrated the following phenomena that seemingly are unexplainable:

- Dispersion of Li in LiCl is associated with the formation of a “metal fog” that cannot be explained by physical dissolution [104, 108].
- The reported values of the solubility limit of Li in LiCl measured by different methods of analyses vary significantly and are in disagreement [1, 70-74, 91].
- The electrical conductivity exhibited by LiCl-Li solutions under metal saturated conditions is unexpectedly low [71].
- Electrochemical measurements of Li in the presence of LiCl appear as if the thermodynamic activity of Li is significantly lower than unity [72].

- An intermediate electrochemical potential, between that of $Li|Li^+$ and that of the electrode material, is observed when Li disperses from an electrode [87].

An example of the unique physical chemistry of molten solutions of LiCl-Li_2O-Li can be demonstrated by visual observation of molten LiCl-Li_2O in the presence and absence of Li. A digital image of a molten solution of LiCl-3wt%Li_2O before and after conducting electrolysis of Li_2O is shown in Figure 4.10. In this experiment, a stainless steel 316L cathode was polarized at -3.2V against a Pt working anode in molten LiCl-3wt%Li_2O at 650°C for approximately ten minutes. This polarization, conducted between when the two images in Figure 4.10 were captured is highly analogous to the polarization that occurs during the electrolytic reduction of actinide oxides [32, 68].

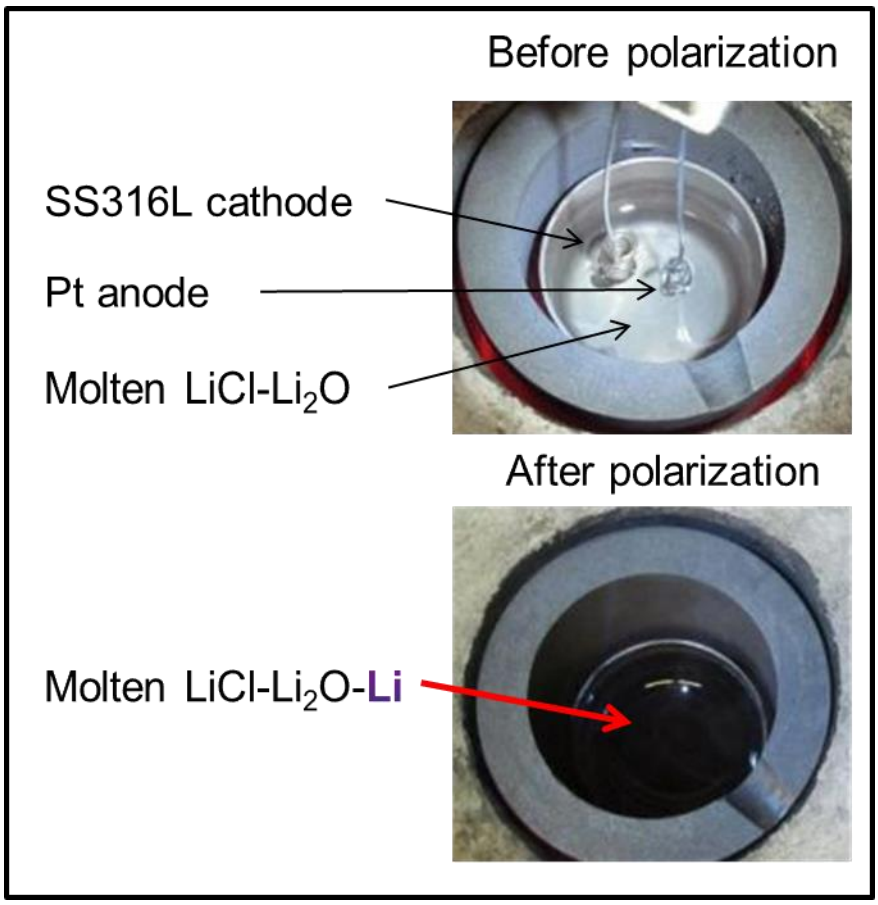


Figure 4.10: Images of molten LiCl-3wt%Li_2O before and after conducting electrolysis of Li_2O using a SS316L cathode and a Pt working anode. The coloring of the molten solution is the result of the formation of a ternary molten solution of LiCl-Li_2O-Li.

The formation of the deeply purple colored molten solution shown in Figure 4.10 that occurs when Li is reduced in molten LiCl is indicative a shift in the physical chemistry of the melt. Alkali-halide molten salts are almost exclusively optically transparent due to the strongly ionic bonding of the salt constituents. The ionic bonding of molten salts results in tightly bound electron states that do not typically absorb visible light. Alternatively, liquid metals are electronic conductors and appear silver as they reflect a broad portion of the visible spectrum. However, the observed coloring of molten LiCl-Li, in the presence and absence of Li_2O, is different. The characteristic purple color of these solutions indicates the existence of relatively loosely bound electron states that

are capable of absorbing visible light. While this is a purely qualitative measure, this effect clearly indicates that these solutions do not exclusively exhibit the physical properties of either molten salts or liquid metals.

An electrochemical investigation of Li in contact with molten LiCl provides a second example of the unique physical properties of these molten solutions. First observed by Liu *et al.,* this effect was used in the current work to demonstrate the success of the developed Li-Bi reference electrode [72, 87, 94]. Electrochemical investigations of the interface between liquid Li and LiCl-Li_2O were conducted after developing the Li-Bi reference electrode discussed in Chapter 2. The phenomena of interest is observed by recording the potential of an electrode while Li^+ is reduced on it, then observing the open circuit potential (OCP) of the electrode as a function of time after ceasing the polarization. This experiment was conducted by polarizing a SS316L working electrode to -1.25 V vs Li-Bi using a Pt counter electrode for 300 seconds in LiCl-2wt%Li_2O, and observing the OCP of the working electrode for the following 2000 seconds. The potential of the working electrode throughout this experiment is shown in Figure 4.11.

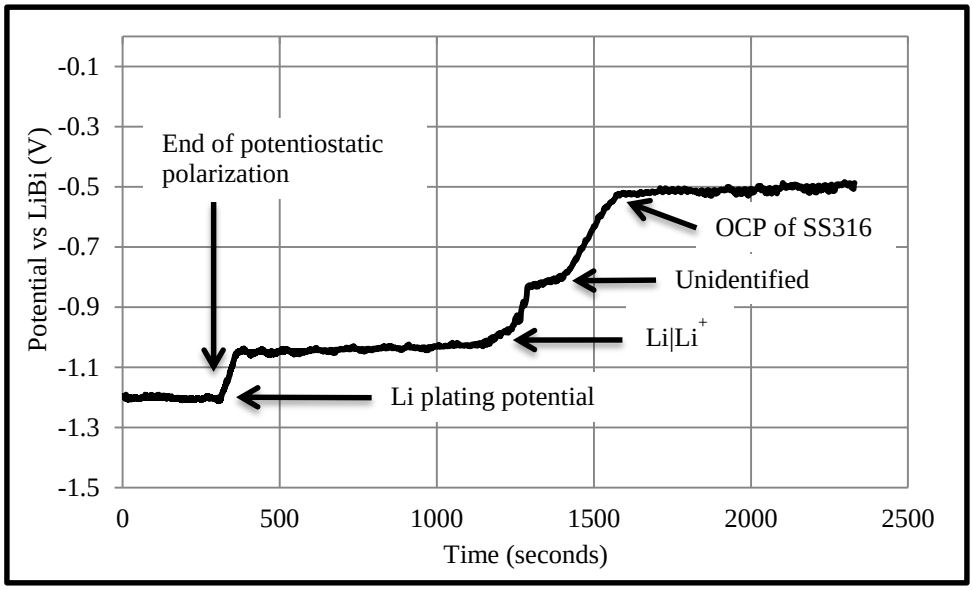


Figure 4.11: Potential vs time plot of a SS316L electrode during and after plating metallic Li on its surface. Potentiostatic polarization to -1.25V vs LiBi was conducted for 300 seconds followed by 2000 seconds of open circuit potential monitoring. The observed second stable potential plateau after polarization is indicative of the formation of an unidentified salt soluble compound.

The potential vs time data shown in Figure 4.11 demonstrates a fascinating aspect of the LiCl-Li_2O-Li system. Initially, during the period of potentiostatic polarization the working electrode potential is maintained below the Li^+ reduction potential at -1.25V vs Li-Bi. After the polarization is ceased, the potential increases to the $Li|Li^+$ potential of approximately -1.05V vs Li-Bi were it is stable for approximately 800 seconds. The potential measured during this period is attributed to the measurement of the OCP of Li existing at unit activity on the electrode. Due to the solubility of Li in the molten LiCl-Li_2O, this activity of Li dissolves into the melt over the course of time. Once sufficient Li has dissolved from the electrode that the activity of Li is no longer unity, the OCP increases again to a second stable potential were it stays for roughly 100 seconds before increasing finally to the OCP of the bare SS316L electrode. The observation of this intermediate potential (between the OCPs of metallic Li and the working electrode) suggests the existence of a salt soluble compound that has not yet been identified. This

effect has been observed in LiCl, LiCl-Li_2O, and LiCl-KCl and has been hypothesized as evidence of the existence of a hyperlithiated compound, such as Li_2Cl [72, 87, 94].

Previous attempts to explain these properties have led to extensive theoretical research on the existence of "hyperlithiated" compounds, such as Li_2Cl [87, 94, 197, 198]. While mass spectrometry experiments [198, 199] have shown the presence of hyperlithiated compounds *in vacuo*, there has been no evidence of their existence in a fused phase. Alternatively, theoretical work has postulated the formation of lithium dimers, Li_2, in the molten LiCl matrix as a rationale for explaining the properties of LiCl-Li [81, 200]. Recently, suspensions of nanoparticles in other molten salts have been investigated for a wide variety of applications due to their unique physical properties [201]. Similarly, experimental work by Nakajima *et al.* suggested that the dispersion of Li in LiCl is the sum of two separate processes, i.e., physical dissolution and colloidal suspension [1, 73, 74, 91]. In these studies, micron-sized particles of metallic Li were observed in quenched LiCl-Li. However, it also was noted that the metallic species would require an emulsifying agent to be suspended in the ionic fluid. While it was proposed that impurities, such as Li_2O and Li_3N, act as emulsifying agents, it also was noted that the concentration of dispersed Li in LiCl was not highly dependent on the concentration of either Li_2O or Li_3N.

4.4 Presence of Li Clusters in Molten LiCl-Li:

Validation of the previously discussed hypotheses is experimentally challenging due to the highly reactive nature of molten solutions that contain metallic Li and LiCl. Furthermore, *ex situ* experimental techniques are not reliable because the phase stability

of mixtures of LiCl and Li is temperature dependent [70, 72]. In the current research, Raman spectroscopy was employed for the *in situ* characterization of molten mixtures of LiCl, Li_2O, and Li at 650˚C in an attempt to understand the nature of these solutions.

4.4.1 Methods:

Precursor chemicals of ultra-high purity were employed in all experiments in this section. Melts were contained in Mo or Ta crucibles, and were maintained at 650˚C ± 10˚C throughout all of the experiments.

Molten solutions of LiCl-Li_2O-Li were generated electrochemically via electrolysis of Li_2O from molten LiCl-3 wt%-Li_2O. Electrolysis was conducted using a coil of Pt as the working anode and a coil of stainless steel alloy 316L as the cathode at a cell voltage of 3.2V, analogous to the cell potential utilized in the electrolytic reduction of UO_2 [32, 68]. Polarization was conducted in this manner until sufficient charge was passed through the cell to reduce an equivalent of 1 wt% of the melt to metallic Li. The electrodes were maintained in the melt for one hour following electrolysis prior to removal for characterization using Raman spectroscopy. The LiCl-Li melts were prepared in subsequent experiments by directly adding metallic Li to molten LiCl. In all cases, Li_2O and/or Li were added after drying the LiCl at 500˚C to remove residual H_2O and suppress the formation of LiOH.

Raman spectroscopic measurements were conducted *in situ* using a Thermo-Scientific DXR spectrometer and the custom fiber optic discussed in Chapter 2. A 10mW, 532 nm laser beam was passed through the fiber optic cable and telescope before

being focused on the surface of the melt. In alternative experiments, the laser beam was propagated horizontally, approximately 5 mm above the LiCl-Li mixture, and it was reflected by a metallic surface to characterize the vapor phase that existed on top of the melt. The reported spectra were an average of eight consecutively recorded spectra, each of which was recorded for eight seconds.

4.4.2 Results:

Figure 4.12 shows the in situ Raman spectrum of molten LiCl-Li_2O-Li (923 K) after electrochemically reducing an equivalent of 1 wt% of the melt to metallic lithium as well as a schematic depiction of the experimental setup. It was observed that the primary features at 285.5, 302.8, and 318.2 cm^{-1} exhibited overtones of decreasing intensity with increasing Raman shift.

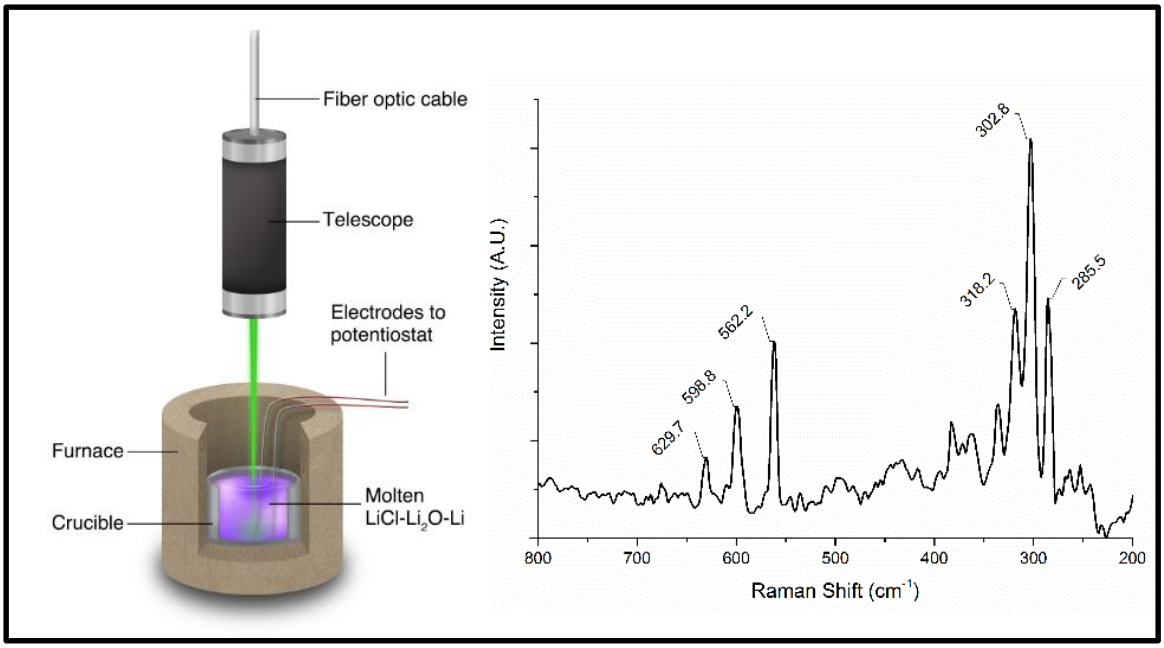


Figure 4.12: (Left) Schematic diagram of the experimental setup used for the measurement of the Raman features of LiCl-Li2O with electrochemically generated Li; (Right): Raman spectrum of LiCl-Li2O-Li at 923 K obtained after reducing the equivalent of 1 wt% Li from LiCl-3 wt% Li2O. The spectrum was recorded using a 10-mW, 532-nm laser focused vertically onto the surface of the molten solution. The spectrum was comprised of three fundamental features at 285.5, 302.8, and 318.2 cm^{-1}, with overtones of decreasing intensity at approximately integer multiples of these Raman shifts.

Additional experiments were conducted to confirm that the spectrum shown in Figure 4.12 was characteristic of the molten metal/molten salt phase of LiCl-Li_2O-Li and not of the vapor. To characterize the vapor phase that existed above the mixture, the excitation laser was maintained parallel to the surface of the melt, approximately 5 mm above the fluid/vapor interface, and it was reflected by a stainless steel mirror. The spectrum recorded in this manner, shown in Figure 4.13, exhibited high intensity Na fluorescence lines at 1818.1 and 1835.3 cm^{-1} (589 and 589.6 nm) [202]. For the sake of clarity, identical features were omitted from the spectrum in Figure 4.12; however, the full spectral range of this spectrum is provided in Figure 4.18.

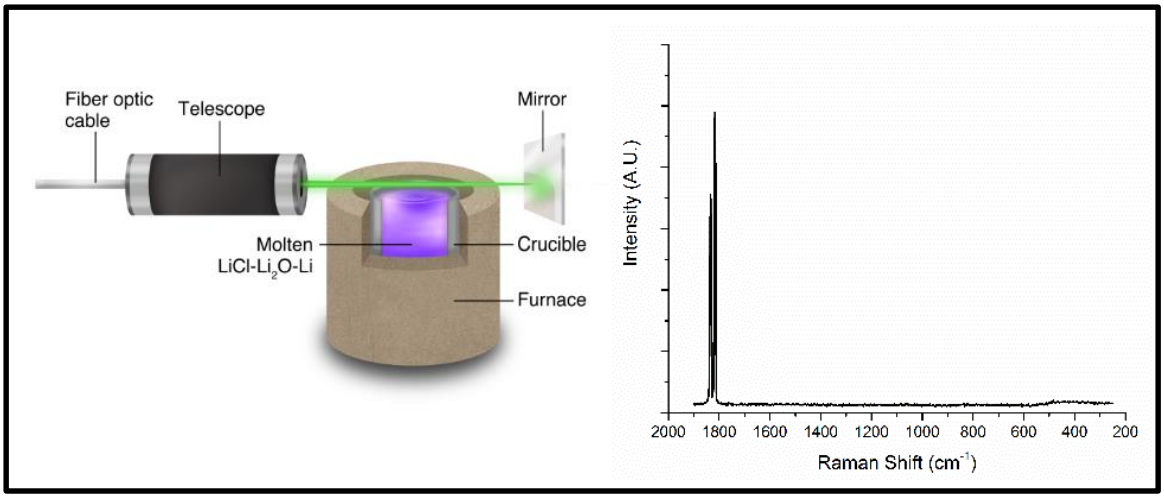


Figure 4.13: (Left) Schematic depiction of the experimental setup used to characterize the vapor phase that existed above the molten LiCl-Li. The excitation laser was maintained horizontally 5 mm above the surface of the LiCl-Li melt and reflected by a stainless steel mirror. (Right) Recorded spectrum of the vapor existing above the surface of LiCl-Li melt maintained at 923 K. The intense features spanning 1800 to 1900 cm^{-1} are characteristic of the fluorescence of Na from NaCl, which is found as a contaminant in LiCl.

The second experiment conducted to demonstrate that the observed Raman spectrum is characteristic of molten LiCl-Li_2O-Li employed a rapid flow of Ar shear gas across the surface of the melt while the Raman spectrum of the melt was recorded. A schematic depiction of this experiment, and the spectra recorded during it, is shown in Figure 4.14. The observed lack of variation in the Raman spectrum recorded in the presence and absence of the Ar shear gas indicates that the spectrum is not the result of a vapor phase exiting above the melt.

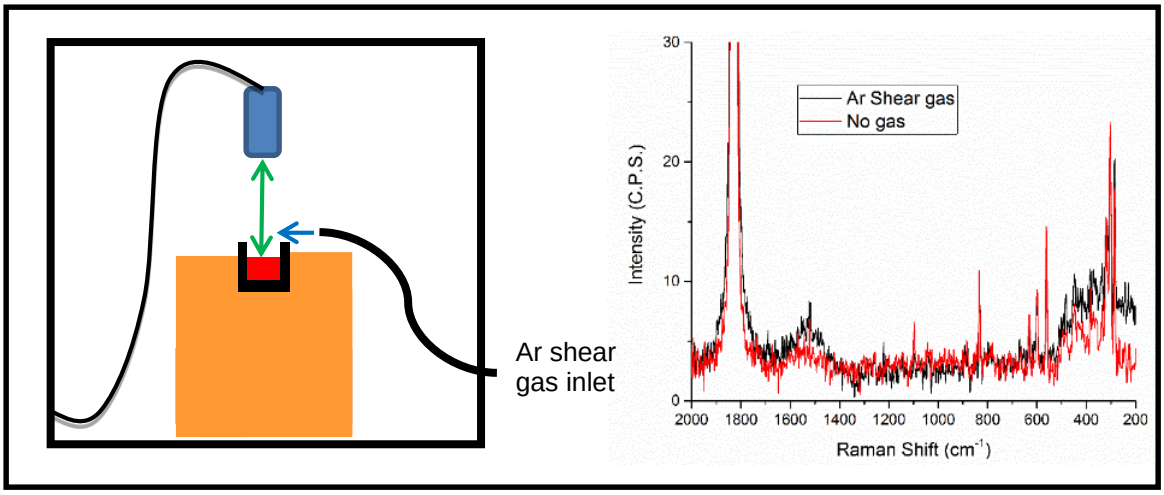


Figure 4.14: (Left) A schematic depiction of the Ar shear gas experiment. (Right) The Raman spectrum of LiCl-1wt%Li at 650ºC with and without passing high velocity Ar shear gas across the surface of the melt. The minimal change in the signal intensity, despite the rapid expulsion of the vapor phase, demonstrates that the Raman spectrum is a property of the fused LiCl-Li phase. The intense feature spanning 1800 to 1900cm^{-1} derives from the fluoresce of impurity Na.

The Raman spectra of LiCl-Li_2O-Li were recorded with varying incident laser power between 0 and 10mW to quantify the dependence of the signal on the power of the laser. Figure 4.15 shows the spectra recorded at various laser powers, along with a plot of the intensity of the Raman feature at 302 cm^{-1} as a function of laser power. A linear response was observed with an R-squared value of 0.979.

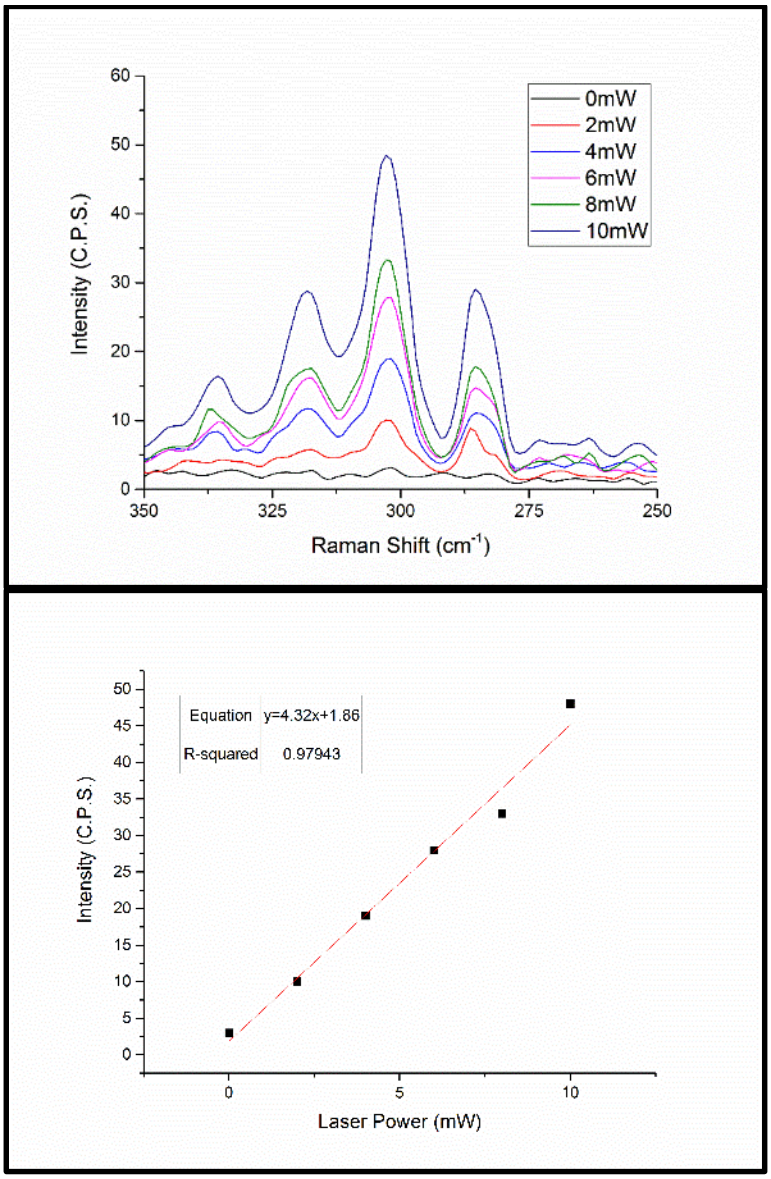


Figure 4.15: (Top) Raman spectra of LiCl-Li at 923 K recorded with an incident laser power increasing from 0 to 10 mW. (Bottom) Plot of the intensity of the 302 cm^{-1} Raman shift as a function of incident laser intensity, showing the linear dependence of signal intensity on the laser power.

To investigate the stability of the LiCl-Li melt as a function of time, Raman spectra of LiCl-Li were recorded 5, 15, 45, and 90 minutes after adding 1-wt% Li to molten LiCl. The spectra recorded at these times are shown in Figure 4.16.

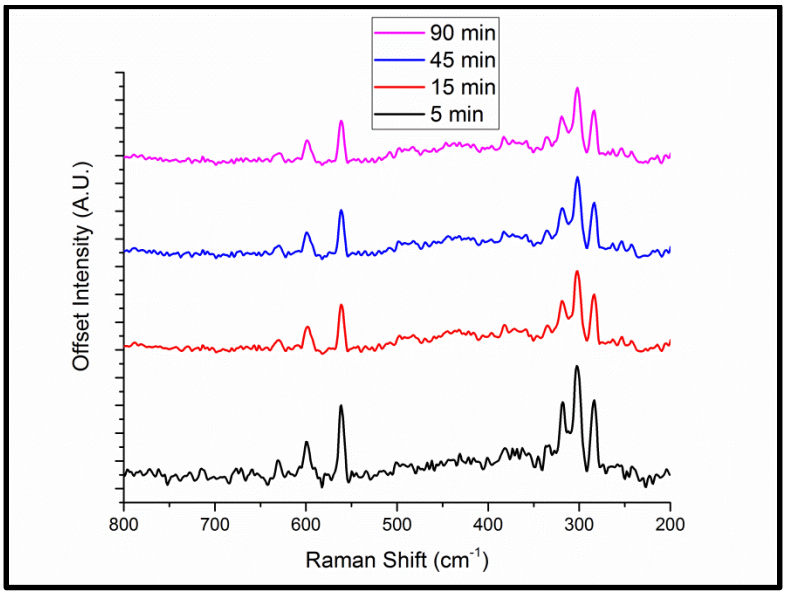


Figure 4.16: Raman spectra of LiCl-Li at 923 K recorded 5, 15, 45, and 90 minutes after adding 1-wt% Li to LiCl. The minimal variation in signal intensity over 90 minutes demonstrates the quasi-stability of the LiCl-Li mixture.

Melts of LiCl-Li were investigated spectroscopically in Mo and Ta crucibles to demonstrate that the observed Raman spectrum of the melt was independent of the crucible material. Raman spectra of LiCl-1-wt% Li recorded in Ta and Mo crucibles are shown in Figure 4.17.

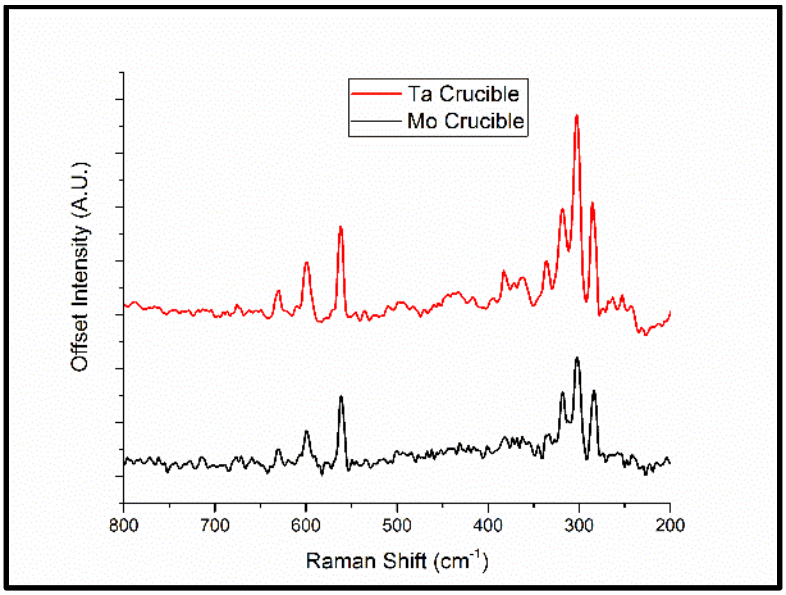


Figure 4.17: Raman spectra of LiCl-Li melt at 923 K contained in Mo and Ta crucibles. The results demonstrate that the observed spectrum is independent of the crucible material.

The Raman spectrum shown in Figure 4.12 was restricted to a narrow spectral band for clarity. Figure 4.16 shows the spectrum in Figure 4.12 across a larger spectral range, and it includes both the Raman features attributed to the presence of Li_8 as well as the Na fluoresce lines exhibited in Figure 4.13.

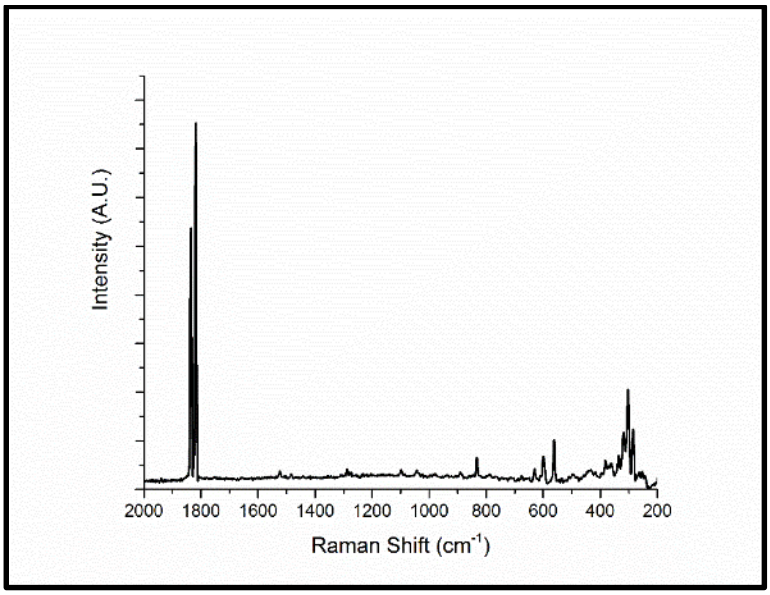


Figure 4.18: Raman spectrum of LiCl-Li_2O-Li at 923 K shown in Figure 4.12 across a larger spectral range. The spectrum exhibits the Raman modes attributed to the presence of Li_8 as well as Na fluoresce.

The Raman spectrum of molten LiCl-3-wt% Li_2O is shown in Figure 4.19 as a control to demonstrate that solutions that do not contain metallic Li lack detectable Raman activity.

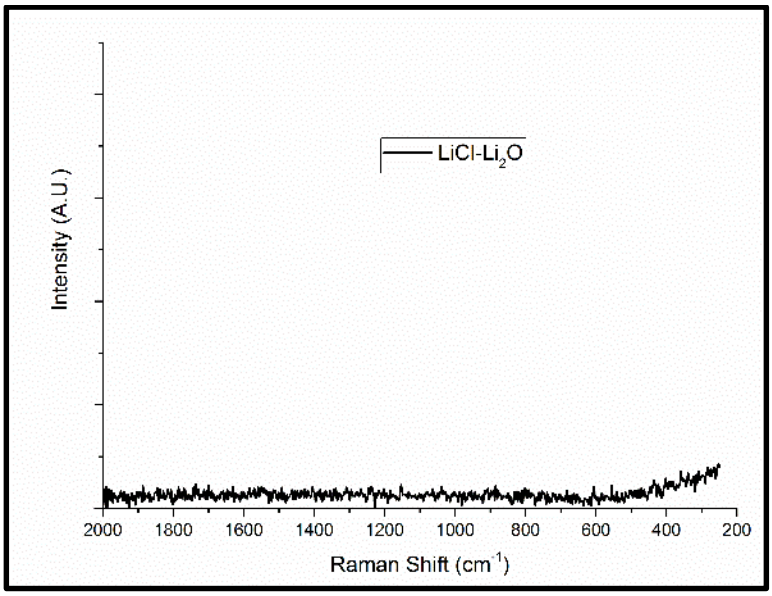


Figure 4.19: Raman spectrum of LiCl-Li_2O at 923 K before the addition of metallic Li to the melt.

4.4.3 Discussions:

The Raman spectrum of molten LiCl-Li_2O-Li at 650˚C, shown in Figure 4.12, is in agreement with the spectrum of the Li cluster, Li_8, previously reported by Kornath *et al.* [203]. The minor discrepancies between the spectra found in the literature and this study are attributed to the difference in the temperatures used in the experiments; the spectra given in this study being recorded 908˚C higher than those in the published work. Despite the vast difference in the temperatures used in the experiments, the symmetry of the two spectra were nearly identical and they consisted of three primary features centered on the A_1 breathing mode of Li_8 at 302.8 cm^{-1} recorded at 650˚C in the current study, and reported at 295.3 cm^{-1} when observed at 15 K. Additionally, the overtones in the spectrum obtained in this study were in agreement with the spectra obtained from Li_8 by Kornath *et al.* [203].

Spectroscopy of the vapor phase that exists above the LiCl-Li melt was conducted to confirm that the reported spectrum was a characteristic of the fused phase. The spectrum in Figure 4.13, obtained with the laser passing horizontally above the surface of the melt, shows only the fluorescence lines from Na and none of the Raman features that have been suggested to be characteristic of Li_8. LiCl has a lower free energy of formation than NaCl at 650˚C, and, as a result, metallic Li will displace Na from NaCl (found as contaminant in LiCl) in the melt to form LiCl and Na [204]. Furthermore, Na has a vapor pressure of 7.43 kPa at 650˚C and is expected to vaporize in significant quantities [205]. Therefore, as a result of the reaction between Li and impurity NaCl, the vapor existing above the LiCl-Li melt consists primarily of Na. Observation of just the Na fluorescence

signal in Figure 4.13, without the Raman features of interest, demonstrated that the vapor phase does not contain detectable quantities of Li clusters, and that the Raman spectrum shown in Figure 4.12 is characteristic of molten LiCl-Li.

Interestingly, the observed Raman spectrum of LiCl-Li does not exhibit the predicted vibrational modes for Li_2Cl [87, 94]. However, it was noted that the original work by Hébant *et al.* hypothesized the existence of Li_2Cl precisely at the interface between liquid Li and LiCl, while the spectrum reported in this study were specifically recorded on the surface of the bulk fluid. Additionally, the Raman mode of the Li_2 dimer at 349 cm^{-1} was not observed in the molten LiCl-Li [206, 207]. Li_2 has been detected under a variety of conditions via Raman spectroscopy, and, previously, it was theorized to be the probable form of Li complexes in molten LiCl-Li [81, 200]. Importantly, however, the dimer molecule possesses $D_{\infty h}$ symmetry [208, 209], while the Li_8 cluster possesses a complex hypertetrahedral T_d geometry [203, 210-212]. The axially-symmetric nature of Li_2 would prevent the dimer from exhibiting a dipole moment and therefore would be immiscible with the pure electrolyte. Alternatively, the asymmetric electronic structure of Li_8 may enable the suspension of these clusters in an ionic fluid. Colloids of lithium clusters are known to form in solid LiF and Li_2O crystals when subjected to sufficient irradiation [213-215]. Furthermore, Li_8 clusters have been observed to be stable in LiF at temperatures up to 1143 K [216]. These reports demonstrated that Li clusters are stable in ionically-bound systems at temperatures exceeding those of the current study.

The variance in reported values of the solubility limit of Li in molten LiCl is suspected to derive from the colloidal suspension of Li clusters in molten LiCl-Li. Should Li clusters exist in molten solutions of LiCl-Li, a well-defined solubility limit may not exist due to the dispersion mechanism of colloidal suspension in addition to physical dissolution. In this case, the quantity of Li that may be suspended or dispersed under a given set of conditions would be highly dependent upon experimental factors such as thermally induced mixing of the melt or mechanical agitation.

The conglomeration of Li atoms in the form of clusters may explain why the F^- center model notably overestimates the electrical conductivity of the LiCl-Li system while accurately predicting such properties for alternative solutions of alkali metal–alkali halide salts [71, 83, 85]. The F^- center model used to describe electron mobility in metal-salt solutions operates on the assumption that each metal atom acts as an electron donor to the electronic structure of the molten system [82, 102, 160, 217]. Under this assumption, the melt should exhibit a rapid increase in electrical conductivity with the inclusion of a small concentration of electron donor atoms. Alternatively, if Li^0 atoms suspended in molten LiCl-Li form clusters their valance electrons would be confined to the clusters instead of extending into shared electron states of the melt as a whole. This effect can therefore account for the consumption of what would be “free” electrons under metal saturated conditions, resulting in a suppression of the electrical conductivity of the melt [82, 83, 102, 103, 160, 217]. Similarly, the F^- center model does not apply to polyvalent metal-salt solutions such as Bi-BiI_3 [79, 86]. In a manner analogous to the proposed formation of Li clusters, metal salt solutions containing transition metals form

abnormally reduced complexes referred to as subhalides. The formation of these subhalides localizes what would otherwise be delocalized electrons causing the electron mobility in the melt to be lower than that predicted by the F^- center model.

The presence of Li clusters in molten LiCl-Li may additionally elucidate the unattributed electrochemical phenomena exhibited by these solutions shown in Figure 4.11. As mentioned previously, electrochemical measurements of Li in contact with molten LiCl exhibits two distinct electrochemical potentials [87, 94]. Furthermore, the alteration to the $Li|Li^+$ open circuit potential that occurs with varying concentrations of Li^0 in the melt is not Nernstian; it behaves as if the activity of the reduced form, Li^0 is not unity and changes based on concentration [72]. These facts suggest that molten solutions of LiCl and Li contain additional Li complexes other than LiCl and Li; a hypothesis that has been debated without confirmation for decades [1, 73, 74, 81, 87, 91, 94, 197, 198, 200]. It was noted that Li clusters possess significantly different ionization potentials than metallic Li [210, 211]; therefore they are expected to exhibit thermodynamic activity that is different from the metallic phase. As a result, the anomalous electrochemical properties of LiCl-Li can be attributed to the simultaneous existence of multiple, variable-activity Li phases. The multiple electrochemical potentials exhibited by Li, as well as the appearance of Li^0 not maintaining unit activity are hypothesized to be due to the presence Li clusters and metallically bonded Li in physical contact with the molten solution concurrently.

4.5 Conclusions:

Chemical analysis of molten solutions of $LiCl-Li_2O$-Li suggests that the solubility limit of Li in these melts is on the order of 0.3wt%, however these measurements yielded

a high degree of experimental error. A device was developed to measure the magnetic susceptibility of molten LiCl-Li_2O-Li and approximated the solubility limit of Li in LiCl-2wt%Li_2O to be in the range of 1 wt%. The Raman spectra of molten LiCl-Li_2O-Li and LiCl-Li were recorded *in situ* at 923 K. It is reported that a Raman active phase forms in the fused salt when Li is electrochemically reduced from Li_2O in molten LiCl-Li_2O, and the recorded spectrum was consistent with previously-reported characteristic spectrum of the lithium cluster Li_8. These spectra were seen to be characteristic of the bulk fluid rather than the vapor phase that existed above the melt, and it was observed to be stable over a 90-minute period. The presence of a colloidal suspension of lithium clusters in the molten salt may explain the anomalous physical behavior of LiCl-Li solutions. Furthermore, should Li clusters exist in molten solutions of LiCl-Li, a well-defined solubility limit may not exist due to the dispersion mechanism of colloidal suspension in addition to physical dissolution.

Chapter 5 Effect of Li on the Corrosion Stainless Steel Alloy 316L Exposed to Molten LiCl-Li_2O

Characterization of the effect of the presence of Li on the corrosion of stainless steel exposed to molten LiCl-Li_2O is presented as the culmination of this dissertation. The results presented in this Chapter examine this effect by systematically characterizing the corrosion of SS316L that results from exposure to melts of varying chemistry; molten LiCl with varying concentration of Li_2O as well as Li. These studies are found to agree with, and explain the findings of, Chapter 3 of this dissertation. Coupons of SS316L were independently exposed to dried reagent grade LiCl with 1 and 2wt%Li_2O, each with 0, 0.2, 0.4, 0.6, 0.8 or 1wt%Li for 20 hours at 650°C.

5.1 Results and Discussion:

5.1.2 Hardness:

The hardness of SS316L exposed to molten LiCl-Li_2O-Li was evaluated using micro-indentation. Indentations were made using loads of 100, 250 and 500 g to facilitate an analysis of the hardness as a relative function of depth. Samples were rinsed in methanol for 10 minutes prior to indentation to remove residual salt from the surface. The evaluated micro-Vickers hardness of the SS316L samples is shown in Figure 5.1. The hardness of an as-received sample is included for comparison.

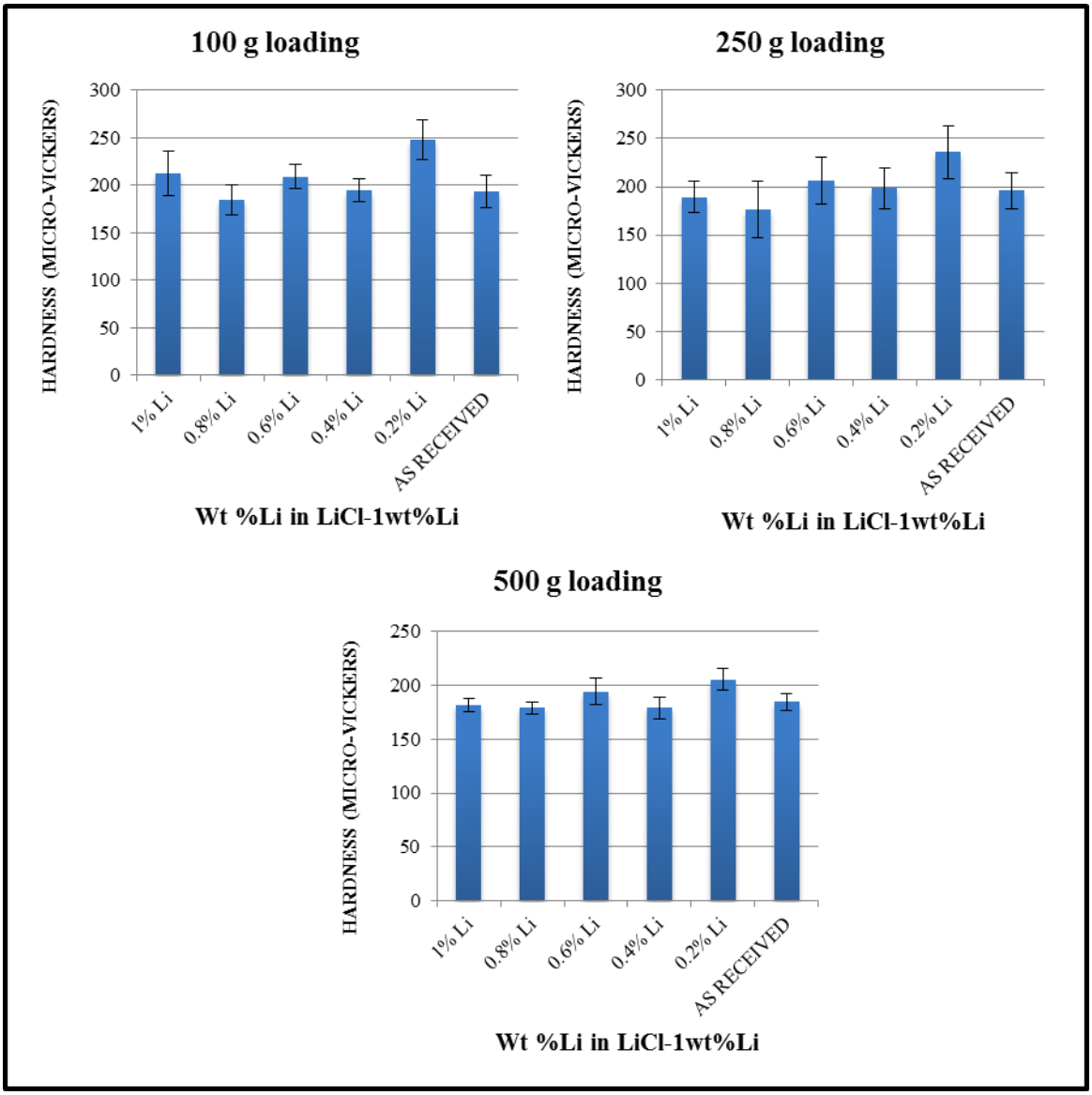


Figure 5.1 Micro-Vickers hardness of SS316L samples exposed to molten LiCl-1wt%Li_2O containing up to 1wt%Li at 650˚C for 20 hours, compared to an as-received sample. No trend in hardness is observed to correlate to the concentration of Li in the melt.

As shown in Figure 5.1, no alteration to the hardness of SS316L occurred as a result of 20 hours of exposure to molten LiCl-Li_2O-Li, nor was a trend of hardness observed to correlate to the concentration of Li in the melt. A slight trend of decreasing hardness with increasing load is observed, however the experimental uncertainty is too great to make strong conclusions from this data. Further investigations are required to

evaluate the alteration to the mechanical properties of materials that results from exposure to molten LiCl-Li_2O-Li.

5.1.2 SEM / EDS:

SEM micrographs of SS316L following 20 hours of exposure to molten LiCl with 1 or 2wt%Li_2O, each containing 0, 0.2, 0.4, 0.6, 0.8 and 1wt%Li are shown in Figure 5.2. Formations with dimensions on the order of micrometers are observed on the surface of samples exposed to melts in the absence of Li are attributed to the presence of oxides. These formations are observed in greater numbers on the surface of samples exposed to melts containing the higher concentration of Li_2O. No trend in morphological alteration to the material surface followed the concentration of Li in the melt with the exception of the samples exposed to melts containing 0.6wt%Li. The surfaces of SS316L exposed to melts containing 0.6wt%Li, with both 1 and 2wt%Li_2O, exhibit irregular features that are different from the observed morphology of all other post exposure alloy surfaces.

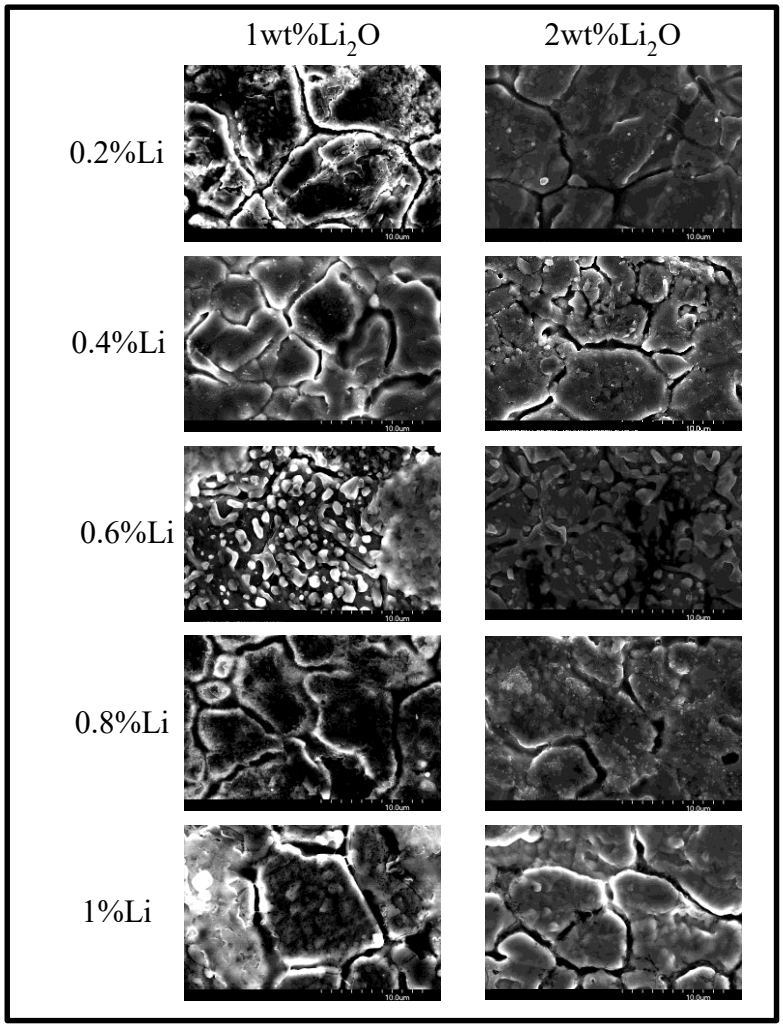


Figure 5.2: SEM micrographs of the surface of SS316L subjected to 20 hours of exposure to molten LiCl with 1 and 2wt%Li_2O, each with 0, 0.2, 0.4, 0.6, 0.8 and 1wt%Li after 2 hours of baking at 650°C in Ar. No trend in morphology follows the concentration of Li in the melt with the exception of melts containing 0.6wt%Li were irregular formations are observed.

The elemental composition as determined by EDS analysis of the surface of SS316L following exposure to molten LiCl with 1 and 2wt%Li_2O, each with varying Li concentration is shown in Figures 5.3 and 5.4, respectively. The elemental composition of the as-received alloy as determined by EDS analysis is included for comparison, however EDS analysis of samples exposed to melts that did not contain Li is excluded due to the high concentration of O detected on these samples. The strong O signal detected on

samples exposed to melts that did not contain Li was found to make the trends in alternative elemental compositions indistinguishable. EDS was performed using accelerating voltages of 10kV (less penetrating) and 20kV (more penetrating) to observe differences in elemental composition as a function of relative depth. The content of Fe in the samples is observed to have varied minimally from the as-received concentration (recorded at 20kV), and no obvious difference in the Fe content was observed when the analysis was conducted at different accelerating voltages. The concentration of Cr detected on all samples is observed to be approximately equivalent to, or decreased from the as-received alloy composition. A clear distinction in Ni concentration is observed in EDS conducted using accelerating voltages of 10kV and 20kV. The concentrations of Ni on the surface of SS316L recorded using an acceleration voltage of 10kV are observed to be approximately half of those recorded using an accelerating voltage of 20 kV. This suggests that Ni is depleted from the alloy surface as a result of exposure to molten LiCl-Li_2O-Li, however no trend is observed to follow Li concentration in the melt. It is noted that the decreased Ni content detected at 10 kV could also be the result of enrichment in Cr and or Fe on the alloy surface causing the relative concentration of Ni to appear to be diminished.

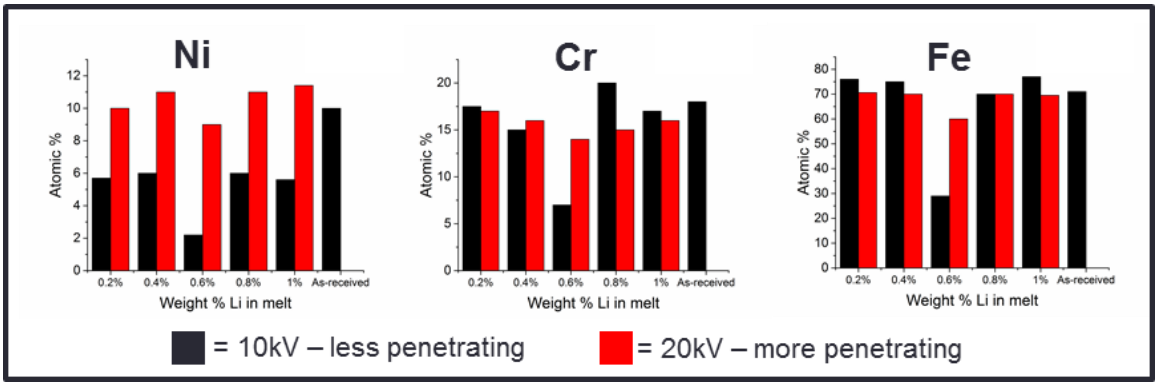


Figure 5.3: Elemental composition of alloying elements Ni, Cr and Fe detected by EDX analysis of SS316L subjected to 20 hours of exposure to molten LiCl-2wt%Li_2O with 0, 0.2, 0.4, 0.6, 0.8 and 2wt%Li after 2 hours of baking at 650°C in Ar recorded at 25,000x magnification. Data recorded using acceleration voltages of 10kV and 20KV is provided to allow for relative depth profiling. The concentration of Cr and Fe are not significantly altered from the as-received alloy, while Ni is observed to be depleted from the exterior surface.

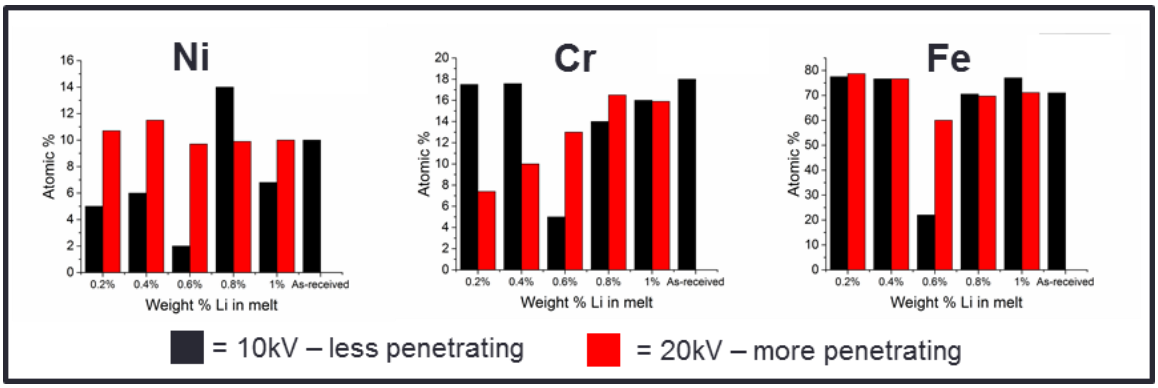


Figure 5.4: Relative concentration of alloying elements Ni, Cr and Fe detected by EDX analysis of SS316L subjected to 20 hours of exposure to molten LiCl-1wt%Li_2O with 0, 0.2, 0.4, 0.6, 0.8 and 1wt%Li after 2 hours of baking at 650°C in Ar recorded at 25,000x magnification. Data recorded using acceleration voltages of 10kV and 20KV is provided to allow for relative depth profiling. Ni is observed to be depleted from the exterior surface. Data obtained from the surface of samples exposed to molten LiCl-Li_2O in the absence of Li are omitted due to the large quantity of O present.

The composition of the surfaces of SS316L samples exposed to molten LiCl-Li_2O containing 0.6wt%Li are anomalous compared to samples exposed to molten solutions containing either lower or higher concentrations of Li. The concentrations of Ni, Cr and Fe on the surface of SS316L exposed to molten LiCl-Li_2O-0.6wt%Li appear low due to the relatively strong O signal detected on these surfaces by EDS. This effect was observed on samples exposed to melts containing 0.6wt%Li with either 1 or 2wt%Li_2O.

The reason why these surfaces contain an increased quantity of O compared to samples exposed to alternative melts is currently unknown and will be studied in future.

5.1.3 XRD:

Diffraction patterns recorded from a sample of SS316L exposed to a melt of LiCl-2wt%Li_2O in the absence of Li, before and after being subjected to the baking procedure, are shown in Figure 5.5. Multiple diffraction peaks attributed to the presence of $LiCrO_2$ are observed in both patterns, notably the characteristic peak from the (0,0,3) plane at 2θ=18.4° [218]. XRD identified the presence of $LiCrO_2$ on the surface of all samples exposed to molten LiCl-Li_2O in the absence of Li. However, XRD analysis did not identify any oxide or chloride surface film on samples exposed to melts containing dissolved Li. XRD analyses identified phases of LiCl, LiCl-H_2O, γ-Fe, and α-Fe on all of the SS316L surfaces exposed to ternary melts of LiCl-LI_2O-Li; however, no trend in the relative proportion of austenite to ferrite was observed by XRD as a function of Li concentration in the melt. Diffraction patterns indicating the presence of LiCl-H_2O were detected on sample surfaces with various levels of intensity. The existence of hydrated compounds on the samples is attributed to trace amounts of atmospheric moisture reacting with hygroscopic LiCl during the sealing of the bag.

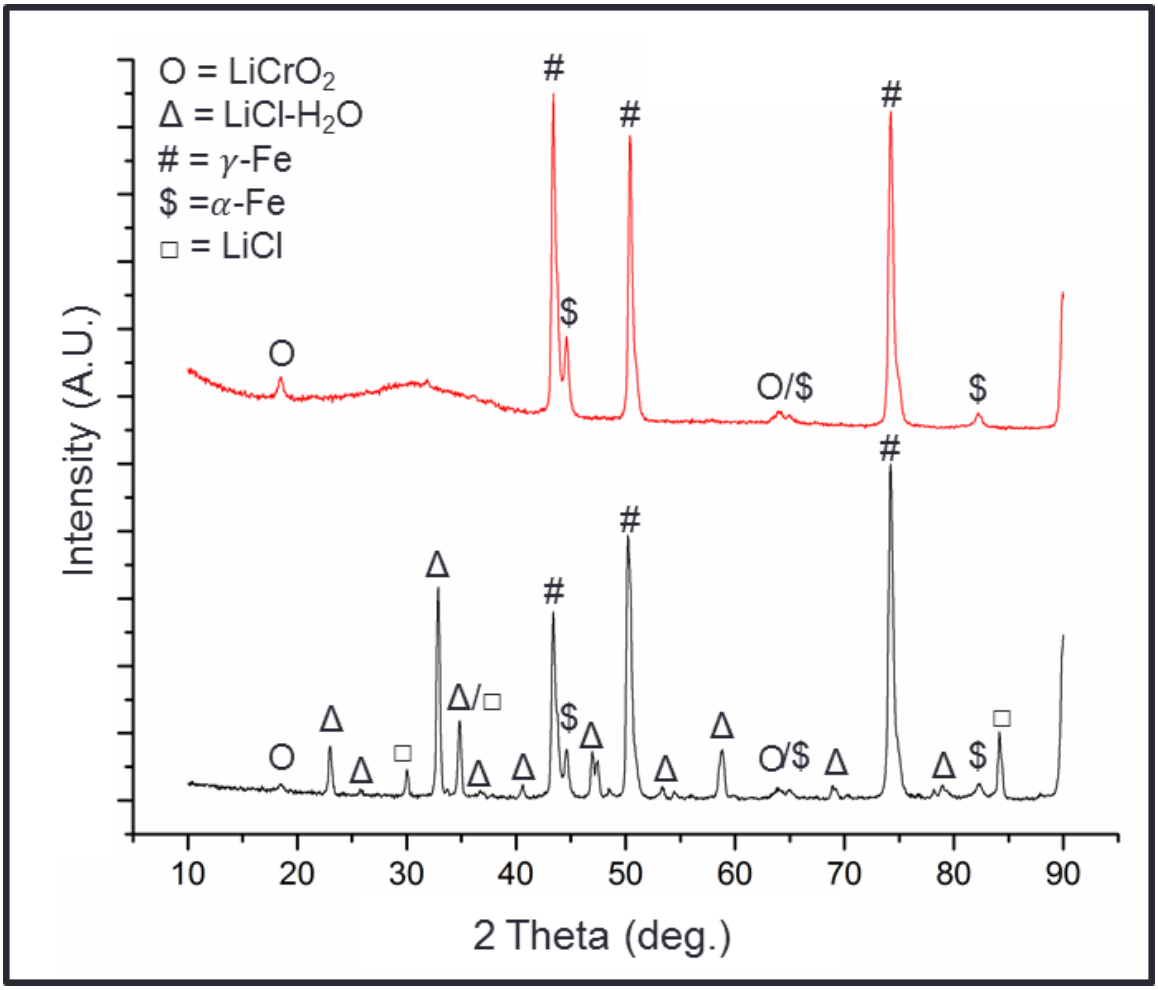


Figure 5.5: X-ray diffraction patterns obtained from a coupon of SS316L exposed to ultra-high purity LiCl-1wt%Li_2O in the absence of Li before baking (Bottom) and after 2 hours of baking at 650°C in Ar (Top). Diffraction from the (0,0,3) plane of $LiCrO_2$ at $2\theta = 18.4^{\circ}$ 2θ is observed in both patterns.

5.1.4 Raman:

Raman spectra collected from the surfaces of SS316L coupons exposed to ultra-high purity and reagent grade melts of LiCl-1wt%Li_2O in the absence of Li are shown in Figure 5.6. The characteristic Raman mode of $LiCrO_2$ at ~590cm^{-1} is observed in both spectra [188]. The surface of samples exposed to melts containing metallic Li did not exhibit detectable Raman signal. These findings corroborate the results from XRD

analyses, showing that $LiCrO_2$ is formed on the surface of SS316L exposed to molten LiCl-Li_2O at 650°C in the absence of dissolved Li.

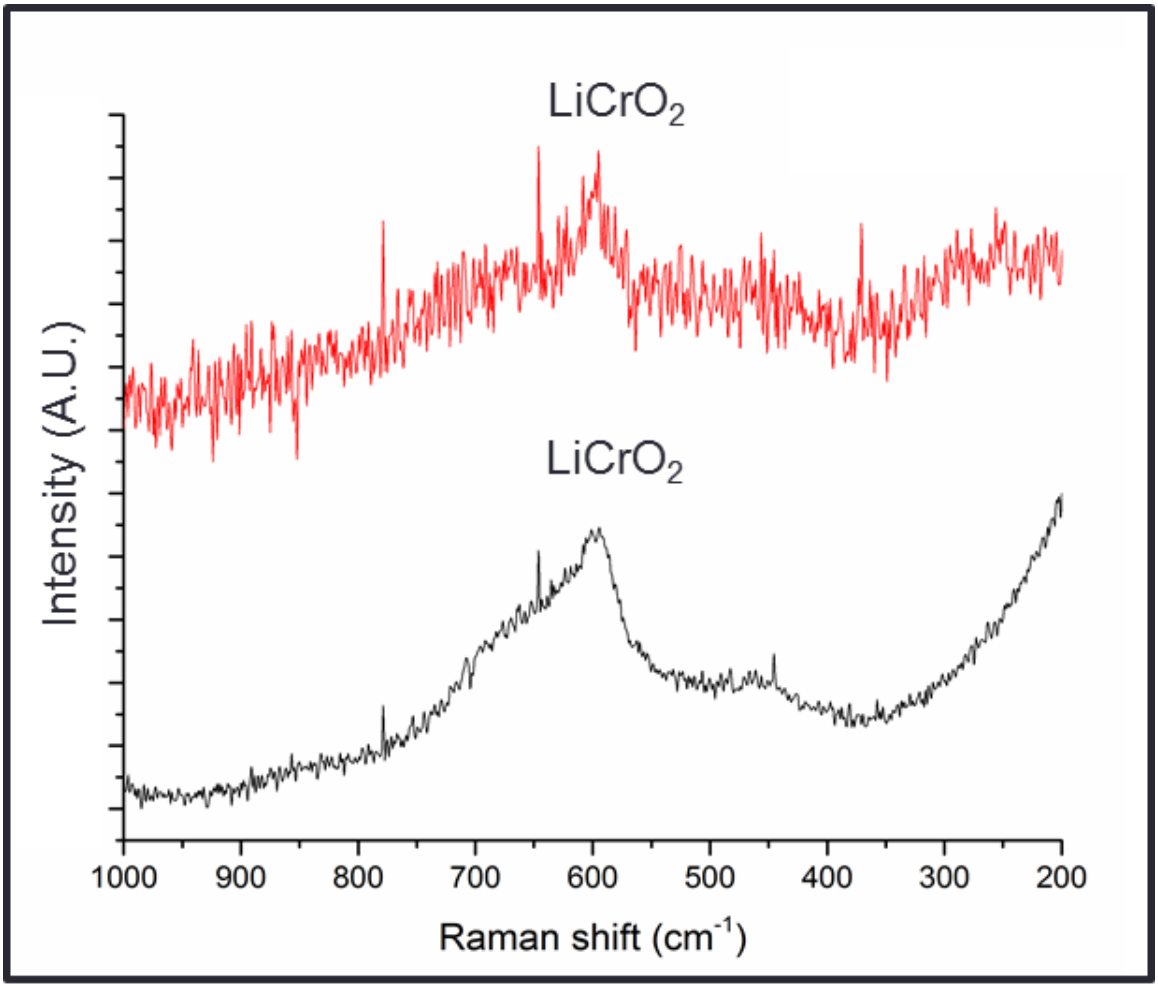


Figure 5.6: Raman spectra obtained from the surface of SS316L exposed to ultra-high purity LiCl-1wt%Li_2O (Top) and reagent grade LiCl-1wt%Li_2O (Bottom) both after baking at 650°C for 2 hours in Ar. The feature at approximately 590cm^{-1} is attributed to the presence of $LiCrO_2$.

5.1.5 XPS:

XPS survey spectra recorded from the surface of SS316L exposed to melts of LiCl with 1 and 2wt%Li_2O, each with concentrations of Li ranging from 0 to 1wt% are shown in Figures 5.7 and 5.8, respectively. Signals indicating the presence of Cr, O, Cl

and C are detectable on the surface of samples exposed to molten LiCl-Li_2O in the absence of Li, while Ni, Fe, Cr, O, Ti, N, C, and Cl are detectable on samples exposed to LiCl-Li_2O melts containing Li. The presence of Ti and N on the surface of materials exposed to molten LiCl-Li_2O-Li has been previously reported [219]. The relative concentration of the alloying elements Fe, Ni and Cr along with possible anions Cl and O detected on the separate sample surfaces by XPS are provided in Figure 5.9. It is observed that Cr constitutes an increasing percentage of the surface when Li is present in the melt at concentrations of 0.2 and 0.4wt% compared to samples exposed to melts of LiCl-Li_2O in the absence of Li. However, the surfaces of SS316L samples exposed to melts containing Li in concentrations exceeding 0.4wt% possess dramatically reduced contents of Cr compared to those exposed to melts containing no Li, as well as 0.2 and 0.4wt%Li. The reduction in Cr signal intensity between samples exposed to 0.4wt% and 0.6wt%Li solutions is observed to coincide with an increase in the intensity of the Fe and Ni signals. The shift from surfaces primarily composed of Cr to ones consisting of Fe and Ni is indicative of an alteration to alloy / melt interfacial chemistry occurring at ~0.4 and 0.6wt%Li. This effect is observed in the XPS spectra obtained from samples exposed to melts of LiCl containing 1 as well as 2wt%Li_2O.

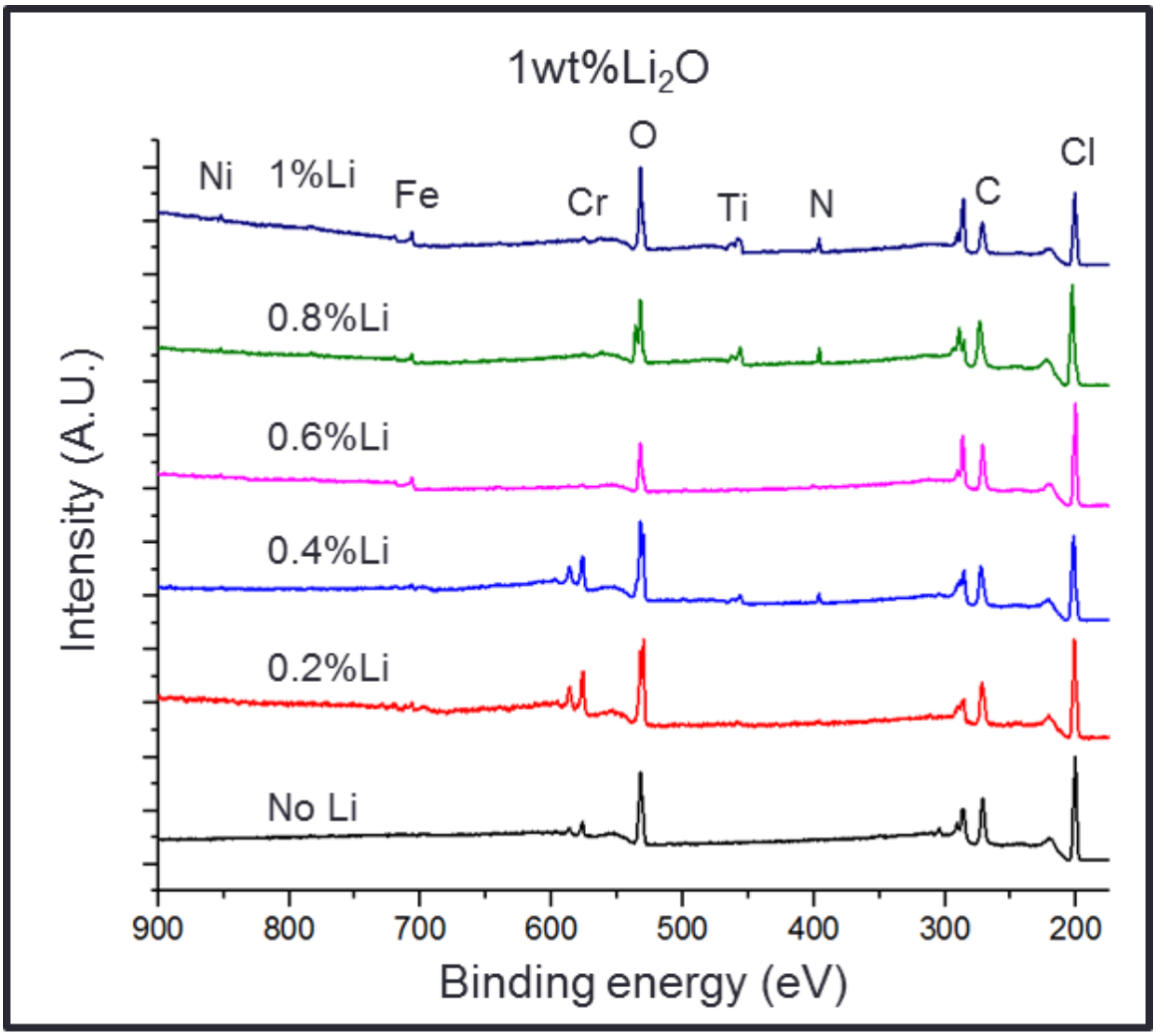


Figure 5.7: XPS survey spectra obtained from the surface of SS316L following exposure to LiCl-1wt%Li_2O with 0, 0.2, 0.4, 0.6, 0.8 and 1wt%Li at 650˚C for 20 hours after 2 hours of baking at 650°C in Ar. Ni, Fe, Cr, O, Ti, N, C, and Cl were present in detectable quantities on samples exposed to LiCl-Li_2O melts containing Li while only Cr, O, Cl and C were detectable on the surface of samples exposed to molten LiCl-Li_2O in the absence of Li. A sharp decrease in the intensity of the Cr signal is observed between samples exposed to melts containing 0.4 and 0.6wt%Li.

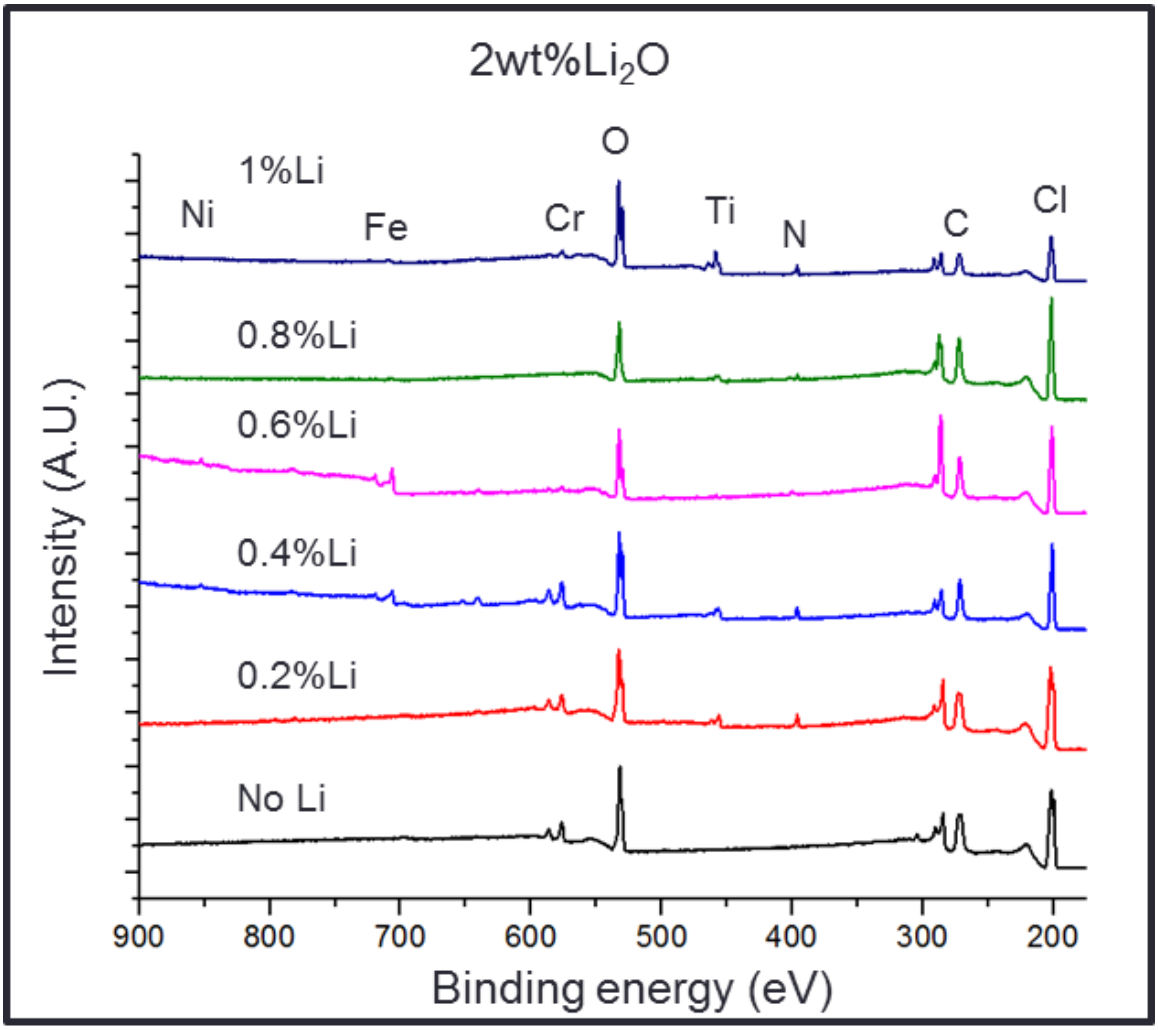


Figure 5.8: XPS survey spectra obtained from the surface of SS316L following exposure to LiCl-1wt%Li_2O with 0, 0.2, 0.4, 0.6, 0.8 and 2wt%Li at 650˚C for 20 hours after 2 hours of baking at 650°C in Ar. Ni, Fe, Cr, O, Ti, N, C, and Cl were present in detectable quantities on samples exposed to LiCl-Li_2O melts containing Li while only Cr, O, Cl and C were detectable on the surface of samples exposed to molten LiCl-Li_2O in the absence of Li. A sharp decrease in the intensity of the Cr signal is observed between samples exposed to melts containing 0.4 and 0.6wt%Li

Narrow XPS scans of the Fe 2p and Ni 2p lines recorded from a SS316L coupon exposed to molten LiCl-1wt%Li_2O-0.2wt%Li are shown in Figure 5.10. These spectra are representative of the bonding of Fe and Ni observed on the surface of all samples following exposure to melts containing dissolved Li. The Fe $2p_{3/2}$ and Ni $2p_{3/2}$ spectra possess single peaks at 706.7eV and 852.8eV, respectively, indicating that these elements are only present in significant quantities in metallically bonded states. It is noted that

these spectra did not require charge correction to be peak fit in accordance with their metallic binding energies. This fact further indicates that the Fe and Ni being analyzed were metallically bonded and in electrical contact with the specimen holder. The lack of oxidized species of Fe or Ni on the surface of SS316L exposed to molten LiCl-Li_2O-Li indicates that these elements do not form stable surface films under these conditions. It should be noted that narrow scans of the Cr 2p line obtained from the same sample surfaces, shown in Figure 5.11, demonstrate the presence of exclusively oxidized forms of Cr. Therefore, it is reported that surface films formed on SS316L in molten LiCl-Li_2O-Li, consist primarily of oxidized Cr and not Ni nor Fe. However, it is noted that it cannot be discerned if the metallically bonded Fe and Ni are located physically below the Cr surface film, or if the Cr surface film is incomplete and does not cover the sample surface and thus allows the metallic signal to be detected.

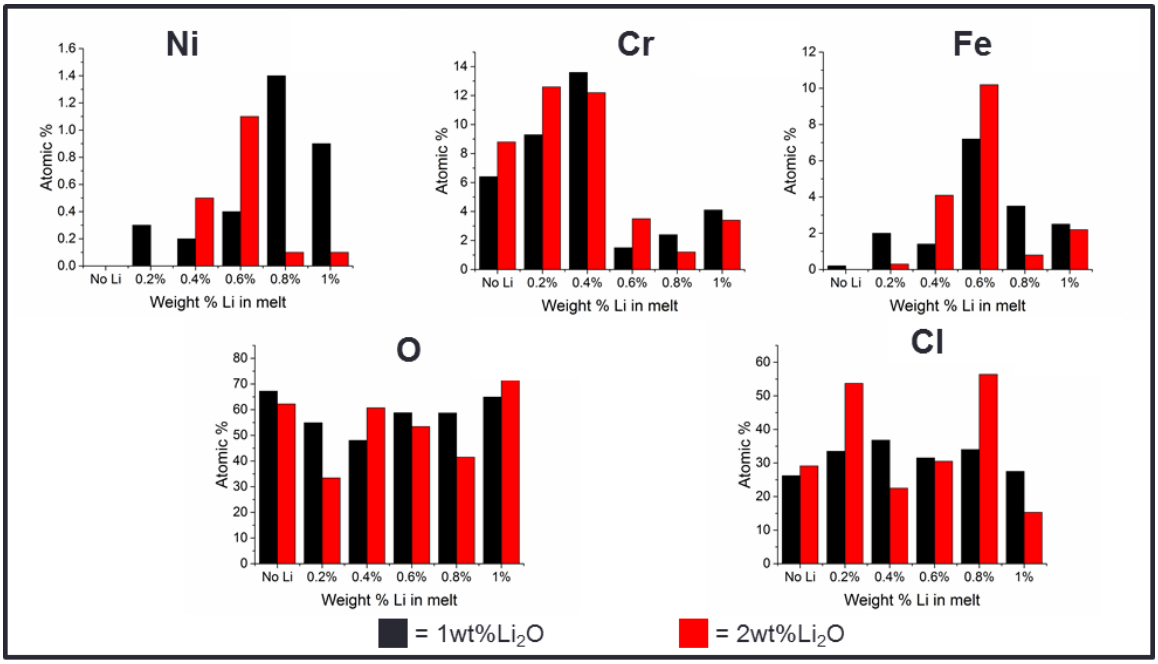


Figure 5.9: Elemental composition of alloying elements Ni, Cr and Fe and potential anions O and Cl detected by XPS analysis of SS316L subjected to 20 hours of exposure to molten LiCl with 1 and 2wt%Li_2O, each with 0, 0.2, 0.4, 0.6, 0.8 and 1wt%Li after 2 hours of baking at 650°C in Ar. A sharp decrease in Cr concentration is observed between samples exposed to melts containing 0.4 and 0.6wt%Li

The ability to detect XPS signal of metallically bonded Fe and Ni on sample surfaces exposed to melts containing Li demonstrates that the Cr surface films formed in these melts are thinner than the inelastic mean free path of the Fe and Ni 2p electrons in these materials. This observation suggests that the surface films formed under these conditions are on the order of nanometers thick. Furthermore, the XPS signal of Fe and Ni was below the level of detection on the surfaces of SS316L coupons exposed to molten LiCl-Li_2O solutions that did not contain metallic Li. The lack of detectable Fe or Ni signal indicates that thicker Cr based surface films formed when metallic Li was not present in the melt.

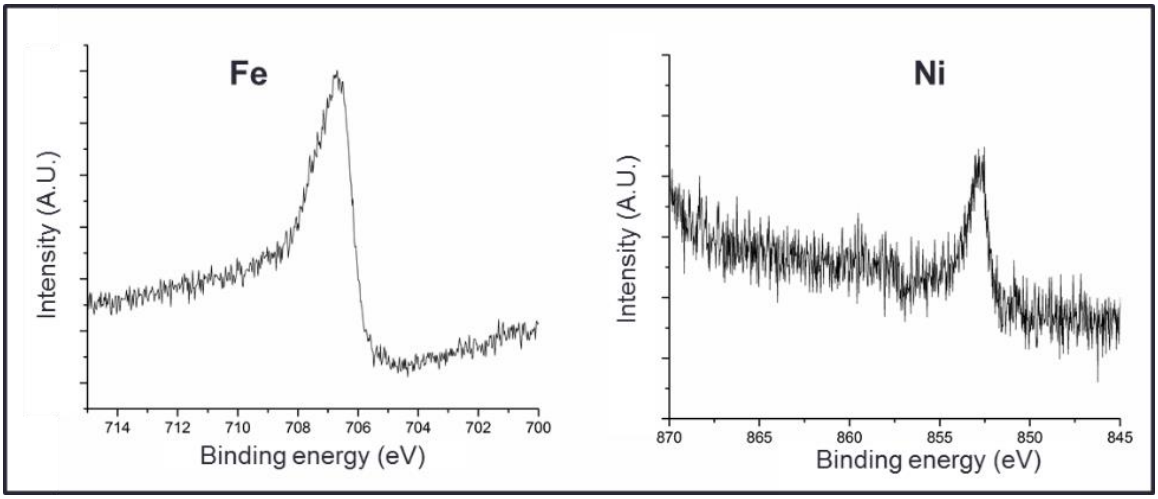


Figure 5.10: Fe 2p (Left) and Ni 2p (Right) spectra obtained from the surface of SS316L exposed to molten LiCl-1wt%Li_2O-0.2wt%Li at 650°C for 20. Only metallically bonded Fe and Ni were present in significant quantities on the surface of samples exposed to molten LiCl-Li_2O containing Li.

The Cr 2p XPS spectra obtained from the surface of SS316L coupons exposed to molten LiCl with 1 and 2wt%Li_2O, each with 0, 0.2, and 0.4wt%Li are shown in Figure 5.11. Additionally, Cr 2p XPS spectra obtained from samples exposed to ultra-high purity melts of LiCl-1wt%Li_2O, LiCl-1wt%Li_2O-0.2wt%Li and LiCl-2wt%Li_2O-0.2wt%Li are included in Figure 5.11 to demonstrate that the films formed in reagent grade and ultra-high purity melts are consistent. It is assumed that the $LiCrO_2$ detected by XRD and Raman analysis of samples exposed to melts of LiCl with 1 or 2wt%Li_2O in the absence of Li constitutes the predominant oxide on these sample surfaces. Under this assumption, the single Cr 2p XPS feature observed on these samples is attributed to the presence of $LiCrO_2$. This Cr $2p_{3/2}$ feature is fit with a binding energy of 576.4eV and is in agreement with previously reported binding energies for $LiCrO_2$ [220]. The Cr spectra obtained from samples exposed to melts containing 0.2 and 0.4wt%Li are fit with the same peak fitting parameters as the Cr spectra obtained from samples exposed to molten LiCl-Li_2O in the absence of Li. Therefore, the Cr surface films observed on SS316L following

exposure to LiCl-Li_2O with 0.2 and 0.4wt%Li are reported to consist of $LiCrO_2$. This observation is in agreement with the Cr spectra obtained from samples exposed to ultra-high purity melts of LiCl-1wt%Li_2O-0.2wt%Li and LiCl-2wt%Li_2O-0.2wt%Li. The existence of oxidized Cr on the surface of SS316L following exposure to molten LiCl-Li_2O with 0, 0.2 and 0.4wt%Li, and a lack of detectable quantities of Cr in these melts as determined by ICP-OES, indicates that $LiCrO_2$ forms a stable and protective surface film under these conditions. It is therefore concluded that SS316L exposed to the LiCl-Li_2O-Li system can form stable $LiCrO_2$ films despite the inclusion highly reducing metallic Li in the melt.

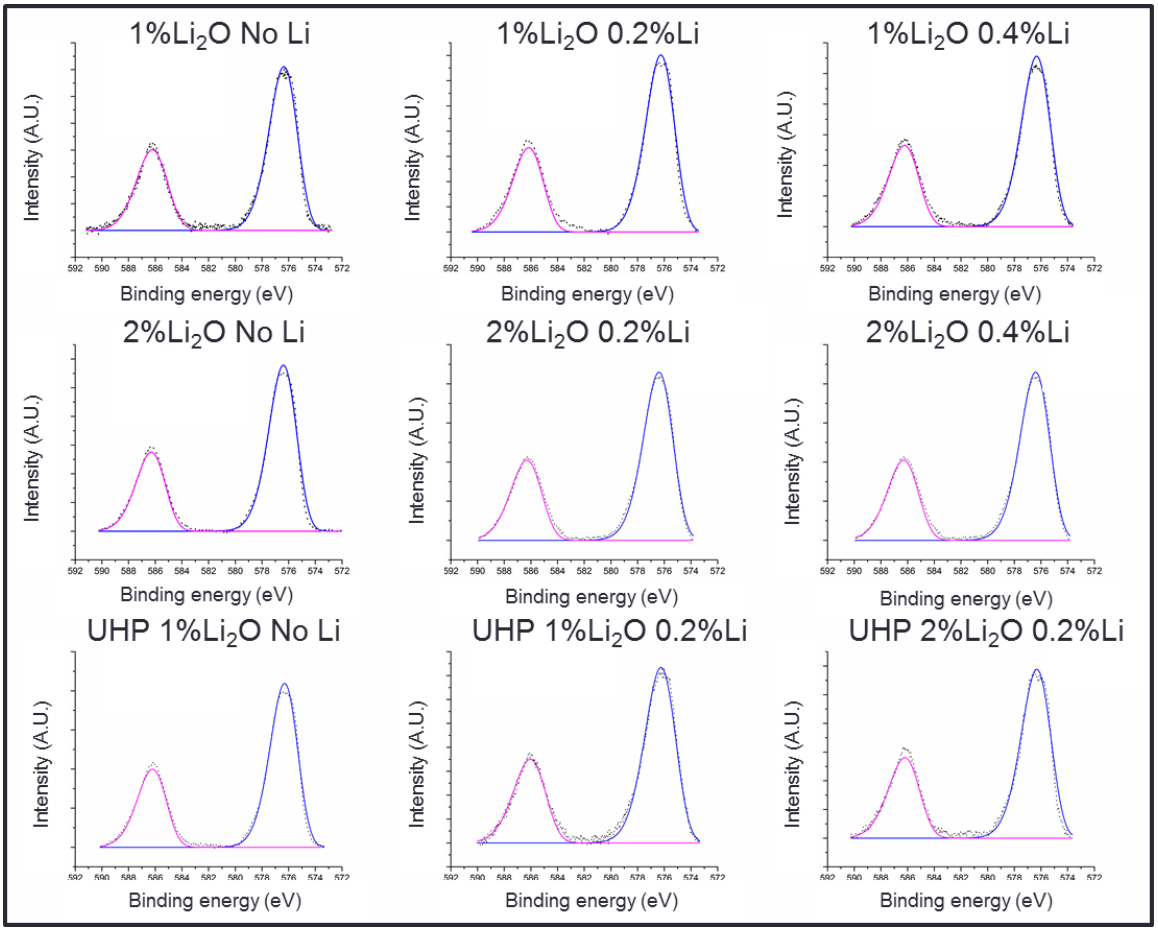


Figure 5.11: Cr 2p spectra obtained from the surface of SS316L subjected to 20 hours of exposure to molten LiCl with 1wt%Li_2O (Top row) and 2wt%Li_2O (Middle row), each with 0, 0.2, 0.4, 0.6wt%Li, as well as ultra-high purity melts of LiCl-1wt%Li_2O, LiCl-1wt%Li_2O-0.2wt%Li, LiCl-2wt%Li_2O-0.2wt%Li, and LiCl-1wt%Li_2O-0.6wt%Li (Bottom row) after 2 hours of baking at 650°C in Ar. All Cr 2p spectra obtained from the surface of these samples have been fit with peak fitting parameters attributed to $LiCrO_2$.

It is hypothesized that the presence of $LiCrO_2$ on the surfaces of SS316L exposed to melts containing 0.2 and 0.4wt% Li could not be detected by Raman or XRD analysis due to the thin nature of the surface films formed under these conditions. This hypothesis is supported by the previously discussed detection of XPS signal from base alloy through the films formed in melts containing Li. Furthermore, as presented subsequently, XPS depth profiling demonstrated that the films formed in the presence of dissolved Li are on

the order of 10s of nm thick. Films of this thickness are not expected to be detectable by Raman or XRD analysis.

XPS analysis of Fe, Ni and Cr bound on the surface of samples exposed to melts containing 0.8 and 1wt%Li demonstrated nearly exclusively metallic bonding. As previously stated, the quantities of these elements that leached into melts containing 0.8 and 1wt%Li were below the level of detection by ICP-OES analysis. Therefore, neither the $LiCrO_2$ surface films formed on SS316L exposed to melts containing less than 0.6wt%Li, nor the metallic surfaces formed in melts containing greater 0.6wt%Li resulted in detectable leaching of alloying elements into the melt. It is hypothesized that the oxidation processes that must occur prior to the solvation of alloying elements by the ionic molten salt do not occur when sufficient concentrations of Li are present in the melt. This would suggest that material interactions with the molten LiCl-Li_2O-Li system are governed by separate mechanisms depending on the content of Li in the melt. At low Li concentrations the oxidizing nature of dissolved O^{2-} allows for the formation of stable $LiCrO_2$ films. Alternatively, the oxidation of alloying elements does not occur when the melt is sufficiently reducing due to the presence of high quantities of Li.

Data obtained from ICP-OES, SEM, EDS and XPS analyses suggest that an intermediate regime between electrochemical oxidation and liquid metal type effects may exist when approximately 0.6wt%Li is present in molten LiCl-Li_2O. As stated previously, Cr leaching only occurred in melts containing 0.6wt%Li. Additionally, SEM analysis demonstrated that irregular surface features formed on SS316L exposed to these melts, as shown in Figure 5.2, while EDS detected a skewed concentration of alloying elements on

these sample surfaces. Furthermore, the shift in surface chemistry demonstrated by XPS to occur at 0.6wt%Li, from oxidized Cr to metallically bonded Fe, Ni and Cr strongly indicates a shift in alloy-melt interfacial chemistry. Thus, it is proposed that the competition between electrochemical and liquid metal effects may to lead to the instability and dissolution of partially formed surface films when approximately 0.6wt%Li is present in the melt.

Figure 5.12 shows XPS spectra obtained from the surface of a SS316L coupon exposed to molten LiCl-2wt%Li_2O-0.4wt%Li with and without being subjected to 30 seconds of Ar ion sputtering. For comparison, at the current density employed in this study, 30 seconds of Ar sputtering was observed to remove 3.5nm of Ta_2O_5. It is observed that the relative signal of spectral features of Cr and O^{2-} varied minimally when subjected to the sputtering, while the binding energy state of the O 1s spectra attributed to OH^- bonding is observed to have reduced considerably. The presence of OH^- bonding on the exterior of the sample surface is attributed to hygroscopic LiCl reacting with minor quantities of moisture during the transfer of the sample from the glove box to the XPS vacuum chamber. This result is similar in effect to the detection of LiCl-H_2O by XRD. While the presence of moisture may alter the exterior salt on the sample surfaces, the removal of the majority of OH^- bonding with 30 seconds of sputtering demonstrates that this degradation does not penetrate more than a few nanometers into the material surface. The minimal difference in the Cr spectra obtained from the surface before and after sputtering, shown in Figure 5.12, demonstrates that the $LiCrO_2$ surface film is beneath the moisture affected LiCl, and largely unaffected by the presence of OH^-.

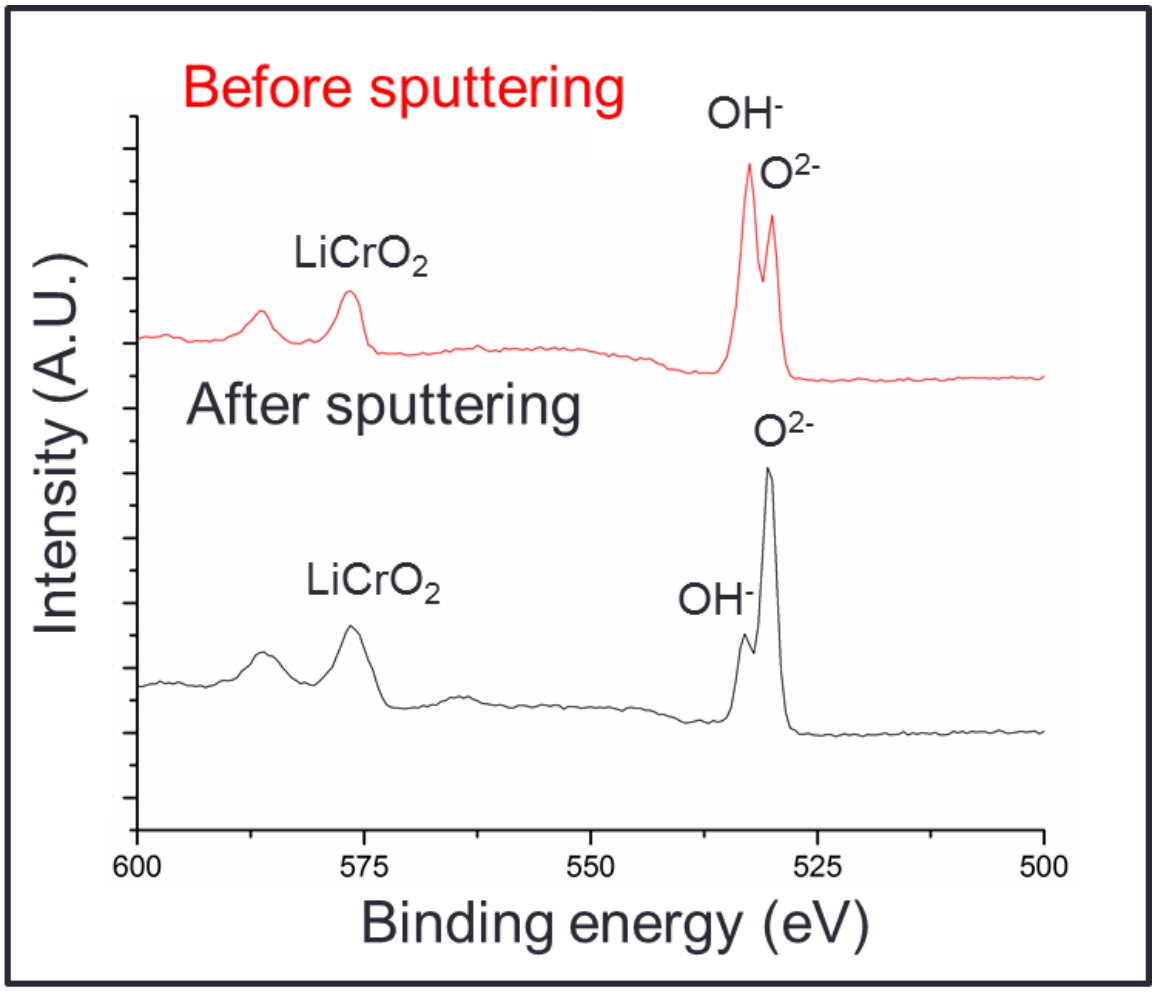


Figure 5.12: XPS spectra obtained from the surface of SS316L exposed to molten LiCl-2wt%Li_2O-0.4wt%Li at 650˚C for 20 hours after 2 hours of baking at 650°C in Ar before sputtering (Top), and after subjecting the surface to 30 seconds of Ar ion sputtering (Bottom). The application of Ar sputtering is observed to have removed the majority of the OH^- bonding from the sample surface, without impacting the Cr 2p or O^{2-} signals. It is therefore reported that the $LiCrO_2$ film is beneath, and unaffected by the presence of OH^-.

The XPS survey spectra obtained from samples of SS316L independently exposed to molten LiCl with 1 and 2wt%Li_2O, each with 0, 0.2, 0.4, 0.6, 0.8 and 1wt%Li at 650˚C for 20 hours, following 5 minutes of Ar ion sputtering, are shown in Figures 5.13 and 6.14, respectively. The relative concentrations of Ni, Cr and Fe on these sample surfaces, as detected by XPS following 5 minutes of Ar ion sputtering, are shown in Figure 5.16.

For reference, at the current density employed in this study 5 minutes of Ar sputtering was observed to remove 35nm of Ta_2O_5. It can be observed that the surfaces of the samples exposed to molten LiCl with 1 and 2wt%Li_2O in the absence of metallic Li are primarily comprised of Cr, O and Cl. This indicates that the layer of $LiCrO_2$ formed on SS316L during 20 hours of exposure to molten LiCl-Li_2O at 650°C is at least 35 nm thick. The detection of Cl on samples following sputtering is expected due to the micrometer dimension islands of LiCl that remain on the sample surface following the baking procedure. While a minor signal of the Fe 2p line was detectable on the surface of SS316L exposed to LiCl-1wt%Li_2O following 5 minutes of sputtering, the signal was below the level of detection on the sample exposed to LiCl-2wt%Li_2O. This indicates that oxide films formed in melts containing higher concentrations of Li_2O are thicker, as expected.

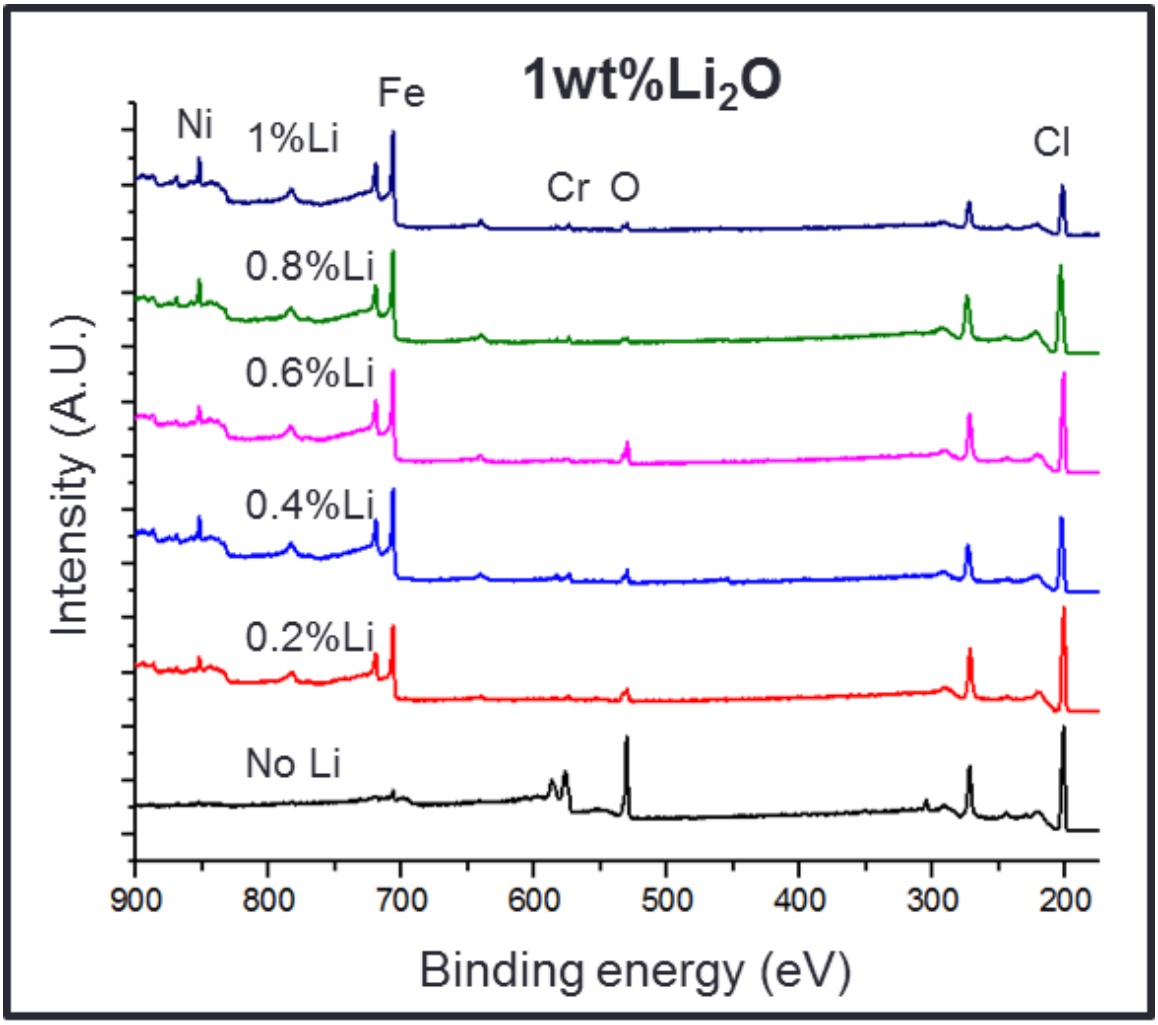


Figure 5.13: XPS survey spectra obtained from SS316L following exposure to LiCl-1wt%Li_2O with 0, 0.2, 0.4, 0.6, 0.8 and 1wt%Li at 650°C for 20 hours after 2 hours of baking at 650°C in Ar and being subjected to 5 minutes of Ar ion sputtering. The surface of SS316L exposed to LiCl-1wt%Li_2O in the absence of Li is comprised of Cr and O, while samples exposed to melts containing Li are primarily comprised of Fe, and Ni with minor quantities of Cr and O detectable.

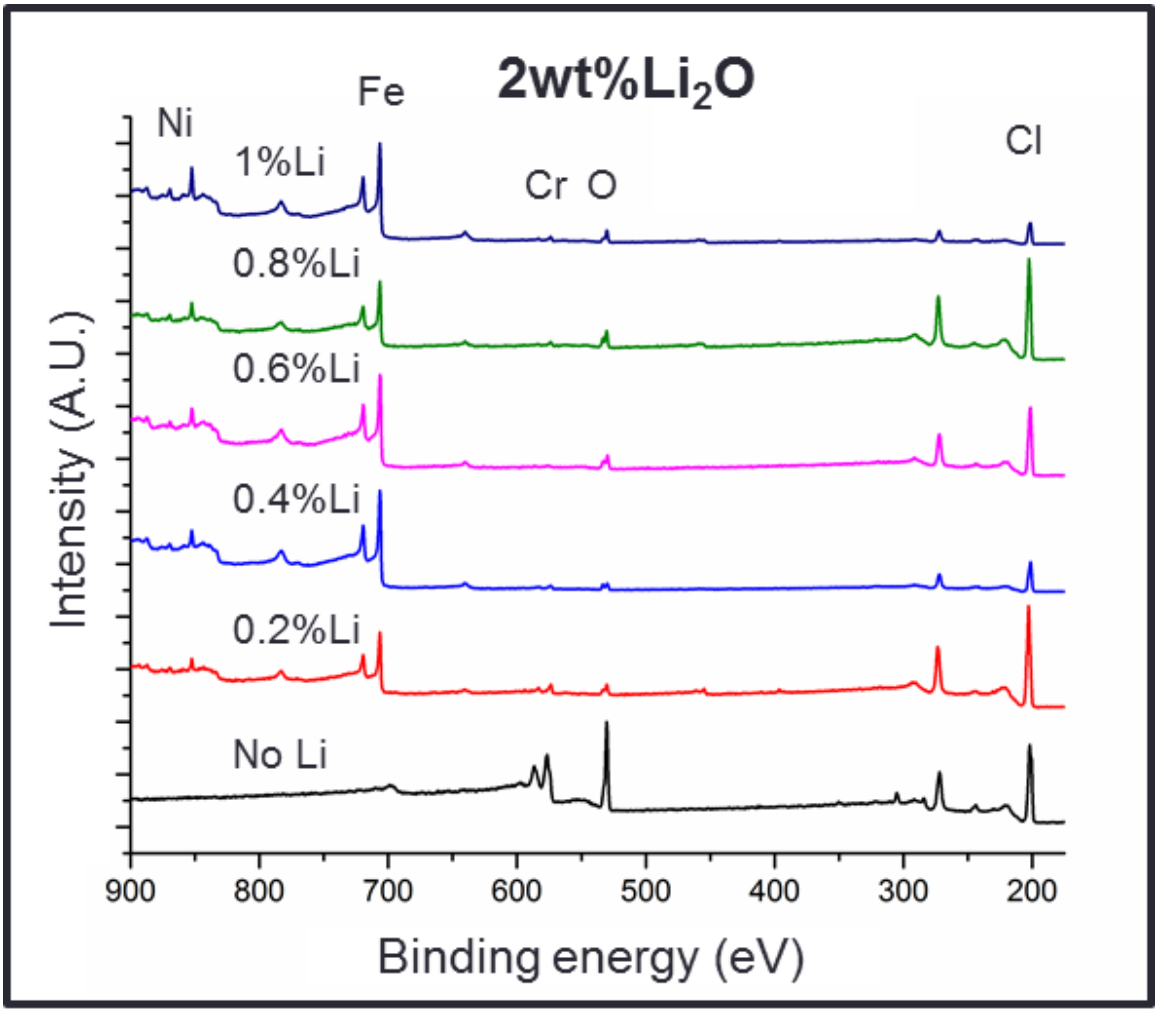


Figure 5.14: XPS survey spectra obtained from SS316L following exposure to LiCl-2wt%Li_2O with 0, 0.2, 0.4, 0.6, 0.8 and 1wt%Li at 650˚C for 20 hours after 2 hours of baking at 650°C in Ar and being subjected to 5 minutes of Ar ion sputtering. The surface of SS316L exposed to LiCl-2wt%Li_2O in the absence of Li is comprised of Cr and O, while samples exposed to melts containing Li are primarily comprised of Fe, and Ni with minor quantities of Cr and O detectable.

After being subjected to 5 minutes of Ar sputtering the surface of all samples exposed to melts containing Li consist primarily of Fe, Ni, Cr and Cl. It is observed that the concentration of Cr on the surface of SS316L is diminished, after sputtering, compared to the as-received alloy following exposure to melts containing Li. The depletion of Cr is observed to have occurred as a result of exposure to all molten solutions containing Li. The content of Cr in SS316L exposed to molten LiCl-1wt%Li_2O-

0.6wt%Li was found be below the level of detection indicating that severe leaching of Cr occurred during exposure of the alloy to this melt. This result is in agreement with the high level of Cr leaching that occurred during exposure of SS316L to the LiCl-1wt%Li_2O-0.6wt%Li melt detected by ICP-OES analysis.

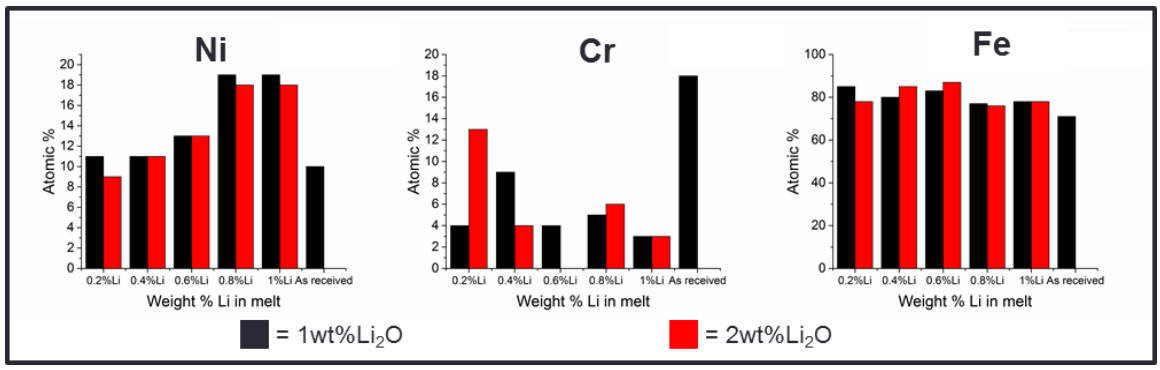


Figure 5.15: Elemental composition of alloying elements Cr, Ni and Fe as determined by XPS analysis of SS316L exposed to molten LiCl with 1 and 2wt%Li_2O, each with 0, 0.2, 0.4, 0.6, 0.8 and 1wt%Li for 20 hours after 2 hours of baking at 650°C in Ar and being subjected to 5 minutes of Ar ion sputtering. It is observed that the surface of all samples exposed to molten LiCl-Li_2O-Li are depleted of Cr. Additionally, samples exposed to melts containing greater than 0.6wt%Li are enriched in Ni. Data obtained from the surface of samples exposed to molten LiCl-Li_2O in the absence of Li are omitted due to the large quantity of O present.

XPS analysis of the surface of SS316L coupons exposed to molten LiCl-Li_2O-Li following 5 minutes of sputtering demonstrates a trend of increasing Ni content with increasing Li concentration in the melt. The concentration of Ni detected on samples exposed to molten solutions containing 0.2 and 0.4wt%Li is observed to be approximately that of the as-received alloying composition. However, the Ni concentration on the surface of samples exposed to melts containing 0.8 and 1wt%Li following five minutes of sputtering is observed to be nearly double the as-received composition. This observation is suspected to be due to two potential effects: preferential alloying of Ni by molten Li, or electroless plating of Ni from the crucible to the sample through the melt. Preferential leaching of Ni from austenitic stainless steels is known to

be the primary mode of degradation of these materials under exposure to molten Li [112, 127, 221]. The increased concentration of Ni observed on samples exposed to melts containing greater than 0.6wt%Li may indicate that metallic Li existed on the surface of these samples during the exposure, resulting in an analogous mode of degradation. Alternatively, it is possible that melts containing high concentrations of Li form electrical pathways between the Ni crucible and the samples. Such an electrical connection may be formed via a transformation of the melt to a metallically conductive state [102, 160, 217] or by the formation of a float of metallic Li on the surface of the melt. Should either of these scenarios occur, then the electroless transport of Ni from the crucible to the sample surface is possible. Further investigations are required to discern between these two mechanisms.

5.2 Conclusions:

The corrosion of stainless steel alloy 316L exposed to molten LiCl containing various concentrations of Li_2O and Li was investigated. Drying LiCl at 550˚C for two hours prior to the addition of Li_2O and Li was found to suppress preferential leaching of Cr and Mo from the alloy. $LiCrO_2$ was observed on SS316L exposed to molten LiCl containing 1 and 2wt%Li_2O, as well as LiCl-Li_2O containing 0.2 and 0.4wt%Li. The observation of $LiCrO_2$ formed in melts containing the strong reducing agent, metallic Li, indicates that material interactions with molten LiCl-Li_2O containing low quantities of Li are governed by electrochemical oxidation effects, and that corrosion of SS316L under these conditions is governed by the formation and stability of protective surface films. Alternatively, the surfaces of samples containing concentrations of Li exceeding 0.6wt%

were observed to not possess oxidized surface films, suggesting that these molten solutions were sufficiently reducing to suppress nearly all oxidation of the alloy. The surface of SS316L exposed to molten solutions containing 0.8 and 1%Li were enriched in Ni indicating effects similar to those resulting from exposure to liquid lithium had occurred. Molten solutions containing 0.6wt%Li were found to result in unstable surfaces, and leached Cr from the alloy.

Chapter 6 Electroless Deposition of Titanium Compounds on Stainless Steel Alloy 316L in Molten LiCl-Li_2O-Li

The electroless deposition of Ti compounds was observed during the course of characterizing material interactions with molten LiCl-Li_2O-Li. Characterization of these compounds, and the dependence of their chemical composition on variations in LiCl-Li_2O-Li melt composition was conducted using X-ray photoelectron spectroscopy. Ironically, despite being present as impurities in the system, characterization of these compounds yields important information demonstrating the ternary nature of the LiCl-Li_2O-Li system.

6.1 Introduction:

The formation of Ti compounds on material surfaces during static exposure testing is hypothesized to be the result of electroless plating of Ti, present as an impurity, by metallic Li present in the melt. Previous research demonstrated that reduction of TiO_2 to metallic Ti in molten LiCl-Li_2O proceeds through the formation of multiple intermediate compounds, namely $LiTi_2O_4$, $LiTiO_2$, TiO and Ti_2O [33, 222]. Alternative research investigating Li intercalation into TiO_2 has demonstrated the formation of non-stoichiometric $Li_{1+x}Ti_{2-x}O_4$ [223, 224]. This partially reduced form of TiO_2 exhibits a spinel structure with a mixture of Ti^{3+} and Ti^{4+} oxidation states, i.e. the value of x, depending upon the extent of Li intercalation. Similar non-stoichiometric transition metal doped TiO_2 materials have been formed in molten lithium salts [225]. Furthermore, TiO_2 reduces through a purely trivalent intermediate compound of Ti^{3+}, $LiTiO_2$, in the presence of an excess of Li [226]. Finally, it has been demonstrated that Ti_3SiC_2 corrodes via the formation of Li_2TiO_3 in the presence of molten LiCl-KCl [227].

In this work, the Ti compounds formed on the surface of stainless steel alloy 316L (SS316L) as a result of exposure to molten LiCl-Li_2O-Li are investigated using X-ray photoelectron spectroscopy. Characterization of these films was conducted as a function of Li_2O concentration in the melt in an attempt to understand the dependence of surface chemistry on the activity of O^{2-} in molten solutions.

Samples of SS316L were independently exposed to molten LiCl-2wt%Li_2O containing no Li, as well as LiCl containing 0.4wt% metallic Li and either 0, 1, 2, 3 or 4wt%Li_2O for 20 hours at 650ºC. The precursor chemicals of LiCl, Li_2O and Li, were investigated for Ti impurities by ICP analysis of aqueous solutions of these chemicals. The solutions were analyzed before and after being adjusted to a pH of 13 and 1 through the addition of NaOH and HCl, respectively, to ensure complete dissolution of all Ti compounds. The reported concentrations of Ti in these chemicals are the maximum values obtained through this analysis. All identified concentrations resulted in relative standard deviations less than 5%. The Ti $2p_{3/2}$ and $2p_{1/2}$ lines were fit using peak fitting parameters shown in Table 6.1 for spectral features attributed to the presence of Ti^{4+}, Ti^{3+}, and TiN.

Table 6.1 XPS fitting parameters used in the devolution of the Ti 2p spectra.

Element	Label	BE (eV)	FWHM (eV)
Ti $2p_{3/2}$	TiN	455.3	1.5
	Ti^{3+}	456.5	1.6
	Ti^{4+}	458.5	1.8
Ti $2p_{1/2}$	TiN	460.9	1.6
	Ti^{3+}	462.4	1.6
	Ti^{4+}	464.2	1.9

6.2 Ti Compounds Formed as a Function of Li_2O Concentration:

The concentration of Ti in LiCl and Li was below the level of detectability by ICP-OES; however the impurity level of Ti in Li_2O was 0.03at%. While this quantity of impurity Ti is high, it is considered an appropriate impurity level for industrial scale processes. With a total surface area of approximately 68 cm^2 of material exposed to the melt, including two SS316L samples and the Ni crucible, the amount of Ti in the 0.5 g of Li_2O in a LiCl-1wt%Li_2O solution can be calculated to constitute a uniform deposited film thickness of ~10 nm. The formation of Ti films on this order of magnitude is sufficient for detection by XPS analysis yet it is likely below the level of detection by alternative analytical techniques.

XPS survey spectra obtained from the surface of SS316L following 20 hours of exposure to LiCl-2wt%Li_2O-0.4wt%Li, LiCl-2wt%Li_2O-0wt%Li, and LiCl-0wt%Li_2O-0.4wt%Li, are shown in Figure 6.1. It is observed that the surfaces of all samples show the presence of Cr, O, C and Cl. However, Ti and N signals are seen only in the spectrum when the molten solution contained both Li_2O and Li.

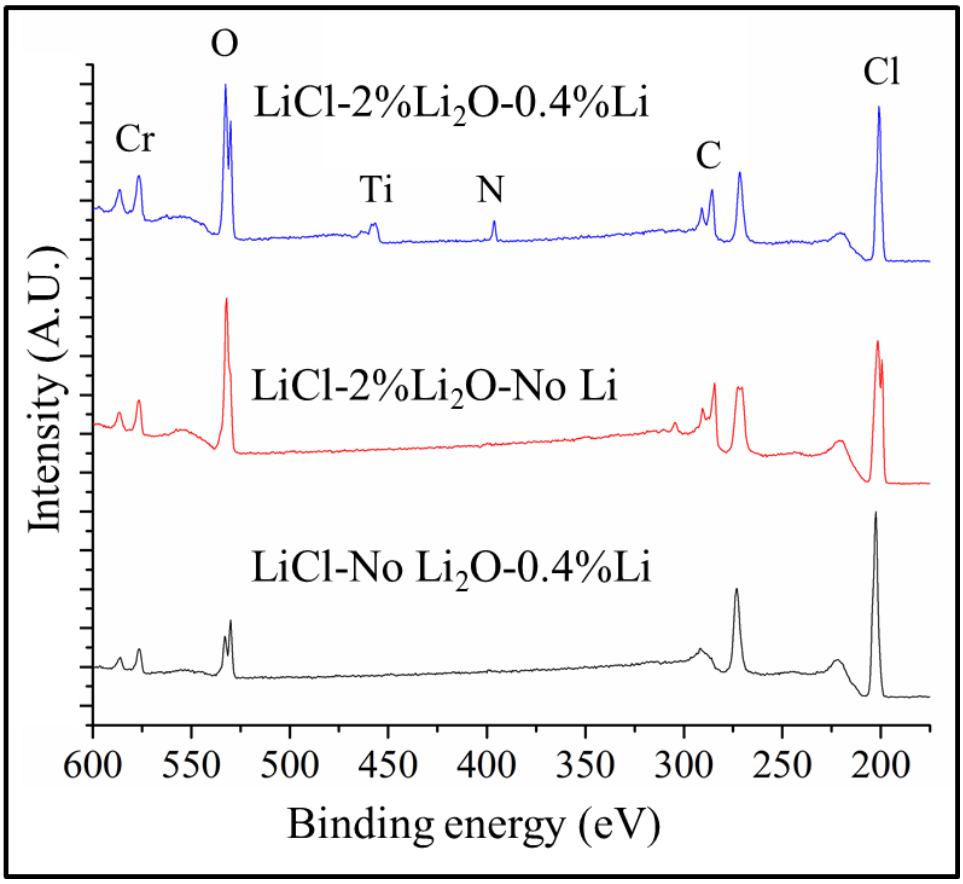


Figure 6.1 XPS survey spectra obtained from the surface of SS316L following exposure to (Top) LiCl-2wt%Li_2O-0.4wt%Li, as well as (Middle) LiCl-2wt%Li_2O in the absence of Li, and (Bottom) LiCl-0.4wt%Li in the absence of Li_2O at 650˚C for 20 hours. Cr, O, C, and Cl are detectable on samples exposed to binary LiCl-Li_2O and LiCl-Li melts, while Ti and N are additionally detectable on the surface of samples exposed to ternary LiCl-Li_2O-Li melts.

To study the effect of O^{2-} activity on surface chemistry, samples were exposed to solutions of LiCl-xwt%Li_2O-0.4wt%Li, where x was 1, 2, 3, or 4. The Ti 2p spectra obtained from the surfaces of coupons of SS316L exposed to molten LiCl with 1, 2, 3 and 4 wt%Li_2O, each containing 0.4wt%Li, are shown in Figures 6.2-5. These spectra each contain three features attributed to the presence of Ti^{4+}, Ti^{3+}, and TiN for the Ti $2p_{3/2}$ and $2p_{1/2}$ lines. The Ti^{4+} feature at 458.5 eV is suspected to be derived from TiO_2, Li_2TiO_3, and or the Ti^{4+} bonding state in $Li_{x+1}Ti_{2-x}O_4$. The intermediate binding energy feature observed at 456.5 eV, labeled Ti^{3+}, is attributed to the trivalent state of Ti in either

$Li_{x+1}Ti_{2-x}O_4$ or $LiTiO_2$, and is in agreement with previous studies of these materials [228-230]. The lowest binding energy peak (455.5 eV) is attributed to the presence of TiN, and is fit using binding energy and FWHM parameters obtained from a commercial standard of this material.

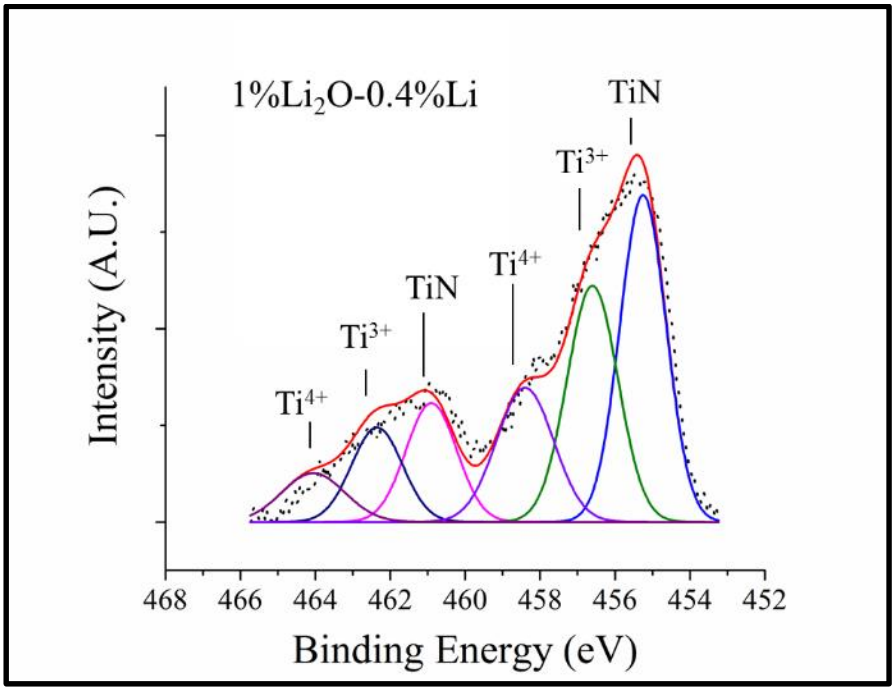


Figure 6.2: Ti 2p spectrum obtained from the surface of SS316L exposed to molten LiCl-1wt%Li_2O-0.4wt%Li at 650°C for 20 hours. Three peaks attributed to the presence of Ti^{4+}, Ti^{3+}, and TiN are observed. TiN constitutes the majority of Ti bonding on the sample surface

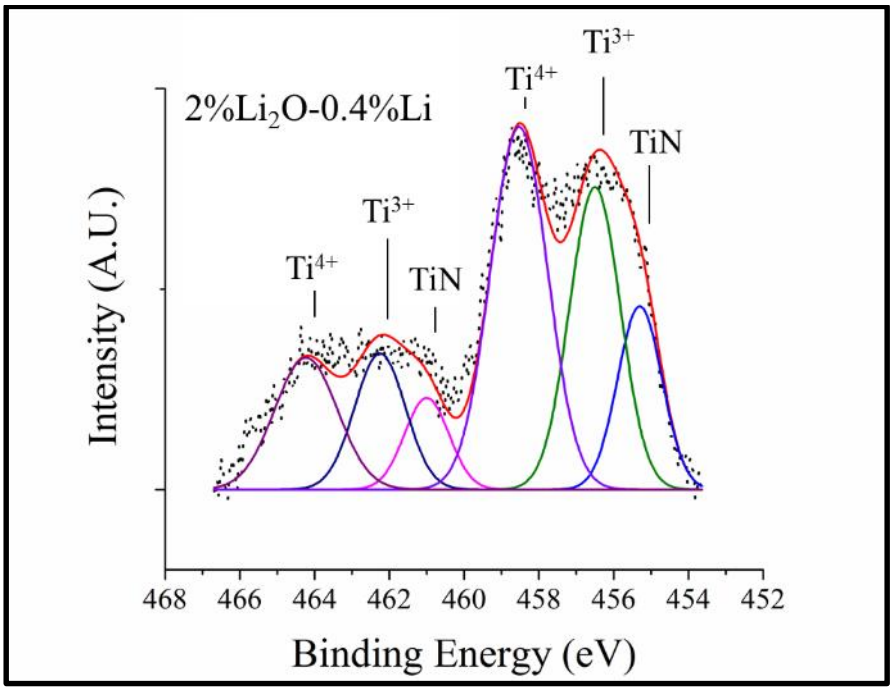


Figure 6.3: Ti 2p spectrum obtained from the surface of SS316L exposed to molten LiCl-2wt%Li_2O-0.4wt%Li at 650°C for 20 hours. Three peaks attributed to the presence Ti^{4+}, Ti^{3+}, and TiN are observed.

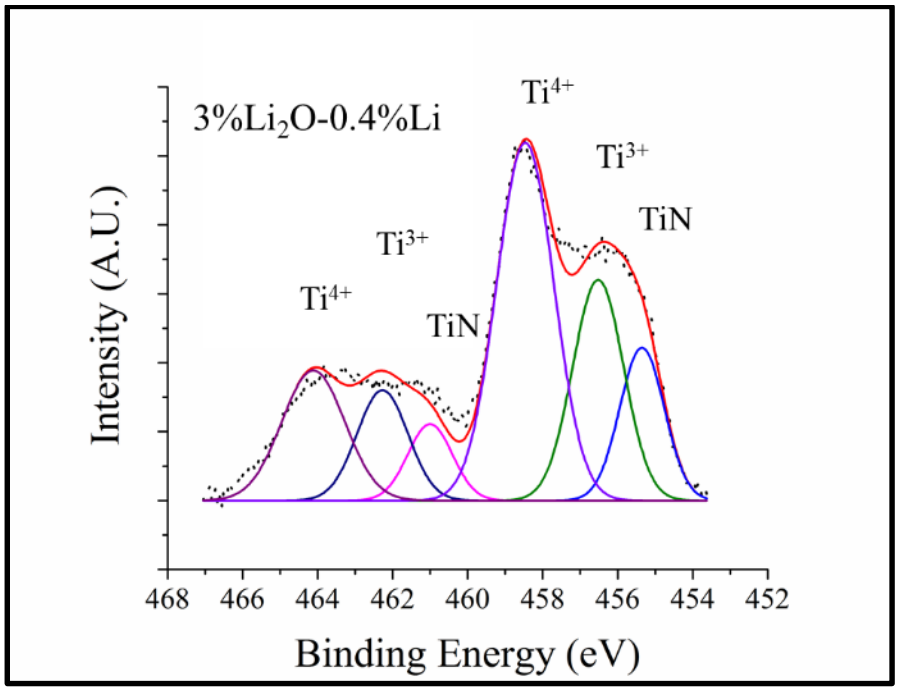


Figure 6.4: Ti 2p spectrum obtained from the surface of SS316L exposed to molten LiCl-3wt%Li_2O-0.4wt%Li at 650°C for 20 hours. Three peaks attributed to the presence of Ti^{4+}, Ti^{3+}, and TiN are observed.

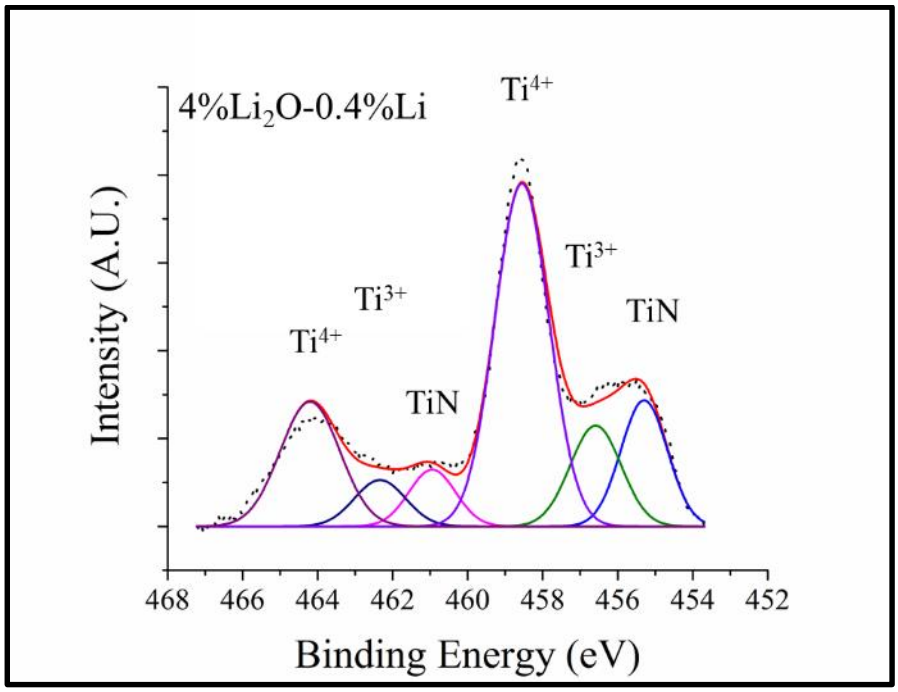


Figure 6.5: Ti 2p spectrum obtained from the surface of SS316L exposed to molten LiCl-4wt%Li_2O-0.4wt%Li at 650°C for 20 hours. Three peaks attributed to the presence of Ti^{4+}, Ti^{3+}, and TiN are observed. Ti^{4+} is observed in significantly higher concentration compared to the more reduced species of Ti.

The N 1s spectra recorded from the surface of SS316L samples exposed to molten LiCl containing 0.4wt%Li with either 1, 2, 3 or 4wt%Li_2O are shown in Figure 6.6. The N 1s spectrum obtained from a standard of TiN is included in Figure 6.6 for reference. While slight variations in the peak position of the N 1s line is observed, all peaks possess binding energies in the range of nitride bonding [231]. The variation in peak position is attributed to the non-ideal yet unavoidable method of internal charge correction used in this study.

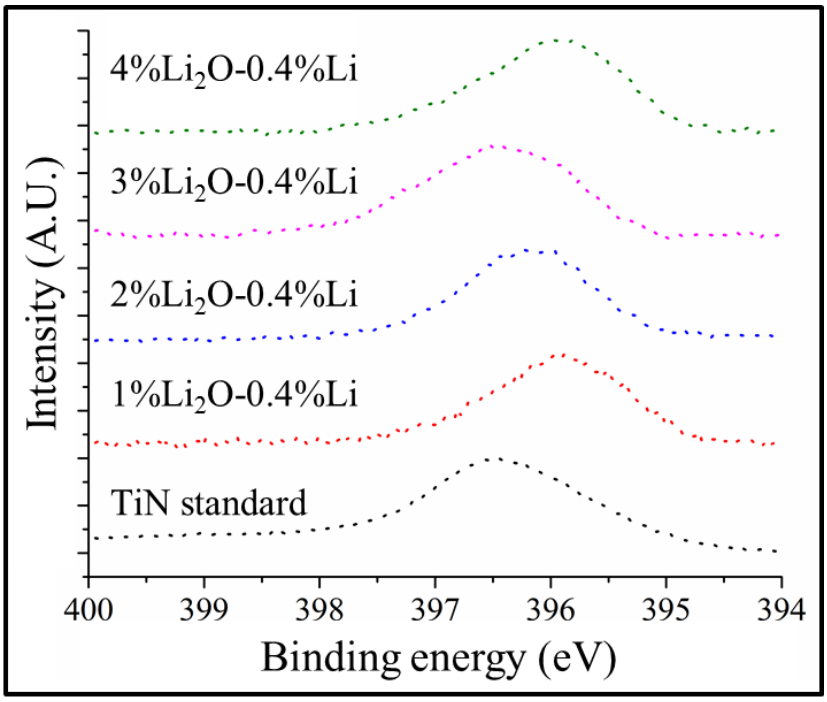


Figure 6.6: N 1s spectra obtained from the surface of SS316L exposed to molten LiCl with 1, 2, 3, and 4wt%Li_2O, each with 0.4wt%Li, at 650°C for 20 hours.

As noted in Chapter 2, gas chromatography analysis measured the concentration of N_2 to be 2% of the Ar glove box atmosphere in which the experiment was conducted. The formation of TiN from Ti contacting N_2 at 650ºC is thermodynamically favorable [232]; a fact that is indicated by the Ti-N phase diagram [233]. At high temperatures, Ti

is known to be an effective getter of nitrogen and has been used extensively to remove impurity nitrogen from both liquid Li as well as Ar gas [234]. However, it has been reported that the electrochemical formation of TiN in molten LiCl-KCl-Li_3N at 500ºC requires anodic polarization at potentials exceeding +0.4 V vs $Li|Li^+$; potentiostatic polarization of Ti at +0.4 V vs $Li|Li^+$ was found to be insufficient to form a TiN surface, and polarization at +0.8 V vs $Li|Li^+$ resulted in a well-developed TiN film [235, 236]. The need to anodically polarize Ti in order to reduce Li_3N and form TiN suggests that Li_3N is more stable than TiN in molten LiCl salt environments. It is noted that these studies were conducted at lower temperature than those considered in the current study (500°C vs 650°C in the present study). However, they provide an insight into the relative stability of these substances in molten salt environments. This is counter to the liquid Li metal system were Ti is known to be a getter for nitrogen from Li due to the lower free energy of TiN compared to Li_3N in liquid Li at 650˚C [158]. The observation of TiN on the surface of SS316L exposed to molten LiCl-Li_2O-Li in the current study suggests that TiN forms to some degree in the presence of molten LiCl-Li_2O-Li, and that these systems possess some thermodynamic qualities analogous to liquid metal environments.

The bonding of Ti on the surface of SS316L exposed to molten LiCl-Li_2O-Li was characterized with varying Li_2O concentration in the melt to investigate the chemistry of the surface films formed in melts of varying O^{2-} ion activity. The Ti species that are not identified as TiN on the surface of SS316L in the current study are attributed to the presence of lithium titanium oxides (Li-Ti-O) with a mixture of Ti^{4+} and Ti^{3+} valance states. It is suggested that the relative concentration of Ti^{4+} and Ti^{3+} in the Li-Ti-O

formed in a given molten solution of LiCl-Li_2O-Li is governed by the redox properties of the melt. In a manner similar to the well accepted Lux-Flood model of molten salt basicity (pO^{2-} defined as the negative log of the O^{2-} ion activity) molten LiCl-Li_2O solutions containing higher concentrations of Li_2O are expected to favor the formation of Li-Ti-O containing more oxidized species of Ti.[125] Quantification of the percentages of the Ti 2p spectra on the surface of SS316L exposed to LiCl-xwt%Li_2O-0.4wt%Li (where x=1, 2, 3 or 4) attributed to Ti^{4+}, Ti^{3+}, and TiN is shown in Figure 6.7. As expected, the percentage of the Ti spectra attributed to the higher oxidation state of Ti^{4+} is observed to increase with increasing Li_2O concentration (O^{2-} ion activity) in the melt. This observation demonstrates the dependence of the nature of the Li-Ti-O on the redox properties of the molten solution, favoring more reduced forms in the presence of lower O^{2-} ion activity. The concentration of Li_2O in the melt was found to additionally affect the propensity to form TiN compared to Ti oxides. The percent of the Ti spectra attributed to TiN is observed to be highly dependent upon the Li_2O concentration at low O^{2-} activity, yet this effect is lower in melts with higher Li_2O concentrations. Alternatively, the percentage of Ti^{3+} in the Li-Ti-O is less dependent on the activity of the O^{2-} ion in the melts with low O^{2-} activity, but becomes increasingly dependent on the O^{2-} activity as the activity increases.

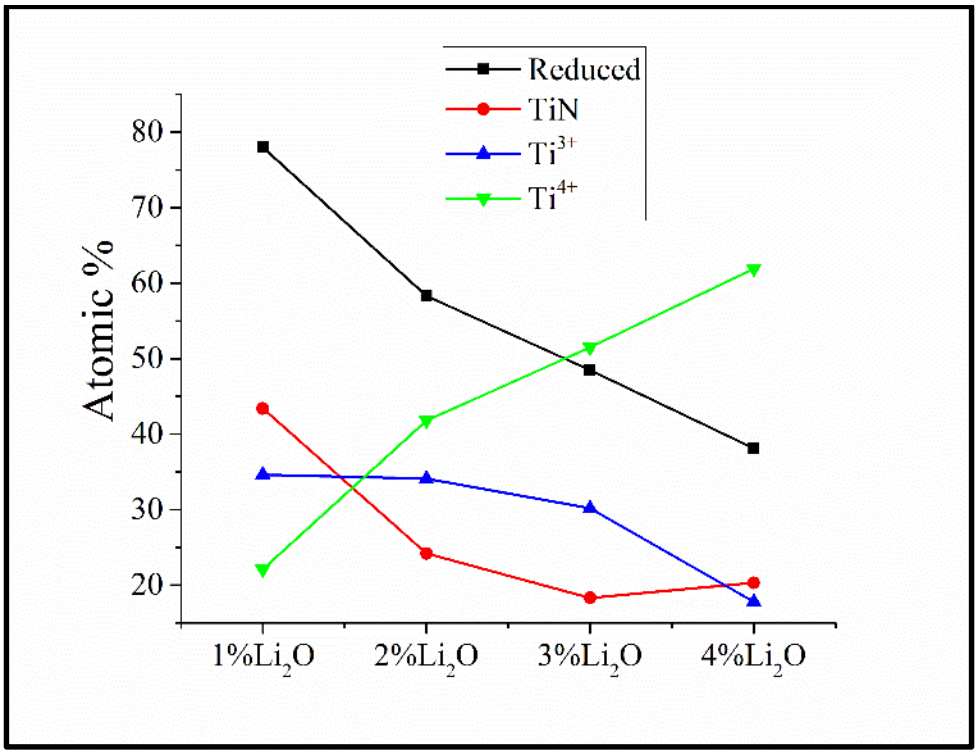


Figure 6.7: The percentage of the Ti 2p spectra observed on the surface of SS316L exposed to molten LiCl-0.4wt%Li with 1, 2, 3 and 4wt%Li_2O attributed to the existence of Ti^{4+}, Ti^{3+}, and TiN. TiN exists in the highest concentration on the sample exposed to LiCl-1wt%Li_2O-0.4wt%Li, while Ti^{4+} constitutes the majority of Ti bonding on all other sample surfaces. A decrease in the concentration of the reduced forms of Ti, Ti^{3+}, and TiN, is observed with an increase in the concentration of Li_2O in the melt.

It is therefore reported that the activity of the O^{2-} ion affects the electrochemistry of the LiCl-Li_2O-Li system despite the presence of the strong reducing agent metallic Li. Alternatively, the formation of TiN in molten LiCL-Li_2O containing metallic Li is suspected to be a liquid Li metal effect. These observations highlight the ternary nature of the LiCl-Li_2O-Li solution chemistry. It is proposed that the chemical properties of the LiCl-Li_2O-Li system and material interactions with these melts are governed by the relative concentrations of Li_2O and Li dissolved in the melts.

6.3 Interactions of TiO_2 with Molten LiCl-Li_2O-Li:

Control experiments were conducted using TiO_2 to verify that the formation of TiN occurred as a result of exposure of Ti compounds to molten LiC-Li_2O-Li. Sample coupons of TiO_2 were independently exposed to molten LiCl-2wt%Li_2O-0wt%Li, and LiCl-2wt%Li_2O-0.4wt%Li at 650°C for 20 hours. The sample of TiO_2 exposed to molten LiCl-2wt%Li_2O-0wt%Li was found to have completely dissolved into the melt during the period of exposure. Images of the TiO_2 samples exposed to molten LiCl-2wt%Li_2O-0wt%Li, and LiCl-2wt%Li_2O-0.4wt%Li are shown in Figure 6.8. The material shown on the right in Figure 6.8 is the portion of the sample that was physically above the melt of LiCl-2wt%Li_2O-0wt%Li and never exposed to the molten solution. The sample on the left in Figure 6.8 is the portion of the TiO_2 sample that was submerged in molten LiCl-2wt%Li_2O-0.4wt%Li and was cut off the sample holder for XPS analysis. Small deposits of residual salt are observable on this sample while the majority of the surface is visibly not corroded. The complete dissolution of the TiO_2 sample exposed to molten LiCl-2wt%Li_2O-0wt%Li, and the lack of visible corrosion on the sample exposed to molten LiCl-2wt%Li_2O-0.4wt%Li indicates that the solution chemistry changes drastically when metallic Li is present in the melt. This change in solution chemistry is hypothesized to result in a shift in the affinity of the melt to dissolve Ti compounds. This hypothesis is supported by the presence of Ti on SS316L samples exposed to molten LiCl-Li_2O that contained metallic Li, and the absence of Ti on samples exposed to molten LiCl-Li_2O that did not contain Li.

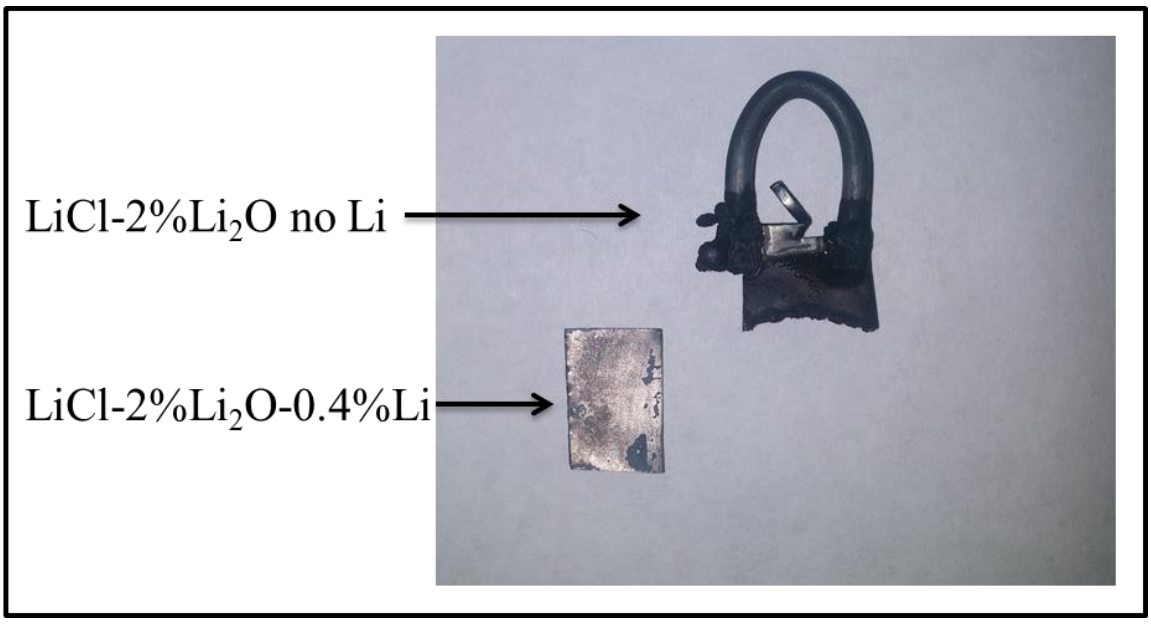


Figure 6.8: An image (Right) TiO_2 following exposure to LiCl-2wt%Li_2O, and (Left) a TiO_2 sample exposed molten LiCl-2wt%Li_2O-0.4wt%Li each for 20 hours at 650°C. The sample exposed to LiCl-2wt%Li_2O-0.4wt%Li was cut for XPS analysis but was visually unaffected by exposure to the molten solution containing metallic Li. The sample exposed to LiCl-2wt%Li_2O in the absence of Li failed at the interface with the melt.

XPS analysis was conducted on the sample of TiO_2 exposed to LiCl-2wt%Li_2O-0.4wt%Li, as well as a coupon of TiO_2 that was not exposed to molten salt, but baked in the manner used to remove salt from sample surfaces (two hours at 650˚C in the glove box atmosphere). The XPS survey spectra obtained from the surface of TiO_2 exposed to molten LiCl-2wt%Li_2O-0.4wt%Li for 20 hours, and the sample that was baked in the glove box without exposure to the molten solution are shown in Figure 6.9. Signal of the N 1s line is clearly visible in the spectrum obtained from the surface of TiO_2 exposed to molten LiCl-2wt%Li_2O-0.4wt%Li; however, the nitrogen was below the level of detectability on the surface of TiO_2 subjected to the baking procedure. This observation clearly demonstrates that bonding of nitrogen to the surface of TiO_2, as well as the formation of TiN on the surface of SS316L exposed to molten LiCl-Li_2O-Li, occurred in the melt and not as a result of the baking procedure. The presence of nitrogen on the

sample of TiO_2 exposed to molten LiCl-2wt%Li_2O-0.4wt%Li was confirmed by EDS, as shown in Figure 6.10.

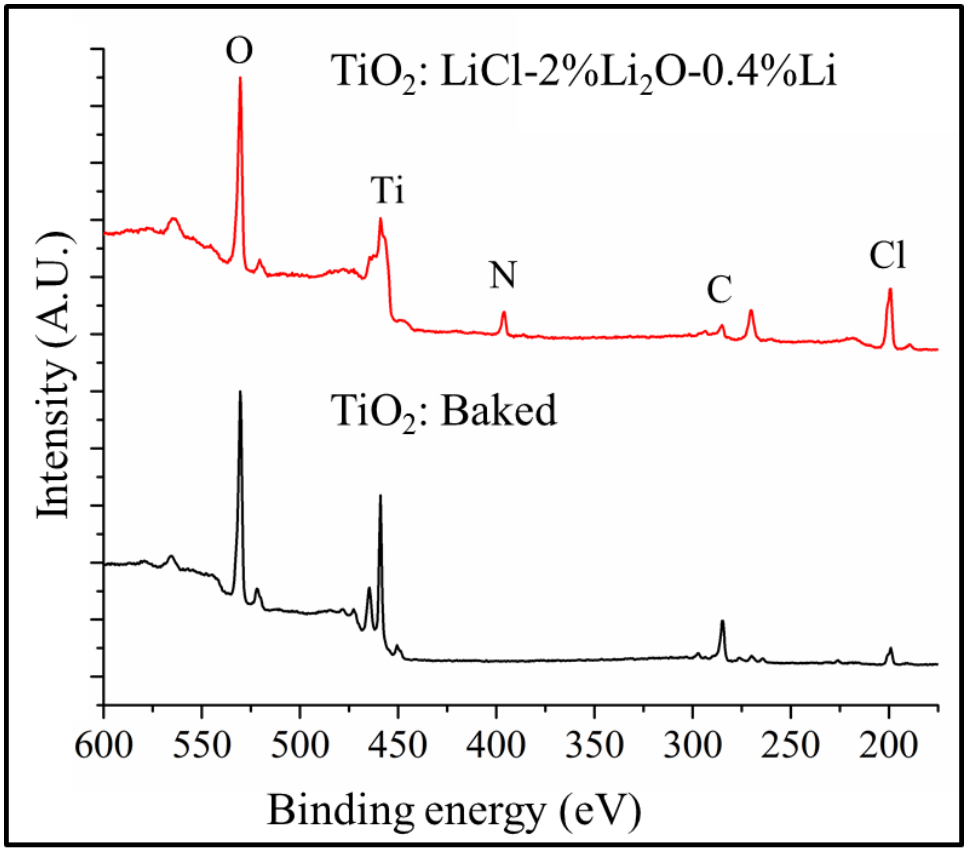


Figure 6.9: XPS survey spectra obtained from the surface of (Top) TiO_2 following exposure to LiCl-2wt%Li_2O-0.4wt%Li, and (Bottom) a TiO_2 sample not exposed to molten salt but baked at 650°C for two hours in the glove box atmosphere. The presence of N on the surface of TiO_2 exposed to molten LiCl-Li_2O-Li and not on the sample baked in the glove box demonstrates that the formation of TiN occurs in the molten solutions and not during the post exposure treatment.



Element	Wt%	At%
C K	2.68	6.86
N K	5.08	11.16
O K	19.04	36.62
Ti K	70.61	45.36

Figure 6.10 SEM micrograph and elemental composition obtained from EDS analysis of TiO_2 exposed to molten LiCl-2wt%Li_2O-0.4wt%Li at 650°C for 20 hours. N was present on the sample surface at every location analyzed.

6.4 Ti Compounds Formed as a Function of Li Concentration:

The Ti compounds formed on SS316L in molten LiCl-Li_2O-Li were further characterized as a function of Li concentration in the melt. SS316L was exposed to LiCl-2wt%Li_2O containing concentrations Li between 0.2 and 1wt%, in 0.2wt% increments. SS316L samples were subjected to the same exposure conditions as in the Section 5.2 with this exception of the change in melt compositions studied. The Ti 2p XPS spectra obtained from the surfaces of SS316L samples exposed to molten LiCl-2wt%Li_2O containing up to 1wt%Li are shown in Figure 6.11. These spectra were curve fit using the previously discussed fitting parameters attributed to the presence of Ti^{4+}, Ti^{3+}, and TiN.

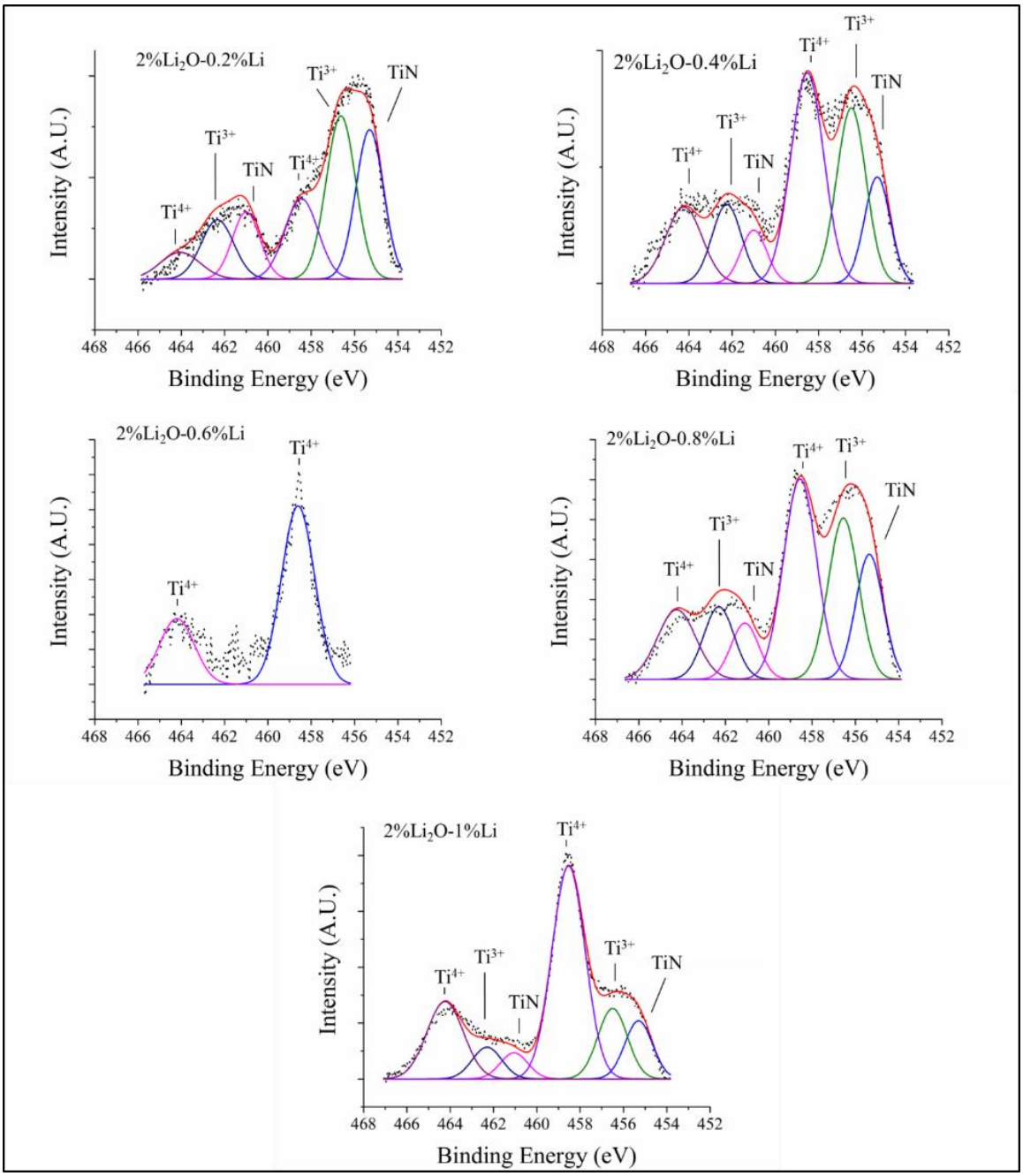


Figure 6.11: Ti 2p XPS spectra obtained from the surface of SS316L exposed to molten LiCl-2wt%Li_2O containing 0.2, 0.4, 0.6, 0.8 and 1wt%Li at 650°C for 20 hours. The spectra are fit with three peaks attributed to the presence of Ti^{4+}, Ti^{3+}, and TiN.

As shown in Figure 6.11, with the exception of the sample exposed to LiCl-2wt%Li_2O-0.6wt%Li, the spectra obtained from each SS316L sample exposed to molten

LiCl-Li_2O containing between 0.2 and 1wt%Li exhibit spectral features of Ti^{4+}, Ti^{3+}, and TiN. It is important to note that TiN is present on the surface of SS316L exposed to molten LiCl-Li_2O containing 0.2wt%Li. As discussed in Chapter 4, 0.2wt%Li is below the limit of physical dissolution in LiCl at 650°C. The formation of TiN (attributed to a liquid metal induced reaction) in molten solutions of LiCl-Li_2O containing Li below 0.3wt% is a strong indication that physically dissolved Li facilitates liquid metal type chemical reactions. Should this hypothesis be correct it would have a dramatic impact on the understanding of material interactions with molten solutions of LiCl-Li_2O-Li. Further, it is proposed that this observation may support the contested theory of electron delocalization in metal salt solutions [82, 84, 217]. More in depth investigations of these effects are required to validate such observations.

The Ti 2p spectrum recorded from SS316L exposed to molten LiCl-2wt%Li_2O-0.6wt%Li was characterized by a single feature indicating presence of exclusively Ti^{4+}. As discussed in more detail in the following chapter, corrosion studies conducted in melts containing 0.6wt%Li where observed to exhibit anomalous results due to a shift in melt chemistry that occurs at approximately this melt composition. It is proposed that the mechanism for why 0.6wt%Li deviates from this trend is the transition between the electrochemical and liquid metal controlled regimes discussed in Chapter 5.

The variation in the percentage of the Ti 2p spectra attributed to the presence of Ti^{4+}, Ti^{3+}, and TiN on the surface of SS316L as a function of Li in the melt is shown in Figure 6.12. The data obtained from the sample exposed to molten LiCl-2wt%Li_2O-

0.6wt%Li was excluded from this analysis due to the previously discussed anomalous characteristics of melts containing 0.6wt%Li.

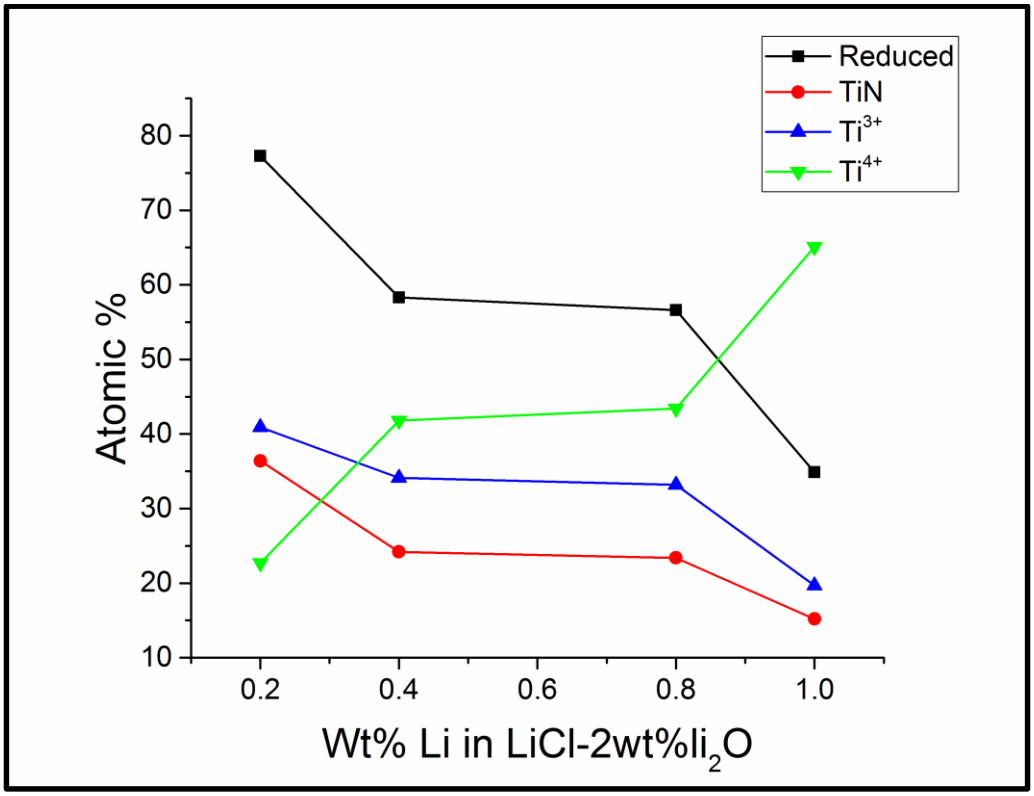


Figure 6.12: The percentage of the Ti 2p spectra obtained from the surface of SS316L exposed to molten LiCl-2wt%Li_2O containing 0.2, 0.4, 0.6, 0.8 and 1wt%Li at 650°C for 20 hours attributed to the existence of Ti^{4+}, Ti^{3+}, and TiN.

As shown in Figure 6.12, an unexpected trend of increasing the ratio of Ti^{4+} to Ti^{3+} is observed to coincide with increasing Li concentration in the melt. This result indicates for the first time that a synergistic relation between Li and Li_2O dissolved in molten LiCl may exist. As previously discussed, the ratio of Ti^{4+} to Ti^{3+} in a given lithium titanium oxide is related to the basicity of the environment in which it was formed. It was demonstrated in Section 5.2 that the ratio of Ti^{4+} to Ti^{3+} in lithium titanium oxides formed in molten LiCl-Li_2O-Li (containing a fixed concentration of Li) increases with increasing melt basicity. The results shown in Figure 6.12 suggest that an

increase in Li concentration in the melt has a similar effect, increasing the ratio of Ti^{4+} to Ti^{3+}. Should this result be an accurate interpretation of the true melt chemistry, it could be described as the Li concentration in the melt affecting the affinity of the melt to donate O^{2-} ions to the Ti system. Specifically, this would indicate that the activity of Li in the melt is affects the activity of the O^{2-} ion.

It is noted that this is strong conclusion based on a single set of results, and that alternative hypotheses can be proposed to explain these observations. For example, the results shown in Figure 6.12 could be explained by Li present in the melt reacting with atmospheric O_2 (less than 5ppm in the glove box) to increase the Li_2O concentration in the melt. Further investigations are required to validate these potential mechanisms.

6.5 Conclusions:

The electroless deposition of Ti compounds on the surface of stainless steel alloy 316L exposed to molten solutions of LiCl-Li_2O-Li was demonstrated using X-ray photoelectron spectroscopy. Three binding energy features of Ti were observed on the surface of the samples and are attributed to the presence of Ti^{4+}, Ti^{3+} and TiN. The formation of TiN in the presence of Li and N_2 is similar to liquid Li environments and counter to molten LiCl salt systems. Additionally, it was demonstrated that the proportion of Ti^{3+} and Ti^{4+} observed in the form of lithium titanium oxides on the sample surfaces was dependent on the concentration of Li_2O in the molten solutions. Coupons of TiO_2 were exposed to molten LiCl-2wt%Li_2O and LiCl-2wt%Li_2O-0.4wt%Li at 650°C for 20 hours. It was observed that the TiO_2 sample exposed to the melt that did not contain metallic Li dissolved during this period of exposure while the sample exposed to the

molten solution containing Li was visually unaffected. Furthermore, N was observed on the surface of TiO_2 exposed to molten LiCl-2wt%Li_2O-0.4wt%Li indicating that liquid metal type reactions occurred to some extent in the melt. Therefore, it is reported that while the activity of O^{2-} plays a role in the electrochemistry of molten solutions of LiCl-Li_2O-Li, chemical reactions analogous to liquid Li systems may also occur in these systems. Characterization of the Ti compounds formed in melts containing varying Li concentrations provided the first evidence of a synergistic effect between dissolved Li and Li_2O.

Chapter 7 Conclusions and Future Work

7.1 Conclusions:

The molten ternary LiCl-Li_2O-Li system has been studied both in terms of its physical chemistry and the ways in which it interacts with materials. Published literature on the electrolytic reduction of actinide oxides was reviewed with an emphasis on the role that metallic Li plays in the process. It was concluded that the physical chemistry of Li in these systems is not well understood and that multiple physical properties of the LiCl-Li_2O-Li system were unattributed. Furthermore, literature review demonstrated that a knowledge gap existed prior to this study regarding to what extent material interactions with molten LiCl-Li_2O-Li are governed by electrochemical and or liquid metal mechanisms.

Experimental methodologies were developed to study the degradation of materials that occurs as a result of exposure to molten LiCl-Li_2O-Li. Development of an experimental apparatus for exposing materials to molten LiCl-Li_2O-Li at 650°C for extended periods of time in accordance with the highest degree of corrosion testing rigor was achieved. Ni crucibles were shown to exhibit a low and uniform level of corrosion when used to contain melts of varying Li concentration. Finally, methodologies were established for analyzing surface films formed in molten LiCl-Li_2O-Li using X-ray photoelectron, energy dispersive X-ray and Raman spectroscopies, as well as X-ray diffraction and electron microscopy.

Evaluation of the miscibility of Li with molten LiCl was completed using chemical, magnetic and spectroscopic analysis. Chemical analysis of the amount of Li that was present in quenched samples of LiCl-Li_2O-Li indicated that the limit of physical dissolution of Li in LiCl is approximately 0.3wt% at 650°C and nearly independent of Li_2O concentration. A device capable of measuring the magnetic susceptibility of molten LiCl-Li_2O-Li was designed to quantify the concentration of Li at which the magnetic susceptibility became independent of the addition of further Li. The results obtained from this technique approximated the solubility limit of Li in LiCl-2wt%Li_2O to be 1wt% at 650°C. Finally, an optical system was developed for simultaneously conducting *in situ* Raman spectroscopy and electrochemical studies in molten LiCl-Li_2O-Li. This system was used to observe the spectroscopic signature of the Li nanocluster Li_8 in molten LiCl-Li_2O-Li. This finding indicates that molten solutions of Li and LiCl are nanofluid-type suspensions of Li_8 in a LiCl matrix. This mechanism of dispersion is theorized to be separate from the quantity of Li that can be physically dissolved in LiCl at 650°C (approximately 0.3wt%). It is concluded that a defined dispersion limit of Li in molten LiCl does not exist due to the mechanism of colloidal suspension.

Preliminary exposure testing of Inconel alloys 625 and 718, along with stainless steel alloy 316L and Hastelloy N was conducted to identify the general corrosion behavior of materials exposed to molten LiCl-Li_2O-Li. The inclusion of low quantities ($\leq$0.6wt%) of Li in molten LiCl-Li_2O suppresses material leaching into the melt and promotes the development of Cr based surface films. Alternatively, the inclusion of a high concentration ($>$0.6wt%) of Li in the melt results in the preferential leaching of Cr

and Mo. This trend in degradation as a function of Li concentration was observed for all three classifications of alloys tested and is independent of the crucible material employed. It is concluded that the mode of degradation that occurs in melts containing a high concentration of Li is not strictly analogous to liquid metal attack or molten salt induced corrosion. Additional tests identified the importance of removing trace quantities of moisture from LiCl prior to exposure testing. The efficacy of drying reagent grade LiCl to induce corrosion analogous to that which occurs in melts of ultra-high purity was demonstrated. Finally, it was observed that the rate of dissolution from Inconel 625 and stainless steel alloy 316L was below the level of detection upon exposure to anhydrous LiCl-Li_2O containing up to 0.3wt% Li for as long as 100 hours.

The alteration to the corrosion of stainless steel alloy 316L that occurs in molten LiCl-Li_2O due to the presence of Li was investigated as the culmination of this study. It was demonstrated that SS316L develops a protective $LiCrO_2$ film when exposed to molten LiCl-Li_2O in the absence of Li, as well as in LiCl-Li_2O containing a low concentration of Li. However, the $LiCrO_2$ films formed in melts containing Li were thinner than those formed in the absence of Li. The surface of SS316L exposed to molten LiCl-Li_2O containing greater than 0.6wt%Li was observed to be metallic. It is suggested that material interactions with LiCl containing 1 or 2wt%Li_2O and bellow approximately 0.6wt%Li are governed by electrochemical oxidation phenomena dictated by the basicity of the melt. Alternatively, material interactions with melts containing Li in excess of 0.6wt% are governed by liquid metal effects. Material leaching from SS316L was observed to be very low when exposed to molten LiCl-Li_2O-Li in either of these regions,

however Cr leaching was observed when an intermediate concentration of Li (~0.6wt%) was present in the melt.

The identification and characterization of Ti compounds formed on stainless steel during exposure to molten LiCl-Li_2O-Li yielded important information regarding the mechanisms of material interactions with these non-trivial systems. It was demonstrated that the presence of physically dissolved (0.2wt%) Li in molten LiCl-Li_2O facilitates chemical reactions previously observed in liquid metal environments and counter to those observed in molten salts. Furthermore, despite the inclusion of 0.4wt%Li in the melt the activity of the O^{2-} ion affects the melt chemistry in a manner predicted by classical molten salt basicity theory. These findings demonstrate that Li and Li_2O dissolved in molten LiCl behave independently, at least to some degree, despite the presence of the alternative dissolved component. Finally, evidence suggesting the existence of a synergistic effect between the concentration of Li and Li_2O in the melt was observed. Further studies are required to confirm what effect, if any, the concentration of Li in molten LiCl-Li_2O-Li has on the activity of the O^{2-} ion.

7.2 Future Work:

Future studies of material interactions with molten LiCl-Li_2O-Li systems should focus on the following areas of study:

1. Verify that the corrosion that occurred as a result of the relatively short term exposures in the current study is an accurate representation of the degradation that occurs over longer periods of time. Specifically, it should be demonstrated that the $LiCrO_2$ surface films formed as a result of 20 hours of exposure are stable and protective throughout hundreds of hours of exposure to molten LiCl-Li_2O containing less than 0.6wt%Li.
2. Evaluate the alteration to the mechanical properties of alloys that results from exposure to molten LiCl-Li_2O-Li. The hardening effect reported in Section 3.9 of this study needs to be confirmed and its cause elucidated.
3. The effect of cycling the concentration of Li in the melt in a manner analogous to the repeated operation of a batch electrolytic reduction process needs to be studied. It is currently unknown if the thin $LiCrO_2$ films formed in the presence of Li will provide protection in LiCl-Li_2O melts in the absence of Li. Further, the range of Li concentrations that result from the full scale operation of the electrolytic reduction process needs to be quantified as it is currently unknown if the liquid metal regime (associated with the presence of >0.6wt%Li) is relevant to the process.
4. The formation of a nanofluid suspension of Li nanoparticles in the molten salt needs to be verified using a secondary analytical technique. Should the

mechanism of colloidal suspension of Li_8 in the pure electrolyte be verified, alternative systems should be investigated to identify if this mechanism of miscibility is a general aspect of metal salt solutions or if it is restricted to the LiCl-Li system.

7.3 Scholarly Work from this Study:

Peer-reviewed Publications:

3. **A. Merwin**, W. Phillips, M. A. Williamson, J. Willit, P. N. Motsegood, and D. Chidambaram, Presence of Li clusters in molten LiCl-Li, *Scientific Reports,* (2016) SREP-15-30186

2. **A. Merwin** and D. Chidambaram, Corrosion of Inconel 625 in molten LiCl-Li_2O-Li, *Nuclear Technology,* (2016) NT15-126R1

1. **A. Merwin** and D. Chidambaram, Alternate anodes for the electrolytic reduction of UO_2, *Mettalurgical and Materials Transactions A,* 46 (2015) Pg. 536-544

Publication Under Review:

3. **A. Merwin** and D. Chidambaram, The electroless deposition of titanium compounds on stainless steel alloy 316L in molten LiCl-Li_2O-Li, *RSC Advances* RA-ART-03-2016-007025

2. **A. Merwin** and D. Chidambaram, The effect of Li(0) on the corrosion of SS316 exposed to molten LiCl-Li_2O – Part 2: X-ray photoelectron spectroscopy, *Journal of Nuclear Materials,* JNM-D-16-00146

1. **A. Merwin** and D. Chidambaram, The effect of Li(0) on the corrosion of SS316 exposed to molten LiCl-Li_2O – Part 1: material leaching and morphology, *Journal of Nuclear Materials* JNM-D-16-00146

Publications Under Preparation:

1. **A. Merwin,** M. A. Williamson, J. Willit, P. N. Motsegood and D. Chidambaram, Metallic lithium and the reduction of actinide oxides: a review

Abstracts and Scholarly Presentations:

5. **A. Merwin** and D. Chidambaram, Material interactions with LiCl-Li_2O-Li, Idaho National Laboratory, Idaho Falls, ID, Nov. 2014

4. **A. Merwin** and D. Chidambaram, Tungsten anodes for the electrolytic reduction of UO_2, International Pyroprocessing Research Conference, Idaho Falls, ID, Oct. 2014

3. **A. Merwin** and D. Chidambaram, Chromium oxide films on stainless steel alloy-316 in molten LiCl-Li_2O, American Nuclear Society Annual Conference, Reno, NV, Jun. 2014

2. **A. Merwin** and D. Chidambaram, Material stability in molten salts, The 224th Meeting of the Electrochemical Society, San Francisco, CA, Oct. 2013

1. **A. Merwin**, Alternative anodes for the electrolytic reduction of uranium dioxide, Master's Thesis Defense, Reno, NV, Dec. 2011

References:

[1] T. Nakajima, K. Nakanishi, N. Watanabe, Study of Emulsions in Molten Salts III. The concentration stability and particle-size distribution of dispersed lithium in molten lithium chloride, Bulletin of the Chemical Society of Japan, 49 (1975) 994-997.

[2] J.J. Laidler, J.E. Battles, W.E. Miller, J.P. Ackerman, E.L. Carls, Development of pyroprocessing technology, Progress in Nuclear Energy, 31 (1997) 131-140.

[3] T. Inoue, L. Koch, Development of Pyroprocessing and its Future Directions, Nuclear Engineering and Technology, 4 (2008) 183-190.

[4] Y. Sakamura, Effect of alkali and alkaline-earth chloride addition on electrolytic reduction of UO_2 in LiCl salt bath, Journal of Nuclear Materials, 412 (2011) 177-183.

[5] Y. Sakamura, T. Omori, T. Inoue, Application of Electrochemical Reduction to Produce Metal Fuel Material from Actinide Oxides, Nuclear Technology, 162 (2007).

[6] S.M. Jeong, S.B. Park, S.S. Hong, C.S. Seo, S.W. Park, Electrolytic production of metallic uranium from U_3O_8 in a 20-kg batch scale reactor, Journal of Radioanalytical and Nuclear Chemistry, 268 (2006) 349-356.

[7] E.-Y. Choi, J.-M. Hur, I.-K. Choi, S.G. Kwon, D.-S. Kang, S.S. Hong, H.-S. Shin, M.A. Yoo, S.M. Jeong, Electrochemical reduction of porous 17kg uranium oxide pellets by selection of an optimal cathode/anode surface area ratio, Journal of Nuclear Materials, 418 (2011) 87-92.

[8] S.D. Herrmann, S.X. Li, B.R. Westphal, Separation and Recovery of Uranium and Group Actinide Products From Irradiated Fast Reactor MOX Fuel via Electrolytic Reduction and Electrorefining, Separation Science and Technology, 47 (2012) 2044-2059.

[9] T.M. Besmann, R.H.J. Cooper, Chemical thermodynamic assessment of the Li-U-O system for possible space nuclear applications, in, 1985, pp. 13.

[10] E. Karell, R. Pierce, T. Mulcahey, Treatment of oxide spent fuel using the lithium reduction process, in, Argonne National Laboratory 1996.

[11] J.L. Willit, W.E. Miller, J.E. Battles, Electrorefining of uranium and plutonium — A literature review, Journal of Nuclear Materials, 195 (1992) 229-249.

[12] L.I. Redey, K. Gourishankar, Direct electrochemical reduction of metal-oxides in: Patent: US6540902 B1, 2001.

[13] K.V. Gourishankar, E.R. Karell, R.E. Everhart, E. Indacochea, Electrometallurgical treatment of degraded N-reactor fuel, in: Embedded Topical Meeting on DOE Spent Nuclear Fuel and Fissile Material Management, The American Nuclear Society San Diego, CA, 2000, pp. 65-72.

[14] E.J. Karell, K.V. Gourishankar, L.S. Chow, R.E. Everhart, Electrometallurgical Treatment of Oxide Spent Fuels, in: Global '99: "Nuclear Technology - Bridging the Millennia", Jackson Hole, WY, 1999, pp. 78-84.

[15] E. Karell, K. Gourishankar, J. Smith, L. Chow, L. Redey, Seperation of Actinides from LWR Spent Fuel Using Molten-Salt-Based Electctrochemical Processes, Nuclear Technology, 136 (2001) 343-353.

[16] E.J. Karell, K.V. Gourishankar, Electrometallurgical treatment of oxide spent fuel - engineering-scale development, in: T.A.N. Society (Ed.) Third Topical Meeting on DOE Spent Nuclear Fuel and Fissile Materials Management, Charleston, SC., 1998, pp. 682-688.

[17] G.Z. Chen, D.J. Fray, T.W. Farthing, Direct electrochemical reduction of titanium dioxide to titanium in molten calcium chloride, Nature, 407 (2000) 361-364.

[18] A.M. Abdelkader, K.T. Kilby, A. Cox, D.J. Fray, DC Voltammetry of Electro-deoxidation of Solid Oxides, Chemical Reviews (Washington, DC, United States), 113 (2013) 2863-2886.

[19] W. Xiao, D. Wang, The electrochemical reduction processes of solid compounds in high temperature molten salts, Chemical Society Reviews, 43 (2014) 3215-3228.

[20] K.S. Mohandas, Direct electrochemical conversion of metal oxides to metal by molten salt electrolysis: a review, Mineral Processing and Extractive Metallurgy, 122 (2013) 195-212.

[21] P. Kar, J.W. Evans, A shrinking core model for the electro-deoxidation of metal oxides in molten halide salts, Electrochimica Acta, 53 (2008) 5260-5265.

[22] E.-Y. Choi, S.M. Jeong, Electrochemical processing of spent nuclear fuels: An overview of oxide reduction in pyroprocessing technology, Progress in Natural Science: Materials International, 25 (2015) 572-582.

[23] Y. Sakamura, Solubility of Li_2O in Molten LiCl-MCl_x (M=Na, K, Cs, Ca, Sr, or Ba) Binary Systems, Journal of the Electrochemical Society, 157 (2010) E135-E139.

[24] Y. Kado, T. Goto, R. Hagiwara, Dissolution Behavior of Lithium Oxide in Molten LiCl−KCl Systems, Journal of Chemical and Engineering Data, 53 (2008) 2816-2819.

[25] T. Usami, M. Kurata, T. Inoue, H.E. Sims, S.A. Beetham, J.A. Jenkins, Pyrochemical reduction of uranium dioxide and plutonium dioxide by lithium metal, Journal of Nuclear Materials, 300 (2002) 15-26.

[26] B. Park, S. Park, S. Jeong, C. Seo, S. Park, Electrolytic reduction of spent oxide fuel in a molten LiCl-Li_2O system, Journal of Radioanalytical and Nuclear Chemistry, 270 (2006) 575-583.

[27] J. Hur, C. Seo, S. Hong, D. Kang, S. Park, Semi-Continuous Electrowinning of Li in a LiCl-Li_2O Molten Salt, Journal of the Korean Radioactive Waste Society, 2 (2004) 211-217.

[28] K. Gourishankar, L. Redey, M. Williamson, Electrolytic Reduction of Metal Oxides in Molten Salts, in: Light Metals, The Minerals, Metals & Materials Society, 2002, pp. 1075.

[29] T. Usami, T. Kato, M. Kurata, T. Inoue, H.E. Sims, S.A. Beetham, J.A. Jenkins, Lithium reduction of americium dioxide to generate americium metal, Journal of Nuclear Materials, 304 (2002) 50-55.

[30] S. Jeong, J. Hur, S. Hong, D. Kang, M. Choung, X. Seo, J. Yoon, S. Park, An Electrochemical Reduction of Uranium Oxide in the Advanced Spent Fuel Conditioning Process, Nuclear Technology, 162 (2007) 184-191.

[31] M. Kurata, T. Inoue, J. Serp, M. Ougier, J.-P. Glatz, Electro-chemical reduction of MOX in LiCl, Journal of Nuclear Materials, 328 (2004) 97-102.

[32] E.-Y. Choi, J.W. Lee, J.J. Park, J.-M. Hur, J.-K. Kim, K.Y. Jung, S.M. Jeong, Electrochemical reduction behavior of a highly porous SIMFUEL particle in a LiCl molten salt, Chemical Engineering Journal (Lausanne), 207–208 (2012) 514-520.

[33] J.-M. Hur, S.-C. Lee, S.-M. Jeong, C.-S. Seo, Electrochemical Reduction of TiO_2 in Molten LiCl-Li_2O, Chemistry Letters, 36 (2007) 1028-1029.

[34] S.-C. Lee, J.-M. Hur, C.-S. Seo, Silicon powder production by electrochemical reduction of SiO_2 in molten LiCl–Li_2O, Journal of Industrial and Engineering Chemistry, 14 (2008) 651-654.

[35] S.M. Jeong, J.-Y. Jung, C.-S. Seo, S.-W. Park, Characteristics of an electrochemical reduction of Ta_2O_5 for the preparation of metallic tantalum in a LiCl–Li_2O molten salt, Journal of Alloys and Compounds, 440 (2007) 210-215.

[36] S.M. Jeong, H.Y. Yoo, J.-M. Hur, C.-S. Seo, Preparation of metallic niobium from niobium pentoxide by an indirect electrochemical reduction in a LiCl-Li_2O molten salt, Journal of Alloys and Compounds, 452 (2008) 27-31.

[37] Chemical Reaction and Equilibrium Software with Extensive Thermochemical Database, Version 5.1, in, Outotec Research HSC Chemistry, 2002.

[38] S. Herrmann, S. Li, M. Simpson, Electrolytic Reduction of Spent Light Water Reactor Fuel Bench-Scale Experiment Results, Journal of Nuclear Science and Technology, 44 (2007) 361-367.

[39] B.H. Park, I.W. Lee, C.S. Seo, Electrolytic reduction behavior of U_3O_8 in a molten LiCl–Li_2O salt, Chemical Engineering Science, 63 (2008) 3485-3492.

[40] J.-M. Hur, C.-S. Seo, S.-S. Hong, D.-S. Kang, S.-W. Park, Metallization of U_3O_8 via catalytic electrochemical reduction with Li_2O in LiCl molten salt, Reaction Kinetics and Catalysis Letters, 80 (2003) 217-222.

[41] E.-Y. Choi, C.Y. Won, J.-S. Cha, W. Park, H.S. Im, S.-S. Hong, J.-M. Hur, Electrochemical reduction of UO_2 in LiCl–Li_2O molten salt using porous and nonporous anode shrouds, Journal of Nuclear Materials, 444 (2014) 261-269.

[42] S. Phongikaroon, S. Herrmann, M. Simpson, Diffusion Model for Electrolytic Reduction of Uranium Oxides in Molten LiCl-Li_2O Salt, Nuclear Technology, 174 (2010).

[43] S. Herrmann, S. Li, B. Serrano-Rodriguez, Observations of Oxygen Ion Behavior in the Lithium-Based Electrolytic Reduction of Uranium Oxide in: GLOBAL 2009, American Nuclear Society 2009.

[44] W. Park, J.-K. Kim, J.-M. Hur, E.-Y. Choi, H.S. Im, S.-S. Hong, Application of a boron doped diamond (BDD) electrode as an anode for the electrolytic reduction of UO_2 in Li_2O–LiCl–KCl molten salt, Journal of Nuclear Materials, 432 (2013) 175-181.

[45] Y. Sakamura, Determination of E–pO^{2-} diagram for lanthanum in LiCl melt at 923K, Electrochimica Acta, 80 (2012) 308-315.

[46] T.B. Joseph, N. Sanil, L. Shakila, K.S. Mohandas, K. Nagarajan, A cyclic voltammetry study of the electrochemical behavior of platinum in oxide-ion rich LiCl melts, Electrochimica Acta, 139 (2014) 394-400.

[47] S.M. Jeong, H.-S. Shin, S.-H. Cho, J.-M. Hur, H.S. Lee, Electrochemical behavior of a platinum anode for reduction of uranium oxide in a LiCl molten salt, Electrochimica Acta, 54 (2009) 6335-6340.

[48] J.M. Hur, J. Cha, E.Y. Choi, Can Carbon Be an Anode for Electrochemical Reduction in a LiCl-Li_2O Molten Salt?, ECS Electrochemistry Letters, 3 (2014) E5-E7.

[49] A. Merwin, D. Chidambaram, Alternate Anodes for the Electrolytic Reduction of UO_2, Metallurgical and Materials Transactions A, 46 (2015) 536-544.

[50] P. Motsegood, Development of Carbon Anodes for Use in Electrolytic Reduction of Used Oxide Fuel, in: International Pyroprocessing Research Conference, Idaho Falls, ID, 2014.

[51] M.K. Yoshiharu Sakamura, and Tadashi Inoue, Electrochemical Reduction of UO_2 in Molten $CaCl_2$ or LiCl, Journal of the Electrochemical Society, 153(3) (2006).

[52] W.I. Ko, H.H. Lee, S. Choi, S.-K. Kim, B.H. Park, H.J. Lee, I.T. Kim, H.S. Lee, Preliminary conceptual design and cost estimation for Korea Advanced Pyroprocessing Facility Plus (KAPF+), Nuclear Engineering and Design, 277 (2014) 212-224.

[53] J. Park, I. Jung, J. Shin, Development of Voloxidation Process for Treatment of LWR spent Fuel, in, Korea Atomic Energy Research Institute, Daejeon (Korea, Republic of), 2007.

[54] B.P. Westphal, K.J. Bateman, C.D. Morgan, J.F. Berg, P.J. Crane, D.G. Cummings, J.J. Giglio, M.W. Huntley, R.P. Lind, D.A. Sell, Effect of Process Variables During the Head-End Treatment of Spent Oxide Fuel, Nuclear Technology, 162 (2008) 153-157.

[55] M.F. Simpson, Development of Spent Nuclear Fuel Reprocessing Technology at Idaho National Laboratory, in, Idaho National Laboratory, Idaho Falls, Idaho, 2012.

[56] K.C. Song, G.I. Park, J.W. Lee, J.J. Park, M.S. Yang, Fractional Release Behavior of Volatile and Semivolitile Fission Products During a Voloxidation and OREOX Treatment of Spent PWR Fuel, Nuclear Technology, 162 (2008) 158-168.

[57] E.-Y. Choi, J.-K. Kim, H.-S. Im, I.-K. Choi, S.-H. Na, J.W. Lee, S.M. Jeong, J.-M. Hur, Effect of the UO_2 form on the electrochemical reduction rate in a LiCl–Li_2O molten salt, Journal of Nuclear Materials, 437 (2013) 178-187.

[58] B.H. Park, I.W. Lee, C.-S. Seo, Reduction of U_3O_8 in a High Temperature Molten LiCl-Li_2O Salt, Journal of Chemical Engineering of Japan, 41 (2008) 294-297.

[59] S.M. Jeong, H.-S. Shin, S.-S. Hong, J.-M. Hur, J.B. Do, H.S. Lee, Electrochemical reduction behavior of U_3O_8 powder in a LiCl molten salt, Electrochimica Acta, 55 (2010) 1749-1755.

[60] J.-M. Hur, I.-K. Choi, S.-H. Cho, S.-M. Jeong, C.-S. Seo, Preparation and melting of uranium from U_3O_8, Journal of Alloys and Compounds, 452 (2008) 23-26.

[61] Y. Sakamura, T. Omori, Electrolytic Reduction and Electrorefining of Uranium to Develop Pyroprocessing of Oxide Fuels, Nuclear Technology, 171 (2010) 266-275.

[62] Y. Sakamura, Pyrochemical Reprocessing Tests to Collect Uranium Metal From Simulated Spent Oxide Fuel, Nuclear Technology, 179 (2012) 220-233.

[63] J.-M. Hur, S.-S. Hong, H. Lee, Electrochemical reduction of UO_2 to U in a LiCl–KCl-Li_2O molten salt, Journal of Radioanalytical and Nuclear Chemistry, 295 (2013) 851-854.

[64] E.-Y. Choi, C.Y. Won, S.-J. Lee, D.-S. Kang, S.-W. Kim, J.-S. Cha, W. Park, H.S. Im, J.-M. Hur, Use of a single fuel containment material during pyroprocessing tests, Annals of Nuclear Energy, 76 (2015) 305-314.

[65] E. Choi, H. Im, J. Hur, Effect of Anode-to-Cathode Distance on the Electrochemical Reduction in a LiCl-Li_2O Molten Salt, Journal of the Korean Electrochemical Society, 16 (2013) 138-144.

[66] S. Herrmann, S. Li, M. Simpson, S. Phongikaroon, Electrolytic Reduction of Spent Nuclear Oxide Fuel as Part of Integral Proces to Separate and Recover Actinides from Fission Products, Separation Science and Techology, 41 (2006) 1965-1983.

[67] S. Herrmann, S. Li, Separation and Recovery of Uranium and Group Actinide Products from Irradiated Fast Reactor MOX Fuel via Electrolytic Reduction and Electrorefining, Nuclear Technology, 171 (2010) 247-265.

[68] W. Park, J.-M. Hur, S.-S. Hong, E.-Y. Choi, H.S. Im, S.-C. Oh, J.-W. Lee, An experimental study for Li recycling in an electrolytic reduction process for UO_2 with a Li_2O–LiCl molten salt, Journal of Nuclear Materials, 441 (2013) 232-239.

[69] M. Iizuka, Y. Sakamura, T. Inoue, Electrochemical reduction of (U–40Pu–5Np)O_2 in molten LiCl electrolyte, Journal of Nuclear Materials, 359 (2006) 102-113.

[70] A.S. Dworkin, H.R. Bronstein, M.A. Bredig, Miscibility of Metals with Salts. VI. Lithium-Lithium Halide Systems, The Journal of Physical Chemistry, 66 (1962) 572-573.

[71] J. Liu, J.C. Poignet, Electronic conductivity of salt-rich Li−LiCl melts, Journal of Applied Electrochemistry, 22 (1992) 1110-1112.

[72] J. Liu, J.C. Poignet, Measurement of the activity of lithium in dilute solutions in molten lithium chloride between 650°C and 800°C, Journal of Applied Electrochemistry, 20 (1990) 864-867.

[73] T. Nakajima, K. Nakanishi, N. Watanabe, The Dispersion of Metallic Lithium in Various Molten Salts, Nippon Kagaku Kaishi, 1975 (1975) 617-621.

[74] N. Watanabe, K. Nakanishi, T. Nakajima, The Dissolution of Lithium in Molten Lithium Chloride, Nippon Kagaku Kaishi, 1974 (1974) 401-404.

[75] S. Herrmann, S. Li, B. Westphal, Separation and Recovery of Uranium and Group Actinide Products from Irradiated Fast Reactor MOX Fuel via Electrolytic Reduction and Electrorefining, in: 3rd International Pyroprocessing Research Conference, U.S. DOE, Dimitrovgrad, Russia, 2010.

[76] S. Herrmann, S. Li, Separation and Recovery of Uranium metal from Spent Light Water Reactor Fuel via Electrolytic Reduction and Electrorefining, Nuclear Technology, 171 (2010) 247 - 265.

[77] M. Simpson, S. Herrmann, Modeling the Pyrochemical Reduction of Spent UO_2 Fuel in a Pilot Scale Reactor, Nuclear Technology, 162 (2008) 179 - 183.

[78] P. Kar, J.W. Evans, A model for the electrochemical reduction of metal oxides in molten salt electrolytes, Electrochimica Acta, 54 (2008) 835-843.

[79] M.A. Bredig, Mixtures of Metals with Molten Salts, in: J.W.a. Sons (Ed.) Molten Salt Chemistry, 1964.

[80] G.M. Haarberg, J. Thonstad, Electrochemical properties of metal-molten salt mixtures, Journal of Applied Electrochemistry, 19 (1989) 789-801.

[81] J.D. Corbett, The Solutions of Metals in their Molten Salts, in: M. Hill (Ed.) Fused Salts, 1964.

[82] J. W.W. Warren, Electronic Properties of Metal / Molten Salt Solutions, in: M. Gaune-Escard (Ed.) Molten Salts: From Fundamentals to Applications, Kluwer Academic Publishers, 2001.

[83] H.R. Bronstein, M.A. Bredig, The Electrical Conductivity of Solutions of Alkali Metals in their Molten Halides, Journal of the American Chemical Society, 80 (1958) 2077-2081.

[84] W.W. Warren, Metal-Metal Salt Solutions, in: R. Publishing (Ed.) Advances in Molten Salt Chemistry, 1983.

[85] W. Freyland, Bulk and Surface Characteristics of Metal-Molten Salt Solutions, Journal of Non-Crystalline Solids, 117 (1990) 613-622.

[86] L.F. Grantham, S.J. Yosim, Electrical Conductivities of Molten Bi–BiI_3 Solutions, The Journal of Chemical Physics, 38 (1963) 1671-1676.

[87] P. Hébant, G.S. Picard, Electrochemical investigations of the liquid lithium/(LiCl–KCl eutectic melt) interface. Chronopotentiometric and electrochemical impedance spectroscopy measurements, Electrochimica Acta, 43 (1998) 2071-2081.

[88] A.S. Dworkin, M.A. Bredig, Miscibility of liquid metals with salts. IX. Pseudobinary alkali metal-metal halide systems: cesium iodide-sodium, cesium iodide-lithium, and lithium fluoride-potassium, The Journal of Physical Chemistry, 74 (1970) 3828-3829.

[89] M.A. Bredig, H.R. Bronstein, Miscibility of Liquid Metals with Salts IV The Sodium-Sodium Halide Systems at High Temperature The Journal of Physical Chemistry, 64 (1960) 64-67.

[90] A.S. Dworkin, H.R. Bronstein, M.A. Bredig, Miscibility of liquid metals with salts. VIII. Strontium-strontium halide and barium-barium halide systems, The Journal of Physical Chemistry, 72 (1968) 1892-1896.

[91] T. Nakajima, R. Minami, K. Nakanishi, N. Watanabe, Miscibility of Lithium with Lithium Chloride and Lithium Chloride - Potassium Chloride Eutectic Mixture, Bulletin of the Chemical Society of Japan, 47 (1974) 2071-2072.

[92] H. Moriyama, T. Nagae, Y. Ito, Solubility of molten salt into liquid lithium, Journal of Nuclear Materials, 211 (1994) 231-235.

[93] K. Chang, B. Hallstedt, Thermodynamic assessment of the Li–O system, Calphad, 35 (2011) 160-164.

[94] P. Hébant, G.S. Picard, Computational investigations of the liquid lithium/(LiCl-KCl eutectic melt) interface, Journal of Molecular Structure: THEOCHEM, 426 (1998) 225-232.

[95] R.O. Jones, A.I. Lichtenstein, J. Hutter, Density functional study of structure and bonding in lithium clusters Li_n and their oxides Li_nO, The Journal of Chemical Physics, 106 (1997) 4566-4574.

[96] C.H. Wu, H. Kudoa, H.R. Ihle, Thermochemical properties of gaseous Li_3O and Li_2O_2, The Journal of Chemical Physics, 70 (1979) 1815-1820.

[97] H. Kudo, K. Yokoyama, The Structures and Bonding of Hyperlithiated Molecules, Bulletin of the Chemical Society of Japan, 69 (1996) 1459-1469.

[98] S. Neukermans, E. Janssens, H. Tanaka, R.E. Silverans, P. Lievens, K. Yokoyama, H. Kudo, Visible and near-infrared photoabsorption spectrum of Li_3O: Resonance enhanced two-photon ionization spectroscopy and ab initio calculations, Journal of Chemical Physics, 119 (2003) 7206-7213.

[99] M. Gutowski, J. Simons, Anionic and Neutral States of Li_3O, The Journal of Physical Chemistry, 98 (1994) 8326-8330.

[100] S. Zein, J.V. Ortiz, Interpretation of the photoelectron spectra of superalkali species: Li_3O and Li_3O^-, The Journal of Chemical Physics, 135 (2011).

[101] V.L. Cherginets, Oxide ion electrodes and oxide ion donors in molten alkaline halogenides. A consideration of potentiometric studies, Electrochimica Acta, 42 (1997) 1507-1514.

[102] M.P. Tosi, Nonmetal-Metal Transition in Solutions of Metals in Molten Salts, J. Mater. Sci. Technol., 14 (1998).

[103] P. Masset, R.A. Guidotti, Thermal activated (thermal) battery technology: Part II. Molten salt electrolytes, Journal of Power Sources, 164 (2007) 397-414.

[104] T. Takenaka, K. Shigeta, H. Masuhama, K. Kubota, Influence of Some Factors upon Electrodeposition of Liquid Li and Mg, ECS Transactions, 49 (2009) 441-448.

[105] A. Merwin, W. Phillips, M.A. Williamson, J. Willit, P.N. Motsegood, D. Chidambaram, Presence of Li Clusters in Molten LiCl-Li, Scientific Reports, (2015).

[106] N. Gese, B. Pesic, Electrochemistry of LiCl-Li_2O-H_2O Molten Salt Systems in: TMS (Ed.) 2013 TMS Annual Meeting & Exhibition, TMS, 2013.

[107] S.M. Jeong, B.H. Park, J.-i.-m. Hur, C.-S. Seo, H. Lee, K.-C. Song, An Experimental study on an Electrochemical Reduction of an Oxide Mixture in the Advanced Spent-Fuel Conditioning Process Nuclear Engineering and Technology, 42 (2010) 183-192.

[108] T. Takenaka, T. Morishige, M. Umehara, Cathodic Phenomena in Li Electrolysis in LiCl-KCl Melt, in: Molten Salts Chemistry and Technology, John Wiley & Sons, Ltd, 2014, pp. 143-148.

[109] S. Herrmann, S. Li, M. Simpson, Electrolytic Reduction of Spent Oxide Fuel – Bench-Scale Test Results in: GLOBAL 2005, INL, 2005.

[110] I.K. Choi, Y.H. Cho, J.W. Yeon, W. Kim, T.J. Kim, Method of in-situ monitoring a reduction of uranium oxides by lithium metal, in, 2008.

[111] T.-J. Kim, Y.-H. Cho, I.-K. Choi, J.-G. Kang, K. Song, K.-Y. Jee, Application of a chronoamperometric measurement to the on-line monitoring of a lithium metal reduction for uranium oxide, Journal of Nuclear Materials, 375 (2008) 275-279.

[112] D.W. Jeppson, J.L. Ballif, W.W. Yuan, B.E. Chou, Lithium Literature Review: Lithium's Properties and Interactions, in, Handford Engineering Development Laboratory, 1978.

[113] E.R. Van Artsdalen, I.S. Yaffe, Electrical Conductance and Density of Molten Salt Systems: KCl–LiCl, KCl–NaCl and KCl–KI, The Journal of Physical Chemistry, 59 (1955) 118-127.

[114] M. Simpson, Develupments of Spent Nuclear Fuel Pyroprocessing Technology at Idaho National Laboratory, in, INL, Idaho Falls, Idaho, 2012.

[115] D.M. Kolb, M. Przasnyski, H. Gerischer, Underpotential deposition of metals and work function differences, Journal of Electroanalytical Chemistry and Interfacial Electrochemistry, 54 (1974) 25-38.

[116] G. Kokkinidis, Underpotential deposition and electrocatalysis, Journal of Electroanalytical Chemistry and Interfacial Electrochemistry, 201 (1986) 217-236.

[117] D.M. Kolb, H. Gerischer, Further aspects concerning the correlation between underpotential deposition and work function differences, Surface Science, 51 (1975) 323-327.

[118] O.A. Oviedo, P. Vélez, V.A. Macagno, E.P.M. Leiva, Underpotential deposition: From planar surfaces to nanoparticles, Surface Science, 631 (2015) 23-34.

[119] Y. Xue, Y. Yan, M. Zhang, W. Han, Z. Zhang, Electrochemical formation of Mg-Li-Y alloys by co-deposition of magnesium, lithium and yttrium ions in molten chlorides, Journal of Rare Earths, 30 (2012) 1048-1054.

[120] Q. Xu, C. Schwandt, G.Z. Chen, D.J. Fray, Electrochemical investigation of lithium intercalation into graphite from molten lithium chloride, Journal of Electroanalytical Chemistry, 530 (2002) 16-22.

[121] J.-M. Hur, S.M. Jeong, H. Lee, Underpotential deposition of Li in a molten LiCl–Li_2O electrolyte for the electrochemical reduction of U from uranium oxides, Electrochemistry Communications, 12 (2010) 706-709.

[122] S. Herrmann, S. Li, D. Sell, B. Westphal, Electrolytic Reduction of Spent Nuclear Oxide Fuel – Effects of Fuel Form and Cathode Containment Materials on Bench-Scale Operations, in, Idaho National Laboratory 2007.

[123] V. Ignatiev, A. Surenkov, 5.10 - Material Performance in Molten Salts, in: J.M.K. Editor-in-Chief: Rudy (Ed.) Comprehensive Nuclear Materials, Elsevier, Oxford, 2012, pp. 221-250.

[124] K. Sridharan, T. Allen, Corrosion in Molten Salts, in: Molten Salt Chemistry, Elsevier, 2013.

[125] A. Nishikata, H. Numata, T. Tsuru, Electrochemistry of molten salt corrosion, Materials Science and Engineering: A, 146 (1991) 15-31.

[126] R. Rapp, Corrosion by Molten Salts, in: Corrosion: fundamentals, testing and protection, ASM International, Materials Park, OH, 2003.

[127] W.D. Manly, Fundamentals of Liquid Metal Corrosion, in: M. Division (Ed.), Oak Ridge National Laboratory, 1956.

[128] N. Gese, The Electrochemistry of Li-LiCl-Li_2O Molten Salt Systems and the Role of Moisture, in: Nuclear Engineering, University of Idaho, 2015.

[129] W.J. Burkhard, J.D. Corbett, The Solubility of Water in Molten Mixtures of LiCl and KCl, Journal of the American Chemical Society, 79 (1957) 6361-6363.

[130] H.A. Laitinen, W.S. Ferguson, R.A. Osteryoung, Preparation of Pure Fused Lithium Chloride-Potassium Chloride Eutectic Solvent, Journal of the Electrochemical Society, 104 (1957) 516-520.

[131] X.K. Feng, C.A. Melendres, Anodic Corrosion and Passivation Behavior of Some Metals in Molten LiCl - KCl Containing Oxide Ions, Journal of the Electrochemical Society, 129 (1982) 1245-1249.

[132] T. Nohira, Y. Ito, Electrochemical Behavior of Hydride Ion in a LiCl-KCl Eutectic Melt, Journal of the Electrochemical Society, 149 (2002) E159-E165.

[133] R.E. Thoma, Chemical Aspects of MSRE Operations, in, Oak Ridge National Laboratory, 1972.

[134] D. Olander, Redox condition in molten fluoride salts: Definition and control, Journal of Nuclear Materials, 300 (2002) 270-272.

[135] B.C. Kelleher, Purification and Chemical Control of Molten Li_2BeF_4 for a Fluoride Salt Cooled Reactor, in, The University of Wisconsin - Madison, 2015.

[136] H. Nakajima, T. Nohira, Y. Ito, Thermodynamic Investigations of a Hydrogen Electrode Reaction in a Molten LiCl-KCl-LiH System, Electrochemical and Solid-State Letters, 5 (2002) E17-E20.

[137] D. Jones, Principles and Prevention of Corrosion Prentice Hall, 1996.

[138] S.H. Cho, J.S. Zhang, Y.J. Shin, S.W. Park, H.S. Park, Corrosion behavior of Fe–Ni–Cr alloys in the molten salt of LiCl–Li_2O at high temperature, Journal of Nuclear Materials, 325 (2004) 13-17.

[139] Y.S. Zhang, Solubilities of Cr_2O_3 in Fused Na_2SO_4 at 1200K, Journal of the Electrochemical Society, 133 (1986) 655.

[140] M. Spiegel, P. Biedenkopf, H.J. Grabke, Corrosion of iron base alloys and high alloy steels in the Li_2CO_3-K_2CO_3 eutectic mixture, Corrosion Science, 39 (1997) 1193-1210.

[141] E. Mohammadi Zahrani, A.M. Alfantazi, Molten salt induced corrosion of Inconel 625 superalloy in $PbSO_4$–Pb_3O_4–$PbCl_2$–Fe_2O_3–ZnO environment, Corrosion Science, 65 (2012) 340-359.

[142] J.E. Indacochea, J.L. Smith, K.R. Litko, E.J. Karell, A.G. Rarez, High-Temperature Oxidation and Corrosion of Structural Materials in Molten Chlorides, Oxidation of Metals, 55 (2001) 1-16.

[143] S. Cho, J. Lim, K. Yun, S. Park, Corrosion Behavior of Ni 200 and Ni-base Alloys in Hot Lithium Molten Salt, Korean Journal of Materials Research, 14 (2004).

[144] S.H. Cho, S.B. Park, J.H. Lee, J.M. Hur, H.S. Lee, Hot corrosion behavior of ZrO_2–MgO coatings in LiCl–Li_2O molten salt, Materials Chemistry and Physics, 131 (2012) 743-751.

[145] J. Indacochea, J. Smith, Corrosion performance of ferrous and refractory metals in molten salts under reducing conditions, Journal of Materials Research, 14 (1999) 1990-1995.

[146] W.A. Averill, D.L. Olson, A review of extractive processes for lithium from ores and brines, Energy, 3 (1978) 305-313.

[147] A.-M. Sapse, P.v.R. Schleyer, Lithium chemistry: a theoretical and experimental overview, John Wiley & Sons, 1995.

[148] F.L. Tabarés, Lithium: Technology, Performance and Safety Nova Science Publishers, Inc, 2013.

[149] H. Kudo, C.H. Wu, Vaporization of $Li_2C_{2(s)}$ and thermochemical properties of gaseous CLi_3, CLi_4, and CLi_6, Journal of Nuclear Materials, 201 (1993) 261-266.

[150] D.L. Smith, K. Natesan, Influence of Nonmetalic Impurity Elements on the Comparability of Liquid Lithium with Potential CTR Containment Materials, Nuclear Technology, 22 (1973) 392-404.

[151] S.V.N. Naidu, P.R. Rao, Phase diagrams of binary tungsten alloys, Indian Institute of Metals, Calcutta, 1991.

[152] H. Okamoto, Phase diagrams of binary iron alloys, ASM International, Materials Park, OH, 1993.

[153] P.F. Tortorelli, O.K. Chopra, Corrosion and compatibility considerations of liquid metals for fusion reactor applications, Journal of Nuclear Materials, 103 (1981) 621-632.

[154] A. Merwin, Alternative Anodes for the Electrolytic Reduction of Uranium Dioxide, in: Chemical and materials engineering, University of Nevada, Reno, 2012.

[155] W. Phillips, Corrosion performance of Monel 400 and the electrochemical behavior of LiBi reference electrode in molten LiCl-Li_2O-Li, in: Chemical and materials engineering, University of Nevada, Reno, 2015.

[156] M.S. Foster, S.E. Wood, C.E. Crouthamel, Thermodynamics of Binary Alloys. I. The Lithium-Bismuth System, Inorganic Chemistry, 3 (1964) 1428-1431.

[157] J. Sangster, A.D. Pelton, The Bi-Li (Bismuth-Lithium) system, Journal of Phase Equilibria, 12 (1991) 447-450.

[158] T. Sakurai, T. Yoneoka, S. Tanaka, A. Suzuki, T. Muroga, Control of the nitrogen concentration in liquid lithium by the hot trap method, Journal of Nuclear Materials, 307–311, Part 2 (2002) 1380-1385.

[159] C.H. Liu, K.E. Johnson, H.A. Laitinen, Electroanalytical Chemistry of Molten Salts, in: Molten Salt Chemistry, John Wiley & Sons, 1964.

[160] D. Nattland, B.v. Blanckenhagen, R. Juchem, E. Schellkes, W. Freyland, Localized and mobile electrons in metal - molten-salt solutions, Journal of Physics: Condensed Matter, 8 (1996) 9309.

[161] A. Ravi Shankar, S. Mathiya, K. Thyagarajan, U. Kamachi Mudali, Corrosion and Microstructure Correlation in Molten LiCl-KCl Medium, Metallurgical and Materials Transactions A, 41 (2010) 1815-1825.

[162] P. Motsegood, in, 2015.

[163] S.-H. Cho, S.-B. Park, J.-H. Lee, J.-M. Hur, H.-S. Lee, Cyclic Corrosion Behavior of Ni-Based Superalloys in Hot Lithium Molten Salt, Oxidation of Metals, 78 (2012) 153-165.

[164] S.-H. Cho, J.-M. Hur, C.-S. Seo, S.-W. Park, High temperature corrosion of superalloys in a molten salt under an oxidizing atmosphere, Journal of Alloys and Compounds, 452 (2008) 11-15.

[165] M. Liu, J. Zheng, Y. Lu, Z. Li, Y. Zou, X. Yu, X. Zhou, Investigation on Corrosion Behavior of Ni-Based Alloys in Molten Fluoride Salt Using Synchrotron Radiation Techniques, Journal of Nuclear Materials, (2013).

[166] E. Mohammadi Zahrani, A.M. Alfantazi, Molten salt induced corrosion of Inconel 625 superalloy in PbSO4–Pb3O4–PbCl2–Fe2O3–ZnO environment, Corrosion Science.

[167] H.E. McCoy, R.L. Beatty, W.H. Cook, R.E. Gehlbach, C.R. Kennedy, J.W. Koger, A.P. Litman, C.E. Sessions, J.R. Weir, New Developments in Materials for Molten-Salt Reactors, Nuclear Applications & Technology, 8 (1969) 156.

[168] J.W. Koger, Evaluation of Hastelloy N alloys after nine years exposure to both a molten fluoride salt and air at temperatures from 700 to 560°C, in, Oak Ridge National Laboratory, 1972.

[169] J. H. E. McCoy, Status of Materials Development for Molten Salt Reactors, in, Oak Ridge National Laboraty, 1978.

[170] J.J. Roy, L.F. Grantham, D.L. Grimmett, S.P. Fusselman, C.L. Krueger, T.S. Storvick, T. Inoue, Y. Sakamura, N. Takahashi, Thermodynamic Properties of U, Np, Pu, and Am in Molten LiCl-KCl Eutectic and Liquid Cadmium, Journal of the Electrochemical Society, 143 (1996) 2487-2492.

[171] J.M. Hur, I.S. Kim, L. W. K, S.H. Cho, C.S. Seo, S.W. Park, A study of the stability of MgO in a LiCl-Li_2O molten salt system, Journal of Industrial and Engineering Chemistry, 10 (2004) 442-444.

[172] H.W. Jenkins, G. Mamantov, D.L. Manning, E.M.F. measurements on the nickel-nickel(II) couple in molten fluorides, Journal of Electroanalytical Chemistry and Interfacial Electrochemistry, 19 (1968) 385-389.

[173] C.G. Kontoyannis, Pyrolytic boron nitride coated graphite as a container of reference electrodes for molten fluorides, Electrochimica Acta, 40 (1995) 2547-2551.

[174] P.F. Tortorelli, O.K. Chopra, Corrosion and compatibility considerations of liquid metals for fusion reactor applications, Journal of Nuclear Materials, 103 (1981) 621-632.

[175] O.K. Chopra, P.F. Tortorelli, Compatibility of materials for use in liquid-metal blankets of fusion reactors, Journal of Nuclear Materials, 123 (1984) 1201-1212.

[176] Glassy Carbon Product Information, in, SPI Supplies.

[177] M. Anderson, K. Sridharan, T. Allen, Liquid Salt Heat Exchanger Technology for VHTR-based Applications: Final Report, in, University of Wisconsin – Madison, 2012.

[178] B. Mishra, D.L. Olson, Corrosion of Refractory Alloys in Molten Lithium and Lithium Chloride, Mineral Processing and Extractive Metallurgy Review, 22 (2001) 369-388.

[179] A. Merwin, D. Chidambaram, Corrosion of Inconel 625 in Molten LiCl-Li_2O-Li, Nuclear Technology, NT15-126R1 (in press) (2016).

[180] P. Masset, J.-Y. Poinso, J.-C. Poignet, Water uptake by salts during the electrolyte processing for thermal batteries, Journal of Power Sources, 137 (2004) 140-144.

[181] T. Gnanasekaran, R.K. Dayal, B. Raj, 10 - Liquid metal corrosion in nuclear reactor and accelerator driven systems, in: D. Féron (Ed.) Nuclear Corrosion Science and Engineering, Woodhead Publishing, 2012, pp. 301-328.

[182] Q. Xu, M. Kondo, T. Nagasaka, T. Muroga, M. Nagura, A. Suzuki, Corrosion characteristics of low activation ferritic steel, JLF-1, in liquid lithium in static and thermal convection conditions, Fusion Engineering and Design, 83 (2008) 1477-1483.

[183] Y.Z. Shen, K.H. Oh, D.N. Lee, Nitriding of steel in potassium nitrate salt bath, Scripta Materialia, 53 (2005) 1345-1349.

[184] H. Tsujimura, T. Goto, Y. Ito, Surface Nitriding of SUS 304 Austenitic Stainless Steel by a Molten Salt Electrochemical Process, Journal of the Electrochemical Society, 151 (2004) D67-D71.

[185] H. Dong, S-phase surface engineering of Fe-Cr, Co-Cr and Ni-Cr alloys, International Materials Reviews, 55 (2010) 65-98.

[186] J. Wang, Y. Lin, J. Yan, D. Zen, Q. Zhang, R. Huang, H. Fan, Influence of time on the microstructure of AISI 321 austenitic stainless steel in salt bath nitriding, Surface and Coatings Technology, 206 (2012) 3399-3404.

[187] Q. Jiapu, C. Jiming, C. Jinbiao, X. Zengyu, W. Weihao, P. Chuanjie, Corrosion of austenitic stainless steel in liquid lithium, Journal of Nuclear Materials, 179–181, Part 1 (1991) 603-606.

[188] M. Suzuki, I. Yamada, H. Kadowaki, F. Takei, A Raman scattering investigation of the magnetic ordering in the two-dimensional triangular lattice antiferromagnet $LiCrO_2$, Journal of Physics: Condensed Matter, 5 (1993).

[189] R.Y. Liu, X. Wang, J.S. Zhang, X.M. Wang, Corrosion of nickel in molten LiCl–Li_2O at 750 °C, Journal of Nuclear Materials, 327 (2004) 194-201.

[190] H. Lee, G.-I. Park, K.-H. Kang, J.-M. Hur, J.-G. Kim, D.-H. Ahn, Y.-Z. Cho, E.H. Kim, Pyroprocessing technology development at KAERI, Nuclear Engineering and Technology, (2011) 317-328.

[191] H.-Y. Lee, K.-H. Baik, Comparison of corrosion resistance between Al_2O_3 and YSZ coatings against high temperature LiCl-Li_2O molten salt, Metals and Materials International, 15 (2009) 783-787.

[192] S.-H. Cho, J.-M. Hur, C.-S. Seo, J.-S. Yoon, S.-W. Park, Hot corrosion behavior of Ni-base alloys in a molten salt under an oxidizing atmosphere, Journal of Alloys and Compounds, 468 (2009) 263-269.

[193] J.M. Hur, S.B. Park, C.S. Seo, K.J. Jung, S.W. Park, Melting and vaporization of salts in a U-LiCl-Li_2O system, Journal of Radioanalytical and Nuclear Chemistry, 270 (2006) 489-493.

[194] J.-M. Hur, S.-M. Jeong, H. Lee, Molten salt vaporization during electrolytic reduction, Nuclear Engineering and Technology, 42 (2010) 73-78.

[195] S.O. Kasap, Principles of Electronic Materials and Devices, Mc Graw Hill, 2006.

[196] N.H. Nachtrieb, Magnetic Susceptibility of some Liquid Metals, Molten Salts, and their Solutions The Journal of Physical Chemistry, 66 (1962) 1163-1167.

[197] S.R. Veličković, J.B. Djustebek, F.M. Veljković, B.B. Radak, M.V. Veljković, Formation and ionization energies of small chlorine-doped lithium clusters by thermal ionization mass spectrometry, Rapid Communications in Mass Spectrometry, 26 (2012) 443-448.

[198] S. Veličković, V. Djordjević, J. Cvetićanin, J. Djustebek, M. Veljković, O. Nešković, Ionization energies of Li_nX (n = 2, 3; X = Cl, Br, I) molecules, Rapid Communications in Mass Spectrometry, 20 (2006) 3151-3153.

[199] O.M. Nešković, M.V. Veljković, S.R. Veličković, L.T. Petkovska, A.A. Perić-Grujić, Ionization energies of hypervalent Li_2F, Li_2Cl and Na_2Cl molecules obtained by surface ionization electron impact neutralization mass spectrometry, Rapid Communications in Mass Spectrometry, 17 (2003) 212-214.

[200] L. Bengtsson, B. Holmberg, S. Ulvenlund, Fluorodilithium(1+) and hydroxodilithium(1+) in molten alkali-metal nitrate, Inorganic Chemistry, 29 (1990) 3615-3618.

[201] J. Xu, L. Chen, H. Choi, H. Konish, X. Li, Assembly of metals and nanoparticles into novel nanocomposite superstructures, Sci. Rep., 3 (2013).

[202] P. Juncar, J. Pinard, J. Hamon, A. Chartier, Absolute Determination of the Wavelengths of the Sodium D 1 and D 2 Lines by Using a CW Tunable Dye Laser Stabilized on Iodine, Metrologia, 17 (1981) 77.

[203] A. Kornath, A. Kaufmann, A. Zoermer, R. Ludwig, Raman spectroscopic investigation of small matrix-isolated lithium clusters, The Journal of Chemical Physics, 118 (2003) 6957-6963.

[204] L.B. Pankratz, Thermodynamic Properties of Halides, in, United States Department of the Interior, 1964.

[205] M.M. Makansi, C.H. Muendel, W.A. Selke, Determination of the Vapor Pressure of Sodium, The Journal of Physical Chemistry, 59 (1955) 40-42.

[206] F.W. Froben, W. Schulze, Raman Measurements of Matrix-Isolated Small Metal Clusters, Berichte der Bunsengesellschaft für physikalische Chemie, 88 (1984) 312-314.

[207] A. Briley, M.R. Pederson, K.A. Jackson, D.C. Patton, D.V. Porezag, Vibrational frequencies and intensities of small molecules: All-electron, pseudopotential, and mixed-potential methodologies, Physical Review B, 58 (1998) 1786-1793.

[208] I. Boustani, W. Pewestorf, P. Fantucci, V. Bonaić-Koutecký, J. Koutecký, Systematic *ab initio* configuration-interaction study of alkali-metal clusters: Relation between electronic structure and geometry of small Li clusters, Physical Review B, 35 (1987) 9437-9450.

[209] S. Ishii, K. Ohno, Y. Kawazoe, S.G. Louie, *Ab initio GW* quasiparticle calculation of small alkali-metal clusters, Physical Review B, 65 (2002) 245109.

[210] P. Dugourd, D. Rayane, P. Labastie, B. Vezin, J. Chevaleyre, M. Broyer, Measurements of lithium cluster ionization potentials, Chemical Physics Letters, 197 (1992) 433-437.

[211] W.A. de Heer, The physics of simple metal clusters: experimental aspects and simple models, Reviews of Modern Physics, 65 (1993) 611-676.

[212] A. Grassi, G.M. Lombardo, G.G.N. Angilella, N.H. March, R. Pucci, Equilibrium geometries of low-lying isomers of some Li clusters, within Hartree–Fock theory plus bond order or MP2 correlation corrections, The Journal of Chemical Physics, 120 (2004) 11615-11620.

[213] A.T. Davidson, K. Schwartz, J.D. Comins, A.G. Kozakiewicz, M. Toulemonde, C. Trautmann, Vacuum ultraviolet absorption and ion track effects in LiF crystals irradiated with swift ions, Physical Review B, 66 (2002) 214102.

[214] G. Krexner, M. Prem, F. Beuneu, P. Vajda, Nanocluster Formation in Electron-Irradiated Li_2O Crystals Observed by Elastic Diffuse Neutron Scattering, Physical Review Letters, 91 (2003) 135502.

[215] E.M. Ibragimova, M.A. Mussaeva, S.N. Buzrikov, Recombination gamma-luminescence at the nanometal Li – dielectric LiF interfaces, Radiation Physics and Chemistry, 111 (2015) 40-45.

[216] F. Beuneu, P. Vajda, O.J. Zogal, Li colloids created by electron-irradiation of LiF: A great wealth of properties, Nuclear Instruments and Methods in Physics Research Section B: Beam Interactions with Materials and Atoms, 191 (2002) 149-153.

[217] U. Beck, T. Koslowski, W. Freyland, Electronic structure of metal-molten salt solutions: Electron localization and the metal-non-metal transition, Journal of Non-Crystalline Solids, 205-207 (1996) 52-56.

[218] JCPDS, 01-072-7839, in, ICDD.

[219] A. Merwin, D. Chidambaram, The electroless deposition of titanium compounds on stainless steel alloy 316L in molten LiCl-Li_2O-Li, Applied Surface Science, (publication under development).

[220] C. Wu, Z. Wang, F. Wu, L. Chen, X. Huang, Spectroscopic studies on cation-doped spinel LiMn2O4 for lithium ion batteries, Solid State Ionics, 144 (2001) 277-285.

[221] I.E. Schreinlechner, P.F. Sattler, Contribution of minor steel constituents to the behaviour of stainless steels in liquid lithium, Journal of Nuclear Materials, 155–157, Part 2 (1988) 736-739.

[222] H.-S. Shin, J.-M. Hur, S.M. Jeong, K.Y. Jung, Direct electrochemical reduction of titanium dioxide in molten lithium chloride, Journal of Industrial and Engineering Chemistry, 18 (2012) 438-442.

[223] E. Setiawati, M. Hayashi, M. Takahashi, T. Shodai, K. Saito, Effect of annealing on the electrochemical properties of ramsdellite-type lithium titanium oxide, Journal of Power Sources, 196 (2011) 10133-10140.

[224] P.P. Edwards, R.G. Egdell, I. Fragala, J.B. Goodenough, M.R. Harrison, A.F. Orchard, E.G. Scott, A study of the spinel materials $LiTi_2O_4$ and $Li_{43}Ti_{53}O_4$ by photoelectron spectroscopy, Journal of Solid State Chemistry, 54 (1984) 127-135.

[225] M.V. Reddy, N. Sharma, S. Adams, R.P. Rao, V.K. Peterson, B.V.R. Chowdari, Evaluation of undoped and M-doped TiO_2, where M = Sn, Fe, Ni/Nb, Zr, V, and Mn, for lithium-ion battery applications prepared by the molten-salt method, RSC Advances, 5 (2015) 29535-29544.

[226] T. Ebina, T. Iwasaki, Y. Onodera, H. Hayashi, T. Nagase, A. Chatterjee, K. Chiba, Ab initio study on the topological Li insertion in titanium oxide, Journal of Power Sources, 81–82 (1999) 393-396.

[227] N. Wang, C. Cheng, J. Tian, S. Hu, H. Zhang, T. Jiang, Hot-corrosion behavior of Ti3SiC2 in a eutectic mixture of LiCl-KCl salts in air, RSC Advances, 5 (2015) 21629-21633.

[228] M. Łapinski, B. Kościelska, A. Winiarski, W. Sadowski, XPS Study of Superconducting $LiTi_2O_4$ and $LiTi_{2-x}Cu_xO_4$ Sol-Gel Derived Powders and Thin Films, Acta Physica Polonica A, 126 (2014).

[229] L.-Q. Wang, D.R. Baer, M.H. Engelhard, Creation of variable concentrations of defects on TiO_2 (110) using low-density electron beams, Surface Science, 320 (1994) 295-306.

[230] S. Södergren, H. Siegbahn, H. Rensmo, H. Lindström, A. Hagfeldt, S.-E. Lindquist, Lithium Intercalation in Nanoporous Anatase TiO_2 Studied with XPS, The Journal of Physical Chemistry B, 101 (1997) 3087-3090.

[231] D. Jaeger, J. Patscheider, A complete and self-consistent evaluation of XPS spectra of TiN, Journal of Electron Spectroscopy and related Phenomena, 185 (2012) 523-534.

[232] C. Li, X. Lv, J. Chen, X. Liu, C. Bai, Kinetics of titanium nitride synthesized with Ti and N_2, International Journal of Refractory Metals and Hard Materials, 52 (2015) 165-170.

[233] H.A. Wriedt, J.L. Murray, The N-Ti (Nitrogen-Titanium) system, Bulletin of Alloy Phase Diagrams, 8 (1987) 378-388.

[234] M.L. Kyle, R.D. Pierce, L.F. Coleman, J.D. Arntzen, Removal of Nitrogen from Argon with Titanium-Metal Sponge, Industrial & Engineering Chemistry Process Design and Development, 7 (1968) 447-453.

[235] Y. Ito, T. Nohira, Non-conventional electrolytes for electrochemical applications, Electrochimica Acta, 45 (2000) 2611-2622.

[236] T. Goto, M. Tada, Y. Ito, Electrochemical surface nitriding of titanium in molten salt system, Electrochimica Acta, 39 (1994) 1107-1113.

A2 Long term exposure of stainless steel and Inconel with $LiCl\text{-}Li_2O\text{-}Li^0$

Table of Contents

Introduction 2
Experimental 2
Development of high-throughput long term exposure capabilities 2
Li evaporation study 3
Methods and Experimental Design 5
Results and Discussion 9
Gravimetric Analysis 9
XRD 11
SEM-EDS 24
Micro-Vickers Hardness Testing 39
Raman 40
XPS 51
Inductively Coupled Plasma – Optical Emission Spectroscopy 62
Conclusions and Future Work 62
References 65

Introduction

To verify the findings of our short term exposure experiments, expand on the understanding of the corrosion mechanisms that occur in LiCl-Li_2O-Li solutions, and give an estimate of corrosion rates in this environment, long term exposure experiments were conducted. For this study, SS316L and I625 samples were exposed to LiCl containing 1 or 2wt%Li_2O and 0, 0.3, 0.6, or 1wt%Li for 500 or 1000hr at 650°C. In total, 16 unique conditions were studied for each material. Post exposure surface analysis was performed using X-ray diffraction (XRD), scanning electron microscopy (SEM) with energy dispersive X-ray spectroscopy (EDS), micro-Vickers hardness testing, Raman spectroscopy, and X-ray photoelectron spectroscopy. The corrosion rate was calculated via gravimetric analysis, and the relative dissolution rates of alloying elements into the salt was examined using inductively coupled plasma – optical emission spectroscopy (ICP-OES) of the dissolved salt ingots.

Experimental

All experiments were performed in an Ar atmosphere contained within a Vacuum Atmospheres glovebox. O_2 and H_2O concentrations were maintained at less than 5pmm, and typically less than 1ppm each over the course of the exposures.

Development of high-throughput long term exposure capabilities

In order to increase the consistency and expediency of long term exposure testing, the experimental apparatus were constructed to allow for multiple exposures to be ran in parallel. For this purpose, a custom graphite block was machined for the purpose of positively locating both the Ni crucibles used to hold the molten LiCl-Li_2O-Li solution as well as the exposure samples suspended within the melt. Figure 1a shows a computer generated drawing of the furnace assembly, while Figure 1b shows the finished assembly within the glovebox in operation. Not shown is a stainless steel lid that is used to prevent contamination of the solutions and limit the rate of evaporation of Li from the system.

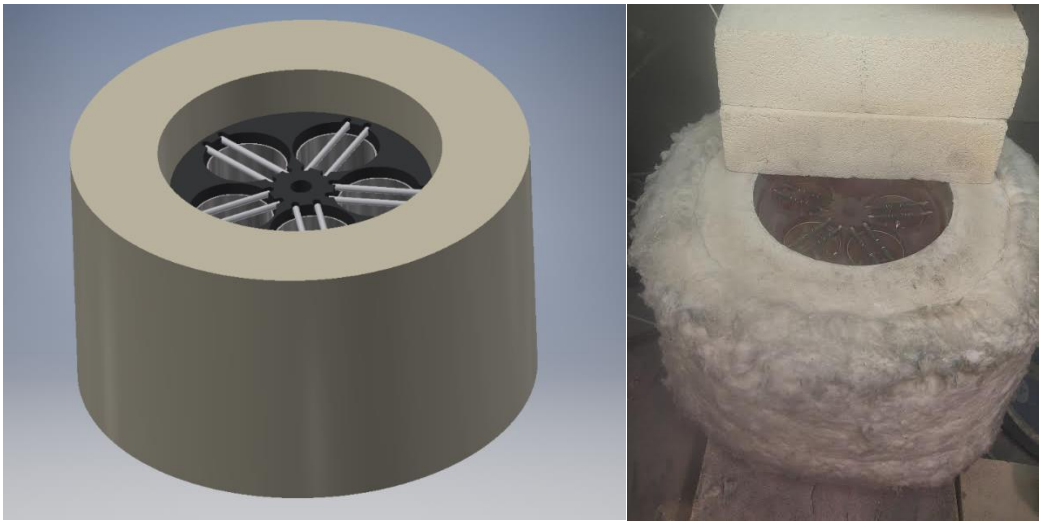


Figure 1: A) Computer generated model of the long term exposure furnace, graphite crucible holder, Ni crucibles, and sample hanging rods (left). Furnace diameter is 6.5" and the Ni crucibles are XX" in diameter. B) The same furnace assembly installed and in operation inside one of the Ar gloveboxes at UNR. Not shown is the SS304 lid used to prevent contamination of the molten salt solutions and escape of Li vapors.

Two of these assemblies were constructed in independent gloveboxes, for a total of 10 crucible locations. In operation with the current set of experiments, 8 of these locations are in use simultaneously to allow for one slot to remain available for salt replacement purposes. Details of the experimental design and salt replacement procedure are given below.

Li evaporation study

In our previous exposure studies, the required mass of Li and Li_2O necessary to achieve a desired melt composition were added at the beginning of the experiment 1 hour prior to the immersion of the samples. Due to the reactive and volatile nature of metallic Li at the operating temperature of 650°C, the mass of metallic Li present in the initial salt charge is depleted over time if no additional action is taken. In our previous work, the length of exposure (20-100 hours) was short enough to allow the depletion of Li to be negated. However, as the primary objective of the present study is to investigate the effects of metallic Li on container materials in the LiCl-Li_2O system over exposure periods of 500 and 1000 hours, it was deemed necessary to replenish the Li periodically to maintain the desired Li concentration. To ensure the accuracy of the salt composition, it was determined that the entire salt

charge would be replaced periodically, and the addition of make-up Li to the existing melt was to be avoided.

To determine the frequency with which the salt must be replaced for these exposures, the evaporation rate of Li in our system was qualitatively observed by calculating the Li concentration in LiCl based on the volume of H_2 gas generated upon reaction of a salt sample with water. This was performed by sampling the salt using a graphite dipstick, weighing the salt sample, and measuring the H_2 volume generation upon reaction with water using the apparatus shown in Figure 2.

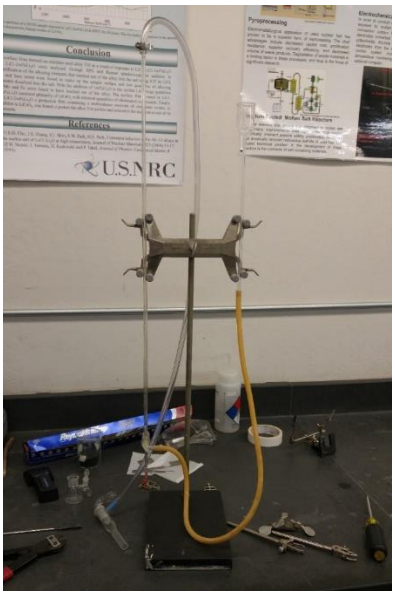


Figure 2: Gas measurement apparatus used for determination of H_2 volume generated from reaction of Li with H_2O. The salt sample is placed in a sealed reaction vessel with 10mL of DI H_2O that is connected via a flexible tube to the top of a 5mL burette, which is filled with water. The pressure inside the closed system is maintained at atmospheric pressure via a movable reservoir connected to the bottom of the burette via a second piece of flexible tubing.

The sample masses were recorded to 1 mg precision, and the burette used for measuring the volume of H_2 produced was accurate to 0.05 ml. The calculation of the mass of Li necessary to evolve the volume of gas produced was performed using the ideal gas law, accounting for the atmospheric pressure in Reno, NV and the temperature of the laboratory, and assuming complete reaction according to the equation:

$$2Li(s) + 2H_2O(l) \rightarrow 2LiOH(aq.) + H_2(g)$$

The conversion factor was updated daily based on barometric pressure data from the National Weather Service. The value of the conversion factor varied between 0.484 and 0.488 mg Li/mL H_2 over the course of the study. The results of this analysis are shown in Figure 3. It is important to note that the solubility limit of Li in LiCl is approximately 0.3wt%, but is not well defined due to the possibility of multiple dissolution mechanisms [1, 2]. This accounts for the upper limit of around 0.35wt%Li observed, and the high variance associated with the measurements at high Li concentrations.

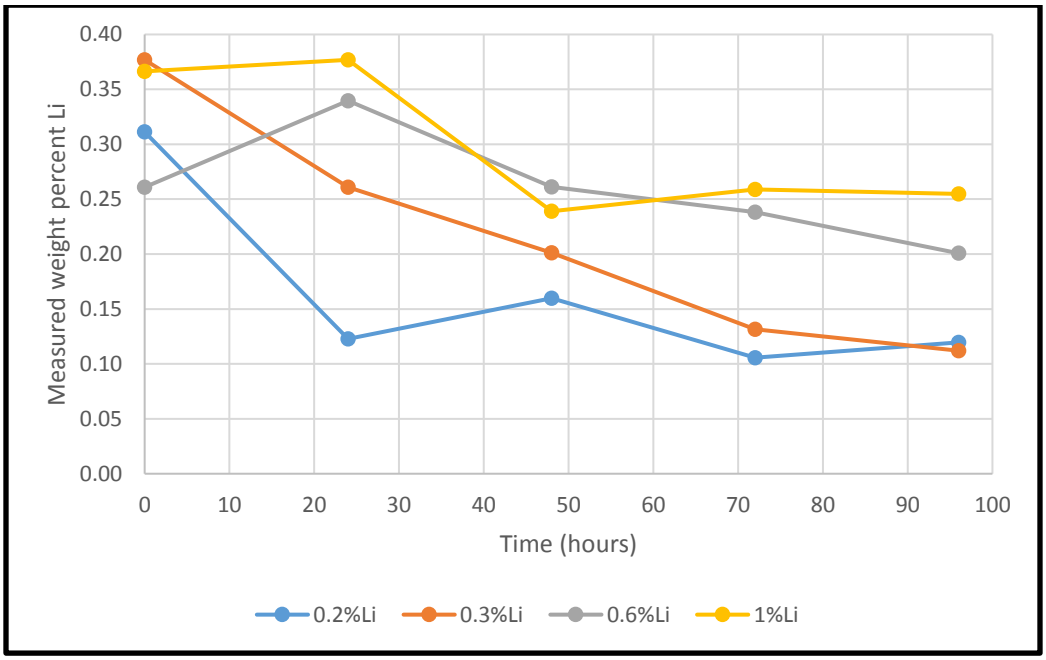


Figure 3: Measured Li concentration vs. time for four initial starting compositions of Li.

Methods and Experimental Design

SS316L and I625 samples were cut from 1/8" thick plate into ½" by ½" squares using a computer controlled CO_2 laser, as was done for our previous exposure studies. The alloys were obtained from McMaster-Carr and are of the composition given in Table 1, below. The samples were prepared by polishing to a mirror finish on both sides with 1 µm diamond abrasive. Hooks for hanging the samples at the correct location in the melt were fabricated by spot welding wire loops of the same material to both

sides of each sample. The second hook was added for redundancy and prevented the samples from being lost should a single spot weld fail. Prior to exposure, each sample was engraved on the edge to allow for identification, and the mass was recorded to mg precision.

Table 1: Elemental compositions for the alloys used in this study.

Alloy	Fe	Cr	Ni	Mo	Mn	C	Al	Ti	Si
SS316L	Bal	16.5	10	2	1.3	0.014			
I625	5	20-23	58	8.0-10	0.5		0.4	0.4	0.5

For exposure, the samples were suspended from rods of similar material to the samples. These rods are positively located above the crucibles via slots machined into the lip of the graphite, as shown in Figure 1. Initially, alumina rods were used for this purpose to prevent galvanic coupling of the samples and the crucible, however, this material was not able to withstand the extremely reducing atmosphere present above the high Li content melts, which resulted in the failure of several tests within 3 days of initial exposure. This reaction was much more severe than was observed for alumina parts used in previous studies, and is hypothesized to be a result of the partially sealed nature of the crucible wells in the graphite block with the SS lid in place, which lead to a highly reducing atmosphere of concentrated metallic Na and Li vapors. Currently, a suitable ceramic material for this extremely reducing environment is not known. Analysis of the degradation of ceramic materials in the conditions experienced during the electroreduction of oxide nuclear fuel is a planned future study, and is necessary for the development of stable reference electrodes for the system. An image of the degradation of the Al_2O_3 rods that were initially used for sample placement is shown in Figure 4, below.



Figure 4: Degradation of Al_2O_3 sample suspension rod following 3 days of exposure to the vapor phase above a LiCl-2wt%Li_2O-1wt%Li solution at 650°C. The degradation was severe enough to cause complete failure of 6 out of 8 rods in 3 days and consequently required the exposure tests to be restarted. The degradation is most severe directly above the center of the crucible, while the ends are relatively unaffected, as they were shielded from direct exposure to the vapor phase by the graphite block in which they were positioned. Due to this severe degradation, the rods were replaced with metallic rods of similar materials to the samples, i.e. SS316L for SS316L, and I625 for I625. Also visible here is the sample coupon geometry used for long term exposure testing.

Based on the results of the Li evaporation study and the logistics of operating the furnace apparatus, the salt replacement interval was set at once every 96 hours for each test. All masses for the chemicals used for the salt replacements were measured to an accuracy 5mg or better, and the total mass of each salt charge was held at 50g. For these experiments, each furnace was operated with 4 of the 5 crucible locations occupied at any one time, with the 5th reserved for salt replacement purposes. Therefore, the salt could be replaced for one out of the four experiments being performed in each furnace on any given day, without the need to shut down the furnace or allow the samples to appreciably cool before being re-submerged in the fresh salt. The movement of the samples between crucibles was quick enough that salt solidification was not typically observed on the surface of the samples.

Impurity H_2O was removed from the replacement salt by baking the necessary mass of LiCl for 2 hours in a dedicated 3" diameter furnace set to 550°C. The salt was then transferred to the empty location in the graphite crucible holder, where it was allowed to heat to the furnace temperature of 650°C for 1 hour. The required masses of Li_2O and Li for each test were then added to the molten LiCl, and the resulting solution was again allowed to equilibrate for 1 hour prior to transferring the samples from the old salt melt to the new melt. The crucible containing the old salt melt was then removed from the furnace and allowed to cool to room temperature overnight. The cooled salt ingot was dissolved in 750ml of 18 MΩ DI water the following day. 65mL of the resulting solution was collected, labeled, and stored for future analysis via ICP-OES.

The crucibles used for these studies were Ni crucibles of 99% purity obtained from Alfa Aesar, and are identical to those used for our previous work. For each material and salt composition, two crucibles were alternated between. Once the salt ingot was dissolved, the crucibles were sanded using 600 grit SiC paper, cleaned with isopropyl alcohol, dried with a heat gun, and placed under vacuum in the glovebox transfer chamber before being reused for the next salt change. In total, 11 salt replacements were conducted for each material/salt composition combination over the course of the 1000hr exposure period.

Following exposure, the samples were removed from the furnace and allowed to cool overnight inside the glovebox. The duplicate sample for each condition was reserved for future studies at this point. These reserve samples are being stored in the Ar glovebox inside labeled and sealed plastic bags and will be used in the event of damage to the sample used for surface analysis. The samples to be analyzed were then baked at 650°C for 2 hours to redistribute the residual salt layer and facilitate surface analysis, as was demonstrated to be effective in our previous short term exposures. However, the usefulness of this technique was diminished for the long term exposures due to the increased surface roughness resulting from the increased exposure period, as is discussed below. Consequently,

the samples were each rinsed with 25mL of ACS reagent grade methanol for 15 minutes with continuous agitation to remove the residual salt layer. We have verified this method to effectively remove the residual salt layer without affecting the surface chemistry or morphology of the samples, and the details of this verification are given below. Following methanol rinsing, post exposure surface analysis was performed again for each sample. The use of the methanol rinsing procedure has allowed for the collection of much higher quality data than was otherwise possible.

Results and Discussion

The results presented here were selected to highlight the observations made during the course of this study. Due to the large quantity of spectra and images obtained for this work, additional information that supports these observations is included in the Appendices at the end of this report. Additionally, critical analysis of all of the data collected thus far is not yet complete, meaning that the results presented here are preliminary in nature.

Gravimetric Analysis

As stated previously, the initial mass of each sample was recorded prior to the start of exposure testing. Following methanol rinsing, the mass of each sample was again recorded using the same balance as used for the initial mass measurements. As the duplicate sample for each exposure condition is currently being reserved for future analysis, only half of the samples have had their final mass recorded, and the statistics of these measurements are consequently less accurate than will be possible once all samples have been analyzed. The surface area of the samples exposed to the molten LiCl-Li_2O-Li solutions was calculated for each sample based on the submerged depth. Overall, the mass loss was very low, with some samples experiencing minor weight gain. The corrosion rate for each sample was calculated based on the mass loss, the density of the base alloy, the surface area exposed to the LiCl-Li_2O-Li solution, and the exposure period. The maximum corrosion rate observed in this study was for

the SS316L sample exposed to LiCl-1wt%Li_2O-1wt%Li for 500hr, where the corrosion rate was 0.665mm/year. This particular sample's measured corrosion rate was well above the average corrosion rate observed for all SS316L samples which was 0.115mm/year with a standard deviation of 0.161mm/year. The maximum corrosion rate for I625 was observed on the sample exposed to LiCl-1wt%Li_2O-0.3%Li for 500hr, where the corrosion rate was 0.558mm/year. Again, this sample was well above the average corrosion rate of 0.122mm/year for all I625 samples, with a standard deviation of 0.176mm/year. The high variance observed is thought to be a result of the relatively low corrosion rates and correspondingly low absolute weight change per sample, which was on the order of 10s of mg for most samples. No overall trend in corrosion rate as a function of material, Li_2O concentration, Li concentration, or exposure period was observed. The calculated corrosion rates for each sample recorded thus far are listed below in Table 2.

Table 2: Calculated corrosion rates for SS316L and I625 samples exposed to LiCl-Li_2O-Li solutions at 650°C for 500hr and 1000hr. Positive corrosion rates indicate weight loss, while negative corrosion rates indicate weight gain. The I625 sample exposed to LiCl-1wt%Li_2O-0.3wt%Li for 1000hr was dropped into the main chamber of our XPS following data collection, but prior to weight loss measurements. This sample will be retrieved during maintenance of the system and measured at that time.

Material	Wt% Li2O	Wt% Li	Exposure (hr)	Corrosion Rate (mm/year)
SS316L	1	0	500	-0.005
SS316L	1	0.3	500	0.211
SS316L	1	0.6	500	0.126
SS316L	1	1	500	0.665
SS316L	2	0	500	0.115
SS316L	2	0.3	500	0.055
SS316L	2	0.6	500	0.016
SS316L	2	1	500	-0.134
SS316L	1	0	1000	0.050
SS316L	1	0.3	1000	0.062
SS316L	1	0.6	1000	0.179
SS316L	1	1	1000	0.112
SS316L	2	0	1000	0.082
SS316L	2	0.3	1000	0.130
SS316L	2	0.6	1000	0.101
SS316L	2	1	1000	0.073
I625	1	0	500	-0.080
I625	1	0.3	500	0.558
I625	1	0.6	500	-0.024
I625	1	1	500	0.444
I625	2	0	500	0.057
I625	2	0.3	500	0.066
I625	2	0.6	500	0.107
I625	2	1	500	0.227
I625	1	0	1000	0.196
I625	1	0.3	1000	*
I625	1	0.6	1000	-0.106
I625	1	1	1000	0.215
I625	2	0	1000	0.040
I625	2	0.3	1000	0.045
I625	2	0.6	1000	0.027
I625	2	1	1000	0.061

XRD

X-ray diffraction was performed using a Rigaku Smartlab diffractometer with a Cu kα source operating at 44kV and 40mA. Parallel beam optics in a grazing incidence angle configuration were used to allow for detection of the surface films formed on the samples as a result of exposure to LiCl-Li_2O-Li

solutions. Data collection was performed prior to and following the methanol rinsing procedure for each sample. Prior to methanol rinsing, XRD was performed with the sample in a plastic bag, which was sealed inside the Ar atmosphere of the glovebox to prevent atmospheric contamination of the sample. This technique was identical to that used for XRD collection in our short term studies. Following methanol rinsing, XRD patterns were collected with the sample in open air, which allowed for the use of the automated thin film precise measurement technique available in the Smartlab software suite. This technique first performs a quick preliminary scan to detect the locations and intensity of the diffraction peaks for a particular sample, and then optimizes the step size and scan speed to maximize the resolution of the final collected data. The step size was chosen to be 1/5 the full width at half maximum (FWHM) of the narrowest peak, while the scan speed was chosen to result in a total of 5000 counts at the peak of the most intense peak. Diffraction patterns were recorded from 10°-90° 2θ, with an incidence angle of 1°. This technique allowed for the collection of very high resolution diffraction patterns of the corrosion products formed on the samples.

Prior to methanol rinsing, the dominant features of the diffraction patterns were the residual salt phase and the base material. The presence of both FCC (γ) to BCC (α) iron was observed on some SS316L samples, indicating the de-austenization of the base material. The degradation of the base material had been observed in our previous work with short term exposures of SS316L to the LiCl-Li_2O-Li system, and was observed on other SS316L samples in this study, as shown below. No correlation between the exposure period or the concentrations of Li_2O and Li could be drawn. We hypothesize that the de-austenization observed is a combined effect of corrosion and temperature induced segregation, but more work is necessary to confirm this. For the SS316L samples exposed to LiCl-2wt%Li_2O containing no Li for 500 and 1000 hours, a peak at 18.4° 2θ was observed, which correlates to similar observations from our previous short term exposures where we identified this peak as being indicative of the (003)

plane of $LiCrO_2$ [3]. The diffraction patterns of SS316L samples exposed to LiCl-2wt%Li_2O solutions containing various quantities of Li for 500hr and 1000hr are shown in Figures 5 and 6, respectively.

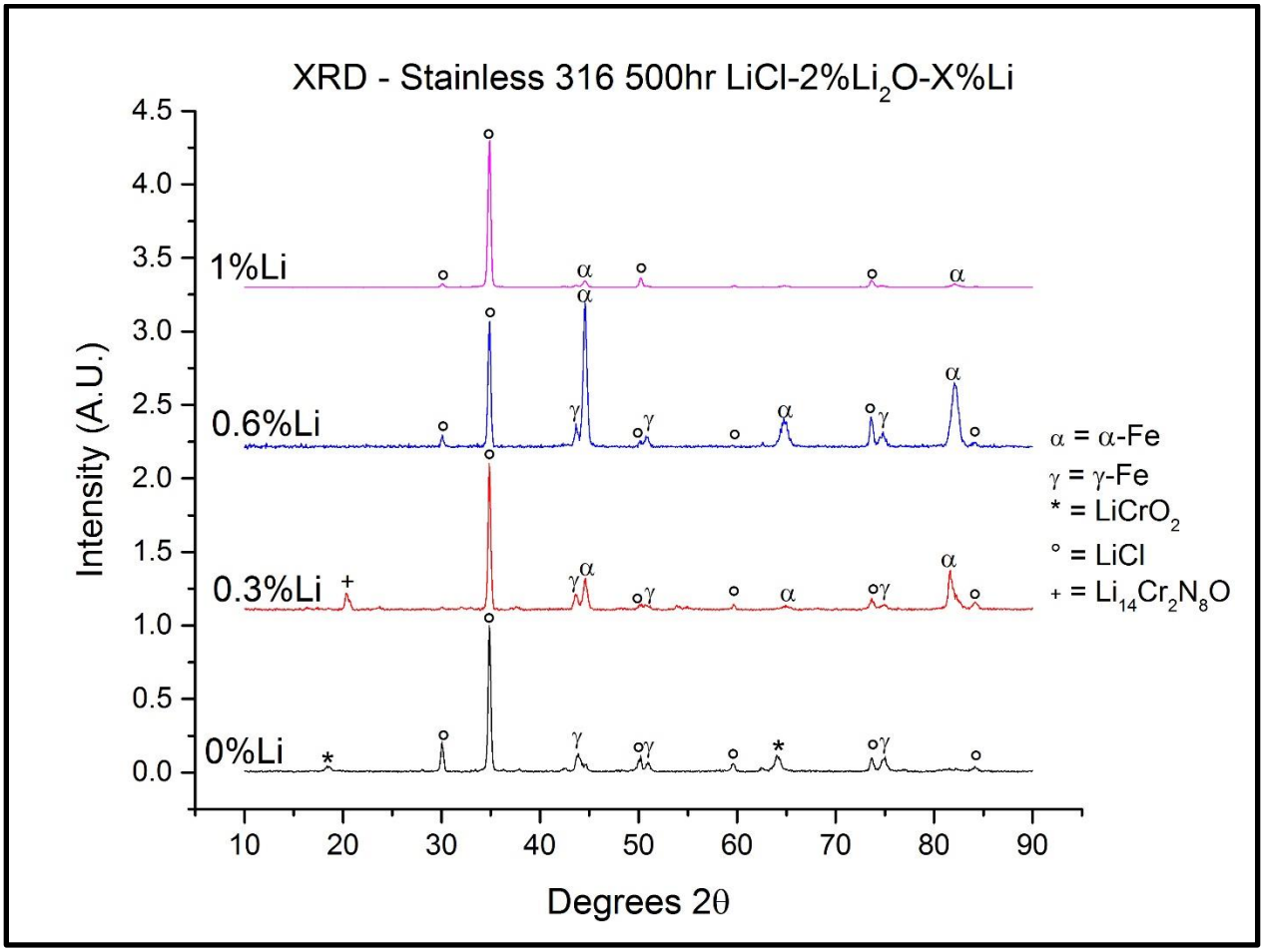


Figure 5: XRD patterns for SS316L samples exposed to LiCl-2wt%Li_2O containing 0, 0.3, 0.6, and 1wt% Li for 500 hours.

For the SS316L sample exposed to LiCl-2wt%Li_2O-0.3wt%Li for 500 hours, a peak at 20.6° 2θ was observed. This observation correlates with the Raman feature observed at 864cm^{-1} on the same sample prior to methanol rinsing and SEM-EDS observations of this area which show high nitrogen, oxygen, and chromium content as well as a unique surface morphology. The results from Raman spectroscopy and SEM-EDS are presented in their respective sections, however, the combination of these techniques possibly indicates a lithium-chromium-oxynitride layer. This correlates well with PDF card number 01-079-1125 for $Li_{14}Cr_2N_8O$, whose most prominent peak is located at 20.68° 2θ. These features were not

observed on any other sample, including the 1000hr sample exposed to the same conditions. This sample was also unique in that the surface layer was mechanically removed during the methanol rinsing procedure, indicating that the compound was not well bonded to the base material. As shown below in Figure 10, XRD of this sample following methanol rinsing detected the peak for $Li_{14}Cr_2N_8O$; however, its intensity was very low, indicating that the majority of the compound was indeed removed during the methanol rinsing procedure. Further analysis of the reserve sample exposed in parallel with this sample is planned for the future to positively identify the compound unique to these samples. As the gloveboxes in our laboratory do not actively monitor or scrub N_2 in their atmospheres, this is the likely source for the nitrogen in this compound. We have observed similar gettering of N from the glovebox atmosphere via XPS both in this work and in our previous studies, where thin titanium oxynitride films on the surface of samples exposed to LiCl-Li_2O-Li solutions have routinely been detected due to impurity TiO_2 in Li_2O. As $Li_{14}Cr_2N_8O$ was only detected on this particular sample, the mechanism for its formation is unknown.

The length of exposure did not appear to have an appreciable difference on the diffraction patterns. The diffraction patterns for SS316L samples exposed to LiCl-2wt%Li_2O solutions containing 0, 0.3, 0.6, and 1wt% Li for 1000hr, shown in Figure 6, show the presence of LiCl and the base material under all conditions, and additionally $LiCrO_2$ in the absence of Li. The primary difference is the absence of the peak at 20.6° on the diffraction pattern obtained from the SS316L sample exposed to LiCl-2wt%Li_2O-0.3wt%Li for 1000hr that was observed on the SS316L sample exposed to identical conditions for 500hr. Similar diffraction patterns were obtained for SS316L samples exposed to LiCl-1wt%Li_2O solutions. For brevity, the diffraction patterns obtained for SS316L samples exposed to LiCl-1wt%Li_2O solutions containing 0, 0.3, 0.6, and 1wt%Li for 500hr and 1000hr are shown in Figures A1 and A2 in Appendix A.

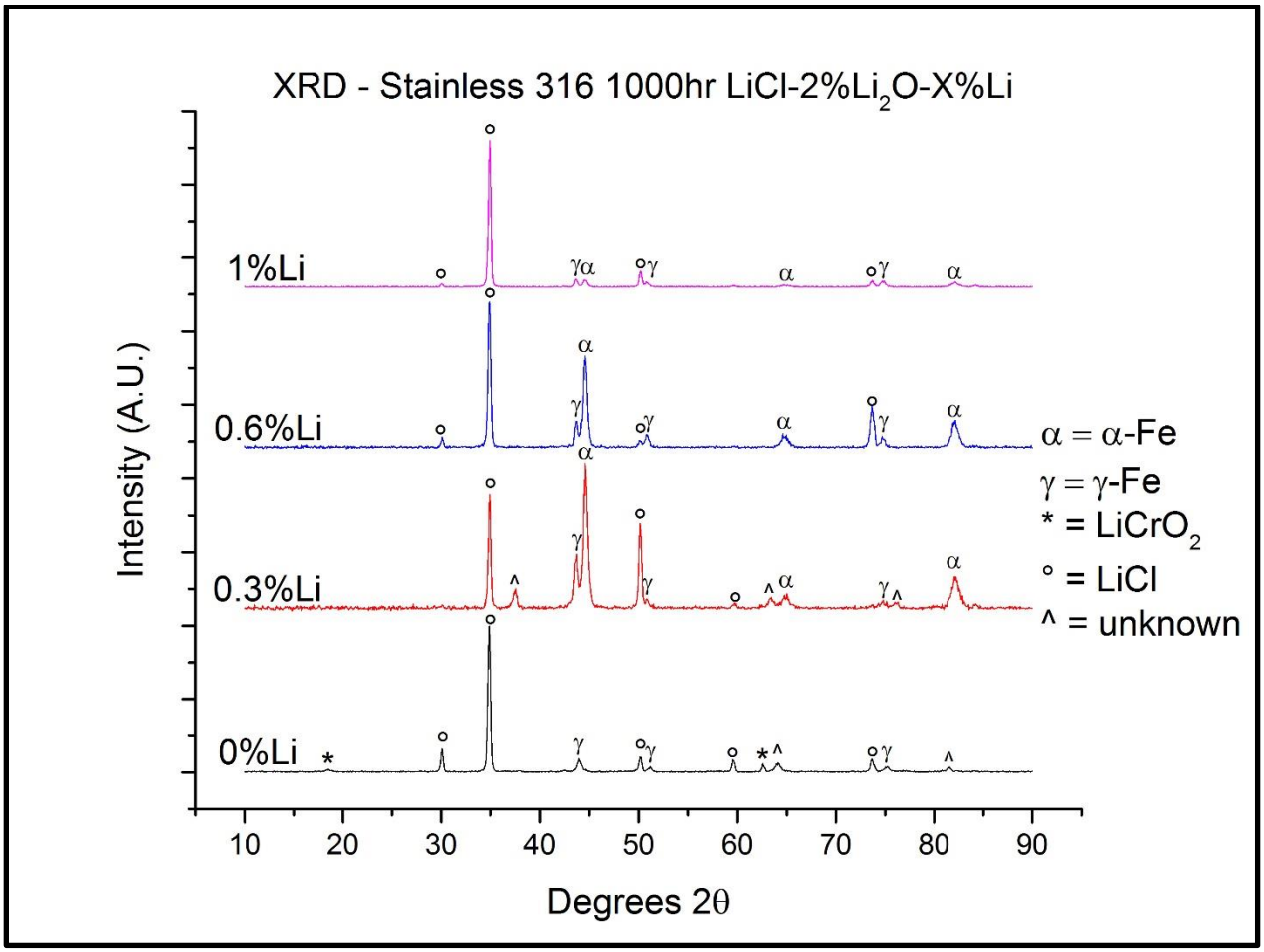


Figure 6: XRD patterns for SS316L samples exposed to LiCl-2wt%Li_2O containing 0, 0.3, 0.6, and 1wt% Li for 1000 hours.

XRD analysis of the I625 samples prior to methanol rinsing showed similar trends as with SS316L samples. Figures 7 and 8 show the XRD patterns collected for I625 samples exposed to LiCl-2wt%Li_2O containing 0, 0.3, 0.6, and 1wt%Li for 500 hours and 1000 hours, respectively. As with SS316L, peaks characteristic of the base alloy and LiCl were observed on all samples, and the peak characteristic of $LiCrO_2$ at 18.4° 2θ was observed on both 500 and 1000 hour samples exposed to LiCl-2wt%Li_2O containing no Li. The diffraction patterns obtained for I625 exposed to LiCl-1wt%Li_2O containing 0, 0.3, 0.6, and 1wt%Li for 500 and 1000hr are shown in Figures A3 and A4 in Appendix A.

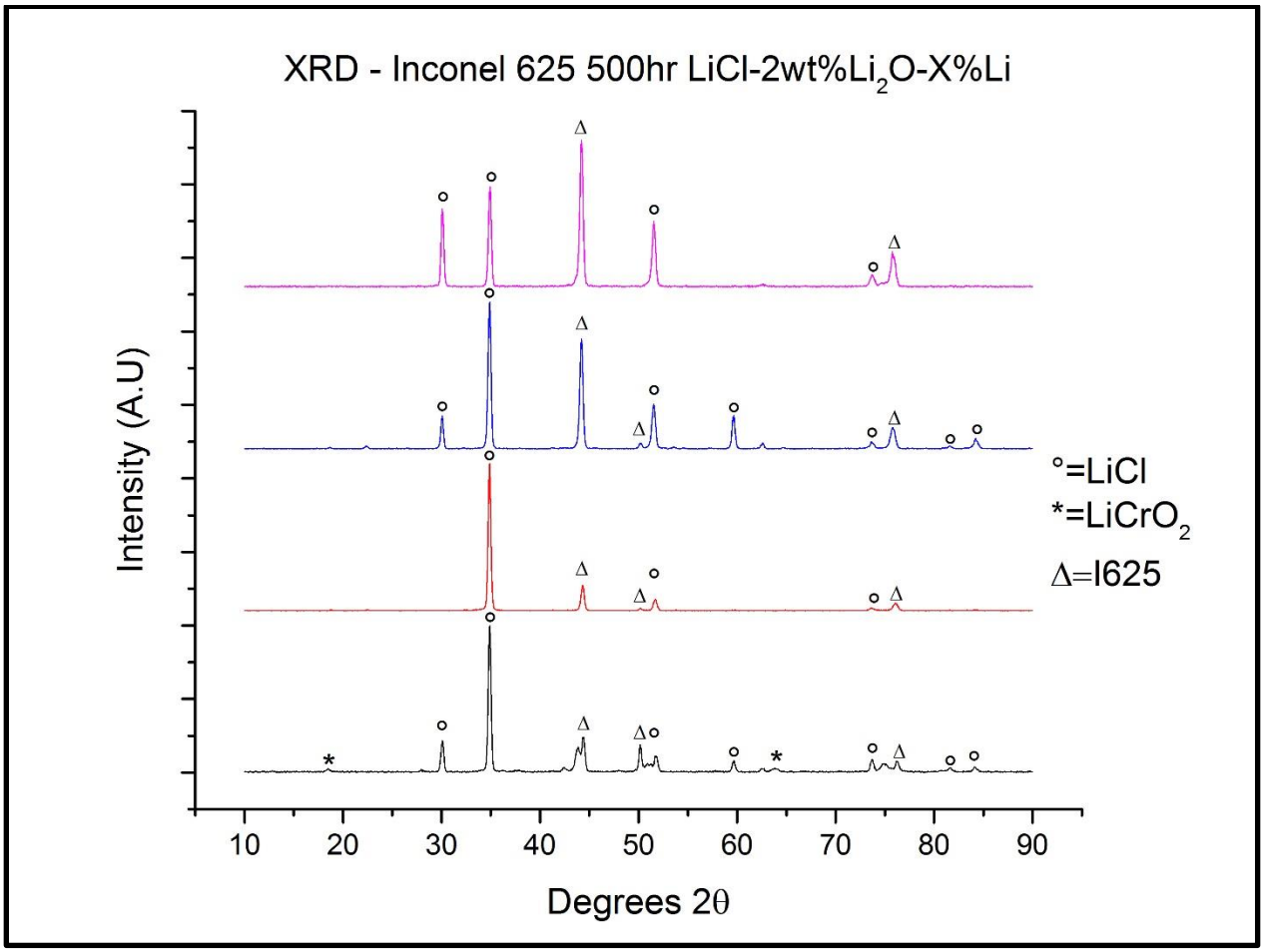


Figure 7: XRD patterns for I625 samples exposed to LiCl-2wt%Li_2O containing 0, 0.3, 0.6, and 1wt% Li for 500 hours.

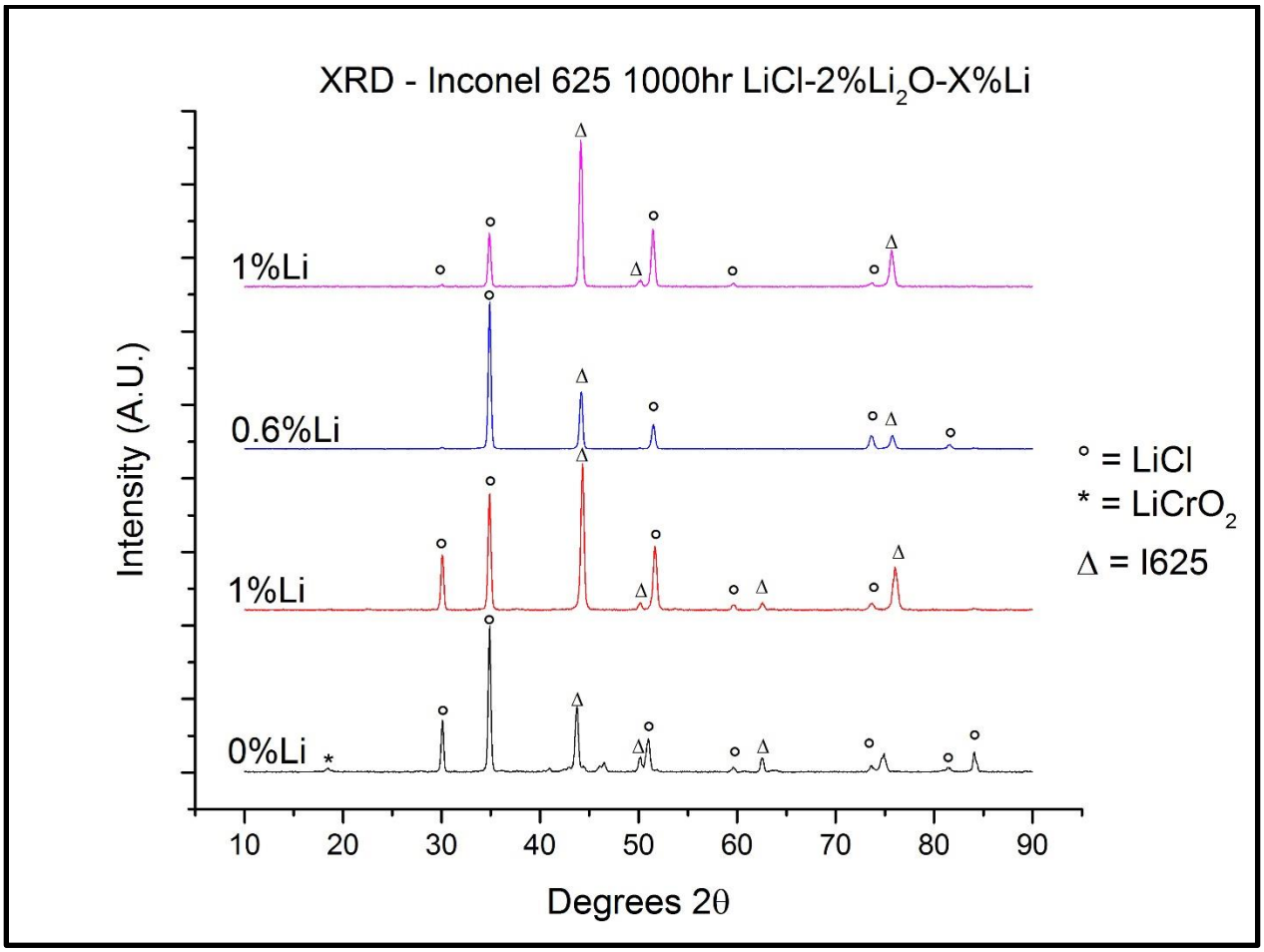


Figure 8: XRD patterns for I625 samples exposed to LiCl-2wt%Li_2O containing 0, 0.3, 0.6, and 1wt% Li for 1000 hours.

After surface analysis had been completed with the salt layer intact and the methanol rinsing procedure had been performed, hi-resolution XRD patterns were collected for all samples exposed to LiCl-1wt%Li_2O solutions. Data collection for samples exposed to LiCl-2wt%Li_2O solutions is currently in progress. For these patterns, the diffractometer was operated using the thin-film precise measurement routine described above. Figure 9 shows the high resolution diffraction pattern obtained for SS316L exposed to LiCl-1wt%Li_2O-0wt%Li at 650°C for 500hr. The removal of the salt layer and the increased resolution of the thin-film precise measurement profile meant that it was possible to resolve all of the

peaks characteristic of $LiCrO_2$ in the scan range of 10°-90° 2θ, based on PDF card number 01-072-7839. Peaks characteristic of the base material were also observed. No other phases were detected on the sample surface, indicating that the $NiFe_xCr_{2-x}O_4$ and Li_2CrO_4 phases predicted by Raman spectroscopy, SEM-EDS, and XPS observations presented below are minor components of the oxide layer present on samples exposed to LiCl-Li_2O solutions in the absence of Li.

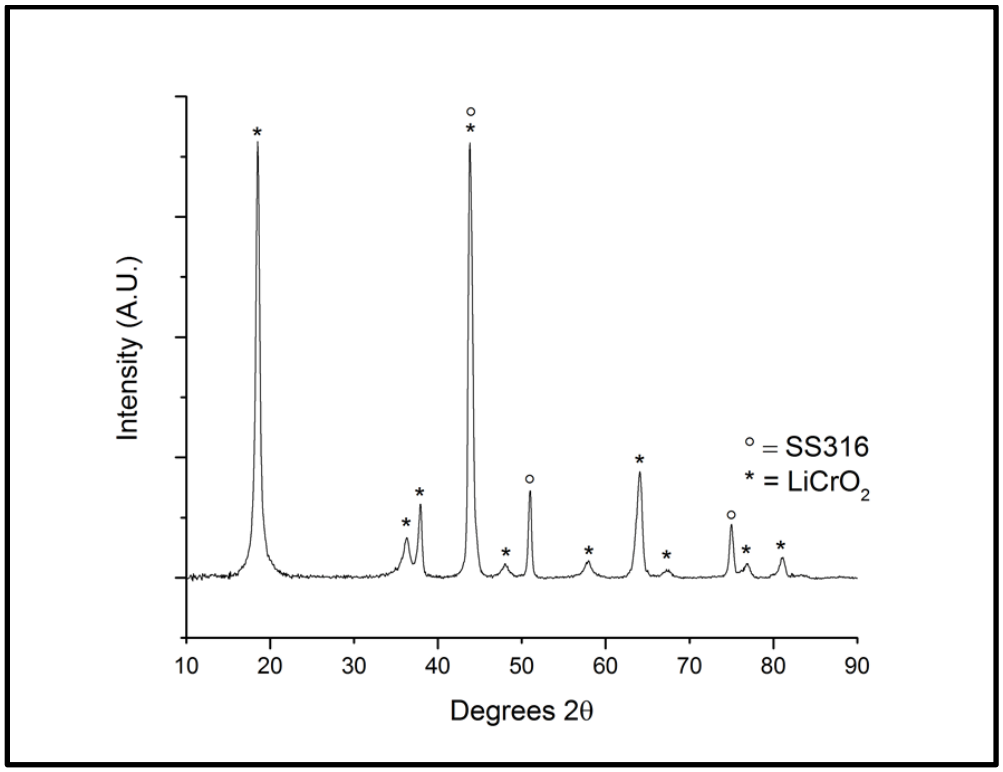


Figure 9: Hi-resolution grazing incidence X-ray diffraction pattern of SS316L exposed to LiCl-2%Li_2O-0%Li for 500hr after methanol rinsing. Peaks corresponding to $LiCrO_2$ (*) and the base material (°) were observed. Resolution of the minor peaks of $LiCrO_2$ was made possible due to the removal of the residual salt layer, and this is the first time that these minor peaks have been observed on any sample studied in the LiCl-Li_2O system. This pattern confirms that the oxide layer formed on SS316L exposed to LiCl-Li_2O in the absence of Li is primarily composed of $LiCrO_2$.

Figure 10 shows the hi-resolution X-ray diffraction pattern obtained for SS316L exposed to LiCl-2wt%Li_2O-0.3wt%Li at 650°C for 500hr after methanol rinsing. Two minor peaks were also observed at 21.2° and 37.8° 2θ. The peak at 21.2° correlates to the peak observed at 20.6° on this sample prior to methanol rinsing discussed above, but with significant loss in intensity due to the removal of most of this surface film during methanol rinsing. The peak at 37.8° has not been identified. No peaks

corresponding to $LiCrO_2$ were detected, further confirming that bulk oxide surface films are not stable in the presence of Li.

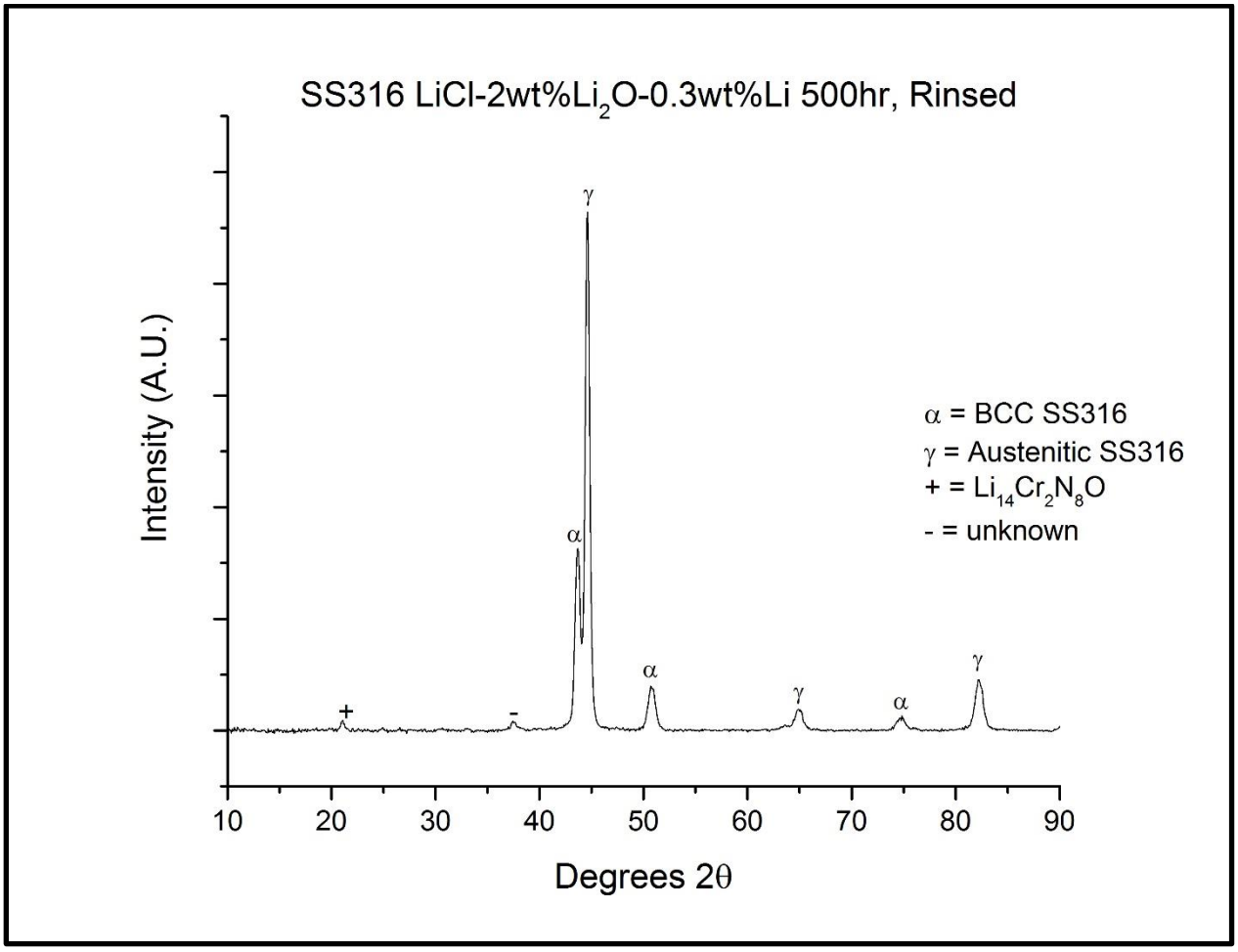


Figure 10: Hi-resolution grazing incidence X-ray diffraction pattern for SS316L exposed to LiCl-2wt%Li_2O-0.3wt%Li at 650°C for 500hr and rinsed with methanol. The peaks detected are indicative of FCC (γ) and BCC (α) steel were observed. A peak at 21.2° was observed which correlates with the peak hypothesized to be indicative of $Li_{14}Cr_2N_8O$ observed on this sample prior to methanol rinsing, although signal intensity is greatly diminished.

Figure 11 shows the high resolution grazing incidence XRD patterns for SS316L samples exposed to LiCl-1wt%Li_2O solutions containing 0, 0.3, 0.6, or 1wt%Li at 650°C for 500hr after methanol rinsing, while Figure 12 shows the diffraction patterns for SS316L samples exposed to identical conditions for 1000hr.

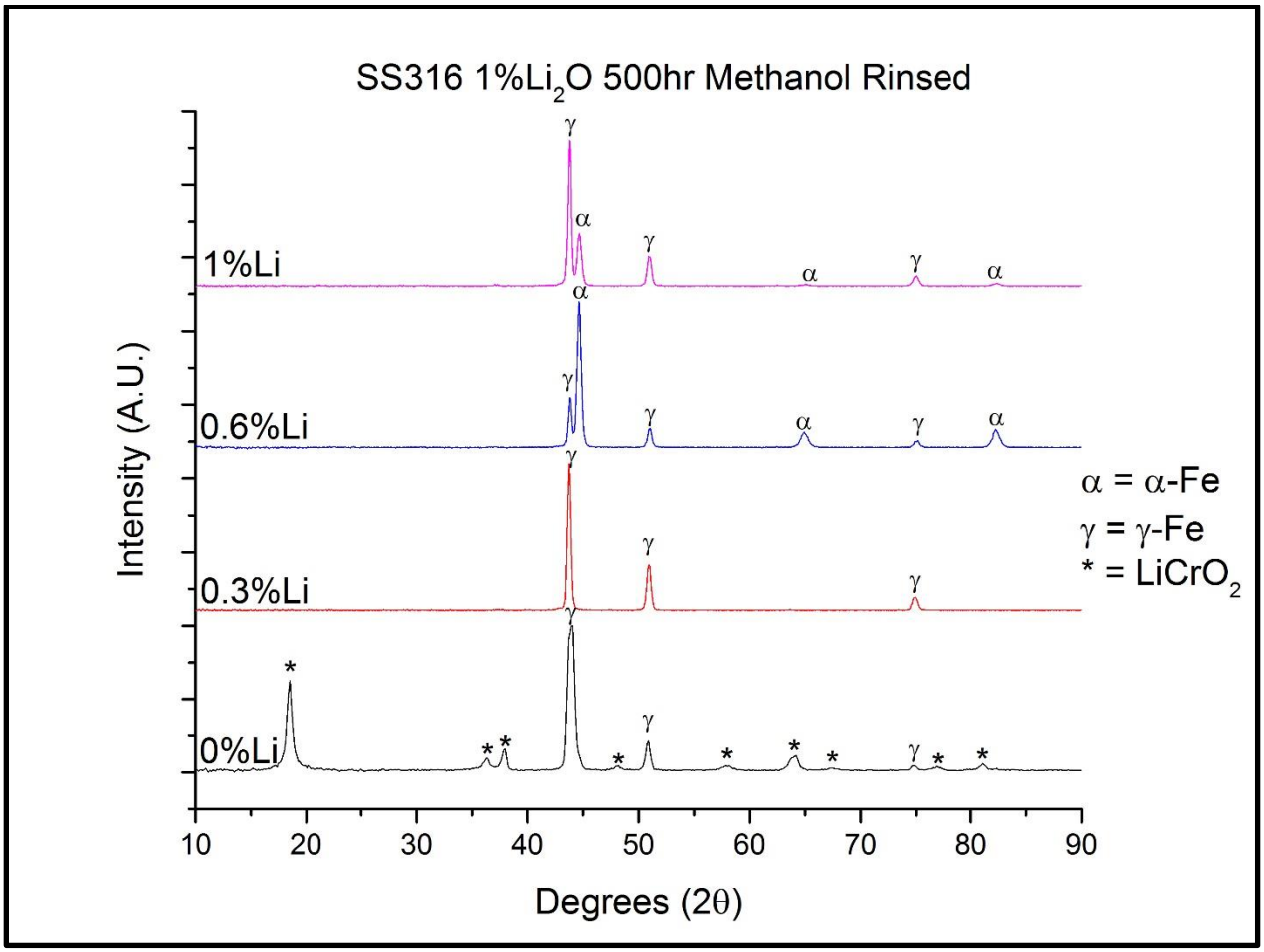


Figure 11: Hi-resolution grazing incidence XRD patterns for SS316L samples exposed to LiCl-1wt%Li_2O solutions containing 0, 0.3, 0.6, or 1wt%Li at 650°C for 500hr. The diffraction pattern for the SS316L sample exposed to LiCl-1wt%Li_2O-0wt%Li shows the peaks identified as $LiCrO_2$ in Figure 10, above. The peaks of $LiCrO_2$ were not observed on any sample exposed to LiCl-Li_2O in the presence of Li. De-austenization of samples exposed to LiCl-1wt%Li_2O containing 0, 0.6, and 1wt%Li for 500hr was observed.

From these figures, it can be observed that the $LiCrO_2$ surface films that form in the absence of Li are not detectable via XRD in the presence of Li, corroborating observations made via SEM-EDS, Raman spectroscopy, and XPS analysis that is presented below. These techniques all show that the presence of Li prevents the formation of appreciable quantities of $LiCrO_2$ and results in liquid metal based attack. The de-austenization of the base material was observed on the SS316L samples exposed to LiCl-1wt%Li_2O containing 0, 0.6, and 1wt%Li for 500hr, and LiCl-1wt%Li_2O containing 0 and 0.3wt%Li for 1000hr. The inconsistency with which this phenomena was observed indicates that the solution chemistry does not affect the probability that a particular sample will undergo de-austenization. This is

particularly highlighted by the SS316L samples exposed to LiCl-1wt%Li_2O containing 0.3, 0.6, and 1wt%Li for 500 or 1000hr, as the samples exposed to identical solution chemistries for different exposure periods did not display similar de-austenization behavior.

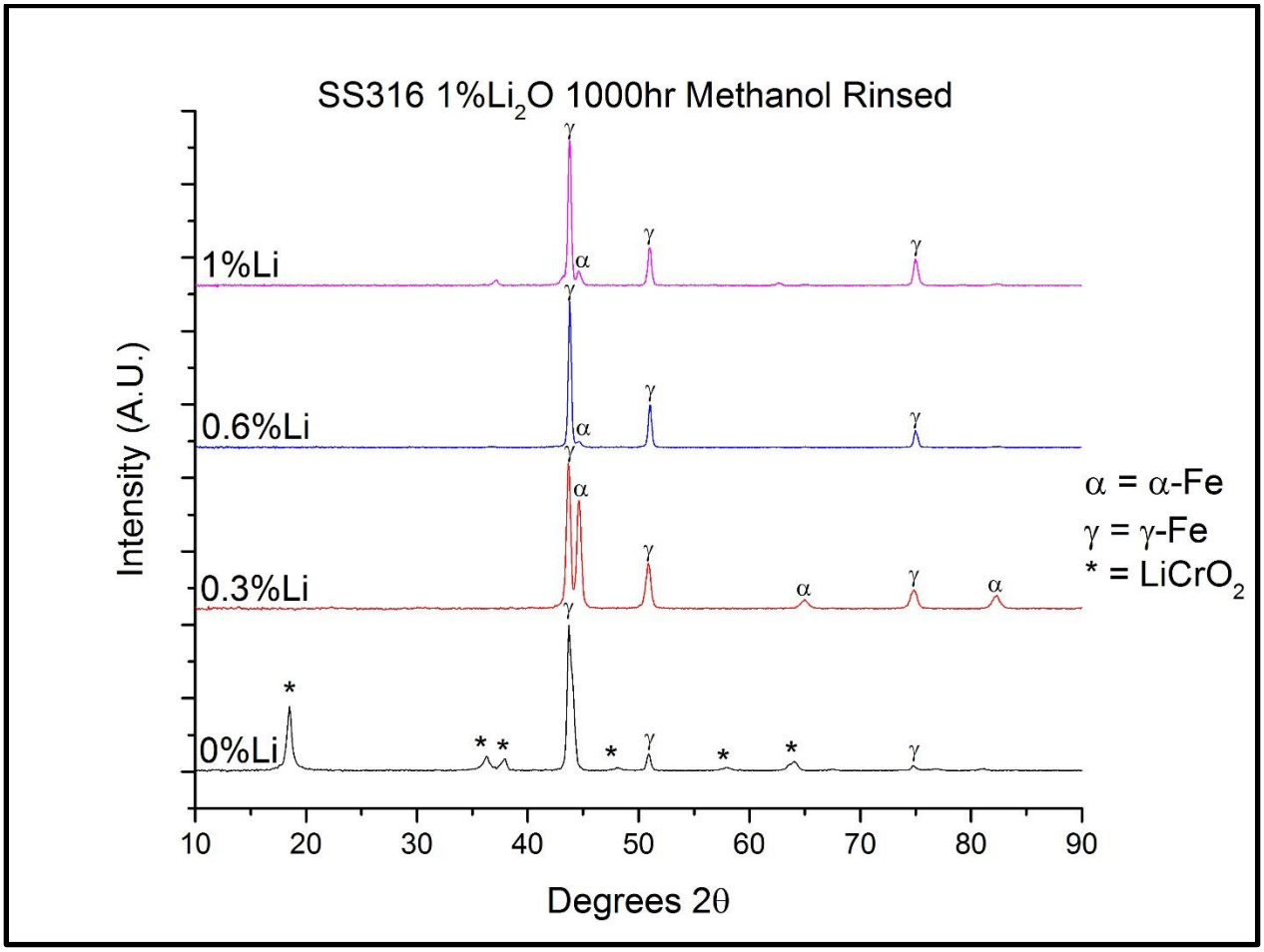


Figure 12: Hi-resolution grazing incidence XRD patterns for SS316L samples exposed to LiCl-1wt%Li_2O solutions containing 0, 0.3, 0.6, or 1wt%Li at 650°C for 1000hr. The diffraction pattern for the SS316L sample exposed to LiCl-1wt%Li_2O-0wt%Li shows the peaks identified as $LiCrO_2$ in Figure 10, above. The peaks of $LiCrO_2$ were not observed on any sample exposed to LiCl-Li_2O in the presence of Li. De-austenization of samples exposed to LiCl-1wt%Li_2O containing 0, 0.6, and 1wt%Li for 500hr was observed.

Similarly, the high resolution grazing incidence XRD patterns obtained for I625 samples exposed to LiCl-1wt%Li_2O containing 0, 0.3, 0.6, and 1wt%Li for 500 and 1000hr show trends consistent with the SS316L samples. These diffraction patterns are shown in Figure 13 for 500hr exposure periods and Figure 14 for 1000hr exposure periods.

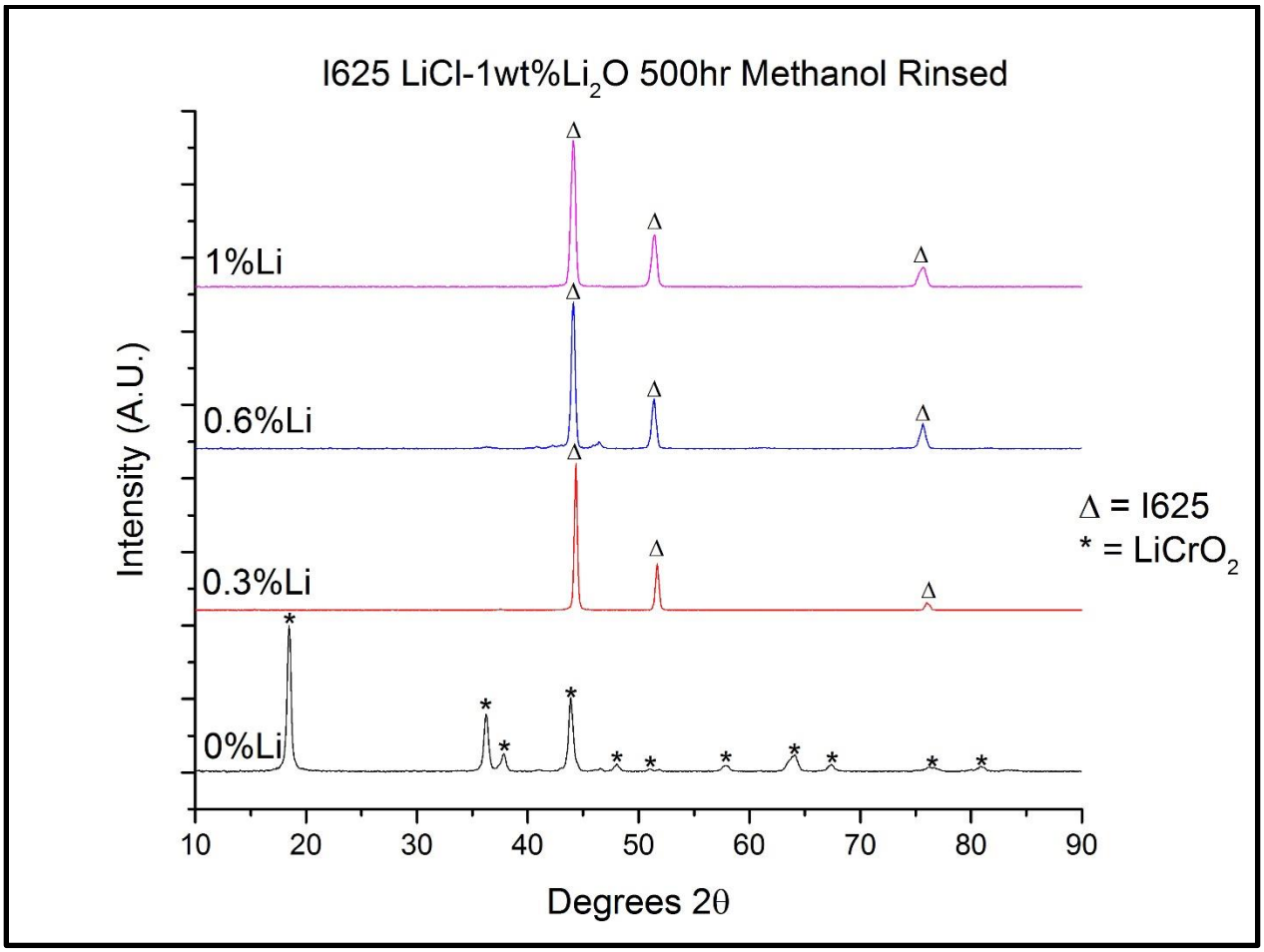


Figure 13: Hi-resolution grazing incidence XRD patterns for I625 samples exposed to LiCl-1wt%Li_2O solutions containing 0, 0.3, 0.6, or 1wt%Li at 650°C for 500hr.

Again, in the absence of Li, samples exposed to LiCl-Li_2O have a surface film primarily composed of $LiCrO_2$, while the addition of Li to the salt solution destabilizes these oxide compounds, leading to an essentially bare alloy surface. In contrast with the $LiCrO_2$ layers detected on the surfaces of SS316L samples, the diffraction pattern for the I625 sample exposed to LiCl-1wt%Li_2O in the absence of Li for 500hr exclusively shows diffraction peaks indicative of $LiCrO_2$, with the base material being undetected. Qualitatively, this indicates that the surface films formed on this particular I625 sample was thicker than those formed on SS316L. This observation correlates with SEM micrographs of I625 and SS316L samples exposed to LiCl-Li_2O in the absence of Li, which show consistently better formed surface oxides on I625 compared to SS316L samples. This may imply superior corrosion resistance for I625; however, peaks for

the base material were detected on the I625 sample exposed to identical conditions for 1000hr, as shown in Figure 14, so the difference in the oxide layer thickness is likely not significant on average.

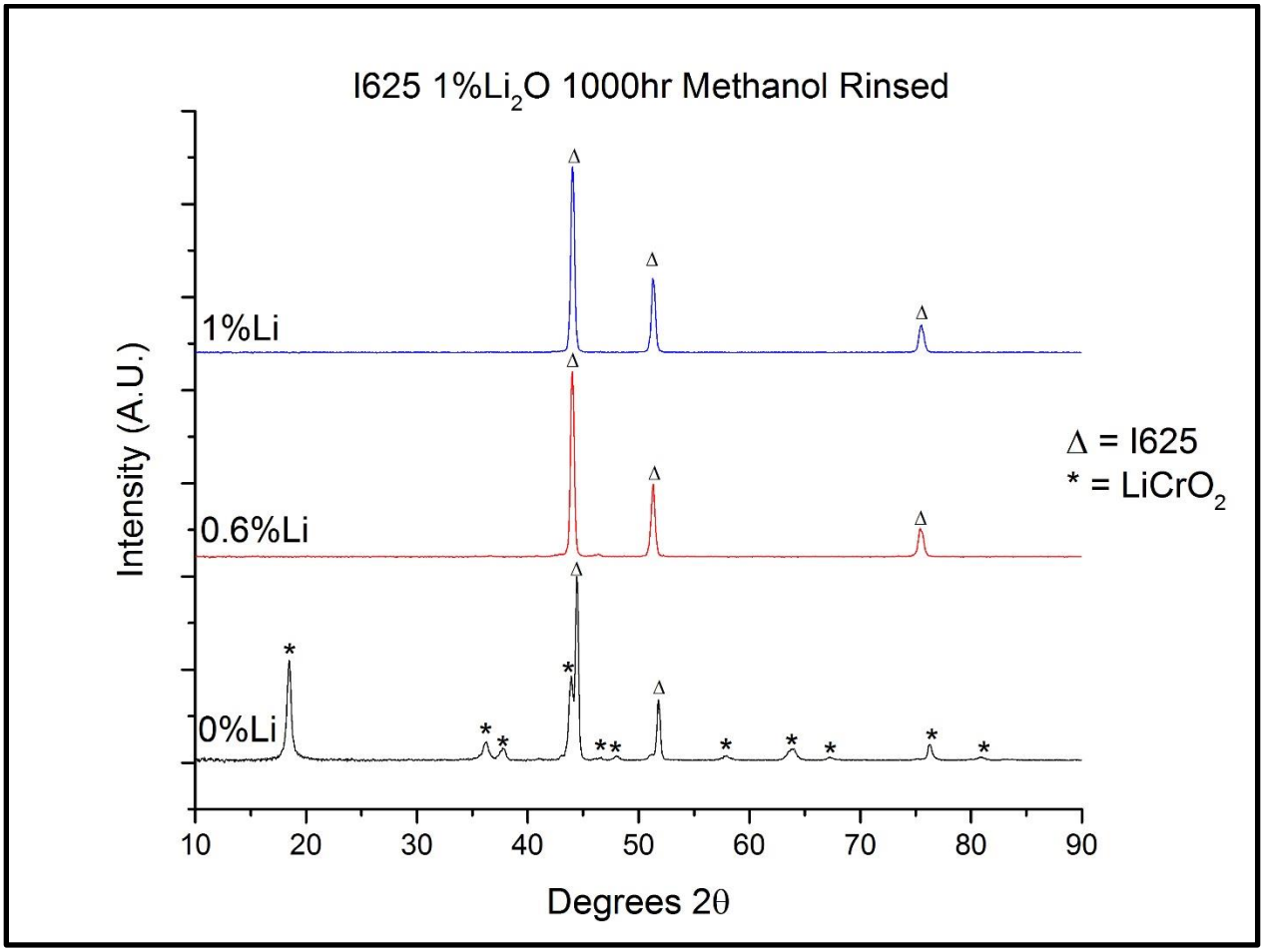


Figure 14; Hi-resolution grazing incidence XRD patterns for I625 samples exposed to LiCl-1wt%Li_2O solutions containing 0, 0.3, 0.6, or 1wt%Li at 650°C for 500hr.

Unfortunately, the I625 sample exposed to LiCl-1wt%Li_2O-0.3wt%Li for 1000hr was accidentally dropped into the main chamber of the XPS after collection of the XPS spectra. As removal of this sample necessitates bringing the system up to atmospheric pressure, this sample will not be recovered until other maintenance of the system is required. XPS was performed prior to XRD, Raman, and micro-Vickers hardness testing for this sample, so it has not been analyzed completely and its diffraction pattern is missing from Figure 14. Fortunately, storage in the ultrahigh vacuum environment of the XPS

is ideal for preventing chemical changes of an alloy surface. Analysis of this sample or the reserve sample to complete the dataset will occur in the future.

SEM-EDS

Scanning electron microscopy was performed using a Hitachi S-4700 equipped with an Oxford Instruments energy dispersive X-ray spectrometer (EDS) and a LaB_6 field emission source. Images of the sample morphology were collected at 5kV and 20kV at a working distance of 12±0.2mm. EDS maps and point analysis were collected at 20kV. Samples were analyzed prior to, and immediately following methanol rinsing. Prior to methanol rinsing, the samples were loaded onto the sample stage in the Ar glovebox and transported to the SEM in a sealed plastic bag. Introduction into the SEM required exposure to atmosphere for approximately 15 seconds before evacuation of the transfer chamber was initiated. Previous work in our lab has shown this period of air exposure to be acceptable for analysis of samples exposed to molten LiCl-Li_2O-Li [4]. Following initial data collection, the samples were required to be exposed to atmosphere due to the design of the instrument, which led to the decision to perform the methanol rinsing procedure for each sample at this time. After methanol rinsing according to the procedure outlined above, the samples were immediately re-analyzed via SEM-EDS using the same parameters as used prior to the rinsing procedure. Due to the quantity of images collected during this analysis, the following discussion is intended to address the general trends observed, as well as the observations unique to particular samples where applicable. More SEM micrographs are included in Appendix B.

The morphologies observed via SEM were highly dependent on the Li concentration in the molten salt solution. Figure 15 shows the SEM micrographs of SS316L exposed to LiCl-2wt%Li_2O containing 0, 0.3, 0.6, and 1wt%Li at 650°C for 1000hr. These images were taken following baking at 650°C, but prior to the methanol rinsing procedure. Consequently, residual salt can be observed in some

locations. In the absence of Li, a surface characteristic of the $LiCrO_2$ oxide layer is observed, with the lighter toned areas being enriched in Ni and Fe compared to the underlying oxide layer. At 0.3wt%Li, the surface appears highly degraded, and has significantly increased surface area. When the Li concentration was beyond the solubility limit at 0.6 and 1wt%Li, the surface appears to have been etched by the solution, and it is possible to see topographical detail of specific crystal planes, indicating preferential attack along thermodynamically favorable directions.

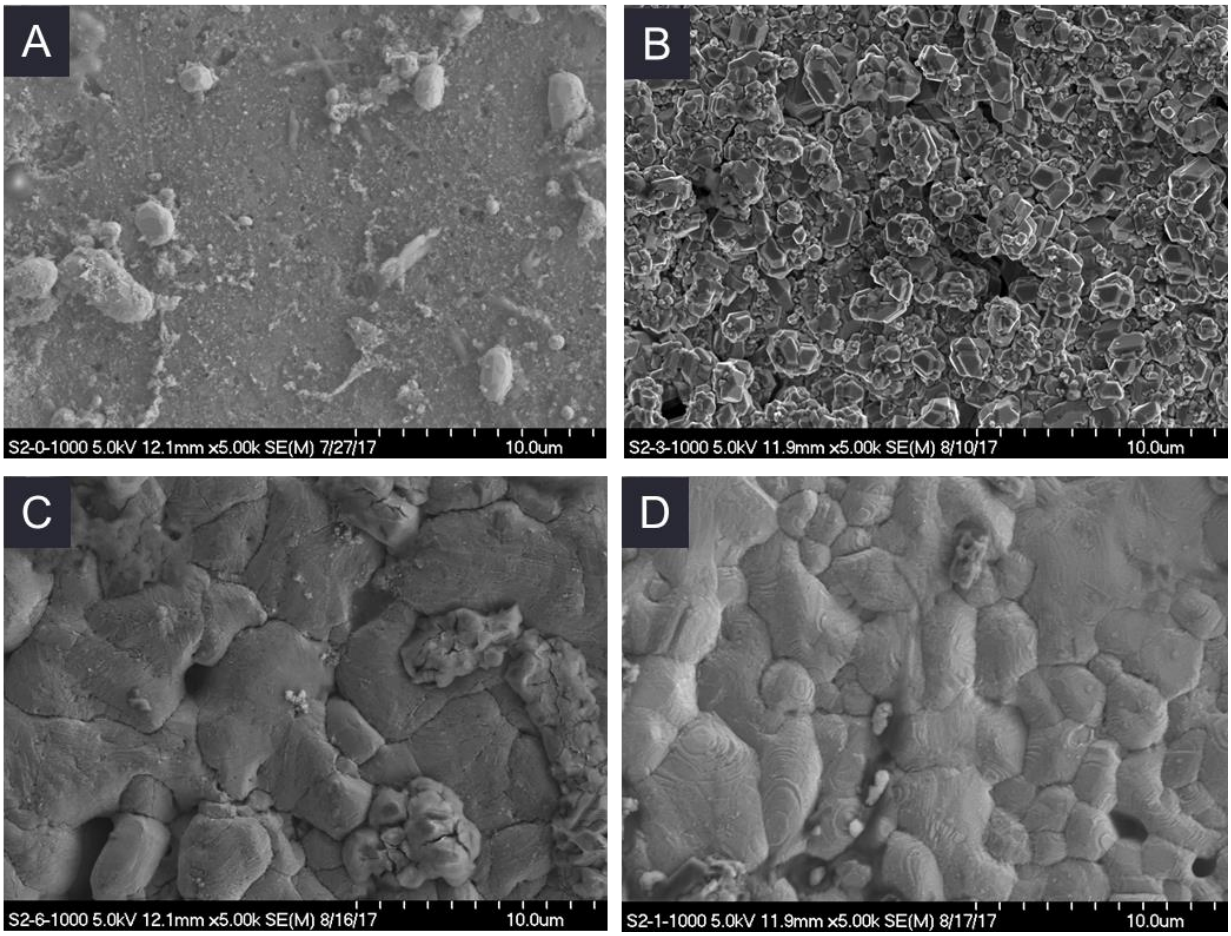


Figure 15: SEM micrographs of SS316L exposed to LiCl-2wt%Li_2O at 650°C containing A) no Li, B) 0.3wt%Li, C) 0.6wt%Li, and D) 1wt%Li for 1000hr prior to the methanol rinsing procedure. Residual salt can be seen in some locations in these images, particularly in the lower right corner of C where the grains appear cracked and in some of the crevices in B.

The differences in the surface morphology caused by the varying concentrations of Li in LiCl-2wt%Li_2O correlates to the changes in surface chemistry observed via Raman, XPS, and XRD. The unique

surface morphology observed at 0.3wt%Li may be indicative of the simultaneous action of electrochemical corrosion and liquid metal attack, while the similarity between the morphologies observed at 0.6 and 1wt%Li indicate that corrosion at these concentrations is firmly within the liquid metal attack regime. Morphologies similar to those observed here were reported in a recent publication by researchers at KAERI who investigated the corrosion behavior of Ni in molten LiCl-Li_2O-Li [5].

The micrographs shown in Figure 15 were taken from areas of voids in the residual salt layer, which electron microscopy is uniquely suited for. The difficulty of obtaining meaningful information from these sample surfaces using XPS and XRD with the salt layer present is highlighted by the micrographs in Figure 16, below.

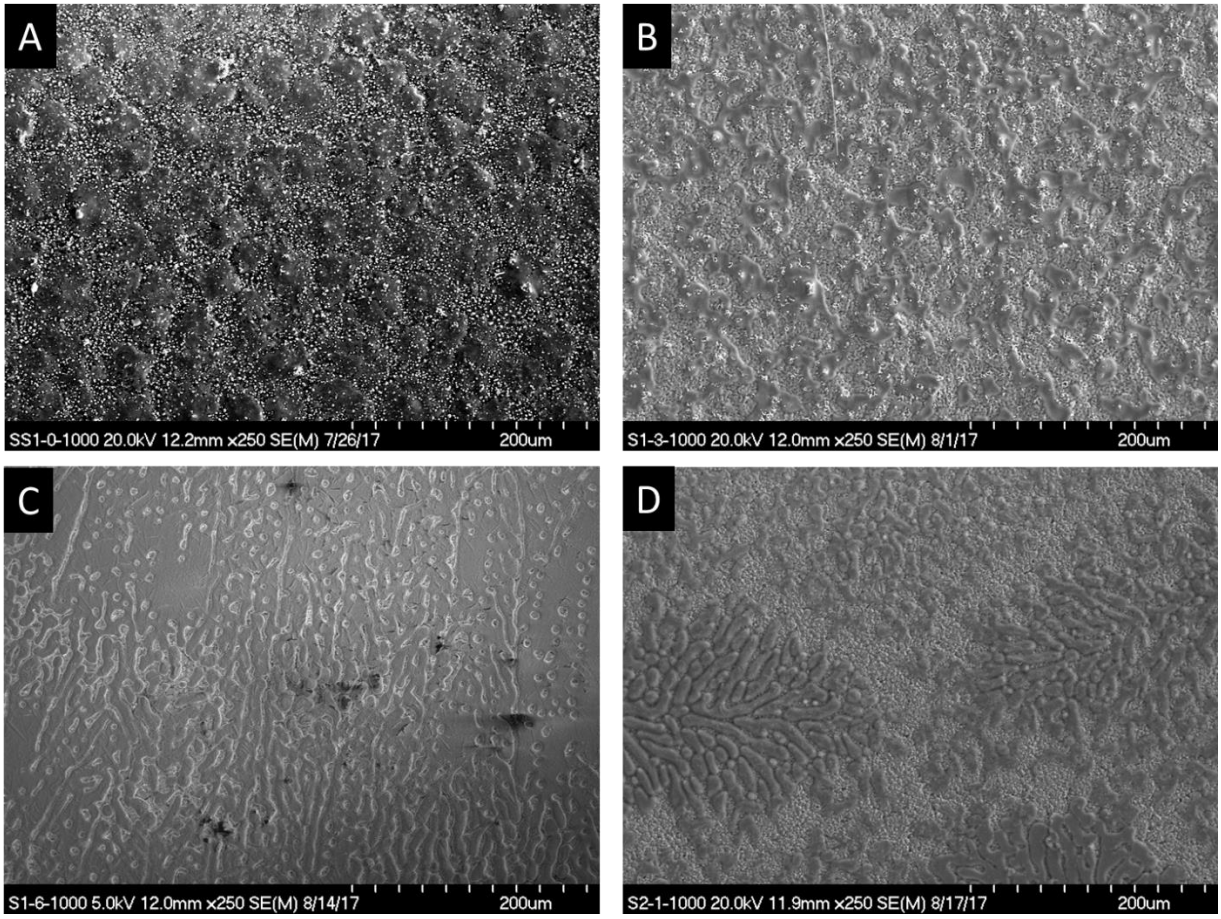


Figure 16: Low magnification SEM micrographs of SS316L exposed to LiCl-2wt%Li_2O at 650°C containing A) no Li, B) 0.3wt%Li, C) 0.6wt%Li, and D) 1wt%Li for 1000hr prior to the methanol rinsing procedure. The residual salt layer is shown to obviously obscure the sample surface, particularly in B, C, and D.

The micrographs in Figure 16 show that the residual salt layer remains well adhered to the sample surface following the baking procedure, particularly at high Li concentrations in the melt. The adhesion of the salt layer is increased by the surface roughness caused by the extended exposure length compared with our previous studies. None of the surface analytical techniques we employed during this study are capable of locating the voids in the residual salt layer as precisely as SEM, and consequently the data collected prior to methanol rinsing was of lower quality for all surface analytical techniques when compared to that obtained after methanol rinsing.

Our previous studies avoided dissolution of the salt layer as the corrosion products formed during exposure to LiCl-Li_2O-Li were unknown at the time, and it was not certain that they would be

unaffected by the solvents employed for the removal of the salt. Due to the increased adhesion of the salt layer caused by the longer exposure periods in this study, it was necessary to physically dissolve the residual salt. Methanol was chosen for this purpose as it has a high solubility limit for LiCl compared to other organic solvents and was deemed less likely to cause additional oxidation of the sample surface than water. The details of the methanol rinsing procedure used in this study are outlined in the experimental section above. Following the methanol rinsing procedure, SEM analysis was performed again to observe any changes in morphology caused by methanol rinsing, as well as to allow for more accurate elemental composition measurements via EDS. The SEM micrographs obtained from SS316L samples exposed to LiCl-2wt%Li_2O containing 0, 0.3, 0.6, and 1wt%Li at 650°C for 1000hr and washed with methanol are shown in Figure 17.

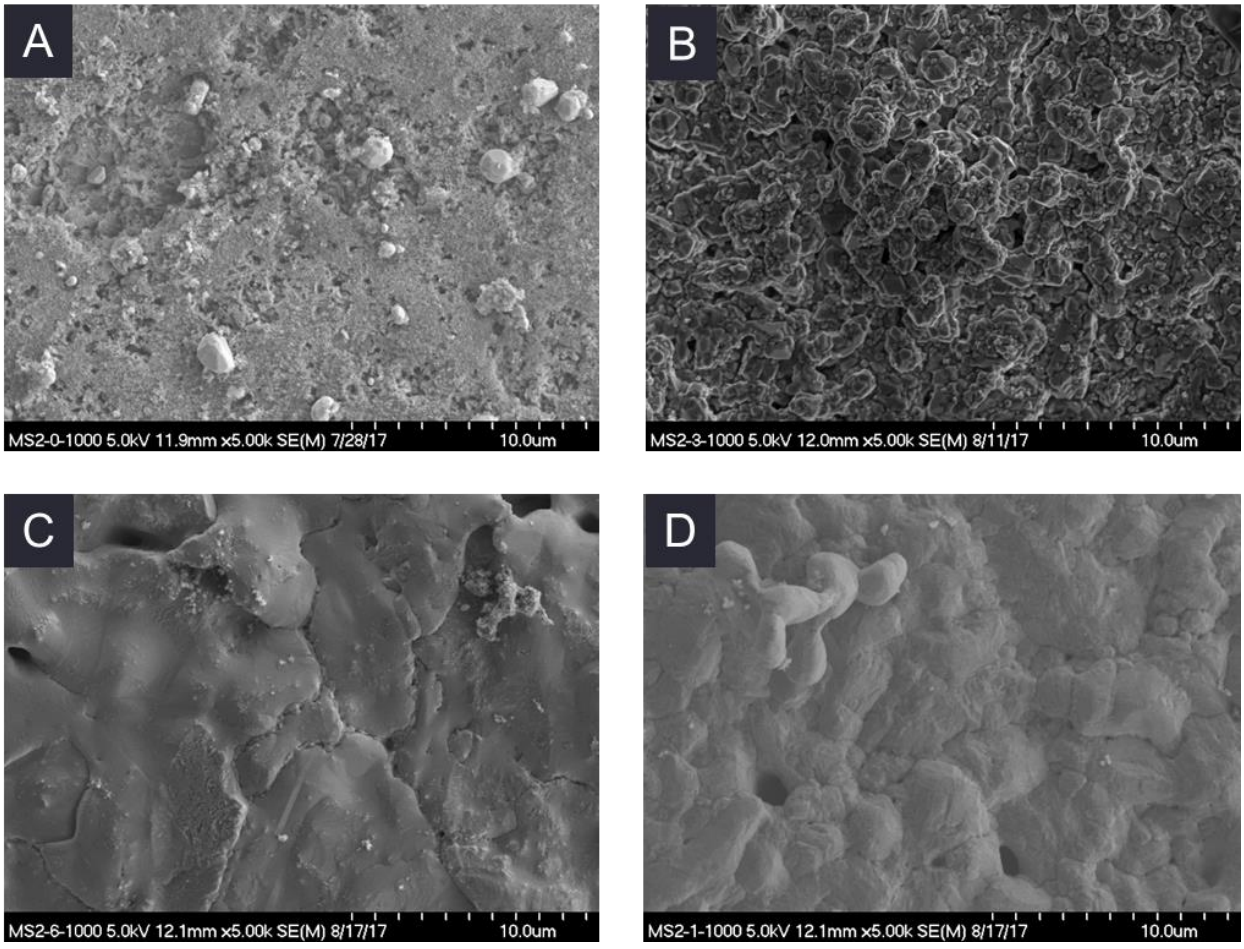


Figure 17: SEM micrographs of SS316L exposed to LiCl-2wt%Li2O at 650°C containing A) no Li, B) 0.3wt%Li, C) 0.6wt%Li, and D) 1wt%Li for 1000hr, following the methanol rinsing procedure. Minimal differences between the morphology of the samples can be observed following the methanol rinsing procedure other than the removal of the residual salt, indicating that this procedure effectively removes the residual salt layer without affecting the underlying surface morphology.

Comparison between Figure 15 and Figure 17 shows that there is minimal change in the surface morphology following methanol rinsing. The variations observed between these figures are due to small differences between specific locations on the sample surface, as it was not possible to return to the exact position in which the images in Figure 15 were taken for re-examination following the methanol rinsing procedure. Additional evidence to support the lack of chemical or physical changes to the sample surface as a result of methanol rinsing is given in the Raman, XRD, and XPS sections of this report, all of which show that no change to the sample surface was caused by methanol rinsing. The removal of the residual salt layer also allowed for more accurate determination of the surface composition with EDS

analysis due to the removal of Cl. The results of EDS analysis for the areas shown in Figure 17 are summarized in Figure 18 below.

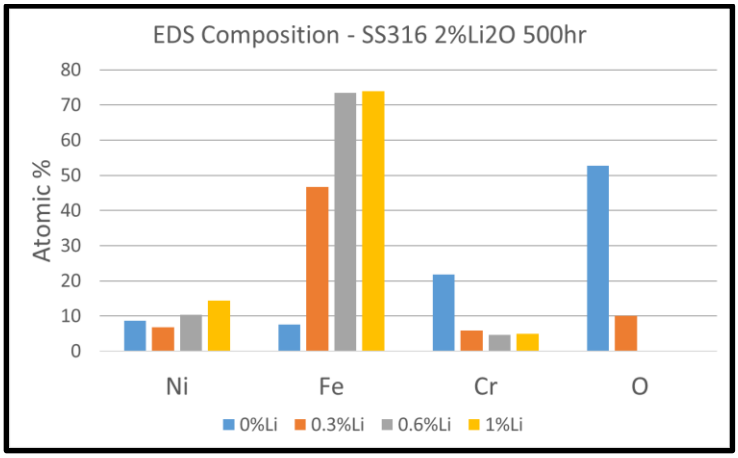


Figure 18: EDS composition corresponding to the SEM micrographs presented in Figure 20 for SS316L samples exposed to LiCl-2wt%Li_2O solutions containing 0, 0.3, 0.6, and 2wt%Li at 650°C for 500hr.

From figure 18, it can be observed that the surface of the SS316L sample exposed to LiCl-2wt%Li_2O-0wt%Li at 650°C for 1000hr is primarily composed of Cr-based oxide films, with minor contributions of Ni and Fe. This is in good agreement with the Raman, XRD, and XPS data presented in their respective sections, which all indicate that these surfaces are composed primarily of $LiCrO_2$, while small quantities of Li_2CrO_4 and $NiFe_xCr_{2-x}O_4$ are predicted by Raman and XPS. When the Li concentration in the molten salt solution is 0.3wt%, the Cr content of the surface is depleted compared to the base alloy and the O concentration is also decreased compared to the surface of the SS316L sample exposed to LiCl-2wt%Li_2O in the absence of Li, while the Fe content is increased. Beyond the solubility limit of Li, at 0.6 and 1wt%Li, Cr is depleted slightly further and O is not detectable, while both Fe and Ni are present at levels nominal for SS316L, indicating a bare metallic surface. A slight enrichment of Ni on the SS316L sample exposed to LiCl-2wt%Li-1wt%Li for 1000hr is in agreement with our previous work, and is indicative of liquid metal like attack by Li.

Similar morphological and compositional patterns were observed for SS316L samples exposed to the other LiCl-Li_2O-Li solution chemistries and exposure periods studied. Micrographs similar those in

Figure 17 are given in Appendix B for these other samples in Figures B1, B2, and B3. The remainder of the discussion of SS316L samples will highlight the observations unique to particular samples.

As noted in the XRD section above, the SS316L sample exposed to LiCl-2wt%Li_2O-0.3wt%Li for 500hr exhibited an anomalous surface film that was removed during methanol rinsing. SEM-EDS analysis of this surface prior to and following methanol rinsing showed a unique morphology and composition that was not observed on any other sample. Figure 19 shows three SEM micrographs of this sample. The leftmost image is a low magnification image following methanol rinsing, showing the base material in dark grey, and the dispersed surface film that remained after methanol rinsing as lighter toned spots. The image labeled with a 1 in the top left corner shows the morphology of the underlying base material, which is consistent with other SS316L samples exposed to LiCl-Li_2O-0.3wt%Li solutions for extended periods of time. Finally, the image labeled with a 2 in the top left corner shows the morphology of the surface film prior to methanol rinsing, which allows for direct observation of the film prior to its removal. The average composition for these areas detected via EDS are given in Table 3.

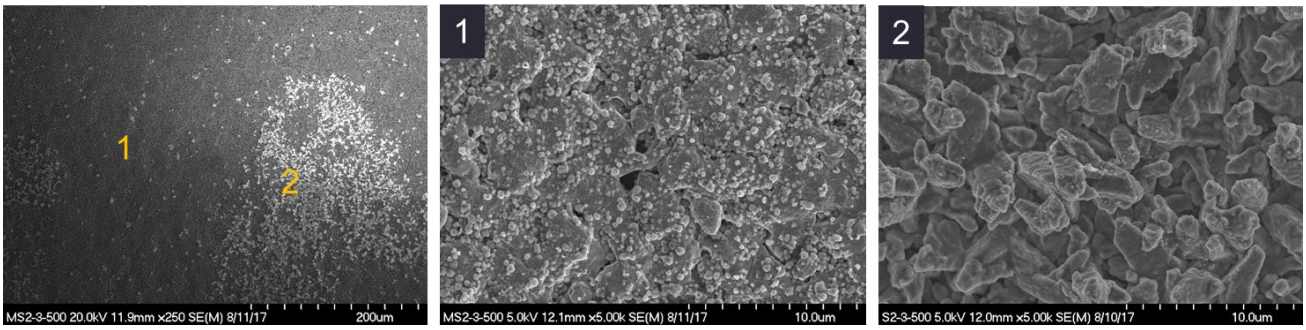


Figure 19: SEM micrographs for the surface of the SS316L sample exposed to LiCl-2wt%Li_2O-0.3wt%Li for 500hr, showing the location of the anomalous surface layer. The image on the left shows a broad view of the surface following methanol rinsing, while the morphologies of areas 1 and 2 are shown in the corresponding images. Area 1 is indicative of the typical surface morphology of the sample, while Area 2 shows the morphology of the anomalous surface layer, in this case prior to methanol rinsing. The composition of these areas detected via EDS are shown in Table 3 below.

Table 3: EDS compositional analysis of the locations shown in Figure 19 for the SS316L sample exposed to LiCl-2wt%Li_2O-0.3wt%Li for 500hr. The compositions given are an average for the entire area shown for each location.

	Area 1	Area 2
Element	Atomic %	Atomic%

N	12.28	43.3
O	7.49	29.68
Si		0.43
Cl	0.19	3.76
Ti	1.52	0.26
Cr	7.02	21.39
Mn	1.34	0.13
Fe	61.26	0.71
Ni	8.69	0.11
Mo		0.17
S	0.22	

The composition of the anomalous surface film detected via EDS consists primarily of N, O, and Cr, which implies a chromium oxynitride-based compound. Li is not detectable via EDS, however the presence of 0.3wt%Li in the melt, along with the identification of the peak at 20.6° as being the primary peak of $Li_{14}Cr_2N_8O$ implies that Li is likely a component of this compound. Additionally, all other samples exposed to melts containing Li show that oxidized transition metal compounds are very unstable in the highly reducing conditions caused by Li^0. This makes it extremely likely that the compound observed on this sample would necessarily incorporate Li to stabilize the compound with respect to the LiCl-2wt%Li_2O-0.3wt%Li solution. Unfortunately, XPS characterization of this sample surface prior to methanol rinsing showed only the residual salt layer, which prevented this technique from being applied to this unique compound.

Also of interest is the observation of sensitization on a small area on the SS316L sample exposed to LiCl-2wt%Li_2O-0.6wt%Li at 650°C for 1000hr. Sensitization of austenitic stainless steels is a well-known issue at high temperatures, where the formation of chromium carbides and their subsequent concentration at the grain boundaries leads to intergranular corrosion and loss of strength [6]. The characteristic enrichment of Cr at the grain boundaries typical of sensitization can clearly be observed in the Cr Kα EDS map in Figure 20, while the specific compositions for spots 1 and 2 marked on the SEM micrograph and EDS map are given in Table 4.

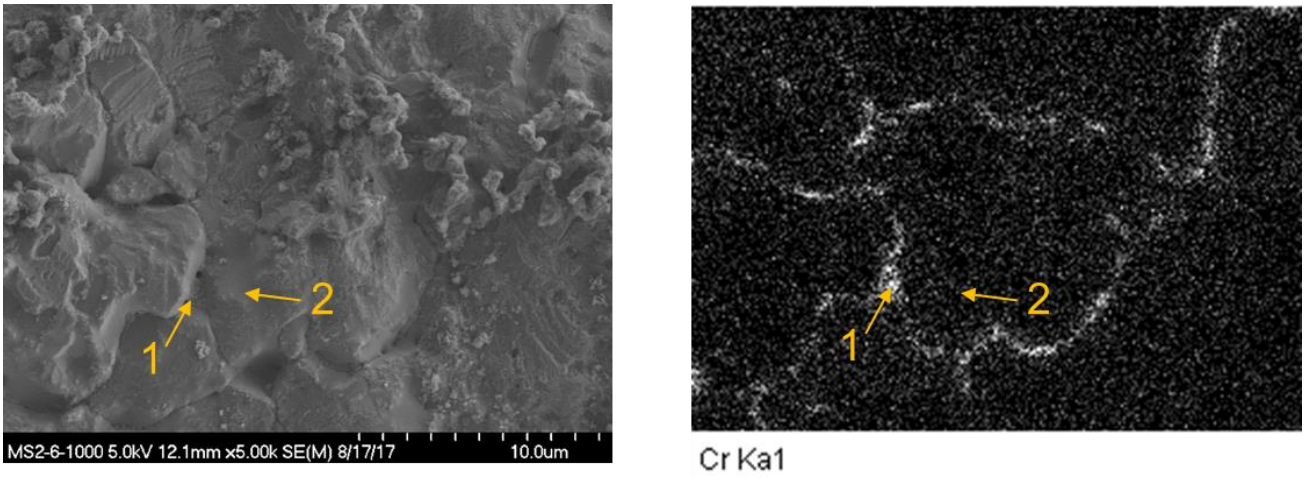


Figure 20: SEM micrograph (left) and EDS map of Cr of the same location (right) for the SS316L sample exposed to LiCl-2wt%Li_2O-0.6wt%Li at 650°C for 1000hr. It can easily be observed that Cr segregation at the grain boundaries occurred at this location on this sample. The elemental compositions obtained via EDS analysis for spots 1 and 2 are given in Table 3.

Table 4: EDS composition spot analysis for the locations marked on the SEM micrograph in Figure 20, above.

Element	Spot 1 Atomic%	Spot 2 Atomic%
C	26.69	
S	1.21	
Cr	27.05	4.28
Mn	1.09	1.46
Fe	28.52	50.05
Ni	15.44	44.21

The detection of S along with chromium carbide formation at Spot 1 is in good agreement with literature, as S is known to accelerate the sensitization of austenitic stainless steels. The low carbon content of the SS316L used for this study is intended to minimize this issue by preventing the formation of carbides, and it is important to note that this was a very localized region only observed near the edge of this particular sample. However, this highlights the necessity of quality control during manufacturing, as localized corrosion is difficult to predict and is therefore difficult to deal with when designing systems. That this was observed at the edge of the sample is unsurprising due to the use of a CO_2 laser to cut these sample coupons from the plate. Laser ablation causes localized heating to high temperatures which allows for the formation of carbides in the vicinity of the cut, and other research scientists in our

laboratory have observed similar behavior in their work when using samples cut using a CO_2 laser. Welding is also well known to cause similar changes in the microstructure that result in sensitization of fabricated assemblies due to the changes in the microstructure of the heat affected zone. Of great importance to the present work, the operating temperature of the electrolytic reduction of UNF at 650°C is also ideal to cause sensitization of austenitic stainless steels, as chromium carbides are insoluble at this temperature and the diffusion of C through the microstructure allows for their formation and migration to the grain boundaries. Consequently, any vessel intended for containment of the electrolyte used during the electrolytic reduction of UNF should be designed with this in mind if SS316L or another austenitic stainless steel is chosen for its construction. For a more thorough discussion of sensitization and its prevention, the reader is directed to *Principles and Prevention of Corrosion* by Denny A. Jones [6].

Of all of the analytical techniques employed in this study, SEM observed the most stark differences in the corrosion behavior exhibited by SS316L and I625. The oxide layer formed on the surface of I625 samples exposed to LiCl-Li_2O solutions in the absence of Li displayed a much more defined grain structure compared to the relatively featureless morphology observed on SS316L samples exposed to the same conditions. Additionally, the presence of Li in the melt had a much more dramatic effect on the microstructure of I625 samples than SS316L samples. To illustrate these points, the SEM micrographs taken of the I625 samples exposed to LiCl-1wt%Li_2O containing 0, 0.3, 0.6, and 1wt%Li for 500hr are shown in Figure 21, below.

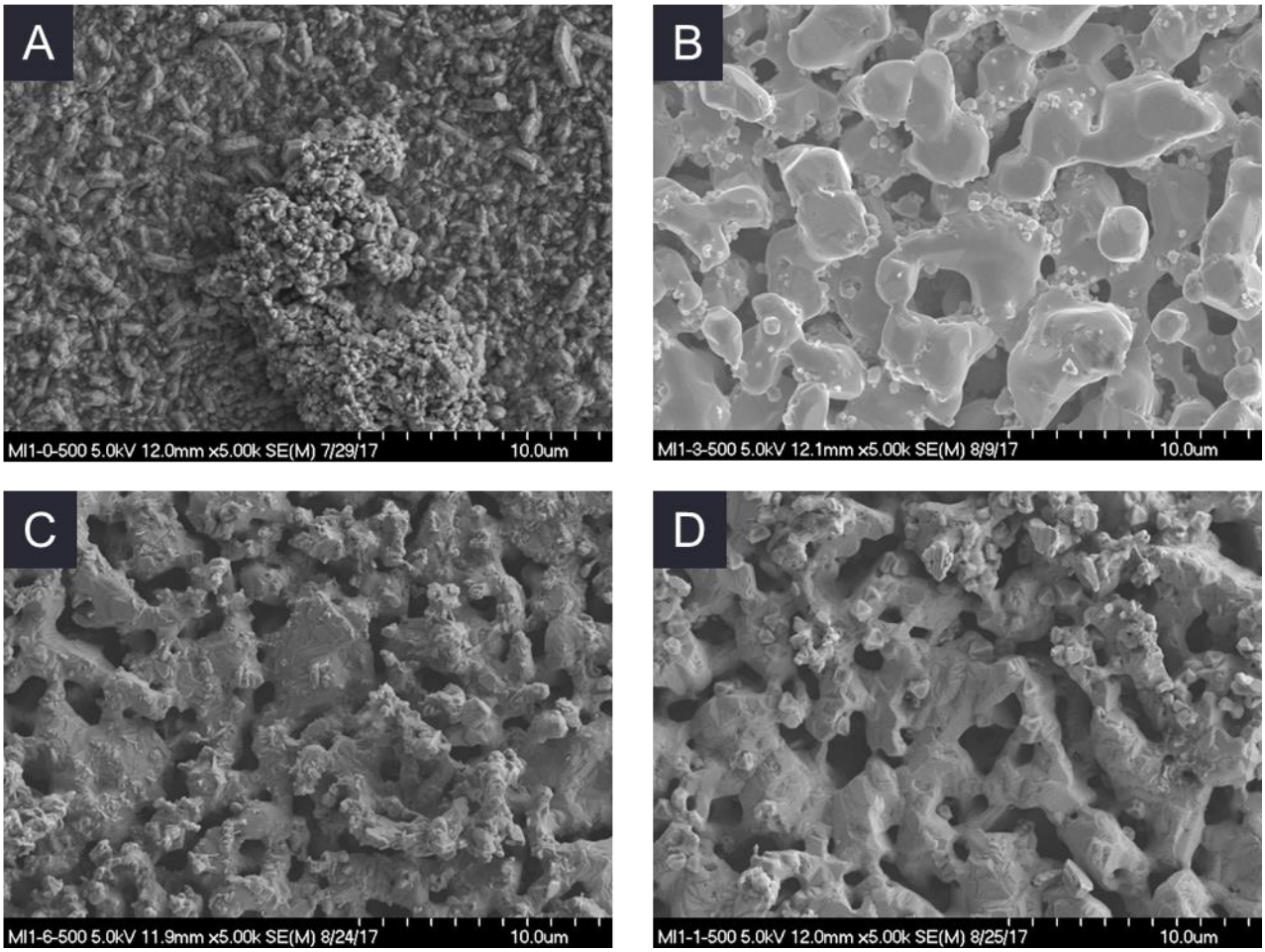


Figure 21: SEM micrographs of I625 exposed to LiCl-1wt%Li2O at 650°C containing A) no Li, B) 0.3wt%Li, C) 0.6wt%Li, and D) 1wt%Li for 500hr and rinsed with methanol.

In the absence of Li, the oxide layer is very well formed and shows evidence of a multi layered structure that is discussed in greater detail below. The presence of Li in the molten LiCl-Li_2O solution destabilizes the oxide layer as is the case with SS316L; however, with I625 this manifests itself as a very porous microstructure that is similar in appearance to a Ni foam. The extent to which this porosity penetrates into the sample surface is currently unknown. Cross sectional analysis of these samples is planned for the future to elucidate this and other questions. Also contrary to the observations of SS316L, there is little difference between the microstructures observed at low and high Li concentrations, with the microstructure of the I625 samples exposed to melts containing 0.3wt%Li displaying microstructures nearly identical to samples exposed to melts containing 1wt%Li. Exposure

periods of 500hr and 1000hr both yielded nearly indistinguishable microstructures, as can be observed by comparing the micrographs of I625 samples exposed to LiCl-1wt%Li_2O containing 0, 0.3, 0.6, and 1wt%Li for 1000hr shown in Figure 24 below to the micrographs presented in Figure 23.

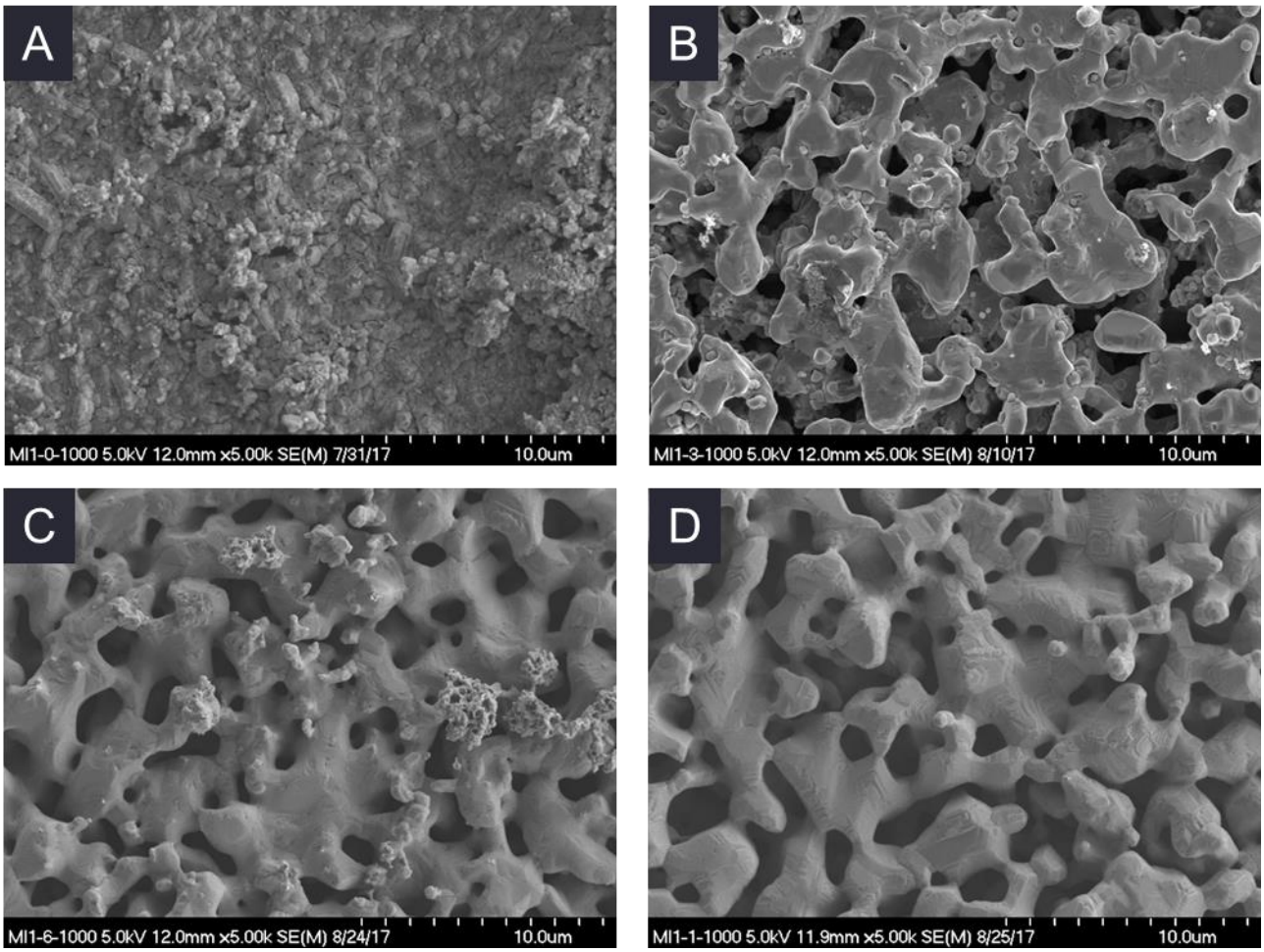


Figure 22: SEM micrographs of I625 exposed to LiCl-1wt%Li2O at 650°C containing A) no Li, B) 0.3wt%Li, C) 0.6wt%Li, and D) 1wt%Li for 1000hr and rinsed with methanol.

Overall, the surfaces of I625 samples were more homogenous, and fewer anomalous behaviors were observed to deviate from the trends outlined above. However, the I625 sample exposed to LiCl-2wt%Li_2O-0wt%Li for 500hr had a small number of locations where the oxide layer had partially delaminated, which allowed for direct observation of the layered structure of the oxide layers formed on I625 during exposure to LiCl-Li_2O in the absence of Li. SEM micrographs of one of these locations are shown in Figure 21, and the compositions of locations 1 through 4 detected via EDS are given in Table 5.

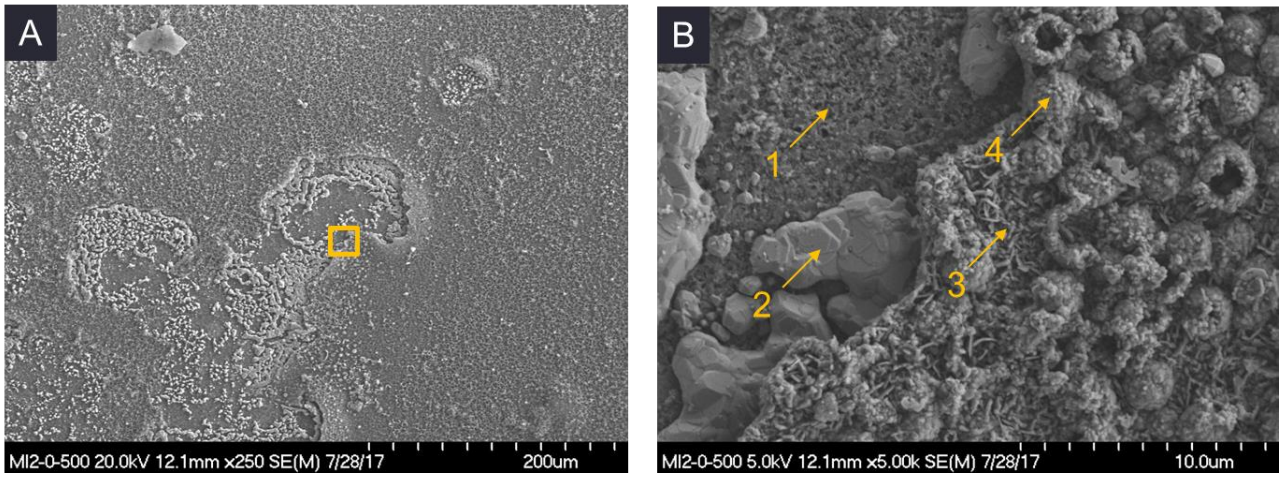


Figure 23: SEM micrographs taken at (A) low magnification and (B) high magnification of the highlighted area on the I625 sample exposed to LiCl-2wt%Li_2O-0wt%Li at 650°C for 500hr after methanol rinsing. The delamination of the outer surface layer on this sample provided a unique opportunity to examine the layered structure of the oxide films that form on I625 upon exposure to molten LiCl-Li_2O in the absence of Li. The compositions of Layers 1 through 4 in image B were obtained via EDS analysis and are given in Table 4, below.

Table 5: EDS compositional analysis obtained for locations 1 through 4 marked in Figure 21B for the I625 sample exposed to LiCl-2wt%Li_2O-0wt%Li at 650°C for 500hr.

Element	Layer 1 Atomic%	Layer 2 Atomic%	Layer 3 Atomic%	Layer 4 Atomic%
C				5.07
O	62.43	11.22	61.07	65.48
Mg	1.35		2.56	3.14
Cl	0.41		0.27	0.47
Cr	18.34	3.33	12.99	20.07
Fe	0.61	3.74	1.21	0.32
Ni	15.23	80.97	21.44	5.13
Nb	0.9			
Mo	0.73	0.74		
Ti			0.46	0.32

The presence of a multilayered oxide structure is easily discerned in this image, and each layer was analyzed via EDS at the spots marked by the arrows. Layer 1 is the innermost layer, and is composed primarily of O, Cr, and Ni. Due to the composition of Layer 2 and the lack of Ti in both Layers 1 and 2, which is present as an impurity in the Li_2O used in this study, it is thought that Layer 1 is either the result of the inward diffusion of O into the base material or the native oxide present after polishing. Interestingly, the morphology of this innermost layer is similar to the morphology observed on SS316L

samples exposed to similar conditions. The O concentration of Layer 2 is much lower than in any of the other layers observed here, and its composition is the most similar to the base alloy. The size of the grains in Layer 2 and their relative orientations are also similar to the morphology of the I625 samples exposed to LiCl-Li_2O in the presence of Li, as can be observed by comparison with Figures 21 and 22, indicating that this is likely the base material which has been depleted in Cr to facilitate the outward growth of Layers 3 and 4. These outermost layers differ in both morphology and composition, suggesting a difference in the compounds that compose them. Layer 3 is the layer closest to the base material, and has a plate-like morphology. The high Ni content of Layer 3 compared to Layer 4 implies that Layer 3 is composed of primarily $NiFe_xCr_{2-x}O_4$ with a relatively low value of x, while Layer 4 is primarily $LiCrO_2$ based. Both Layer 3 and Layer 4 have incorporated Ti from the impurities present in Li_2O. The spheroidal morphology of Layer 4 suggests that its growth begins at specific nucleation sites. Some of these spheroids from Layer 4 appear to be broken or incompletely formed, showing that they are hollow. Figure 24 shows the results of EDS mapping of Ni, Fe, Cr, and O for the same location shown in Figure 23 which further highlights the differences between the layers observed on this sample.

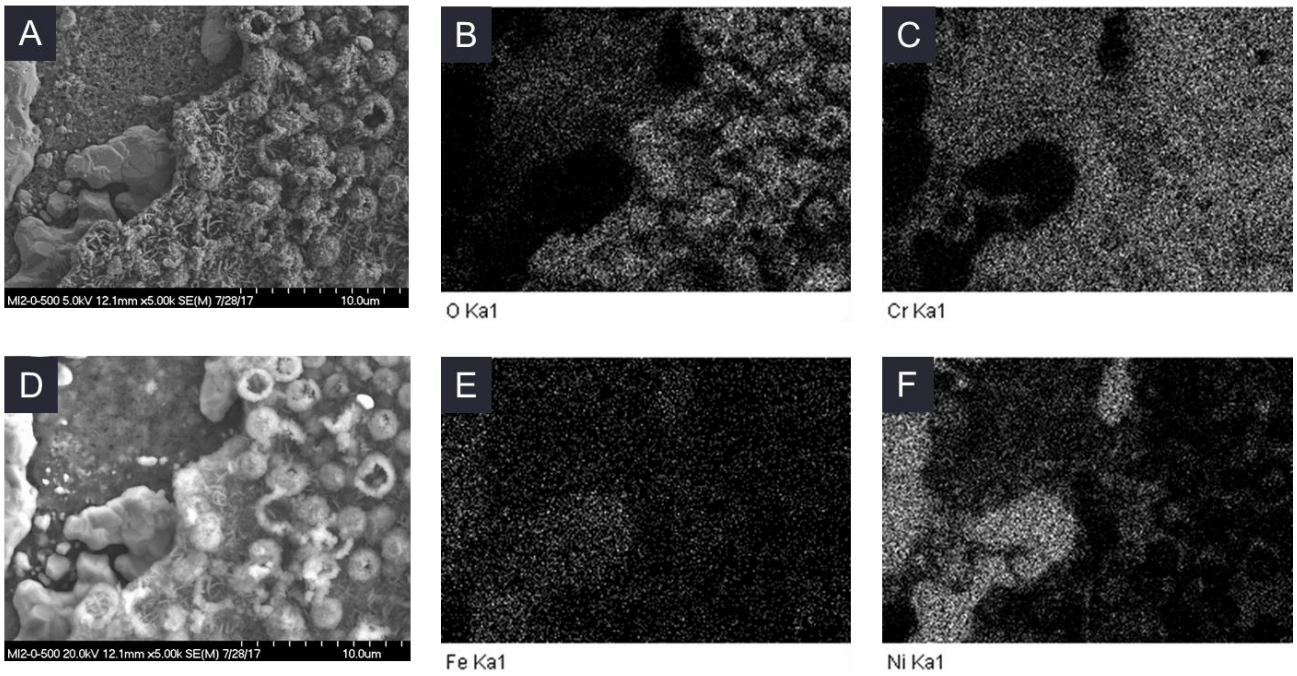


Figure 24: SEM images and EDS maps of the same area for the I625 sample exposed to LiCl-2wt%Li_2O-0wt%Li for 500hr. (A) SEM micrograph same as in Figure 21B given for reference, taken at 5kV accelerating voltage, (B) EDS map of O Kα, (C) EDS map of Cr Kα, (D) SEM micrograph of same area, taken at 20kV accelerating voltage (E) EDS map of Fe Kα, and (F) EDS map of Ni Kα. For the EDS maps, lighter tones indicate higher concentrations of that element.

These observations give a unique insight into the mechanisms governing the corrosion of I625 in the LiCl-Li_2O-Li system. Cross sectional investigations of these samples will be performed in the future to provide further insight into the corrosion processes at play in this system.

Micro-Vickers Hardness Testing

In an attempt to obtain information on the degradation of mechanical properties as a result of exposure to LiCl-Li_2O-Li solutions, micro-Vickers hardness testing was performed on all samples after methanol rinsing. These measurements were performed on a Wilson Tukon 1202 hardness tester using a micro-Vickers square pyramidal indenter. The load force of 500g was applied for 10s per indentation, and 10 indentations were made per sample. Unfortunately, the results of this testing were directly influenced by the morphologies of the samples, meaning that no conclusions about the bulk mechanical properties of the samples could be obtained. The presence of the oxide layer on the surface artificially increased the measured hardness values for all SS316L and I625 samples exposed to LiCl-Li_2O in the

absence of Li due to the higher hardness of covalently bonded compounds compared to metals. Similarly, the highly porous morphologies observed on the SS316L samples exposed to LiCl-Li_2O solutions containing 0.3wt%Li, as well as all I625 samples exposed to LiCl-Li_2O in the presence of Li, lead to artificially lower hardness values. As the SS316L samples exposed to LiCl-Li_2O solutions containing 0.6 and 1 wt%Li showed less porous morphology, the softening due to the microstructure was reduced when compared to the 0.3wt%Li samples. This can be observed in Figure 25, which shows the hardness measurements made for SS316 samples exposed to LiCl-2wt%Li_2O solutions containing 0, 0.3, 0.6, and 1wt%Li for 1000hr.

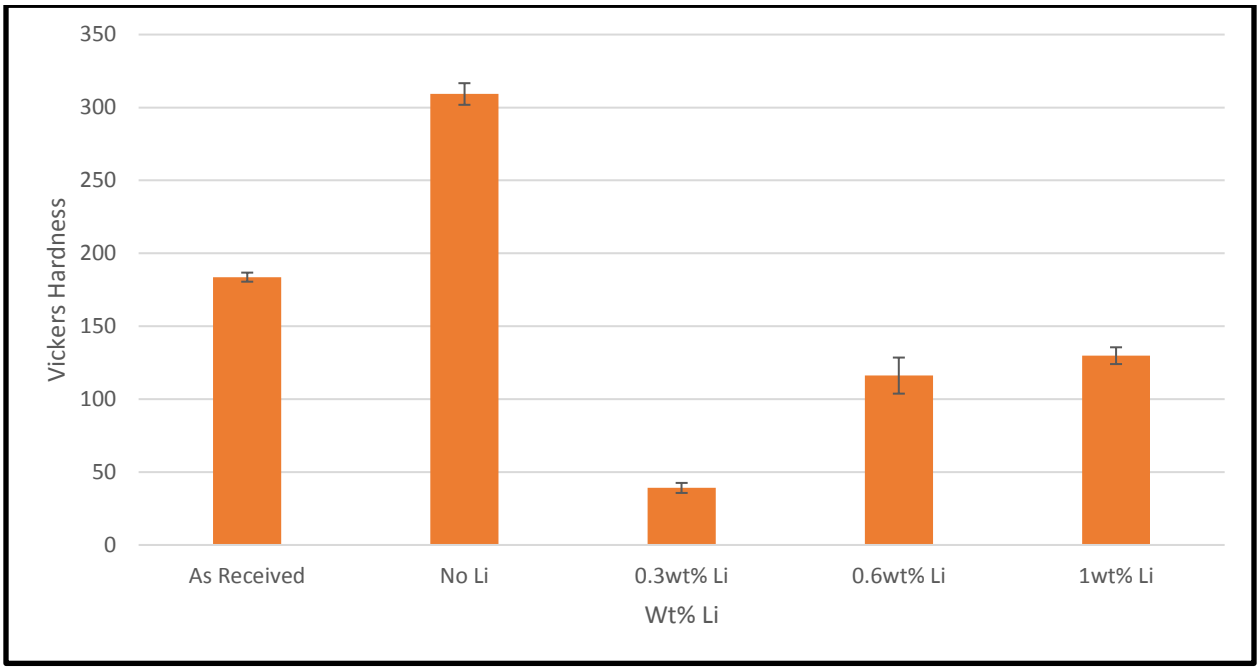


Figure 25: Micro-Vickers hardness measurements made for as received SS316 and SS316 samples exposed to LiCl-2wt%Li_2O containing 0, 0.3, 0.6, and 1wt%Li for 1000hr. Comparison to the morphologies shown in the SEM images presented above shows a direct correlation between surface morphology and hardness, indicating that the hardness measurements made are not representative of the base material.

Raman

Prior to methanol rinsing, Raman spectroscopy was performed in the Ar atmosphere of the glovebox using a Thermo-Fischer DXR Raman microscope equipped with a fiber probe procured from InPhotonics. The laser power was set to 10mW at an excitation wavelength of 532nm, however,

coupling of the laser to the fiber probe results in a loss of laser power of approximately 90% at the sample. Focus of the incident beam was achieved by maximizing the intensity of the recorded spectrum using the vertical translation stage installed in the glovebox. The spectra collected prior to methanol rinsing reported here are an average of 32 spectra obtained with a collection time of 16 seconds per spectra.

Figure 26 shows the Raman spectra obtained prior to methanol rinsing for SS316L samples exposed to LiCl-2wt%Li containing 0, 0.3, 0.6, and 1 wt% Li for 500 hours (left) and 1000 hours (right). The samples exposed to LiCl-2wt%Li in the absence of Li displayed Raman modes at 590cm^{-1}, which our previous work has shown to be indicative of the A_{1g} mode of $LiCrO_2$ [7]. Additionally, the sample exposed to LiCl-2wt%Li_2O-0.3wt%Li exhibited a Raman mode at 864cm^{-1}, which is in the vicinity of some Cr^{6+} compounds. As stated previously, it is hypothesized that this may indicate the presence of $Li_8Cr_2N_8O$ on the surface of this sample. To the best of our knowledge, a Raman investigation of this compound has been reported in the open literature, and a commercial source for this compound to use as a standard could not be found. Consequently, the peak at 864cm^{-1} has not been be positively identified, but is corroborating evidence for the presence of a unique compound on this sample surface. The location of the peak at 864cm^{-1} is sufficiently different from the Li_2CrO_4 peak at 850cm^{-1} observed on methanol rinsed samples exposed to LiCl-Li_2O in the absence of Li that it is unlikely to indicate the presence of Li_2CrO_4 on the surface of this sample. This Raman feature was not observed for the SS316L sample exposed to the same solution chemistry for 1000 hours. No Raman active modes were observed on the samples exposed to melts containing 0.6wt%Li or greater. The discrete peak seen at 484cm^{-1} on some spectra is an artifact of residual light in the laboratory, and the features above approximately 2000cm^{-1} as well as the step up in intensity seen from 500cm^{-1} and below are indicative of fiber probe induced artifacts.

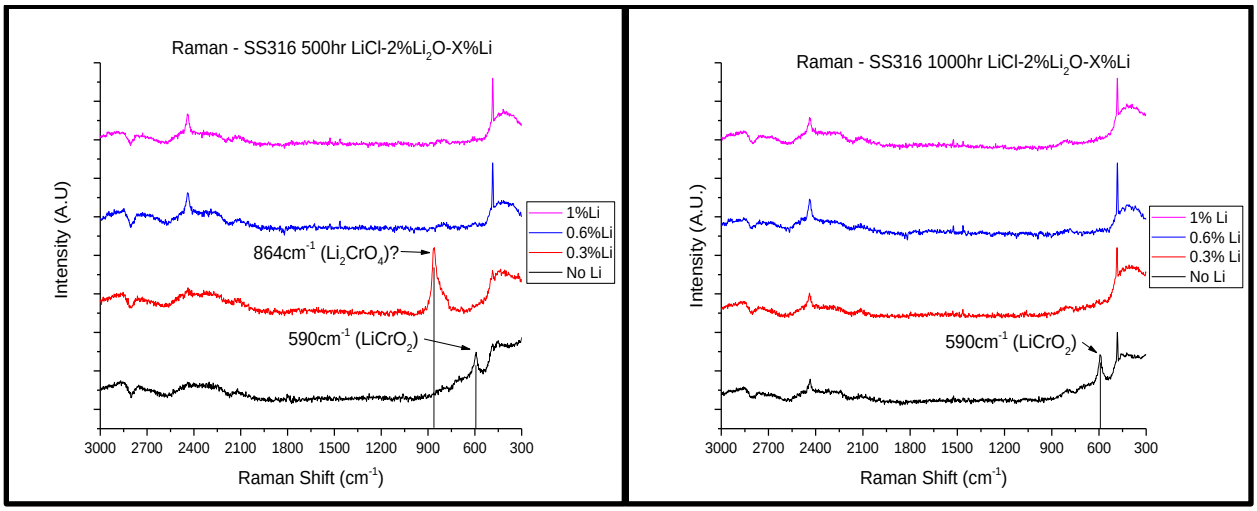


Figure 26: Raman spectra obtained for SS316L samples exposed to LiCl-2wt%Li_2O solutions containing 0, 0.3, 0.6, and 1 wt% Li for (left) 500 hours, and (right) 1000 hours. The characteristic peak of $LiCrO_2$ at 590 cm^{-1} was observed on both 500hr and 1000hr SS316L samples exposed to LiCl-2wt%Li_2O melts without Li present, as was observed in our previous work with short term exposures. A peak hypothesized to be the result of the presence of Li_2CrO_4 at 864 cm^{-1} was observed on the SS316L sample exposed to LiCl-2wt%Li_2O-0.3wt%Li for 500 hours, but not on the surface of the sample exposed to the same solution chemistry for 1000 hours.

Figure 27 shows the Raman spectra obtained for I625 samples exposed to LiCl-2wt%Li containing 0, 0.3, 0.6, and 1 wt% Li for 500 hours (left) and 1000 hours (right). Similar to the SS316L samples, the I625 samples exposed to LiCl-2wt%Li_2O with no Li for both 500 and 1000 hours displayed the Raman mode at 590cm^{-1} indicative of $LiCrO_2$. No Raman modes were observed for any other I625 samples. However, the samples exposed to LiCl-2wt%Li_2O-0.3wt%Li for both 500 and 1000 hours and LiCl-2wt%Li_2O-0.6wt%Li for 500 hours produced anomalous Raman spectra that are indicative of perfect reflectance of the incident laser beam. Multiple attempts were made for each sample with differing incidence angles with no improvement in Raman signal. The cause of this anomalous behavior remains unknown.

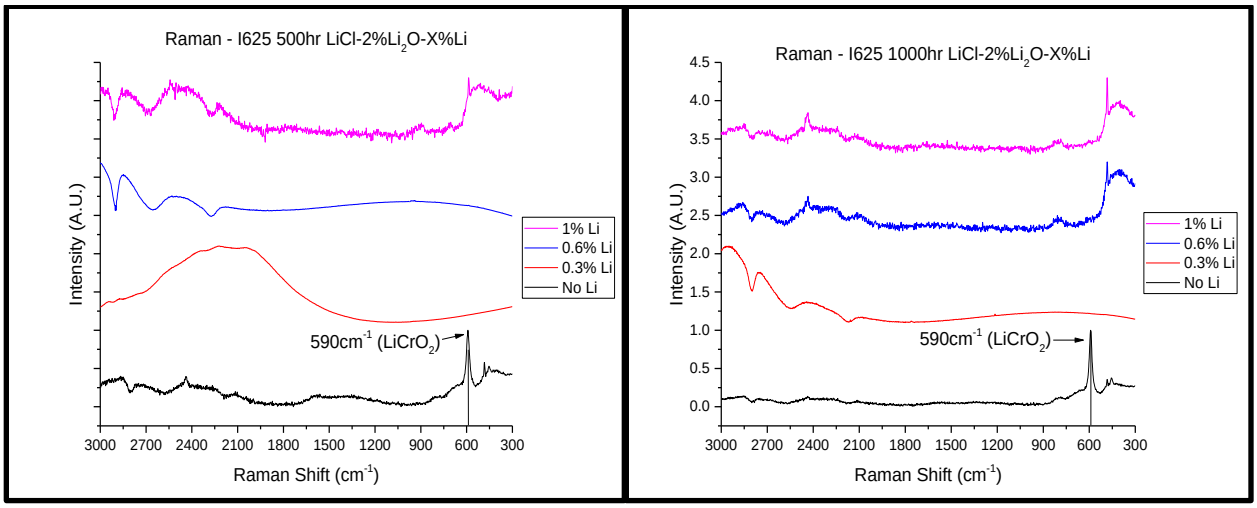


Figure 27: Raman spectra obtained for I625 samples exposed to LiCl-2wt%Li_2O solutions containing 0, 0.3, 0.6, and 1 wt% Li for (left) 500 hours, and (right) 1000 hours. The characteristic peak of $LiCrO_2$ at 590 cm^{-1} was observed on both 500hr and 1000hr I625 samples exposed to LiCl-2wt%Li_2O melts without Li present. Three of the samples (I625 exposed to LiCl-2wt%Li_2O-0.3wt%Li for 500 and 1000 hours, and exposed to LiCl-2wt%Li_2O-0.6wt%Li for 500 hours) exhibited near perfect reflectance of the laser beam, and thus did not provide useful Raman data, despite numerous attempts.

The spectra obtained prior to methanol rinsing for the SS316L and I625 samples exposed to LiCl-1wt%Li_2O containing 0, 0.3, 0.6, and 1wt%Li for 500 and 1000hrs are shown in Figure 28 below. As with the 2wt%Li_2O samples, a peak at 590cm^{-1} was observed for all samples exposed to LiCl-Li_2O solutions in the absence of Li, indicating the presence of $LiCrO_2$ on these samples. No Raman active modes were observed on the surface of any sample exposed to LiCl-1wt%Li_2O in the presence of Li of any quantity in the molten salt solution. As stated above the features of the Raman spectra for SS316L and I625 samples exposed to Li-containing solutions are indicative of fiber probe artifacts and background light present in the laboratory.

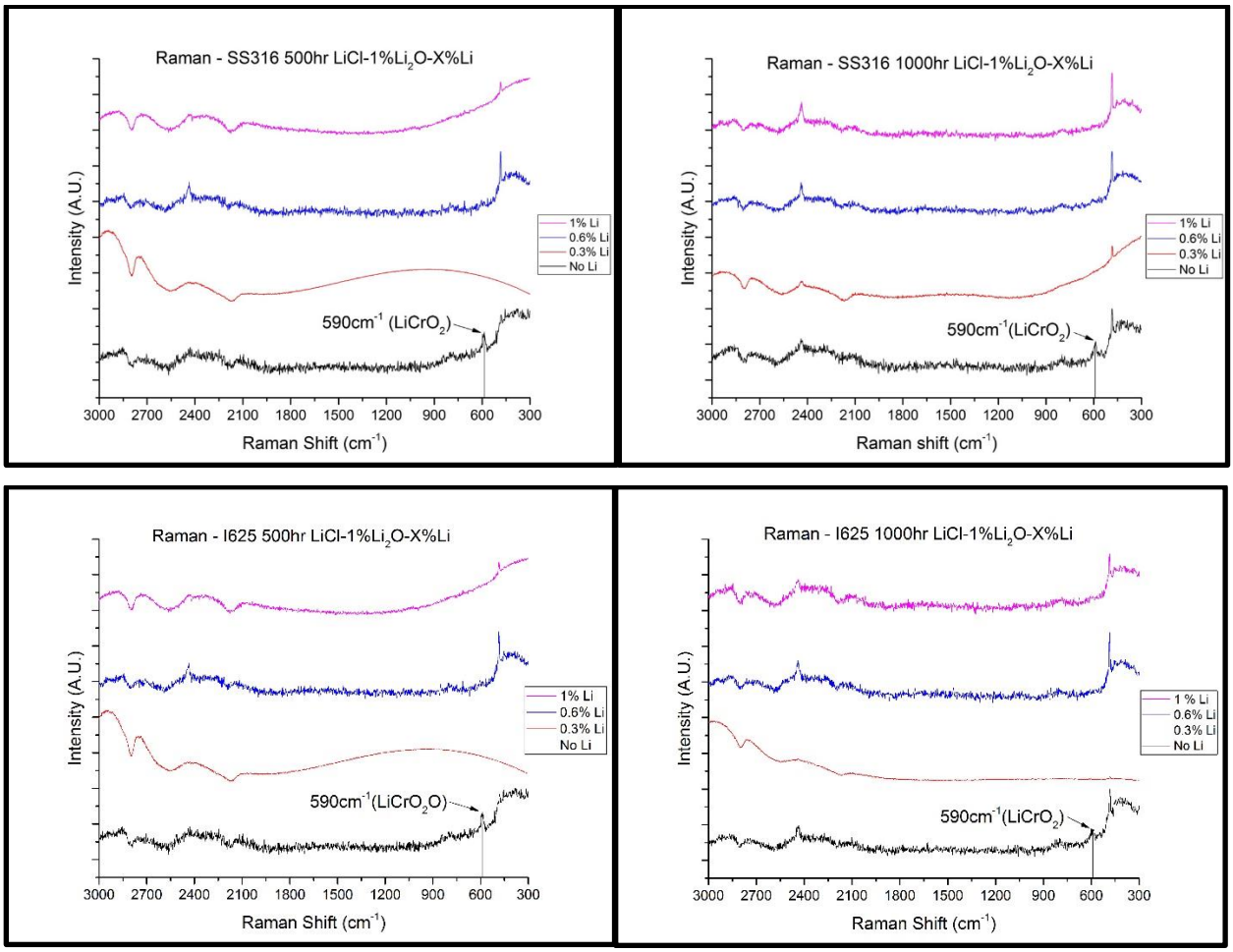


Figure 28: Raman spectra of SS316L (top row) and I625 (bottom row) exposed to LiCl-1wt%Li_2O containing 0, 0.3, 0.6, and 1wt%Li at 650°C for 500hr (left) and 1000hr (right), performed in-situ in the Ar glovebox prior to methanol rinsing to remove the residual salt layer. The features at wavenumbers between 2000 and 3000 cm^{-1} are artifacts caused by the fiber probe.

Following methanol rinsing, Raman analysis was performed a second time with the samples in the Raman microscope. For this data collection, spectra were obtained through the 50x magnification objective lens using a laser power of 10mW, an exposure period of 4 seconds, and 16 exposures were averaged for the spectra reported here. The increased signal intensity and removal of the artifacts introduced by the fiber probe, along with the removal of the residual salt layer resulted in dramatically improved spectra quality. This allowed for minor Raman active modes to be resolved that had previously remained un-detected. To illustrate this, the Raman spectrum of the SS316L sample exposed to LiCl-1wt%Li_2O-0wt%Li at 650°C for 500hr is shown in Figure 29. This spectrum displays peaks that were

observed in various ratios on all samples exposed to LiCl-Li_2O solutions in the absence of Li, and is therefore used as a representative spectra for this set of spectra.

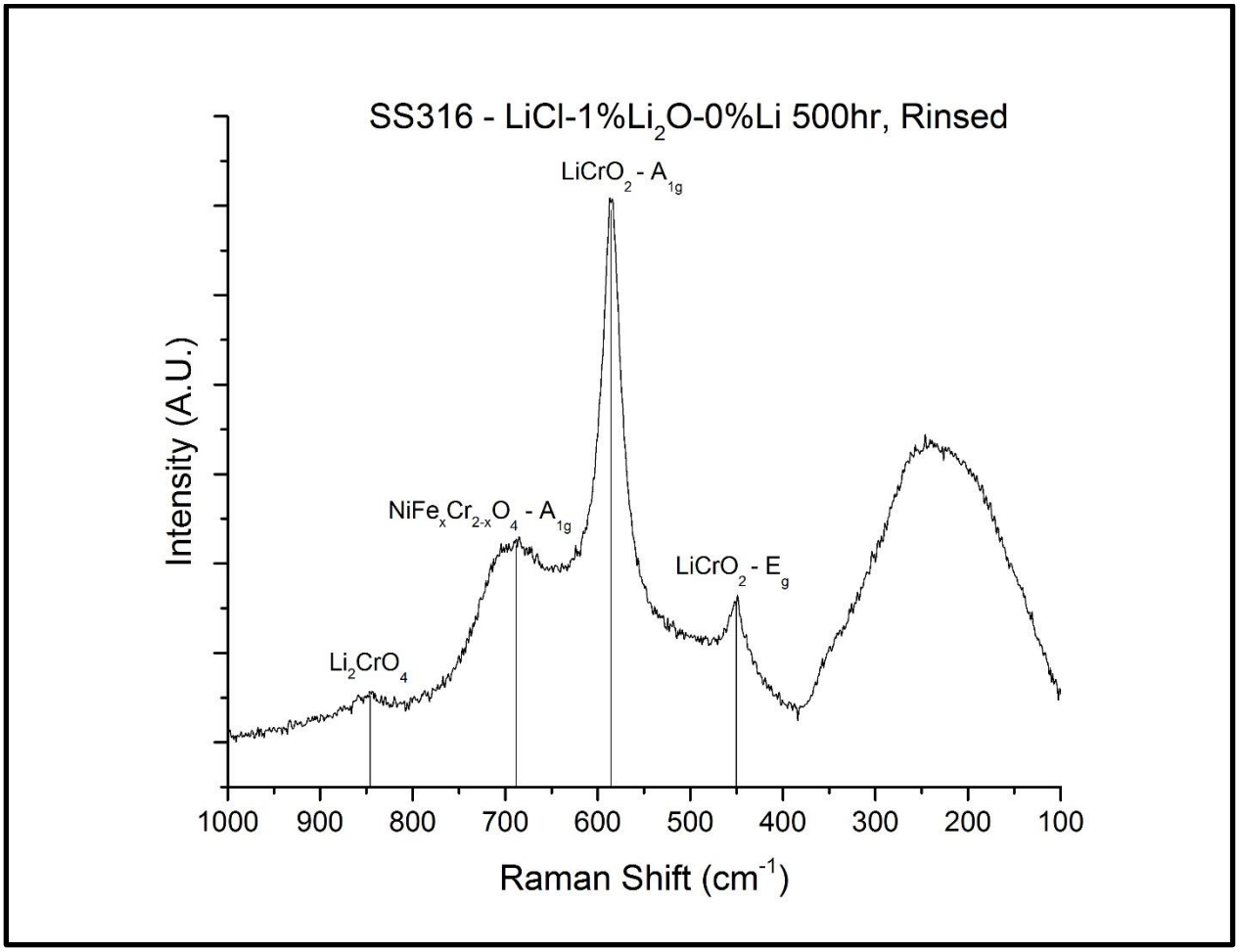


Figure 29: Raman spectrum of SS316L exposed to LiCl-1wt%Li_2O-0wt%Li at 650°C for 500hr, following methanol rinsing. The peaks at 590cm^{-1} and 450cm^{-1} are indicative of the A_{1g} and E_g modes of $LiCrO_2$, respectively [7]. The broad peak at approximately 590cm^{-1} is indicative of nickel-iron-chromium spinel oxides [8], and the small peak at approximately 850cm^{-1} is indicative of Li_2CrO_4.

The spectrum obtained through the microscope is of significantly higher quality than that obtained with the salt layer intact using the fiber probe, with both the A_{1g} and the E_g modes of $LiCrO_2$ clearly defined following the methanol rinse [7]. Prior to methanol rinsing, the E_g mode of $LiCrO_2$ had not been observed for these samples. The observation of these features supports evidence from other analytical techniques that the surface was not degraded by the methanol rinsing procedure. Additionally, Raman active modes not discernible prior to the methanol rinsing procedure can also be

observed, with broad peaks centered at 250cm^{-1}, 690cm^{-1}, and 845cm^{-1}. Based on EDS and XPS analysis shown in their respective sections, the peak at 690cm^{-1} can be attributed to the A_{1g} mode of a mixed Ni, Fe, Cr spinel oxide of the form $NiFe_xCr_{2-x}O_4$, although the exact composition of this oxide is not easily identified [8]. The position of this peak was also observed to shift slightly on other samples, which can likely be attributed to variations in the stoichiometry of the spinel oxide due to differing exposure periods, melt compositions, and base materials. The peak at 845cm^{-1} is hypothesized to originate from Li_2CrO_4, based on the presence of Cr^{6+} in the XPS spectra collected from SS316L samples exposed to LiCl-Li_2O solutions in the absence of Li. The broad feature centered around 250cm^{-1} could not be positively attributed to any single compound, but may be caused by the combination of the minor modes of Li_2CrO_4 shown in Figure 31 below and minor components of the $NiFe_xCr_{2-x}O_4$ spectrum. This broad feature at 250cm^{-1} was observed only on this sample.

When exposed to LiCl-Li_2O solutions containing Li, these oxide based surface films are destabilized due to the highly reducing nature of metallic Li. To illustrate the changes to the surface layer present on samples exposed to LiCl-Li_2O solutions as a function of Li concentration, Figure 30 shows the Raman spectra obtained from SS316L samples exposed to LiCl-1wt%Li_2O solutions containing 0, 0.3, 0.6, and 1wt%Li at 650°C for 500hr. The spectra for the SS316L sample exposed to LiCl-1wt%Li_2O-0wt%Li for 500hr is identical to that shown in Figure 29, above, but is shown again to allow direct comparison to the spectra for samples exposed to melts containing Li under otherwise identical conditions.

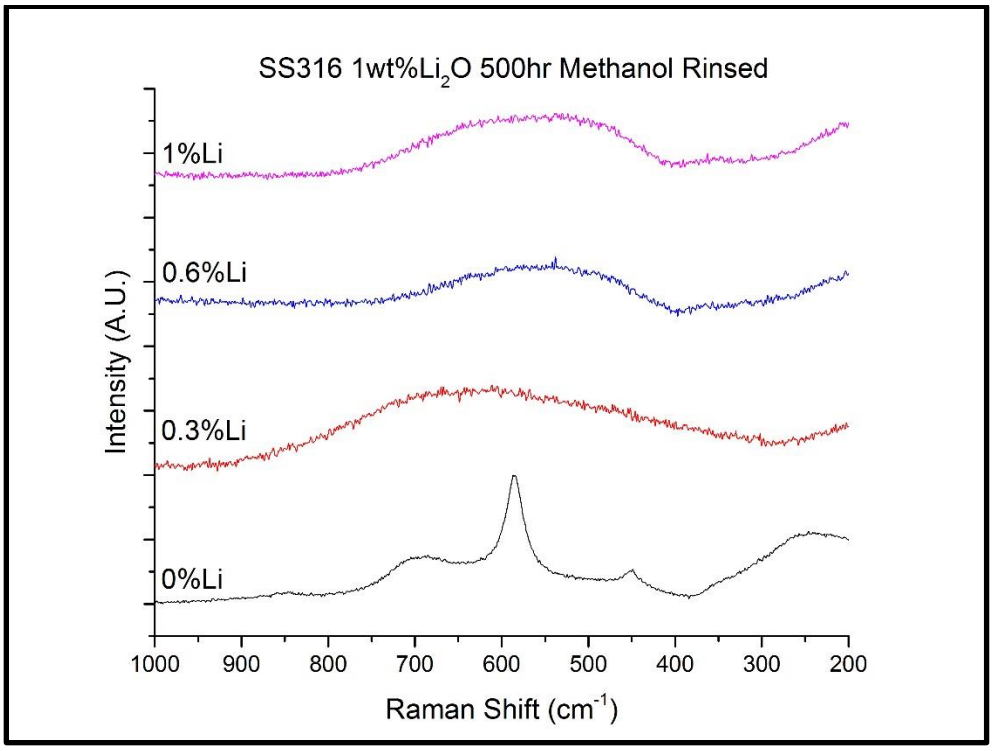


Figure 30: Raman spectra of SS316L exposed to LiCl-1wt%Li_2O containing 0, 0.3, 0.6, and 1wt%Li at 650°C for 500hr. The spectra for the SS316L sample exposed to LiCl-1wt%Li_2O-0wt%Li for 500hr is identical to that shown in Figure 31. For samples exposed to LiCl-Li_2O solutions in the presence of Li, no discernible peaks are present in the Raman spectra. The broad features observed on these samples are currently unidentified.

As no investigations into the Raman spectra of Li_2CrO_4 could be found in literature, the spectra of pure Li_2CrO_4 was collected to confirm that the peak seen at 845cm^{-1} in Figure 29 could be attributed to this compound. For this purpose, Li_2CrO_4 of 95% purity was obtained from Strem Chemicals. The Raman spectrum collected from pure Li_2CrO_4 is shown in Figure 31 below.

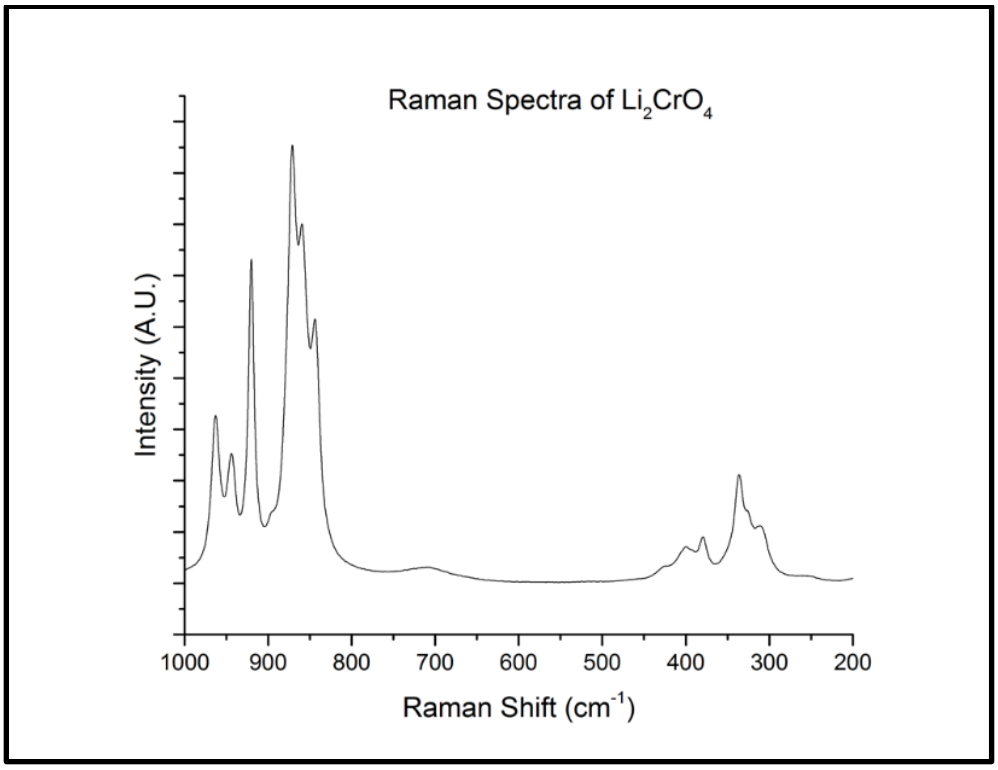


Figure 31: Raman spectrum obtained from Li_2CrO_4. Collection parameters were identical to those used for methanol rinsed samples. The primary features of the Li_2CrO_4 spectrum occur around 850cm^{-1}, with minor features in the range of 450cm^{-1} to 300cm^{-1}.

The assignment of specific vibrational and rotational modes to each of the peaks observed in Figure 31 is beyond the scope of this study. However, it can be seen that the primary features of pure Li_2CrO_4 occur between 1000cm^{-1} and 800cm^{-1}, with the dominant peak occurring at approximately 850cm^{-1}. Additional minor features are present between 450cm^{-1} and 375cm^{-1}. As the oxide layer of the samples is non-homogenous and consists primarily of $LiCrO_2$ with small amounts of $NiFe_xCr_{2-x}O_4$ and Li_2CrO_4, the smearing of the features of the Li_2CrO_4 spectrum to form the single, broad peak centered around 850cm^{-1} observed on the samples exposed to LiCl-Li_2O is plausible [8].

SS316L samples exposed to LiCl-2wt%Li_2O-Li solutions displayed similar behavior to those exposed to LiCl-1wt%Li_2O-Li solutions. Figure 32 shows the Raman spectra collected from SS316L samples exposed to LiCl-2wt%Li_2O containing 0, 0.3, 0.6, and 1wt%Li at 650°C for 500hr.

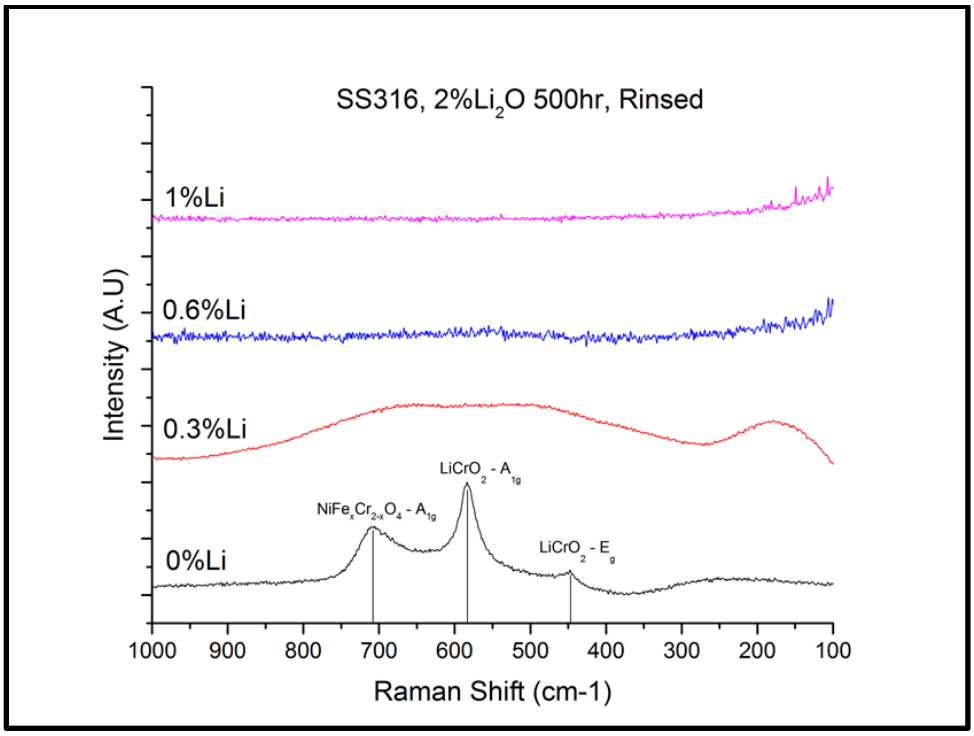


Figure 32: Raman spectra obtained from SS316L samples exposed to LiCl-2wt%Li_2O containing 0, 0.3, 0.6, and 1wt%Li at 650°C for 500hr. The features indicative of $LiCrO_2$ and $NiFe_xCr_{2-x}O_4$ are easily observable in the absence of Li. The peak corresponding to Li_2CrO_4 was not observed on this sample. In the presence of 0.3wt%Li, the features observed in the absences of Li are broadened, with no individual features being discernible in the spectrum. At higher Li contents, the spectra obtained show no features at all, with only background noise present, indicative of a bare metallic surface.

The sample exposed to LiCl-2wt%Li_2O for 500hr in the absence of Li shows a very similar Raman spectrum to that of the sample exposed to LiCl-1wt%Li_2O for 500hr in Figure 29, however, the peak indicative of Li_2CrO_4 was not observed. When 0.3wt%Li is present in the system, the features seen in the absence of Li are broadened, with no peaks defined well enough to be attributed to a particular compound, indicating that the surface film is destabilized by the addition of Li. At higher Li concentrations of 0.6 and 1wt% Li, no Raman active modes were present on the samples surfaces, and the spectra are indicative of the base alloy, showing only background noise of the system.

As exposure period increases in the absence of Li, the Raman spectra indicate that further oxidation of the surface occurs, as illustrated in Figure 33, which shows the Raman spectrum collected for SS316L exposed to LiCl-2wt%Li_2O at 650°C for 1000hr in the absence of Li.

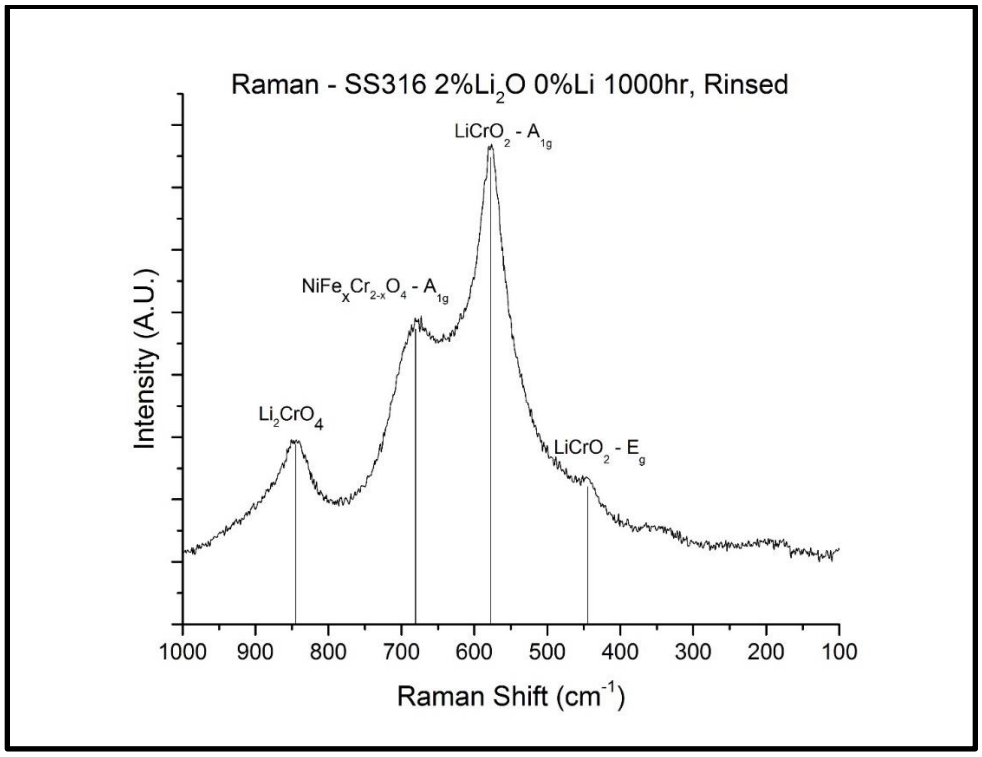


Figure 33: Raman spectrum of SS316L exposed to LiCl-2wt%Li_2O-0%Li at 650°C for 1000hr and rinsed with Methanol. Features associated with $LiCrO_2$, $NiFe_xCr_{2-x}O_4$ and Li_2CrO_4 are observed.

Compared to the spectrum for SS316L exposed to LiCl-2wt%Li_2O-0wt%Li at 650°C for 500hr shown in Figure 32, the SS316L sample exposed to the same conditions for 1000hr prominently shows the Li_2CrO_4 peak at 845cm^{-1}, and the peak position for the $NiFe_xCr_{2-x}O_4$ A_{1g} mode shifts from approximately 705cm^{-1} to approximately 690cm^{-1}. According to the work done by Hosterman, this indicates an increase in the chromium content of the spinel oxide as a function of time, i.e., the value of x in $NiFe_xCr_{2-x}O_4$ decreases over time [8].

Overall, Similar trends were observed for the Raman spectra of I625 samples following methanol rinsing. These spectra, as well as additional spectra for SS316L samples are shown in Appendix C.

XPS

XPS data was collected using a PHI 5600 spectrometer utilizing Al K_α source emitting radiation of 1486.6eV, and operated at an accelerating voltage of 15kV and emission power of 300W. The Ag $3d_{3/2}$ line at 368.3eV was used for calibration of the spectrometer to an accuracy of ±0.05eV. Sputtering was performed using an Ar^+ ion source, which was measured to remove 7nm of Ta_2O_5 per minute. Data collection and analysis for XPS is the primary bottleneck of all of the surface analytical techniques employed in this study. Currently, survey spectra from binding energies (BE) of 1400eV to 0eV, as well as narrow scans for each element detect in the survey scans have been collected prior to and following 2 minutes of Ar^+ sputtering for all samples exposed to LiCl-1wt%Li_2O solutions, following methanol rinsing. The data presented below is representative of the data collected thus far, although rigorous analysis of all spectra has not been completed at this time.

The surface sensitivity of XPS, which is on the order of 10nm, meant that the residual salt layer obscured the sample surface from direct observation using this technique on most of the samples exposed to melts containing Li, and severely decreased the ability of the instrument to resolve the sample surface on samples exposed to LiCl-Li_2O in the absence of Li. To illustrate this point, XPS survey spectra of SS316L samples exposed to LiCl-2wt%Li_2O in the absence of Li and the presence of 0.3%Li prior to methanol rinsing are shown in Figure 34. These spectra are typical of those collected for both SS316L and I625 prior to the methanol rinsing procedure in that only salt is observable.

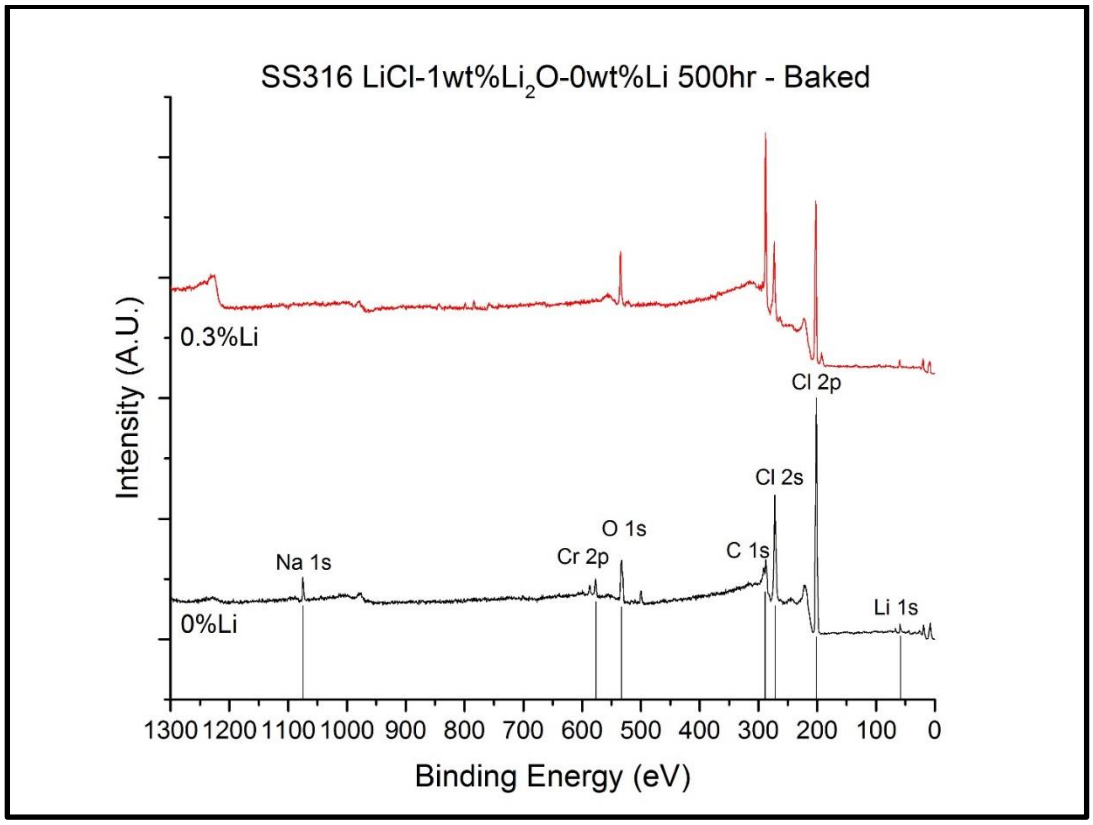


Figure 34: XPS spectra of SS316L samples exposed to LiCl-2wt%Li_2O containing 0 and 0.3wt%Li for 500hr prior to methanol rinsing. The residual salt layer largely prevented observation of the observation of the base material.

For all samples exposed to LiCl-Li_2O in the presence of Li, the XPS spectra only indicate the presence of elements from the salt, namely, Li, Cl, and O due to the nearly uniformly distributed residual salt layer. It can also be observed that the signal from the residual salt is significantly stronger than that of Cr on the sample exposed to LiCl-X%Li_2O in the absence of Li. In contrast, Figure 35 shows the XPS spectra recorded for the same samples following the 15 minute methanol rinsing procedure described previously. These spectra have significantly reduced Cl content, and the elements comprising the sample surfaces are readily observed.

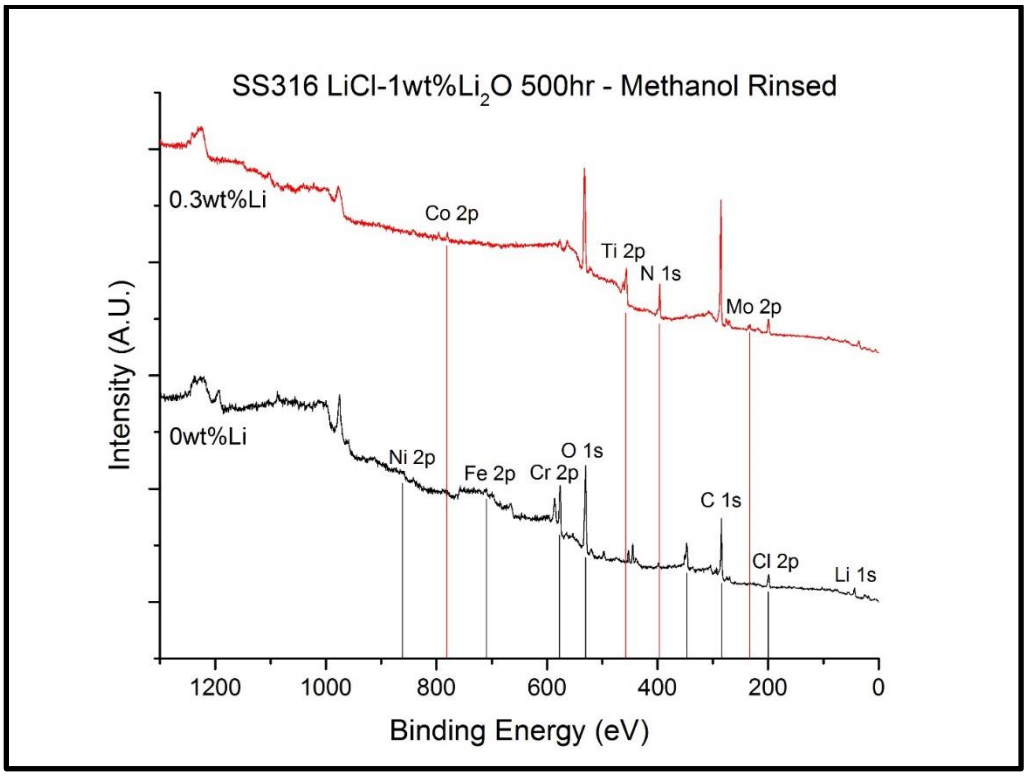


Figure 35: Survey spectra recorded on the same SS316L samples exposed to LiCl-1wt%Li_2O containing 0wt%Li (bottom) and 0.3wt%Li (top) at 650°C for 500hr after rinsing in methanol for 15 minutes. The spectra recorded before rinsing with methanol (Figure 34, above) show primarily salt constituents (Li, Cl, and O), and small amounts of Cr in the absence of Li. Following the methanol rinsing procedure, the spectrum shows a significantly reduced Cl content, and the constituent elements of the surface are clearly observable.

In Figure 35, the Cl content has been significantly decreased, indicating an almost complete removal of the residual salt layer. For the SS316L sample exposed to LiCl-1wt%Li_2O at 650°C for 500hr in the absence of Li, the surface is primarily composed of Cr and O, with Ni and Fe detectable in small quantities. Surface contamination from Ca, as well as adventitious C was also observed. Adventitious carbon is routinely observed on all samples via XPS, and is broadly accepted as the standard used for charge correction of XPS spectra. Additionally, Ca has been observed on a number of samples in our laboratory.

For the SS316L sample exposed to LiCl-1wt%Li_2O-0.3wt%Li at 650°C for 500hr, the surface shows a relatively thick Ti-based surface deposit, with high quantities of N and O present. The deposition of Ti based compounds on samples exposed to LiCl-Li_2O in the presence of Li was extensively studied during

our previous short term studies. TiO_2 is a common impurity in Li_2O, and the observation of the deposition of Ti compounds on this sample is not surprising, and will not be detailed more here. More interestingly, Co was also observed on this sample, as well as some of the other samples exposed to LiCl-Li_2O in the presence of Li. Co is not an alloying element of SS316L, but is present as the primary impurity in the Ni crucibles used for these studies, at concentrations of less than 1wt%. Consequently, the presence of Co on the surface of the samples exposed to LiCl-Li_2O solutions in the presence of Li indicates that there is mass transport from the crucible to the samples. Further investigation of the crucibles used for this study is planned, with the goal of determining a more complete view of the degradation of materials and mass transport in the system. Mass transport of Co from the crucible to the samples had not been observed in our previous short term experiments. Additionally, Mo was also observed in small quantities on this sample. Further analysis of the narrow scans for each of these samples are given below, following the discussion of the effects the methanol rinsing procedure.

Detailed analysis of the alloying elements, especially the Cr 2p spectra is necessary to tease out the details of the corrosion mechanisms of SS316L, as Cr is the primary element responsible for the formation of oxide films in the absence of Li. Prior to the removal of the residual salt layer, the spectra of the sample surface originates from a small area between “islands” of residual salt that can be observed in Figure 16. Consequently, the effects of differential charging are difficult to deconvolute for these samples, as charging is non-homogenous between the Cr-based oxide layer and the residual salt layer, which can lead to errors when peak fitting the spectra for quantification of oxidation states. The presence of LiCl on the sample surface further complicates charge correction, as the C 1s peak lies on the shoulder of the Cl 2s peak. To demonstrate these difficulties and the benefits of methanol rinsing for analysis of XPS spectra obtained from these samples, Figure 36 shows the narrow scans of the C 1s spectra obtained from the same spot on the SS316L sample exposed to LiCl-2wt%Li_2O-0%Li for 500hr, the survey scans of which are shown in Figures 34 and 35, above.

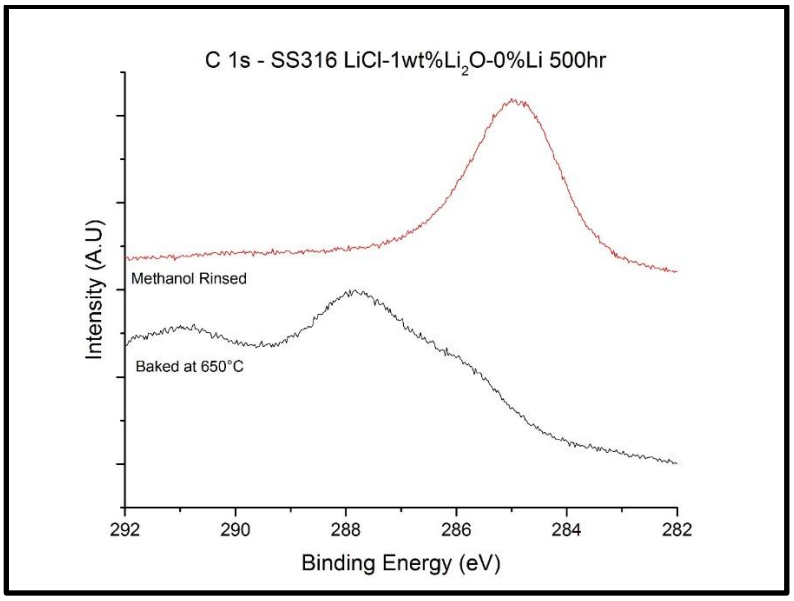


Figure 36: XPS narrow scan of the adventitious C 1s spectra of SS316L exposed to LiCl-1wt%Li_2O-0%Li for 500hr at 650°C before (bottom) and after methanol rinsing (top). It can be easily observed that the C1s spectra is significantly more complex when the residual salt layer is still present on the sample surface (before methanol rinsing). This is a result of the convolution of differential charging and the location of the Cl 2s shoulder, which overlaps significantly with the C1s spectra. The binding energy of the adventitious C1s peak for the methanol rinsed sample shows very minimal charging of 0.1eV, which drastically simplifies the analysis of the other elements, presented below.

It can be observed in Figure 42 that the C 1s spectrum prior to methanol rinsing shows the effects of differential charging, exhibited by the presence of a hump on the lower binding energy side of the primary peak at 287.8eV, as well as a sloping baseline caused by the Cl 2s shoulder, which peaks at ~291eV. Following methanol rinsing, the C 1s spectra is typical of adventitious carbon on a conductive sample, showing only minor charging of 0.1eV from the standard value of 284.8eV typically used for charge correction during XPS analysis. The simplification of interpretation for the C 1s spectra has a significant impact on further analysis of the chemical structure of these samples, in addition to the other benefits obtained by removal of the salt.

To verify that the methanol rinsing procedure had minimal impact on the surface chemistry of the samples, the Cr 2p spectra for the SS316L sample exposed to LiCl-1wt%Li_2O-0wt%Li at 650°C for 500hr was collected before and after methanol rinsing. Both of these narrow scans are shown in Figure 37, below.

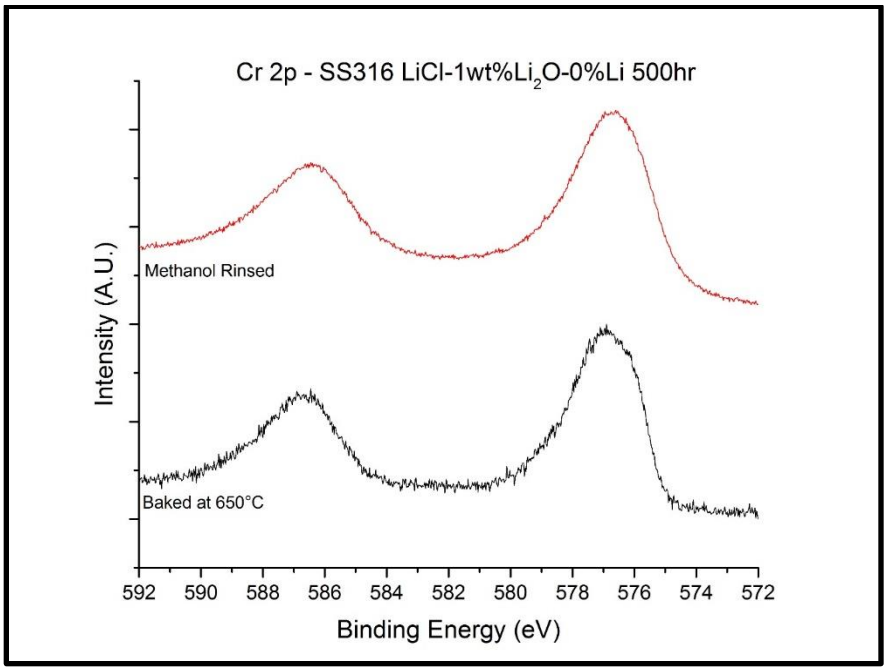


Figure 37: Comparison between methanol rinsed (top) and non-rinsed (bottom) SS316L surfaces after exposure to LiCl-1%Li_2O-0%Li for 500hr at 650°C. Identical collection parameters were used for both spectra. It can be seen that there is minimal change in the spectrum collected, indicating that there was no change of chemical state caused by the methanol rinsing procedure. The decreased noise of the spectrum collected following the methanol rinsing procedure is a product of the increased signal available for detection from the analysis area following removal of the residual salt layer.

It can be observed that the methanol rinsing procedure had a negligible impact on the Cr 2p spectrum, indicating that there was no chemical alteration to the Cr compounds on the surface of the sample. Along with the evidence collected via SEM/EDS, XRD, and Raman spectroscopy, it can be concluded that the methanol rinsing procedure employed in this study effectively removes the residual salt layer without affecting either the morphology or chemistry of the alloy/oxide layer surfaces exposed to LiCl-Li_2O-Li solutions.

Identification of the oxidation state of Cr present on the surface of the SS316L sample exposed to LiCl-1wt%Li_2O-Li at 650°C for 500hr was performed by peak fitting the Cr $2p_{3/2}$ spectra using previously published peak fitting parameters [9]. The peak fit data is shown in Figure 38, while the peak fitting parameters are given in Table 6.

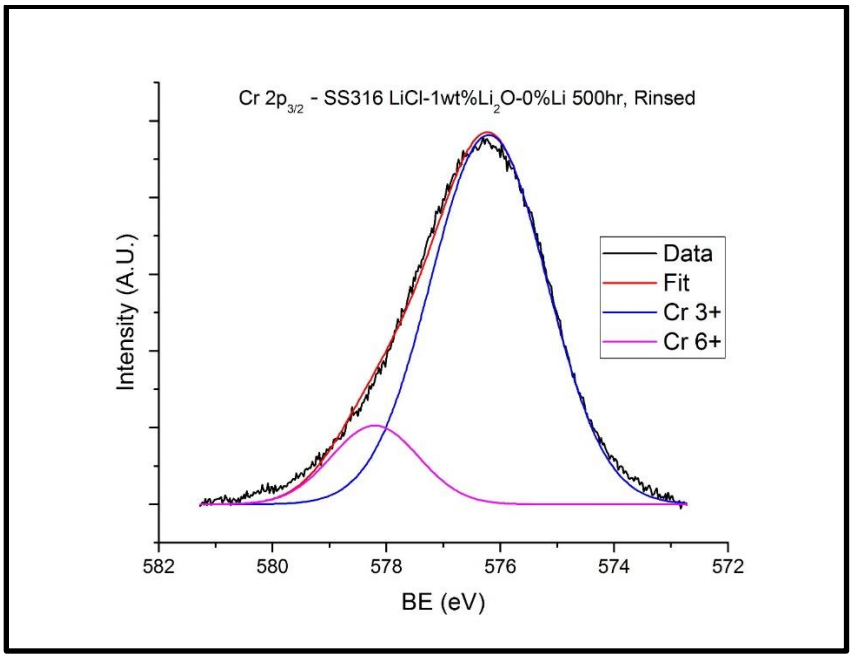


Figure 38: Peak fit Cr $2p_{3/2}$ spectra of SS316L exposed to LiCl-1wt%Li_2O-0%Li for 500hr at 650°C after removal of the salt layer with methanol, showing the presence of both Cr^{3+} and Cr^{6+} on the sample surface. The presence of both oxidation states of Cr confirms the simultaneous presence of both $LiCrO_2$ (Cr^{3+}) and Li_2CrO_4 (Cr^{6+}) on the sample surfaces in the absence of Li.

Table 6: Peak fitting parameters used for analysis of the Cr $2p_{3/2}$ spectra of SS316L exposed to LiCl-1wt%Li_2O-0%Li for 500hr at 650°C and rinsed with methanol, shown in Figure 12.

Peak	BE	FWHM	Area%
Cr 3+	576.2	2.4	86.2
Cr 6+	578.2	1.8	13.8

This analysis shows that there is the simultaneous presence of Cr^{3+} and Cr^{6+} on the sample, further supporting the presence of both $LiCrO_2$ (Cr^{3+}) and Li_2CrO_4 (Cr^{6+}) on the surfaces of samples exposed to LiCl-Li_2O solutions in the absence of Li. The presence of Cr^{3+} is also required for $NiFe_xCr_{2-x}O_4$, as both Fe and Cr are in the 3+ oxidation state in this compound, while Ni is present in the 2+ oxidation state. Further confirmation of the presence of $NiFe_xCr_{2-x}O_4$ is given by the narrow scans of the Ni 2p and Fe 2p spectra for SS316L exposed to LiCl-1wt%Li_2O-0wt%Li for 500hr, which are shown in Figure 39, below.

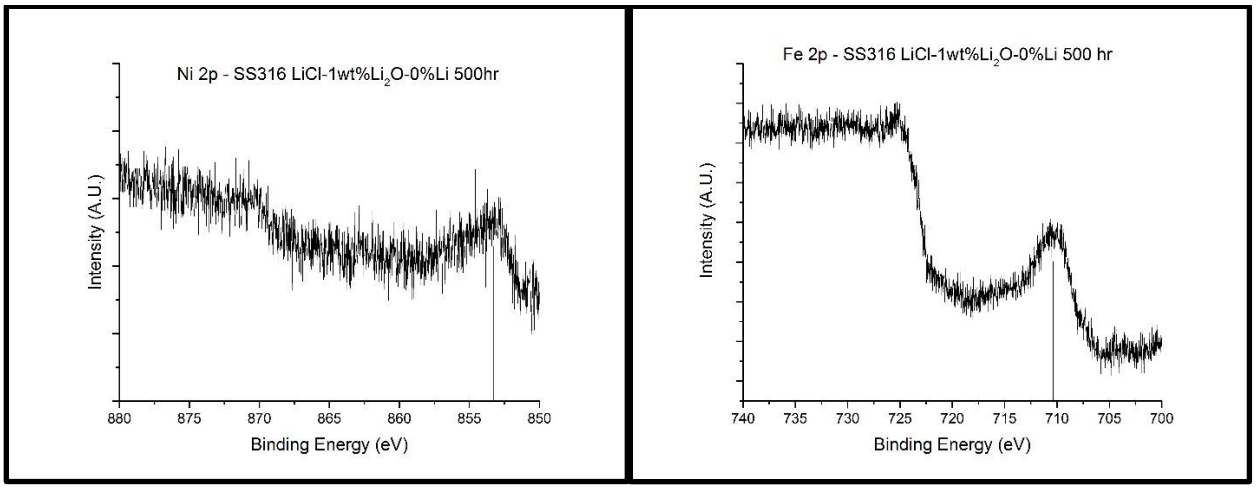


Figure 39: XPS narrow scans for Ni 2p (left) and Fe 2p (right) collected from SS316L exposed to LiCl-1%Li_2O-0%Li at 650°C for 500hr. The Ni $2p_{3/2}$ peak is located at 853.5eV, while the Fe $2p_{3/2}$ peak is located at 710.1eV. These binding energies correspond to Ni^{2+} and Fe^{3+}, respectively. Neither element was detected in the metallic state, confirming the presence of Ni and Fe based oxides on the sample surface. In conjunction with Raman spectroscopy and EDS analysis, this is further evidence supporting the presence of a $NiFe_xCr_{2-x}O_4$ based spinel present on the surface of the samples exposed to LiCl-Li_2O in the absence of Li.

These narrowscans show that Ni and Fe are present as Ni^{2+} and Fe^{3+}, respectively, based on the binding energy of the most prominent peak of the $2p_{3/2}$ spectrum for each element. This is in accordance with the presence of $NiFe_xCr_{2-x}O_4$ on the surface of samples exposed to LiCl-Li_2O in the absence of Li.

In the presence of Li, the highly reducing nature of metallic Li destabilizes the oxide films that are present on the sample surfaces in the absence of Li. However, the transition between electrochemical oxidation of the samples in the absence of Li and liquid metal attack in the presence of high Li concentrations is not abrupt. Our previous short term studies have shown that at concentrations at or below the apparent solubility limit of Li in the system (around 0.3wt%Li) [1], there exists a transition region where both modes of attack occur simultaneously. The Cr $2p_{3/2}$ spectra shown in Figure 40 gives further evidence for this hypothesis. The peak fitting parameters used for this Figure are given in Table 7.

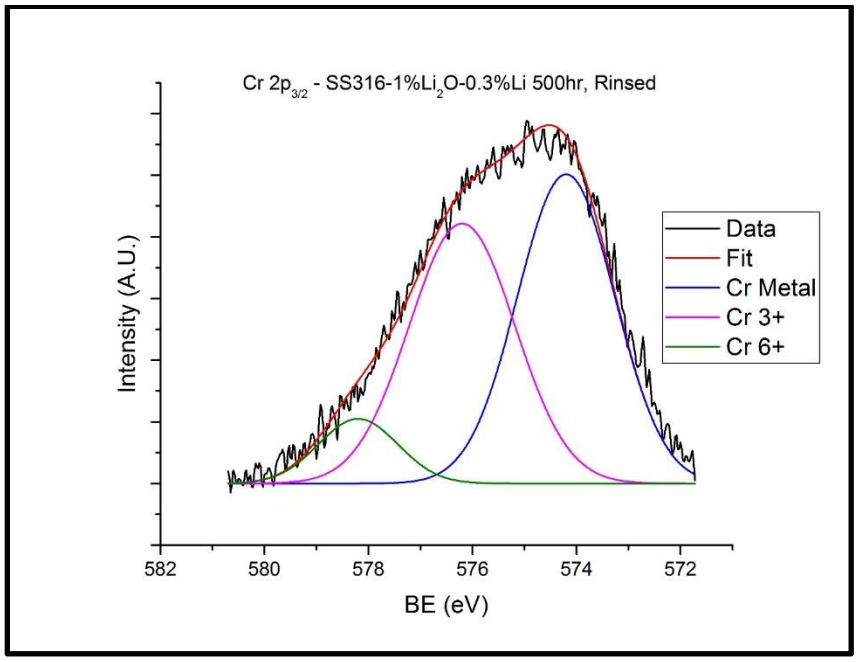


Figure 40: Peak fit Cr $2p_{3/2}$ spectra of SS316L exposed to LiCl-1wt%Li_2O-0.3%Li for 500hr at 650°C, showing the presence of Cr^{3+}, Cr^{6+}, and Cr metal on the sample surface. Charge correction of 1.2eV was applied based on the adventitious C 1s peak at 284.8eV. The simultaneous observation of the three oxidation states of Cr on the sample surface following exposure to 0.3wt%Li supports the hypothesis of a transition region between electrochemical corrosion and liquid metal attack at intermediate Li concentrations.

Table 7: Parameters used for peak fitting the Cr $2p_{3/2}$ XPS spectrum collected for the SS316L sample exposed to LiCl-1wt%Li_2O-0.3wt%Li at 650° for 500hr following methanol rinsing.

Peak	BE	FWHM	Area%
Cr Metal	574.2	2.2	47.9
Cr 3+	576.2	2.4	43.9
Cr 6+	578.2	1.8	8.2

As can be observed in Figure 40, the Cr $2p_{3/2}$ spectrum for the SS316L sample exposed to LiCl-1wt%Li_2O-0.3wt%Li at 650°C for 500hr and subsequently rinsed with methanol has components attributable to Cr^0, Cr^{3+}, and Cr^{6+}. This indicates that Cr-based oxides are present on the sample, but are significantly reduced in thickness and/or coverage of the surface when compared to the oxide films observed on samples exposed to LiCl-Li_2O solutions in the absence of Li. Importantly, the presence of Cr in the metallic state on this sample also serves to confirm that the methanol rinsing procedure does not oxidize the sample surfaces. As Cr is the most active metal present in both SS316L and I625, it will be the most likely to be affected chemically by the methanol rinsing procedure. As mentioned previously, Ti,

Co, and Mo were the other transition metals observed in the survey spectrum of SS316L exposed to LiCl-1wt%Li_2O-0.3wt%Li at 650°C for 500hr. The narrow scans of these elements are given in Figures 41, 42, and 43, respectively.

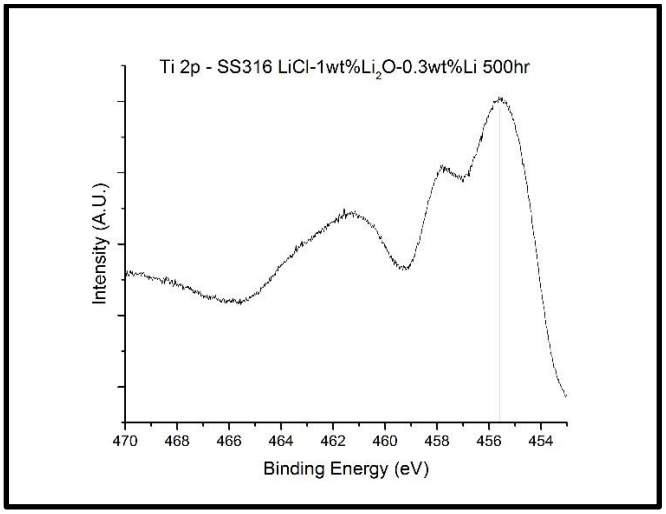


Figure 41: XPS narrow scan of the Ti 2p peak observed on SS316L exposed to LiCl-1wt%Li_2O-0.3wt%Li at 650°C for 500hr and rinsed with methanol. Charge correction of 1.2eV was applied based on the adventitious C 1s peak at 284.8eV. The peak position demarcated by the line at 455.4eV is indicative of TIN. Furthermore, the peak shape is indicative the presence of TiN, Ti^{3+}, and Ti^{4+}, in accordance with our previous work.[4]

As mentioned previously, the presence of Ti compounds on the surfaces of samples exposed to LiCl-Li_2O-Li solutions was observed during our short term exposure studies. In our previous work, Mo was observed to behave similarly to Cr in some respects, becoming enriched on the surface in the absence of Li, and depleted at higher Li concentrations. As Mo is a minor alloying element of SS316L at around 2wt%, the exact details of its behavior in the LiCl-Li_2O-Li system remains uncertain. Figure 42 shows the narrow scan for the Mo 3d peak observed on SS316L exposed to LiCl-1wt%Li_2O-0.3wt%Li at 650°C for 500hr following the methanol rinsing procedure.

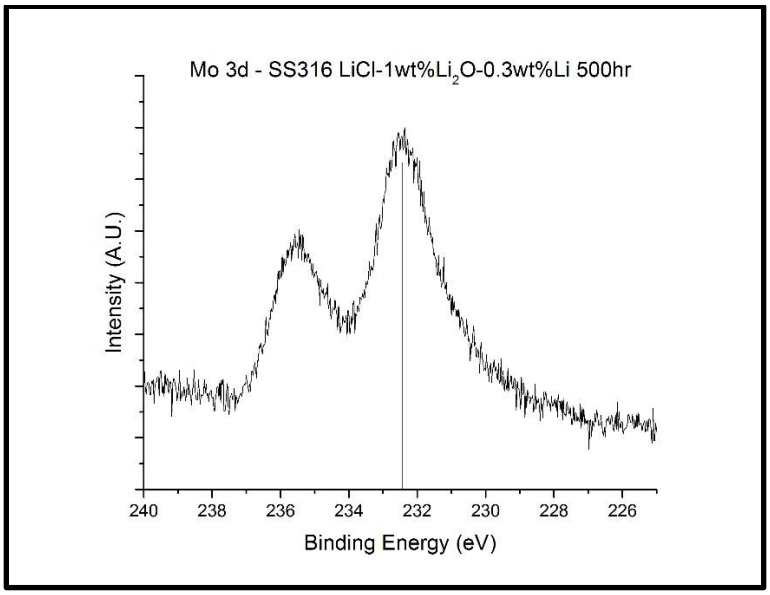


Figure 42: XPS narrow scan of the Mo 3d peak observed on SS316L exposed to LiCl-1wt%Li_2O-0.3wt%Li at 650°C for 500hr and rinsed with methanol. Charge correction of 1.2eV was applied based on the adventitious C 1s peak at 284.8eV. The binding energy of the $3d_{5/2}$ peak of 232.3eV is consistent with the presence of Mo^{6+}.

The binding energy of the Mo $3d_{5/2}$ peak of 232.3eV is consistent with the presence of Mo^{6+}. The exact nature of the compound that Mo forms on the SS316L surface is unknown at this time, however, it is likely that the chemistry of Mo may be similar to that of Cr.

As mentioned previously, the presence of Co on the sample surface was not expected, as it is not an alloying element of SS316L, and it had not been observed in our short term studies. Interestingly, the Co 2p spectra, which is presented in Figure 43, is typical of Co^{3+}, due to its binding energy and peak shape. The only source of Co in the system is from the Ni crucibles, indicating that there is mass transport occurring between the crucibles and samples. The cause of this, and its implications to the degradation of materials in the system as a whole requires further investigation.

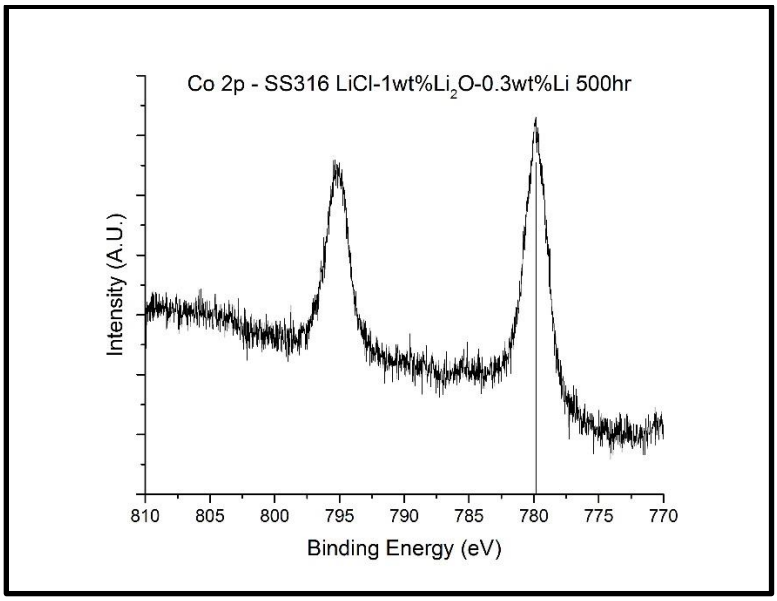


Figure 43: XPS narrow scan of the Co 2p peak observed on SS316L exposed to LiCl-1wt%Li_2O-0.3wt%Li at 650°C for 500hr and rinsed with methanol. Charge correction of 1.2eV was applied based on the adventitious C 1s peak at 284.8eV. The binding energy and shape of the $2p_{3/2}$ peak of 789.8eV is consistent with the presence of Co^{3+}.[10]

Inductively Coupled Plasma – Optical Emission Spectroscopy

Inductively Coupled Plasma – Optical Emission Spectroscopy (ICP-OES) was used to detect the leaching of alloying elements into the molten salt. For each salt change, the cooled salt ingot was dissolved in 750mL of DI H_2O. 65mL of the resulting solution was saved for analysis via ICP-OES. 15mL of this sample was acidified with HNO_3 and HCL to a pH of 1 to dissolve any precipitate. This acidified solution was analyzed via a Perkin Elmer Optima 8000 ICP-OES. As salt changes were performed every 96 hours, 11 salt samples were collected over the course of each 1000hr exposure. Unfortunately, the data from ICP-OES did not provide any conclusive information, and is therefore not reported here.

Conclusions and Future Work

The present study has investigated the corrosion behavior of SS316L and I625 when exposed to molten LiCl-Li_2O-Li solutions at 650°C for periods of 500 and 1000hr. For this work, the composition of Li_2O was varied between 1 and 2wt%Li_2O, and the Li concentrations studied were 0, 0.3, 0.6, and 1wt%Li. At the present time, all exposures have been completed, as has the bulk of the post exposure

surface analysis. Post exposure surface analysis has been performed using XRD, SEM-EDS, Raman spectroscopy, XPS, and micro-Vickers hardness testing. Significant progress has been made with analysis of the collected data, although there is still much work to be done. Gravimetric analysis of the samples showed relatively low corrosion rates for both materials studied under all test conditions. The concentration of Li was shown to be the primary factor governing the mechanisms of material degradation in the LiCl-Li_2O-Li system. When Li is not present in the system, both SS316L and I625 form stable oxide layers that are composed primarily of $LiCrO_2$ with minor contributions of Li_2CrO_4 and $NiFe_xCr_{2-x}O_4$. These surface layers were observed to be relatively insensitive to Li_2O concentration or exposure period. At high Li concentrations of 0.6 and 1wt%Li, these oxide films are completely destabilized and the degradation of the base material is primarily governed by liquid metal like attack. In the presence of Li concentrations around 0.3wt%Li the formation of bulk oxide layers is destabilized, however, some oxide formation is still observed, indicating a transition region where both methods of degradation occur simultaneously.

Consequently, to minimize the corrosion of the vessel and other components in contact with molten LiCl-Li_2O, the electroreduction of UO_2 be should conducted so as to minimize the dissolution of Li into the bulk electrolyte. As dissolution of Li into the electrolyte also represents a significant source of inefficiency in the process [11], work towards this goal will benefit the development of the electroreduction process in a number of ways. Further corrosion studies should be conducted using samples exposed to the electrolyte during the electroreduction of UO_2 to verify that the corrosion mechanisms presented here are typical of those that are present in the electroreduction vessel. The presence of O_2 gas is likely to affect the corrosion of materials exposed to these conditions.

To complete the present study, post methanol rinse XPS and XRD data must be collected for the SS316L and I625 samples exposed to LiCl-2wt%Li_2O solutions containing 0, 0.3, 0.6, and 1wt%Li for 500 and 1000hr. Following completion of surface analysis, the samples will be cross sectioned and

investigated via SEM-EDS to provide insight into the variations of the surface chemistry and structure as a function of depth into the sample surface. Once analysis is complete, the residual salt layer will be removed from the reserve samples and their mass loss recorded to complete the gravimetric study. Presently, data collection has outstripped the pace of data analysis, so analysis of the data that has been collected but not presented above is also necessary. Investigation into the degradation of the crucibles used for this study is also planned, and will likely lead to additional insights into the effects of Li on the degradation of materials exposed to molten LiCl-Li_2O-Li.

References

[1] T.N. Nakajima, K., N. Watanabe, Nippon Kagaku Kaishi 1974 (1974) 401-404.

[2] A. Merwin, W.C. Phillips, M.A. Williamson, J.L. Willit, P.N. Motsegood, D. Chidambaram, Scientific Reports 6 (2016) 25435.

[3] PDF Card No. : 01-079-5397, in: T.I.C.f.D. Data (Ed.) 2017.

[4] A. Merwin, Material Interactions with Molten LiCl-Li_2O-Li, Materials Science and Engineering, vol Doctor of Philosophy in Materials Science and Engineering, University of Nevada, Reno, 2016, p. 241.

[5] E.-Y. Choi, J. Lee, Journal of Nuclear Materials 495 (2017) 85-90.

[6] D.A. Jones, Principles and Prevention of Corrosion, Prentice Hall, Upper Saddle River, NJ, 1996.

[7] M. Suzuki, I. Yamada, H. Kadowaki, F. Takei, Journal of Physics: Condensed Matter 5 (1993) 4225-4232.

[8] B.D. Hosterman, Raman Spectroscopic Study of Solid Solution Spinel Oxides, Physics and Astronomy, vol Doctor of Philosophy in Physics, UNLV, 2011, p. 155.

[9] D. Chidambaram, C.R. Clayton, G.P. Halada, Journal of the Electrochemical Society 150 (2003) B224-B237.

[10] M.C. Biesinger, B.P. Payne, A.P. Grosvenor, L.W.M. Lau, A.R. Gerson, R.S.C. Smart, Applied Surface Science 257 (2011) 2717-2730.

[11] A. Merwin, M.A. Williamson, J.L. Willit, D. Chidambaram, Journal of the Electrochemical Society 164 (2017) H5236-H5246.

Appendix A – Supplemental XRD Figures

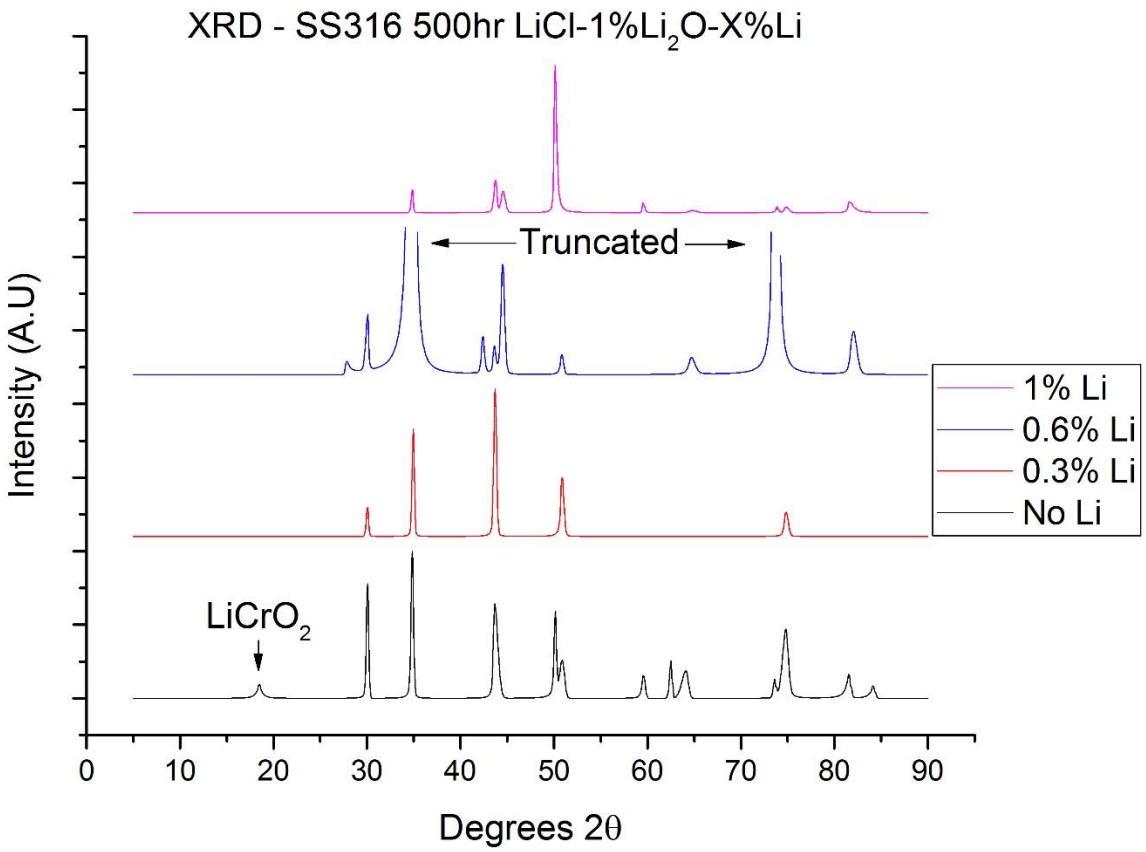


Figure A44: GI-XRD patterns for SS316 samples exposed to LiCl-1wt%Li containing 0, 0.3, 0.6, or 1wt%Li at 650°C for 500hr prior to methanol rinsing. The peak at 18.4° indicative of $LiCrO_2$ was observed on the sample exposed to LiCl-1wt%Li_2O in the absence of Li. All other peaks displayed in these patterns originate from LiCl or the base material.

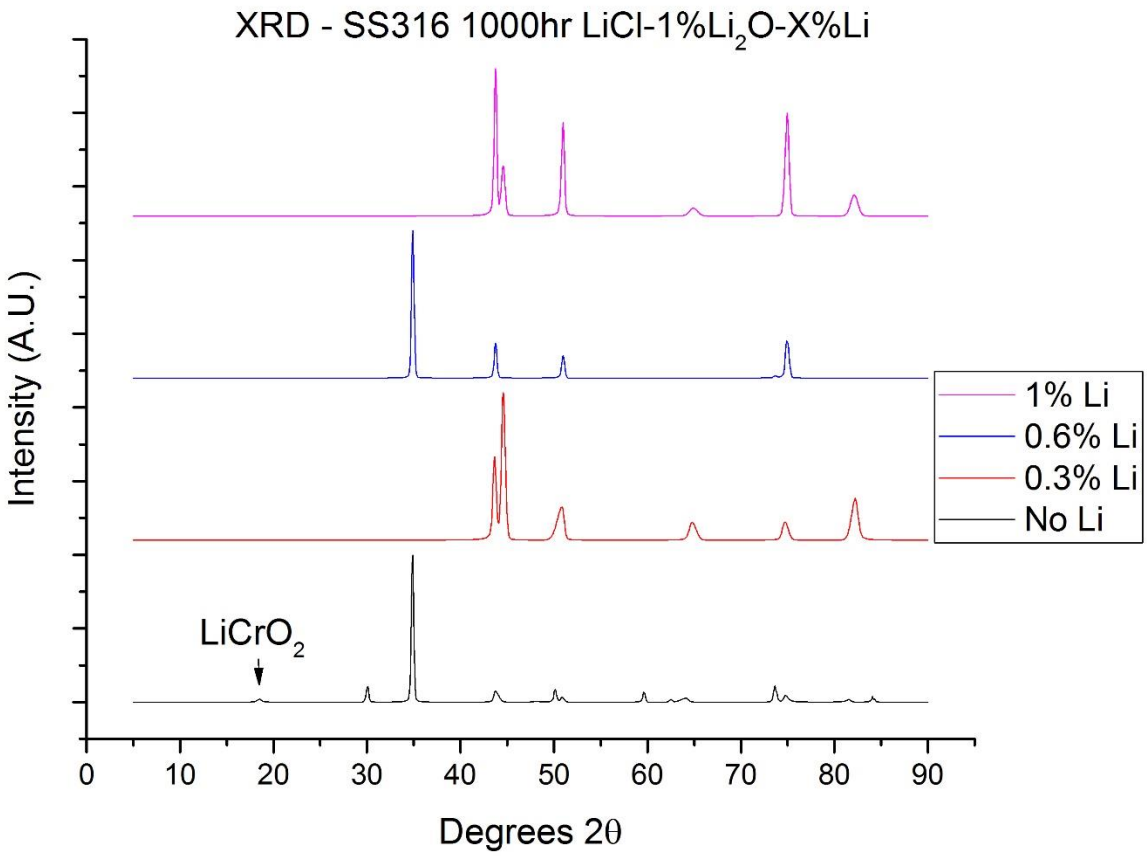


Figure A45: GI-XRD patterns for SS316 samples exposed to LiCl-1wt%Li containing 0, 0.3, 0.6, or 1wt%Li at 650°C for 1000hr prior to methanol rinsing. The peak at 18.4° indicative of $LiCrO_2$ was observed on the sample exposed to LiCl-1wt%Li_2O in the absence of Li. All other peaks displayed in these patterns originate from LiCl or the base material.

Appendix B – Supplemental SEM-EDS Figures

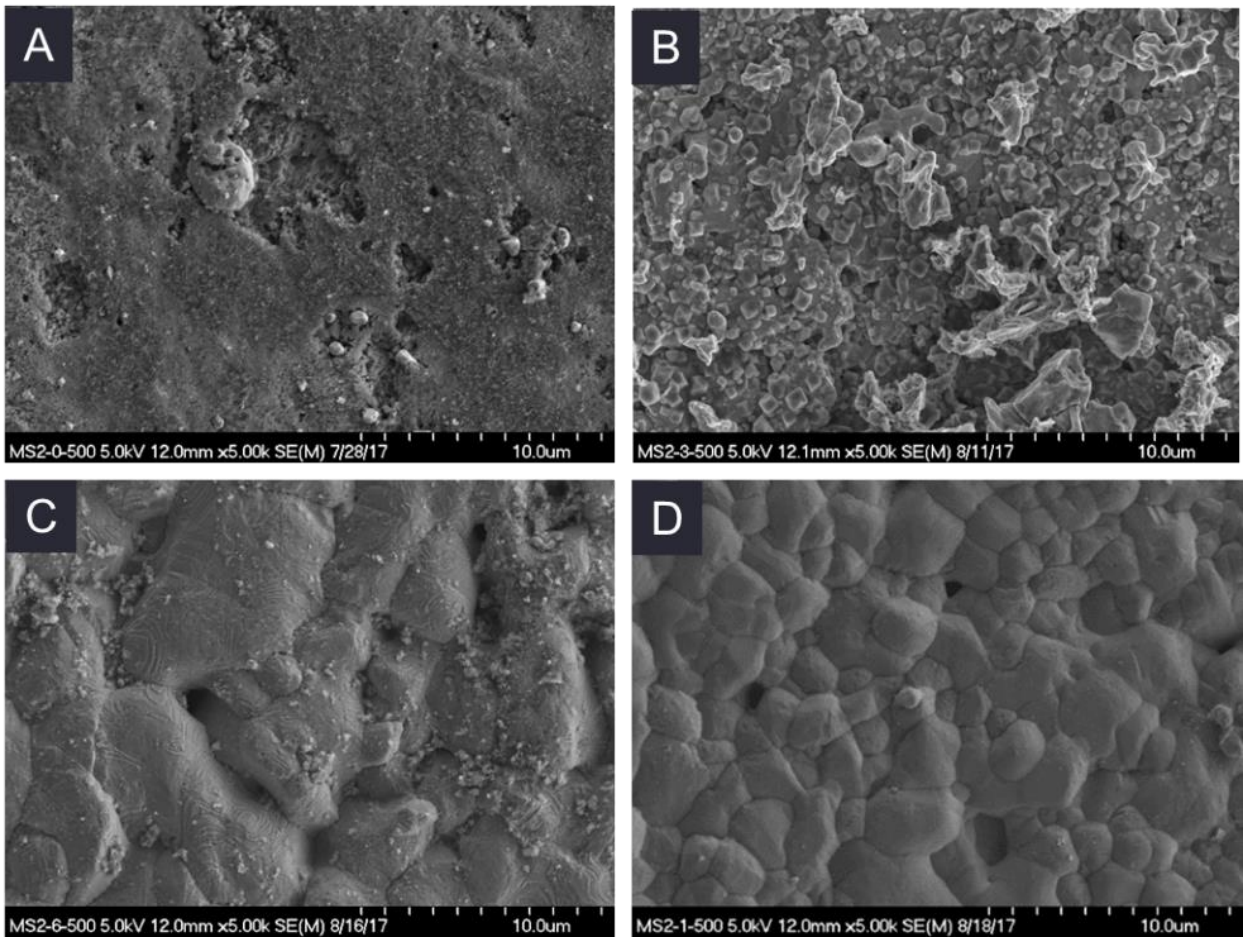


Figure B1: SEM micrographs of SS316L exposed to LiCl-2wt%Li2O at 650°C containing A) no Li, B) 0.3wt%Li, C) 0.6wt%Li, and D) 1wt%Li for 500hr, following the methanol rinsing procedure.

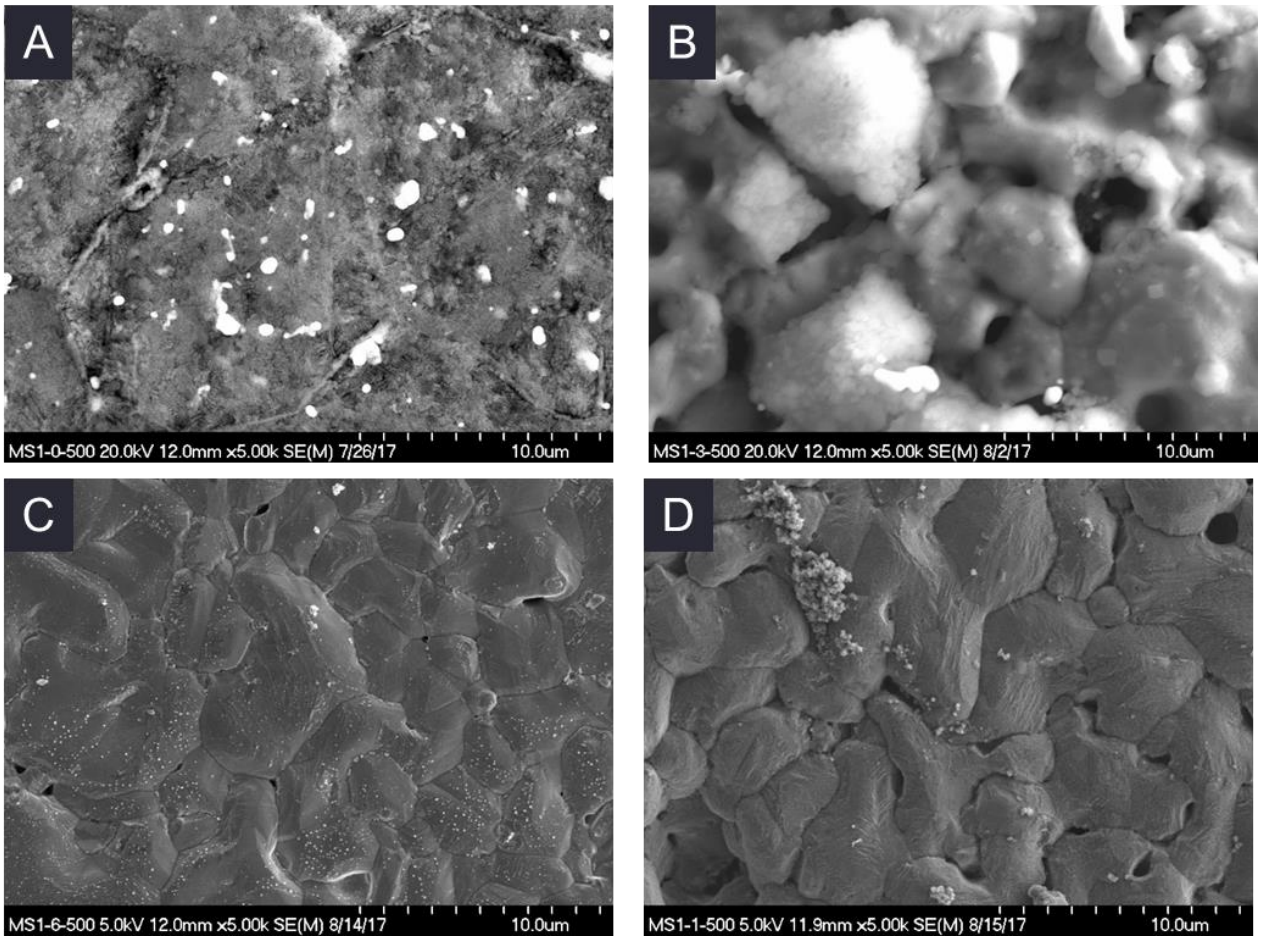


Figure B2: SEM micrographs of SS316L exposed to LiCl-1wt%Li2O at 650°C containing A) no Li, B) 0.3wt%Li, C) 0.6wt%Li, and D) 1wt%Li for 500hr, following the methanol rinsing procedure.

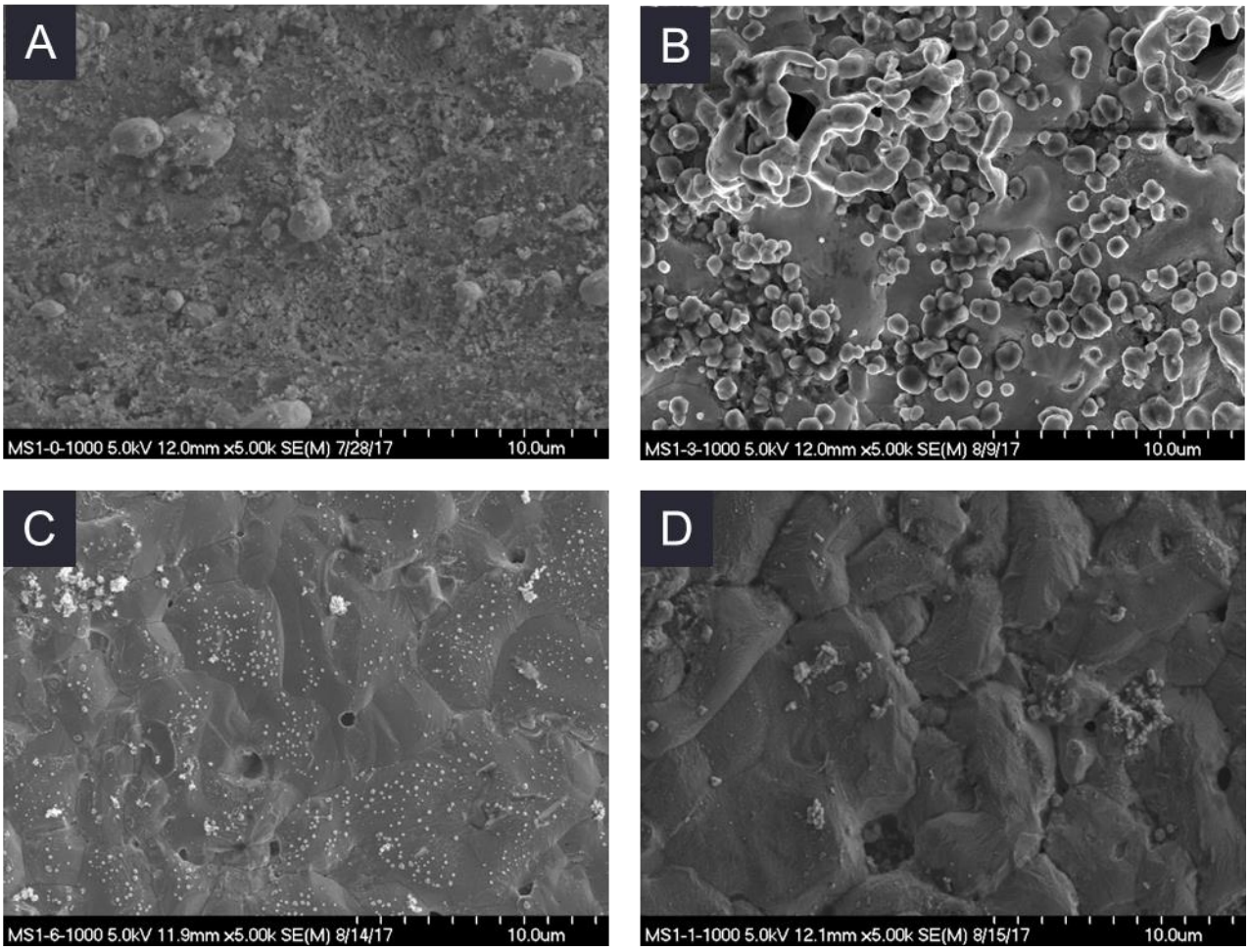


Figure B3: SEM micrographs of SS316L exposed to LiCl-1wt%Li2O at 650°C containing A) no Li, B) 0.3wt%Li, C) 0.6wt%Li, and D) 1wt%Li for 1000hr, following the methanol rinsing procedure.

Appendix C – Supplemental Raman Figures

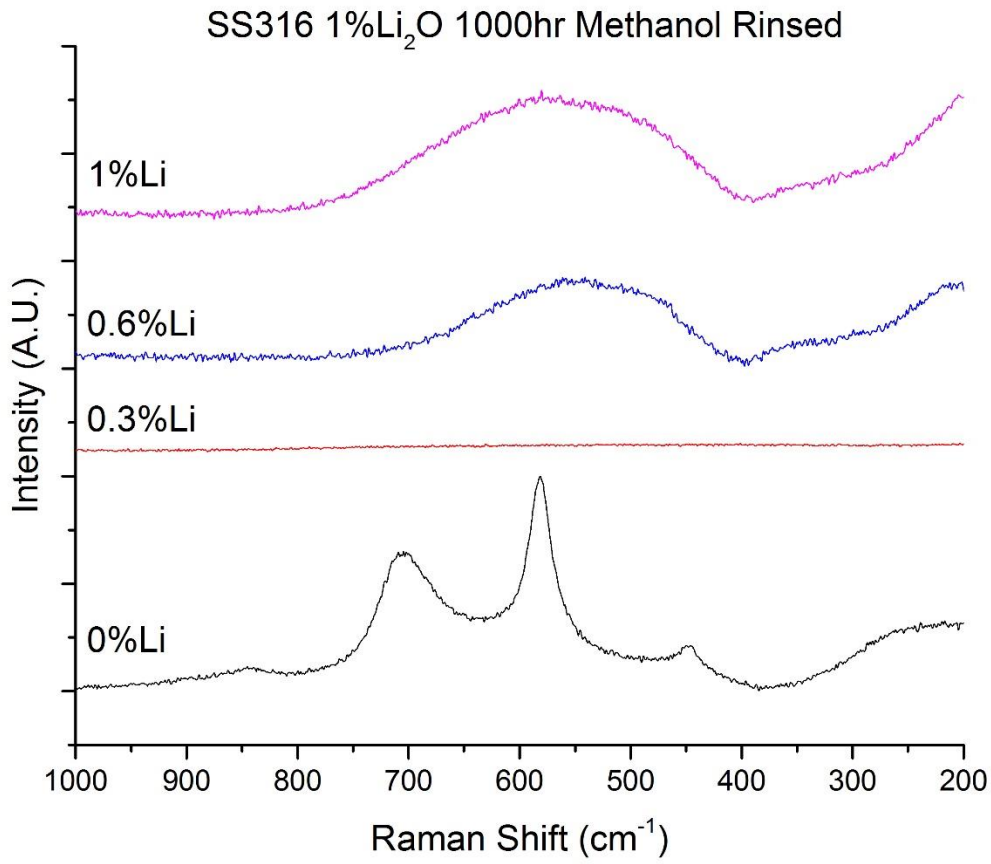


Figure C1: Raman spectra obtained from methanol rinsed SS316L samples exposed to LiCl-2wt%Li solutions containing 0, 0.3, 0.6, and 1wt%Li at 650°C for 500hr.

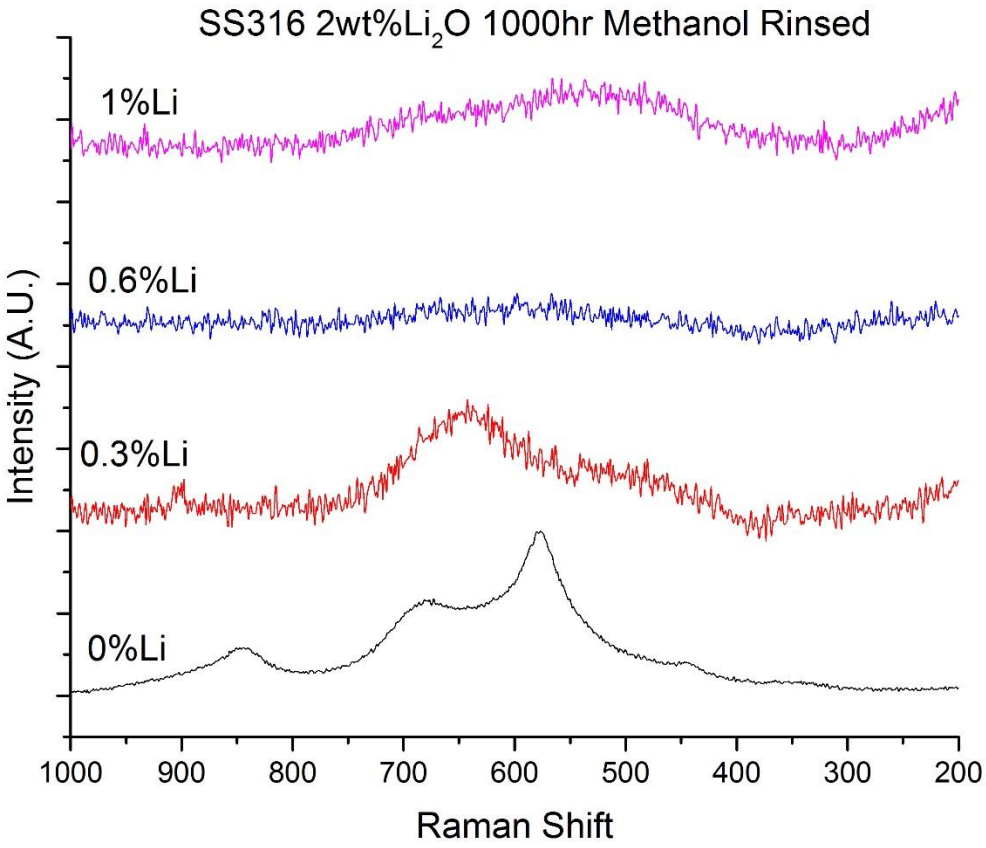


Figure C2: Raman spectra obtained from methanol rinsed SS316L samples exposed to LiCl-2wt%Li solutions containing 0, 0.3, 0.6, and 1wt%Li at 650°C for 1000hr.

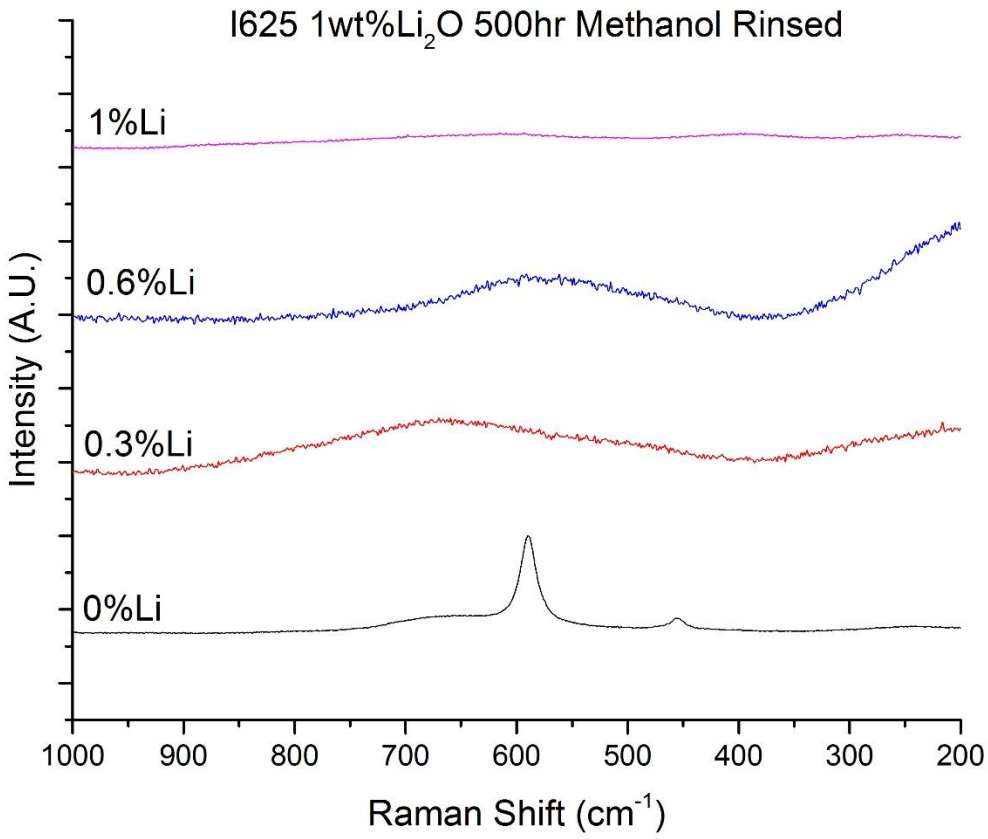


Figure C3: Raman spectra obtained from methanol rinsed I625 samples exposed to LiCl-1wt%Li solutions containing 0, 0.3, 0.6, and 1wt%Li at 650°C for 500hr.

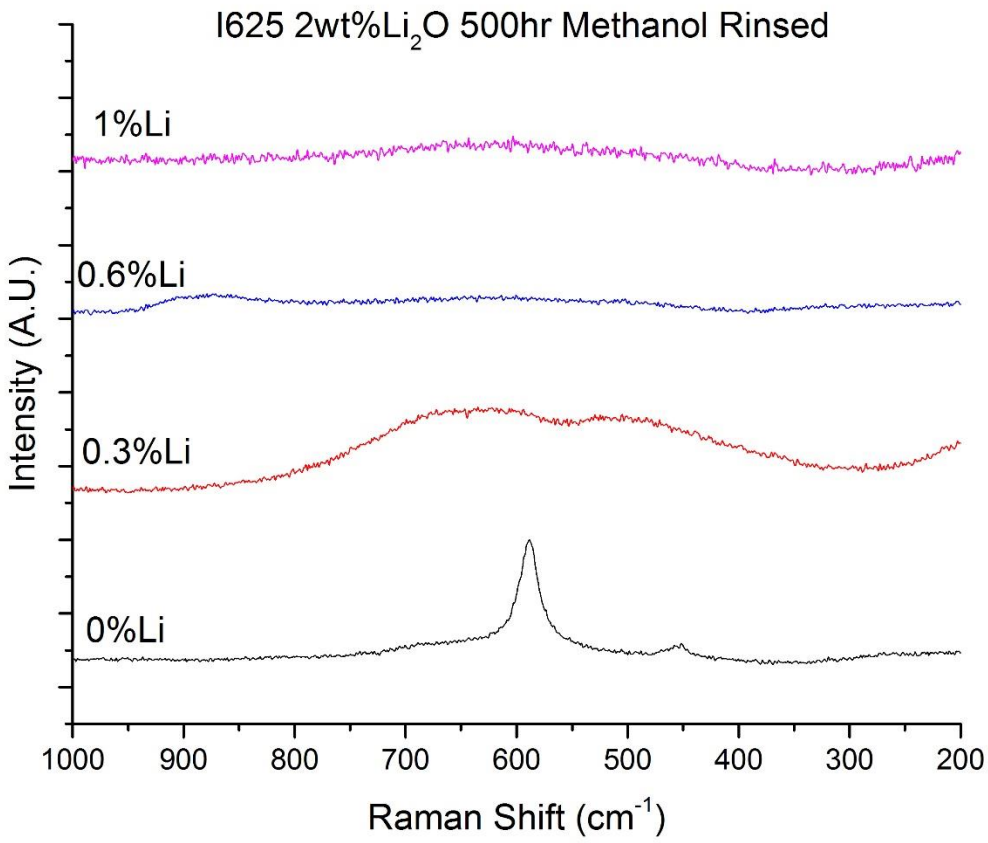


Figure C4: Raman spectra obtained from methanol rinsed I625 samples exposed to LiCl-2wt%Li solutions containing 0, 0.3, 0.6, and 1wt%Li at 650°C for 500hr.

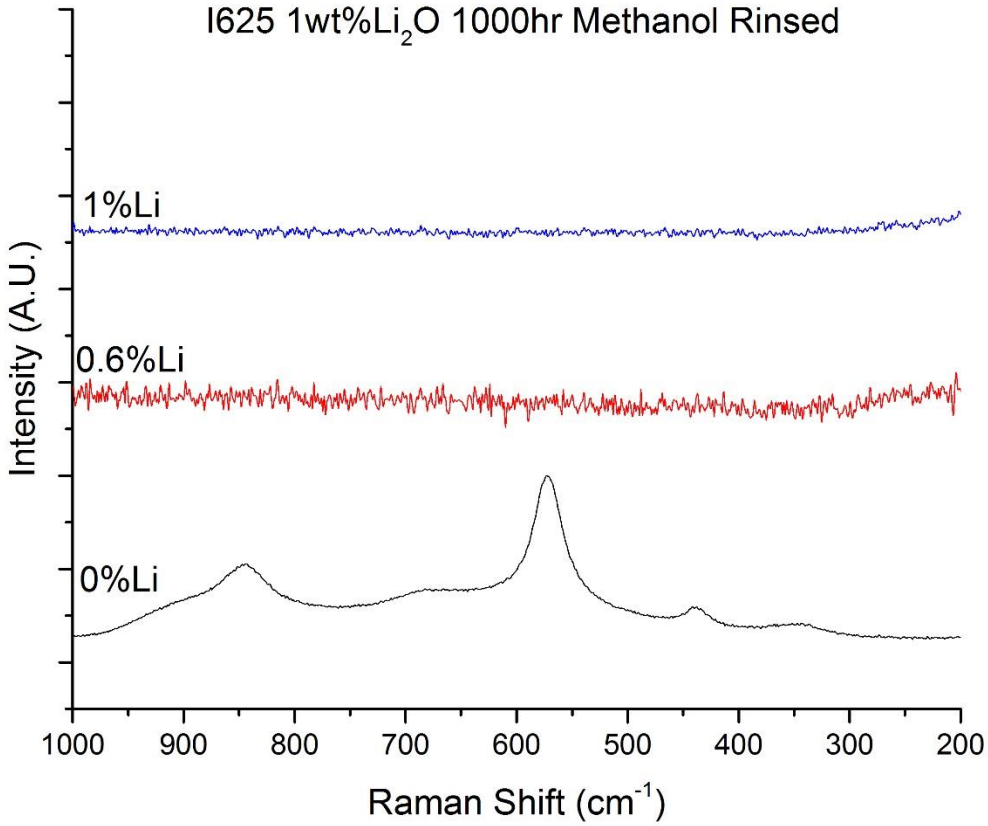


Figure C5: Raman spectra obtained from methanol rinsed I625 samples exposed to LiCl-1wt%Li solutions containing 0, 0.3, 0.6, and 1wt%Li at 650°C for 1000hr.

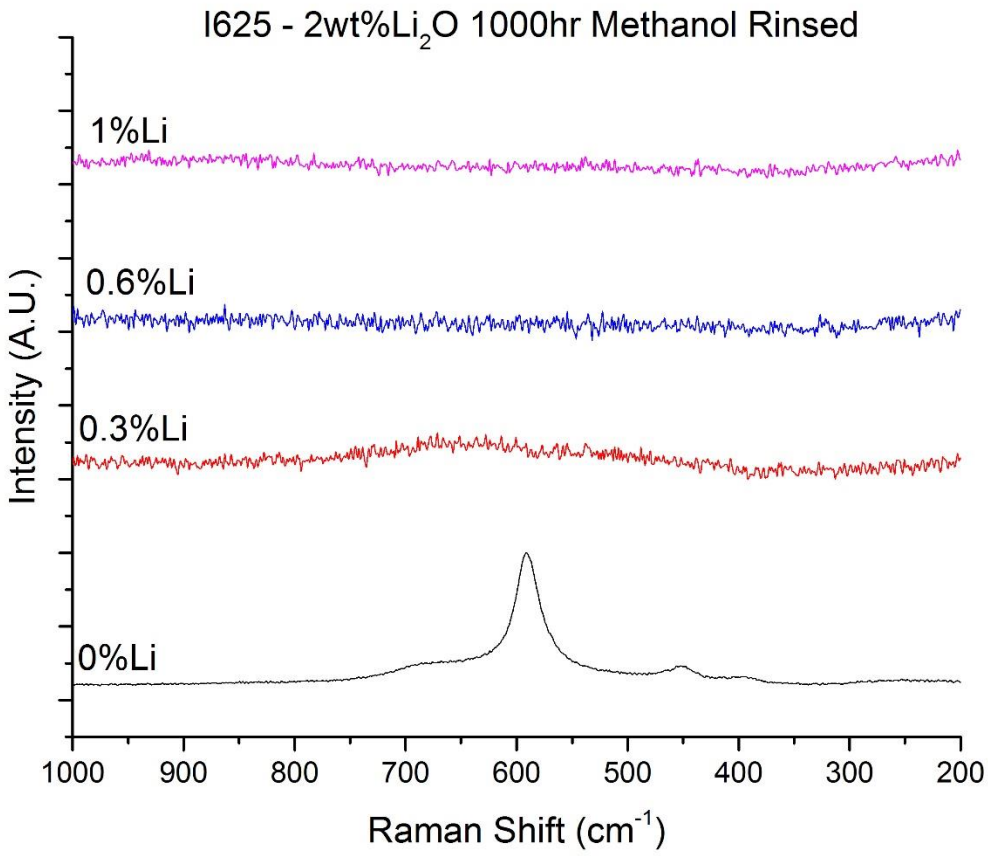


Figure C6: Raman spectra obtained from methanol rinsed I625 samples exposed to LiCl-2wt%Li solutions containing 0, 0.3, 0.6, and 1wt%Li at 650°C for 1000hr.

Appendix D – Supplemental XPS Figures

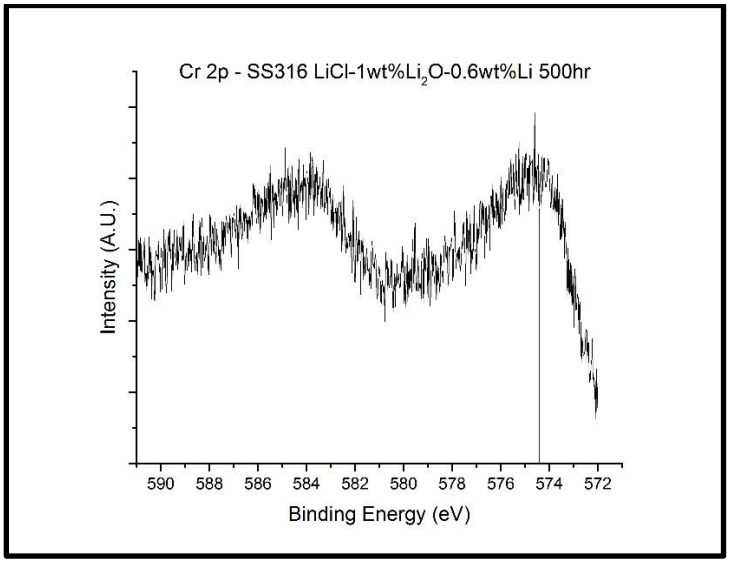


Figure D1: XPS narrow scan of the Cr 2p peak observed on SS316L exposed to LiCl-1wt%Li_2O-0.6wt%Li at 650°C for 500hr and rinsed with methanol. Charge correction of 0.9eV was applied based on the adventitious C 1s peak at 284.8eV. The binding energy of the Cr $2p_{3/2}$ peak is 574.2eV, indicating that Cr is in the metallic state on this sample.

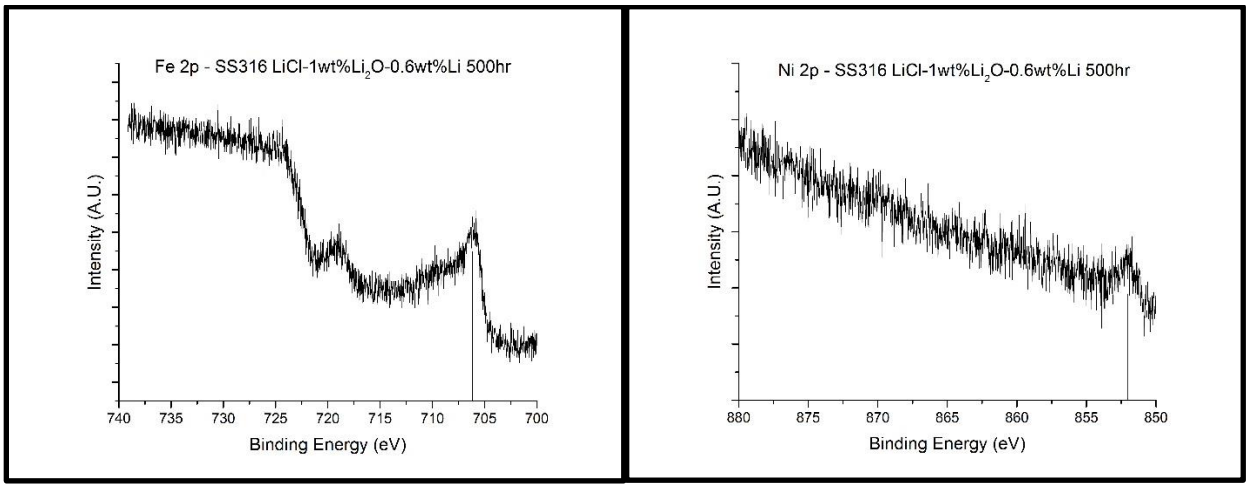


Figure D3: XPS narrow scans of the Fe 2p (left) and Ni 2p (right) peaks observed on SS316L exposed to LiCl-1wt%Li_2O-0.6wt%Li at 650°C for 500hr and rinsed with methanol. Charge correction of 0.9eV was applied based on the adventitious C 1s peak at 284.8eV. The binding energies for Fe $2p_{3/2}$ and Ni $2p_{3/2}$ are 706.0eV and 852.0eV, respectively, indicating these elements are present in the metallic state.

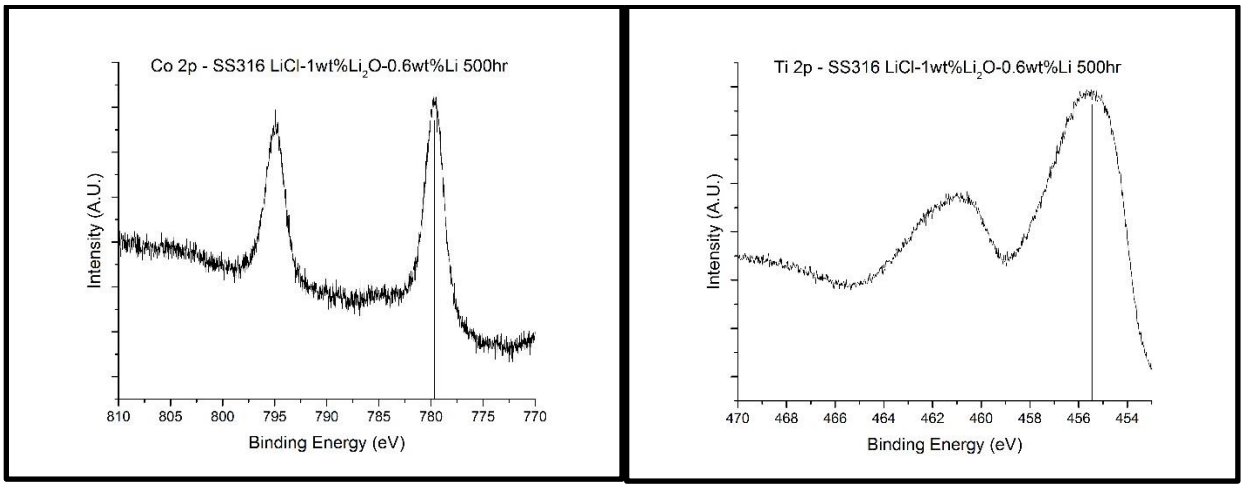


Figure D4: XPS narrow scans of the Co 2p (left) and Ti 2p (right) peaks observed on SS316L exposed to LiCl-1wt%Li_2O-0.6wt%Li at 650°C for 500hr and rinsed with methanol. Charge correction of 0.9eV was applied based on the adventitious C 1s peak at 284.8eV. The binding energies for Co $2p_{3/2}$ and Ti $2p_{3/2}$ are 789.8eV and 455.4eV, respectively.

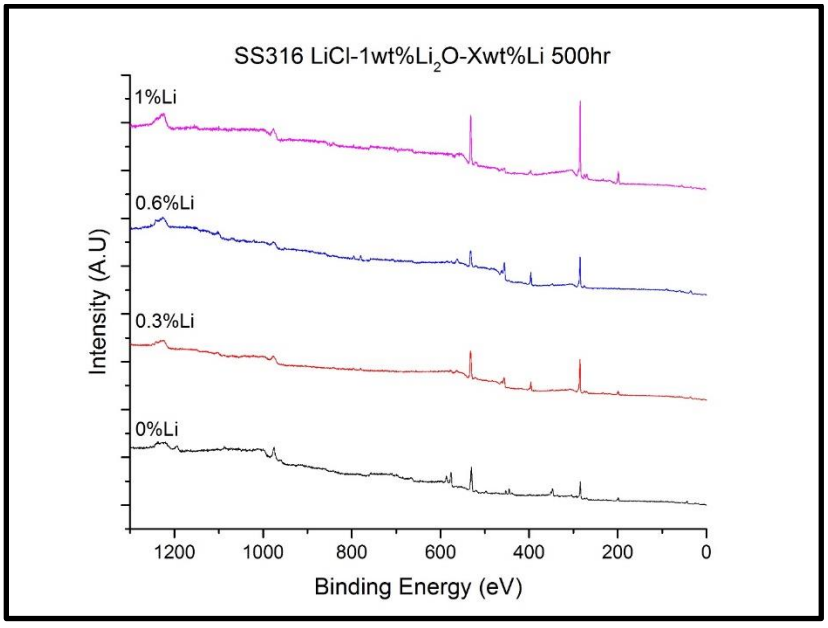


Figure D5: XPS survey scans for SS316L exposed to LiCl-1wt%Li_2O containing 0, 0.3, 0.6, and 1wt%Li at 650°C for 500hr as Li content increases, Cr is depleted from the sample surfaces, and Ti compounds become more prominent. The deposition of Ti compounds on samples surfaces exposed to LiCl-Li_2O in the presence of Li was observed in our previous work as well, and is a result of TiO_2 impurities present in Li_2O.

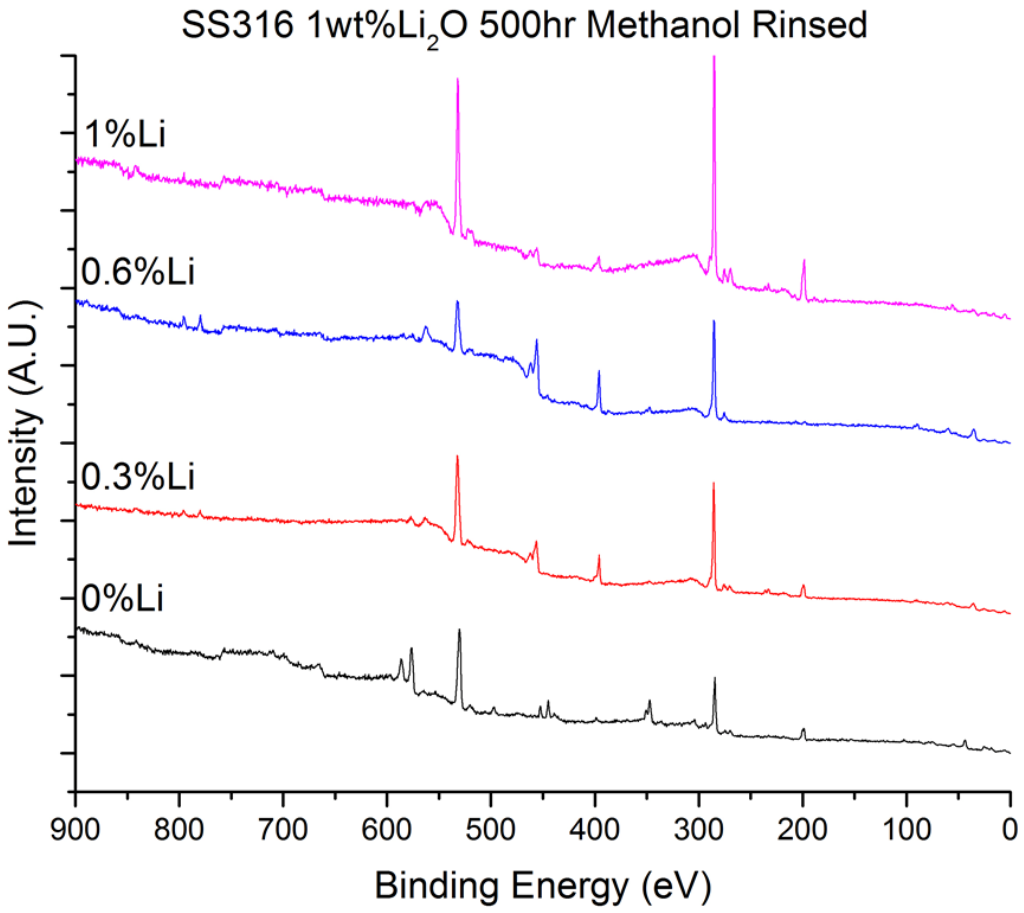


Figure D6: XPS survey spectra obtained from methanol rinsed SS316 samples exposed to LiCl-1wt%Li solutions containing 0, 0.3, 0.6, and 1wt%Li at 650°C for 500hr.

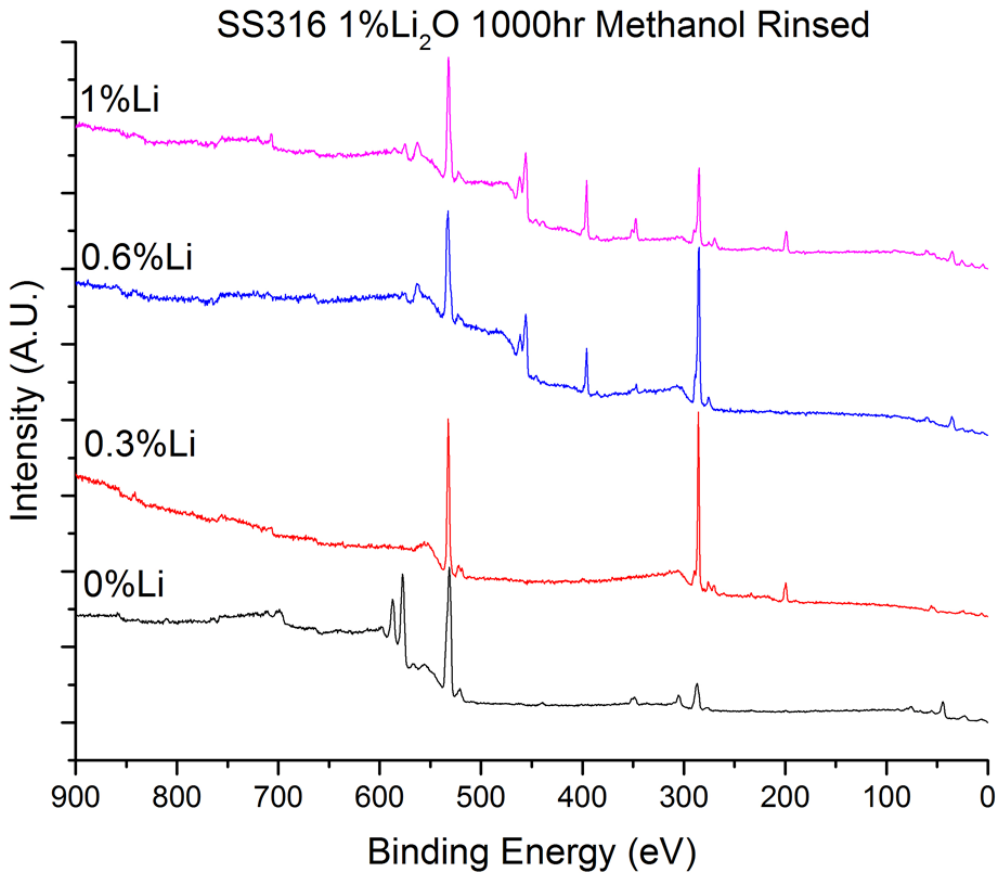


Figure D7: XPS survey spectra obtained from methanol rinsed SS316 samples exposed to LiCl-1wt%Li solutions containing 0, 0.3, 0.6, and 1wt%Li at 650°C for 1000hr.

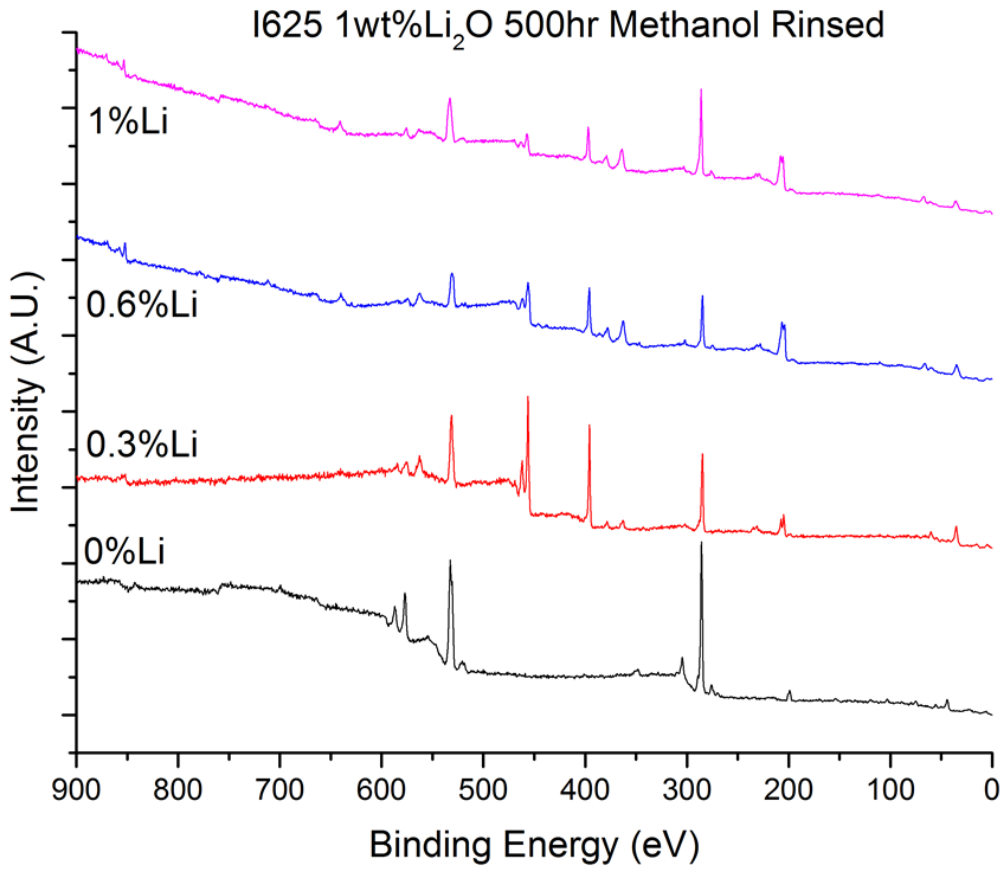


Figure D8: XPS survey spectra obtained from methanol rinsed I625 samples exposed to LiCl-1wt%Li solutions containing 0, 0.3, 0.6, and 1wt%Li at 650°C for 500hr.

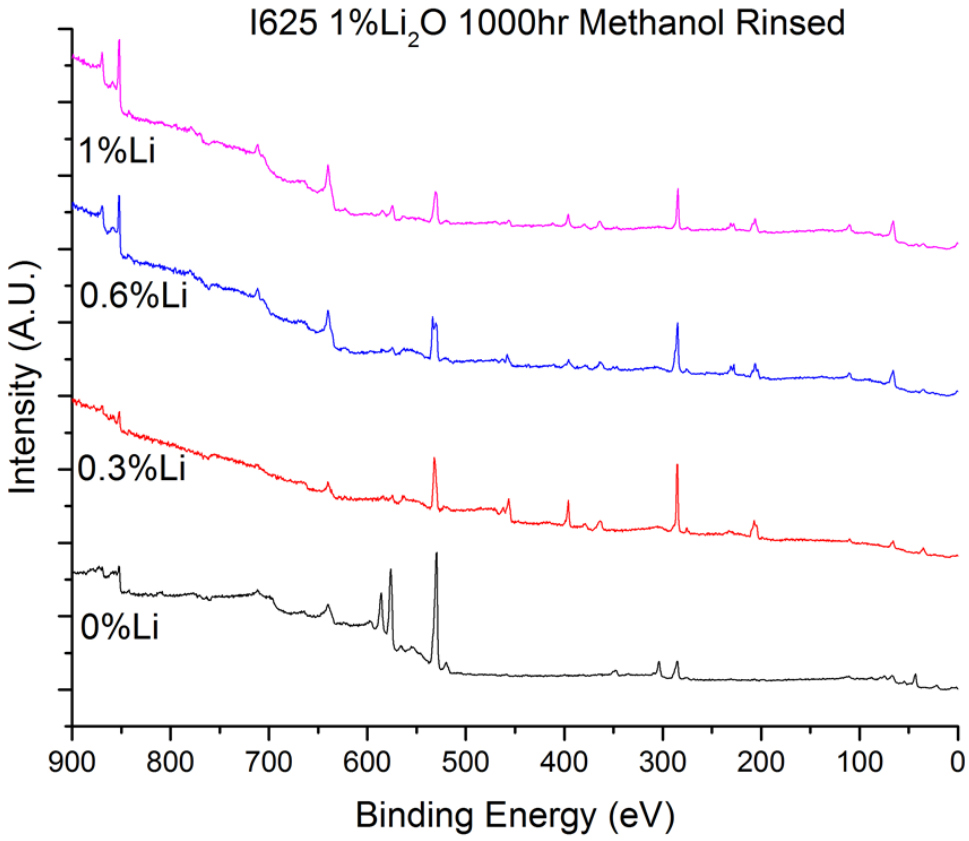


Figure D9: XPS survey spectra obtained from methanol rinsed I625 samples exposed to LiCl-1wt%Li solutions containing 0, 0.3, 0.6, and 1wt%Li at 650°C for 1000hr.

A3 Corrosion behavior of Monel 400 and electrochemical performance of Li-Bi reference electrode in LiCl-Li_2O-Li

Contents

Abstract i
Acknowledgements iii
Contents v
List of Figures vii
List of Tables xii
Chapter 1: Introduction 1
1.1 Energy Needs 1
1.2 Nuclear Energy 2
1.3 Nuclear Waste 4
1.4 Reprocessing 5
1.5 Pyroprocessing 7
1.6 Electroreduction of Spent Nuclear Fuel in LiCl-Li_2O-Li 9
1.7 Corrosion in Molten Salts 11
1.8 Corrosion in Molten LiCl-Li_2O-Li 17
1.9 Material Selection 17
Chapter 2: Experimental 19
2.1 Materials 19
2.2 Sample Preparation 20
2.3 Glove box 21
2.4 Furnace, Temperature Control, and Crucibles 21
2.5 Exposure Testing 23
2.6 Electrochemical Measurements 23
2.7 Post Exposure Analytical Methods 24
2.7.1 X-Ray Diffraction 24
2.7.2 Scanning Electron Microscopy and Energy Dispersive X-Ray Spectroscopy 26
2.7.3 Micro-Vickers Hardness Testing and Optical Microscopy 27
2.7.4 Raman Spectroscopy 29
2.7.5 X-Ray Photoelectron Spectroscopy 30
2.7.6 Inductively Coupled Plasma - Optical Emission Spectrometry 31
Chapter 3: Lithium-Bismuth Reference Electrode Development 33
Chapter 4: Results and Discussion 38

4.1 Exposure Testing 38
4.1.1 Visual Observations 38
4.1.2 X-Ray Diffraction 39
4.1.3 Field Emission Scanning Electron Microscopy and Energy Dispersive X-Ray Spectroscopy 47
4.1.4 Micro-Vickers Hardness Testing and Optical Microscopy 60
4.1.5 Raman Spectroscopy 62
4.1.6 X-Ray Photoelectron Spectroscopy 63
4.1.7 Inductively Coupled Plasma Optical Emission Spectrometry 69
4.2 Electrochemical Measurements 74
4.3 Proposed Mechanism of material interaction 78
Chapter 5: Conclusions 81
Chapter 6: Future Work 83
References 85

Chapter 1: Introduction

"If there is a danger to mankind from nuclear energy it does not lie in the use of nuclear energy to generate electric power. It lies in the armaments and in the risk of proliferation; it could lie in the political tensions which may follow the failure to develop nuclear power and other resources as replacements to declining petroleum resources." – Dr. Sigvard Eklund, former director of the International Atomic Energy Agency (*1*)

1.1 Energy Needs

The increasing use of fossil fuels such as coal, oil, and natural gas for power generation since the dawn of the industrial revolution has transformed human society, and has caused noticeable changes to the planet we inhabit. The rise in energy consumption over this time period has given benefits to mankind far too numerous to detail. Quality of life has increased considerably along with average life expectancy, both of which have been directly correlated to an increase in per-capita energy consumption (*2, 3*). However, 1.3 billion people in developing countries currently lack access to electricity. The United Nations has set a goal of providing access to electricity to the remainder of the world by 2030 (*4*). When this is combined with the projected increase in demand for electricity in the industrialized world and expected population growth of approximately 2 billion people, projections indicate that global energy consumption will increase by 37% by 2040 (*5, 6*). To meet the supply requirements for such a large increase in energy consumption while simultaneously reducing reliance on non-renewable and carbon intensive energy sources, considerable investments in sustainable and carbon neutral energy technologies must be made. It is important to note that no single energy technology can solve these problems and all options must be fully explored. Therefore, this thesis will not attempt to compare the merits of the various energy technologies, but will instead delve into the technical details of one of the most stable components of our energy portfolio: nuclear fission. This

chapter will give a brief history of the nuclear industry to provide the motivation for the research presented in the following chapters is given in this introduction.

1.2 Nuclear Energy

Nuclear reactors currently supply 19.5% of the electricity in the United States, while globally 10.9% of electricity demand is met by nuclear energy (*7*). In 2014, there were 13 countries generating more than 25% of their electricity via nuclear fission, with France relying on nuclear power for 76.9% of total electricity generation (*7*). The majority of the nuclear reactors in operation are of the Generation II light-water reactor (LWR) (*8*) type; specifically of the pressurized water reactor (PWR) and boiling water reactor (BWR) designs. Most reactors currently under construction are Generation III+ designs, which are evolutions of the PWR and BWR designs that include passive safety features to reduce the risk of a major accident. There are also a small number of research and prototype reactors of other designs currently in operation.

One of the main problems with the current reactor fleet is the large amount of waste they produce. This is due to the inefficient use of fissionable materials associated with the so called “open fuel cycle” that is employed. In an open fuel cycle, the fuel is inserted into the core of the reactor, burned for a period of time, and then stored indefinitely. Thermal reactors can only initiate fission in fissile isotopes, such as ^{235}U and ^{239}Pu. Alternatively, fertile isotopes such as ^{238}U, are only fissionable in a fast, high average neutron energy, spectrum reactor. This means that the fuel for a LWR must have a minimum concentration of fissile isotopes in order to maintain criticality.

To solve this issue and close the nuclear fuel cycle, while simultaneously enhancing the economics, safety, and proliferation resistance of nuclear energy generation, the Generation IV

reactor initiative was created (*9*). Generation IV reactors are designed to be passively safe; they safely shut themselves down due to inherent physical phenomena such as gravity, thermal expansion, natural convection, or melting, in the event of an accident. The designs for Generation IV reactors are summarized below in Table 1 (*9*).

Table 1: Generation IV reactor types and primary design characteristics (*9*).

Reactor Type	Abbreviation	Coolant	Fuel type	Operating temp (°C)	Neutron spectrum
Gas Cooled Fast Reactor	GFR	He	Ceramic	850	Fast
Lead Cooled Fast Reactor	LFR	Pb/Bi	Metallic/oxide	500-600	Fast
Molten Salt Reactor	MSR	LiF/UF_4	Liquid	800	Thermal/Epithermal
Sodium Cooled Fast Reactor	SFR	Na	Metallic/oxide	550	Fast
Supercritical Water Cooled Reactor	SCWR	H_2O	Oxide	550-600	Thermal/Epithermal
Very High Temperature Reactor	VHTR	He	Ceramic	>1000	Thermal/Epithermal

Each of the reactors listed in Table 1 was designed to achieve a specific goal, and the implementation of these reactor types, in addition to the current reactor fleet, will provide a robust, economical, efficient, and environmentally friendly source of power to humanity. The Generation IV designs are expected to come online around 2030, while some may be able to be commercialized before this date (*9*). A discussion of all of the Generation IV reactor designs is beyond the scope of this thesis. The fuel cycle for the sodium cooled fast reactor (SFR) will be subsequently discussed in detail, as it is the focus of this work.

1.3 Nuclear Waste

As mentioned previously, one of the major concerns with large scale usage of nuclear power is the need for long term storage of the used fuel. Although nuclear fuel is said to be 'burned' in the core of the reactor, only a very small amount of mass is actually converted to energy, and the mass of the fuel assemblies upon discharge is essentially unchanged from the initial fuel loading. However, the isotopic composition of the fuel changes significantly as a direct result of fission and various neutron capture reactions that take place during the fuel's residence in the core (*10, 11*).

Due to the statistical nature of these reactions, irradiated fuel contains a broad range of radioactive isotopes, some of which decay with half-lives on the order of tens of thousands of years (*12*). Therefore, extreme care must be taken when dealing with Used Nuclear Fuel (UNF). These isotopes can be classified into three primary groups: fission products with atomic number $Z<92$, Trans-Uranic Isotopes (TRU) with $Z>92$, and unburnt uranium with $Z=92$. The main concern associated with the long term storage of UNF lies with the TRU. These isotopes are generally long lived radioisotopes created via successive neutron absorption reactions beginning with ^{238}U (*13*). Due to the long lived nature of some of the TRU, UNF must be isolated from the biosphere until it decays to an extent that it does not pose a threat to human life. For LWR spent fuel, this storage period is on the order of 20,000 years.

At the end of 2012, the inventory of UNF in the United States exceeded 70,000 tons, and is currently increasing at a rate of 2000 tons per year (*14*). Upon discharge from the core, the fuel assemblies are placed underwater in spent fuel pools until the residual decay heat is reduced to a level that is manageable with air cooling (*11*). At that time, the assemblies are placed in dry casks and stored on site at the reactor facility to await long term storage in a

geologic repository. In the United States, the construction and commissioning of a geologic repository for permanent storage of UNF has been mired in political gridlock since the early 1980s. A large volume of research, at considerable expense, was performed to evaluate the proposed Yucca Mountain repository located on the Nevada Test Site approximately 100 miles north of Las Vegas, Nevada, however the future of the site remains uncertain (*15*).

Geologic storage of UNF is controversial due primarily to concerns stemming from the need to keep the material isolated from the environment for tens of thousands of years. The federal government is responsible for the construction of a geologic repository due to the complex nature of the storage of UNF. To pay for the construction of such a site, the DOE imposed a fee on utilities of 0.1cent/kWh of electricity generated by a nuclear reactor from 1983 through 2014 (*16*). In total, the fund exceeded $39.8 billion available to dispose of the nation's nuclear waste at the close of the 2014 fiscal year (*17*).

1.4 Reprocessing

The name used nuclear fuel implies that the useful aspects of the material have been exhausted. However, this is most assuredly not the case, as only 3-5% of the fuel actually undergoes fission. The UNF no longer has the reactivity required to sustain criticality in the LWR core due to the buildup of fission products that act as neutron absorbers, the thermal neutron spectrum used, and the burning of fissile material present in the initial fuel loading. However, the potential energy contained in the fertile isotopes remaining in the fuel is enormous. Many of the fission products are also valuable for medical and industrial applications (*10*). The value of the elements and potential energy stored in UNF make geologic disposal both extremely costly and wasteful. An alternative to this method of disposal is to reprocess the UNF so that the remaining fertile and fissile material, along with the TRU, are burned in a suitable reactor to

generate power, leaving only a small amount of hazardous material to be sent to a geologic repository (*11*).

Various isotopes of Pu are bred from ^{238}U in the core along with other, heavier transuranic isotopes such as Np, Cm, and Am. The TRU isotopes cause difficulties in the handling and disposal of UNF due to their long half-lives, however they are able to be burned in a reactor to generate power if a fast or epithermal neutron spectrum is used (*10*). Additionally, 97% of the UNF is ^{238}U, which remains capable of generating more fissile ^{239}Pu. If a closed fuel cycle were to be implemented, the energy stored in the UNF in the United States is enough to meet 100% of the projected energy demand for several hundred years (*18*). By burning the TRU elements, the final waste product consists primarily of short lived fission products with high specific activity, meaning that the waste will initially be much hotter, physically and radiologically, but will decay over a significantly reduced time period. Only 300-500 years of isolated storage would be necessary for the UNF from a closed fuel cycle, as opposed to the tens of thousands of years of isolation necessary with LWR UNF (*11*).

There are two primary methods used to reprocess UNF; aqueous chemical processing and molten salt electrochemical pyrometallurgical processing (*11*). The most commonly used aqueous process is the PUREX process, which stands for plutonium-uranium redox extraction and was developed for the Manhattan project during WWII to isolate Pu for use in weapons production (*11*). All countries currently operating large scale reprocessing operations use the PUREX method. Due to the stream of isolated Pu inherent to PUREX, there is a nuclear proliferation risk associated with the use of this process. This has limited the adoption of this technology for peaceful civilian nuclear energy due to U.S. regulations based on fears that it will eventually be used to develop a nuclear weapons program in hostile countries.

To address the concerns about the economics, safety, efficiency, scalability, and proliferation resistance of traditional nuclear energy, the Integral Fast Reactor (IFR) project was created in the United States during the 1970's and 80's. The sodium-cooled fast reactor designed for this project utilized metallic fuel, which allows for the implementation of a method for reprocessing UNF utilizing high temperature molten salts, called pyroprocessing (*19-30*). The project was terminated before completion in the early 1990's for political reasons, but remains one of the greatest achievements of American nuclear engineering (*31*).

1.5 Pyroprocessing

As part of the IFR program, Argonne National Labs (ANL) developed a molten salt based electrometallurgical reprocessing technology to recycle spent oxide fuel from LWRs into the metallic fuel used in the IFR (*19*). The integral portion of the name refers to the integration of medium scale fuel reprocessing facilities at the reactor site to minimize the hazards and proliferation concerns associated with transportation of UNF. The recycling operation was termed pyroprocessing due to its high temperature pyrometallurgical nature and is the key technological aspect of the entire IFR program (*31*).

The entire pyroprocessing operation consists of an oxide reduction unit, an electrorefiner, a cathode processor, and a fuel fabrication unit. A process flow diagram of this operation is depicted in Figure 2. Various salt purification and recycling steps are also utilized to minimize salt waste, but are omitted here for clarity. Reduction of LWR used fuel from the oxide form into a metallic product is accomplished by cathodic polarization of the UNF beyond the reduction potential of U in a LiCl-Li_2O electrolyte at 650°C. While, gaseous fission products are removed during this step, many of the more reactive fission products remain dissolved in the electrolyte. Therefore, the oxide reduction step process also serves as an initial refining

operation. The oxide reduction process is discussed in greater detail in the following section, as it is the focus of the research in this thesis. Metallic UNF, either from the oxide reduction step or directly from reactors using a metallic fuel cycle, such as the IFR, is then placed in the electrorefining unit, which operates at 550°C. Here, a eutectic mixture of LiCl-KCl saturated with UCl_3 electrolyte and, the UNF is anodically polarized, and the elements are separated based on their reduction potentials. The U, Pu, other TRU actinides, and some of the fission products are plated onto a stainless steel cathode, while the lanthanide fission products form a liquid alloy with a liquid cadmium cathode. The residual salt is removed from the refined fuel cathode by distillation in the cathode processor. The salt is recycled back to electrorefiner, and the refined fuel is sent to the fuel fabrication furnace where it is cast into the proper geometry for reuse in the core of a metallically fueled reactor. The final waste product contains most of the fission products and is in a solid form suitable for geologic storage.

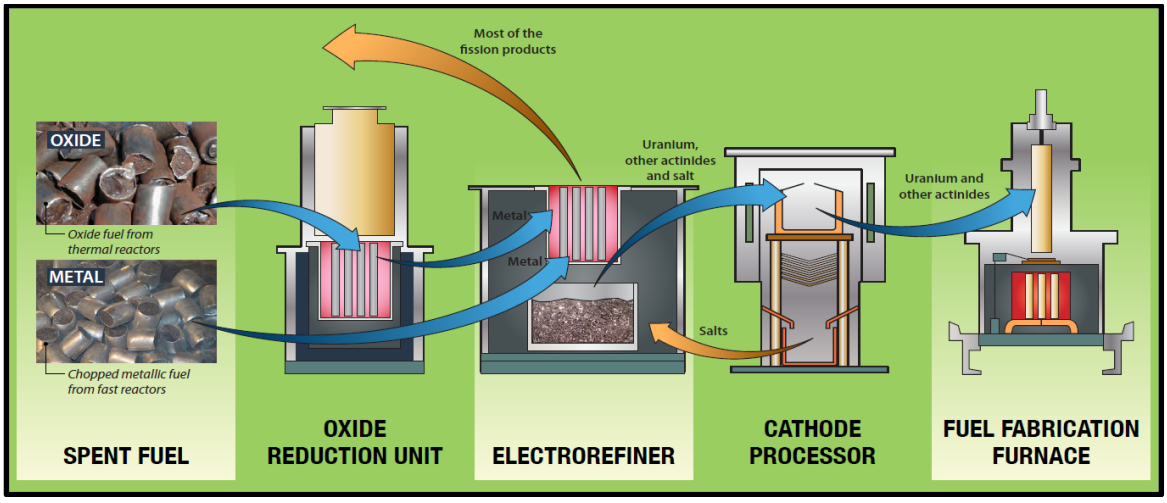


Figure 1: Process flow diagram for the pyroprocessing operation developed by Argonne National labs for the reprocessing of spent nuclear fuel as part of the Integral Fast Reactor program. The process consists of an oxide reduction unit, an electrorefiner, a cathode processor, and a fuel fabrication furnace. Other salt recycling steps have been omitted for clarity. The current research focuses on material reliability concerns in the oxide reduction unit (*32*).

One of the main advantages of this process is the inherent proliferation resistance of the electrorefining operation. In contrast with the PUREX process, pyroprocessing never isolates

weapon grade material, meaning that the technology is inherently more resistant to nuclear proliferation than aqueous reprocessing (*33*). The Pu recovered in electrorefining is always mixed with fission products and minor actinides that are highly radioactive or are strong neutron absorbers, making weapon fabrication difficult or impossible without subsequent refinement (*34*). Researchers at INL, ANL, and the Korean Atomic Energy Research Institute (KAERI) have successfully conducted the entire pyroprocessing operation on a kilogram scale, and no major technological barriers remain in the process development stage. Additionally, KAERI has performed a large amount of research and development on this process, and has designed and constructed an engineering pilot scale facility to validate the economic and technical viability of a commercial scale operation (*35-39*).

1.6 Electroreduction of Spent Nuclear Fuel in LiCl-Li_2O-Li

As mentioned previously, the reduction of oxide UNF is performed in a molten LiCl-Li_2O electrolyte at 650°C and utilizes potentiostatic polarization to reduce LWR UNF to a metallic form so that it can then be fed into the electrorefiner (*40, 41*). In addition to the reduction of oxide UNF, electro-reduction in LiCl-Li_2O has been used to reduce TiO_2, SiO_2, Ta_2O_5, and Nb_2O_5, making this process of significant interest to both nuclear and non-nuclear industries (*42-45*). This process is based on the Fray-Farthing-Chen (FFC) process, which pioneered the use of molten salts for the electrochemical reduction of metal oxides (*46*).

The original reduction process developed by ANL for the IFR project was developed before the FFC process and utilized a direct chemical reduction using metallic Li added to pure molten LiCl. The metallic Li chemically reduced the metal oxides according to Reaction 1.

$$4Li + MO_2 \rightarrow M + 2Li_2O \qquad \textbf{Reaction 1}$$

In this process, the concentration of Li_2O in the molten electrolyte gradually increases as Reaction 1 goes to completion. The FFC electrochemical process replaced this chemical process in the early 2000's as it is much more controllable, and the interaction of metallic Li with container materials causes severe corrosion (*47, 48*).

In the FFC process, Li_2O is added as a catalyst to the molten LiCl to allow for oxygen gas to evolve on the anode as current is applied. In theory, the concentration of Li_2O does not vary as the reduction proceeds. The equations for the cathodic reduction of the metal oxide and anodic formation of oxygen gas are given below.

U cathodic reaction: $$UO_2 + 4e^- \rightarrow U + 2O^{2-}$$ **Reaction 2a**

U anodic reaction: $$2O^{2-} \rightarrow O_{2(g)} + 4e^-$$ **Reaction 2b**

Li cathodic reaction: $$Li_2O + 2e^- \rightarrow 2Li + O^{2-}$$ **Reaction 2c**

Li anodic reaction: $$O^{2-} \rightarrow \frac{1}{2}O_{2(g)} + 2e^-$$ **Reaction 2d**

Reduction yields of greater than 99% have been observed for UO_2, and this process has been used to successfully reduce mixed oxide fuel, as well as simulated high burnup fuel (SIMFUEL) (*49-51*).

The reduction of the actinide oxides UO_2 and PuO_2 in LiCl-Li_2O is complicated due to the extremely close reduction potentials of the actinide oxides and Li_2O. Li_2O has a reduction potential 70mV higher than UO_2, which is in theory large enough to allow for the reduction of U without deposition of Li on the cathode; however, in practice it is necessary to provide overpotential beyond the reduction potential of Li_2O in order to decrease processing time and increase reduction yields (*47, 52-56*). This overpotential causes Li to be reduced on the cathode

surface, thereby acting as an additional reduction pathway for the actinides, causing the reduction to proceed through both the chemical and electrochemical reduction routes given by Reactions 1 and 2. It has been shown that the reduction of UO_2 proceeds from the surface of the pellet inwards, with metallic Li being formed on the surface. The reduction process becomes diffusion limited by the transport of O and/or Li through the porous metallic U pellet as the reaction goes to completion (*54, 55*). Due to the solubility of Li in LiCl a portion of the metallic Li on the cathode surface dissolves into the molten solution, forming a tertiary LiCl-Li_2O-Li electrolyte (*57-62*). The scientific community has yet to reach a consensus on the quantity of Li that dissolves into solution and the mechanisms of this dissolution; however, an understanding of the interactions of this complex system with engineering materials is of considerable importance to the development of this process.

1.7 Corrosion in Molten Salts

In order for process equipment to withstand the high temperature molten salt environments present in the pyroprocessing operation, materials must be evaluated to determine their ability to withstand these conditions. Molten salts have low vapor pressure and high chemical stability at high temperature, while exhibiting high ionic conductivity, high heat capacity, and high boiling points. These properties have led to their wide range of high temperature process applications in industry. A detailed understanding of the corrosion mechanisms responsible for the degradation of the materials used to construct industrial process equipment is necessary to improve the economics, safety, and efficiency of processes utilizing molten salt solutions and their commercial implementation. Therefore, the mechanisms of corrosion and material degradation in these high temperature fluids have been

extensively studied, with a number of books and review articles published on the subject (*63-67*).

The current consensus amongst researchers in the field is that there are two primary methods for degradation of a metal in contact with a molten salt: dissolution of metallic atoms from the surface of the metal into the salt without oxidation, and oxidation to metallic ions and subsequent dissolution (*63, 65, 67*). The first mechanism is only applicable if there is appreciable solubility of the metallic species in the salt, this occurs when the salt is composed of the same cation as the base metal as is the case with Li in LiCl. This is largely analogous to the corrosion mechanisms in liquid metal interactions. The second mechanism is more widely applicable, and implies an electrochemical redox reaction with a requisite exchange of electrons between species of differing electrochemical potential. It is important to note that the two mechanisms are not mutually exclusive, and both may occur in the same solution for different elements in an alloy.

It is useful to compare molten salts to aqueous solutions due to the many similarities between the two and the vast amount of experience with the latter. Due to the ionic nature of molten salts, their behavior can be theoretically understood as an infinitely concentrated electrolyte in aqueous solution (*63*). Using this analogy, a molten salt solution can be described by its electrolytic character, its oxidation potential, and its acid/base character (*65*). Consequently, the interactions between metals and molten salts can be described largely by the reduction potentials for each system and their relative basicities. Salt basicity is defined as the negative log of the oxygen ion activity in the salt, as shown below in Equation 1.

$$pO^{2-} = -\log\{O^{2-}\}$$ **Equation 1**

This is analogous to pOH in aqueous solutions, with higher values indicating acidic solutions, and lower values indicating basic solutions (*63*). Each molten salt system has different thermodynamic potentials for a given species; therefore, the optimum basicity for each solution/solute combination at which corrosion will be minimized varies significantly. This is analogous to increased corrosion rates at high or low pH values in aqueous solution. The change in oxide solubilty as a function of O^{2-} activity can be seen in Figure 2 below, which gives the solubility of corrosion products in Na_2SO_4 as a function of the negative log of Na_2O activity: analogous to O^{2-} activity previously discussed. There is a narrow range of optimum O^{2-} activity in which corrosion is minimized for each solute, which contrasts to the generally broad range of pH values over which surface films are stable in aqueous solutions. However, it is important to note that solubility never goes to zero and there is always a thermodynamic driving force for corrosion (*65)*. The slope on each side of the minima of solubility of the curves on the graph below can be described by the formation of acidic (high pO^{2-}) or basic (low pO^{2-}) corrosion products. The chemical formulae for these corrosion processes are given by Reactions 3 and 4. The slopes of the experimentally determined curves in Figure 2 are in good agreement with the slope predicted thermodynamically (*66*).

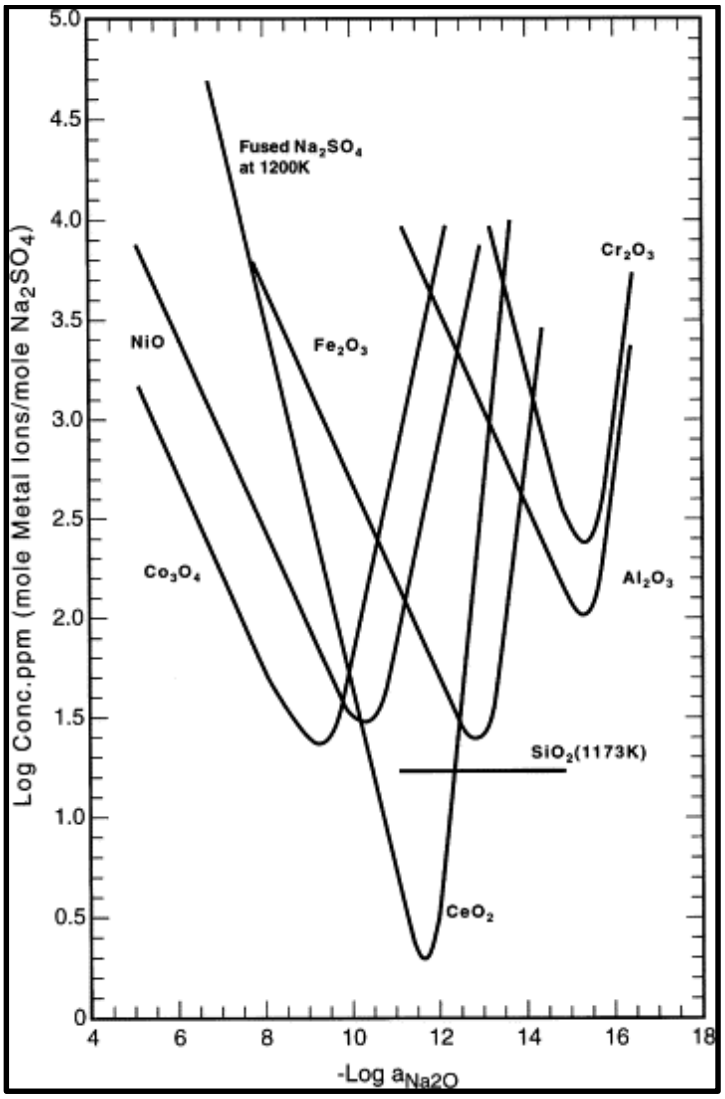


Figure 2: Compilation of measured solubilities for several oxides in fused pure Na_2SO_4 at 1200 K. The solubility of an oxide is highly dependent on the oxygen activity, and narrow regions of stability exist (*66*).

Basic dissolution: $$2NiO + Na_2O + \frac{1}{2}O_2(g) = 2NaNiO_2$$ **Reaction 3**

Acidic dissolution: $$NiO + Na_2SO_4 = NiSO_4 + Na_2O$$ **Reaction 4**

Corrosion in molten salts has been shown to be dependent to a large extent on the impurity levels in the salt (*63, 67*). The hygroscopic nature of some salts will cause moisture from the air to be included in the salt, forming dissolved oxides and hydroxides in the molten

solution. Salts that have absorbed moisture result in dramatically increased corrosion rates in comparison to dry salts (*67*). However, once the impurities are consumed, the corrosion process is controlled by other factors and the corrosion rate decreases based on the kinetics of the previously discussed mechanisms. For short term exposure tests, this can have a large impact on the observed corrosion rate if strict purity levels are not maintained. Consequently, the environment used to conduct experiments must closely match the environment of the process in question such that the impurity levels in the test salt match those encountered in the field (*65*). For the LiCl-Li_2O-Li system, moisture content is an issue, as reactions 5, 6, and 7 generate corrosive products that increase the corrosion rate of the base material (*67, 68*).

$$H_2O + LiCl = LiOH + HCl \qquad \textbf{Reaction 5}$$

$$H_2O + Li_2O = 2LiOH \qquad \textbf{Reaction 6}$$

$$H_2O + Li = LiOH + \frac{1}{2}H_2 \qquad \textbf{Reaction 7}$$

Systems with large thermal gradients, such as those found in the thermal energy storage loops at concentrated solar power facilities and in the heat exchangers of MSRs, can experience increased corrosion rates. This is caused by the difference in alloying element solubility and electrochemical potential between the hot and cold portions of the loop, leading to plating reactions on the cold side simultaneously with dissolution on the hot side. This causes a net mass transfer from hot to cold regions of the loop. Due to the primarily electrochemical nature of this mass transfer, it has been termed Faradaic mass transfer to indicate its dependence on electrical and ionic currents (*63*). Prevention of corrosion by Faradaic mass transfer can be accomplished by breaking the electrical path between the affected areas to prevent charge transfer.

As elements of low nobility are preferentially removed from the surface, the exterior of the material becomes depleted in that element and a concentration gradient between the bulk and the surface is created. Since diffusion occurs relatively rapidly at high temperatures, these elements migrate from the bulk to the surface, leaving vacancies in the alloy. These vacancies then migrate and coalesce at grain boundaries due to the Kirkendall effect, which can give the appearance of intergranular corrosion (*67, 69*).

The similarity between aqueous corrosion and molten salt corrosion extends to the techniques used to study these systems. The electrochemical techniques that are used extensively for understanding the behavior of aqueous corrosion processes can also be used for studies in molten salt environments. However, such methods must be modified for use in specific molten salt systems. For example, reference electrodes must be devised that are unique to molten salts, and those that work in one system are not necessarily applicable to another (*65*). The redox potential is a very useful quantity for predicting corrosion processes, and the redox potential of a species, M, can be determined using the Nernst equation in the form below (*67*):

$$M^{n+} + ne = M \qquad \textbf{Equation 2}$$

$$e_M = e_M^0 + 2.303\frac{RT}{nF}\log\left(\frac{[M^{n+}]}{[M]}\right) \qquad \textbf{Equation 3}$$

Where e_M is the redox potential of species M, e_M^0 is the standard potential for species M, R is the ideal gas constant, T is the temperature in Kelvin, F is the Faraday constant, $[M^{n+}]$ is the activity of the oxidized species, and $[M]$ is the activity of the reduced species. For a given system, lower redox potentials indicate a reducing environment that will tend to lower the corrosion rate, while higher redox potentials indicate an oxidizing environment that will tend to

corrode materials at a faster rate. The redox potential can be determined experimentally through electrochemical means (*63, 65, 67*).

1.8 Corrosion in Molten LiCl-Li_2O-Li

An understanding of the corrosion mechanisms in binary molten salt solutions such as LiCl-Li_2O is important to give a background for the corrosion processes present in the tertiary LiCl-Li_2O-Li system found in the electroreduction step of the pyroprocessing operation. However, the addition of metallic Li to the system has major implications on the corrosion mechanisms. As the LiCl-Li_2O-Li system is the focus of this thesis, it is important to note that to date, there have only been a handful of reports published studying corrosion in these solutions. Despite its significant impact on the electrolytic reduction of UNF, corrosion in the LiCl-Li_2O-Li system remains largely unstudied. The papers that have been published report conflicting results and do not adequately explain the mechanisms responsible for corrosion (*70-72*).

Unpublished work from this research group has shown that corrosion in the LiCl-Li_2O-Li system is highly dependent on the concentration of each element in solution, as well as the impurities that contribute to the overall solution chemistry. Due to the reducing nature of metallic Li and the oxidizing nature of Li_2O, a number of interesting phenomena have been observed, including the formation of Li_8 nanoclusters in solution at 650°C, which was observed by this research group (*73*).

1.9 Material Selection

Previous corrosion studies of stainless steel alloy 316 and nickel based Inconel alloys 625 and 718 performed by this lab group indicates that at high concentrations of lithium metal in the salt solution, chromium leaches from the alloy, leading to increased corrosion rates. All three of

these alloys were observed to exhibit high rates of Cr and Mo dissolution. The corrosion performance of the Ni based Inconel alloys were superior to that of the Fe based stainless steel. For these reasons, it was decided to study a Ni based alloy that was stabilized by elements other than Cr. This led to the selection of the Ni-Cu alloy Monel 400 (M400).

The elemental composition of M400 is given in Table 2 (*74, 75*). This alloy was developed in the early 20th century based on a naturally occurring ore found at a mine in Canada, and has proven to be remarkably corrosion resistant in a number of harsh environments. It is commonly used for marine applications, and has numerous industrial uses in chemical and hydrocarbon processing operations (*76-78*). The corrosion performance of M400 has been shown to be excellent in carbonate salts at 650°C and sulphate salts at 600°C, which gave theoretical justification for testing this material in the LiCl-Li_2O-Li system at 650°C (*77, 79*). No studies of M400 in molten chloride salts could be found in the open literature.

Table 2: Elemental composition typical of M400, from ASTM UNS N04400

Ni wt%	Cu wt%	Fe wt%	Mn wt%
63 min	28-34	2.5 max	2.0 max

Chapter 2: Experimental

This chapter focusses on the materials, equipment, experimental procedures, and analytical techniques used to characterize the corrosion behavior of M400 in molten LiCl-Li_2O-Li. Technical details, parameters, and other background information required to conduct experiments and accurately study material interactions in this complex environment are emphasized. The high temperature and highly reactive nature of these molten solutions necessitate the use of specialized experimental setups and methodologies in order to minimize experimental error, ensure repeatability, and to maintain the safety of those involved in performing the experiments. The results from these experiments are given in Chapter 4.

2.1 Materials

The composition of the M400 plate was obtained from California Metals, with a certified composition provided in Table 3. The plate was factory cold rolled and annealed.

Table 3: Elemental composition of the M400 sheet used in this study.

Ni wt%	Cu wt%	Fe wt%	Mn wt%	Minor Components
63.9	33.0	1.55	1.1	Si, C, Al, P, Co, S, Pb, Sn, Zn

Anhydrous LiCl of 99wt% purity, li_2O of 99.5wt% purity, and metallic Bi powder of 99.5wt% purity, all packed in an Argon atmosphere, were obtained from Alfa Aesar. Metallic Li pellets of 99wt% purity, also packed in an Argon atmosphere, was obtained from Strem Chemicals. All powders and metals were opened and stored in the Ar environment of the glove box. Methanol was procured from Fisher Scientific and was of HPLC grade at 99.9% purity. 55mL Nickel crucibles were obtained from Alfa Aesar. Graphite tubes, used for the Li-Bi reference electrode, were obtained from Weaver Industries and were manufactured using NAC-200 grade

extruded graphite. M400 and Nickel wires were obtained from ESPI metals. Commercial grade Copper wire was obtained from Arcor metals.

2.2 Sample Preparation

A schematic diagram of the sample geometry and submersion depth during exposure is given in Figure 3. M400 samples were cut into ½" by ½" squares from a 1/16" thick plate using a CO_2 laser. Sample coupons were exposed to the molten solutions in their as-received condition to simulate real world conditions. The samples were spot welded to 0.032" diameter M400 wire on one corner for suspension from the sample holder. The sample height was fixed such that the maximum surface area could be exposed to the salt melt without exposure of the heat affected zone from the spot weld.

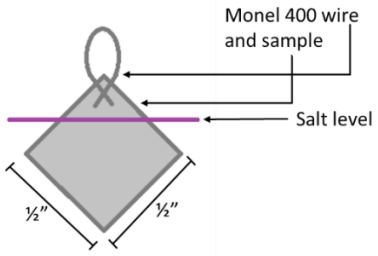


Figure 3: Exposure testing sample geometry showing the approximate depth of immersion in the molten LiCl-Li_2O-Li salt.

The design shown in Figure 3 allowed samples to be made on a jig in a repeatable manner that gave an exposed surface area of $3.2cm^2 \pm 0.16cm^2$ (5%). Two samples were used for each test, resulting in a total exposed surface area of $7.2cm^2$. The samples were degreased using 99.95% pure acetone and dried in the vacuum antechamber of the glove box prior to being subjected to the exposure testing.

2.3 Glove box

The highly reactive nature of molten salts containing metallic Li as well as the hygroscopic qualities of room temperature LiCl require that these experiments be conducted in an inert atmosphere in the absence of significant quantities of O_2 or H_2O. For this purpose a Vacuum Research Systems OmniLab glove box with an argon atmosphere was used to contain the furnace, balance, and chemicals used in this study. The glove box employed a copper plate type purification system to maintain the oxygen concentration at less than 10ppm, and a molecular sieve to keep water content below 2ppm. Glove box electronics were kept below 40°C by an exterior water cooling loop.

2.4 Furnace, Temperature Control, and Crucibles

The exposure testing setup, shown in Figure 4, used three concentric crucibles inside of a furnace to contain the salt in the event of failure of the inner crucible or accidental spillage of the molten salt. The outermost crucible was a 2 ½" inner diameter schedule 40 steel pipe welded to a 1/8" steel plate designed to both contain liquid metallic lithium and to stabilize the furnace temperature by increasing the thermal inertia of the system. The total height of the steel crucible was 3". The second crucible was a 3" tall, 2" inner diameter graphite crucible purchased from the Graphite Store that fit within the steel crucible. In the event of an unexpected system failure, the graphite crucible is designed to contain any spilled LiCl and Li_2O. The use of the steel crucible is essential as metallic Li diffuses through the porous graphite. The inner crucibles, used to directly contain the molten LiCl-Li_2O-Li, were nickel crucibles obtained from Alfa Aesar of 55mL capacity. The use of a metallic crucible is necessary since metallic lithium is known to react readily with all commercially available ceramics (*80*). This crucible allows for safe containment of 50g of LiCl-Li_2O-Li.

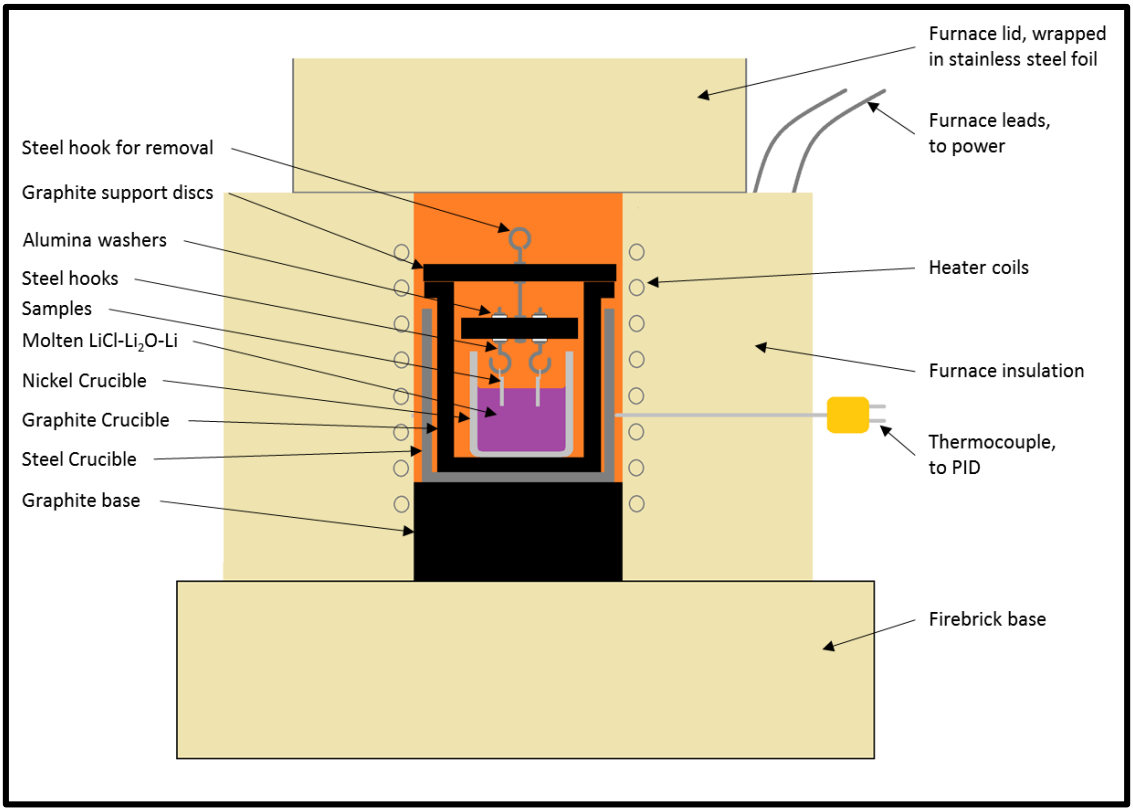


Figure 4: Schematic of the furnace, crucibles, sample holder and other various equipment contained within the furnace used for the experiments conducted in this study.

A three inch inner diameter Watlow furnace was controlled by a PID using a type K thermocouple for continuous temperature control. The tip of the thermocouple was inserted through a small hole in the side of the furnace and was placed in contact with the outside of the steel containment vessel. The temperature set point was calibrated using a second type K thermocouple inserted directly into a salt melt used specifically for this purpose. To minimize contamination in the salt melt due to insertion of a thermocouple, the temperature of the salt itself was not monitored directly during individual experiments, and temperature control relied on the proper calibration of the external thermocouple. However, all temperatures when reported are the molten salt temeperature. Temperature during exposure was maintained in this manner at 650±5°C.

2.5 Exposure Testing

The total mass of LiCl, Li_2O and Li used for each experiment was 50g. The salt melt was composed of LiCl-2wt%Li_2O with concentrations of Li ranging from 0wt% to 1wt% in 0.1wt% increments. All masses were measured to ± 0.001g accuracy using a balance with a 0.0001g precision. Exposures in LiCl-2wt%Li_2O with 0, 0.2, 0.4, 0.6, 0.8, and 1.0 wt%Li solutions were conducted in duplicates to ensure repeatability of the calculated corrosion rates, resulting in a total of 17 exposure experiments.

In accordance with Gese *et al.,* impurity H_2O in hygroscopic LiCl was removed from the salt prior to the addition of Li_2O and Li by heating the required mass of LiCl for each experiment to 550°C for 2 hours in a Ni crucible (*68*). Following the drying procedure, the required mass of Li_2O and Li were added to the LiCl at 550°C and the temperature of the melt was raised to 650°C. The temperature was allowed to stabilize for one hour to ensure the solution was completely melted (*81*). Sample coupons were then connected to the sample holder, the assembly was lowered into the furnace, and covered with the furnace lid. All exposure tests were conducted for 20 hours. Once the allotted exposure time had elapsed, the samples were removed from the furnace and allowed to cool to room temperature before being stored, while the salt was allowed to cool and solidify in the Ni crucible inside the furnace.

2.6 Electrochemical Measurements

The open circuit potentials (OCP) of Cu and Ni wire electrodes versus a Li-Bi reference electrode were measured in various molten solutions of LiCl-Li_2O-Li in order to elucidate the mechanisms driving the corrosion of M400 in the LiCl-Li_2O-Li system. The LiCl-Li_2O-Li electrolyte used in these OCP studies was prepared in a similar manner to that used for exposure testing outlined above. Ni and Cu wire electrodes were prepared by polishing with 600 grit SiC paper in

the glove box to remove any surface contamination. For tests using the Li-Bi reference electrode, the electrode was heated along with the salt to minimize potential damage due to thermal shock. Wire electrodes were suspended in alumina tubes and attached to a vertical translation stage to allow for immersion in the electrolyte at temperature. A Gamry PC4 potentiostat was used in all experiments in conjunction with Gamry Framework and Echem Analyst software. The potential was measured every second for 200 seconds after the voltage stabilized.

2.7 Post Exposure Analytical Methods

A suite of surface analytical techniques were used to characterize the samples following exposure testing. This section will cover the methodology and parameters used for each instrument as well as the types of data each technique was used to collect, while the results of these studies will be presented in Chapter 4.

2.7.1 X-Ray Diffraction

Grazing incidence X-ray diffraction (GI-XRD) was used to characterize the crystalline phases present on the samples following exposure. A Rigaku Smartlab was used to conduct XRD analysis. The x-ray tube had a copper target and was operated at 40KV and 44mA. Cu K_β radiation was removed by the use of a Ni filter. Grazing angle diffraction was performed in a parallel beam optical configuration with an incidence angle of 0.5° in order to study the surface films formed as a result of exposure testing. In this configuration, the X-ray source was held fixed relative to the sample, with only the detector arm moving to collect the diffraction pattern. A scan range from 2θ=5° to 90° was employed using a step size of 0.06° and a rate of 1° per minute. Due to the hygroscopic nature of the LiCl that remains on the sample surface after

removal from the salt melt, all measurements were performed in an inert atmosphere by maintaining the sample in a plastic bag that was sealed in the Ar environment of the glove box. This technique has been successfully employed by previous researchers studying hygroscopic samples, and has been confirmed by our research group (*82, 97*). The bag was held off the surface of the sample with plastic tubes to minimize its interference.



Figure 5: Top: Rigaku X-Ray Diffractometer used for characterization of phases present on samples. Bottom: Internal components of the Rigaku XRD.

2.7.2 Scanning Electron Microscopy and Energy Dispersive X-Ray Spectroscopy

Field emission scanning electron microscopy (FESEM) was used to characterize sample morphology. A Hitachi S-4700 FESEM equipped with an Oxford Instruments energy dispersive X-ray spectrometer (EDS) was used in this study. The LaB_6 field emission electron source was operated at 20kV and 15mA. The working distance was set at 11.9±1mm. The samples and puck were sealed in a plastic bag in the Ar atmosphere glove box to prevent atmospheric contamination during transport to the FESEM; however, the design of the instrument necessitated exposure of the samples to air for approximately 15 seconds before being introduced to the FESEM vacuum chamber. Micrographs were taken at 50x, 500x, 5,000x, and 25,000x magnification. EDS spectroscopy was performed at 25,000x magnification on areas of exposed alloy to give a quantification of the elemental composition of the sample surface. A collection time of 124 seconds for EDS was used, and the microscope was operated under the same conditions as during imaging.



Figure 6: Hitachi S-4700 Field Emission Scanning Electron Microscope and Oxford Instruments energy dispersive X-Ray spectrometer used to characterize surface morphology and composition

2.7.3 Micro-Vickers Hardness Testing and Optical Microscopy

A Shimadzu Seisakusho LTD NT-M001 hardness tester was used to indent the samples for micro-Vickers hardness measurement in order to study the variation of surface mechanical properties that occurred as a result of exposure to molten LiCL-Li_2O-Li. The samples were rinsed with methanol for 10 minutes to remove the LiCl remaining on the surface prior to indentation. A load of 500g was applied for 30 seconds per indentation. Each sample had 10 indentations performed in order to provide statistically accurate determination of surface hardness. For micro-Vickers hardness testing, the indentation created is square pyramidal in geometry and the length of the diagonal (d), in µm, and the load (L), in g, are used to calculate the Vickers hardness (HV) through the formula given in equation 4 (*83*).

$$HV = \frac{1854.4 * L}{d^2} \qquad \textbf{Equation 4}$$

Images of the indentations were captured using the 200x objective lens of a Leica MC170 HD operating with the Leica Application Suite version 4.3. This software package was also used to measure both diagonal lengths of each indentation. The average of the two diagonal lengths was used for the calculation of each indentation. The hardness measurement made using this equipment was verified to be accurate using a NIST certified hardness standard. These images were also used to observe changes in surface morphology following exposure to differing melt conditions.



Figure 7: Shimadzu Seisakusho LTD. NT-M001 used for micro-Vickers hardness testing.



Figure 8: Leica MC170 HD microscope and computer used to capture images of sample surfaces and measure indentation size.

2.7.4 Raman Spectroscopy

Raman spectroscopy was used to study the surface of the exposed samples and to characterize the rotational and vibrational modes of the sample surface following exposure to molten LiCl-Li_2O-Li. A Thermo Scientific DXR Raman spectrometer equipped with a 10 mW 532nm laser that was passed through a custom fiber optic probe designed by InPhotonics was used for this study. The use of the fiber probe allowed the Raman spectroscopic analysis to be conducted in the Ar atmosphere of the glove box. The fiber probe, which had a focal length of 5mm, functioned as both the focusing and the receiving optics for the system for these measurements. The beam was focused by a computer controlled vertical translation stage from Zaber Technologies with a precision of 10µm. The height of the fiber probe was adjusted until the strongest signal was recorded by the Raman microscope. The spectra reported are an average of 16 individual exposures of 16 seconds each.



Figure 9: Thermo Scientific DXR Raman microscope used to characterize the rotational and vibrational modes of the sample surfaces.

2.7.5 X-Ray Photoelectron Spectroscopy

X-ray photoelectron spectroscopy (XPS) was used to quantify the elemental composition of the sample surface. All samples were rinsed with methanol for 10 minutes prior to XPS analysis to remove the residual salt layer from the sample surface. A Phi 5600 XPS using Mg K_α radiation of 1253.6eV at an accelerating voltage of 14kV and operating at 300W was used for this study. The Ag $3d_{5/2}$ line at 368.3eV was used to calibrate the spectrometer to an accuracy of ±0.05eV. The variation of composition as a function of depth was analyzed through the use of Ar^+ sputtering. The ion gun was operated at a current density of approximately 0.1mA/cm^2 and was measured to remove approximately 7nm of Ta_2O_5 per minute over 9mm^2 of surface area. XPS spectra were collected from an area of 1.6mm^2 for binding energies between 1100eV and 0eV with a step size of 0.5eV, using a pass energy of 29.35eV and a dwell time of 50ms. The reported spectra are the average of 10 individual spectra.

Elemental composition was determined using the XPS spectra and normalizing the elemental line intensity by the respective photoelectron emission cross sections. Quantification of the relative atomic ratios of Ni and Cu on the sample surfaces was performed using the AugerScan software. The area of the Cu $2p_{3/2}$ peak was determined using a Shirley background from an upper binding energy of 936.0eV to a lower binding energy of 928.5eV for all samples, as Cu was only observed in the metallic state. Fitting of the Ni $2p_{3/2}$ spectrum is known to be complex due to the multiplet, shake-up, and plasmon loss structures unique to Ni spectra (*84*). Therefore, the area of the Ni $2p_{3/2}$ peak was determined using a Shirley background from an upper binding energy varying between 865eV and 862.5eV to a lower binding energy of 848.5eV for surfaces analyzed prior to Ar^+ sputtering. The upper binding energy for Ni was fixed at

862.5eV for the sputtered spectra, as Ni was only observed to be in the metallic state after sputtering.

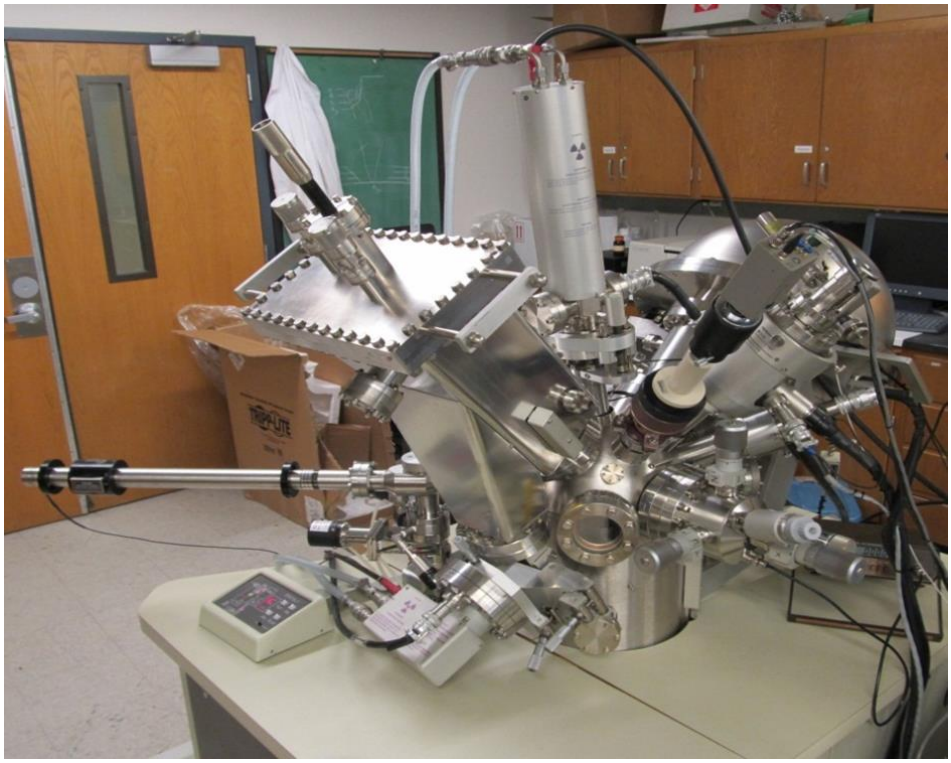


Figure 10: The Phi 5600 X-Ray photoelectron spectrometer used to quantify sample surface composition.

2.7.6 Inductively Coupled Plasma - Optical Emission Spectrometry

Inductively coupled plasma optical emission spectrometry (ICP-OES) was used to quantify the alloying elements that dissolved into the salt as a result of each exposure test. The cooled salt ingot was dissolved in 750ml of 18 MΩ deionized water. The resulting solution was analyzed using a Perkin Elmer Optima 8000 ICP-OES. SCP Scientific supplied spectroscopic standards for calibration. The concentrations were reported in mg/L by the instrument and had a relative standard deviation of less than 5%.

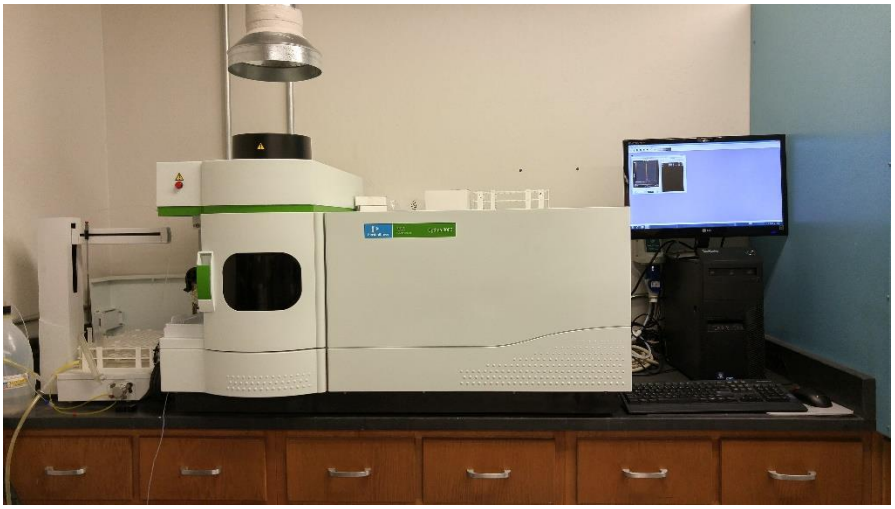


Figure 11: Perkin Elmer Optima 8000 Inductively Coupled Plasma Optical Emission Spectrometer used to quantify the dissolution of alloying elements into the molten salt

Chapter 3: Lithium-Bismuth Reference Electrode Development

As stated in Chapter 1, in order to conduct electrochemical experiments for a given molten salt system a suitable reference electrode must be devised. For an electrode to act as a reference, it must be able to maintain a stable electrochemical potential independent of changes in the solution chemistry. To accomplish this, a redox couple that maintains a constant Gibbs free energy of formation over the range of electrolyte solution chemistries needs to be utilized. The $Ni|Ni^{2+}$ couple is typically used as a quasireference in the LiCl-Li_2O system (*40, 85*). However, the LiCl-Li_2O-Li system studied in this work contains significant quantities of dissolved metallic Li, negating the usefulness of the $Ni|Ni^{2+}$ electrode. This is due to the inclusion of both Li and Li_2O in the electrolyte, since any oxidized species (M^+) that would not be reduced by Li would have a corresponding reduced species (M) that would be oxidized by Li_2O. The inverse of this argument is also true. This paradox is summarized by Reactions 8 and 9 below

If $\Delta G_{M|M^+} > \Delta G_{Li|Li^+}$ then $2M + Li_2O \rightarrow M_2O + 2Li$ **Reaction 8**

If $\Delta G_{M|M^+} < \Delta G_{Li|Li^+}$ then $M_2O + 2Li \rightarrow 2M + Li_2O$ **Reaction 9**

Consequently, the selection of a redox couple ($M|M^+$) for this system that acts as a true reference electrode is near impossible, as no species exists that spans the electrochemical window necessary to maintain a stable reference voltage in LiCl-Li_2O-Li. For this reason, a reference electrode was designed for the LiCl-Li_2O-Li system based on the $Li|Li^+$ couple utilizing a liquid alloy of Li and a more reactive element. For thermodynamic reasons discussed below, at the interface between the liquid alloy and molten LiCl-Li_2O-Li, the $Li|Li^+$ couple is in equilibrium and a nearly stable potential will be maintained regardless of fluctuations in solution chemistry.

Two such liquid metal reference electrode systems have been reported in the literature, those being Li-Pb and Li-Bi (*86, 87*). Due to the toxicity of Pb, the Li-Bi system was chosen in this study. Ideally, the Li-Bi composition for a stable reference electrode is 60at% Li-40at%Bi (*88*). This composition was chosen by studying the Li-Bi phase diagram; shown in Figure 12 (*89, 90*). In this diagram, it can be seen that intermetallic $BiLi_3$ is formed at 75at% Li, and the liquidus at 923K occurs at approximately 52at%Li. Additionally, it has been shown that the intermetallic phase exists at deviations of as much as 22at%Li from the ideal stoichiometry (*90*). Therefore, in this concentration range, a mixture consisting of liquid Li-Bi and solid $BiLi_3$ is formed. Under the operating conditions, Reaction 10 describes the equilibrium in the reference electrode.

$$Bi(l) + 3Li(l) \leftrightarrow BiLi_3(s) \qquad \textbf{Reaction 10}$$

Analogous to common pyrometallurgical practices, the intermetallic $BiLi_3$ acts as a sink and source for any fluctuations in Li concentration while maintaining a constant activity of Li in the reference electrode (*25*). This is due to the fact that Li will maintain unit activity when dissolved in the liquid metal containing intermetallic $BiLi_3$. Consequently, the potential of the Li-Bi reference electrode will theoretically remain constant over a wide range of Li concentrations in the electrolyte. A thin walled graphite tube with a closed end was used as an ion bridge between the Li-Bi alloy and molten LiCl-Li_2O-Li.

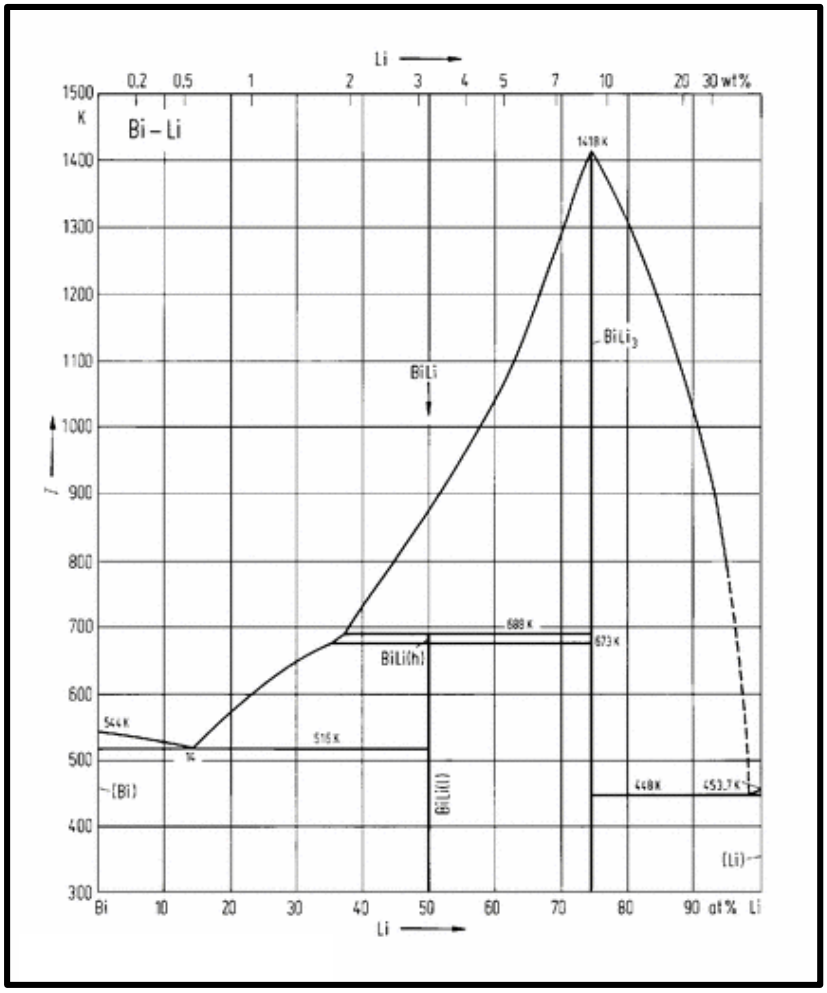


Figure 12: Phase diagram for the Bi-Li system.

The reference electrode was constructed by mixing metallic Li and Bi in the proper ratio to form 3g of the desired alloy in a 1mm walled graphite tube at room temperature. The same furnace used for exposure testing was used to assemble the Li-Bi reference electrode. The assembly was heated to 200°C for 30 minutes to melt the Li component, whereupon the formation of the intermetallic Li_3Bi phase occurred (*91*). This was followed by heating at 300°C for 30 minutes to melt any unreacted Bi. Final annealing was performed at 800°C for 5 hours to ensure thorough mixing and saturation of the wall of the graphite tube.

All attempts at forming the intermetallic Li_3Bi phase resulted in the failure of the graphite cell. McDeavitt noted that the formation of Li_3Bi is highly exothermic with a standard heat of mixing of -251.3kJ/mol, which in an adiabatic system would equate to a temperature rise of more than 2000°C due to the compound's low specific heat of 115J/mol·K (*91*). Consequently, a different formulation for the Li-Bi alloy was chosen for the construction of the final electrodes. Previous research has shown that the activity of Li in Bi is relatively constant with respect to fluctuations in Li content, with variations in composition from 10 to 50at%Li having a potential variation of only 20mV (*92*). Variations in composition are expected to be much smaller than this for the reference electrode developed in this study, allowing for a fairly stable voltage to be maintained. Therefore, the composition of 30at%Li-70at%Bi was chosen for the final design. This Li-Bi composition has been successfully used as a reference electrode in the LiCl system by previous researchers (*93*). Two Li-Bi reference electrodes were successfully constructed using this composition. An image of one of the completed reference electrodes used in this study is shown in Figure 13. The stability of the Li|Li-Bi couple observed in this study is presented in section 4.3.



Figure 13: Image of a Li-Bi reference electrode following the completion of one of the electrochemical tests presented in Section 4.2. The alloy is composed of 30at%Li-70at%Bi and is contained in a graphite tube with 1mm wall thickness. A dark band at the bottom of the graphite tube, indicated by the red arrow, showed the level of the alloy in the tube as a result of diffusion of Li through the wall. The electrode was wrapped in fiberglass for electrical insulation and supported with a metal test tube clamp. A Ni wire in contact with the outer wall of the graphite tube allowed for connection to the potentiostat.

Chapter 4: Results and Discussion

This chapter will present and discuss the results of the experiments, as outlined in the Chapter 2 of this study. Observations are presented in sections 4.1 and 4.2, and interpretation of these observations is presented in Section 4.3. The overall conclusions and recommendations drawn from this work are given in Chapter 5.

4.1 Exposure Testing

4.1.1 Visual Observations

Upon removal from the LiCl-Li_2O salt melts containing metallic Li, visual inspection indicated the M400 samples showed no visible signs of degradation by the exposure. However, the samples exposed to LiCl-2wt%Li_2O without metallic Li showed signs of corrosion not seen on the samples that had been exposed to melts containing metallic Li, as can be seen in Figure 14. The amount of visible degradation was not as severe as that with Inconel and stainless steel samples in other similar studies conducted by this research group. These visual observations, although qualitative in nature, are indicative of high resistance to corrosion in the environment studied.

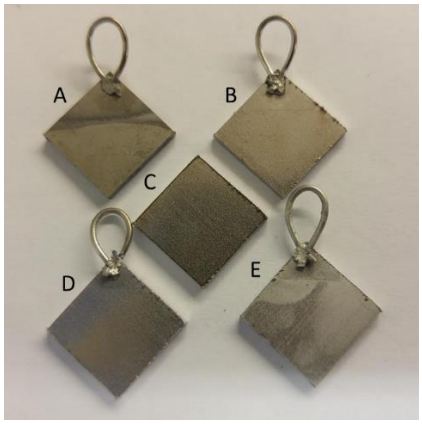


Figure 14: Optical image of Monel 400 samples. (A) Exposed to LiCL-2wt%Li_2O in the absence of Li at 650°C for 20 hours. (B) Exposed to LiCL-2wt%Li_2O-0.1wt%Li at 650°C for 20 hours. (C) As-received. (D) Exposed to LiCL-2wt%Li_2O-0.5wt%Li at 650°C for 20 hours. (E) Exposed to LiCL-2wt%Li_2O-0.9wt%Li at 650°C for 20 hours.These samples are representative of all samples following exposure to molten LiCl-Li_2O-Li. Degradation was seen at the liquid level for the sample exposed to LiCl-2wt%Li_2O in the absence of Li, but not on samples exposed to LiCl-2wt%Li_2O containing Li.

4.1.2 X-Ray Diffraction

GI-XRD was performed to detect changes in the lattice parameter of the base alloy and the crystalline phases present on the sample surface following exposure to molten LiCl-Li_2O-Li. GI-XRD of M400 samples exposed to molten LiCl-2%Li_2O-Li solutions was performed in a plastic bag sealed in the Ar atmosphere of the glove box in order to preserve any corrosion products that are unstable in air. The diffraction pattern of an as-received sample was recorded in the same manner to serve as a control that could be used to account for any changes in the diffraction pattern caused by the plastic bag. Figure 15 shows the diffraction pattern of an as-received M400 sample analyzed in a plastic bag. The peaks occurring at 2θ = 44.1°, 51.3°, and 75.5°, are characteristic of M400 and correspond to the (1,1,1), (2,0,0), and (2,2,0) planes, respectively. ICDD card number 01-077-7711 was used for identification of the M400 crystal planes. A minor additional peak at 2θ = 23.1° is caused by the plastic bag. The crystal structure of M400 is FCC, owing to its primarily Ni-Cu composition, and has an as-received lattice parameter of 3.56Å.

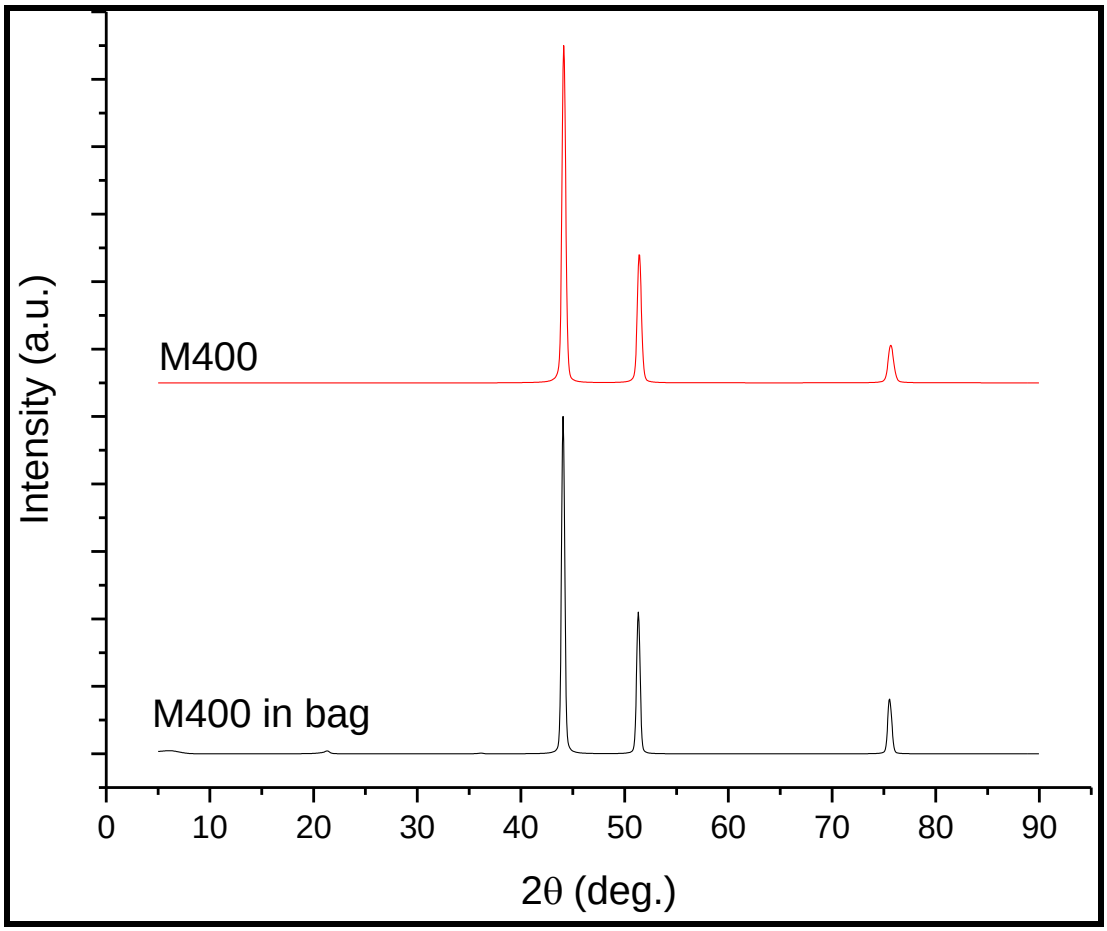


Figure 15: GI-XRD pattern for as-received M400 obtained in air and while contained in a plastic bag. The primary diffraction peaks occur at 2θ = 44.1°, 51.3°, and 75.5°, corresponding to the (1,1,1), (2,0,0), and (2,2,0) planes respectively. A minor amorphous peak centered on 2θ = 21° is attributed to the plastic bag, as this peak is not present on the sample analyzed in atmosphere. The plastic bag did not cause any shift in the primary diffraction peaks of M400. The lattice parameter of M400 is 3.65Å, as calculated from the peak positions of these diffraction patterns.

Figure 16 shows the diffraction pattern of a M400 sample exposed to LiCl-2wt%Li_2O-0.9%Li at 650°C for 20 hours. This pattern is typical of the diffraction patterns obtained for M400 samples following exposure to LiCl-Li_2O-Li at 650°C for 20 hours. The peak positions obtained from this pattern are given in Table 4. This sample is presented separate from the bulk of the diffraction patterns collected as it displays all of the peaks found on the other samples. Not all samples displayed all of the diffraction peaks found in this pattern and the relative intensity of each peak varied from sample to sample. The use of both grazing incidence and parallel beam

optics for the collection of these diffraction patterns prevents comparison of peak heights between samples. The phases present were M400, LiCl, and LiCl-monohydrate. No correlation was observed between the presence of any given peak or group of peaks and the Li concentration in the melt.

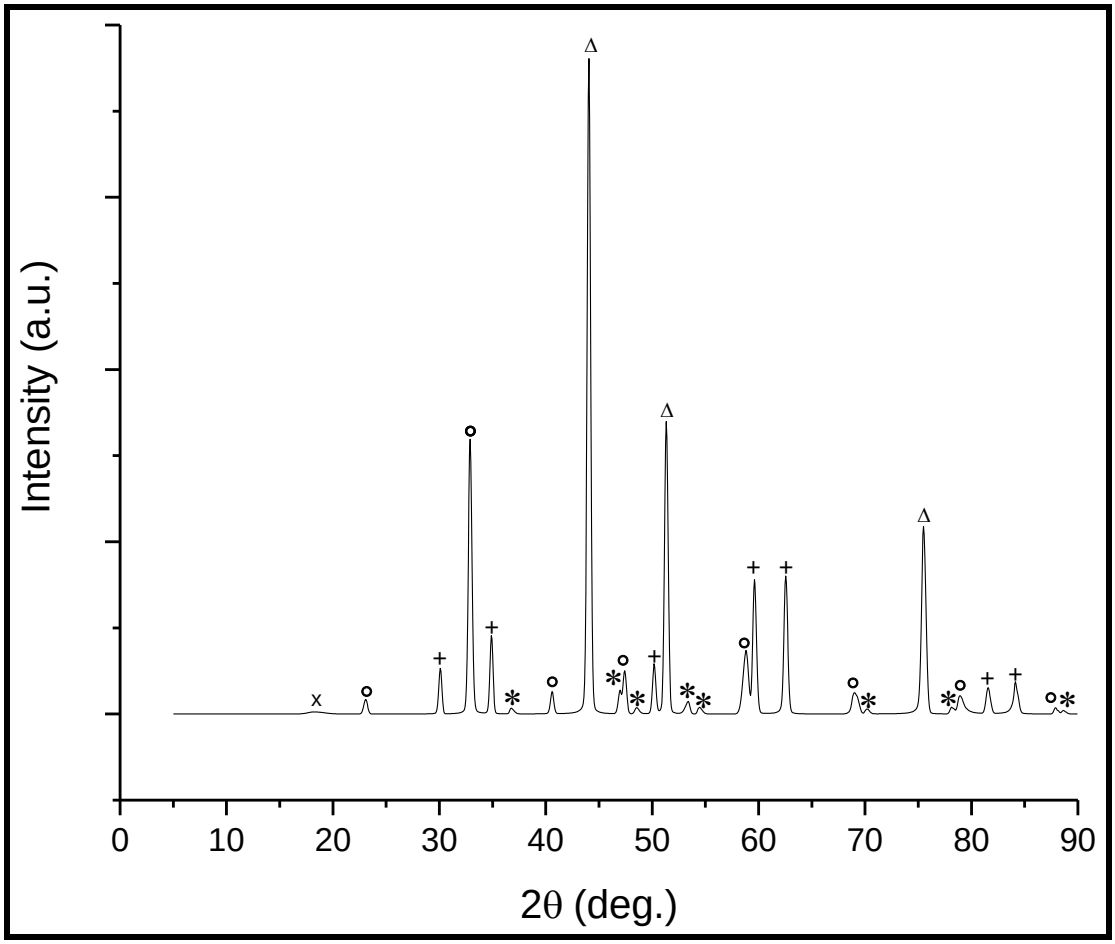


Figure 16: GI-XRD pattern of M400 exposed to LiCl-2wt%Li_2O-0.9wt% Li at 650°C for 20 hours. Diffraction peaks corresponding to M400, LiCl, and LiCl-monohydrate phases, labeled as Δ, +, and o, respectively Minor peaks were not identified (*), but are suspected to be oxides of the base alloy and Li, and are labeled as *. The diffraction peak of the plastic bag (x) is also present.

Table 4: Peak positions and of the diffraction peaks detected on M400 exposed to LiCl-2wt%Li_2O-0.9wt%Li, and the symbol corresponding to peaks in Figure 16 above.

Peak No.	2θ (deg)	Phase	Plane (h,k,l)	Symbol
1	18.23	Plastic Bag		X
2	23.06	Lithium Chloride-Monohydrate	(1,0,0)	o
3	30.07	Lithium Chloride	(1,1,1)	+
4	32.86	Lithium Chloride-Monohydrate	(1,1,0)	o
5	34.87	Lithium Chloride	(2,0,0)	+
6	36.69	Unknown		*
7	40.57	Lithium Chloride-Monohydrate	(1,1,1)	o
8	44.02	M400	(1,1,1)	Δ
9	46.95	Unknown		*
10	47.37	Lithium Chloride-Monohydrate	(2,0,0)	o
11	48.48	Unknown		*
12	50.15	Lithium Chloride	(2,2,0)	+
13	51.28	M400	(2,0,0)	Δ
14	53.39	Unknown		*
15	54.35	Unknown		*
16	58.79	Lithium Chloride-Monohydrate	(2,1,1)	o
17	59.56	Lithium Chloride	(3,1,1)	+
18	62.49	Lithium Chloride	(2,2,2)	+
19	68.86	Unknown		*
20	69.25	Lithium Chloride-Monohydrate	(2,2,0)	o
21	70.12	Unknown		*
22	75.45	M400	(2,2,0)	Δ
23	78.11	Unknown		*
24	78.86	Lithium Chloride-Monohydrate	(3,1,0)	o
25	81.52	Lithium Chloride	(3,3,1)	+
26	84.12	Lithium Chloride	(4,2,0)	+
27	87.88	Lithium Chloride-Monohydrate	(2,2,2)	o
28	88.62	Unknown		*

Phases identified via XRD were M400, LiCl, and LiCl-monohydrate. The as-received M400 sample served as baseline for the M400 phase, while ICDD card numbers 00-004-0664 and 01-072-4565 were used for identification of LiCl and LiCl-monohydrate, respectively minor peaks did not match any diffraction pattern for compounds containing the elements present in the base alloy or salt phases. These are suspected to be resulting from the presence of Li intercalated oxides of the base alloy due to the evidence of oxygen on the sample surface obtained from EDS analysis of unrinsed samples, which is presented in Section 4.1.3. These films would be very thin, as observed by the low relative intensity of these peaks on the XRD patterns and the XPS analysis of rinsed samples in section 4.1.6.

The diffraction patterns collected from the surfaces of M400 samples following exposure to molten LiCl-Li_2O-Li had peak positions consistent with those detected on the 0.9wt%Li sample. The diffraction patterns collected for all M400 samples exposed to molten LiCl-Li_2O-Li solutions at 650C for 20 hours are given in Figure 17. Analysis of the M400 peak positions, shown in Table 5, indicates that there was minimal contraction or expansion of the M400 lattice due to exposure to LiCl-2wt%Li_2O-Li at 650°C for 20 hours.

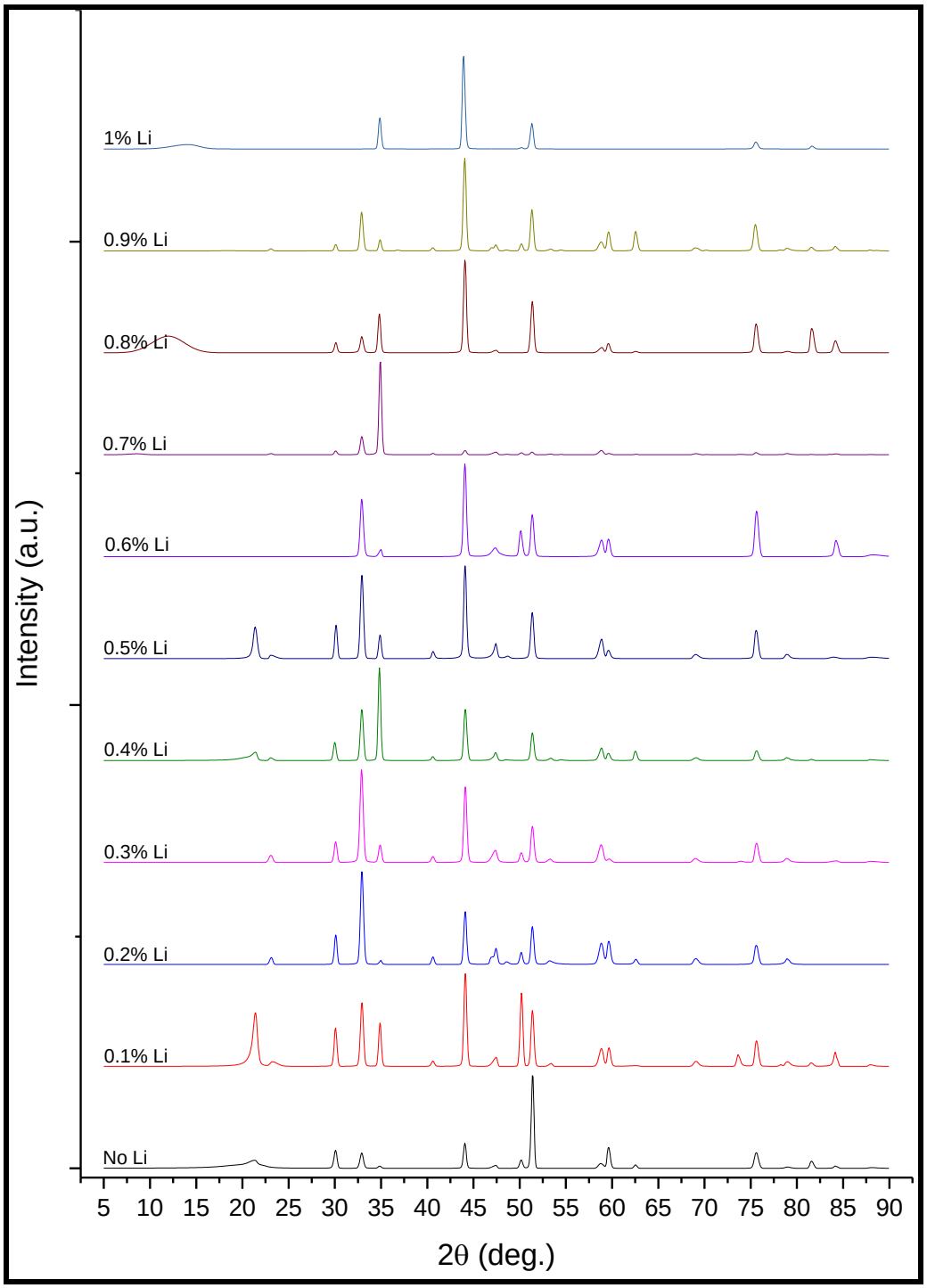


Figure 17: GI-XRD patterns obtained from M400 samples exposed to molten LiCl-2wt%Li_2O-Li at 650°C for 20 hours. The weight percent metallic Li content of the salt melt is indicated on each diffraction pattern. LiCl, LiCl-monohydrate and M400 were identified on all samples except for the sample exposed to 1wt%Li, which only displayed peaks of M400 and LiCl. Inconsistencies in the ratios of phases between samples can be attributed to varying salt thickness and the susceptibility of parallel beam optics to detection of preferentially oriented crystal planes.

Table 5: M400 peak positions, inter-planar spacing, and lattice parameters for as-received M400 and M400 samples exposed to LiCl-2wt%Li_2O-Li at 650°C for 20 hours. Peak positions varied minimally, and the lattice parameter was unaffected by exposure to the salt melt. This indicates that the base alloy suffered minimal degradation due to exposure to the salt melt.

Weight Percent Li	(1,1,1) (deg 2θ)	(2,0,0) (deg 2θ)	(2,2,0) (deg 2θ)	$d_{(1,1,1)}$ (Å)	$d_{(2,0,0)}$ (Å)	$d_{(2,2,0)}$ (Å)	$a_{(1,1,1)}$ (Å)	$a_{(2,0,0)}$ (Å)	$a_{(2,2,0)}$ (Å)	Average Lattice Parameter (Å)	Percent change (%)
No Li	44.06	51.38	75.56	2.055	1.778	1.258	3.560	3.557	3.559	3.559	0.088
0.1% Li	44.12	51.38	75.56	2.053	1.778	1.258	3.555	3.557	3.559	3.557	0.045
0.2% Li	44.12	51.38	75.62	2.053	1.778	1.257	3.555	3.557	3.557	3.556	0.022
0.3% Li	44.12	51.38	75.56	2.053	1.778	1.258	3.555	3.557	3.559	3.557	0.045
0.4% Li	44.12	51.38	75.68	2.053	1.778	1.257	3.555	3.557	3.554	3.555	0.000
0.5% Li	44.06	51.38	75.56	2.055	1.778	1.258	3.560	3.557	3.559	3.559	0.088
0.6% Li	44.06	51.38	75.56	2.055	1.778	1.258	3.560	3.557	3.559	3.559	0.088
0.7% Li	44.06	51.38	75.62	2.055	1.778	1.257	3.560	3.557	3.557	3.558	0.066
0.8% Li	44.06	51.38	75.56	2.055	1.778	1.258	3.560	3.557	3.559	3.559	0.088
0.9% Li	44.06	51.32	75.62	2.055	1.780	1.257	3.560	3.560	3.557	3.559	0.102
1% Li	43.94	51.32	75.56	2.061	1.780	1.258	3.569	3.560	3.559	3.563	0.211
As-received M400	44.12	51.38	75.68	2.053	1.778	1.257	3.555	3.557	3.554	3.555	n/a

As mentioned previously, GI-XRD patterns were collected with the samples sealed in plastic bags to prevent atmospheric contamination from destroying the species present on the surface that are not stable in air (*82*). To confirm the efficacy of this technique, a sample was exposed to air immediately following the collection of the GI-XRD pattern in a bag and the XRD pattern was collected a second time using the same parameters. The results of this experiment are shown in Figure 18. The M400 sample exposed to molten LiCl-2wt%Li_2O-0.7wt%Li at 650°C was selected for this test, as it had the highest relative intensity of salt in its initial GI-XRD pattern out of all samples, as evident in Figure 17.

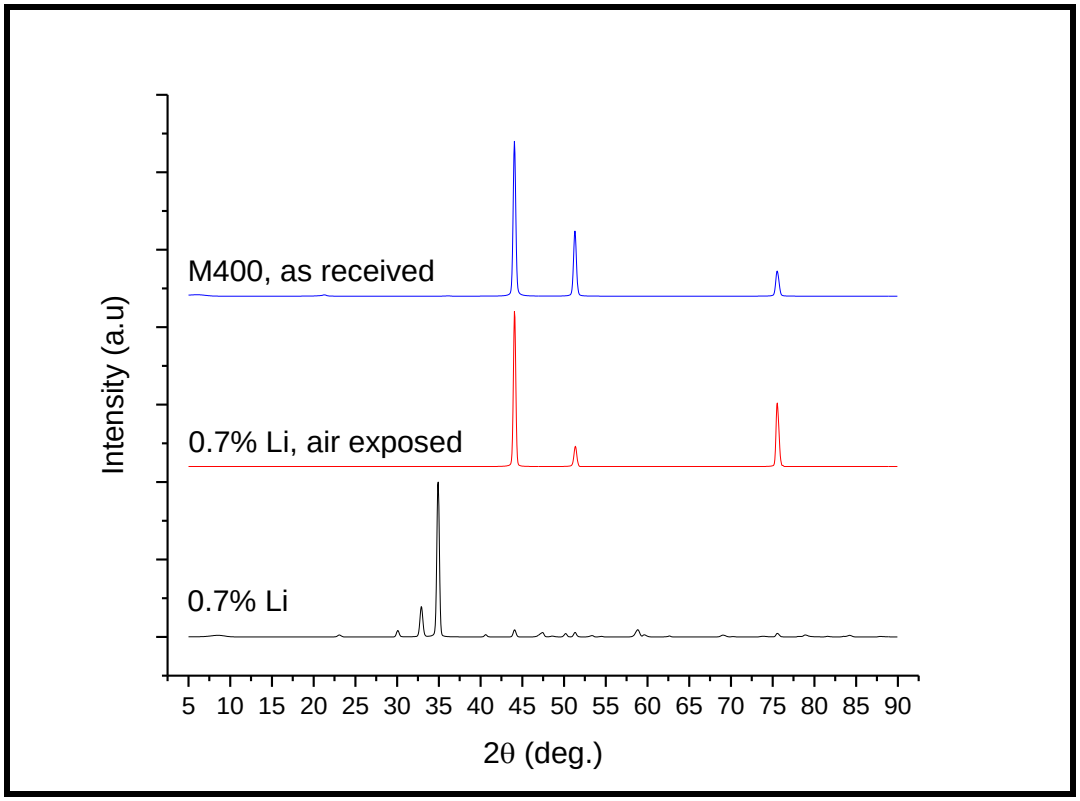


Figure 18: GI-XRD patterns of, from bottom to top, M400 exposed to molten LiCl-2wt%Li_2O-0.7wt%Li at 650°C maintained in an Ar atmosphere in a plastic bag for the duration of the measurement, M400 exposed to molten LiCl-2wt%Li_2O-0.7wt%Li at 650°C as measured in an air filled plastic bag, and as-received M400 measured in a plastic bag. All crystalline phases other than those of M400 are eliminated from the sample surface when exposed to air.

From the data shown in Figure 18, it is evident that the method of using a plastic bag to maintain the as exposed surface of the samples in an inert atmosphere was mostly effective. The presence of LiCl-H_2O indicated that that some contamination of the samples occurred either from storage in the glove box, which is maintained at or below 10ppm H_2O, or from diffusion through the bag during GI-XRD analysis. However, more importantly it demonstrated that the salt phases as well as the surface films on the M400 samples were not stable upon exposure to atmosphere.

4.1.3 Field Emission Scanning Electron Microscopy and Energy Dispersive X-Ray Spectroscopy

Surface morphology of the samples exposed to LiCl-Li_2O-Li at 650°C for 20 hours was characterized using FESEM. Analysis was performed on the exposed samples both before and after rinsing with methanol to remove the residual salt layer, as well as on an as-received sample to serve as a baseline for observation of changes in surface morphology.

Figure 19 shows the FESEM micrographs taken of an as-received M400 sample. The surface was characteristic of mill finished sheet metal. Minor blemishes due to the cold rolling process were observed. These appeared as divots in an otherwise flat surface.

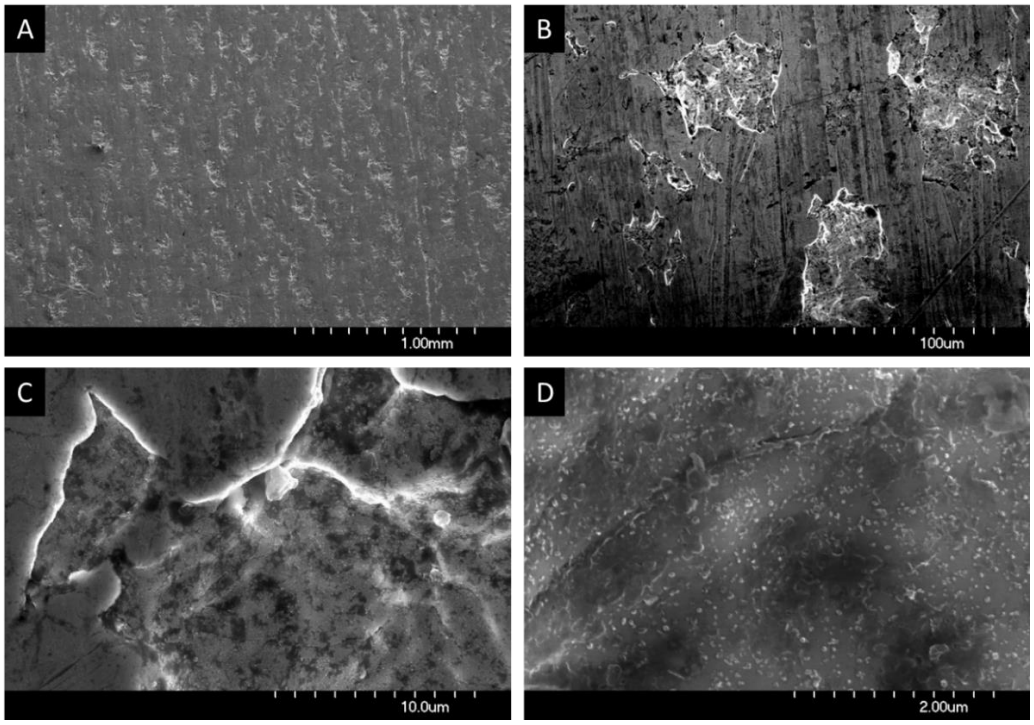


Figure 19: FESEM micrographs of an as-received M400 sample taken at magnifications of (a) 50x, (b) 500x, (c) 5,000x, and (d) 25,000x. The surface is characteristic of mill finished cold rolled sheet metal. Minor surface imperfections are prevalent.

4.1.3.1 FESEM micrographs of non-rinsed samples

Figure 20 shows the FESEM micrographs taken at 50x magnification of unrinsed M400 samples exposed to LiCl-Li_2O with varying concentrations of Li at 650°C. Due to the design of the transfer chamber on the microscope, it was necessary to briefly expose the samples to atmosphere before being inserted into the vacuum chamber of the FESEM. Total exposure to atmosphere was limited to approximately 15 seconds. Consequently, the unrinsed samples adsorbed a small amount of water from the atmosphere due to the highly hygroscopic nature of LiCl and the ambient humidity of the room. The degradation of the surface due to water adsorption from this brief exposure to atmosphere was expected to be minimal. The residual salt layer on the sample surfaces obscured direct observation of the base material. The salt layer on the M400 sample exposed to LiCl-2wt%Li_2O without the addition of Li was heterogeneous

and had obvious cracks throughout. Conversely, the salt layers on the M400 samples exposed LiCl-Li_2O melts containing Li at 650°C were largely homogeneous. This indicates that the inclusion of Li in the molten LiCl-Li_2O solution enhances adhesion of the salt layer to the M400 surface as the samples cool following removal from the furnace.

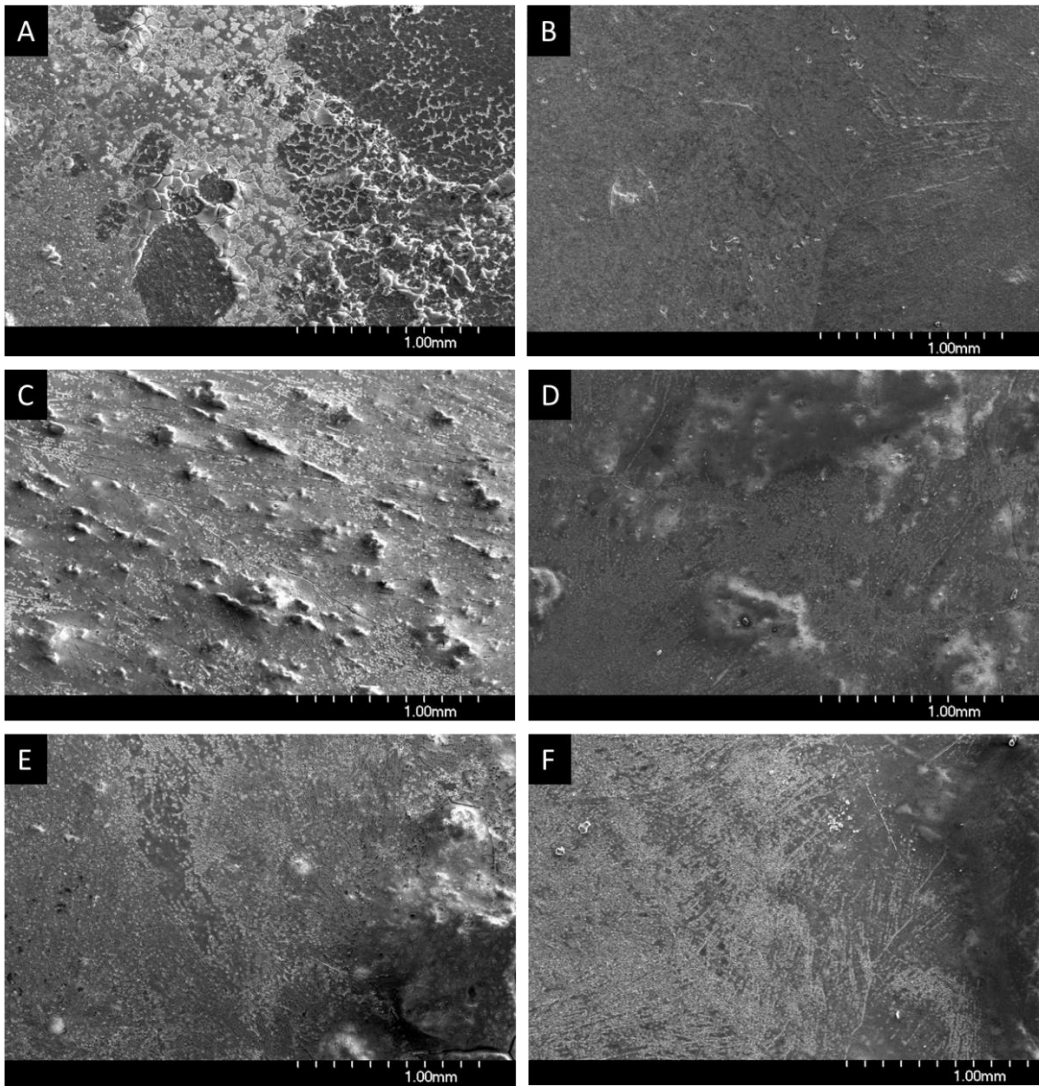


Figure 20: FESEM micrographs taken at 50x magnification for unrinsed M400 samples exposed to LiCl-2wt%Li_2O at 650°C for 20 hours containing (a) 0wt% Li, (b) 0.2wt% Li, (c) 0.4wt% Li, (d) 0.6wt% Li, (e) 0.8wt% Li, (f) 1wt% Li. The salt residue obscured observation of the large scale morphology of the sample surfaces, however cracks in the salt surface were seen that expose small areas of base material.

Figure 21 shows the FESEM micrographs taken at 500x magnification of unrinsed M400 samples exposed to LiCl-Li_2O with varying concentrations of Li at 650°C. The increased adhesion

of the salt layers on the M400 surface formed by LiCl-Li_2O containing Li compared to the layer formed by LiCl-Li_2O in the absence of Li was more apparent at this magnification. The base material was observed in some places as dark patches below the salt layer, although surface morphology of the alloy could not be discerned.

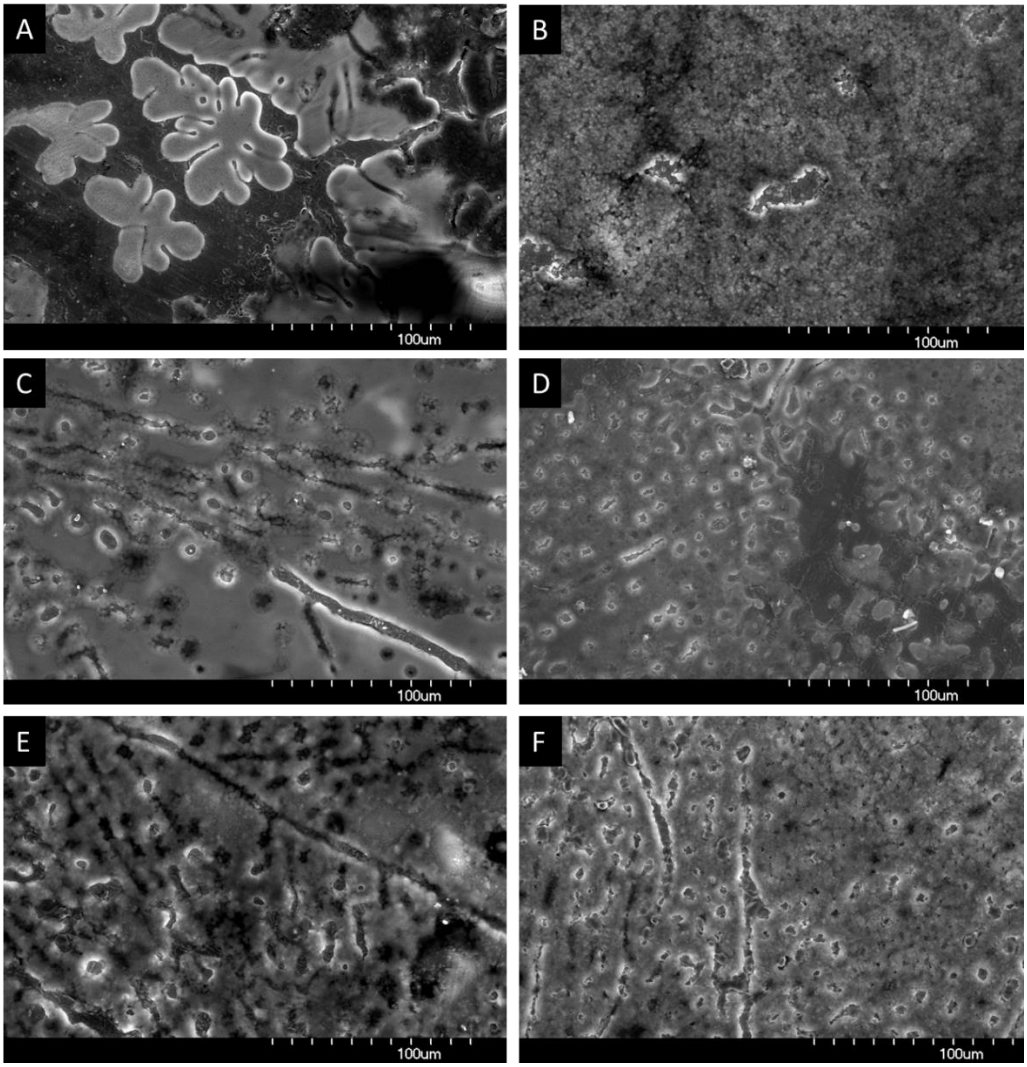


Figure 21: FESEM micrographs taken at 500x magnification for unrinsed M400 samples exposed to LiCl-2wt%Li_2O at 650°C for 20 hours containing (a) no Li, (b) 0.2wt% Li, (c) 0.4wt% Li, (d) 0.6wt% Li, (e) 0.8wt% Li, (f) 1wt% Li. The light areas are residual salt, while the M400 surface was observed in the dark areas. It was apparent that the presence of Li in the salt increased the adhesion of the salt layer to the sample surface.

Figure 22 shows the FESEM micrographs taken at 5,000x magnification of unrinsed M400 samples exposed to LiCl-Li_2O with varying concentrations of Li at 650°C. The alloy surface was seen on the samples exposed to Li concentrations up to 0.6wt%, however, no areas of exposed alloy of considerable size were observed on the samples exposed to LiCl-2wt%Li_2O containing 0.8wt%Li or 1wt%Li. Despite the ability to image the sample surface between cracks in the residual salt layer at this magnification, the area of exposed base alloy was too small to observe enough area to determine what morphology was representative of the sample surfaces.

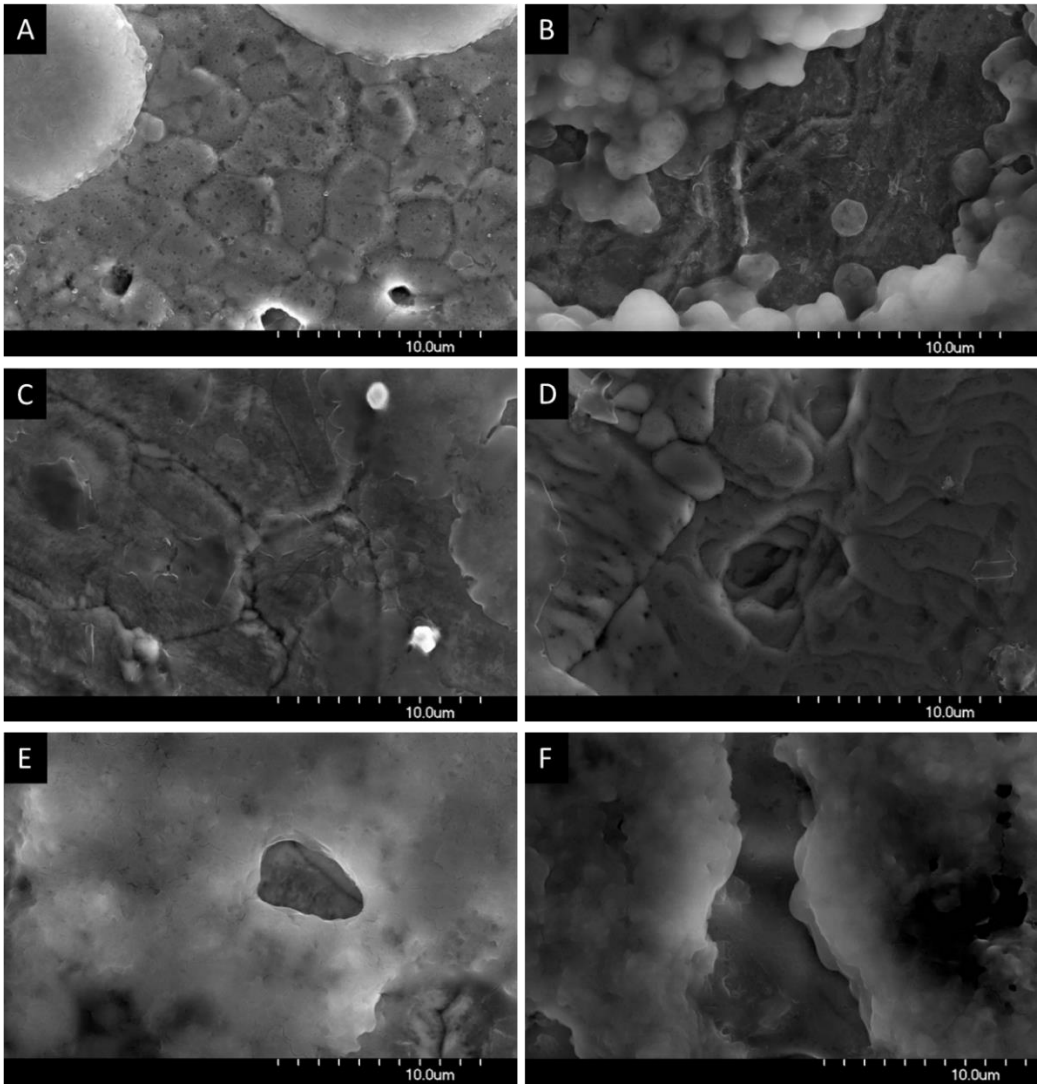


Figure 22: FESEM micrographs taken at 5,000x magnification for unrinsed M400 samples exposed to LiCl-2wt%Li_2O at 650°C for 20 hours containing (a) 0wt% Li, (b) 0.2wt% Li, (c) 0.4wt% Li, (d) 0.6wt% Li, (e) 0.8wt% Li, (f) 1wt% Li. Surface morphology was observed for samples exposed to LiCl-Li_2O containing up to 0.6wt%Li, however surface morphology for samples exposed to melts containing 0.8wt%Li and 1wt%Li was not observable.

Figure 23 shows the FESEM micrographs taken at 25,000x magnification of unrinsed M400 samples exposed to LiCl-Li_2O with varying concentrations of Li at 650°C. Individual surface features were observed at this magnification. These micrographs were obtained primarily to provide context of the EDS analysis presented in Figure 24.

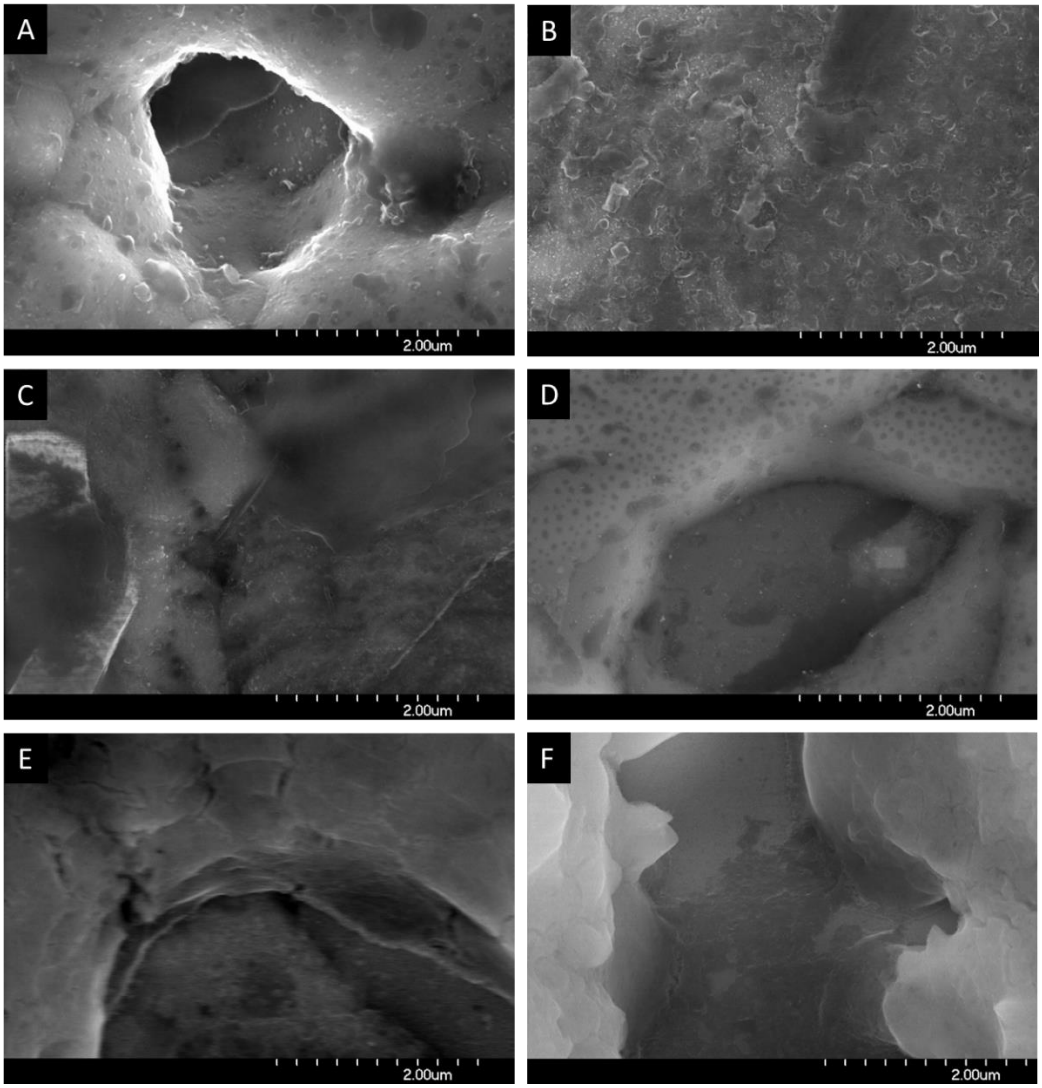


Figure 23: FESEM micrographs taken at 25000x magnification for unrinsed M400 samples exposed to LiCl-2wt%Li_2O at 650°C for 20 hours containing (a) 0wt% Li, (b) 0.2wt% Li, (c) 0.4wt% Li, (d) 0.6wt% Li, (e) 0.8wt% Li, (f) 1wt% Li. EDS spectra were obtained at these locations.

The results of the EDS analysis of the alloying elements present at the locations shown in Figure 23 are shown in Figure 24. At the accelerating voltage of 20kV used for this data collection, penetration depth is approximately on the order of micrometers. The composition detected by EDS was consistent with the composition of as-received M400 given in Table 2. Minor deviations of the Ni to Cu ratio were for samples exposed to 0.6wt%Li and 1wt%Li. No Mn was detected on the M400 sample exposed to LiCl-2wt%Li containing no Li. Oxygen and chlorine

were detected on all unrinsed sample surfaces. The presence of O and Cl was expected on unrinsed samples due to the residual LiCl-Li_2O salt layer. Both O and Cl were omitted from Figure 24 to allow for comparison to the as-received alloy composition.

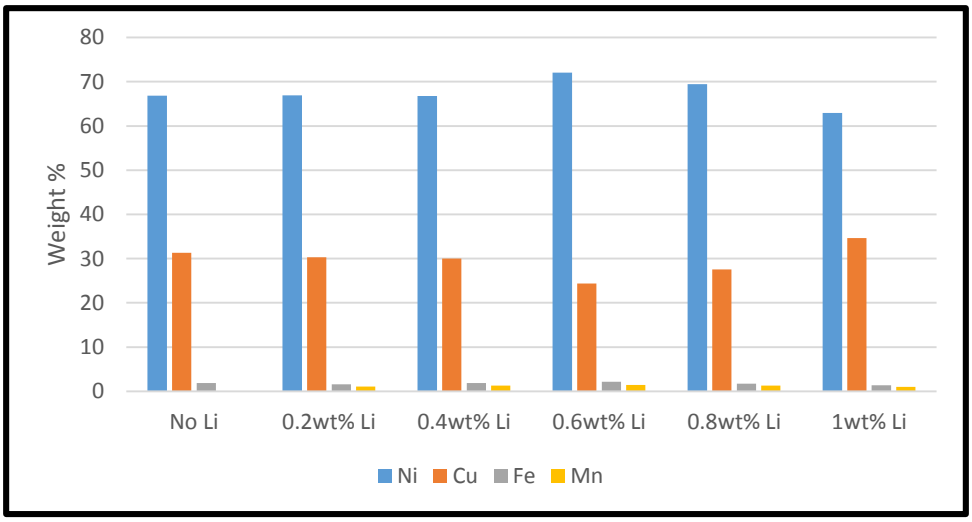


Figure 24: EDS analysis of alloying elements unrinsed M400 samples exposed to LiCl-2wt%Li_2O at 650°C for 20 hours taken at 25,000x magnification for the locations shown in Figure 24 on areas of exposed base alloy.

4.1.3.2 FESEM micrographs of methanol rinsed samples

The M400 samples rinsed with methanol prior to XPS analysis were also analyzed by FESEM to detect changes in surface morphology that were unobservable with the residual salt layer still present. Figure 25 shows the FESEM micrographs taken at 50x magnification of methanol rinsed M400 samples exposed to LiCl-Li_2O with varying concentrations of Li at 650°C. At this magnification, the sample surfaces appeared to be largely unaffected by the exposure to high temperature LiC-2wt%Li_2O containing Li up to 0.8wt% and subsequent methanol rinsing. However, the M400 sample exposed to LiCl-2wt%Li_2O-1wt%Li and rinsed with methanol shows obvious deterioration. The divots in surface finish characteristic of the as-received cold rolled and annealed sample were no longer visible, indicating a substantial removal of material from this sample's surface during the methanol rinse.

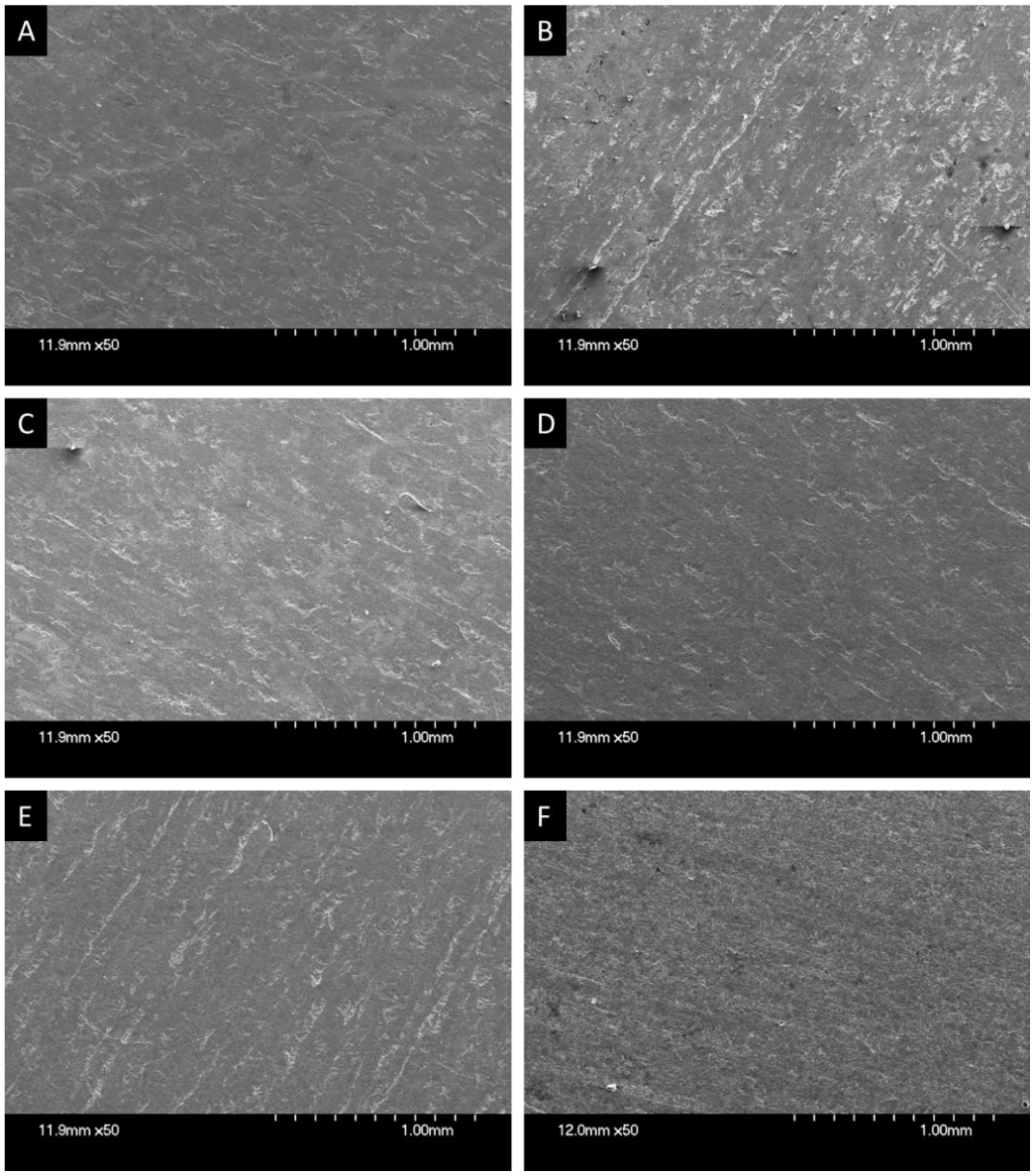


Figure 25: FESEM micrographs taken at 50x magnification for methanol rinsed M400 samples exposed to LiCl-2wt%Li_2O at 650°C for 20 hours containing (a) 0wt% Li, (b) 0.2wt% Li, (c) 0.4wt% Li, (d) 0.6wt% Li, (e) 0.8wt% Li, (f) 1wt% Li. Compared to the as-received micrograph taken at similar magnification, shown in Figure 19A, minimal surface degradation is observed at this magnification for all samples except the M400 sample exposed to LiCl-2wt%Li_2O-1wt%Li.

Figure 26 shows the FESEM micrographs taken at 500x magnification of methanol rinsed M400 samples exposed to LiCl-Li_2O with varying concentrations of Li at 650°C. At this magnification, a trend towards increasing surface damage with increasing Li content was observed on M400 samples exposed to LiCl-2wt%Li_2O containing above 0.2wt%Li. The onset of

this change in surface morphology correlates to the apparent solubility limit of 0.3wt%Li in LiCl-Li_2O, indicating that the effect was a result of excess undissolved Li in the system that is present as Li_8 nanoclusters (*59, 61, 73*). The degradation has the appearance of intergranular corrosion. However, the vigorous reaction between methanol and LiCl-Li_2O containing Li precludes confirmation of this method of corrosive attack to this system.

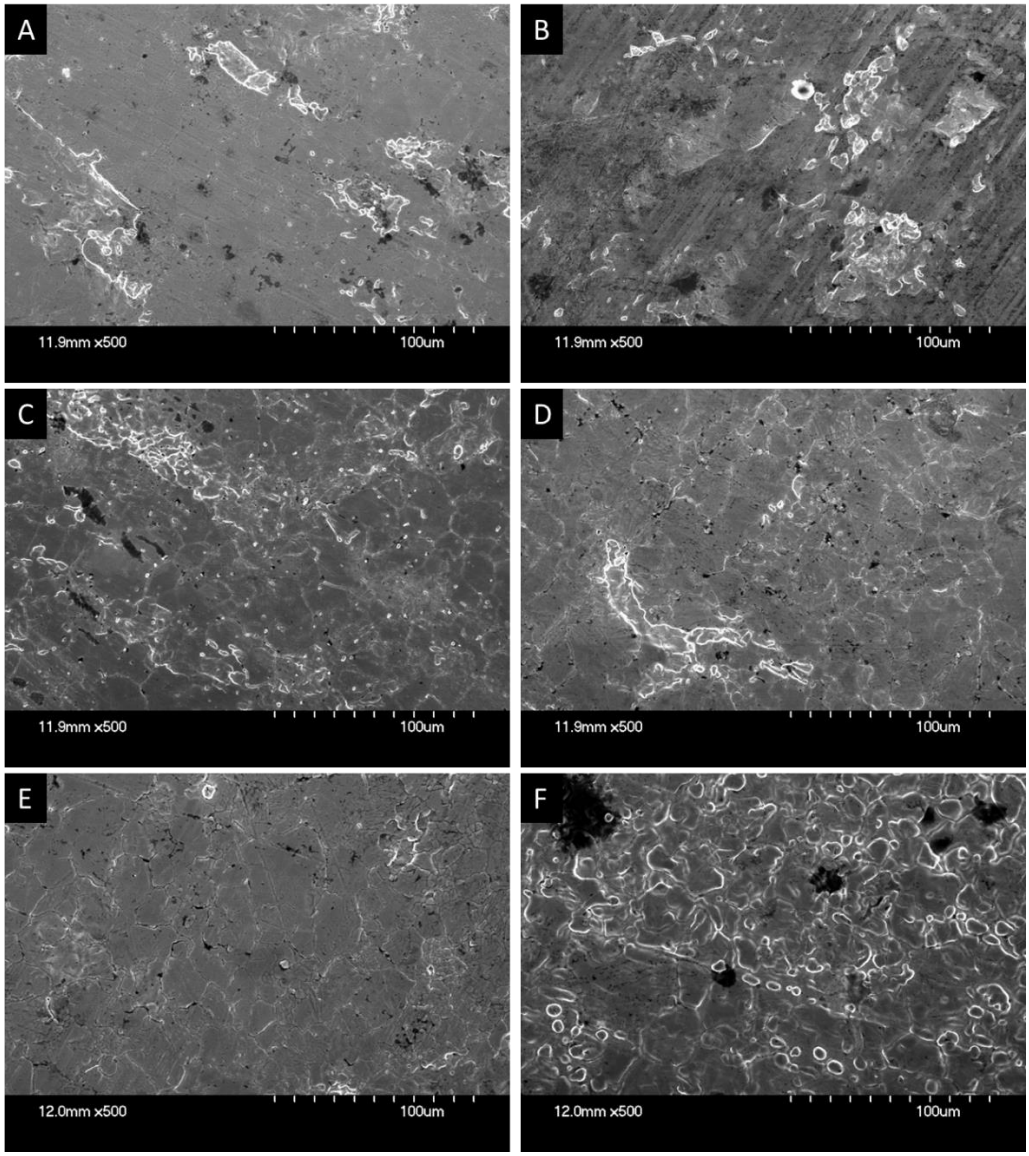


Figure 26: FESEM micrographs taken at 500x magnification for methanol rinsed M400 samples exposed to LiCl-2wt%Li_2O at 650°C for 20 hours containing (a) 0wt% Li, (b) 0.2wt% Li, (c) 0.4wt% Li, (d) 0.6wt% Li, (e) 0.8wt% Li, (f) 1wt% Li. Increased surface damage was proportional to increased Li content beyond the solubility limit of Li in LiCl-Li_2O of 0.3wt%Li.

Figure 27 shows the FESEM micrographs taken at 5,000x magnification of methanol rinsed M400 samples exposed to LiCl-Li_2O with varying concentrations of Li at 650°C. Further morphological detail was seen on the samples exposed to molten LiCl-Li_2O with Li contents above the solubility limit. Increased damage with increasing Li content was apparent.

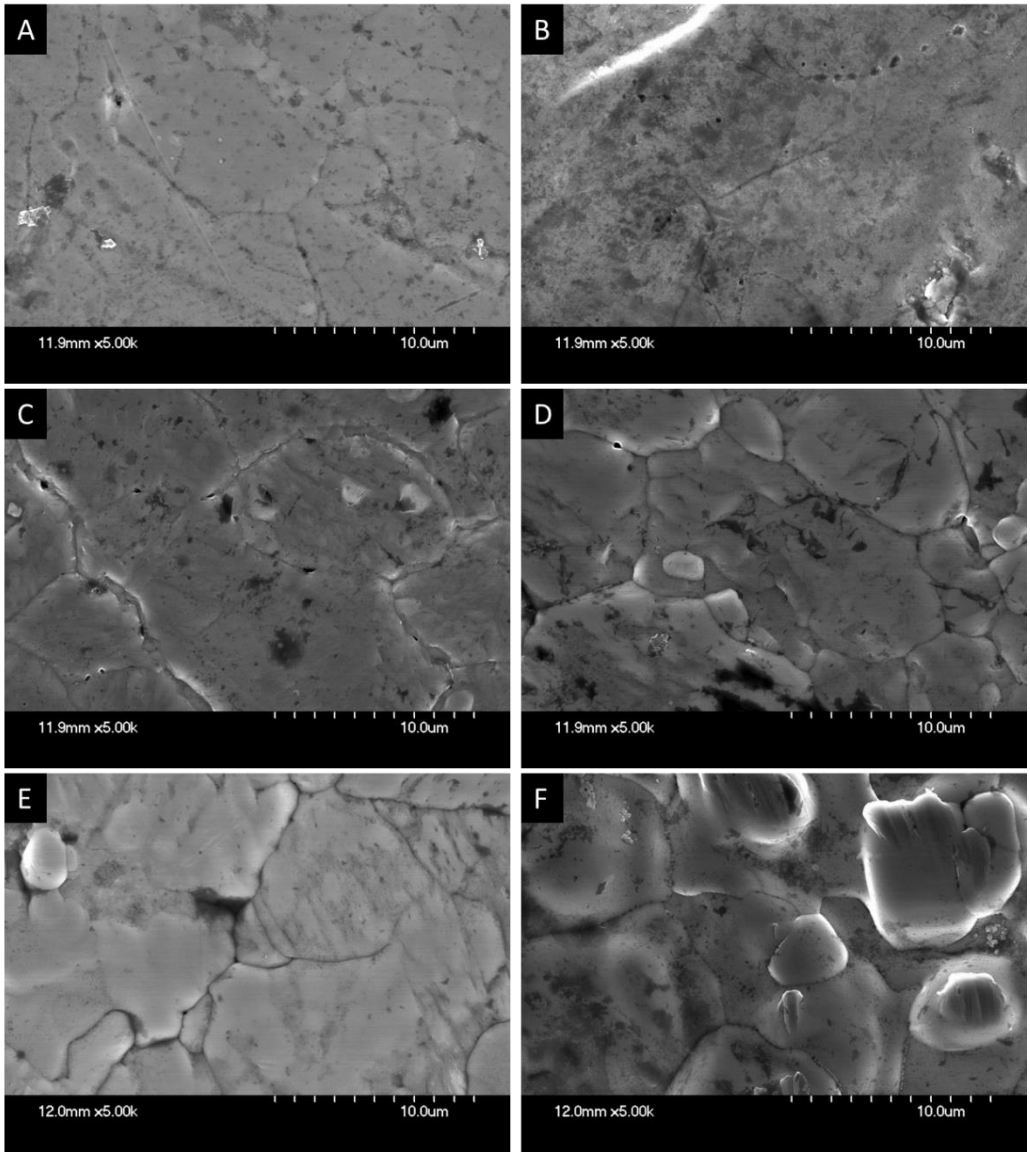


Figure 27: FESEM micrographs taken at 5000x magnification for methanol rinsed M400 samples exposed to LiCl-2wt%Li_2O at 650°C for 20 hours containing (a) 0wt% Li, (b) 0.2wt% Li, (c) 0.4wt% Li, (d) 0.6wt% Li, (e) 0.8wt% Li, (f) 1wt% Li. Increased damage with increasing Li content was apparent.

Figure 28 shows the FESEM micrographs taken at 25,000x magnification of methanol rinsed M400 samples exposed to LiCl-Li_2O with varying concentrations of Li at 650°C. Grain boundary relief can be seen on the samples exposed to molten LiCl-Li_2O with Li content above the solubility limit. The EDS results presented in Figure 29 were obtained at these locations.

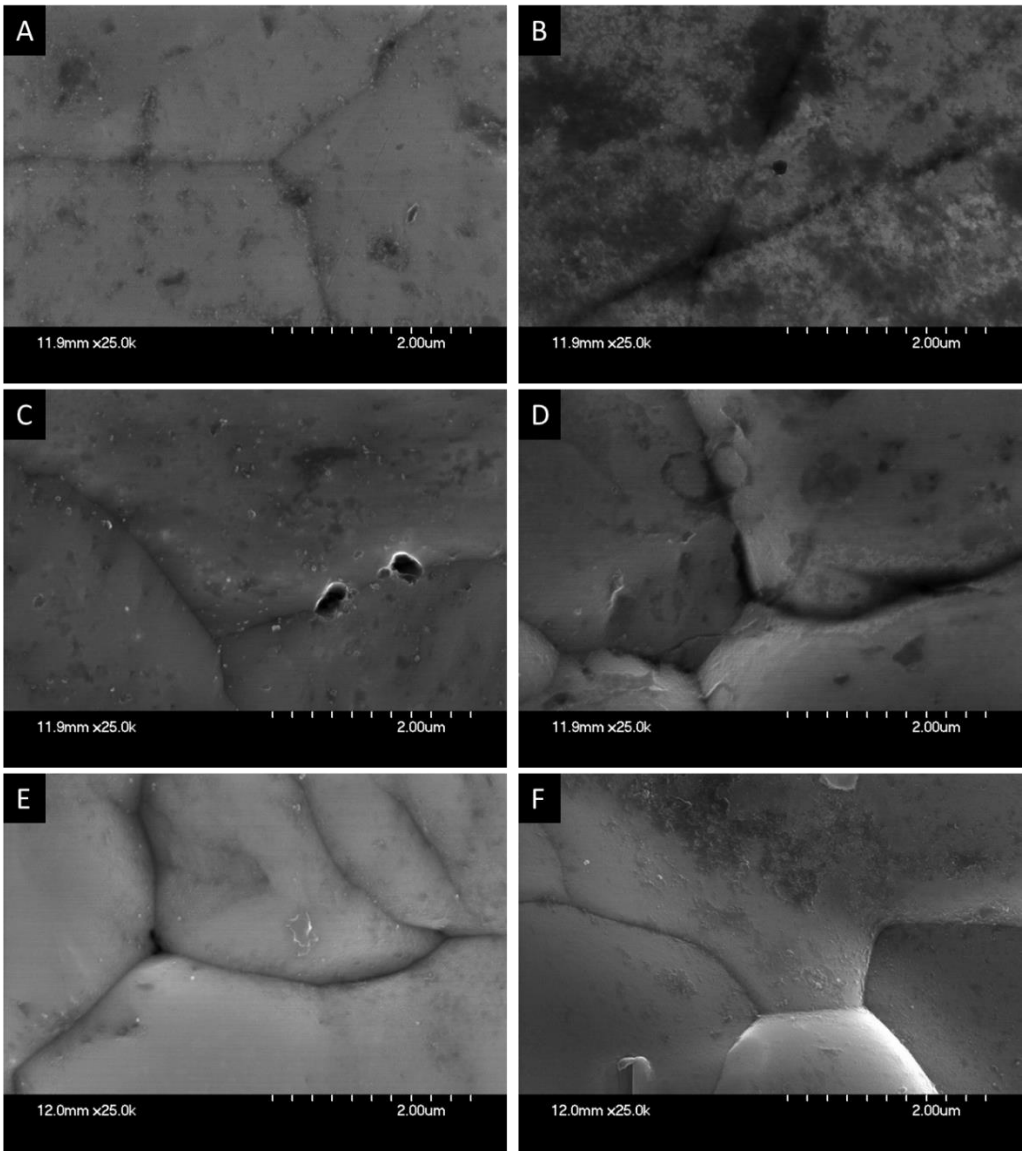


Figure 28: FESEM micrographs taken at 25000x magnification for methanol rinsed M400 samples exposed to LiCl-2wt%Li_2O at 650°C for 20 hours containing (a) 0wt% Li, (b) 0.2wt% Li, (c) 0.4wt% Li, (d) 0.6wt% Li, (e) 0.8wt% Li, (f) 1wt% Li. EDS analysis was performed at these locations.

Figure 29 presents the EDS analysis performed on M400 samples exposed to LiCl-Li_2O-Li at 650°C for 20 hours and rinsed with methanol. The M400 sample exposed to LiCl-2wt%Li_2O-1wt%Li shows depletion of Ni compared to the nominal composition for M400. This depletion of Ni may be due the formation of the proposed Li-Ni-O surface film and its subsequent dissolution during the methanol rinsing procedure. All other samples are typical of the composition of

M400, given in Table 2. No Mn was observed on the sample exposed to LiCl-2wt%Li_2O in the absence of Li. The alloy composition was relatively unaffected by exposure to LiCl-Li_2O with Li contents of up to 0.8wt%Li.

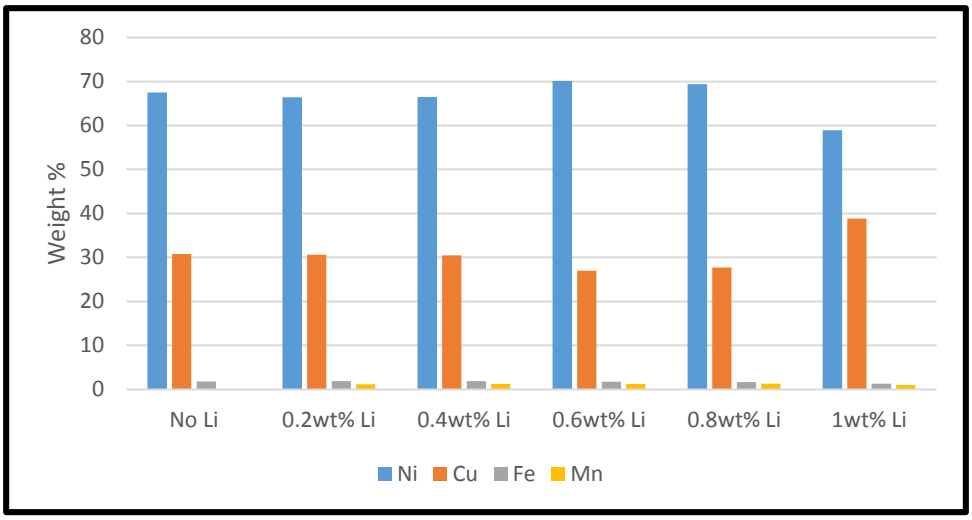


Figure 29: EDS analysis of methanol rinsed M400 samples exposed to LiCl-2wt%Li_2O at 650°C for 20 hours, taken at 25000x magnification for the locations shown in Figure 28 on areas of exposed base alloy. Composition is consistent with as-received M400 for all samples exposed to LiCl-2wt%Li_2O containing up to 0.8wt%Li, however the sample exposed to 1%wt%Li was relatively depleted in Ni.

4.1.4 Micro-Vickers Hardness Testing and Optical Microscopy

Micro-Vickers hardness testing was performed to detect changes in surface mechanical properties of the M400 samples following exposure to molten solutions of LiCl-Li_2O-Li. The samples were rinsed in methanol prior to indentation to remove residual salt from the surface to prevent misrepresentation of the measured hardness. Images of the sample surface following indentation were gathered at 200x magnification and are shown in Figure 30. The indentation diameter was measured to calculate the Vickers hardness. The Images collected allowed for observation of surface morphology of the methanol rinsed samples.

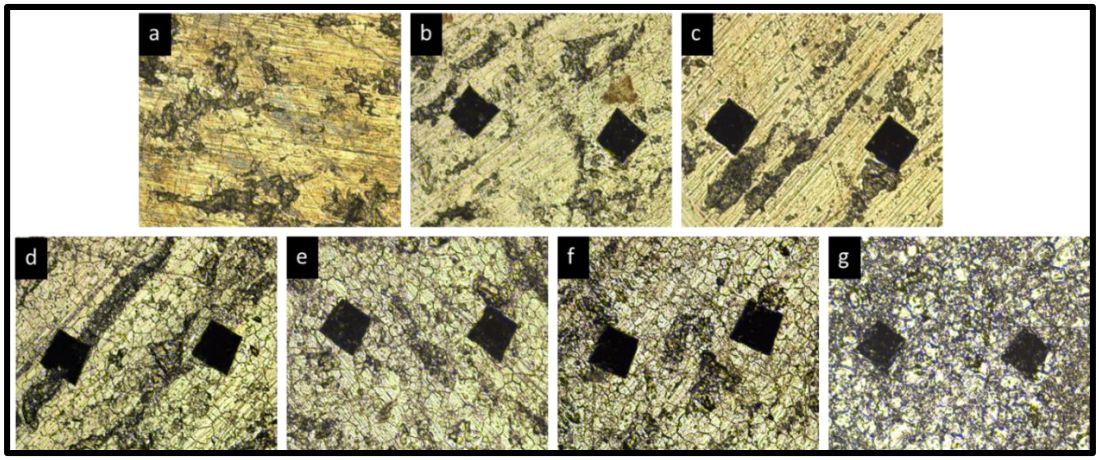


Figure 30: Optical micrographs of M400 samples taken at 200x magnification. (a) As-received M400, (b) M400 exposed to LiCl-2wt%Li_2O, (c) M400 exposed to LiCl-2wt%Li_2O-0.2%Li, (d) M400 exposed to LiCl-2wt%Li_2O-0.4%Li, (e) M400 exposed to LiCl-2wt%Li_2O-0.6%Li, (f) M400 exposed to LiCl-2wt%Li_2O-0.8%Li, (g) M400 exposed to LiCl-2wt%Li_2O-1%Li. The images of the exposed samples show indentations representative of those used to determine micro-Vickers hardness. The solubility limit of Li in LiCl-Li_2O is around 0.3wt% Li, which corresponds to the onset of the apparent intergranular corrosion seen on these samples. Increased surface deterioration strongly correlates with increased Li content.

The surface morphology shown in Figure 30 indicates a strong trend towards increased degradation with increased metallic Li content. The observed degradation has the appearance of intergranular corrosion similar to the observations made via FESEM in section 4.1.3. However, it is noted it was not possible to observe the surface prior to rinsing the samples with methanol. it is possible that the surface degradation observed in Figure 30 is due to the reaction that may occur during the rinsing procedure for samples exposed to salt melts containing Li.

Figure 31 shows the results of the micro-Vickers hardness tests for M400 samples exposed to LiCl-Li_2O with varying concentrations of Li at 650°C. Softening of the alloy occurred due to the exposure to LiCl-Li_2O at 650°C for 20 hours, and further softening occurred when Li was present; however, there was no observable trend correlating hardness to Li content in the molten LiCl-Li_2O solution. The change in hardness can likely be attributed to annealing of the base alloy due to the sustained exposure to high temperature.

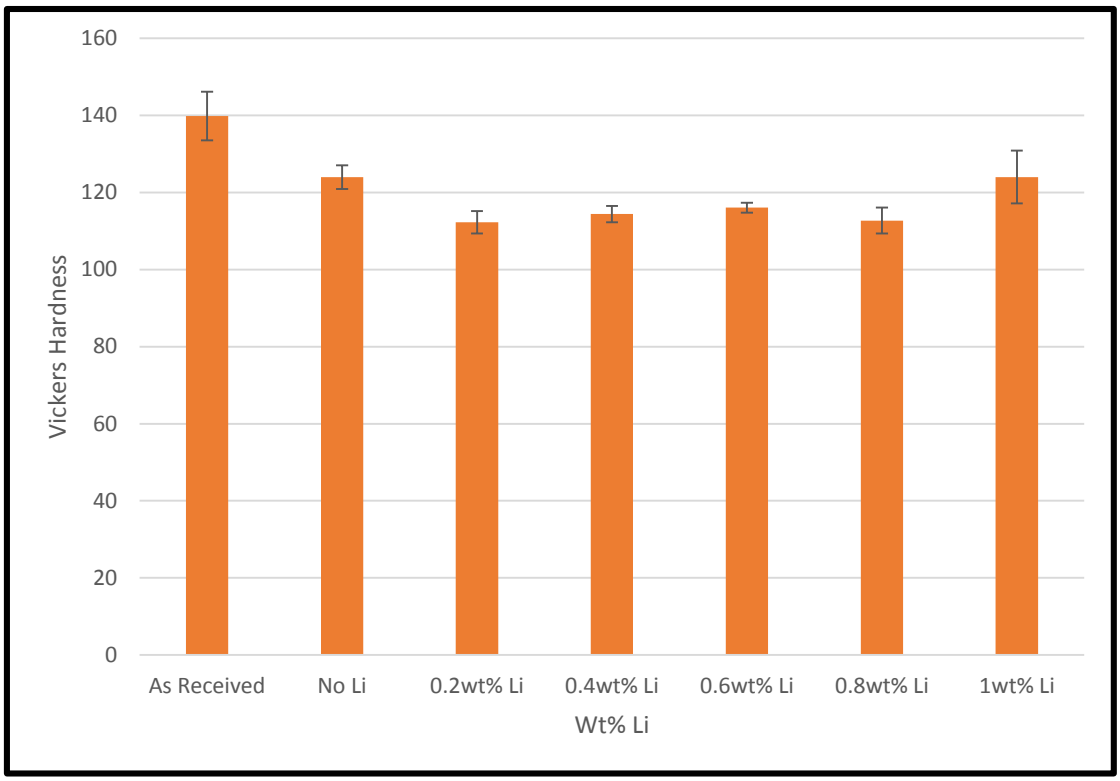


Figure 31: Micro-Vickers hardness of as-received M400 and M400 samples exposed to molten LiCl-2wt%Li_2O with various concentrations of metallic Li. The reported values are an average of 10 individual measurements on each sample, and the error bars show the standard deviation for these measurements. Softening due to the 20 hour exposure to molten LiCl-Li_2O-Li was observed for all samples relative to the as-received sample, however, the change in hardness was independent of the concentration of Li in the LiCl-L_2O system.

4.1.5 Raman Spectroscopy

Raman spectroscopy was performed to characterize the Raman active modes of any surface films formed on M400, if present, following exposure to molten LiCl-Li_2O-Li solutions. The Raman spectra presented in Figure 32 were collected in the glove box via a fiber probe to maintain the integrity of the hygroscopic samples. This technique avoided the possibility of atmospheric contamination and allowed for examination of the samples in the as-exposed state. As demonstrated in section 4.1.6, the surface films formed on M400 were on the order of 10nm. The thin surface films and the micron-level interaction volume of Raman spectroscopy caused

the vibrational and rotational modes of the surface to not be detectable. This can be seen by the essentially flat Raman spectra obtained from the surface of every sample.

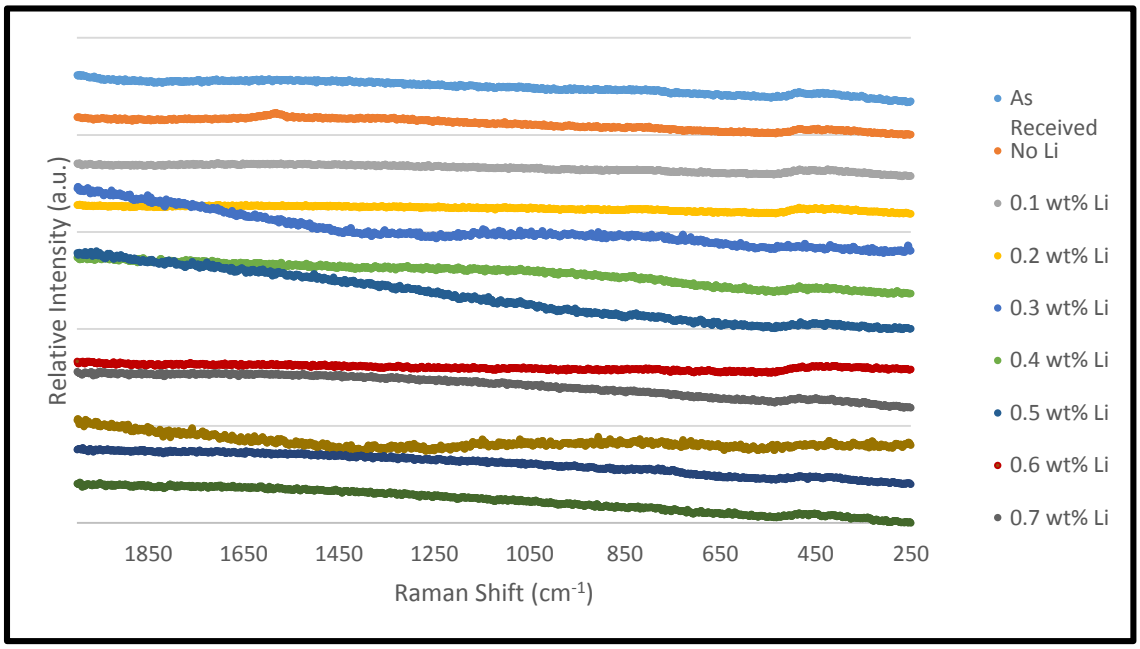


Figure 32: Raman spectra of M400 samples in the as-received state and following exposure to molten LiCl-2wt% Li_2O-Li solutions, collected via fiber optic probe in an inert atmosphere. No Raman active modes were detected on the surface of any sample. This indicates that the thickness of the surface films formed on M400 were on the order of nanometers due to the micron-scale interaction depth of Raman spectroscopy.

4.1.6 X-Ray Photoelectron Spectroscopy

M400 samples exposed to LiCl-2wt%Li_2O-Li at 650°C for 20 hours were rinsed with methanol and characterized using XPS. The methanol rinse precluded the use of XPS to determine the chemical nature of the surface films formed in the salt melt, as the film would be affected by methanol. However, this rinse was necessary to remove the bulk salt layer from the sample surfaces and allow for characterization of the alloy surface as unrinsed samples showed only the presence of salt. The necessity of the methanol rinse limited the usefulness of XPS analysis to quantification of the atomic composition of the sample surfaces and qualitative estimation of surface film thickness. Survey scans obtained from the surface of M400 samples

exposed to LiCl-2wt%Li_2O-Li were collected immediately following the methanol rinse, as well as after 2 minutes of Ar^+ sputtering. XPS was used to characterize M400 samples exposed to LiCl-2wt%Li_2O at 650°C at increments of 0.2wt%Li to observe general trends in surface alterations.

The XPS survey scans collected for M400 samples exposed to LiCl-Li_2O-Li at 650°C for 20 hours and rinsed with methanol are shown in Figure 33. All samples display prominent oxygen peaks, which is suspected to be the result of oxidation from the methanol rinse. Mn and Fe were not present in detectable quantities on the unsputtered surfaces. The relative ratios of Ni and Cu detected by XPS for both unsputtered and sputtered samples are given in Figure 35.

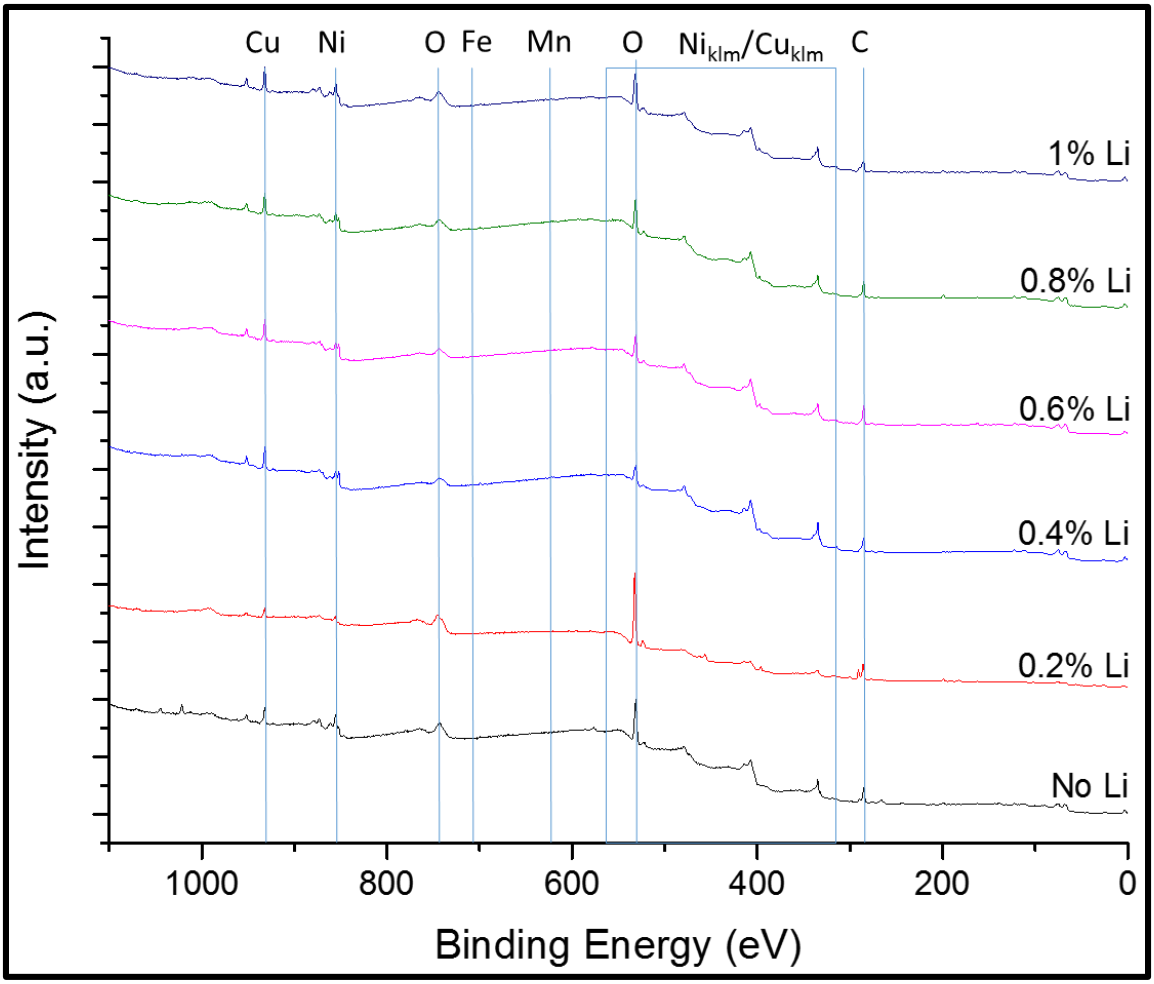


Figure 33: XPS survey scans obtained from the surface of M400 samples exposed to LiCl-2wt%Li_2O-Li at 650°C for 20 hours and subsequently rinsed with methanol. Significant O_{1s} and O_{KLL} signal is observed at 532 eV and 743eV, respectively, which is attributed to the methanol rinse.

The samples whose spectra are shown in Figure 33 were subjected to 2 minutes of Ar^+ sputtering and characterized using XPS. The resultant spectra are shown in Figure 34. This sputtering treatment was sufficient to remove the oxygen and adventitious carbon from all samples with the exception of the sample exposed to LiCl-2wt%Li_2O-0.2wt%Li.

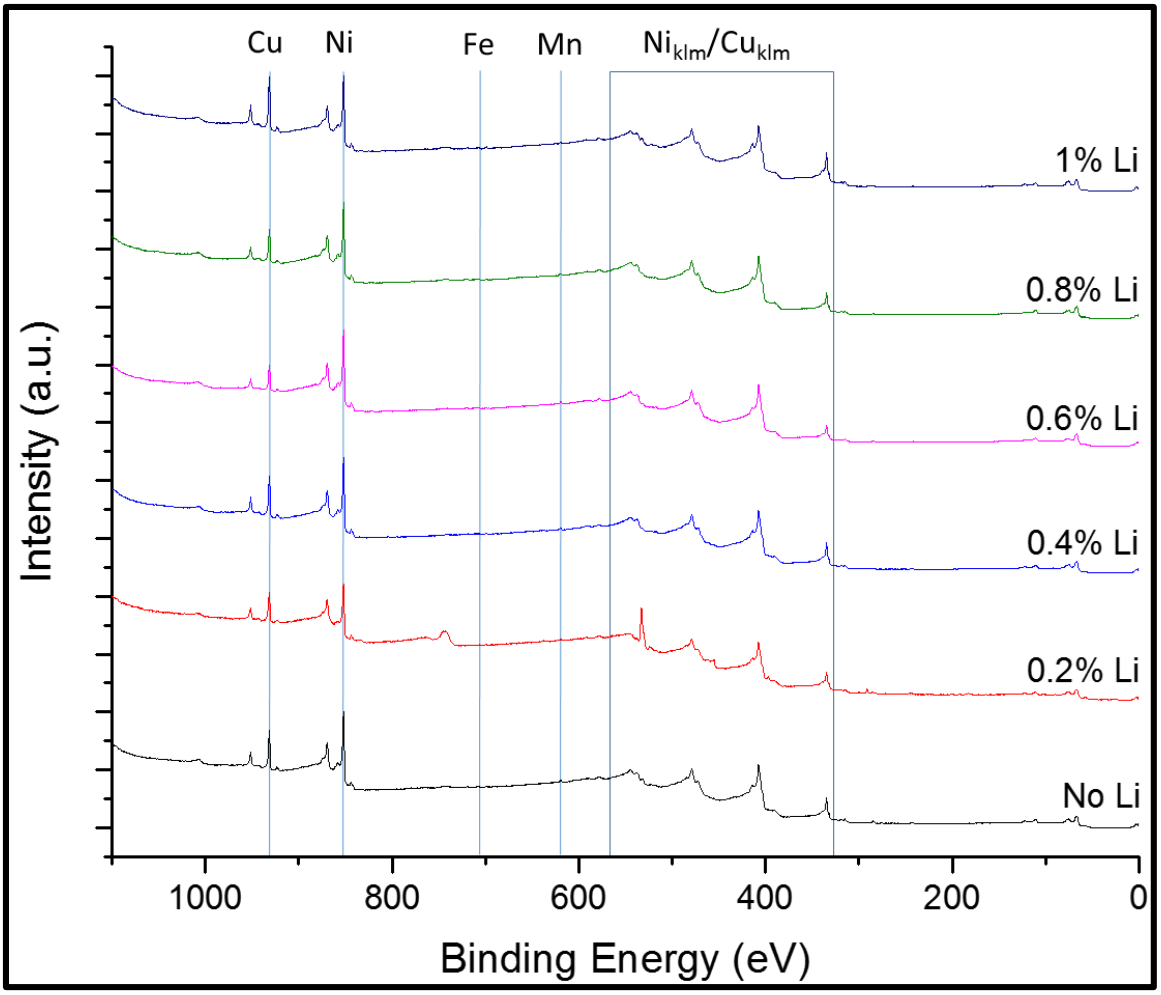


Figure 34: XPS survey scans obtained from the surface of M400 samples exposed to LiCl-2wt%Li_2O with varying concentrations of Li at 650°C for 20 hours, rinsed with methanol, and subjected to 2 minutes of Ar^+ sputtering. Oxygen and adventitious carbon are below the detection level on all samples other than the sample exposed to LiCl-2wt%Li_2O-0.2wt%Li at 650°C for 20 hours. Ni and Cu were both observed to be predominantly in the metallic state.

The relative atomic ratios of Ni and Cu following 2 minutes of sputtering were determined from the spectra shown in Figure 34 in a similar manner to that previously discussed. Mn and Fe were not included in the analysis of surface composition due to their very low signal intensity. It is expected that these low signals could lead to large errors in the quantification of their contribution to the surface composition. It is important to note that detectable levels of signal corresponding to the Mn 2p and Fe 2p lines were observed on all of the samples following sputtering. This indicated that the surface observed after sputtering was

characteristic of the bulk alloy. As previously discussed, the current density of the Ar^+ sputtering employed was sufficient to remove 14nm of Ta_2O_5 in this amount of time, indicating that the thickness of the oxide layers formed on M400 were on the order of 14nm.

The relative atomic ratios of Ni and Cu following 2 minutes of sputtering were determined from the spectra shown in Figure 34 in a similar manner to that previously discussed. Mn and Fe were not included in the analysis of surface composition due to their very low signal intensity. It is expected that these low signals could lead to large errors in the quantification of their contribution to the surface composition. The ratio of Ni to Cu, given in weight percent, for each sample was calculated using the relative atomic percentages of Ni and Cu on the sample surfaces before and after sputtering, to allow for comparison of the composition of the exposed samples to the composition to the as-received alloy. The results of these analyses are shown in Figure 35.

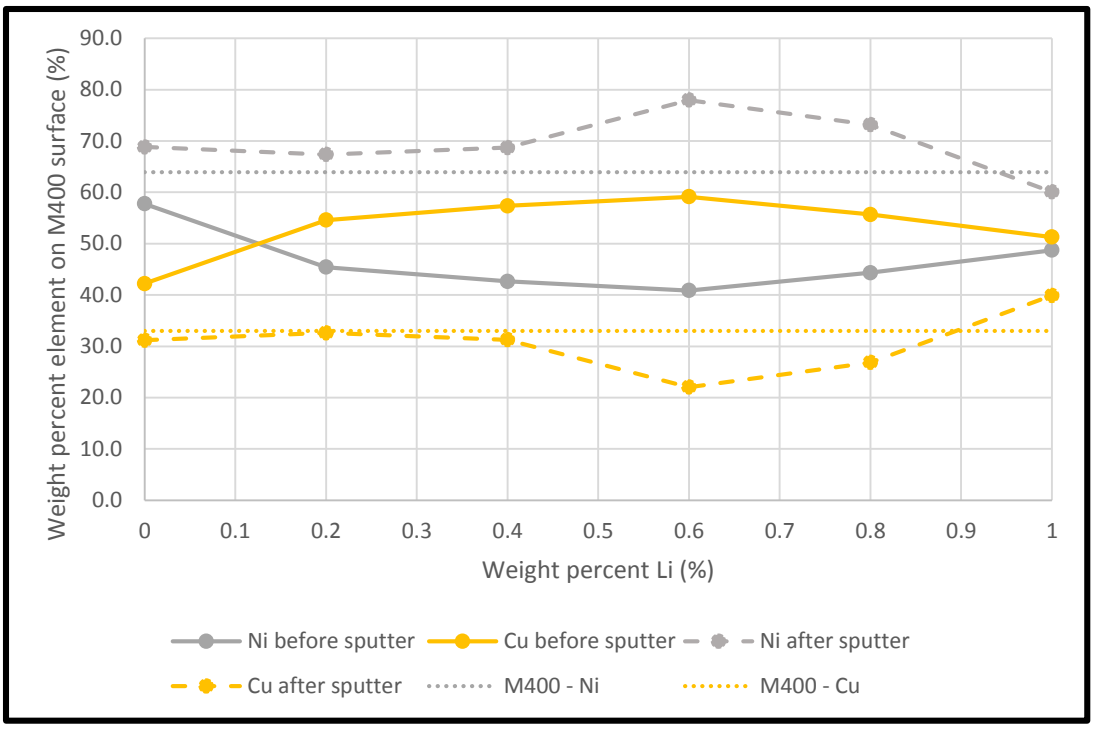


Figure 35: Relative weight percentages obtained by XPS analysis of Ni and Cu before and after 2 minutes of Ar^+ sputtering on the surface of M400 samples exposed to LiCl-2wt%Li_2O-Li at 650°C for 650 hours after rinsing in methanol. The composition of the base alloy is shown by horizontal dotted lines for reference. The unsputtered sample surfaces show enrichment in Cu and depletion of Ni, while the sample surfaces after 2 minutes of Ar^+ sputtering are enriched in Ni.

The surfaces of the unsputtered M400 samples were depleted in Ni relative to the as-received alloy composition of 63.9wt%Ni, while the sputtered surfaces were relatively enriched in Ni. Interpretation of the unsputtered surface was complicated by the methanol rinsing procedure performed prior to XPS analysis, as the methanol rinse had an unknown effect on the chemical state of the surface. The sputtered surface was largely characteristic of the base metal, however, the deviations seen at 0.6wt%Li, 0.8wt%Li and 1wt%Li from nominal M400 composition are in agreement with similar deviations observed with EDS analysis, as shown in Section 4.1.3.

4.1.7 Inductively Coupled Plasma Optical Emission Spectrometry

ICP-OES was used to quantify the elemental composition of the alloying elements present in the cooled salt ingot following exposure of the M400 samples to molten LiCl-Li_2O-Li solutions. The raw data was processed to give the total mass of each alloying element found in the salt following each experiment at 0.1wt%Li intervals. The masses calculated in this manner are given in Figure 36.

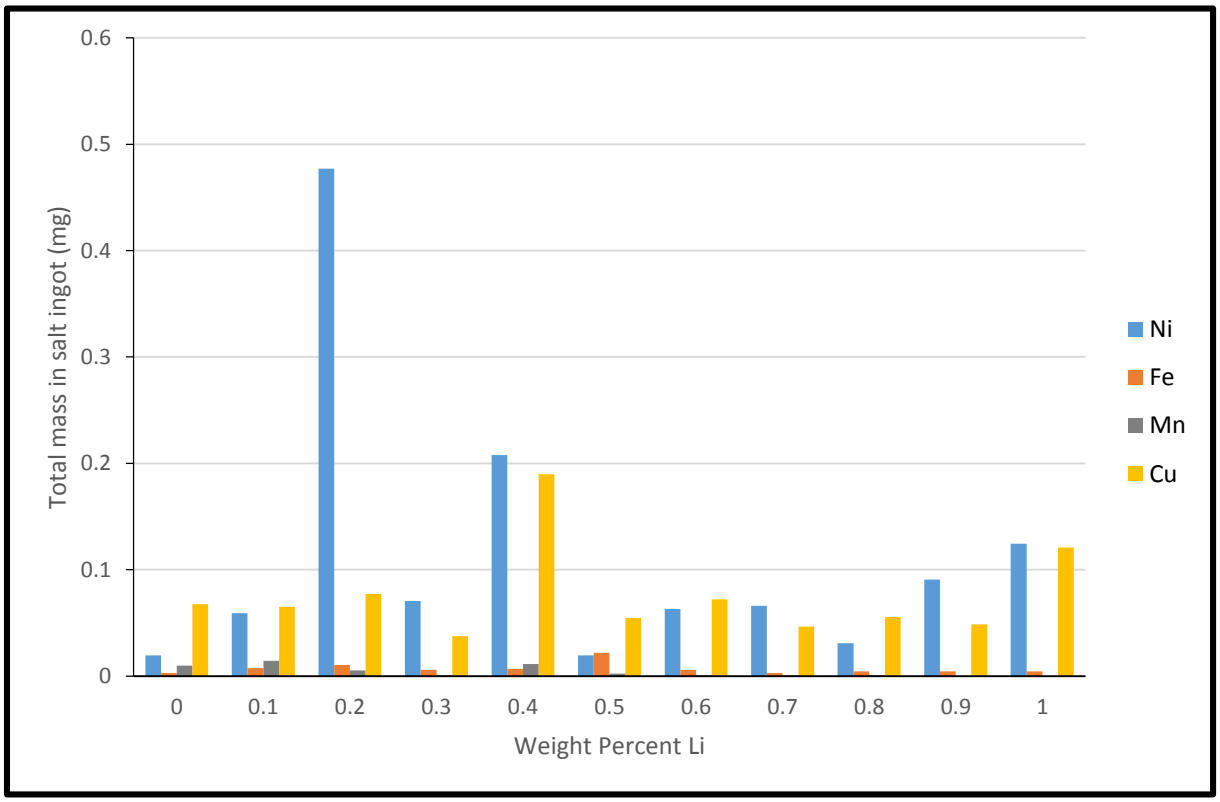


Figure 36: Mass of each alloying element in the cooled salt ingots for the M400 samples exposed to LiCl-2wt%Li_2O performed at 0.1wt%Li increments at 650°C for 20 hours. The large variation in the mass of Ni detected is largely due to the use of Ni crucibles. The concentrations of the other alloying elements detected approached the lower limit of the detection capabilities of ICP-OES.

Similar results were obtained for the experiments repeated at 0.2wt%Li intervals. Figure 37 shows the mass of alloying elements observed at 0.2wt%Li intervals averaged for two

experiments, with error bars indicating the high and low values observed for individual experiments.

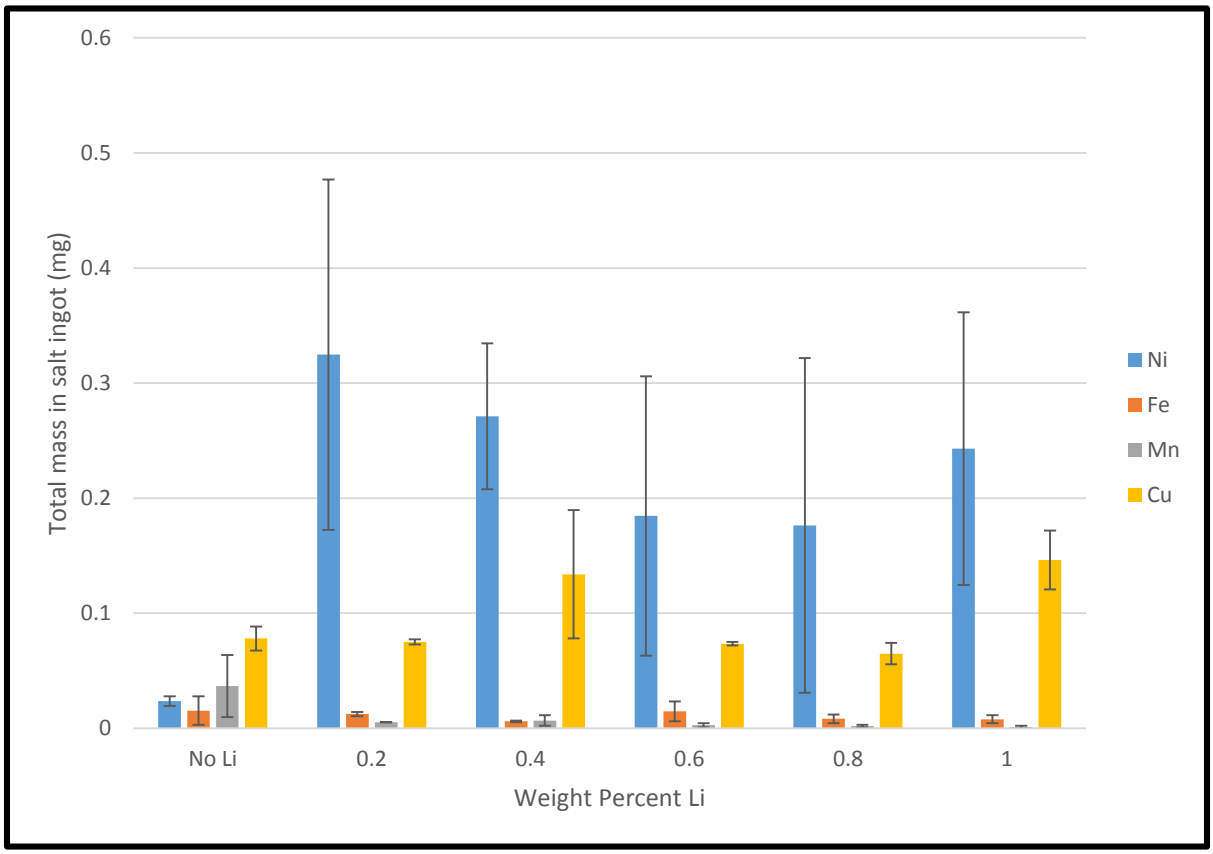


Figure 37: Average total mass of each alloying element detected by ICP-OES in the cooled salt ingot upon completion of the exposure testing of M400 in LiCl-2wt%Li_2O-Li for two experiments at each 0.2wt% Li interval. The error bars give the results of individual experiments. The total mass of the alloying elements other than Ni were roughly constant, while the Ni concentrations were highly variable in the presence of Li. The high variation of Ni with addition of metallic Li was likely a result of the use of Ni crucibles for the exposure tests. The consistently low concentration of the other alloying elements in the salt ingot over the range of Li concentrations studied indicates that M400 was highly resistant to corrosion in the molten LiCl-Li_2O-Li system.

It is noted that both the M400 samples and the Ni crucibles used for containment of the molten LiCl-Li_2O-Li solutions contributed to the Ni content of the salt ingot. Consequently, the quantity of Ni detected by ICP-OES was the result of corrosion of both the M400 samples as well as the Ni crucible. The low concentration of Ni in the salt ingot following the exposure tests of M400 in LiCl-2wt%Li_2O in the absence of Li indicate that Ni is stable in the LiCl-Li_2O system when

metallic Li is not present in the melt. It is likely that the high concentrations and variation of Ni in the Li containing melts was a result of the instability of the Ni crucible in the LiCl-Li_2O-Li system, resulting in its dissolution into the molten salt. Previous studies conducted in our laboratory have seen similar as well as greater dissolution rates of Ni into molten LiCl-Li_2O in the presence of Li (*97)*. The detection of small (mg) quantities of Ni in LiCl-Li_2O-Li in the absence of M400 samples indicates that the majority of the Ni detected in the salt ingot in this study is due to degradation of the crucible. However, all Ni was assumed to come from the M400 samples for the corrosion rate calculations below, as it was not possible to quantitatively differentiate between the sources of the Ni in the salt ingot. This assumption resulted in a conservative (higher) estimate of the corrosion rate calculated from this data.

It can be further observed in Figure 37 that the dissolution rate of the other alloying elements (Cu, Fe and Mn) in molten solutions containing metallic Li remained roughly constant with changes in Li concentration up to 1wt%Li. Alternatively, a high relative rate of Mn dissolution was observed when M400 was exposed to LiCl-2wt%Li_2O in the absence of Li. This observation correlated to the depletion of Mn on this sample's surface seen in the EDS analysis shown in Figures 24 and 29. The change in the relative dissolution rates of the alloying components indicates a shift in the chemical reaction mechanisms driving degradation of M400 in LiCl-Li_2O melts in the presence and absence of metallic Li.

The total mass of alloying elements in the salt ingot was used to calculate the corrosion rate of M400 in LiCl-2wt%Li_2O at 650°C for each 0.2wt%Li interval, according to the methodology outlined below:

The corrosion rate was calculated from the ICP-OES data in the following manner. The mass loss rate (m_i) of each alloying element (i) was calculated by multiplying the concentration

(C_i) by the 0.75L volume (V) of water used to dissolve the salt and dividing by the exposure period (t) of 20 hours.

$$\frac{C_i\left(\frac{mg}{L}\right) \cdot V(L)}{t(h)} = m_i(mg/h) \qquad \textbf{Equation 5}$$

The total mass loss rate (M_T) for the M400 samples was calculated by summing the mass loss rates of the individual alloying elements.

$$M_T\left(\frac{mg}{h}\right) = \sum_i^n m_i(mg/h) \qquad \textbf{Equation 6}$$

The corrosion rate (CR) was then calculated based on the total mass loss rate, the density of M400 (ρ), and the total surface area of the exposed samples (SA).

$$CR\left(\frac{mm}{year}\right) = \frac{M_T\left(\frac{mg}{h}\right) \cdot \frac{8760h}{year}}{\rho\left(\frac{g}{cm^3}\right) \cdot SA(cm^2) \cdot \frac{1cm}{10mm} \cdot \frac{1000mg}{g}} \qquad \textbf{Equation 7}$$

This was simplified to the following formula, where 87.6 is a unit conversion constant.

$$CR\left(\frac{mm}{year}\right) = 87.6\left(\frac{g \cdot h \cdot mm}{mg \cdot year \cdot cm}\right) \cdot \frac{M_T\left(\frac{mg}{h}\right)}{\rho\left(\frac{g}{cm^3}\right) \cdot SA(cm^2)} \qquad \textbf{Equation 8}$$

An example of this calculation is shown in Table 6 below:

Table 6: Example calculation of the corrosion rate observed by ICP-OES for M400 exposed to LiCl-2wt%Li_2O without the presence of Li at 650°C for 750 hours. The formulae derived above were used for this calculations

Ni (mg/L)	Fe (mg/L)	Mn (mg/L)	Cu (mg/L)	m_{Ni} (mg/h)	m_{Fe} (mg/h)	m_{Mn} (mg/h)	m_{Cu} (mg/h)	M_T (mg/h)	CR (mm/y)
0.037	0.037	0.085	0.118	0.00139	0.00139	0.00319	0.00443	0.0104	0.007

The above analysis assumes the density of M400 to be 8.8 g/cm^2, that corrosion occurs uniformly, and that the total exposed surface area for the two samples is 7.2cm^2, as calculated in section 2.4. As stated previously, all Ni was assumed to come from the M400 samples, which

resulted in calculated corrosion rates higher than the true value. The results of this analysis are presented in Figure 38.

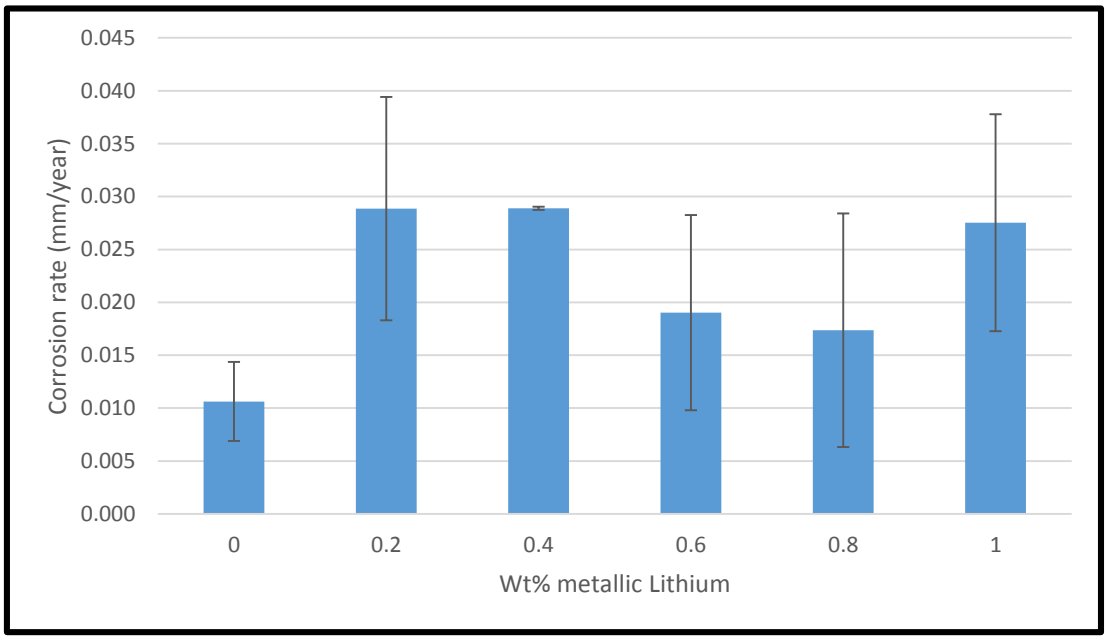


Figure 38: Average corrosion rate for M400 exposed to LiCl-2wt%Li_2O-Li for various concentrations of Li. The calculated average corrosion rate was excellent for all of the experiments performed, despite the large variation in the quantity of Ni detected via ICP-OES.

The corrosion rate of the sample exposed to LiCl-Li_2O containing no Li was calculated to be 0.011±0.004mm/yr. Addition of Li led to an increased corrosion rate, which is in agreement with the optical microscopy and micro-Vickers hardness testing presented in section 4.1.4, however, the corrosion rate did not correlate to the concentration of Li. The change in corrosion rate with the addition of Li was further indication a possible shift in corrosion mechanism between melts containing metallic Li and those not containing metallic Li.

The highest corrosion rate was found to be expressed by the sample exposed to LiCl-Li_2O-0.2wt%Li and was calculated to be 0.029±0.010mm/yr. This corrosion rate is considered to be excellent, and shows that M400 is highly resistant to corrosion in the molten LiCl-Li_2O-Li environment over a broad range of Li metal concentrations (*94*). The stability of M400 over the

range of melt compositions studied indicates that this alloy would perform well when exposed to the process conditions encountered during the electrolytic reduction of UNF. The corrosion performance of M400 in the molten LiCl-Li_2O-Li system at 650°C is superior to the majority of materials that have been studied in this system by this lab group (*97*).

4.2 Electrochemical Measurements

To elucidate the mechanisms responsible for degradation of M400 the OCP was measured between Cu and Ni in LiCl-2wt%Li_2O containing no Li, 0.2wt%Li, and 1wt%Li at 650°C. Ni and Cu were selected as they are the primary alloying components of M400. All measurements of the OCP between Cu and Ni use the potential of the Ni wire as the reference voltage. To verify the design of the Li-Bi reference electrode described in Chapter 3, the OCP of Ni and Cu wires were measured against the Li-Bi reference electrode in LiCl-2wt%Li-0.3wt%Li at 650°C.

The OCP between Cu and Ni was measured in LiCl-2wt%Li_2O-Li at 650°C to observe changes in the electrochemical potentials of these metals as a function of Li content in the molten LiCl-Li_2O electrolyte and to determine their relative ordering in the galvanic series. The results of the measurement of the OCP between Cu and Ni in LiCl-2wt%Li_2O containing no Li, 0.2wt%Li, and 1wt% Li are shown in Figure 39. The potential of Cu was consistently more noble than that of Ni; however, the magnitude of the difference in potential varied between 6.7mV and 63.3mV. While no correlation between electrochemical potential and Li content in the melt was observed, the observation that Cu is more noble than Ni regardless of solution chemistry is important for understanding the mechanisms driving corrosion of M400 in the complex LiCl-Li_2O-Li system. The implications of this observation are discussed in Section 4.3 below.

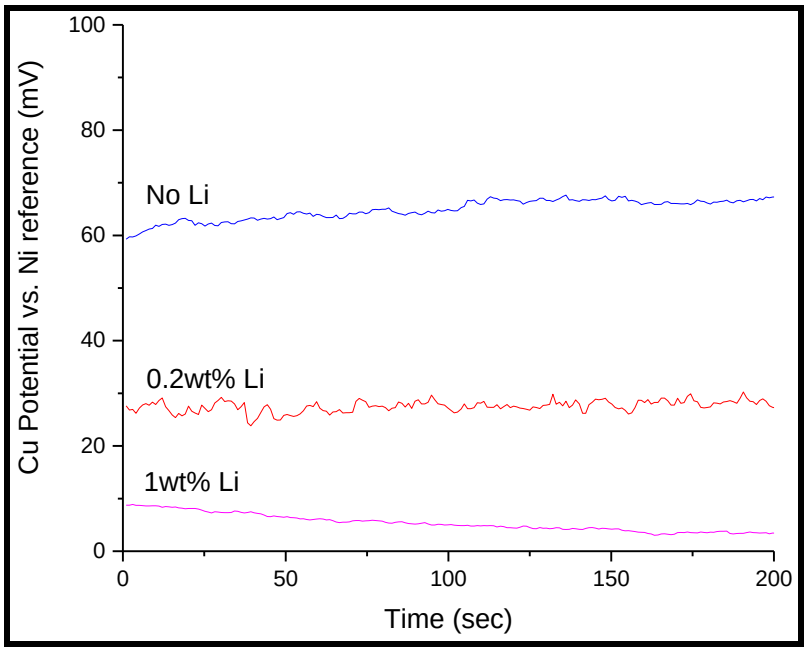


Figure 39: Compilation of the measured OCP between Cu and Ni in LiCl-2wt%Li_2O containing no Li, 0.2wt%Li, and 1wt%Li for 200 seconds. There was no trend observed correlating the OCP measured between Cu and Ni as a function of Li content in the electrolyte. However, Cu was observed to be more noble than Ni in all experiments.

To verify the results observed in Figure 39 in a rigorous electrochemical manner, the OCP of Cu and Ni were measured independently against the Li-Bi reference electrode designed in Chapter 3 and against each other in LiCl-2wt%Li_2O-0.3wt%Li at 650°C. The difference between the OCP of Cu and Ni measured independently against the Li-Bi reference electrode was calculated to compare to the direct measurement of the OCP between Cu and Ni. The results of this experiment are shown in Figure 40.

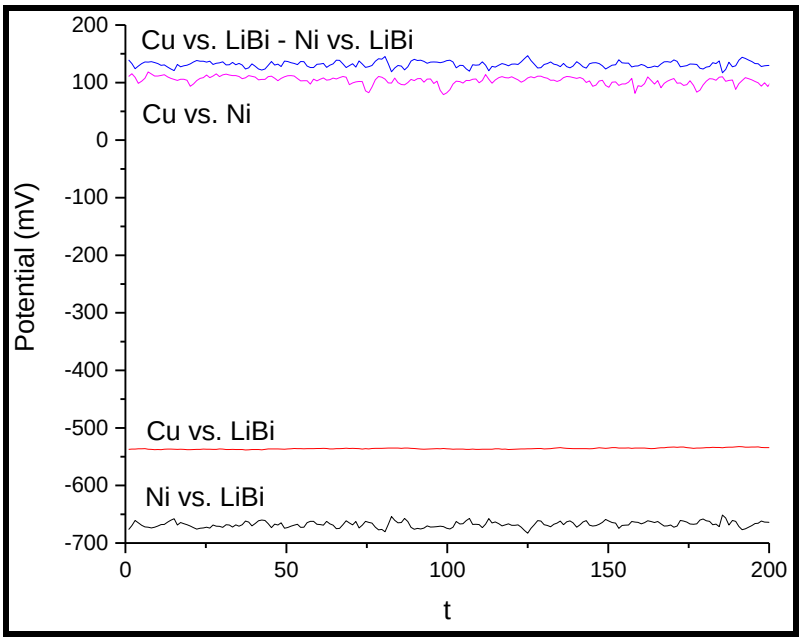


Figure 40: Plot of the OCP for Cu and Ni measured independently against the Li-Bi reference electrode and each other in LiCl-2wt%Li_2O-0.3wt%Li at 650°C for 200 seconds. Very good agreement between the independent measurements of the Cu and Ni potentials against Li-Bi and each other was observed.

If a reference couple exists in thermodynamic equilibrium with a given electrolyte, the difference between two electrochemical couples should not be affected by measurement against the reference couple. Therefore, the difference between the OCP of Cu and Ni measured independently against the Li-Bi reference electrode and each other observed in Figure 40 is a measurement of the deviation from the ideal behavior. This difference is defined as the work function of the system, and is caused by a number of factors, including potential drop across the graphite tube and diffusion of Li through the wall for this system. The variance of the work function observed over time is a measurement of the stability of the Li-Bi reference electrode. Figure 41 shows the histogram for the work function of the Li-Bi reference electrode, calculated from the data presented in Figure 40. The work function was seen to approximately follow a normal distribution, with a mean value of 27.4mV and a standard deviation of 8.0mV. This low and stable potential proves the validity of the Li-Bi reference electrode designed for this study. The stability of the work function of less than 10mV observed for the Li-Bi referenced electrode

is similar to that of well-established reference electrodes used in aqueous electrochemistry, and therefore represents a significant development for electrochemistry in the LiCl-Li_2O-Li system.

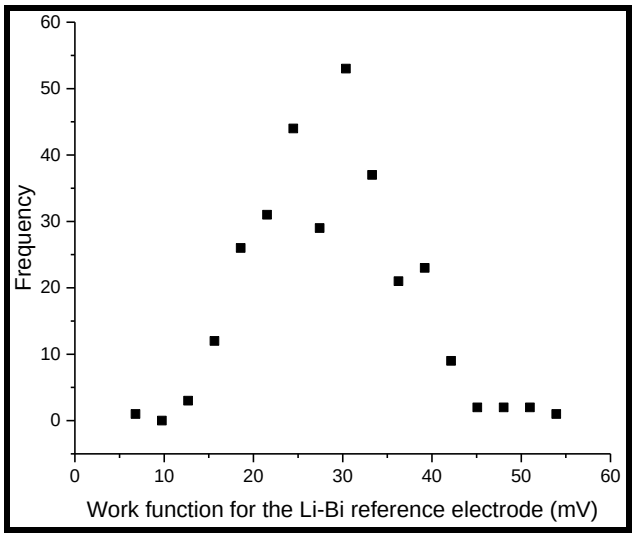


Figure 41: Histogram of the distribution of the work function observed for the Li-Bi reference electrode, calculated from the difference between the OCP of Cu and Ni measured independently against the Li-Bi reference electrode and each other in LiCl-2wt%Li_2O-0.3wt% Li, observed in Figure 40. The mean work function was 27.4mV and the standard deviation was 8.0mV. This demonstrated the stability and validity of the Li-Bi reference electrode designed in Chapter 3.

To ensure the repeatability of the electrode design, a second Li-Bi reference electrode was constructed in a similar manner to the first electrode. Two independent experiments were conducted to measure the OCP of Ni and Cu independently against the Li-Bi reference electrode immersed in LiCl-2wt%Li_2O-0.3wt%Li at 650°C. The results of these experiments are shown in Figure 42. The observed values for the OCP measured for Cu and Ni independently against the Li-Bi reference electrodes differed by approximately 70mV between the two Li-Bi reference electrodes. This difference could be partially attributed to variations in composition of the Li-Bi alloy between the two electrodes, as small errors in the mass of Li and Bi used to form the Li-Bi alloy cause large fluctuations in relative atomic concentration due to the large difference in atomic masses between Li and Bi. However, the difference in potential between the two electrodes was larger than expected theoretically. This may be due to differences in the work

function between the two electrodes. Despite the variation in work function between Li-Bi reference electrodes, the calculated potential between Cu and Ni only differed by approximately 10mV. This indicated that both Li-Bi electrodes maintained self-consistent potentials despite differing in work functions.

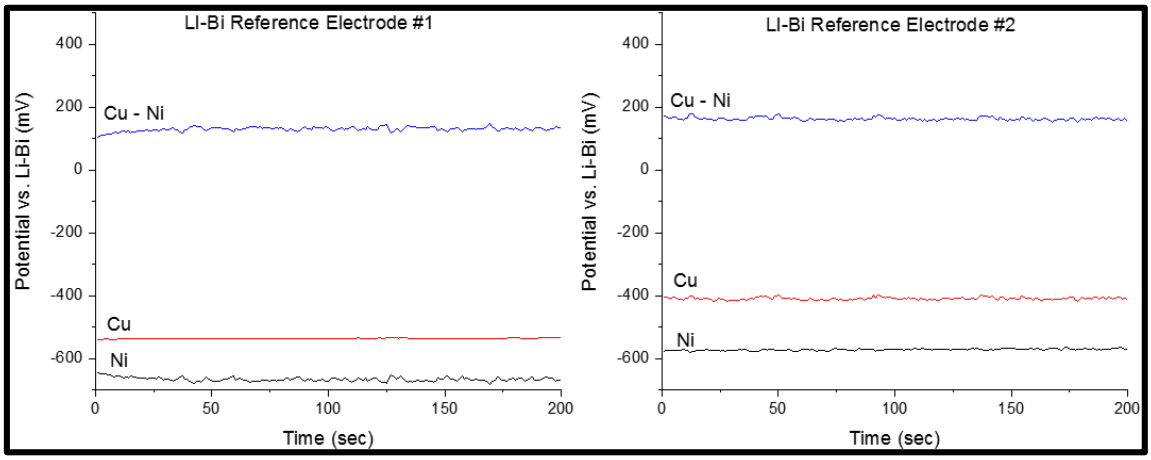


Figure 42: Comparison of the OCP measured for Cu and Ni wires vs. two different Li-Bi reference electrodes in LiCl-2wt%Li_2O-0.3wt%Li at 650°C for 200 seconds. The offset between Li-Bi reference electrode potentials is approximately 70mV, which is attributed to variations in the composition of the Li-Bi alloy between the two electrodes. The difference between the Cu/Ni potential measured by both Li-Bi electrodes differed by approximately 10mV. This indicated that both Li-Bi electrodes maintained a stable, self-consistent potential with respect to the LiCl-Li_2O-Li electrolyte.

4.3 Proposed Mechanism of material interaction

It is proposed that one possible explanation for the observations made throughout this chapter would be that a thin, protective surface film forms on M400 during exposure to LiCl-Li_2O-Li at 650°C, and that this film dissolves during the methanol rinsing procedure. Due to the inclusion of Li in LiCl-2wt%Li_2O at 650°C, the formation of a lithium intercalated oxides on the surface of M400 may be possible. Lithium-transition metal oxides are known to form at 650°C, but are structurally unstable and rapidly decompose when exposed to organic solvents such as methanol due to the high effective equilibrium oxygen partial pressure (*95, 96*). These

compounds are generally non-stoichiometric and have been extensively researched as cathode materials for Li-ion batteries (*95, 96*).

The corrosion rates observed via ICP-OES presented in section 4.1.7 were relatively constant with respect to the Li content of the molten LiCl-Li_2O-Li salt. However, this relatively constant dissolution rate is not consistent with the increased degradation of surface morphology observed by both optical and electron microscopy performed subsequent to the methanol rinsing procedure in sections 4.1.4 and 4.1.3.2, respectively. The combination of these observations indicates that the appearance of intergranular corrosion likely occurred during the methanol rinse and not during exposure to the molten LiCl-Li_2O-Li solutions. Furthermore, evidence supporting the formation of these films can be observed in the XRD, XPS and electrochemical sections of this study in sections 4.1.2, 4.1.6, and 4.2, respectively. The non-stoichiometric nature of lithium intercalated transition metal oxides, such as $Li_{1-x}Ni_{1+x}O_2$, may give rise to the unidentified diffraction peaks observed by XRD in section 4.1.2. Additionally, the decomposition of $Li_{1-x}Ni_{1+x}O_2$ films during the methanol rinsing procedure would explain the observation of a depletion of Ni as observed on the unsputtered sample surfaces during XPS analysis in section 4.1.6. The observation of Ni depletion by XPS following the methanol rinse indicates that the surface film is primarily Ni based. Finally, the observation of the higher nobility of Cu compared to Ni in the LiCl-Li_2O-Li system indicates that Ni would preferentially oxidize to form a surface film over Cu.

Interestingly, if the formation of $Li_{1-x}Ni_{1+x}O_2$ on the surface of M400 is indeed the mechanism of interaction for this alloy with the molten LiCl-Li_2O-Li salt at 650°C, the variable and non-stoichiometric nature of these films would allow for their adaptation to the dynamic solution chemistry experienced during the electrolytic reduction of UNF. As the activity of Li in

the electrolyte increases as the electrolytic reduction proceeds, Li would diffuse into the $Li_{1-x}Ni_{1+x}O_2$ surface film in a manner analogous to the charging cycle for Li-ion batteries (*95*). Once the electrolytic reduction of UNF reaches completion and the next cycle begins, the Li thus diffused into the $Li_{1-x}Ni_{1+x}O_2$ surface would then desorb to the LiCl-Li_2O electrolyte, analogous to a Li battery discharge cycle. Commercialization of Li-ion batteries using Li-transition metal oxides has shown these materials to be capable of undergoing thousands of charge-discharge cycles before failure (*96*). If a stable $Li_{1-x}Ni_{1+x}O_2$ film is formed on M400 in LiCl-Li_2O-Li, it may explain the stability of this alloy in the molten LiCl-Li_2O-Li environment observed in this study. Further investigation would be necessary to confirm this hypothesis.

Chapter 5: Conclusions

Electrolytic reduction of UNF is an important step necessary to integrate current stockpiles of LWR oxide fuel into a pyroprocessing based closed nuclear fuel cycle. Pyroprocessing, accompanied by electrolytic reduction of UNF, offers many advantages over traditional aqueous reprocessing methods. Despite the importance of this process, material degradation in the molten LiCl-Li_2O-Li system has not been extensively studied. Typically, stainless steel 316 and various Inconel alloys are used to construct components exposed to the molten salt solutions used for the electroreduction of UNF. These alloys rely on the formation of stable chromium rich oxides to protect the base material and limit corrosion. Due to fluctuations of the salt chemistry caused by the accumulation of metallic Li on the cathode surface, the stability of these surface films has been shown to be compromised as the dissolved Li content in the melt varies.

A reference electrode was designed and constructed based on the Li-Bi intermetallic system for use specifically in molten solutions of LiCl-Li_2O-Li at 650°C. The stability and repeatability of this electrode was confirmed via measurements of the open circuit potential between the Li-Bi reference electrode and Ni as well as Cu wires. The open circuit potential of Cu relative to Ni was measured, and Cu was confirmed to be more noble than Ni in the LiCl-Li_2O-Li system at multiple Li concentrations.

M400 was investigated as an alternative material for construction of components exposed to the molten LiCl-Li_2O-Li electrolyte due to its well established corrosion performance in a number of extreme environments. M400 samples were exposed to LiCl-2wt%Li_2O solutions

in the absence of Li, as well as LiCl-2wt%Li_2O solutions containing up to 1wt%Li at 650°C for 20 hours.

M400 was found to be highly resistant to degradation in all studied environments. However, the presence of metallic lithium was found to lead to higher degradation of M400 compared to LiCl-Li_2O containing no metallic lithium. Post exposure analysis of the samples was performed using X-ray diffraction, field emission scanning electron microscopy, Raman spectroscopy, X-ray photoelectron spectroscopy, optical microscopy, and micro-Vickers hardness testing. The crystal structure of the base alloy was observed to be unaffected by exposure to LiCl-Li_2O-Li via XRD analysis. FESEM and optical microscopy images of M400 samples exposed to LiCl-Li_2O-Li and subsequently rinsed with methanol showed increased degradation with increased Li content that was similar in appearance to intergranular corrosion. Micro-Vickers hardness testing of methanol rinsed M400 samples showed softening of the alloy due to exposure to LiCl-2wt%Li_2O containing no Li, and further softening when metallic Li was included in the salt melt. Raman spectroscopy was unable to detect the rotational and vibrational modes of the M400 sample surfaces due to the thinness of surface films formed upon exposure to LiCl-Li_2O-Li. The surface films present on M400 samples exposed to LiCl-Li_2O-Li and subsequently rinsed with methanol were observed to be on the order of 14 nm by X-ray photoelectron spectroscopy. The data obtained from inductively coupled plasma – optical emission spectroscopy characterization of the cooled salt ingot was analyzed to determine the corrosion rate for the M400 samples exposed to LiCl-Li_2O-Li. It is proposed that the corrosion resistance of M400 in LiCl-Li_2O-Li is due to the formation of a protective $Li_{1-x}Ni_{1+x}O_2$ surface film which is variable with respect to Li composition.

Regardless of the interaction mechanism between M400 and the molten LiCl-Li_2O-Li system, the corrosion resistance of M400 observed by the analytical techniques employed in this study is excellent. The corrosion rate of M400 was shown to be less than 0.040mm per year and was nearly independent of the concentration of Li in the LiCl-Li_2O-Li system at 650°C. The observed stability of this alloy with varying Li concentrations would extend the useful lifetime of components constructed with M400 that would be exposed to the varying process conditions experienced during the electroreduction of UNF.

Chapter 6: Future Work

Prior to the use of M400 for construction of components exposed to molten LiCl-Li_2O-Li, further laboratory scale investigations into the behavior of M400 in this system should be conducted. The decrease in hardness observed for the M400 samples exposed to LiCl-Li_2O-Li at 650°C compared to the base alloy indicates that the mechanical properties should be further investigated, as the operating temperature of 650°C is roughly half the solidus temperature for the M400 alloy. Collection of *in-situ* creep, fatigue, and slow-strain rate performance data would be necessary to determine mechanical design parameters. It is also suggested that M400 may be explored as a corrosion resistant cladding for higher strength alloys that are not able to withstand the corrosive molten LiCl-Li_2O-Li environment. Further corrosion testing should be performed using crucibles constructed from a different material so that the interaction of the crucible with the molten salt does not affect the analysis of the corrosion performance of the samples.

The Li-Bi reference electrode developed in this work requires further refinement and characterization to verify the ability of this design to provide a stable reference potential for

electrochemical experimentation in LiCl-Li_2O-Li. Further investigation into formation of the Li_3Bi phase may yield a more repeatable reference potential. Formation of metallic Li on the graphite tube via cathodic polarization above the Li_2O reduction potential and its subsequent diffusion into the Bi phase through the graphite wall may provide a means of controlling the reaction rate of Li with Bi and allow for the formation of the intermetallic Li_3Bi phase.

References

[1] G. Greenhalgh, *The Necessity for Nuclear Power*. (Graham and Trotman Limited, London, England, ed. 1, 1980).

[2] C. Pasten, J. C. Santamarina, Energy and quality of life. *Energy Policy* **49**, 468-476 (2012).

[3] O. Burger, J. P. DeLong, M. J. Hamilton, Industrial energy use and the human life history. *Scientific Reports* **1**, 1-7 (2011).

[4] U. N. Foundation. *Achieving universal energy access.* http://www.unfoundation.org/what-we-do/issues/energy-and-climate/clean-energy-development.html?referrer=http://www.washingtonpost.com/blogs/wonkblog/wp/2013/05/29/heres-why-1-2-billion-people-still-dont-have-access-to-electricity/ (2013).

[5] United Nations, *World Population Prospects: The 2012 Revision, Key Findings and Advance Tables* (2012).

[6] International Energy Agency, *World Energy Outlook 2014,* http://www.worldenergyoutlook.org/media/weowebsite/2014/141112_WEO_FactSheets.pdf (2014).

[7] Nuclear Energy Institute, *Nuclear energy Around the World.* http://www.nei.org/Knowledge-Center/Nuclear-Statistics/World-Statistics (2015).

[8] E. J. Wheelwright *et al.*, *Technical summary: Nuclear Waste Vitrification Project*, (U.S. DOE PNL-3038-UC-70) (1979).

[9] OECD Nuclear Energy Agency for the Generation IV International Forum, *Technology Roadmap Update for Generation IV Nuclear Energy Systems* (2014).

[10] J. K. Shultis, R. E. Faw, *Fundamentals of Nuclear Science and Engineering*. (CRC Press, ed. 2, 2008).

[11] N. Tsoulfanidis, *The Nuclear Fuel Cycle*. (American Nuclear Society, ed. 2, 2013), pp. 463.

[12] R. C. Ewing, Long-term storage of spent nuclear fuel. *Nature Materials* **14**, 252-257 (2015).

[13] S. Y. F. Chu, L. P. Ekstrom, R. B. Firestone, The Lund/LBNL Nuclear Data Search Version 2.0, http://nucleardata.nuclear.lu.se/toi/ (Lawrence Berkeley National Laboratory) (1999).

[14] J. C. Wagner, *et. al., Categorization of Used Nucelar Fuel Inventory in Support of a Comprehensive National Nuclear Fuel Cycle Strategy* (U.S. DOE ORNL/TM-2012/308FCRD-FCT-2012-000232) (2012).

[15] U.S. NRC, *Safety Evaluation Report Related to Disposal of High-Level Radioactive Wastes in a Geologic Repository at Yucca Mountain, Nevada*, http://www.nrc.gov/reading-rm/doc-collections/nuregs/staff/sr1949/ (2010-2015).

[16] 42 U.S. Code Chapter 108 *Nuclear Waste Policy Act* (1982).

[17] U.S. DOE, *Nuclear Waste Fund Annual Financial Report,* OAS-FS-15-03, http://energy.gov/sites/prod/files/2014/12/f19/OAS-FS-15-03.pdf (2014).

[18] D. E. Klein, Spent Nuclear Fuel is an Abundant Source of Energy. *21st Century Science and Technology* **Spring**, 33-38 (2011).

[19] C. E. Till, Y. I. Chang, W. H. Hannum, The Integral Fst Reactor - An Overview. *Progress in Nuclear Energy* **31**, 3-11 (1997).

[20] D. C. Wade, R. N. Hill, The design rationale of the IFR. *Progress in Nuclear Energy* **31**, 13-42 (1997).

[21] E. L. Glueker, U.S. advanced liquid metal reactor (ALMR). *Progress in Nuclear Energy* **31**, 43-61 (1997).

[22] D. C. Wade, R. A. Wigeland, D. J. Hill, The safety of the IFR. *Progress in Nuclear Energy* **31**, 63-82 (1997).

[23] G. L. Hofman, L. C. Walters, T. H. Bauer, Metallic fast reactor fuels. *Progress in Nuclear Energy* **31**, 83-110 (1997).

[24] J. I. Sackett, Operating and test experience with EBR-II, the IFR prototype. *Progress in Nuclear Energy* **31**, 111-129 (1997).

[25] J. J. Laidler, J. E. Battles, W. E. Miller, J. P. Ackerman, E. L. Carls, Development of Pyroprocessing Technology. *Progress in Nuclear Energy* **31**, 131-140 (1997).

[26] J. P. Ackerman *et al.*, Treatment of wastes in the IFR fuel cycle. *Progress in Nuclear Energy* **31**, 141-154 (1997).

[27] H. F. McFarlane, M. J. Lineberry, The IFR fuel cycle demonstration. *Progress in Nuclear Energy* **31**, 155-173 (1997).

[28] C. C. McPheeters, R. D. Pierce, T. P. Mulcahey, Application of the pyrochemical process to recycle of actinides from LWR spent fuel. *Progress in Nuclear Energy* **31**, 175-186 (1997).

[29] W. H. Hannum, D. C. Wade, Using the IFR to dispose of excess weapons plutonium. *Progress in Nuclear Energy* **31**, 187-201 (1997).

[30] W. H. Hannum, D. C. Wade, H. F. McFarlane, R. N. Hill, Nonproliferation and safeguards aspects of the IFR. *Progress in Nuclear Energy* **31**, 203-217 (1997).

[31] C. E. Till, Y. I. Chang, *Plentiful Energy: The Story of the Integral Fast Reactor*. (2011).

[32] Argonne National Laboratory, *Pyroprocessing Technologies, Recycling Used Nuclear Fuel for a Sustainable Energy Future* (http://www.ne.anl.gov/pdfs/12_Pyroprocessing_bro_5_12_v14[6].pdf).

[33] R. Bean, *Project Report on Development of a Safeguards Approach for Pyroprocessing* (U.S. DOE INL/EXT-10-20057) (2010).

[34] M. F. Simpson, *Developments of Spent Nuclear Fuel Pyroprocessing Technology at Idaho National Laboratory* (U.S. DOE INL/EXT-12-25124) (2012).

[35] H. Lee *et al.*, Pyroprocessing Technology Development at KAERI. *Nuclear Engineering and Technology* **43**, 317-328 (2011).

[36] J. Ahn, Roles and effects of pyroprossesing for spent nuclear fuel management in South Korea. *Progess in Nuclear Energy* **75**, 49-62 (2014).

[37] P. SangKyu *et al.*, Alloy design of new Ni-based structural materials for electrolytic reduction and its corrosion behavior in lithium molten salt. *Advanced Materials Research* **886**, 41-44 (2014).

[38] W. I. Ko, *e. al.*, Preliminary conceptual design and cost estimation for Korea Advanced Pyroprocessing Facility Plus (KAPF+). *Nuclear Engineering and Design* **277**, 212-224 (2014).

[39] H. J. Lee, W. I. Ko, I. T. Kim, H. S. Lee, Design for integrated pyroprocessing plant level simulator. *Annals of Nuclear Energy* **60**, 316-328 (2013).

[40] S. D. Herrmann, S. X. Li, M. F. Simpson, S. Phongikaroon, Electrolytic Reduction of Spent Nuclear Oxide Fuel as Part of an Integral Process to Separate and Recover Actinides from Fission Products. *Separation Science and Technology* **41**, 1965-1983 (2006).

[41] K. Gourishankar, L. Redey, M. Williamson, in *Light Metals, The Minerals, Metals & Materials Society,* W. A. Schneider, Ed. (2002).

[42] J. M. Hur, S. C. Lee, S. M. Jeong, C. S. Seo, Electrochemical reduction of TiO_2 in molten LiCl-Li_2O. *Chemistry Letters* **36**, 1028-1029 (2007).

[43] S. C. Lee, J. M. Hur, C. S. Seo, Silicon powder production by electrochemical reduction of SiO_2 in molten LiCl–Li_2O. *Journal of Industrial Engineering and Chemistry* **14**, 651-654 (2008).

[44] S. M. Jeong, J. Y. Jung, C. S. Seo, S. W. Park, Characteristics of an electrochemical reduction of Ta2O5 for the preparation of metallic tantalum in a LiCl–Li_2O molten salt. *Journal of Alloys and Compounds* **440**, 210-215 (2007).

[45] S. M. Jeong, J. Y. Jung, C. S. Seo, S. W. Park, Preparation of metallic niobium from niobium pentoxide by an indirect electrochemical reduction in a LiCl-Li_2O molten salt. *Journal of Alloys and Compounds* **452**, 27-31 (2008).

[46] G. Z. Chen, D. J. Fray, T. W. Farthing, Direct electrochemical reduction of titanium dioxide to titanium in molten calcium chloride. *Nature* **407**, 361-364 (2000).

[47] B. Park, S. Park, S. Jeong, C. Seo, Electrolytic reduction of spent oxide fuel in a molten LiCl-Li_2O system. *Journal of Radioanalytical and Nuclear Chemistry* **270**, 575-583 (2006).

[48] J. Hur, C. Seo, S. Hong, D. Kang, S. Park, Semi-Continuous Electrowinning of Li in a LiCl-Li_2O Molten Salt. *Journal of the Korean Radioactive Waste Society* **2**, 211-217 (2004).

[49] S. Jeong *et al.*, An Electrochemical Reduction of Uranium Oxide in the Advanced Spent Fuel Conditioning Process. *Nuclear Technology* **162**, 184-191 (2007).

[50] E. Y. Choi *et al.*, Electrochemical reduction behavior of a highly porous SIMFUEL particle in a LiCl molten salt. *Chemical Engineering Journal (Lausanne)* **207-208**, 514-520 (2012).

[51] M. Kurata, T. Inoue, J. Serp, M. Ougier, J. P. Glatz, Electro-chemical reduction of MOX in LiCl. *Journal of Nuclear Materials* **328**, 97-102 (2004).

[52] J. M. Hur, C. S. Seo, S. S. Hong, D. S. Kang, S. W. Park, Metallization of U_3O_8 via catalytic electrochemical reduction with Li_2O in LiCl molten salt. *Reaction Kinetics and Catalysis Letters* **80**, 217-222 (2003).

[53] E. Y. Choi *et al.*, Electrochemical reduction of UO_2 in LiCl–Li_2O molten salt using porous and nonporous anode shrouds. *Journal of Nuclear Materials* **444**, 261-269 (2014).

[54] S. Phongikaroon, S. Herrmann, M. Simpson, Diffusion Model for Electrolytic Reduction of Uranium Oxides in Molten LiCl-Li_2O Salt. *Nuclear Technology* **174**, 85-93 (2010).

[55] S. Herrmann, S. Li, B. Serrano-Rodriguez, Observations of Oxygen Ion Behavior in the Lithium-Based Electrolytic Reduction of Uranium Oxide, *GLOBAL 2009*. (Paris, France, 2009), pp. 1198-1206.

[56] W. Park *et al.*, Application of a boron doped diamond (BDD) electrode as an anode for the electrolytic reduction of UO_2 in Li_2O–LiCl–KCl molten salt. *Journal of Nuclear Materials* **432**, 175-181 (2013).

[57] A. S. Dworkin, H. R. Bronstein, M. A. Bredig, Miscibility of Metals with Salts. VI. Lithium-Lithium Halide Systems. *The Journal of Physical Chemistry* **66**, 572-573 (1962).

[58] J. Liu, J. C. Poignet, Electronic conductivity of salt-rich Li−LiCl melts. *Journal of Applied Electrochemistry* **22**, 1110-1112 (1992).

[59] J. Liu, J. C. Poignet, Measurement of the activity of lithium in dilute solutions in molten lithium chloride between 650°C and 800°C. *Journal of Applied Electrochemistry* **20**, 864-867 (1990).

[60] T. Nakajima, K. Nakanishi, N. Watanabe, The Dispersion of Metallic Lithium in Various Molten Salts. *Nippon Kagaku Kaishi* **1975**, 617-621 (1975).

[61] T. N. Nakajima, K., N. Watanabe, The Dissolution of Lithium in Molten Lithium Chloride. *Nippon Kagaku Kaishi* **1974**, 401-404 (1974).

[62] T. N. Nakajima, K., N. Watanabe, Study of Emulsions in Molten Salts III. The concentration stability and particle-size distribution of dispersed lithium in molten lithium chloride. *Bulletin of the Chemical Society of Japan* **49**, 994-997 (1975).

[63] A. C. Sequeira, *High Temperature Corrosion in Molten Salts*. (Trans Tech Publications Ltd, 2003).

[64] F. Lantelme, H. Groult, *Molten Salts Chemistry From Lab to Applications*. (Elsevier, Burlington, MA, ed. 1, 2013).

[65] R. A. Rapp, *Corrosion by Molten Salts, Corrosion: fundamentals, testing and protection*. (ASM International, Materials Park, OH, 2003).

[66] R. A. Rapp, Hot corrosion of materials: a fluxing mechanism? *Corrosion Science* **44**, 202-221 (2002).

[67] T. R. Allen, K. Sridharan, *Corrosion in Molten Salts, in Molten salts chemistry from lab to applications*. (Elsevier, Burlington, MA, ed. 1, 2013).

[68] N. Gese, B. Pesic, *Electrochemistry of LiCl-Li_2O-H_2O Molten Salt Systems* (U.S. DOE INL/CON-12-26774) (2013).

[69] A. D. Simigelskas, E. O. Kirkendall, Sinc diffusion in Alpha Brass. *Transactions of the American Institute of Mining, Metallurgical and Petroleum Engineers* **171**, 130-142 (1947).

[70] J. E. Indacochea, J. L. Smith, K. R. Litko, E. J. Karell, Corrosion performance of ferrous and refractory metals in molten salts under reducing conditions. *Journal of Materials Research* **14**, 1990-1995 (1998).

[71] J. E. Indacochea, J. L. Smith, K. R. Litko, E. J. Karell, A. G. Raraz, High-Temperature Oxidation and Corrosion of Structural Materials in Molten Chlorides. *Oxidation of Metals* **55**, 1-16 (1999).

[72] B. Mishra, D. L. Olson, Corrosion of Refractory Alloys in Molten Lithium and Lithium Chloride. *Mineral Processing and Extractive Metallurgy Reviews* **22**, 369-388 (2001).

[73] A. Merwin, W. Phillips, M.Williamson, J.Willit, P. Motsegood, D. Chidambaram, Presence of Li Clusters in Molten LiCl-Li. *Scientific Reports*, **Currently Under Review** (2015).

[74] ASTM standard B127, Standard Specification for Nickel-Copper Alloy (UNS N04400) Plate, Sheet, and Strip (2014).

[75] *Huntington Alloys Corporation Certified Materials Test Report for Monel alloy 400*.

[76] C. Jeyaprabha, S. Muralidharan, G. Venkatachari, Corrosion behaviour of Monel in phosphoric acid. *Anti-Corrosion Meth & Material* **47**, 285-287 (2000).

[77] K. D. Ramkumar, N. Arivazhagan, S. Narayanan, D. Mishra, Hot Corrosion Behavior of Monel 400 and AISI 304 Dissimilar Weldments Exposed in the Molten Salt Environment Containing Na_2SO_4 + 60% V_2O_5 at 600C. *Materials Research* **17**, 1273-1284 (2014).

[78] R. S. Dutta, Corrosion aspects of Ni-Cr-Fe based and Ni-Cu based steam generator tube materials. *Journal of Nuclear Materials* **393**, 343-349 (2009).

[79] J. M. Fisher, P. S. Bennett, Corrosion and wetting behaviour of metals and steels with molten alkali carbonates. *Journal of Materials Science* **26**, 749-755 (1991).

[80] D. W. Jeppson, J. L. Ballif, W. W. Yuan, B. E. Chou, *Lithium literature Review: Lithium's Properties and Interactions* (U.S. DOE HEDL-TME 78-15 UC-20) (1978).

[81] S. Herrmann, S. Li, B. Serrano-Rodriguez, *Observations of Oxygen Ion Behavior in the Lithium-Based Electrolytic Reduction of Uranium Oxide* (U.S. DOE INL/CON-08-15165) (2009).

[82] Y. Sakamura, M. Iizuka, S. Kitawaki, A. Nakayoshi, H. Kofuji, Formation and Reduction behaviors of zirconium oxide compounds in LiCl-Li_2O melt at 923K. *Journal of Nuclear Materials* **466**, 269-279 (2015).

[83] J. F. Shackelford, *Introduction to Materials Science for Engineers*. (Pearson Prentice Hall, Upper Saddle River, NJ, ed. 7, 2009), pp. 533.

[84] M. C. Biesinger, B. P. Payne, L. W. M. Lau, A. Gerson, R. S. C. Smart, X-ray photoelectron spectroscopic chemical state quantification of mixed nickel metal, oxide and hydroxide systems. *Surface and Interface Analysis* **41**, 324-332 (2008).

[85] S. D. Herrmann, S. X. Li, M. F. Simpson, Electrolytic Reduction of Spent Oxide Fuel - Bench-Scale Test Results, *GLOBAL 2005*. (Tsukuba, Japan, 2005).

[86] S. M. Jeong, H. S. Shin, S. H. Cho, J. M. Hur, H. S. Lee, Electrochemical behavior of a platinum anode for reduction of uranium oxide in a LiCl molten salt. *Electrochimica Acta* **54**, 6335-6340 (2009).

[87] M. Iizuka, Y. Sakamura, T. Inoue, Electrochemical reduction of (U-40Pu-5Np)O_2 in molten LiCl electrolyte. *Journal of Nuclear Materials* **359**, 102-113 (2006).

[88] X. Ning *et al.*, Self-healing Li-Bi liquid metal battery for grid-scale energy storage. *Journal of Power Sciences* **275**, 370-376 (2015).

[89] A. D. Pelton, J. Sangster, The Bi-Li (Bismuth-Lithium) system. *Journal of Phase Equilibria* **12**, 447-450 (1991).

[90] B. Predel, *Phase Equilibria, Crystallographic and Thermodynamic Data of Binary Alloys B-Ba – C-Zr, Bi-Li (Bismuth-Lithium)* (Springer Berlin Heidelberg, 1992), vol. 5b, pp. 1-5.

[91] S. M. McDeavitt, *Synthesis and casting of a lithium-bismuth compound for an ion-replacement electrorefiner* (U.S. DOE ANL/CMT/CP-96844) (1999).

[92] M. S. Foster, S. E. Wood, C. E. Crouthamel, Thermodynamics of Binary Alloys. I. The Lithium-Bismuth System. *Inorganic Chemistry* **3**, 1428-1431 (1964).

[93] Y. Sakamura, Effect of alkali and alkaline-earth chloride addition on electrolytic reduction of UO_2 in LiCl salt bath. *Journal of Nuclear Materials* **412**, 177-183 (2011).

[94] D. A. Jones, *Principles and Prevention of Corrosion*. (Prentice Hall, Upper Saddle River, NJ, ed. 2, 1996).

[95] M. S. Whittingham, Lithium Batteries and Cathode Materials. *Chemical Reviews* **104**, 4271-4301 (2004).

[96] M. K. Gulbinska, *Lithium-ion Battery Materials and Engineering: Current Topics and Problems from the Manufacturing Perspective*. (Springer, ed. 1, 2014).

[97] A. Merwin, On the behavior of materials exposed to molten LiCl-Li_2O-Li, PhD dissertation, *University of Nevada, Reno*, **Expected May 2016**